A More Robust Wall Model for Use with the Two-equation Turbulence Model

Kevin Charles Mallone

A thesis submitted in partial fulfilment of the regulations of the University of Hertfordshire for the degree of Doctor of Philosophy.

March 1995

University of Hertfordshire
School of Engineering
Division of Mechanical, Aerospace and Automotive Engineering

Abstract.

The applicability of computational fluid dynamics (CFD) modelling schemes to turbulent wall-bounded flows is a matter of concern. In the near-wall region of bounded flows, the standard high Reynolds number k-ε model is not valid and requires the use of empirical wall models to mimic the behaviour of this region.

A theoretical study of the physics of prevalent wall modelling techniques showed that the velocity distribution took no account of the pressure gradient. To determine the effect of this shortcoming, a typical transient three-dimensional flow was analysed using current CFD methods and the results compared with experimental flow measurements. Consideration of these results showed that the 'traditional' wall model was unable to replicate observed flow features in the near-wall region: further analysis of the computational results confirmed that these poor flow predictions arose from the inability of the model to consider local pressure gradient effects.

Consequently, a strong case was made for a more robust wall model for use in conjunction with the standard high Reynolds number k-ε model. A number of boundary layer analyses were reviewed and Coles' law of the wake (1956) presented as a viable candidate for the development of a new wall modelling scheme. In theory, Coles' law (1956) provides a description of bounded flows under arbitrary pressure gradients up to the point of near-separation and may be extended to the study of reversed flows.

A generic algorithm for Coles' law was prepared and used to study the fundamental test cases of U-bend and backward facing step flows. In a comparison between documented experimentation, 'conventional' CFD modelling and Coles' law models of these flows, the Coles' law model was shown to provide a viable alternative to 'traditional' schemes. Consequently, the Coles' law model of the near-wall region, being valid for pressure-driven flows, offers an extension to the range of flows for which the standard high Reynolds number k-ε model may be used.

To My Family and Other Animals.

Peter, Cheryl, Gordon, Rene and Phil, Chris, Kay and my impending Godchild, Liz and Richard, Roo and Angela, Fi, Mark and the Homunculus, Kate, Fi and Dion, Stevie B., Gwil, Lesley, Julie and Martin, Andy and Daniel.

Sigh no more ladies, sigh no more,
Men were deceivers ever,
One foot in the sea, and one on shore,
To one thing constant never.
Then sigh not so, but let them go,
And be you blithe and bonny,
Converting all your sounds of woe,
Into hey nonny nonny.

W.S.

Acknowledgements.

First and foremost, I would like to give my heartfelt thanks to my principal supervisor, Dr Arne-Erik Holdo, for his singular support, guidance and enthusiasm throughout the course of this study. I am also extremely grateful for his constructive criticism and encouragement during my period of writing up.

Thanks are also extended to my second supervisor, Dr Arvind Kenkare, for his advice and comments, given in preparation of this thesis.

Colin Johnson, Technical Mananger of the Division of Mechanical, Aerospace and Automotive Engineering at the University of Hertfordshire, is to be thanked for his valuable assistance with regard to organizing the refurbishment of the test cell used for practical experimentation. The Technical Officers Jerry Bennett, Mac M^{c}Crystal and Len Harper are to be especially thanked for their hard work and many long hours of help in the preparation of the test rig and the conducting of practical experiments. They were a pleasure to work along side and their friendship much appreciated. For the photographic plates in Chapter Three of this thesis, may I thank Terry Newman.

With regard to the computational part of my studies, I would like to thank Ursula Mullane of Applied Computing and Engineering, Warrington for providing user-support for the FIDAP package. Her help with some of the more arcane features of that programme was most useful.

My thanks to Mum and Dad and to Shaun, Sara, Auntie Roma and Uncle Spike, Nicki, David and Kellie and Auntie Flo and Uncle Brian, my family, for their unconditional love and for their support throughout my entire education.

Of the many other people who have encouraged and, when necessary, cajoled me, I would particularly like to thank Inge Tait, Dawn Lee, Avice Hall, Sylvia Douglas, Christine Shepperson, Liz Byrne, Sarah Wakes, Phil Green, Anne Jones, Paul Kitson, Matt Broom, Jason Irving Fitzwilliam Todd-Morris, the Mackay and Snook families and the denizens of Fleetville and Symondshyde.

Finally, for their inspirational influence, I would like to thank Valerie Singleton, John Noakes, Noel Langley, Sooty and Mr Yoffi and the significant others - Graeme, Karl, Keanu Reeves, River Pheonix, Tim Vincent, Howard, Gary, Mark, Jason and Robbie.

Contents.

List of Symbols.

a	dimensionless constant
A	empirical constant
B	empirical constant
B	integral layer thickness
C_f	coefficient of skin friction
C_p	dimensionless pressure coefficient
C_{ph}	horizontal dimensionless pressure coefficient
C_{pv}	vertical dimensionless pressure coefficient
$C_{\varepsilon 1}$	empirical constant
$C_{\varepsilon 2}$	empirical constant
C_μ	empirical constant
d	channel width
D	empirical function
E	empirical function
f_1	empirical function
f_2	empirical function
f_μ	empirical function
F	force
g	gravitational acceleration
G	shear generation
G_s	shape factor
h	step height
Δh_{dyn}	dynamic pressure head
Δh_h	horizontal pressure head
Δh_v	vertical pressure head
k	kinetic energy of turbulence
k^+	dimensionless kinetic energy of turbulence

k_t	kinetic energy at top of special wall element
K	fluid bulk viscosity
l_m	mixing length
L	distance from wall to point of maximum shear stress in turbulent boundary layer
L	streamwise distance downstream of duct inlet
m	mass
p	pressure
p_o	stagnation pressure
p_∞	freestream pressure
Δp	pressure difference
r_i	inner radius of bend
r_o	outer radius of bend
Re	Reynolds number
R_δ	Reynolds number at edge of boundary layer
t	time
t_o	reference time
t_s	sampling interval
u^+	dimensionless velocity
$\overline{uv}^+$	dimensionless shear stress
v	velocity
v_{Coles}	velocity calculated by Coles' law
v_l	velocity scale
v_r	resultant velocity
v_s	scaling velocity
v_t	tangential velocity
v_t	total velocity
v_x	x-component of velocity

v_y	y-component of velocity
v_z	z-component of velocity
v'_x	fluctuating x-component of velocity
v'_y	fluctuating y-component of velocity
v'_z	fluctuating z-component of velocity
v_∞	freestream velocity
v^*	wall friction velocity
x	scaling factor
y	distance normal to wall
y^+	dimensionless distance
w	Coles' wake function
x_r	normalized length of recirculation zone
β	Clauser's equilibrium pressure gradient parameter
δ	boundary layer thickness
δ^*	displacement thickness
δ_l	length scale
δ_{sub}	viscous length scale of turbulent boundary layer
Δ	defect thickness
ε	dissipation
θ	flow angle
θ	local inclination of computational mesh to the horizontal
θ_h	horizontal component of flow angle
θ_v	vertical component of flow angle
κ	von Karman's constant
λ	skin friction parameter
μ	dynamic viscosity
μ_t	eddy or virtual viscosity

ν	kinematic viscosity
ξ	pressure gradient parameter
Π	Coles' wake parameter
ρ	density
ρ_a	density of fluid continuum
ρ_m	density of manometer fluid
σ_k	turbulent Prandtl/Schmidt number for turbulent kinetic energy, k
σ_ε	turbulent Prandtl/Schmidt number for turbulent dissipation, ε
τ	laminar or viscous stress
τ_{max}	maximum shear stress in turbulent boundary layer
τ_0	shear stress at wall
τ^t	Reynolds or virtual stress
ϕ	generic flow variable
ϕ	inclination of resultant velocity to the horizontal

1. Introduction.

A wide range of practical problems in engineering relate to fluid flow; typically, fluid movement is constrained within a bounded channel or a solid body is moving through a fluid continuum. In either event the interaction of the fluid medium with the solid surface, relative to which it is moving, is a matter of interest.

Many practical situations occur as transient, or time-dependent, flow with the geometry of that flow complicating analysis further. The development of new or improved designs for fluid conduits or of articles that operate within a fluid environment is then demanding. The traditional engineering approach of preparing production prototypes, both as scaled models and for full scale evaluation is costly. The manufacture of scaled models for study in wind-tunnels is a specialist field in itself. In conducting such tests, the measurement techniques used must be considered carefully as the introduction of metering devices will often distort the very flow that they were intended to observe. As such, use of practical experimentation as the sole method of optimizing a design is expensive, both in terms of time and expertise, with the end results often being limited in scope.

Computational fluid dynamics (CFD) offers a scheme for the numerical simulation of fluid flows that occur in real engineering problems. General CFD modelling techniques have been validated and improved upon by comparison with experimental studies for a range of idealised and fundamental flows. However, the assumptions upon which these models are based may not be obvious to the user and the limited experimental data available for comparison of more complex flows may lead to the use of a mathematical model beyond the range of those assumptions upon which it was based. Where the flow is driven by a pressure gradient, for example, pressure-related effects may not necessarily be accounted for.

At the heart of all CFD codes lie the equations of conservation of momentum and of continuity. The accuracy with which they are operated is central to the success of the model. At present, the storage limitations of current computers require discretisation of the fluid continuum on a scale larger than that of the finest scales of fluid motion. For turbulent flow, where the velocity of fluid particles has both mean and fluctuating components, practical solutions to these equations then comment on the time-averaged behaviour of the flow; this is usually sufficient for most engineering practice.

Modelling schemes then operate a time-averaged approximation to the discretised or non-continuous flow field, with the turbulent field being predicted by semi-empirical relationships. Within the core of the flow, such approaches are successful but at the interface between the fluid medium and the solid surface further problems arise. In the near-wall region, the viscosity of the fluid becomes significant. The local velocity gradients become increasingly sheer on approach to the wall and to capture this behaviour would require a great increase in the density of the computational mesh. As the number of points in the mathematical model increases, so do the computational storage needs and the solution time. The necessary mesh density, within a finite computational environment will then limit the range of flow geometries that can be simulated, often requiring mesh over-simplification.

To this end, the computational modelling of turbulent bounded flows has traditionally made use of wall models; the dense mesh of the near-wall region is replaced by an empirical model of the boundary layer, accounting for local viscous effects. The wall model then interfaces with the core model of the freestream at a suitable point beyond which viscosity may be neglected. In practice, many currently used wall models are based on relationships prepared for very simple flow situations. The widely used model of Spalding (1961), for example, is not valid for pressure-driven flows or where there is any departure from turbulent equilibrium in the flow field. The use of such models beyond the range of conditions for which they were prepared leads to a reduced quality of numerical prediction. Where such matters have been taken into account, the conditions for which these models were validated again limit their use in differing flow conditions (Patel, Rodi and Scheurer, 1985).

The use of wall modelling as a practical tool offers many advantages in extending the use of cost-effective schemes to bounded flows, with the inherent saving in the near-wall mesh density allowing more complex environments to be analysed numerically. Whilst models for 'core' flow appear to be very successful, analyses of wall-bounded flows are still based on empirical methods which may not always be applicable. Thus, where the use of a wall model is required, it should be generic in nature, being appropriate across the full range of possible flow conditions. To this end, the improvement of such schemes is required to cater for the pressure and viscous effects observed experimentally both in transient flows and in those having complex geometries. This would increase the range of applicability of wall modelling techniques and provide greater confidence in computational results.

The aims of the present work were thus

i) to study the results of a typical engineering problem with laboratory experimental methods,
ii) to study the transient results of CFD modelling of this engineering problem and
iii) to compare these results and, if necessary, propose and develop a more robust model of the near-wall region.

2. Theoretical Background and Development.

2.1 The Equations of Motion for a Three-dimensional, Isothermal Fluid Flow.

The equations of motion governing three-dimensional fluid flow may be constructed from consideration of the principles of conservation of mass and of momentum. For isothermal conditions, where there is no significant transfer of heat to or from the fluid, flow is described by the Navier-Stokes equations, which are an application of Newton's second law.

In most cases, the only significant body forces acting on the element will be those arising from the fluid pressure, p, and the gravitational force per unit mass, g. Furthermore, for cases where pressure only is to be considered, the sum of forces acting on the system in the x-direction, say, is $\frac{\partial p}{\partial x}$. Further restricting study to the case of a Newtonian fluid (considered to be perfectly elastic, in that stress is held proportional to strain in the fluid body), then the general equations of motion for a Newtonian fluid with varying density and viscosity and neglecting gravitational effects are

$$\rho \frac{Dv_x}{Dt} = \frac{\partial}{\partial x}\left\{2\mu \frac{\partial v_x}{\partial x} + \frac{2}{3}\mu\left(\frac{\partial v_x}{\partial x} + \frac{\partial v_y}{\partial y} + \frac{\partial v_z}{\partial z}\right)\right\} + \frac{\partial}{\partial y}\left\{\mu\left(\frac{\partial v_y}{\partial x} + \frac{\partial v_x}{\partial y}\right)\right\} + \frac{\partial}{\partial z}\left\{\mu\left(\frac{\partial v_z}{\partial x} + \frac{\partial v_x}{\partial z}\right)\right\} - \frac{\partial p}{\partial x} \tag{2.1a}$$

$$\rho \frac{Dv_y}{Dt} = \frac{\partial}{\partial x}\left\{\mu\left(\frac{\partial v_y}{\partial x} + \frac{\partial v_x}{\partial y}\right)\right\} + \frac{\partial}{\partial y}\left\{2\mu \frac{\partial v_y}{\partial y} + \frac{2}{3}\mu\left(\frac{\partial v_x}{\partial x} + \frac{\partial v_y}{\partial y} + \frac{\partial v_z}{\partial z}\right)\right\} + \frac{\partial}{\partial z}\left\{\mu\left(\frac{\partial v_z}{\partial y} + \frac{\partial v_y}{\partial z}\right)\right\} - \frac{\partial p}{\partial y} \tag{2.1b}$$

$$\rho \frac{Dv_z}{Dt} = \frac{\partial}{\partial x}\left\{\mu\left(\frac{\partial v_z}{\partial x} + \frac{\partial v_x}{\partial z}\right)\right\} + \frac{\partial}{\partial y}\left\{\mu\left(\frac{\partial v_z}{\partial y} + \frac{\partial v_y}{\partial z}\right)\right\} + \frac{\partial}{\partial z}\left\{2\mu \frac{\partial v_z}{\partial z} + \frac{2}{3}\mu\left(\frac{\partial v_x}{\partial x} + \frac{\partial v_y}{\partial y} + \frac{\partial v_z}{\partial z}\right)\right\} - \frac{\partial p}{\partial z} \tag{2.1c}$$

The equation of continuity, describing conservation of mass, may then be written as

$$\frac{\partial \rho}{\partial t} = -\left(\frac{\partial}{\partial x}\rho v_x + \frac{\partial}{\partial y}\rho v_y + \frac{\partial}{\partial z}\rho v_z\right) \qquad (2.2)$$

These equations of motion, known as the Navier-Stokes equations, in conjunction with the equation of continuity, the density dependence of viscosity and the boundary and initial flow conditions completely determine the pressure, density and velocity distributions in a flowing isothermal fluid.

Turbulence may be described as a spatially varying mean flow with superimposed three-dimensional random fluctuations, which are self-sustaining and enhance mixing, diffusion, entrainment and dissipation (White, 1991). In the free stream, the flow will display homogeneous and isotropic behaviour but near to solid boundaries, the effects of viscosity become important and homogeneity is not present (Tennekes and Lumley, 1972). The flow contains a large number of three-dimensional, entangled vortices, or eddies, of varying sizes. As such, diffusion of heat, mass and momentum is far greater in turbulent flow than in laminar, where diffusion results from molecular interaction. The nature of turbulence is so complicated that a complete analysis and quantification is not foreseen (White, 1991).

With regard to bounded turbulent flows, a minimal flow analysis should provide

i) velocity profiles and
ii) wall friction data.

Even setting the above limited aims for an analysis, the modelling of the simplest flows involves recourse to a series of empiricisms. Because of the range of flow scales comprising turbulent flow, a complete study of a fluid continuum by direct numerical simulation of the Navier-Stokes equations is impractical. Emmons (1970) demonstrated that to reproduce the fine details of turbulent flow in a pipe at $Re \approx 10^7$ would require 10^{22} numerical operations: even for an optimal computational speed of 1ns per operation, such a study would take several thousand years. Consequently, direct numerical simulation is typically limited to low Reynolds number analysis on supercomputers and to modelling sub-regions of the fluid continuum for specific reasons, such as gaining clearer insight into the nature of turbulence near a solid boundary (Spalart, 1988).

With regard to practical flow studies, two main approaches have evolved as:

i) statistical analysis, as typified by Tennekes and Lumley (1972) and
ii) study of turbulent mean flow.

For the majority of engineering applications, sufficient data is yielded by the latter method as mean velocity and temperature profiles, heat exchange, surface friction and shear layer thickness data (White, 1991).

Study of turbulent flow may then proceed by considering the fluctuating nature of the flow variables. A given property of the flow field, such as velocity or pressure, will fluctuate wildly with time about a mean value. For the generic flow variable, ϕ, the instantaneous value at a point may be written as

$$\phi = \bar{\phi} + \phi' \tag{2.3}$$

where $\bar{\phi}$ is the mean and ϕ' is the fluctuating component of the instantaneous value, ϕ.

For a fluid continuum described by Cartesian co-ordinates, with x as the streamwise co-ordinate, y as the normal direction and z representing the cross-flow, the mean velocity components, $\overline{v_x}$, $\overline{v_y}$ and $\overline{v_z}$, have their fluctuating counterparts as v'_x, v'_y and v'_z. These fluctuating components may be significant in comparison with their mean counterparts: for the turbulent boundary layer on a flat plate, these fluctuations may be locally equivalent to 11% of the freestream velocity. The solution of the Navier-Stokes equations for turbulent flow typically makes use of time-averaging techniques to comment on the mean values of flow variables (as would be measured by a Pitot-static tube or a pressure gauge). This process of obtaining time-smoothed forms of the equations of motion and continuity is known as Reynolds averaging. The time-smoothed equations of continuity and motion are then gained by substitution of equation 2.3, expressed for velocity and for pressure, into equations 2.2 and 2.1 respectively. The time-smoothed equation of continuity is then

$$\frac{\partial \rho}{\partial t} = -\left(\frac{\partial \overline{v_x}}{\partial x} + \frac{\partial \overline{v_y}}{\partial y} + \frac{\partial \overline{v_z}}{\partial z}\right) \tag{2.4}$$

and the x-component of the time-smoothed equation of motion is

$$\frac{\partial}{\partial t}\rho\overline{v_x} = -\left(\frac{\partial}{\partial x}\rho\overline{v_x}\,\overline{v_x} + \frac{\partial}{\partial y}\rho\overline{v_y}\,\overline{v_x} + \frac{\partial}{\partial z}\rho\overline{v_z}\,\overline{v_x}\right)$$

$$-\left[\begin{array}{l} \dfrac{\partial}{\partial x}\left\{2\mu\dfrac{\partial\overline{v_x}}{\partial x} + \dfrac{2}{3}\mu\left(\dfrac{\partial\overline{v_x}}{\partial x} + \dfrac{\partial\overline{v_y}}{\partial y} + \dfrac{\partial\overline{v_z}}{\partial z}\right)\right\} \\ + \dfrac{\partial}{\partial y}\left\{\mu\left(\dfrac{\partial\overline{v_y}}{\partial x} + \dfrac{\partial\overline{v_x}}{\partial y}\right)\right\} + \dfrac{\partial}{\partial z}\left\{\mu\left(\dfrac{\partial\overline{v_z}}{\partial x} + \dfrac{\partial\overline{v_x}}{\partial z}\right)\right\} \end{array}\right] \qquad (2.5)$$

$$-\frac{\partial\overline{p}}{\partial x} - \left\{\frac{\partial}{\partial x}\rho\overline{v_x'v_x'} + \frac{\partial}{\partial y}\rho\overline{v_y'v_x'} + \frac{\partial}{\partial z}\rho\overline{v_z'v_x'}\right\}$$

with similar expressions for the y- and z-components of the equation of motion.

The time-averaged equations may be compared with their instantaneous counterparts, from which it will be seen that the net effect of time-averaging is to substitute $\overline{v}$ for v and $\overline{p}$ for p into the relevant equations. Note, however, the presence of new terms of the form $\frac{\partial}{\partial x}\rho\overline{v_x'v_x'}$, which arise from the fluctuations in the velocity field of the turbulent flow. These turbulent momentum fluxes arise from the product of terms of the form $v\frac{\partial v}{\partial x}$ and are strictly acceleration terms. The turbulent shear, $\overline{v_x'v_y'}$ is not negligible and its analytical form is not known *a priori* (White, 1991); it is not only related to the physical properties of the fluid but also to local flow conditions, including velocity, geometry, surface roughness and the upstream flow history. As no further physical laws are available to model the turbulent shear directly, this inevitably leads to a closure problem.

However, the time-averaged conservation of momentum equation may be rearranged to show the turbulent inertia terms in a form where they behave mathematically as stresses. On a historical basis, many analytical methods achieve closure by modelling these terms as 'turbulent or Reynolds stresses', using an eddy viscosity concept after Boussinesq (1877). Whilst attempts have been made to construct turbulent conservation equations, these too lead to extra unknowns that cannot be evaluated readily from first principles.

2.2. Turbulence Modelling Techniques.

Time-averaging of the equations of motion for isothermal fluid flow then yields six Reynolds stress components that can only be defined by knowledge of the detailed turbulent structure (White, 1991) and thus offers a closure problem, in that there are more unknowns than equations to solve them. Turbulence modelling may be described as the attempt to model equations for the spatial and temporal development of these turbulent fluxes. Such equations can then be used in conjunction with the mean flow equations to solve for the mean flow field. It should be noted though, that in providing approximate or empirical equations to model the Reynolds stresses, that the solution becomes approximate as well.

In seeking to describe the k-ε turbulence model, it is then useful to consider the principles of eddy viscosity modelling upon which it is based. All eddy viscosity models are based on a common hypothesis; by analogy with the molecular flux of momentum, the turbulent flux of momentum is held to be proportional to the gradients of the mean flow field. In a laminar, Newtonian fluid, the molecular fluxes of momentum are given by Stokes' law of viscosity as

$$\tau_{xy} = \mu\left(\frac{\partial v_x}{\partial y} + \frac{\partial v_y}{\partial x}\right) \tag{2.6}$$

The eddy viscosity model assumes that the turbulent fluxes of momentum can be approximated to by analogous expressions of the form

$$-\rho\overline{v_x' v_y'} = \mu_t\left(\frac{\partial \overline{v_x}}{\partial y} + \frac{\partial \overline{v_y}}{\partial x}\right) - \frac{2}{3}\rho k \delta_{xy} \tag{2.7}$$

In the above expression, μ_t is the eddy viscosity, but, unlike the laminar viscosity, μ, it is not dependent upon fluid properties but is determined by the state of turbulence. The eddy viscosity often varies significantly across a given flow field and from one field to another and, as such, no universal value may be ascribed to it. k, in the above expression, represents the kinetic energy of turbulence and may be written as

$$k = \frac{\overline{v_x' v_x'} + \overline{v_y' v_y'} + \overline{v_z' v_z'}}{2} \qquad (2.8)$$

which is half the sum of the variances of the velocity fluctuations per unit mass.

So the Reynolds stresses may then be expressed in terms of one unknown, that being the eddy viscosity, μ_t, and this provides a basis for turbulence modelling. Most models for eddy viscosity relate it to the large scale, energy carrying eddies in the flow field by an expression of the form

$$\mu_t \alpha \rho v_l \delta_l \qquad (2.9)$$

where δ_l and v_l are the length and velocity scales respectively of the largest eddies. This is a physically tangible relationship, in that these characteristic scales can be prescribed across the flow field with greater ease than for the eddy viscosity, μ_t.

The most widespread, and hence most documented, approach is the k-ε model. Furthermore, the k-ε model offers the advantage of being able to mimic the effects of advection. The derivation of the transport equations for the k-ε model for isothermal flow is discussed by Launder and Spalding (1974). By dimensional reasoning, the following arguments are made as

$$v_l \alpha \sqrt{k} \qquad (2.10)$$

and

$$\delta_l \alpha \frac{k^{3/2}}{\varepsilon} \qquad (2.11)$$

These statements are more 'universal' than the use of Prandtl's mixing length theory (1925) upon which simpler zero- and one-equation turbulence models are based. Since the characteristic scales for turbulence are now directly linked to the local turbulent quantities of kinetic energy, k, and dissipation, ε, these quantities may be said to characterize the local state of turbulence.

Substituting for equations 2.10 and 2.11 into equation 2.9, then

$$\mu_t = C_\mu \rho \frac{k^2}{\varepsilon} \qquad (2.12)$$

where C_μ is an empirical constant, constant over a wide range of strong-strain flows (Rodi, 1975).

Values for k and ε are then obtained from the semi-empirical transport equations, which, neglecting bouyancy effects, state

$$\rho \frac{Dk}{Dt} = \frac{\partial}{\partial x}\left(\frac{\mu_t}{\sigma_k} \cdot \frac{\partial k}{\partial x}\right) + \frac{\partial}{\partial y}\left(\frac{\mu_t}{\sigma_k} \cdot \frac{\partial k}{\partial y}\right) + \frac{\partial}{\partial z}\left(\frac{\mu_t}{\sigma_k} \cdot \frac{\partial k}{\partial z}\right) + \rho G - \rho\varepsilon \qquad (2.13)$$

$$\rho \frac{D\varepsilon}{Dt} = \frac{\partial}{\partial x}\left(\frac{\mu_t}{\sigma_\varepsilon} \cdot \frac{\partial \varepsilon}{\partial x}\right) + \frac{\partial}{\partial y}\left(\frac{\mu_t}{\sigma_\varepsilon} \cdot \frac{\partial \varepsilon}{\partial y}\right) + \frac{\partial}{\partial z}\left(\frac{\mu_t}{\sigma_\varepsilon} \cdot \frac{\partial \varepsilon}{\partial z}\right) + C_{\varepsilon 1}\rho \frac{\varepsilon}{k} G - C_{\varepsilon 2}\rho \frac{\varepsilon^2}{k} \qquad (2.14)$$

Note that the above equations are derived from manipulation of the instantaneous flow equations. In equation 2.13, for turbulent kinetic energy, G represents shear generation - the production of turbulent kinetic energy from interactions between the mean and the turbulent fields - and is modelled as

$$\rho G = \mu_t \left\{ \begin{array}{l} \frac{\partial \overline{v_x}}{\partial y}\left(\frac{\partial \overline{v_x}}{\partial y} + \frac{\partial \overline{v_y}}{\partial x}\right) + \frac{\partial \overline{v_x}}{\partial z}\left(\frac{\partial \overline{v_x}}{\partial z} + \frac{\partial \overline{v_z}}{\partial x}\right) \\ + \frac{\partial \overline{v_y}}{\partial x}\left(\frac{\partial \overline{v_y}}{\partial x} + \frac{\partial \overline{v_x}}{\partial y}\right) + \frac{\partial \overline{v_y}}{\partial z}\left(\frac{\partial \overline{v_y}}{\partial z} + \frac{\partial \overline{v_z}}{\partial y}\right) \\ + \frac{\partial \overline{v_z}}{\partial x}\left(\frac{\partial \overline{v_z}}{\partial x} + \frac{\partial \overline{v_x}}{\partial z}\right) + \frac{\partial \overline{v_z}}{\partial y}\left(\frac{\partial \overline{v_z}}{\partial y} + \frac{\partial \overline{v_y}}{\partial z}\right) \end{array} \right\} \qquad (2.15)$$

Equation 2.14, for turbulent dissipation, models the effects of dissipation largely by intuition and dimensional reasoning (Launder, 1984). The term $C_{\varepsilon 1}\rho \frac{\varepsilon}{k} G$ denotes shear generation, $C_{\varepsilon 2}\rho \frac{\varepsilon^2}{k}$ viscous dissipation and $C_{\varepsilon 1}$ and $C_{\varepsilon 2}$ are empirical model constants. The model constants σ_k and σ_ε are the turbulent Prandtl/Schmidt numbers for k and ε respectively.

In both equations, the turbulent diffusion of k and ε, due to the turbulent fluctuations of velocity and pressure, is modelled using the eddy viscosity concept. The transport equations have modelled terms for diffusion and for sources and sinks and hence model the local processes of turbulent generation and destruction. As such, solution of these equations provides the spatial and temporal evolution of the characteristic length and velocity scales, since these are governed by mean advection and diffusion and also by

local processes of turbulent generation and destruction.

The additional computational cost of solving two more transport equations must be considered as the complexity of the overall mathematical model is significantly increased. The model is highly non-linear and shows strong coupling between various of the transport equations - these factors tend to destabilise the convergence of the numerical solution. Furthermore, the standard k-ε model, as presented, is only valid for high Reynolds numbers. For bounded flows then, wall functions are required to connect the fully turbulent region of flow with the conditions prevalent at the wall.

2.3. Computational Modelling of the Equations of Motion.

The equations of motion for isothermal fluid flow, as considered so far, provide a continuous description of the time-averaged mean field of flow, in as much as their solution, if possible, would yield information pertaining to an infinite number of degrees of freedom. Whilst it is believed that the solution of these equations can be used to describe three-dimensional flows completely, current supercomputers are neither fast enough nor have sufficient storage to solve the equations directly for the relevant time and length scales of general engineering problems. Turbulent motion contains scales significantly smaller than the extent of the flow domain, typically in the region of 10^{+3} times smaller. As such, resolution of such fine scales using a numerical procedure would require spatial discretisation far beyond current computational capabilities. Therefore, a solution is sought by making use of a discrete or discontinuous model of the flow; the finite element method (FEM) approach to this problem will now be considered.

2.3.1. Finite Element Modelling.

The purpose of FEM is to reduce the continuous problem, having an infinite number of degrees of freedom, to a discrete problem, with a finite number of degrees of freedom, described by a system of algebraic equations.

As such, the continuum region is divided into a number of simply shaped regions, known as elements. By dint of having used an Eulerian description of fluid motion in the analysis to date, these elements are held to be fixed in space. Inside each finite element then, the flow variables are interpolated spatially in terms of values to be determined at a set of nodal points. The partial differential equations covering the flow region as a whole

are replaced by ordinary differential or algebraic equations within each element, for each nodal point described. The system of equations thus provided may then be solved by a suitable numerical technique to yield values of v, p, k and ε at discrete points throughout the region.

For isothermal fluid flow, the governing equations of motion are seen as the equations of continuity and of conservation of momentum, given by equations 2.4 and 2.5 respectively, on a time-averaged basis. Within each element, the velocity and pressure fields are approximated by functions of the form

$$v_i(x,t) = \varphi V_i(t) \tag{2.16a}$$

$$p(x,t) = \psi P(t) \tag{2.16b}$$

where V_i and P are column vectors of element nodal point unknowns and φ and ψ are column vectors of interpolation functions.

These approximations may then be substituted into the field equations and boundary conditions to provide equations of the form

$$f_1(\varphi, \psi, V_i, P) = R_1 \tag{2.17a}$$

$$f_2(\varphi, V_i) = R_2 \tag{2.17b}$$

where R_1 is a residual, or error, resulting from the use of these approximations for the momentum equation of 2.17a. Likewise, R_2 is the corresponding residual in the conservation of mass relationship, given as equation 2.17b. The Galerkin form of the method of weighted residuals (FIDAP Theory Manual, 1994) then seeks to reduce these errors to zero and hence provide a solution to the flow problem considered.

These matrix equations are used to provide an overall model of the flow region, consisting of an assemblage of elements with interelement continuity of the flow variables being enforced by appropriate summation of equations common to adjacent elements. This approach, known as the direct stiffness approach, gives a global system of matrix equations spanning the entire region of flow.

Principal advantages of the FEM may then be listed as

i) inherent flexibility in treating arbitrarily complex flow geometries and boundary conditions,
ii) use of unstructured grids, such that areas of interest can be studied in greater detail without the need for excessive numbers of nodal points throughout the entire computational grid representing the flow domain,
iii) natural and correct imposition of boundary conditions on curved boundaries and
iv) the mathematical formulation used allows for derivation of comprehensive error estimates; hence the determination of accurate solutions may be performed to user-presribed tolerances.

2.3.2. Solution Procedures.

The solution procedures used to implement the FEM will now be considered in conjunction with the particular computational package used in this project, namely FIDAP, which is a proprietary package, produced by Fluid Dynamics International, for use both as a commercial and a research tool.

In keeping with many current, commercial codes, analysis of the flow regime is subdivided into a number of tasks as

i) generation of a mesh of nodal points pertinent to the problem geometry and specification of boundary and initial conditions,
ii) specification of the class of problem and necessary equations to be solved, the solution procedure, fluid and material properties and integration with the relevant boundary and initial conditions and element data to create a solution input file and
iii) post-processing facilities, allowing for computation and graphical display of derived variables and quantities.

The main solution types may be subdivided into two main categories as

i) steady-state flows and
ii) transient or time-dependent flows.

For steady-state flows, or for transient analyses using an implicit time integrator, a non-linear matrix system of equations requires to be solved - once for steady-state and at each time step for transient analysis.

This solution is the most time-consuming stage of the analysis, typically accounting for up to 80% of computational resources used. Consequently, the choice of solution algorithm can govern and ultimately limit the practical size of the problem considered. Two distinct approaches to the solution of the matrix system of equations may be seen as

i) fully coupled solutions and
ii) sequential, or segregated, solutions.

The fully coupled approach solves all the equations simultaneously whereas the segregated approach decomposes the matrices and solves for each variable in a sequential fashion. Practical experience shows the fully coupled approach to be the best for all but the largest of two-dimensional problems, whilst the segregated solver is most practical for very large two-dimensional and the majority of three-dimensional problems, where the cost and availability of computer resources (in terms of storage of the global systems matrix and CPU time) become of critical interest.

Although the segregated solver has guaranteed substantially reduced disc storage requirements in comparison with the fully coupled solver, its segregated and uncoupled nature requires more iterations to converge on a solution. However, as the size of the mesh of nodes for the problem rises, the cost of each full segregated iteration is increasingly less than for fully coupled iterations. As such, a 'trade-off' is observed between performing a larger number of less expensive iterations or fewer, more expensive ones with the fully coupled solver.

2.4. Study of Bounded Flow Regimes.

When modelling a bounded flow, the local conditions in the region of the wall must be considered. In the freestream, the turbulent fluctuations are largely isotropic in nature but near to the wall, the presence of a solid boundary will limit fluctuations perpendicular to the main flow direction. In considering the fluctuating velocity components, the component v'_x has the greatest magnitude, being unimpeded by the wall and being reinforced by the freestream whereas v'_y is the smallest of the fluctuating components. v'_z

has an intermediate value, even for two-dimensional flow (although it has no direct effect on two-dimensional mean flow). Figure 2.1 shows this phenomenon for turbulent flow through a smooth pipe, with r and z representing the radial and axial flow directions respectively.

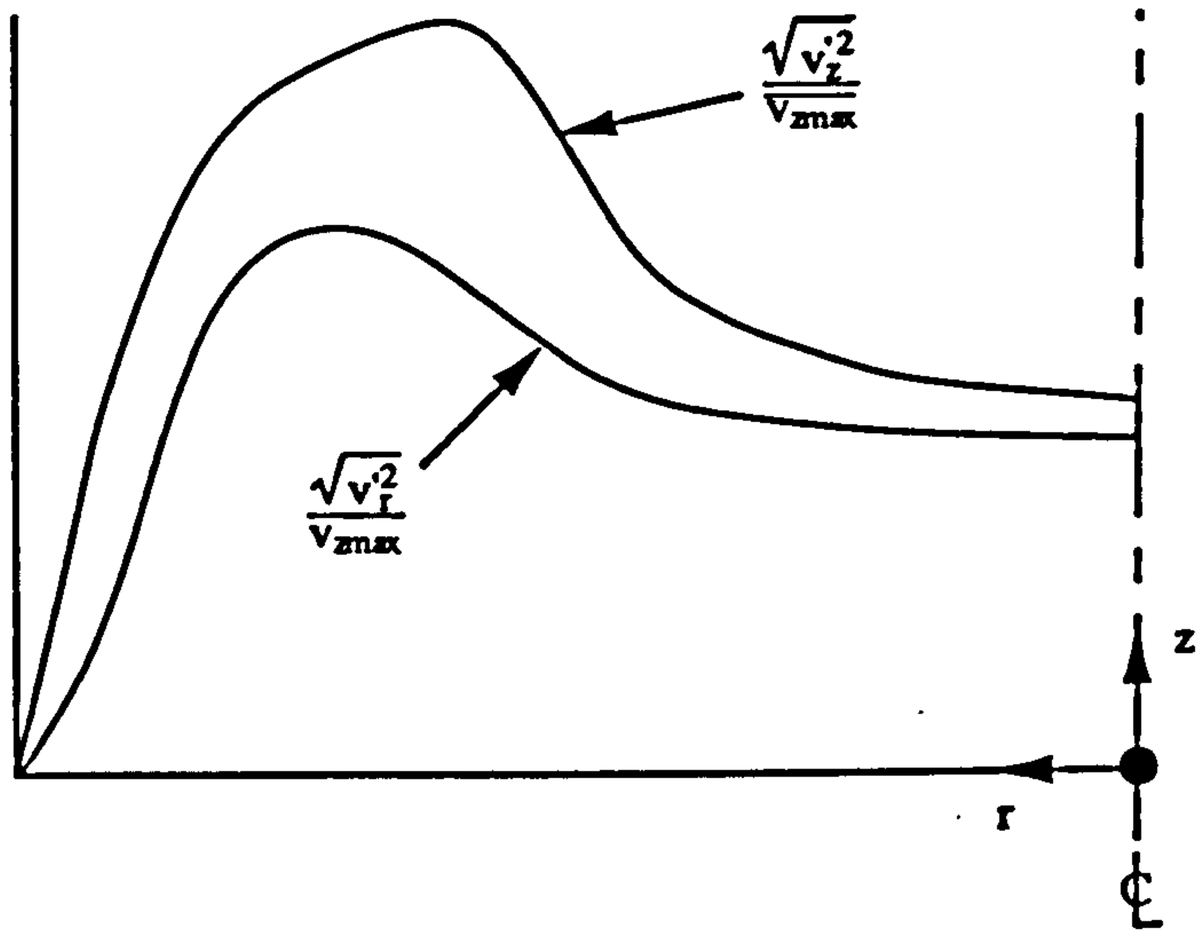

Figure 2.1. Showing turbulent fluctuations in velocity for flow along a pipe.

The fluctuations in the direction of flow are seen to be greater than those perpendicular to the flow. Whilst there is a tendency to isotropy near the centreline of the pipe, there is a marked difference between the two fluctuations as the wall is approached.

The laminar and virtual stresses across the pipe cross-section are shown as Figure 2.2 below.

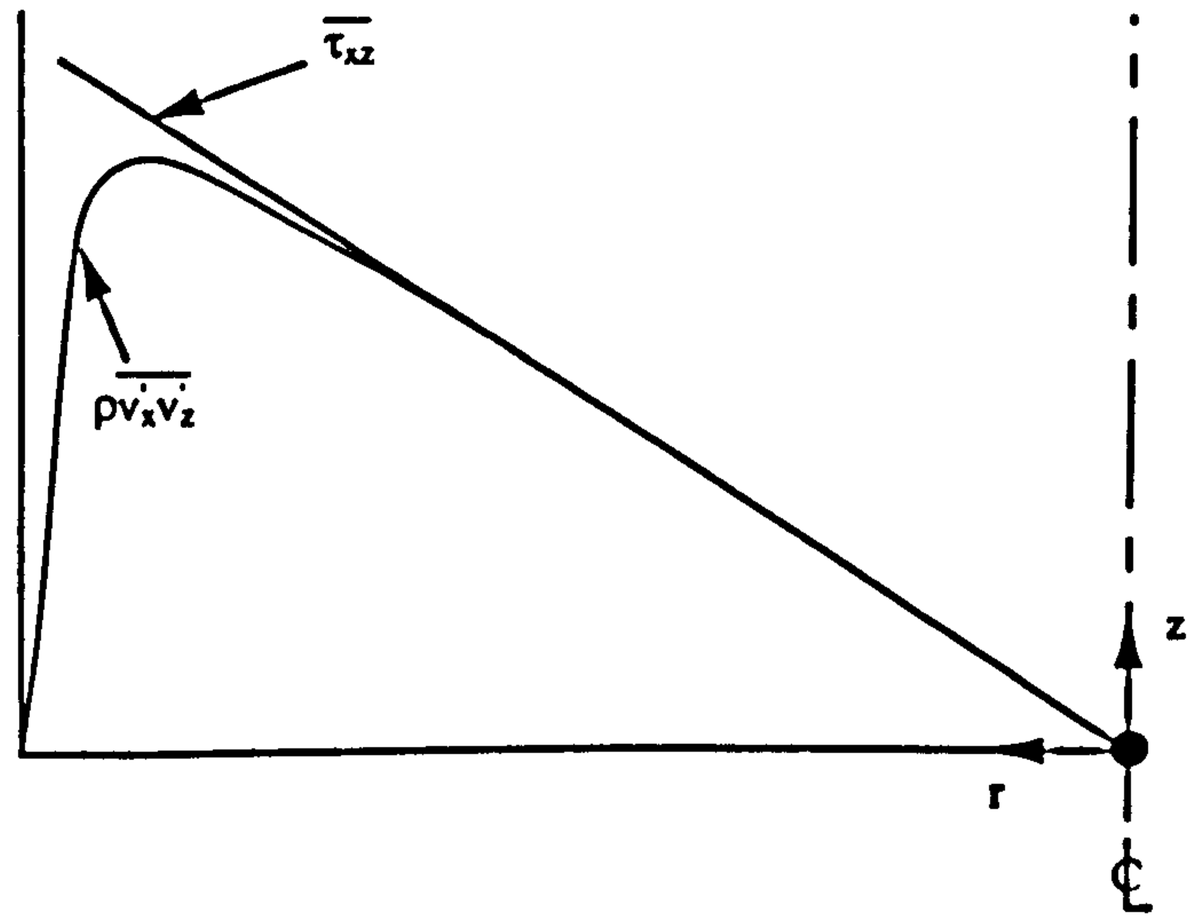

Figure 2.2. Showing the variation of stresses across the flow in a pipe.

On inspecting Figure 2.2, the relative importance of the viscous (laminar) and Reynolds stresses may be compared, with regard to the variation in momentum flux over the cross-section of the flow. Given that $\overline{\tau_{xz}}$ is a summation of the viscous and Reynolds stresses, then the rapid decrease towards zero in the Reynolds stress, $\rho\overline{v_x'v_z'}$, on approaching the wall implies that the major component of the term $\overline{\tau_{xz}}$, which is still significant in this region, is the viscous stress. The decline in the Reynolds stress close to the wall arises from the presence of the wall itself, which acts to damp out the Reynolds stress on final approach to the wall (van Driest, 1956). As such, in the near-wall region, any proposed mathematical model of the flow must be able to model the effects of viscosity in order to be of service. The shear stress, $\overline{v_x'v_y'}$, has a smaller value than any of the fluctuating components but is of fundamental importance as it lies at the root of analytical problems. For an impermeable boundary, a no-slip condition for velocity will prevail, such that the local velocity is zero at the solid surface. However, the fluctuating velocities are resistant to wall damping and are still significant at $y/\delta = 0.0001$ (where δ is the thickness of the boundary layer). As such, to capture the velocity profile close to the wall computationally would require a very fine computational mesh.

This deviation from isotropic or homogeneous turbulence near the wall and the importance of viscous effects near the wall limits the validity of the k-ε model in this region: the k-ε model requires isotropic flow at high Reynolds numbers and also cannot make allowance for viscous effects. Further practical drawbacks to the use of the k-ε model in the near wall region are presented by Figure 2.3.

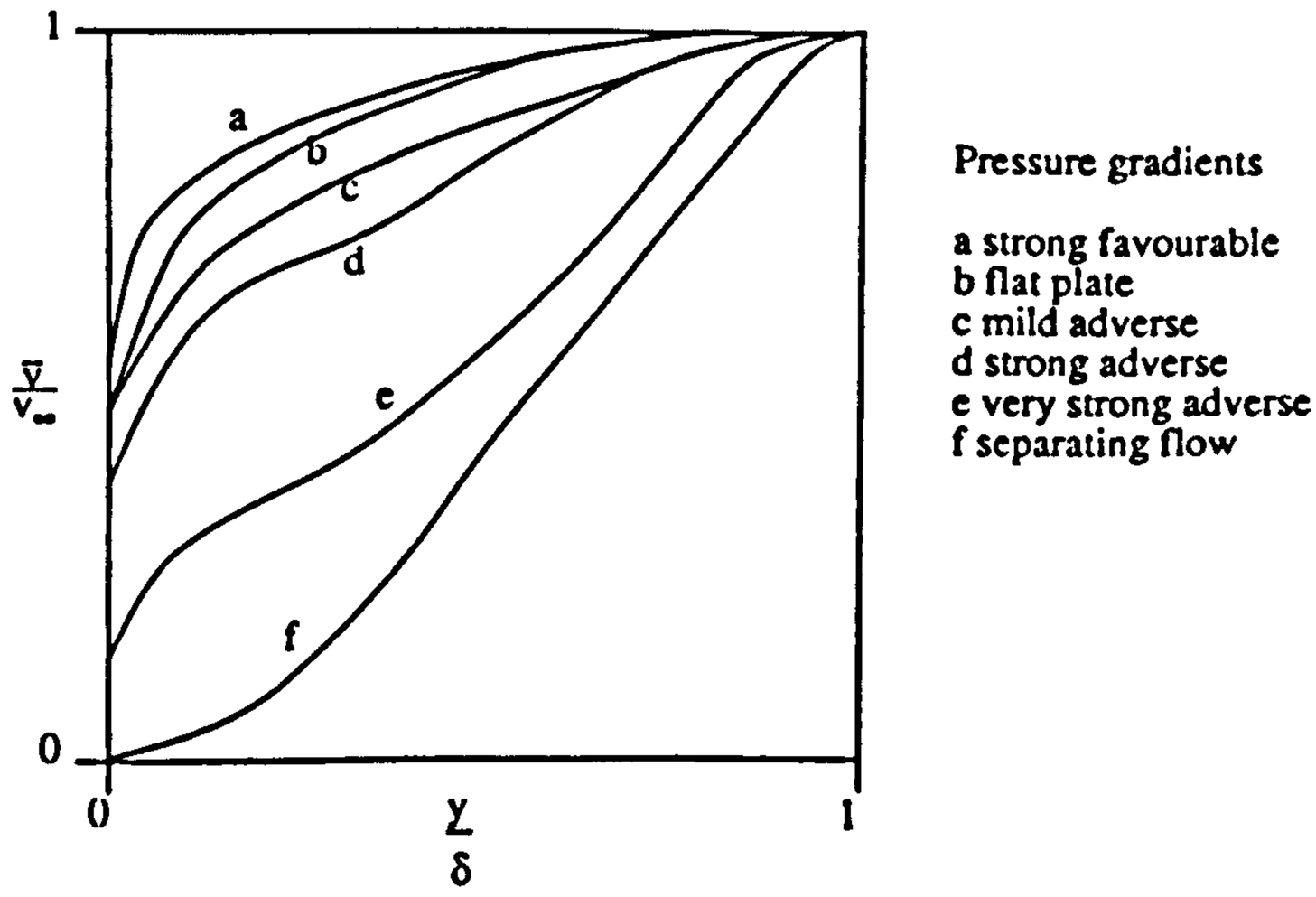

Figure 2.3. Typical turbulent boundary layer velocity profiles for various pressure gradients, after White (1991).

In the above diagram, v_∞ denotes the freestream velocity, y denotes the normal distance from the wall and δ the thickness of the boundary layer. On inspecting the velocity profiles in Figure 2.3, it will be seen that as the pressure gradient becomes progressively more adverse, the general form of the profiles develops an increasing dip below the convex form of profile 'a'. This departure from the response to a favourable pressure gradient begins at about $\frac{y}{\delta} = 0.2$ and corresponds to the onset of a wake-like behaviour in the outer, fully turbulent region of the boundary layer. The velocity profiles appear to 'collide' with the solid boundary at $\frac{y}{\delta} = 0$. Actually, the profiles will all drop linearly to zero within a thickness too small to be seen here. This presents a modelling problem; such sharp velocity gradients would necessitate use of an extremely fine mesh in the vicinity of the wall, leading to excessive computational requirements, both in terms of memory space and solution time.

2.4.1. The Establishment of Wall Laws to Model the Boundary Layer.

Given the inability of the k-ε model to predict the effects of viscosity and coupled with the excessive computational demands that would arise from attempting to mimic the sharply varying velocity gradients in the near-wall region, it would seem practical to model the boundary layer with methods other than the k-ε model. This is typically done by use of so-called wall laws, where the boundary layer is modelled by use of semi-empirical equations that predict variation of the flow properties from the solid boundary out into the flow to such a point as the k-ε model becomes practical and valid.

With regard to these boundary layer profiles, Prandtl and von Karman proposed that they consist of a number of layers as

i) an inner layer, dominated by viscous, or molecular, shear,
ii) an outer layer, dominated by turbulent (eddy) shearing and
iii) an overlap layer, where both types of shear are important.

Prandtl (1933) suggested that the velocity profile for the inner layer is dependent upon the wall shear stress, τ_0, on various fluid properties and upon the distance from the wall, y, but not on the freestream parameters. Therefore, an inner law would be a

function of the form

$$\bar{v} = f(\tau_0, \rho, \mu, y) \tag{2.18}$$

von Karman (1930) proposed an outer law, where the presence of the wall acted as a source of retardation to the flowing fluid, such that $\bar{v}(y) < v_\infty$. He suggested that the outer law would be independent of viscosity but that it would be related to the wall shear stress, the boundary layer thickness, δ, and to the freestream pressure gradient, $\frac{dp_\infty}{dx}$.

Therefore, an outer law would be a function of the form

$$v_\infty - \bar{v} = g\left(\tau_0, \rho, y, \delta, \frac{dp_\infty}{dx}\right) \tag{2.19}$$

Note that this outer law is expressed as a velocity defect, $v_\infty - \bar{v}$.

For the overlap layer, at some finite, intermediate point, a smooth merging is then required between the inner and outer layers as

$$\overline{v_{inner}} = \overline{v_{outer}} \tag{2.20}$$

Practical forms of the above laws may be derived from experiment after the use of dimensional analysis, which provides the following insight:

Inner law $$\frac{\bar{v}}{v^*} = f\left(\frac{yv^*}{\nu}\right) \quad : \quad v^* = \sqrt{\frac{\tau_0}{\rho}} \tag{2.21}$$

Outer law $$\frac{v_\infty - \bar{v}}{v^*} = g\left(\frac{y}{\delta}, \xi\right) \quad : \quad \xi = \frac{\delta}{\tau_0} \cdot \frac{dp_\infty}{dx} \tag{2.22}$$

Equation 2.22 is presented as a velocity defect law - the defect in velocity arising from retardation of the flow due to wall effects. At a given position, x, along the flow then, the defect shape, $g\left(\frac{y}{\delta}\right)$, will depend on the local pressure gradient parameter, ξ.

Note also the use of the wall friction velocity, v^*, used to present the wall laws in a non-dimensional form. The wall friction velocity may be considered to be a measure of the turbulent eddying or, alternatively, to be a correlation between the fluctuating velocity components (Schlichting, 1979).

Inspecting equations 2.21 and 2.22, the overlap law may be written again as

$$\frac{\bar{v}}{v^*} = f\left(\frac{\delta v^*}{\nu} \cdot \frac{y}{\delta}\right) = \frac{v_\infty}{v^*} - g\left(\frac{y}{\delta}\right) \qquad (2.23)$$

Here the function f contains a multiplicative constant, whilst the function g has an additive constant. As such, equation 2.23 can only be true if both f and g are logarithmic constants, yielding for the overlap layer

Inner variables $$\frac{\bar{v}}{v^*} = \frac{1}{\kappa} \ln \frac{yv^*}{\nu} + B \qquad (2.24)$$

Outer variables $$\frac{v_\infty - \bar{v}}{v^*} = -\frac{1}{\kappa} \ln \frac{y}{\delta} + A \qquad (2.25)$$

κ, the von Karman constant, and B are held to be near-universal constants for turbulent flow past smooth, impermeable walls, where κ=0.41 and B=5.0 (Coles and Hirst, 1968). The constant A, however, is seen to vary with the pressure gradient parameter, ξ, the consequences of which will be seen later.

The velocity profiles presented in Figure 2.3 may be usefully redrawn, making use of the following dimensionless variables

$$u^+ = \frac{\bar{v}}{v^*} \qquad (2.26)$$

and $$y^+ = \frac{yv^*}{\nu} \qquad (2.27)$$

It is interesting to note that the normalised distance from the wall, y^+, may also be viewed as a local Reynolds number, hence being useful in describing the nature of the boundary layer flow.

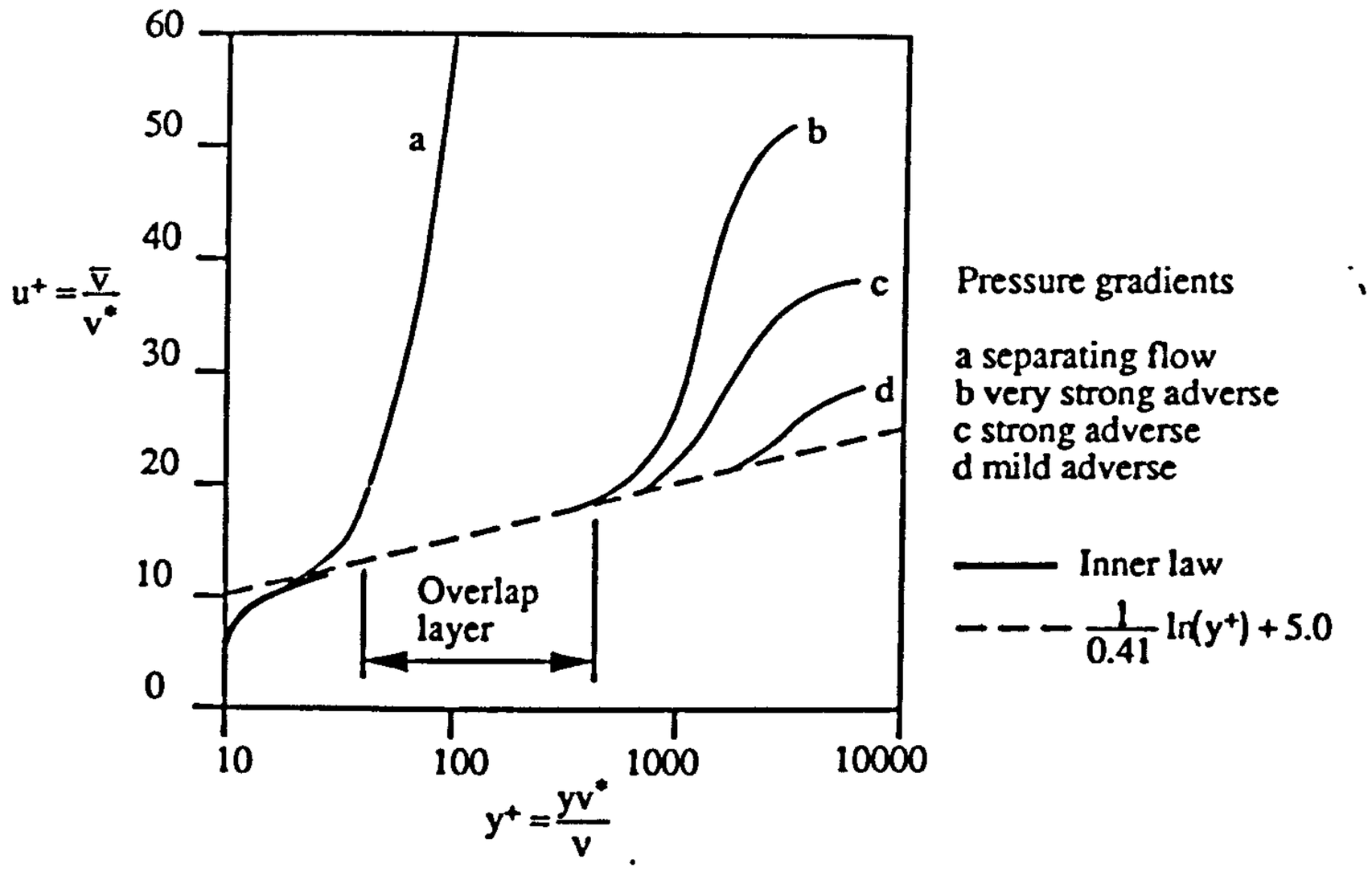

Figure 2.4. Dimensionless velocity profiles for a turbulent boundary layer, after White (1991).

Straight away, it can be seen that, excepting the case of near-separating flow, all the curves for the various pressure gradients condense to one logarithmic relationship in the overlap region, for $35 \leq y^+ \leq 350$. Beyond this point, however, the experimental curves either turn upwards into the outer, wakelike layer or downwards, into the inner (viscous) layer.

For the case of a near-separating flow, as v^* tends to zero, u^+ becomes large and y^+ very small. Hence, near a point of separation, scaling in terms of τ_0 is not useful; the outer law is still of merit, but the corresponding inner and overlap layers become vanishingly small.

Whilst Figure 2.4 validates the inner and overlap laws, in that all the experimental data collapse onto one curve, the outer law is less easy to defend by a similar process. Figure 2.5 demonstrates this by replotting the curves of Figure 2.3 using outer variables as

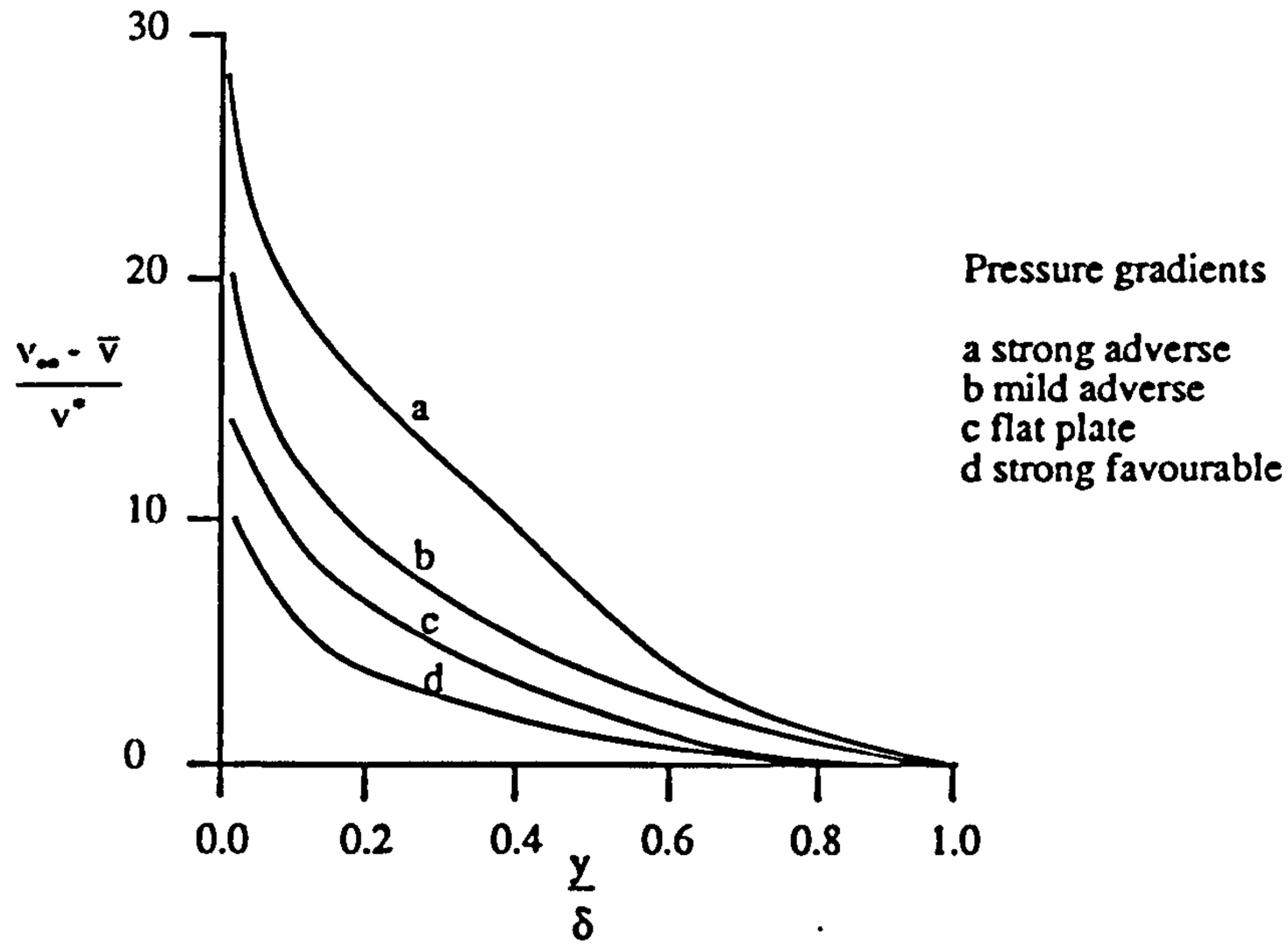

Figure 2.5. Turbulent boundary layer velocity profiles, expressed in terms of outer law variables, after White (1991).

Each velocity profile shown has a different pressure gradient parameter, ξ, and hence a different value for the constant, A. No collapse onto a universal curve is seen but, for a given value of ξ, an unique profile would be obtained.

2.4.2. Practical Use of the Wall Laws.

From Figure 2.4, it can be seen that the inner law rises from the no slip boundary condition at the wall to merge smoothly, at approximately $y^+ = 30$, with the overlap log-law, as expressed by equation 2.24. Very close to the wall, over a region too small to be shown in the diagram, the presence of the wall 'damps out' the effects of turbulence and the boundary layer is thus dominated by viscous shear. As such, for very small values of y, the velocity profile is linear as

$$y^+ \leq 5 \qquad \tau_0 = \frac{\mu \bar{v}}{\bar{y}} \qquad \text{or} \qquad u^+ = y^+ \tag{2.28}$$

This very thin region near the wall is known as the viscous (laminar) sub-layer and, by general agreement, has a thickness $\delta_{sub} = \frac{5\nu}{v^*}$, where $\frac{\nu}{v^*}$ is often referred to as the viscous length scale of the boundary layer.

In the region $5 \leq y^+ \leq 30$, the buffer layer, the velocity profile is neither linear nor logarithmic but is seen to merge smoothly between the two.

As such, separate equations are used to study the sub-layer, buffer layer and log-layer, using the identity y^+ to select the appropriate set of equations. However, various attempts have been made to provide a combined or universal form of these equations for general use.

Reichardt (1951) proposed that

$$u^+ = \frac{1}{\kappa}\ln(1 + 0.4y^+) + 7.8\left\{1 - e(-y^+/11) - \frac{y^+}{11}e(-0.33y^+)\right\} \qquad (2.29)$$

This equation corresponds extremely well with experimental data from the wall up to $y^+ = 300$ and beyond. However, when first proposed, this equation was awkward to implement under the computational conditions then prevalent and so a later and simpler model, proposed by Spalding (1961), has seen widescale usage as

$$y^+ = u^+ + e^{-\kappa B}\left\{e^{-\kappa u^+} - 1 - \kappa u^+ - \frac{(\kappa u^+)^2}{2} - \frac{(\kappa u^+)^3}{6}\right\} \qquad (2.30)$$

Spalding's equation provides a very good fit to inner law data, from the wall all the way to a point (around $y^+ \rangle 100$) where the outer layer begins to rise above the logarithmic curve. Lindgren (1965) showed experimental results for fully developed pipe flow with a favourable pressure gradient (at $\xi = -2$) that gave values for $\bar{v}$ in good agreement with Spalding's work, from very close to the wall up to $y^+ \rangle 300$, at which point a slight wake was evident in the outer layer.

However, it must be noted that neither Reichardt's nor Spalding's models are designed to cater for the effects of advection. As such, in regions where the effects of advection are significant, any results gained must be viewed with suspicion.

As mentioned in Section 2.4.1., the validity of the outer law has proven less easy to verify. The outer region of a turbulent boundary layer displays a complex, nonlinear memory related to upstream events - this means that velocity distributions are dependent upon upstream, as well as local, conditions (Schofield, 1981). Clauser (1954,1956) set

out to address this problem by considering certain boundary layers with adverse pressure gradients. Clauser limited this study to cases where the boundary layer was subject to a constant force history and thus could be described in terms of local parameters alone.

The external forces on a boundary layer may be seen as the pressure gradient, $\frac{dp}{dx}$, and the shear stress at the wall, τ_0. Thus, for a boundary layer with a constant force history, which Clauser termed an 'equilibrium boundary layer', a non-dimensional ratio of forces may be written as

$$\beta = \frac{\delta^*}{\tau_0} \cdot \frac{dp_\infty}{dx} \tag{2.31}$$

where δ^* is the displacement thickness of the boundary layer, defined as

$$\delta^* = \frac{\int_0^\delta (\rho_\infty v_\infty - \rho\bar{v})dy}{\rho_\infty v_\infty} \tag{2.32}$$

The displacement thickness is more rigorously defined than the boundary layer thickness, δ, and may be viewed as the thickness through which the freestream density and velocity would have to act in order to provide the same mass flow deficit as the boundary layer.

Clauser expected that for the equilibrium layer, with constant β, the mean and fluctuating velocity fields would be dynamically similar at all stations (provided fine scale eddies are neglected). Clauser then considered the only documented equilibrium boundary layer then known - the case of zero pressure gradient, for which it is well established that

$$\frac{v_\infty - \bar{v}}{v^*} = f\left(\frac{y}{\delta}\right) \tag{2.33}$$

Such a velocity defect law will predict behaviour from the freestream almost down to the wall. Clauser reasoned that a defect law of the same form as equation 2.33 should be valid for equilibrium layers in flows with a pressure gradient. Clauser then demonstrated experimentally that a boundary layer with varying pressure, $p_\infty(x)$, but with constant equilibrium pressure gradient parameter, β, is in turbulent equilibrium in as much as all the gross properties of the boundary layer can be scaled by a single parameter. Clauser saw the most relevant scaling parameter for equilibrium turbulent flows as the

defect thickness, Δ, where

$$\Delta = \int_0^\infty \frac{v_\infty - \bar{v}}{v^*} dy = \delta^* \lambda \quad : \quad \lambda = \sqrt{\frac{2}{C_f}} \tag{2.34}$$

where λ is a measure of the local skin friction, C_f.

Velocity profiles can then be scaled with $\frac{y}{\Delta}$ and a shape factor, G, which would remain constant throughout the equilibrium layer as

$$G_s = \frac{1}{\Delta} \int_0^\infty \left(\frac{v_\infty - \bar{v}}{v^*} \right)^2 dy \tag{2.35}$$

In fact, it can be shown that for various, discrete values of the equilibrium parameter, β, that the data do collapse beautifully onto one curve for $\frac{v_\infty - \bar{v}}{v^*}$ vs. $\frac{y}{\delta}$, as seen in Figure 2.6.

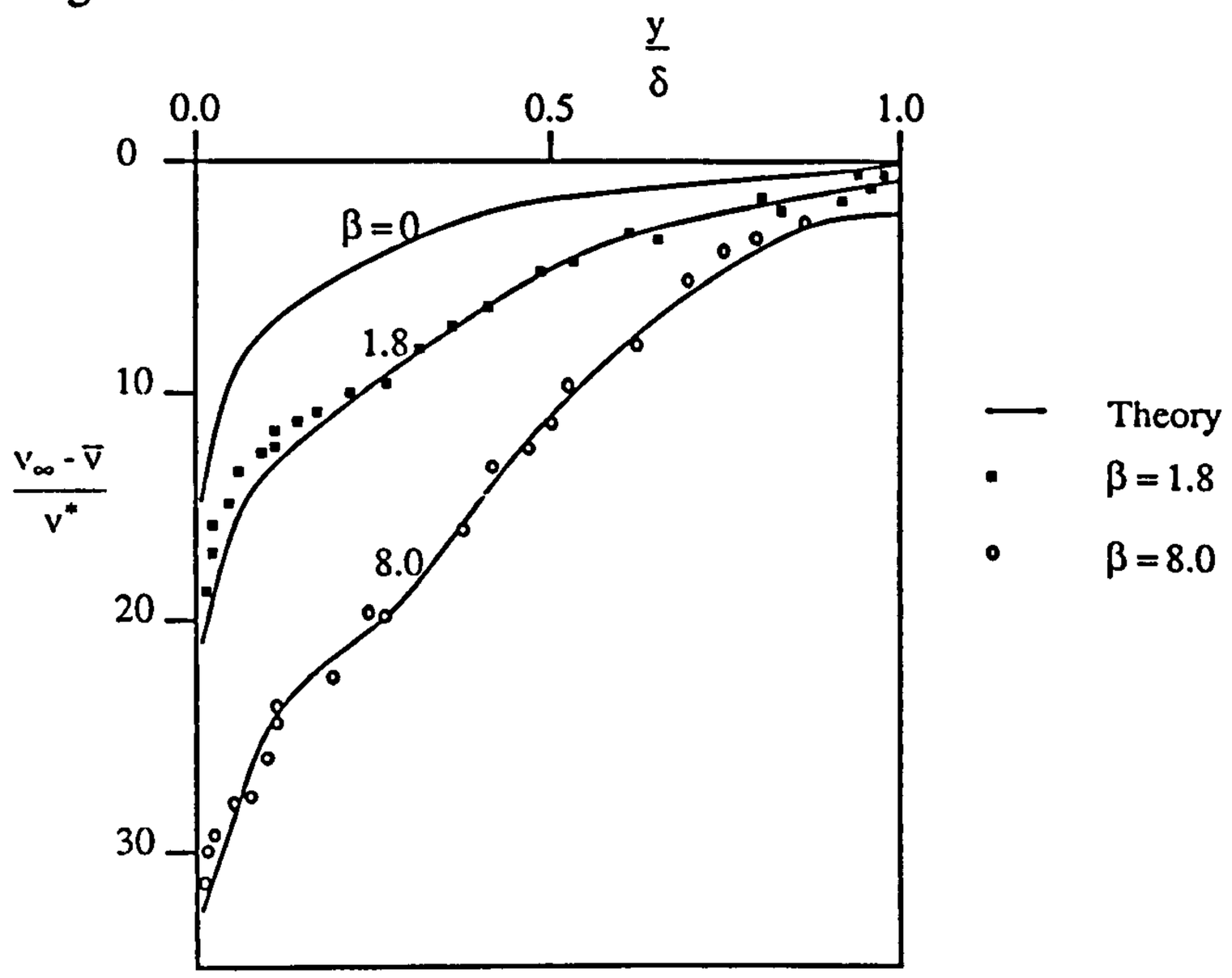

Figure 2.6. Equilibrium defect profiles, as correlated by Clauser's equilibrium pressure gradient parameter, β, after White (1991).

Clauser's work was a significant step forward in modelling the outer region of certain boundary layers but a number of shortcomings were experienced as

i) non-equilibrium flows deviate in shape from the similiarity profiles of Clauser,
ii) the equilibrium shapes have no simple analytical form for use in an engineering theory and
iii) for the case of near-separating flow, v^* approaches zero and so is no longer suitable as a scaling parameter.

As the adverse pressure gradient increases, v^* tends to zero and β to infinity. Furthermore, the logarithmic layer thins and ultimately vanishes and wall co-ordinates become inappropriate (see Figure 2.4); as such, a more appropriate velocity scale is required.

2.4.3. Coles' Law of the Wake.

In modelling the boundary layer, a single, universal equation for the velocity profile, also catering for the effects of advection, would be highly desirable. In reviewing the approaches to boundary layer modelling considered so far, each of these techniques appears to be valid for a limited range of conditions only. Reichardt's and Spalding's models of the inner and overlap layers cannot account for advective effects, given that they are based upon zero pressure gradient flows, and Clauser's model of the outer layer is only valid for equilibrium flows in the absence of separation.

Another approach with much wider potential use was proposed by Coles (1956). Coles studied a considerable range of reported experimental results and observed that deviations, in the form of excess velocity, of the outer layer above the predictions of the logarithmic law (see Figure 2.4) take a 'wake-like' shape when viewed from the freestream.

Coles then reappraised the description of the mean velocity profile for two-dimensional flow near the wall, given by equation 2.21 as

$$\frac{\bar{v}}{v^*} = f\left(\frac{yv^*}{\nu}\right)$$

and that for the overlap layer, given by equation 2.24 as

$$\frac{\bar{v}}{v^*} = \frac{1}{\kappa}\ln y^+ + B$$

and proposed that the mean velocity profile for a turbulent shear flow would be of the form

$$\frac{\bar{v}}{v^*} = f\left(\frac{yv^*}{\nu}\right) + h(x,y) \qquad (2.36)$$

Coles found that for certain common, special cases, such as uniform pipe flow or the boundary layer over a flat plate, that the above expression may be rewritten as

$$\frac{\bar{v}}{v^*} = f\left(\frac{yv^*}{\nu}\right) + g\left(\Pi, \frac{y}{\delta}\right) \qquad (2.37)$$

where Π is a parameter independent of both x and y.

Now, outside the viscous sub-layer, the logarithmic variation of the function f in equation 2.37 led to

$$\frac{\overline{v_1} - \bar{v}}{v^*} = F\left(\Pi, \frac{y}{\delta}\right) \qquad (2.38)$$

where $\bar{v} = \overline{v_1}$ at $y = \delta$.

The above velocity defect law implies that loss of momentum is independent of viscosity of the fluid. This is consistent with the idea that turbulent rather than viscous transport mechanisms are predominent outside the viscous sub-layer. This also agrees with experimental observations that the momentum defect is sensitive to the turbulence intensity outside the boundary layer but not to surface roughness at the solid boundary (FIDAP Theory Manual, 1994).

Coles then studied the function h(x,y) in the general mean velocity equation, equation 2.36, in conjunction with a wide range of experimental data at large Reynolds number. Coles found that various mean velocity profiles were quite systematic, in that they had a common form, once expressed in the co-ordinates (u^+, y^+). Indeed, for a number of such profiles with the same defect law (common Π), despite displaying marked differences in environment, the same form was observed for each, as seen below in Figure 2.7 overleaf.

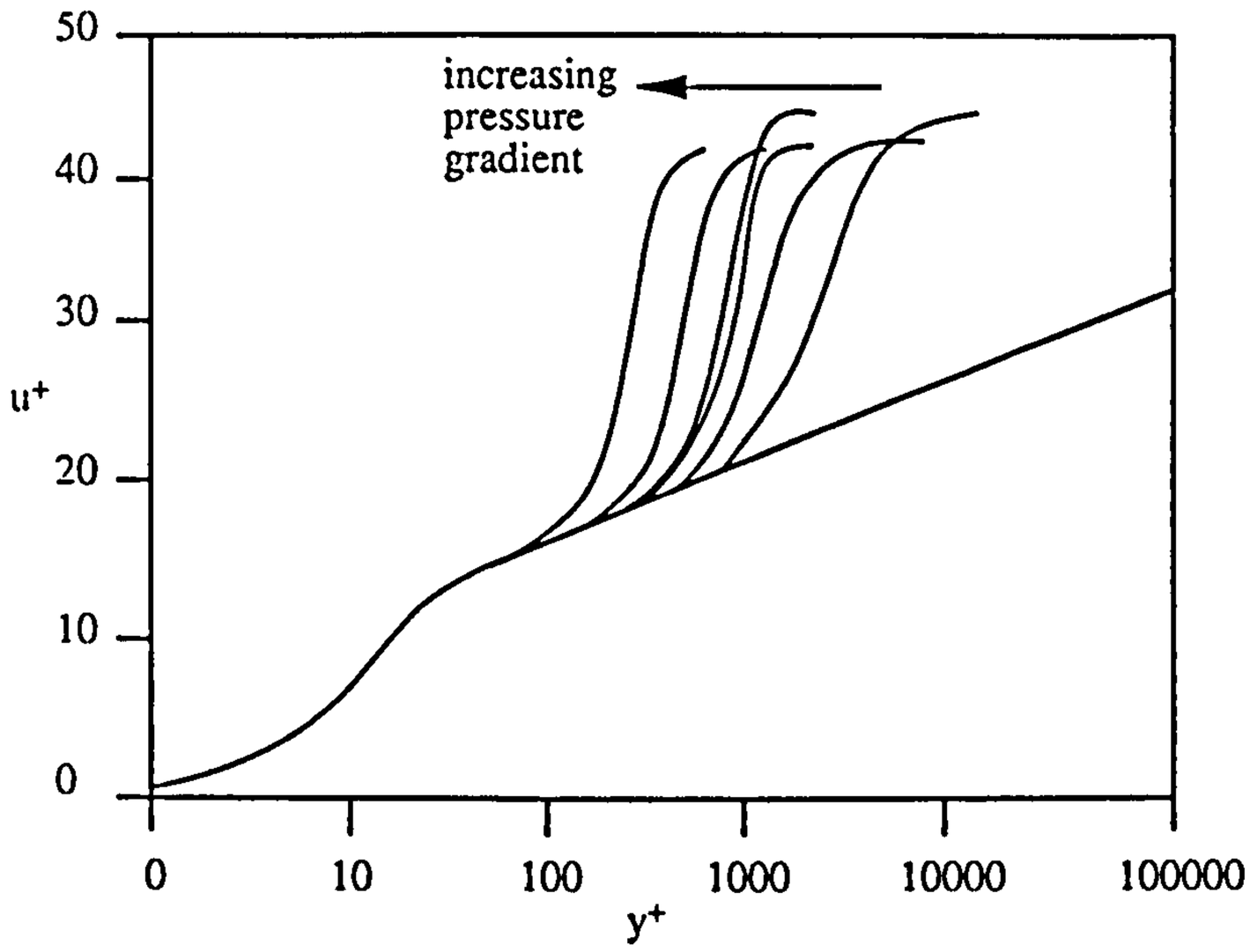

Figure 2.7. Displaying the similarity in velocity profiles having a common wake parameter, Π, but differing wake function, w, and streamwise force histories, after Coles (1956).

This suggested to Coles that the solution to the defect law lay not in the study of the function F in equation 2.38 but in the original function g in equation 2.37, which gives the departure of the mean velocity profile from the logarithmic law.

Figure 2.8 below shows data from three equilibrium flows (Clauser series I and II and from Wieghardt(1943)).

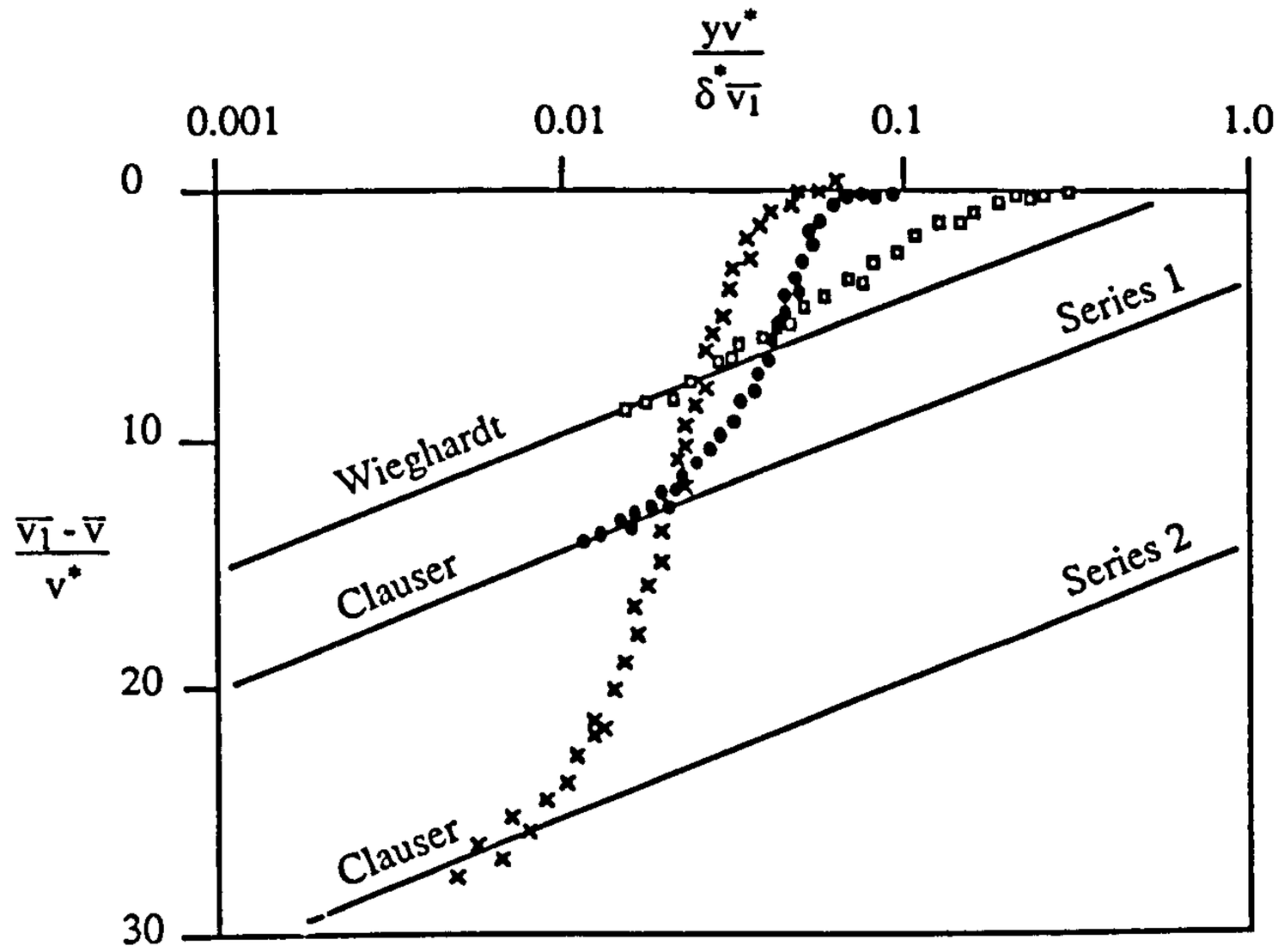

Figure 2.8. A comparison of the flow profiles of three documented experimental equilibrium flows, after Coles (1956).

These results show striking resemblance to one another, each displaying marked 'antisymmetry' about the midpoint. At this stage in the analysis, Coles then plotted an arbitrary profile taken from a non-equilibrium flow and found the same behaviour there. This allowed Coles to rewrite equation 2.36 as

$$\frac{\overline{v}}{v^*} = f\left(\frac{yv^*}{\nu}\right) + \frac{\Pi}{\kappa} w\left(\frac{y}{\delta}\right) \tag{2.39}$$

The introduction of a second universal function to the mean velocity profile, used to describe the departure from the logarithmic law, is then Coles' wake hypothesis, the function $w\left(\frac{y}{\delta}\right)$ being the law of the wake. Coles' law of the wake then provides a complete and fairly accurate description of flows, whether in equilibrium or not (Das, 1988).

Coles argued that if Π were independent of x then the functions $g\left(\Pi, \frac{y}{\delta}\right)$ and $\Pi w\left(\frac{y}{\delta}\right)$ would be functions of $\frac{y}{\delta}$ alone. This argument corresponded with Clauser's definition of an equilibrium flow. However, Coles' work is felt to be more far reaching than that of Clauser; although equation 2.39 is a restricted form of equation 2.37 (in turn a special case of equation 2.36) it is considered to apply to non-equilibrium flow.

To test the validity of the wake hypothesis, Coles required to define the boundary layer thickness, δ, and to prescribe a normalizing factor for the function w. The displacement thickness, δ^*, may be computed from equation 2.32 and used in conjunction with the mean velocity profile of equation 2.39 to provide

$$\delta^* = \delta \frac{v^*}{\overline{v}_1}\left(\frac{1}{\kappa} + \frac{\Pi}{\kappa}\int_0^{w_1} \frac{y}{\delta} dw\right) \tag{2.40}$$

where w_1 is set to be the maximum value of w.

As such, a convenient first normalizing condition is

$$\int_0^{w_1} \frac{y}{\delta} dw = 1 \tag{2.41}$$

and a second condition is suggested by the nearly antisymmetric form of the observed curves. The maximum value of w occurs very near to $\frac{y}{\delta} = 1$ provided that

$$w_1 = w(1) = 2 \tag{2.42}$$

The parameter Π was then found to be related to the local friction coefficient, $C_f = 2v^{*2}/\overline{v_1}^2$, by

$$\frac{\overline{v_1}}{v^*} = \frac{1}{\kappa}\ln\left(\frac{\delta v^*}{\nu}\right) + B + \frac{2\Pi}{\kappa} \tag{2.43}$$

and to the displacement thickness by

$$\kappa\frac{\delta^*\overline{v_1}}{\delta v^*} = 1 + \Pi \tag{2.44}$$

By hypothesis, $w\left(\frac{y}{\delta}\right)$ is an universal function so that δ is uniquely defined in terms of δ^* by the normalizing conditions of equations 2.41 and 2.42. When considered with equations 2.43 and 2.44, plus the identity

$$\left(\frac{\delta^*}{\delta}\right)\left(\frac{\overline{v_1}}{v^*}\right) = \frac{\left(\frac{\delta^*\overline{v_1}}{\nu}\right)}{\left(\frac{\delta v^*}{\nu}\right)} \tag{2.45}$$

all five dimensionless parameters $\frac{\overline{v_1}}{v^*}$, $\frac{\delta^*}{\delta}$, $\frac{\delta v^*}{\nu}$, $\frac{\delta^*\overline{v_1}}{\nu}$ and Π or $\frac{\delta^*\overline{v_1}}{\delta v^*}$ are determined. A complete analytic description of the mean velocity field is then provided, which implies complete knowledge (at least within the boundary layer approximation) of streamline pattern, shearing stress field and the local rate of transfer of energy from the mean flow to the turbulent flow field.

Practical usage of Coles' law of the wake is discussed by White(1991), who notes that a curve fit may be provided for the function w as

$$w\left(\frac{y}{\delta}\right) = \sin^2\left(\frac{\pi}{2}\eta\right) = 3\eta^2 - 2\eta^3 \tag{2.46}$$

where $\eta = \frac{y}{\delta}$.

Typical results of this operation may be seen as Figure 2.9 below

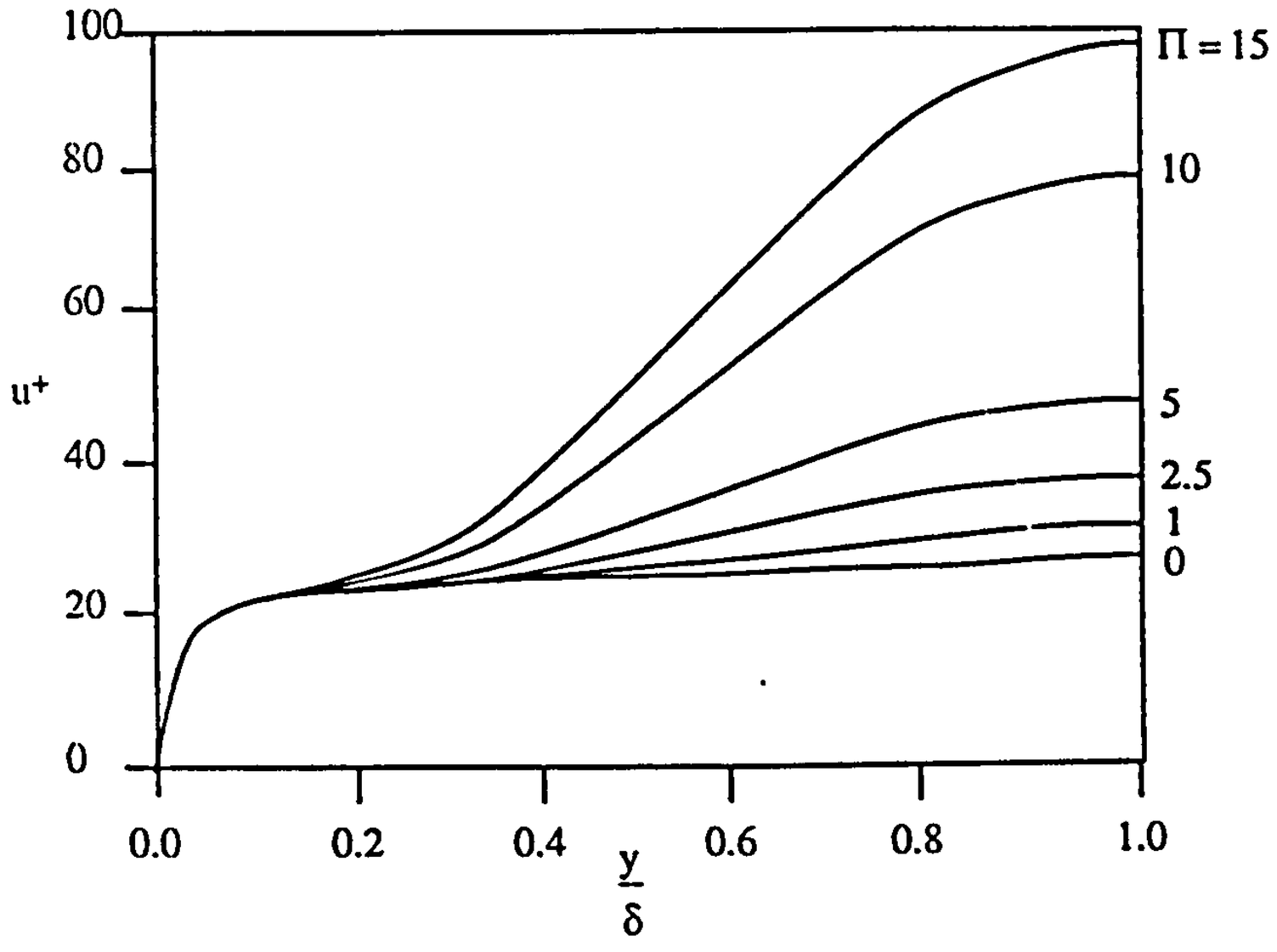

Figure 2.9. Turbulent velocity profiles computed from Coles' law of the wake, after White(1991).

Note that the curve $\Pi = 0$ corresponds to the pure law of the wall. The above curves compare well with observed results, as noted by Coles, and are easy to compute; if normalized to $\frac{\bar{v}}{\bar{v}_\infty}$ and replotted, they give results very similar to Figure 2.4.

The usefulness of the wake component of equation 3.39 may be demonstrated by considering the case where v^* tends to zero, when $\tau_0 \rightarrow 0$, as separation is approached. After expressing Π in terms of δ, δ^*, $\overline{v_1}$ and v^* using equation 2.44, then

$$\frac{\bar{v}}{\overline{v_1}} = \frac{1}{2} w\left(\frac{y}{\delta}\right)$$

This result does not include the terms κ or ν and implies that the flow at a point of separation or reattachment is locally a pure wake flow.

2.4.4. Range of Application of Wall Models.

For an adverse pressure gradient, as separation is approached, the scale v^* tends to zero and the terms in Clauser's and Coles' equations that account for pressure gradient tend to infinity. As the logarithmic layer thins and ultimately vanishes, use of wall co-ordinates and hence of v^* becomes futile. The work of Perry and Schofield (1973) and of Schofield (1981) then proposed an experimental profile correlation based upon $y^{1/2}$, supported by the work of Mellor and Gibson (1966). The Schofield-Perry law gives a good description of flows with strong adverse pressure gradient, where the maximum shear in the boundary layer is $\tau_{max} \geq 1.5\ \tau_0$.

White (1991) compared Coles' and Schofield-Perry's laws with two experimental non-equilibrium flows. Coles' law gave fair agreement, with those discrepancies observed being attributed to uncertainty in prescribing δ, the boundary layer thickness. The Schofield-Perry distribution also performed well, provided an appropriate scaling velocity v_s, was selected.

The preceding similarity laws, describing the boundary layer have been successfully used in a range of momentum integral analyses to study the nature of bounded turbulent flows. However, where knowledge of the entire fluid continuum is desired or where more detailed boundary layer data is required, such as turbulent shear stress, r.m.s. turbulent fluctuations or complete velocity profiles, then recourse is sought to turbulence modelling.

2.5. Approaches to the Modelling of Turbulent Flows.

For a two-dimensional turbulent boundary layer, the only unknown is the turbulent shear, $-\rho\overline{v'_x v'_y}$. The traditional modelling assumption of Boussinesq (1877) draws an analogy to molecular shear, where the turbulent shear is equated with an eddy viscosity, μ_t. Prandtl's mixing length theory (1925) relates μ_t to the local velocity gradient and to a characteristic length scale, l_m. Experimental evidence suggests that for the outer layer, $\mu_t >> \mu$, the laminar viscosity. So a turbulent shear layer has high apparent viscosity in the outer layer, rapidly decreasing across the inner layer. As such, turbulent velocity profiles are very steep close to the wall, notionally requiring mathematical models to concentrate computational effort in the vicinity of the wall. van Driest (1956) provided an eddy viscosity model for the inner and overlap layers that incorporated a damping factor

to cater for the decreasing influence of molecular viscosity moving away from the wall. Again, the presence of a pressure gradient complicates the analysis as the modelling assumption that the total shear stress near the wall is constant no longer holds true.

A number of different approaches to turbulence modelling can be seen to use the eddy viscosity concept (White, 1991) as

i) zero equation models, using a simple mixing length model,
ii) one equation models, using a transport equation for turbulent kinetic energy and
iii) two equation models, using transport equations for both turbulent kinetic energy and turbulent rate of dissipation

and more complex methods, modelling the turbulent stresses directly may be seen as

i) Reynolds stress models, providing either transport equations or algebraic approximations to the turbulent fluctuations and
ii) direct numerical simulation.

In seeking to model a bounded turbulent flow numerically, a compromise must necessarily be drawn between accuracy of results, in comparison with experimental data, and computational expense. Where computational techniques capture boundary layer behaviour by use of dense computational meshes, the storage requirements may outweigh the advantages of increased accuracy and even preclude analysis of the full continuum.

With regard to two-equation eddy viscosity modelling, the k-ε model provides a balance between model sophistication and computational economy (Haroutunian and Engelman, 1991). However, as it does not cater for the effects of molecular viscosity, to model a bounded flow, it requires either to be reformulated in a low Reynolds number form or to be used in conjunction with a wall law model.

The standard k-ε model, proposed by Jones and Launder (1972) offers transport equations for turbulent kinetic energy, k, and the turbulent rate of dissipation, ε. The model contains five empirical constants, determined from experimental data and numerical tuning. As molecular viscosity and sub-layer damping effects are neglected, the model is only valid from the overlap layer outwards into the freestream (White, 1991).

Low Reynolds number versions of the k-ε model typically introduce laminar

viscosity functions into the model equations, as well as viscosity-dependent adjustments to the standard model constants.

Rodi (1991) compared the behaviour of the standard k-ε model with that of a low Reynolds number and a two-layer eddy viscosity model. For two-dimensional thin shear layers, where flow is predominantly in the x-direction, no separation occurs and streamwise turbulent transport is negligible. The turbulent model only has to cater for $\overline{v_x' v_y'}$ and the close alignment of the streamlines precludes numerical diffusion. As such, where poor predictions arise, they are typically due to inaccurate initial conditions or poor coding of the turbulence model.

For wall-bounded flows, the effects of viscosity and turbulence are concentrated in the near-wall region, although the outer inviscid layer is still of interest as flow losses and possible separation in the boundary layer will affect the whole flow regime. For the simplest such flow, being zero pressure gradient flow over an infinite flat plate, with low freestream turbulence and smooth, impermeable walls, Rodi noted that all the models gave good predictions. However, in the instance of significant streamwise curvature, the k-ε model predicted too slow a pressure recovery after the bend. Further, whilst surface roughness could be incorporated into the wall model used, where a pressure gradient was present, the k-ε model predicted rising skin friction with increase in pressure gradient. This was attributed to the dissipation equation where too steep a rise in length scale near the wall was observed in comparison with experimental data, suggesting that the length scale should be largely independent of pressure gradient. As such, this problem might be better analysed with a two-layer model , using a one-equation model with prescribed length scale to simulate the near-wall region.

With regard to accelerating flow, where relaminarisation may arise, the k-ε model offers better results than two-layer models with analytical length scales but as viscous effects are important over a large part of the boundary layer, low Reynolds number models might be better than wall functions.

For separating flows, wall functions have been used historically despite the predominant models of Spalding (1961) and Reichardt (1951) not being strictly valid near separation. For the case of flow over a backward facing step, Rodi noted that the standard k-ε model underpredicted the length of the recirculating zone by some 20%. Whilst the two-layer model gave better results, the necessity for a large number of computational points within the boundary layer limited its range of application.

Having noted that traditional wall law models, in not catering for the effects of

pressure gradient, tend to give poor results for accelerating or decelerating flows, the alternative within a k-ε model framework is the use of a low Reynolds number k-ε model, where the model in modified form is valid right down to the wall.

The standard, high Reynolds number k-ε model, using wall functions, relates the surface boundary conditions to a point in the continuum beyond the viscous sub-layer, hence avoiding the direct modelling of viscosity, and so is restricted to where Reynolds number is high enough for viscous effects to be unimportant. The van Driest damping function for mixing length is an alternative to this approach but in extending the validity of the k-ε model down to the wall, an increase in computational effort arises from the necessary increase in local mesh density.

Low Reynolds number models use a mixture of damping effects and direct molecular viscosity effects on the empirical constants and functions in the parent high Reynolds number k-ε model. Owing to a dearth of reliable near-wall data for low Reynolds number, these models are often prepared and honed by numerical experiments. Patel, Rodi and Scheurer (1985) reviewed eight recent low Reynolds number k-ε models, first discussing the modelling assumptions and modifications to the parent model and then testing each model for a range of cases, including low Reynolds number boundary layers, high Reynolds number flow and equilibrium flows in adverse pressure gradients.

Patel et al (1985) considered the available near-wall and low Reynolds number turbulent data to provide a basis upon which to assess the modelling assumptions. They noted that such data was limited, mainly because of probe interference effects near the wall and also problems in measuring τ_0, necessary for scaling the flow parameters. The available data, mostly for flat plate boundary layers, was important in that all the low Reynolds number models considered attempt to reproduce such near-wall effects.

In brief, the dimensionless kinetic energy, k^+, for a flat plate boundary layer, peaks at about $y^+ = 15$, providing a maximum production of approximately $k^+ = 4.5$. Beyond this, in the range $60 < y^+ < 150$, k^+ is almost constant at $k^+ \approx 3.3$.

The non-dimensional shear stress, $-\overline{uv}^+$, in the log-law region is distributed as $-\overline{uv}^+ = 1 - (1/ky^+)$ but very close to the wall varies as y^{+3}.

With regard to the turbulent dissipation rate, ε, the transport equation in the k-ε model is only truly valid for homogeneous turbulence. In the log-law region, say for $40 < y^+ < 100$, $\varepsilon \approx k$, but in the immediate vicinity of the wall, $\varepsilon = a + by^+$ and so ε is finite at the wall.

The low Reynolds number k-ε models considered by Patel et al included viscous diffusion terms and functions to modify the five constants of the standard model and also extra terms, D and E, to mimic near-wall behaviour. The models were all observed to suffer from a number of the following shortcomings

i) use of the ε transport equation may be avoided by setting $\bar{\varepsilon} = \varepsilon - D$ such that D provides $\bar{\varepsilon} = 0$ at the wall. As such, D should be assymptotic to the non-zero value of ε at the wall, so as to balance the k equation at that point. Whilst all the models did this, beyond $y^+ = 60$, $\bar{\varepsilon}$ should equal ε for vanishing D. Not all models gave this result.

ii) the standard model has five constants as C_μ, $C_{\varepsilon 1}$, $C_{\varepsilon 2}$, σ_k and σ_ε. The low Reynolds number models all employ multipliers of the first three constants as f_μ, f_1 and f_2, all tending to unity for high Reynolds number, at which point the low Reynolds number models operate on their coded values of C_μ, $C_{\varepsilon 1}$ and $C_{\varepsilon 2}$, which were not necessarily equal to those of the parent model. As the k-ε model is very sensitive to the precise values of $C_{\varepsilon 1}$ and $C_{\varepsilon 2}$, this approach results in a reduction in general validity, implying that such models should only be used in the near-wall region. Furthermore, the ε equation for zero pressure gradient relates $C_{\varepsilon 1}$, $C_{\varepsilon 2}$, σ_ε and C_μ to one another and this relationship was not satisfied by all the models.

iii) the function f_μ acts on the eddy viscosity relationship to mimic the effect of molecular viscosity on shear stress but shear stress is also depressed by fluctuations in the pressure field due to the pressure-strain correlation which is independent of viscosity and hence not dependent on Re or y^+. This function then acts to reproduce two effects that are hard to separate, yielding a numerical distribution different to that gained experimentally. Also, beyond $y^+ = 60$, f_μ should tend to unity but some models did not provide this, giving viscous damping too far out into the flow.

iv) the function f_2 modifies the destruction of turbulent dissipation at low Reynolds number. Experiments on the decay of isotropic turbulence suggest that $k \alpha x^{-n}$, for which n = 1.25 at high Reynolds number, tending to 2.5 in the last stages of decay. Some of the models gave lower decay rates near the wall. However, as f_2 tends to unity beyond Re ≈ 15, this effect is limited to the viscous sub-layer.

v) the functions f_1 and E in the ε equation provide quadratic growth in ε with distance from the wall. However, some models yield a decrease in ε as y^4 in the

logarithmic region, disappearing in the viscous sub-layer. This leads to a peak in the buffer zone and this causes a lower peak in the corresponding k value.

As such, Patel et al (1985) concluded that the eight models surveyed lacked a sound physical basis, being at best limited to specific flow regimes for low Reynolds number, from which they were derived.

In practically evaluating model performance, the models were expected to duplicate the behaviour of the high Reynolds number parent model in the freestream and for bounded flows, to mimic low Reynolds number behaviour observed experimentally. The tests included a flat plate with an equilibrium pressure gradient and one with a strong favourable pressure gradient. These flow regimes were not successfully modelled by all of the schemes tested. Patel et al (1985) concluded that for such models to be of general use, the damping function, ε, should be matched to experimental studies, that the functions f_1 and f_2 should be adjusted for mathematical consistency and that all the models reviewed required fine tuning to allow for the prediction of basic features of wall-bounded flows under pressure gradients.

Another approach to the resolution of velocity profiles within turbulent boundary layers is the application of second moment closure methods (Launder and Shima, 1989). Here the turbulent stresses are modelled directly by preparation of suitable transport equations or algebraic approximations. With regard to the problem of closure, an exact, closed set of transport equations can be derived from the instantaneous form of equations of motion (Hinze 1975) (where each Reynolds stress component is defined in terms of turbulent generation, viscous dissipation, destruction and redistribution due to pressure fluctuations and turbulent diffusion) but such equations require knowledge of further unknowns. These new unknown quantities may be clarified by preparation of a further set of transport equations, which, in turn, yield more unknowns. This spiralling process is a classic closure problem and demonstrates why so much attention has been paid to approximations to the Reynolds stresses. Again, as for the low Reynolds number methods, wall functions are dispensed with and the turbulence model is operated right down to the wall. In a paper by Leschziner (1989), the algebraic stress method was used to reproduce the experimental results of Driver and Seegmiller (1985) who studied a range of flows over backward facing steps. Leschziner's results showed better predictions than similar studies using the standard k-ε model. However, the computational effort required is highlighted by a similar study by Launder and Shima (1989). Effective modelling of the

boundary layer required some seventy nodes distributed across the boundary layer, many of which were sited in the viscous sub-layer.

Summing up the various approaches to bounded flows considered so far, it can be seen that the standard k-ε model, in conjunction with traditional wall laws, is unable to replicate the effects of pressure-driven flows, whilst the use of two-layer models, low Reynolds number models and second moment models typically result in excessive computational effort. However, a number of wall laws for pressure gradient analysis have also been considered that might be of merit in enhancing the basic high Reynolds number k-ε model.

2.6. Application of Wall Laws to Complex Flows.

For a wall model, offering a velocity profile for the viscosity-affected region of the boundary layer to be of general use, it must be able to cope with the effects of pressure gradients and hence with separation effects.

Schofield (1986) presented a discussion of the nature of separating flows and detailed an extension to the Schofield-Perry power law (1981). Schofield noted that no single closure hypothesis was available for both developing attached boundary layers in adverse pressure gradients and for detaching and fully detached shear layers and that analysis hinged upon the use of zonal models.

With regard to the use of similarity profiles for separating layers, Schofield suggested that whilst Coles' law (1956) was very robust for attached boundary layers, it was only valid up to the point of separation. Turbulent boundary layer separation is a process and not an event (Kline, Bardina and Strawn, 1983). Flow near the wall spends an increasing proportion of time in backflow as an observer moves downstream through the detachment zone. The region is intermittent in nature as three-dimensional elements of backflow appear and disappear in a random manner near the wall. The appearance, growth rate and lateral position of these elements is unpredictable, leading to multiple instantaneous detachment lines. As the separation bubble develops downstream, the magnitude and duration of flow reversal elements rises and the flow becomes increasingly three-dimensional. With negligible production of kinetic energy in the backflow, classical wall laws fail as they depend upon a local balance between k and ε. Traditional wall laws then become inappropriate as the flow now scales on different variables. Flow reversals first occur near the wall and then, as detachment develops with downstream distance, they

increase in frequency and extend out from the wall. As such, the deviation from the logarithmic law begins at the wall and extends up through the boundary layer with distance downstream.

To get an accurate value of τ_0 from an experimental velocity profile, the method must account for reversed flow contamination effects on the measured mean velocity. As such, any recording technique used to this end must be able to capture both the magnitude *and* direction of the local flow, whilst offering as little disturbance as possible to that flow. In consequence, the quality and quantity of near-wall data for separating flow is limited (Schofield, 1986), which poses a problem when seeking to validate any proposed 'universal' wall model. Whilst turbulence measurements suggest the low values of τ_0 in a detached region have little effect on mean flow development, any analytical approach which scales on v^* will then fail in a region with intermittent flow reversal as τ_0 will have a mean value of zero near separation.

As already noted, Schofield (1981) proposed such a flow to be governed by τ_{max} and gathered experimental evidence to show that boundary layers under adverse pressure gradient and near detachment are dominated by large scale turbulent structures in the outer layer which scale with v_s, directly related to τ_{max}. Schofield's model, for moderate to strong adverse pressure gradients, including attached flow immediately preceding separation, holds for $\tau_{max} \geq \frac{3}{2}\tau_0$, on the assumption that τ_{max} is unaffected by intermittent or mean flow reversals near the wall.

Now the law of the wall is unlikely to cease abruptly at separation but should still hold for the outer portion of the boundary layer, where a large scale coherent turbulent structure still exists, and hence be able to determine part of the mean flow profile. After separation then, the law of the wall should still describe the forward flowing outer portion of the boundary layer, riding over the mean reversed flow. As such, some portion of the separation bubble should be excluded from analysis by positioning the origin for Schofield's defect law away from the wall, the natural choice being the mean dividing streamline, providing continuity between Schofield's analysis and the upstream attached flow. This fits with experimental observations of the outer layer structure being little affected by detachment and of its dominating the flow from the outer edge of the boundary layer down to the dividing streamline.

Hence Schofield provided a power defect law to complement the shrinking law-of-the-wall-zone for all the forward flowing segment of the separation bubble. The analysis still excludes the backflow region, for which little data of common intermittency was

available to Schofield although it was postulated that scaling might be affected by reference to the maximum reversed velocity.

Dengel and Fernholz (1990) investigated a range of pressure gradient flows such that τ_0 was finite but close to zero over a section of the test boundary. Their data suggested that not only was Coles' law unsuited to separating flows but that Schofield's analysis was limited to the immediate vicinity of separation. Their work suggested that intermittent backflow begins well upstream of the mean separation point and that the first portions of reversed flow occur at the point where the log-law vanishes. Dengel and Fernholz then noted that the boundary layer shape changes continuously under adverse pressure gradient and that a universal profile such as that of Schofield is hence unlikely to arise. However, for flow in the immediate vicinity of separation, they presented a seventh-order polynomial profile.

In a slightly different approach, Haroutunian and Engelman (1991) presented a special wall model element for finite element analysis, using van Driest's approach for modelling near-wall viscosity. In order to overcome the problem of excessively fine near-wall meshing, the elements operate a form of Reichardt's law to model the viscous sub-layer and buffer zones up to $y^+ \geq 30$. As such, the standard k-ε model is run right down to the outer edge of this layer of special elements lining the model wall.

Reichardt's law is formulated as shape functions matched to the element by the dimensionless element height, which they related to y^+. However, these shape functions are not scaled on v^* but by $k^{1/2}$ taken at the outer edge of the element. Whilst this offers a more fundamental velocity scale, the wall law is no longer strictly related to near-wall parameters.

As the k-ε model is not solved in the viscosity-affected area, the eddy viscosity is modelled within the elements using the van Driest model, with the length scale related to y^+ in terms of $k^{1/2}$ away from the wall. As the k-ε model operates over a truncated domain, boundary conditions for k and ε are required at the model interface, being given as Neumann conditions for k and with ε set as an analytical function of k.

For the approach to work, the element must fully contain both the viscous sub-layer and the buffer zone lest the k-ε model be applied in a low Reynolds number region. The shape functions resolve the sharply varying flow profile across one elemental layer, hence providing a method with the benefits of van Driest but without the need for a very fine mesh. However, it will be remembered that Reichardt's law was not prepared for pressure-gradient-driven flows.

Whilst Schofield's work is restricted to medium to strong pressure gradients, a number of attempts have been made to extend the more general Coles' law to describe separating flows. The basic problem with Coles' law under such conditions is the use of v^* as a scaling factor since at separation, $\tau_0 = 0$.

Kline, Bardina and Strawn (1983) noted that as the skin friction approaches zero at the separation point, so does τ_0. However, beyond this point, τ_0 becomes negative. As such, either side of the separation point, a viable v^* value denoting the sense of flow may be offered by using the modulus of τ_0 to calculate v^*, which is then given the same sign as τ_0. Kline et al then reformulated Coles' law in terms of a wake amplitude and a dimensionless shear velocity. In comparison with experimental test data, the method appears to work well for both attached and detached flow over impermeable surfaces, such as the data of Kim (1978) for the backward facing step.

Das (1987, 1988) presented an integral method for studying two-dimensional incompressible boundary layers under arbitrary pressure gradients, based on Coles' law. The wall-wake velocity profile and the equations of continuity and conservation of momentum were integrated across the boundary layer in terms of u^+ and y^+ to yield a simple relationship in terms of the shear velocity. This could then be used to calculate the skin friction, boundary layer thickness and shear stress at the wall. Das (1987, 1988) considered experimental data from a range of flows including near-separating, separating, reattaching and six favourable pressure gradient flows, from which an empirical relationship between Coles' wake parameter and Clauser's equilibrium pressure gradient was prepared. Since the equilibrium pressure gradient can be determined simply from knowledge of the shear stress at the wall, the displacement thickness and the streamwise pressure gradient, then this empirical relationship simplifies the application of Coles' law to arbitrary pressure gradient flows. Das's model, relating Coles' wake parameter to the pressure gradient, was also used by Wahls, Burnwell and DeJarnette (1989) in their study of compressible turbulent boundary layers.

Das then extended the method by inverting it such that the displacement thickness profile was used as input to the solution, with the intention of calculating the velocity profile for separating flows. The basic problem of Coles' law failing as τ_0 (and hence v^*) tends to zero at separation was then addressed by re-expressing the wake parameter in terms of a wake velocity which remains finite across the zone of separation, varying smoothly from the attached to the detached flow region. This modified form of Coles' law was then compared with test data for flow separation under strong positive pressure

gradient, in a diffusing passage and for flow around an aerofoil-like body. Das thus demonstrated that this method gave good results for skin friction, the development of displacement thickness and for the velocity distribution within the separating zone.

Having reviewed a range of wall laws for use under a range of diverse flow conditions, Coles' law is felt to provide the widest scope for analysing a variety of flows under arbitrary pressure gradients. To date, Coles' work, subject to various modifications necessary to extend its range of application, has typically been confined to momentum integral analyses. However, as its profile is relatively simple to compute, it is to be forwarded here as a possible tool for use in the construction of an enhanced wall law to complement the standard, high Reynolds number k-ε model.

2.7. The Case for an Improved Wall Law for Use With the Standard k-ε Turbulence Model.

Prior to setting down the projected aims of this study, it is of use to take an overview of the previous work that has been considered in this chapter.

In reviewing the major techniques currently available for analysis of fluid continua, no one method has been found to be universally applicable. In the approach of direct numerical simulation, where an exact solution to the Navier-Stokes equations is sought, the computational effort required in resolving the finest scales of turbulent decay precludes its application to general flow problems; analysis is confined to low Reynolds number flows and even then is regarded as a tool limited to the study of the nature of turbulence. Second moment techniques are similarly computationally expensive - by avoiding the use of empirical approximations to the Reynolds stresses, the increased number of transport equations needing to be solved again limits the complexity of the flow regime that can be modelled on a given computer system.

In turning to the use of eddy viscosity models, the range of approaches, each with their own limitations, presents no obvious general candidate. The Reynolds stresses are modelled by analogy to the viscous stress of the fluid, with models being classified by the number of transport equations used to that end. The two-equation k-ε model has enjoyed widespread use but, whilst it is considered to offer a balance between accuracy of results and computational expense, in the near-wall region, the assumptions upon which it is based break down. Extensions to this scheme, such as low Reynolds numbers adaptations and two-layer models again have drawbacks. In the former case, the physics

of the model are dubious and in the latter, the necessary spatial discretization of the near-wall layer (operating a one-equation turbulence model) limits the range of geometries to which it can be applied usefully.

The end goal of CFD within an engineering environment is to provide a practical and robust tool for the simulation of as wide a range of real flows and geometries as possible. As such, use of the k-ε turbulence model within a finite element framework is expected to prevail for some time to come. Some technique is then required to account for the effects of viscosity in the near-wall region, and hence the sharply varying local velocity gradients, without recourse to an excessively fine computational mesh. Practical engineering problems will typically display complex geometries and transience of flow. As such, any near-wall model must be able to predict the effects of separation and recirculation, thus considering the influence of the local pressure gradient.

Whilst law of the wall models have been used in conjunction with the k-ε model for some time, beyond the specific instances for which they were prepared, their more general applicability has not been greatly questioned. The 'traditional' expressions of the law of the wall, in the works of Reichardt (1951) and of Spalding (1961) make no allowance for pressure gradient and hence should be limited to the simplest of geometries. Furthermore, extensions to this approach, such as that of Haroutunian and Engelman (1991) compound this oversight by calculating the scale for u^+ and y^+ in terms of parameters away from the solid boundary, contrary to the work of Prandtl (1933). Even where the behaviour of recirculating flow has been considered, as with Schofield (1981, 1986), the resulting model is limited to very specific flow regimes.

Of the studies reviewed, it is only in the work of Coles (1956) that a wide-ranging wall law is seen. Coles' law of the wake encompasses the traditional law of the wall and further seeks to cater for the local pressure gradient. The more recent work of Das (1987, 1988) makes the use of Coles' law much more approachable, whilst that of Kline, Bardina and Strawn (1983) seeks to take Coles' law beyond the point of separation. Coles' law then appears to display those characteristics which, in union with the standard high Reynolds number k-ε turbulence model, would provide a general flow modelling technique without the need for superfine spatial discretisation.

With regard to the abandon with which traditional wall laws are erroneously applied, reference may be made to two recent papers. Taklanti (1993) discussed the use of CFD codes in conjunction with turbulence and combustion models for the purpose of simulating three-dimensional gas flow and combustion in "real and complicated"

geometries. Test cases were cited as the three-dimensional inlet ports and inlet manifold to an internal combustion engine, having been identified as instances of highly complex and transient flow. Analysis was then performed using the k-ε model with a basic logarithmic wall law. For steady flow through an idealized, axi-symmetric inlet port, recirculation effects were systematically underpredicted in comparison with the results of laser doppler anemometry experimentation. (This is in keeping with Rodi (1991), who notes the tendency of this type of modelling combination to curtail recirculation processes.) Taklanti went on to model the 'true' geometry of the inlet ports but the resulting very small elements restricted solution to a laminar simulation. Finally, an entire inlet manifold was modelled, first for steady flow (having only one inlet port open) and then for the transient case, with the cycle of inlet port events being reproduced through time.

Taklanti presented no experimental data against which to gauge the efficacy of the manifold simulations, merely noting that further progress in turbulence modelling techniques was necessary. Whilst this comment is no doubt true, no allusion was made to the effect of the demonstrated rapidly varying pressure distribution upon the wall modelling assumptions used. Where there is a marked pressure gradient, changing in both space and time, the traditional wall law is clearly deficient.

Baxendale (1993) similarly used the k-ε - law-of-the-wall combination to model the three-dimensional, non-reacting flow field within various types of catalytic converters, being an instance where gas flow distribution and efficiency of heat exchange are of great interest. Given the fine scales of geometry within such devices, the flow channels were modelled by porous media elements, with the need for fine meshing thus confined to the vicinity of the housing walls. Despite these simplifications, Baxendale was still only able to perform steady-state modelling of the flow, arguing that this at least offered *some* basis for comparison between different catalytic converter designs. Again, the limitations of the wall modelling technique used were not considered. More significantly, Baxendale stressed the need for 'user-friendly' simulation tools, where the user need not be minutely conversant with the mathematics or physics of that tool. If this requirement is to be met, then it is inappropriate to offer up a modelling technique for general use that is so restricted in its range of valid application.

To date, no paper has been encountered that discusses the variation in y^+ under a pressure-gradient-driven flow, let alone for the case where that flow is transient in nature. That the established wall laws are zonal in veracity with regard to the ambient pressure gradient is clear: that their usefulness is dependent upon the local y^+ value falling within

prescribed bands has been less clearly commented upon. In a flow with varying pressure gradient, the shear stress at the wall, and hence y^+, will be a function of time. As such, the wall model used must not only account for local pressure gradient but also be valid across the widest possible range of y^+ values encountered. For instance, the model of Haroutunian and Engelman (1991) collapses when y^+ falls below thirty and that of Spalding (1961) has only been verified up to $y^+ \approx 300$.

2.8. Intended Scope of Current Work.

From the preceding discussion of Section 2.7, the aims of the current work may be summarized as

i) consideration of the effectiveness of currently used wall laws through a comparison between experimental work and CFD simulations,
ii) demonstration of the need for an improved wall model, based upon an investigation of the variation in y^+ and pressure gradient for transient flow and
iii) development of a robust wall law for use within the framework of the standard, high Reynolds number k-ε turbulence model, hence taking advantage of the near-wall saving in spatial discretisation that such schemes offer.

As such, the scope of the work may be seen to include

i) investigation of a pertinent transient flow, using basic laboratory experimentation and contemporaneous computational techniques,
ii) consideration of the observed variation in y^+ and pressure gradient under such conditions, hence commenting on the validity of current methods for transient and/or geometrically involved flows,
iii) development of an enhanced wall model based upon the work of Coles,
iv) identification of test cases suitable to appraise the workings of such a model and
v) demonstration of the behaviour of the Coles' law model and comparison with the response of established techniques for those test cases.

3. Study of Flow in an Inlet Manifold by Practical Experimentation and C.F.D. Modelling.

The validity of 'traditional' wall modelling techniques used to support the standard, high Reynolds number k-ε turbulence model was questioned in the previous chapter. Traditional wall models make no allowance for the influence of pressure gradients on the turbulent boundary layer profile. In that many common engineering flows are transient in nature, then the pressure gradient and y^+ itself would be functions of time, hence compounding the deficiencies in the modelling approach used. In Section 2.8, it was proposed that the need for a more robust wall model might be demonstrated by comparing the computational results of a traditional modelling scheme with experimental velocity profiles taken under laboratory conditions.

In seeking to compare current CFD analysis with practical flow observations, the inlet manifold of an internal combustion engine was selected as a typical engineering problem. Such devices typically possess complex geometries where flow separation might be expected. Furthermore, the time-dependent behaviour of such a flow would lead to variation of pressure gradients and recirculation events in both space and time. The works of Baxendale (1993) and Taklanti (1993) both proposed that CFD was a useful design tool for automotive components. Whilst both papers studied a real transient flow problem of complex geometry, the methods used were suspect in that traditional wall laws were used, with no discussion being given of their suitability in such circumstances. As such, in studying the three-dimensional flow through the inlet manifold of an internal combustion engine here, it is intended to focus on the behaviour of a traditional wall law under unfavourable conditions, hence highlighting any shortcomings in traditional modelling schemes when compared with experimental data.

3.1. Programme of Study for Transient Flow in an Inlet Manifold.

In desiring to compare experimental and computational analyses of the transient flow through an inlet manifold, the task may be subdivided as below

i) measurement and analysis of the practical flow using straightforward, commercial laboratory practice,

ii) development of a suitable computational mesh,
iii) obtaining a steady-state, turbulent solution to the problem, in order to study mesh sensitivity and the solution methods pertinent to three-dimensional, turbulent analysis,
iv) operation of a time-dependent, conventional, turbulent model of flow through the model and
v) comparison of experimental and computational results.

In order to provide a basis for comparison with computational results, a number of experimental velocity profiles were taken at discrete points within the inlet manifold. Flow simulation was then performed at the same nominal Reynolds number as these practical experiments, allowing for comparison of the actual, time-averaged flow with the computational models which use Reichardt's law to simulate the near-wall region.

In using conventional techniques to analyse the flow regime, having first validated the computational mesh, it was then useful to gain a steady-state, turbulent solution prior to time-dependent modelling. This provided experience in selecting suitable solution procedures for use in three-dimensional turbulent modelling, such as the solution algorithm used and what level of solution damping was required - if any - to achieve convergence. The steady-state, turbulent solution also gave a first approximation to flow behaviour in the manifold, indicating likely areas of interest in the flow. Furthermore, this solution would then provide the initial conditions required at the onset of a time-dependent, conventional, turbulent analysis.

The final stage of modelling, being a transient, turbulent model of flow through the inlet manifold, should then provide insight into the time-dependent nature of y^+ and of the local pressure gradient. Such data is expected to illustrate the limitations of established wall laws under such conditions, hence supporting the argument that a more robust wall model is needed for use in conjunction with the standard, high Reynolds number k-ε turbulence model.

3.2. Experimental Analysis of Flow Through the Inlet Manifold.

For the purpose of practical experimentation and in order to provide a basis for computational meshing of a realistic inlet manifold, a suitable engine was made available for study in the Thermodynamics Laboratories of the University of Hertfordshire. The

engine was a Perkins T4.236 direct injection diesel engine, the inlet manifold of which will now be described.

3.2.1. Physical Description of the Inlet Manifold.

The inlet manifold is depicted in Figures 3.1 and 3.2, providing an approximately isometric view of the front and rear elevations of the manifold respectively.

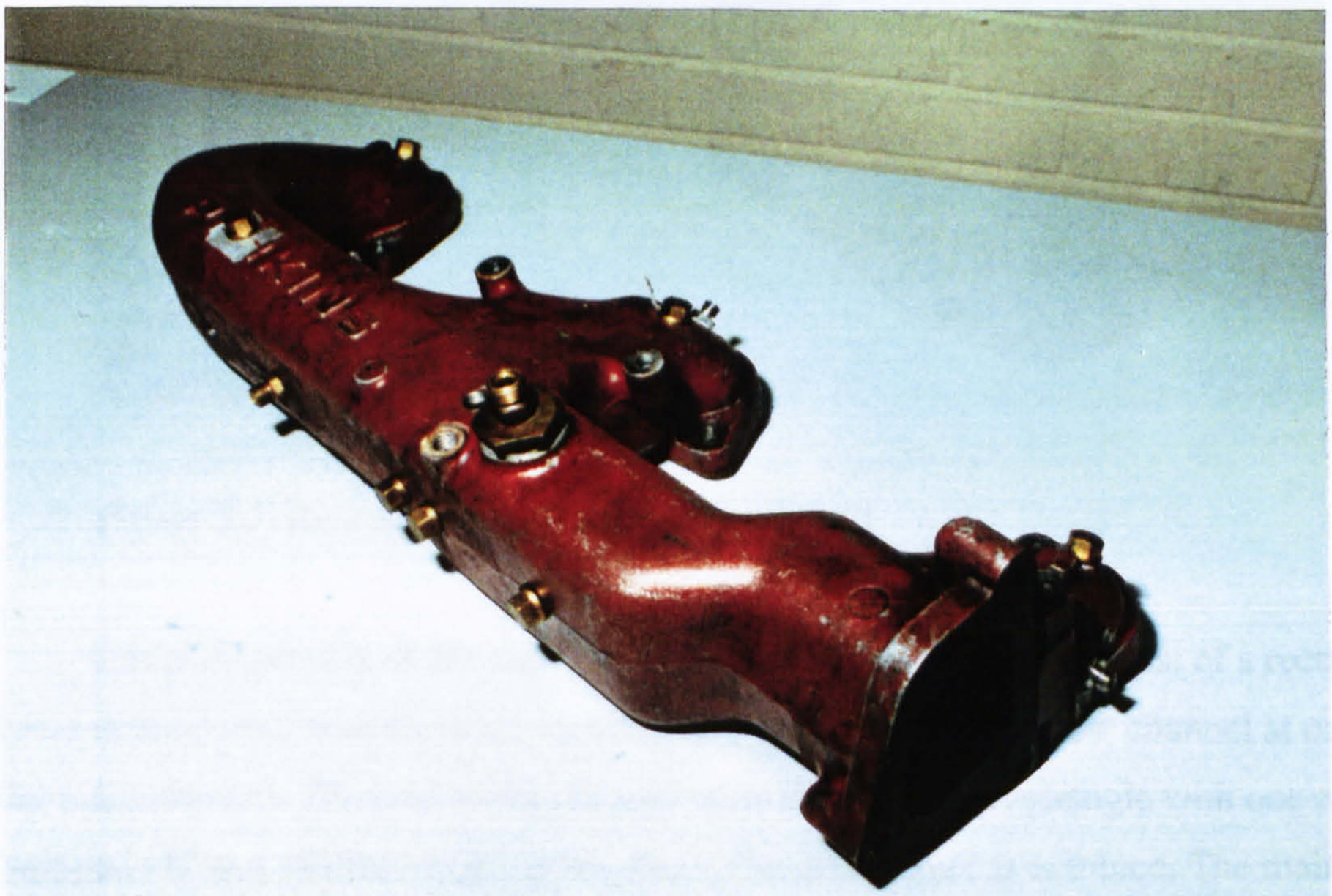

Figure 3.1. Front elevation of the inlet manifold.

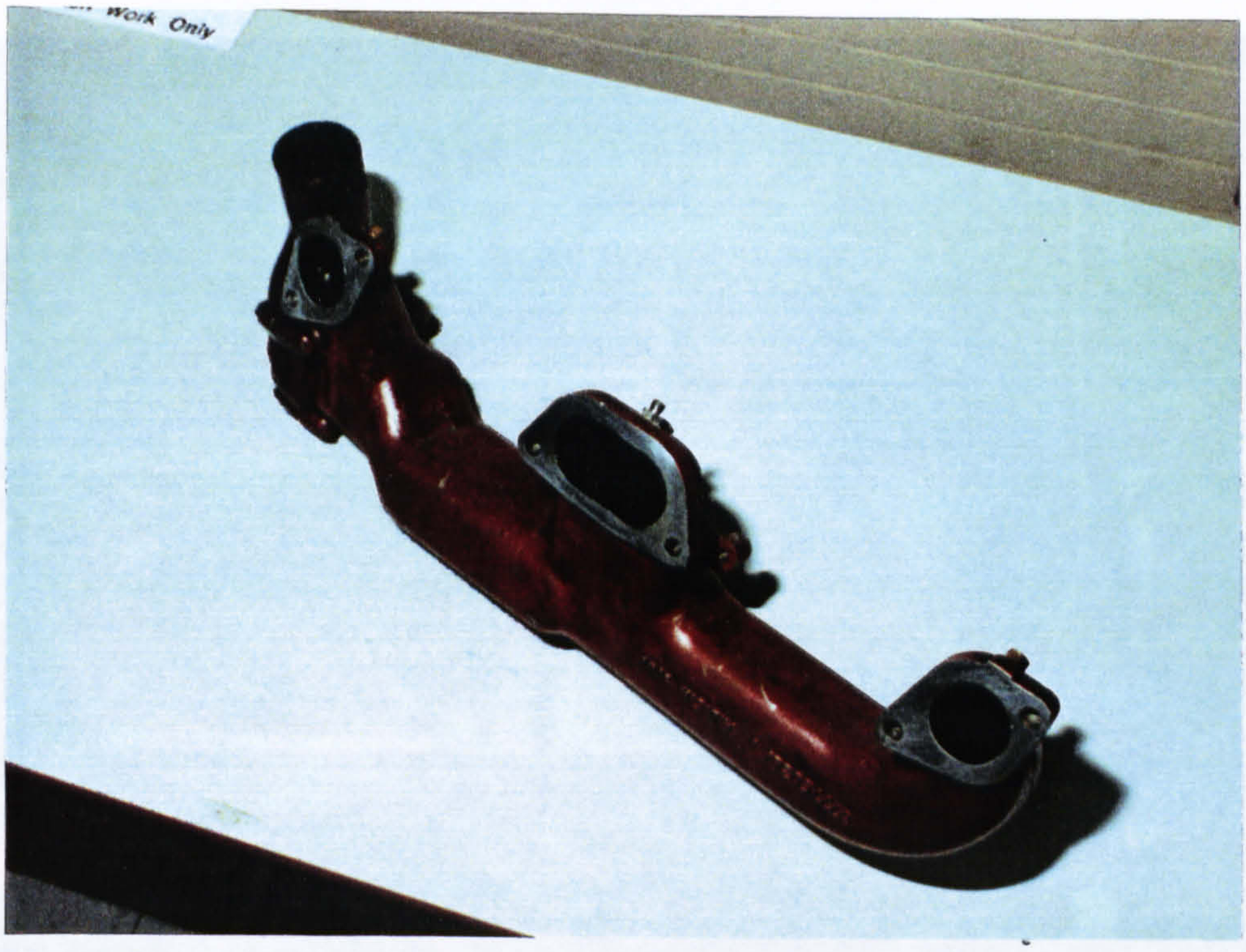

Figure 3.2. Rear elevation of the inlet manifold.

Initial inspection of the above plates shows the manifold to consist of a rectangular cross-section duct with rounded corners, having the inlet to the flow channel at one end of the main channel. The inlet to the channel takes the form of a rectangle with one corner 'snipped off' at a shallow angle, providing a five-sided duct at entrance. The main channel then connects with three side branches, in turn connecting to the four engine inlet ports. Each of these side branches is essentially wedge shaped, terminating in a bend of oval cross-section.

In situ, the inlet manifold is mounted on the engine adjacent to the exhaust manifold, as shown in Figure 3.3 below.

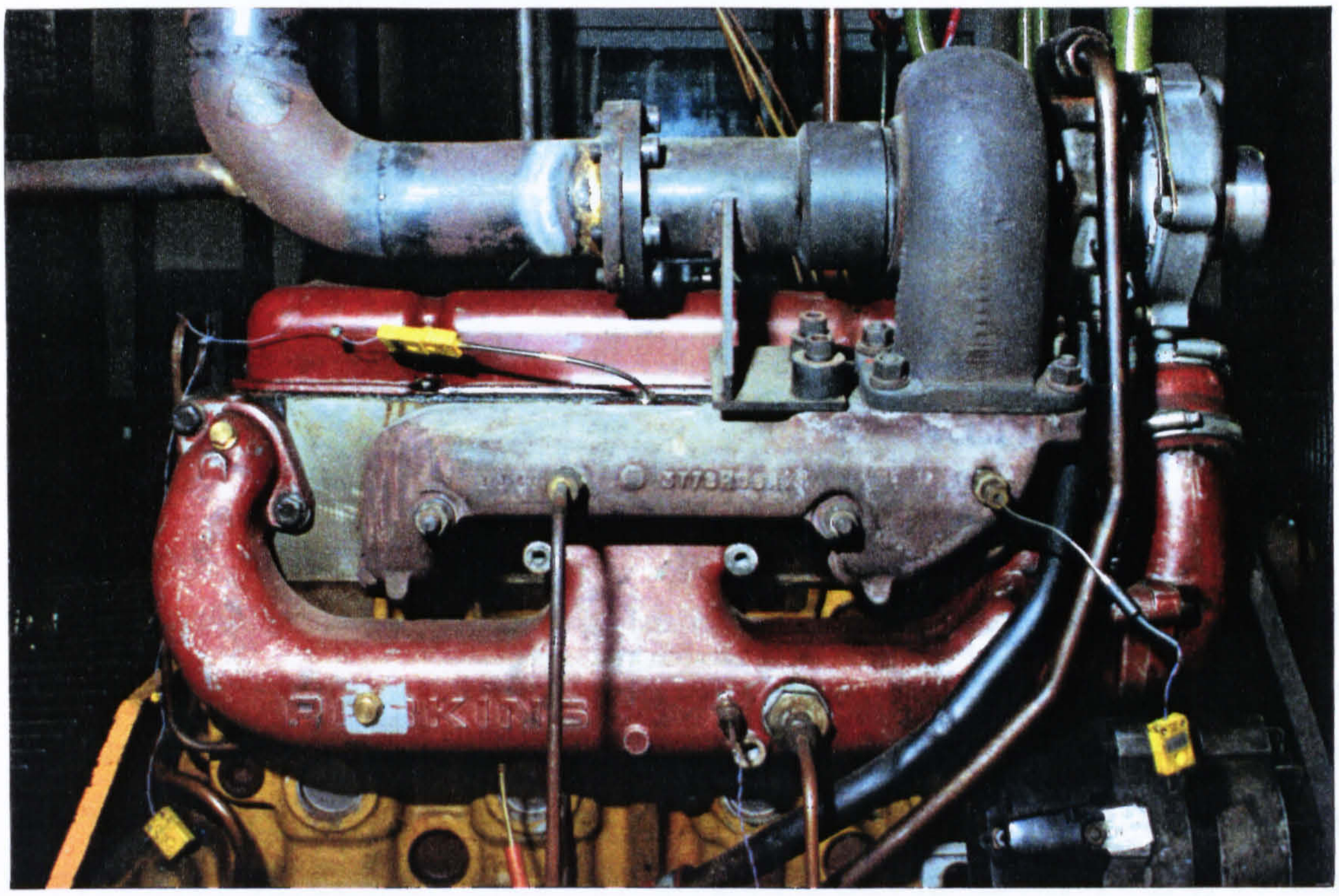

Figure 3.3. Showing the layout of the inlet and exhaust manifolds in situ.

Inspecting Figure 3.3, it can be seen that the complex curvature of the side branches of the inlet manifold partly arises from the need to fit both manifolds into a limited space. Furthermore, the positioning of the turbo-charger unit leads to the air intake to the inlet manifold being placed at one end of this duct, rather than being sited centrally with respect to the engine inlet ports, which might be expected to provide even aspiration of air into the engine cylinders. The inlet manifold layout then presents problems in terms of physical access to the flow for practical experimentation and also to computational meshing for C.F.D. analysis.

3.2.2. Experimental Design.

In designing and performing physical experiments to study flow through the inlet manifold, with a view to providing some basis for comparison with computational experimentation, a range of desirable data may be considered as knowledge of

i) inlet conditions to the manifold and
ii) velocity distributions within the manifold.

Regarding boundary conditions, where the fluid flow is confined by an impervious duct, as is the case here, then at the solid surface a 'no-slip' velocity condition will necessarily prevail. Beyond this, knowledge is then required of the distributions of velocity, kinetic energy of turbulence and rate of turbulent dissipation within the boundary layer. The very nature of flow within the boundary layer, with its attendant rapidly changing variable distributions, makes the practical measurement of such flows difficult. The presence of any probe used may well alter the flow distribution that it was intended to measure.

At inlet to the flow, the distributions of v, k and ε are likewise of great interest. A general velocity distribution might be obtained by use of some form of velocity probe but for kinetic energy and dissipation, more sophisticated techniques would be required. In fact, kinetic energy and dissipation rate data can be provided by methods such as hot-wire anemometry but such analyses are both complicated and specialised. Inspecting Figure 3.3, showing the physical layout of the inlet and exhaust manifolds and the turbocharger unit in situ, it can be seen that the flow at entrance to the inlet manifold will by no means be fully developed: the close proximity of the turbocharger to the inlet manifold (and the two right angle bends in the duct connecting these two units) suggest that a homogeneous or 'uniform' flow is likely to prevail at entrance to the inlet manifold. Access to this entrance, as depicted by Figure 3.3, is somewhat limited and, coupled with the specialised nature of hot-wire techniques, it was decided that such analysis was beyond the scope of this work.

Regarding the study of general velocity distributions within the inlet manifold, however, there are a number of points along its length where there is sufficient room externally to allow the use of a velocity probe. Figure 3.4 below shows two such stations, at 0.165 and 0.345m downstream of inlet respectively.

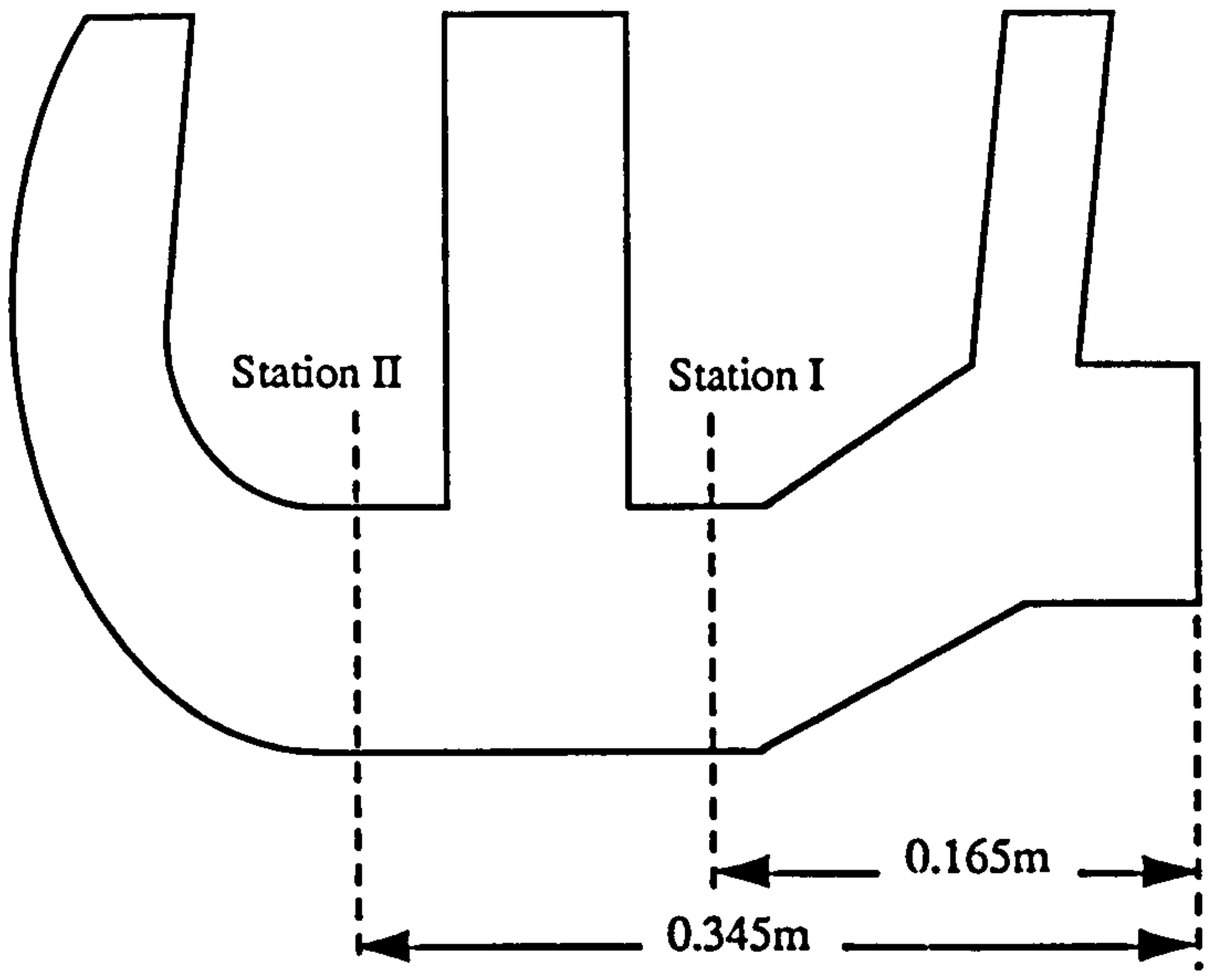

Figure 3.4. Showing the siting of test stations for a velocity probe.

Whilst it would be highly desirable to study the flow in the side branches of the manifold, connecting its main duct with the engine inlet ports, this was precluded by the lack of access to these regions. A velocity probe, such as a pitch probe or a yaw meter, in measuring the local pressures incident upon it, will yield spurious results for the reverse flow found in zones of recirculation. As such zones were predicted in these parts of the manifold by preliminary computational modelling and coupled with the desire not to extend the work to more complex studies involving, say, three-dimensional hot-wire anemometry, experimentation was ultimately limited to taking velocity samples in the main duct of the inlet manifold, at the stations depicted above in Figure 3.4.

Practical experimentation was then limited in scope to provide qualitative insight into the nature of the manifold flow. The results of these simple experiments were intended to act as a basis for comparison with the computational experiments. The design and calibration of suitable metering equipment, in the form of a combined pitch and yaw probe, and the method by which results were processed are described in Appendix A1.

3.2.3. Test Results and Discussion for Practical Experimentation.

The experimental velocity profiles will now be discussed in turn. For each station, the results show the variations in the components of the total flow velocity, v_x, v_y and v_z, for two mutually perpendicular lines drawn through the duct cross-section (and are

given in tabular form in Appendix A1). As such, they should provide some insight into the nature of the flow through the plane of either test station. However, it must be remembered that to either side of the traversing lines the flow was not measured and so care should be exercised in predicting the nature of the flow across the entire plane.

In order to provide a direct comparison between experimental and computational results, each set of results was normalized to its maximum recorded velocity. Where differences existed in the maximum recorded velocity between experimental and computational results, this then allowed for a qualitative comparison of results to be drawn. Figure 3.5 below shows the normalized velocity components for the vertical traverse of the duct at station I.

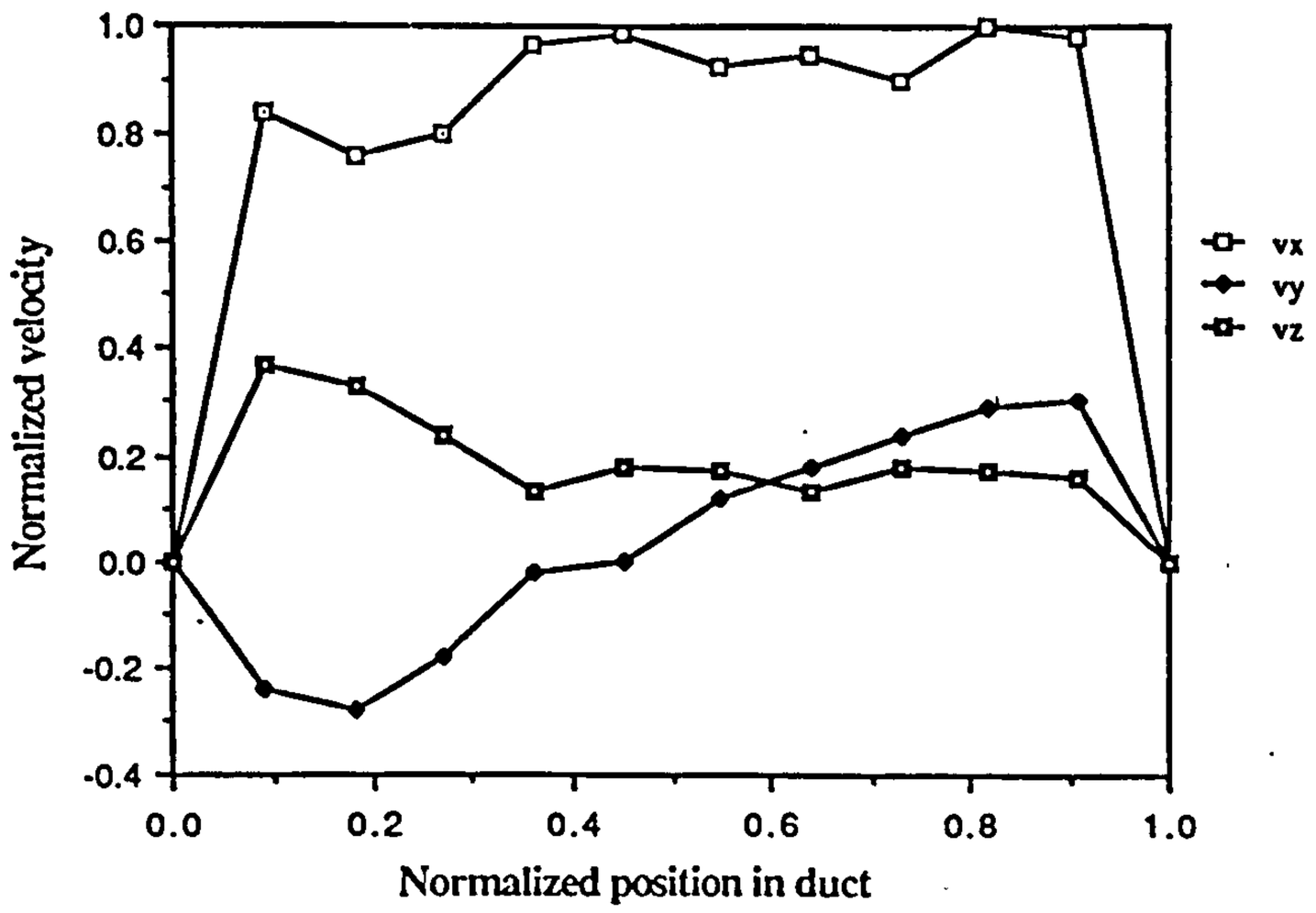

Figure 3.5. The vertical variation of v_x, v_y and v_z across the manifold at station I.

From the above graph, the major flow direction is seen to be in the x-direction, along the main length of the manifold. The velocity components v_y and v_z are less than 40% of v_x. Station I is sited just before the side branch leading to ports 2 and 3 and after the downturn in the main duct after side branch 1. The profile for v_x suggests a rapid rise in velocity away from the wall, with the normalized velocity being near unity in the upper half of the duct. This implies that mass flow through station I is greater in the upper half of the duct. The v_y profile, being negative in the lower half of the duct and positive in the upper half, predicts an anti-clockwise swirl in the flow when moving towards side branch 2/3. The v_z distribution is positive across the duct, being greatest over the bottom third of the duct.

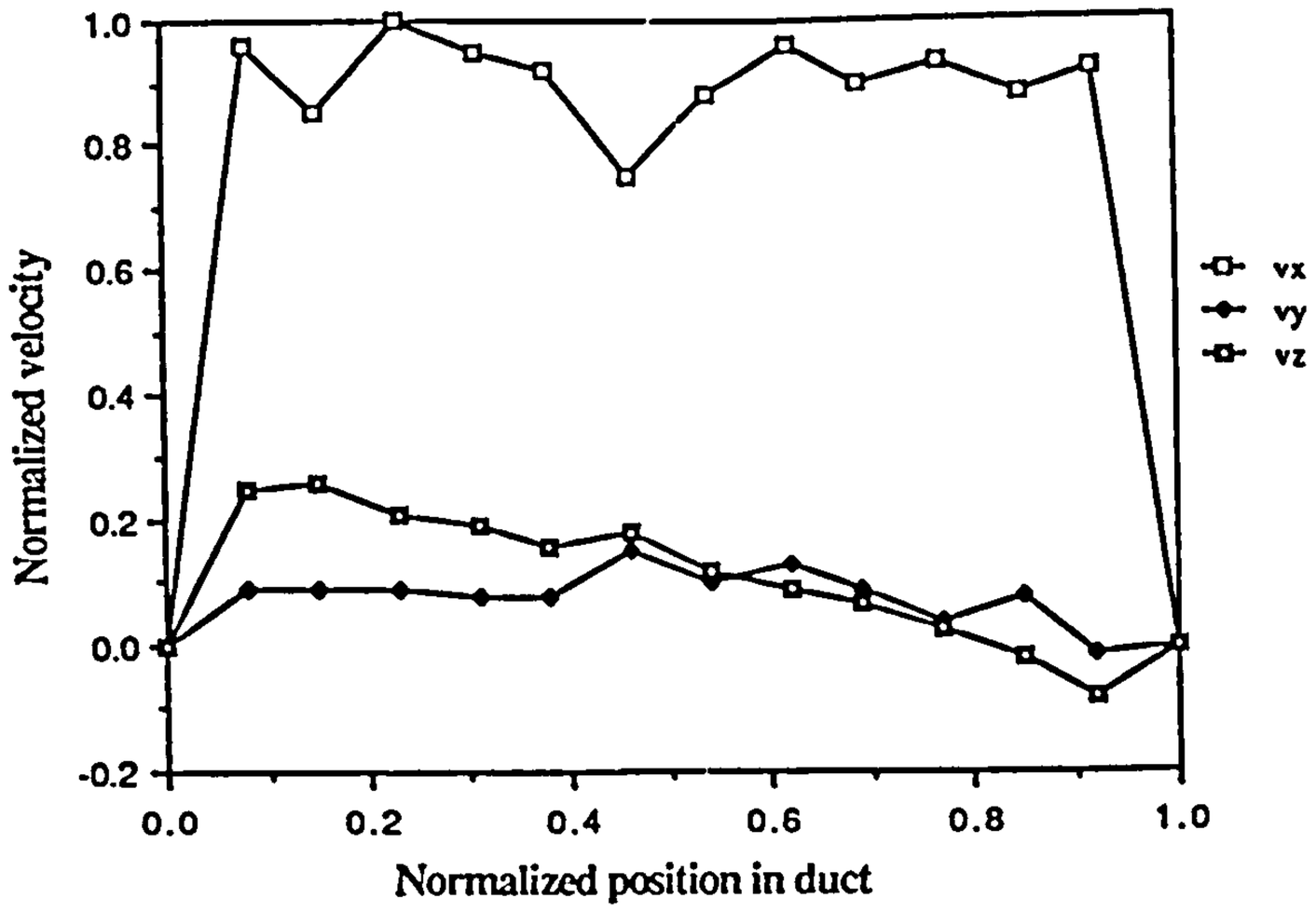

Figure 3.6. The horizontal variation of v_x, v_y and v_z across the manifold at station I.

Figure 3.6 shows the horizontal velocity distribution at station I. As with the vertical distribution of Figure 3.5, the predominant flow direction is along the x-axis, with v_y and v_z being less than 20% of v_x here. The v_y profile predicts a slight deflection in the flow towards the front face of the manifold, with v_z again suggesting movement towards the upper half of the duct.

Whilst the horizontal and vertical distributions of Figures 3.5 and 3.6 suggest that flow is predominantly in the x-direction, the combined results for v_y and v_z suggest that after accelerating around the bend downstream of side branch 1, the flow is concentrated in the upper half of the duct section and that there is a tendency in the flow towards the rear, upper corner of the duct. Side branch 2/3 is just downstream of station I and given that ports 2 and 3 should account for one half of the mass flow through the manifold, then a deflection in the flow towards this side branch is plausible.

Figure 3.7 then shows the vertical velocity distribution at station II.

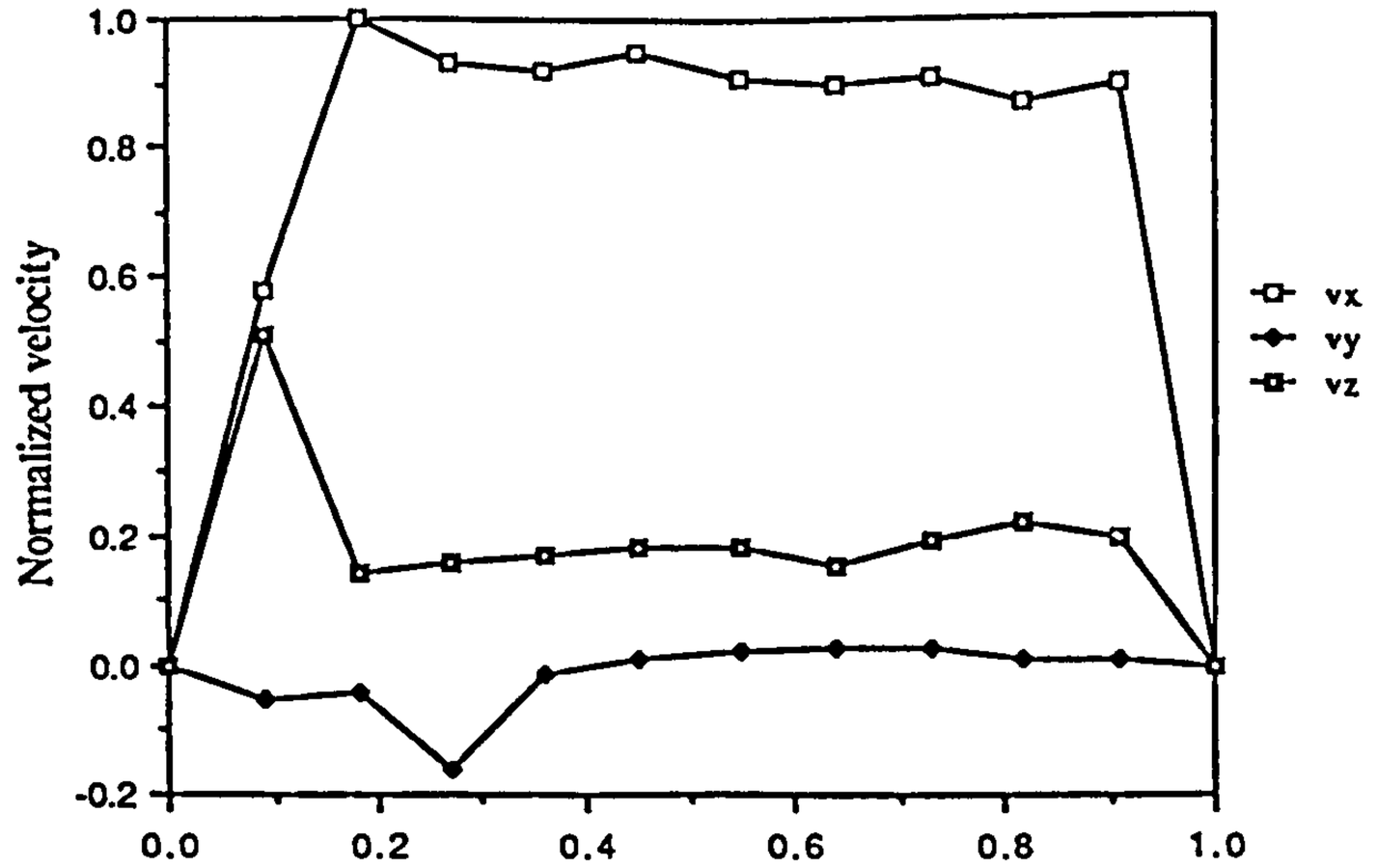

Figure 3.7. The vertical variation of v_x, v_y and v_z across the manifold at station II.

For the vertical section at station II, the flow is mainly in the x-direction, towards port 4. Whilst v_x rises rapidly towards unity away from the upper duct surface, the increase in v_x away from the base of the duct is more gradual. Whilst v_y and v_z are typically less than 20% of v_x, the result for v_z near the base of the duct, being some 50% of v_x is suspect. Such a result arises from a large flow angle, θ_v, implying locally strong shearing of the flow, for which the flow angle meter, as described in Appendix A1, is unsuitable. Generally, the v_y profile, being slightly negative, predicts minor movement towards the rear face of the duct, with the v_z profile suggesting a flow movement towards the upper reaches of the duct.

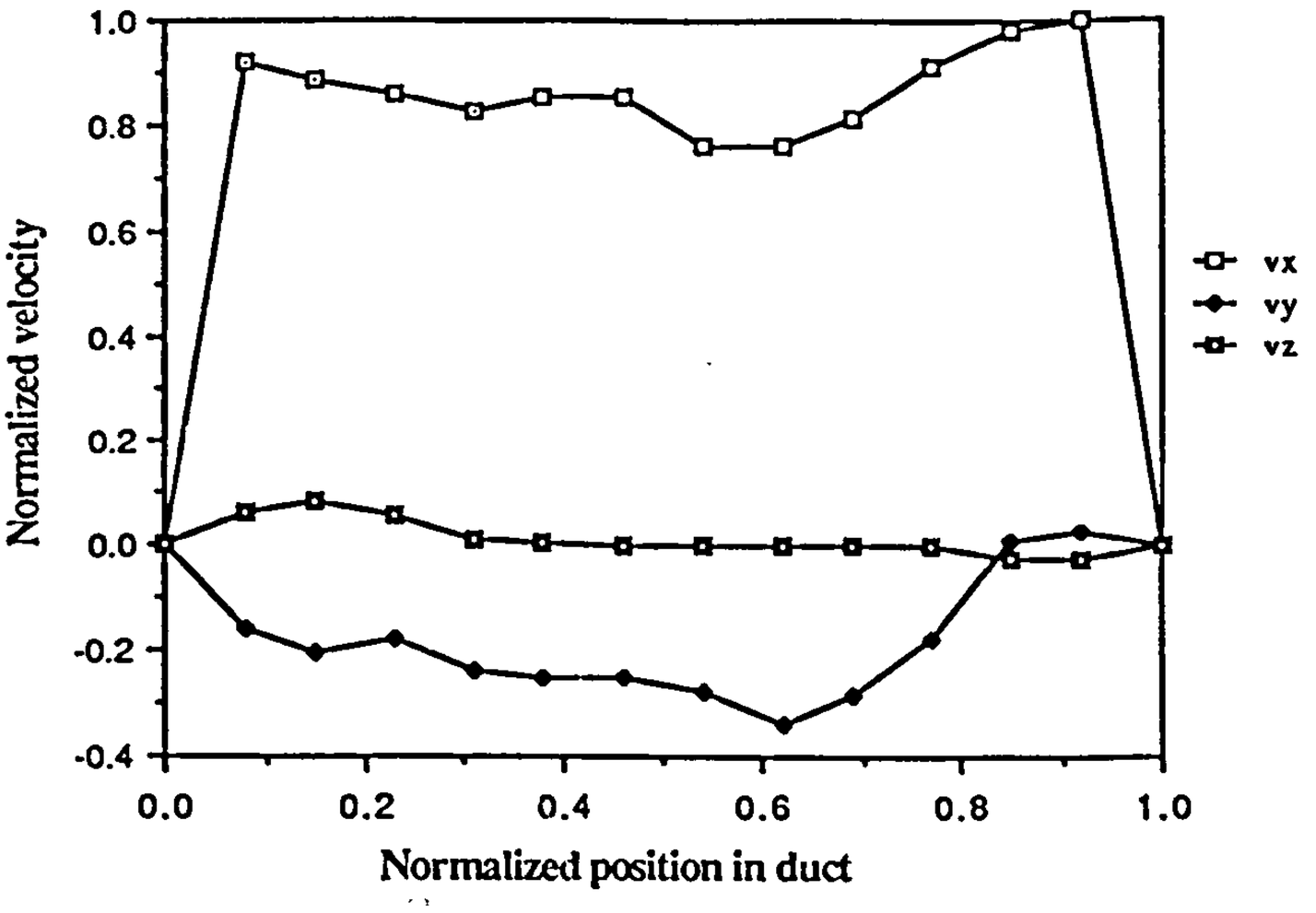

Figure 3.8. The horizontal variation of v_x, v_y and v_z for the manifold at station II.

The horizontal section at station II shows a near-uniform distribution in v_x across the duct, rising rapidly from zero at the walls. The distribution for v_y, being some 20% of v_x, suggests a tendency in the flow towards the rear wall of the duct, whilst the v_z profile, being about 5% of v_x, shows slight motion towards the upper reaches of the duct. Considering the distributions of Figures 3.7 and 3.8 together, the results imply that the main direction of flow in the x-direction is augmented by a slight movement of the flow towards the rear, upper section of the duct. In that station II is just upstream of the entrance to side branch 4, then a tendency in the flow towards the upper section of the duct, before accelerating around the inlet bend to side branch 4, seems reasonable.

In reviewing these results, their somewhat scattered nature is thought to arise from the combined effects of engine speed and recording technique. Experience showed that in moving from one reading point to the next across the duct, the readings took some five minutes to fully stabilize. Given that the engine speed could only be held approximately constant, typically varying by ± 30rev/min over an half hour period, it cannot truly be claimed that all results for a given traverse were taken at the same engine speed and hence for the same mass flow rate. Given that flow velocity is proportional in the first instance to engine speed, then for the nominal speed of 1220 rpm at which tests were conducted, this fluctuation in engine speed would correspond to a variation of up to 3% in flow velocity during the traversing of any given test station.

3.3. Computational Modelling of Flow Through the Inlet Manifold.

In seeking to model the inlet manifold, the computational mesh for such work had to be generated from scratch. The development of the computational model of the manifold centred on the provision of high mesh resolution in the near-wall region, suitable for the intended study of the response of 'traditional' wall modelling philosophies; the preparation of this model is laid out in Appendix A2.

The final version of the manifold model, listed as input file barf.FDREAD in Appendix A2, was operated as a steady-state model. To enable the inlet port faces, being the outlets of the manifold model, to be opened and closed in accordance with the timing sequence of the actual engine, the inlet port faces were declared as 'plot' elements. Whilst plot elements are principally offered in FIDAP to allow for fluid properties, such as pressure, to be studied across a fluid boundary to the modelled continuum during post-processing of results, they present no restriction to the flow at that boundary. In this

instance, the plot elements were used for a different purpose: by placing plot elements at the manifold outlets, individual outlets could then be 'closed' by use of suitable boundary condition commands.

The cycle of events describing the opening and closing of the inlet port faces was equated to a number of separate runs of the model, which collectively simulated the transient flow through the manifold. For the Perkins T4.236 diesel engine studied by practical experimentation in Section 3.2, the firing sequence of the cylinders was 1 - 3 - 4 - 2, where the inlet valves opened 18° before top dead centre and closed 42° after bottom dead centre. For the nominal engine speed of 1220rpm at which the practical tests were conducted, a portion of the complete cycle of events is given as Table 3.1 below.

Model run number	Manifold event	Crank angle		Time	
		at start of run (degrees)	at end of run (degrees)	at start of run (s)	at end of run (s)
1	open port 3	162	222	0.0	0.008334
2	close port 1	222	342	0.008334	0.025002
3	open port 4	342	402	0.025002	0.033360

Table 3.1. Listing of part of the sequence of inlet manifold events.

The initial conditions from which transient modelling commenced were provided by a steady-state solution for the inlet manifold with only port 1 open. Transient run no.1 then simulated the flow in the manifold from 162°, at which crank angle port 3 opened, up to 222°, when port 1 closed. Thus at the start of transient run no.1, boundary condition commands were set to define ports 2 and 4 as 'closed' and the initial conditions for the turbulence and velocity fields were taken from their corresponding fields for the solution to the steady-state problem. Likewise, transient run no.2 took its initial conditions as those prevailing at the end of transient run no.1, with the change in flow conditions being the closure of port 1. Transient run no.3, being the last in this series of experiments, saw the opening of port 4. The modifications to the manifold model, barf.FDREAD, that executed these transient flow experiments are listed in Appendix A2.

It will be realised that to simulate the complete catalogue of events involved in the four-stroke cycle of the engine would require several further transient model runs beyond those listed above. To offer such a description of the flow, it would be advisable to run

the model through one complete cycle of events, prior to collecting any data for analysis, to ensure independence of results from the steady-state initial conditions used at the onset of transient modelling. However, for the study in hand, the principal interest lay in a qualitative comparison of flow tendencies shown by experimental and computional results and in the behaviour of y^+ and the pressure gradients within the flow under transient conditions. As such, the results from the transient runs listed above should suffice.

Throughout these transient runs then, a fixed time step, $\Delta t = 0.001042s$, was used, such that transient run no.s 1 and 3 were subdivided into eight time steps and transient run no.2 into sixteen. The results of each time step, were they to be saved, would occupy the same amount of computer memory as a steady-state run for the same computational mesh. Consequently, it was necessary to limit the number of time steps saved from each transient run to three within the solution procedure.

To allow the variation in y^+ across the solid boundaries of the manifold duct to be inspected as post-processed results, the finite elements prescribing the boundary layer model were reconfigured. The single 'wall' element grouping, combining all such elements together, was replaced by a number of similar sub-groups, each accounting for a distinct portion of those solid boundaries modelled.

These results will now be considered with regard to

i) the general suitability of the model, in comparison with the experimental studies of Section 3.2 and

ii) the variation of y^+ and pressure gradient with time.

3.3.1. Comparison Between Computational and Experimental Results.

Figure 3.9 below shows a longitudinal section of the steady-state solution to the manifold mesh, with all four ports open.

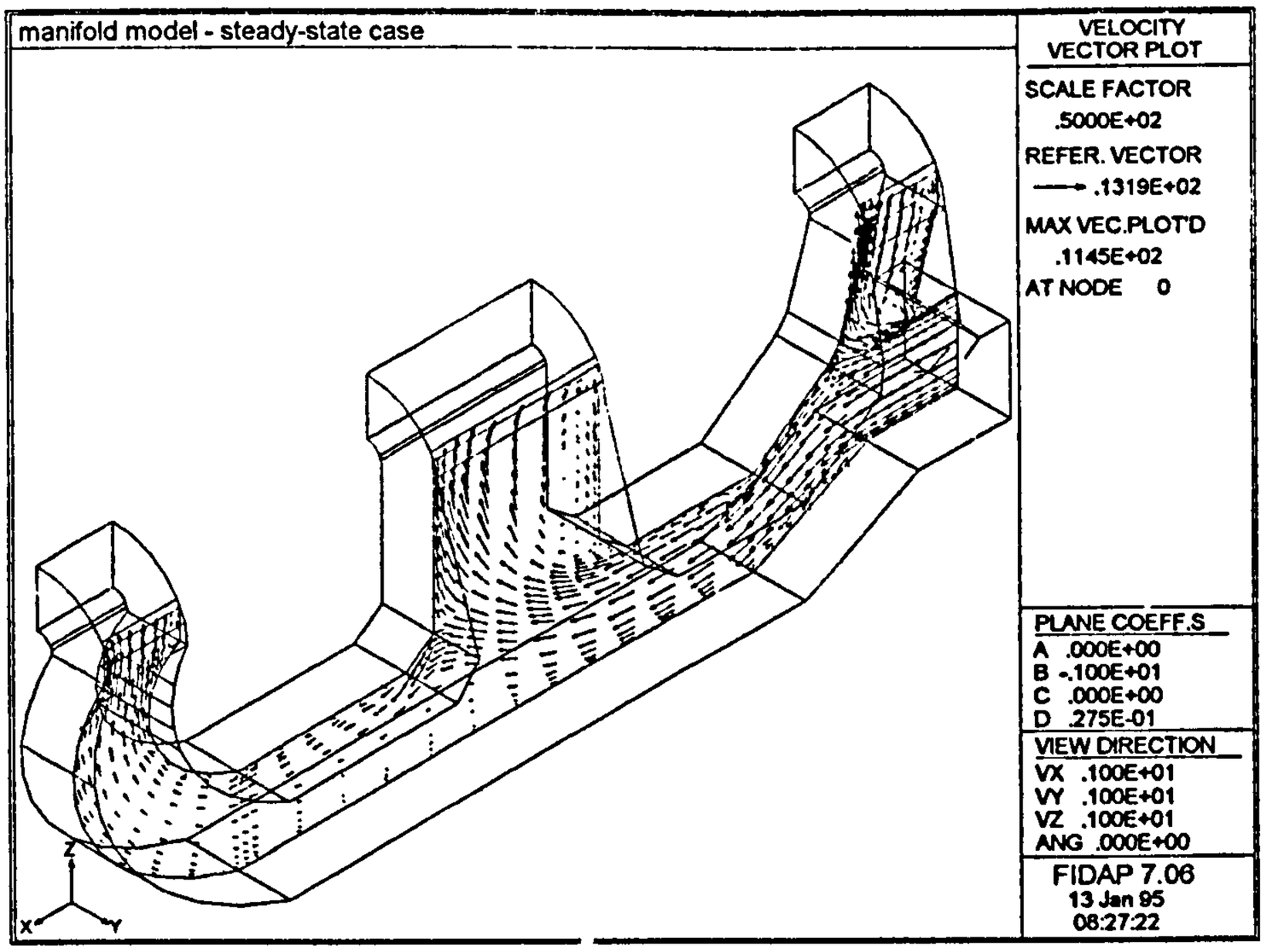

Figure 3.9. A longitudinal section of the steady-state solution to the inlet manifold flow.

In the velocity vector plot of the above figure, the flow distribution observed is a simplified approximation to the practical experimentation of Section 3.2, since all four ports were assumed open. Whilst in the practical experiments the inlet ports were opening and closing through time, they did so on a time scale much less than the response time of the metering equipment. Consequently both the practical experiments and the numerical experiment shown above should provide a time-averaged estimate of the real flow process. Be that as it may, inspection of Figure 3.9 should provide an initial insight into flow patterns within the manifold, prior to studying the time-dependent results.

A uniform velocity of 9.7m/s was specified at inlet to the manifold (see calculation of theoretical inlet velocity in Appendix A1). For the section of the manifold shown, the velocity distribution normal to the length of the main duct is of a similar magnitude to that at inlet, up to that part of the main duct beneath ports 2 and 3. Downstream of the duct inlet, the flow divides at the upper wall of the main duct below side branch 1. Part of the flow is diverted into side branch 1, running up the downstream y-z face of that side branch (Face 2). The upstream face, nominally in the y-z plane, of side branch 1, being Face 1, is abutted by an area of recirculation, which commences at the base of that side

branch. The bulk of the flow, however, runs along the main duct towards side branch 2/3.

As the flow runs beneath the central side branch, it largely turns up towards port 3 and so the main flow direction is again split between that entering side branch 2/3 and that heading towards port 4. This upturn in the flow impacts on the duct wall at the base of Face 4, the wall in the y-z plane on the downstream side of side branch 2/3. The bulk of the flow is then directed towards port 3. At the foot of Face 3, the upstream y-z plane of side branch 2/3, the flow is still mainly parallel to the x-axis, turning up towards port 3 beneath the mid-point of the side branch. Consequently, there is a second recirculating region of fluid adjacent to Face 3.

That lesser portion of the flow turning back down towards the main duct at the base of Face 4 runs along beneath the upper surface of the main duct towards port 4. In the lower regions of this last segment of the main duct, the low fluid velocity is comparable to that within the recirculating pockets of fluid already noted. There is then an acceleration in the flow as it turns to enter the final bend in the x-z plane on approach to port 4.

As Figure 3.9 shows velocity vectors for a vertical section taken through the manifold model, its results may be compared with the experimental vertical velocity distributions at stations I and II, namely Figures 3.5 and 3.7 respectively. Inspecting Figure 3.9 in the vicinity of stations I and II, in either case, the velocity in the upper half of the duct is greater than that near the base of the duct, in keeping with experimental observation. Downstream of station I, Figure 3.9 shows a general tendency in the flow towards the entrance to side branch 2/3, as predicted by experimental Figures 3.5 and 3.6. Likewise, downstream of station II, there is a tendency in the flow towards the upper portion of the duct, as it begins to accelerate around the bend leading into side branch 4, as suggested by experimental Figures 3.7 and 3.8.

Taking an overview of Figure 3.9 then, the upstream y-z faces of side branches 1 and 2/3, being Faces 1 and 3 respectively, provoke initial interest in that the fluid adjacent to them has undergone separation and is recirculating. It is now appropriate to consider corresponding velocity profiles taken from the transient models. In each case, the velocity profiles will be presented along the x-z plane central to the major axis of the model (as was the case for Figure 3.9).

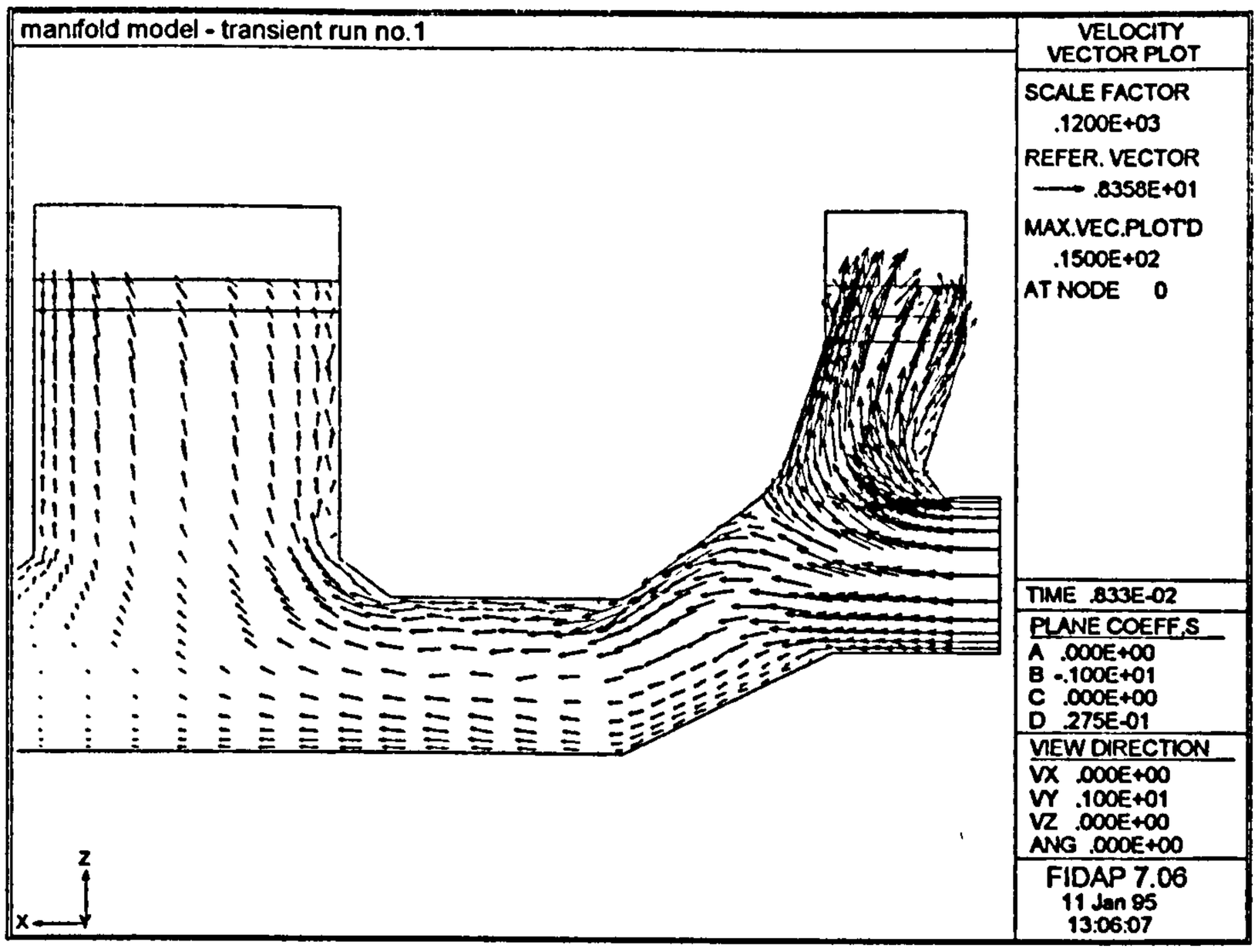

Figure 3.10. Velocity distribution for the final time step of transient run no.1.

Figure 3.10 shows the velocity distribution eight time steps after the opening of port 3. The predominant flow is still towards the open port 1. Where the flow bifurcates at the base of Face 2, there is a local acceleration in the flow. At the lower edge of Face 1, being the upstream face of side branch 1, the flow separates and is seen to reattach approximately halfway up that face, so the length of the recirculating zone is less than in the steady-state case.

On the upstream side of side branch 2/3, there is the seed of a recirculating region at the bottom of Face 3, where the flow having accelerated around the filleted root of the side branch then impacts on the wall. Running up Face 3, the flow is seen to waver in direction between striking the wall there and moving towards port 3. Across the greater cross-section of side branch 2/3, the flow tends towards port 3.

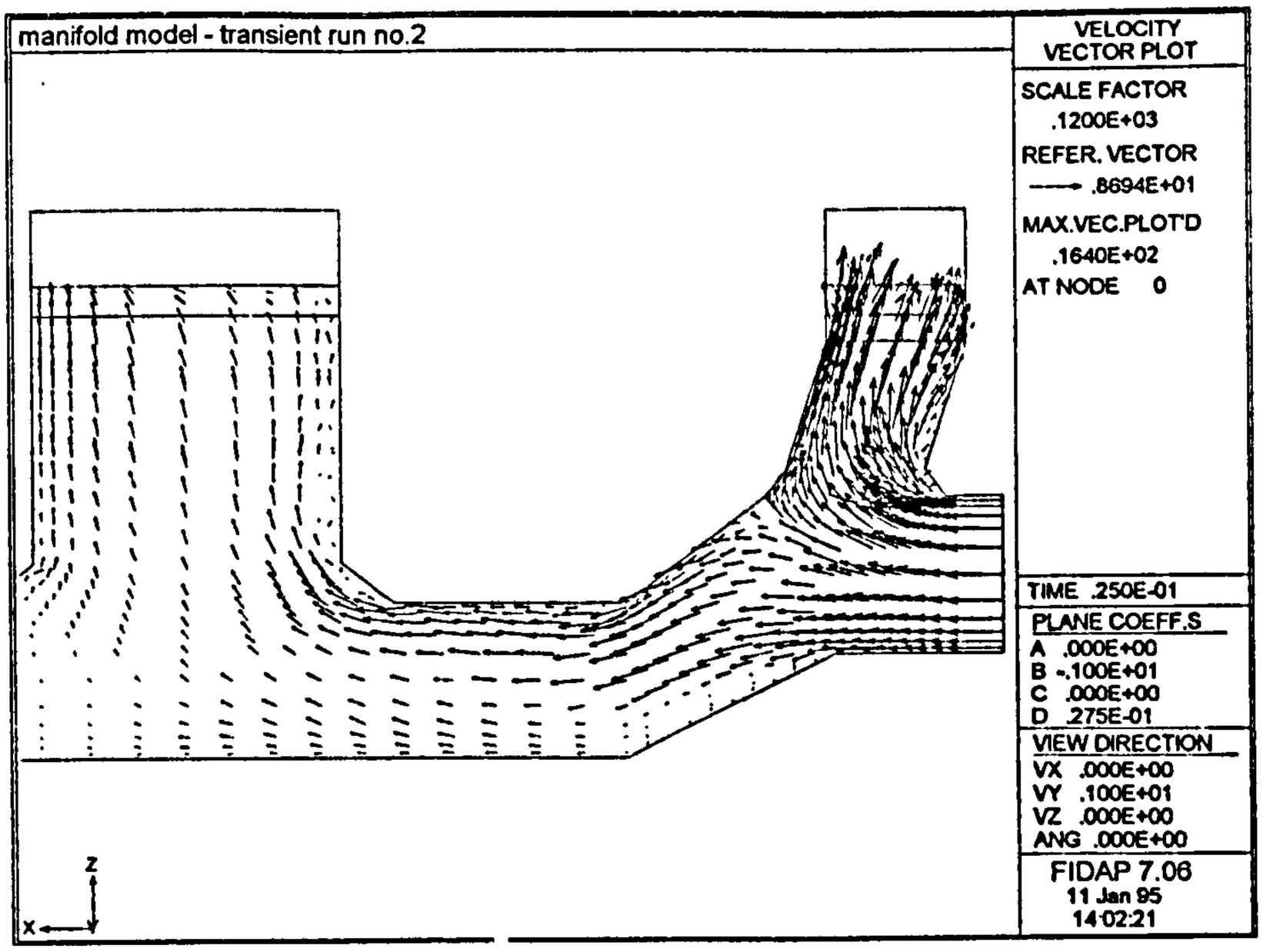

Figure 3.11. Velocity distribution for the final time step of transient run no.2.

Figure 3.11 shows the velocity distribution sixteen time steps after the closure of port 1. At the point of division in the flow against the upper wall of the main duct beneath Face 2, the acceleration of the flow towards ports 2 and 3 is more marked and there is an attendant increase in velocity across the section of the duct at station I, just before side branch 2/3. The velocities within the recirculating region next to Face 1 are greater after the closure of port 1. Furthermore, as the flow turns increasingly towards port 3 in side branch 2/3, the nascent recirculation covering Face 3 has grown in size.

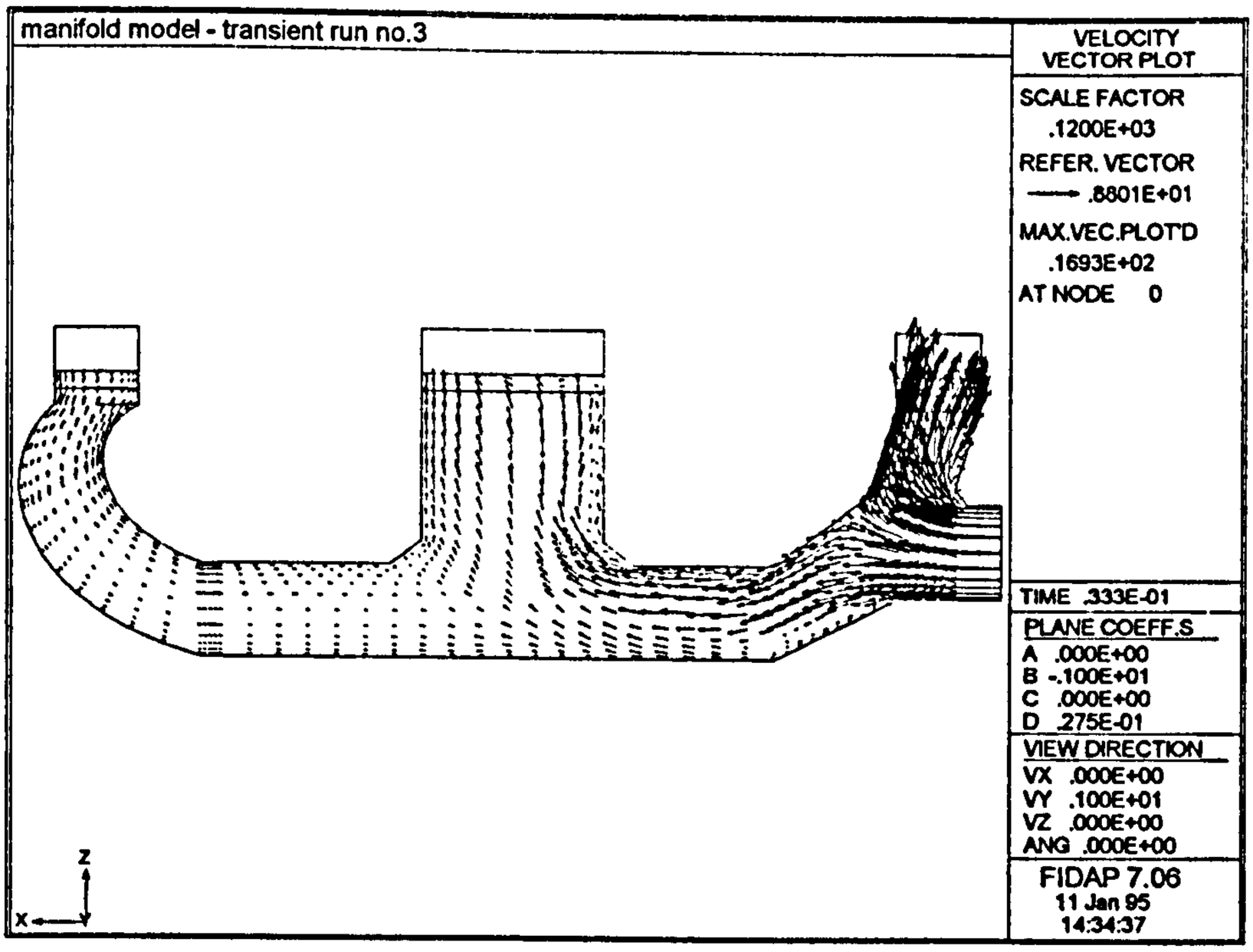

Figure 3.12. Velocity distribution for the final time step of transient run no.3.

Finally, in Figure 3.12, showing the flow some eight time steps after opening port 4, the general trends of Figure 3.11 are seen to continue. The observed recirculations continue to become more prominent. As the closure of port 1 is registered by the flow, a greater portion of the flow turns away from side branch 1 and into the main duct. At the base of Face 4, there are now some early signs of the fluid dividing itself between ports 3 and 4, rather than heading in the main towards port 3.

The velocity profiles at stations I and II, as predicted by both steady-state and transient modelling, will now be considered.

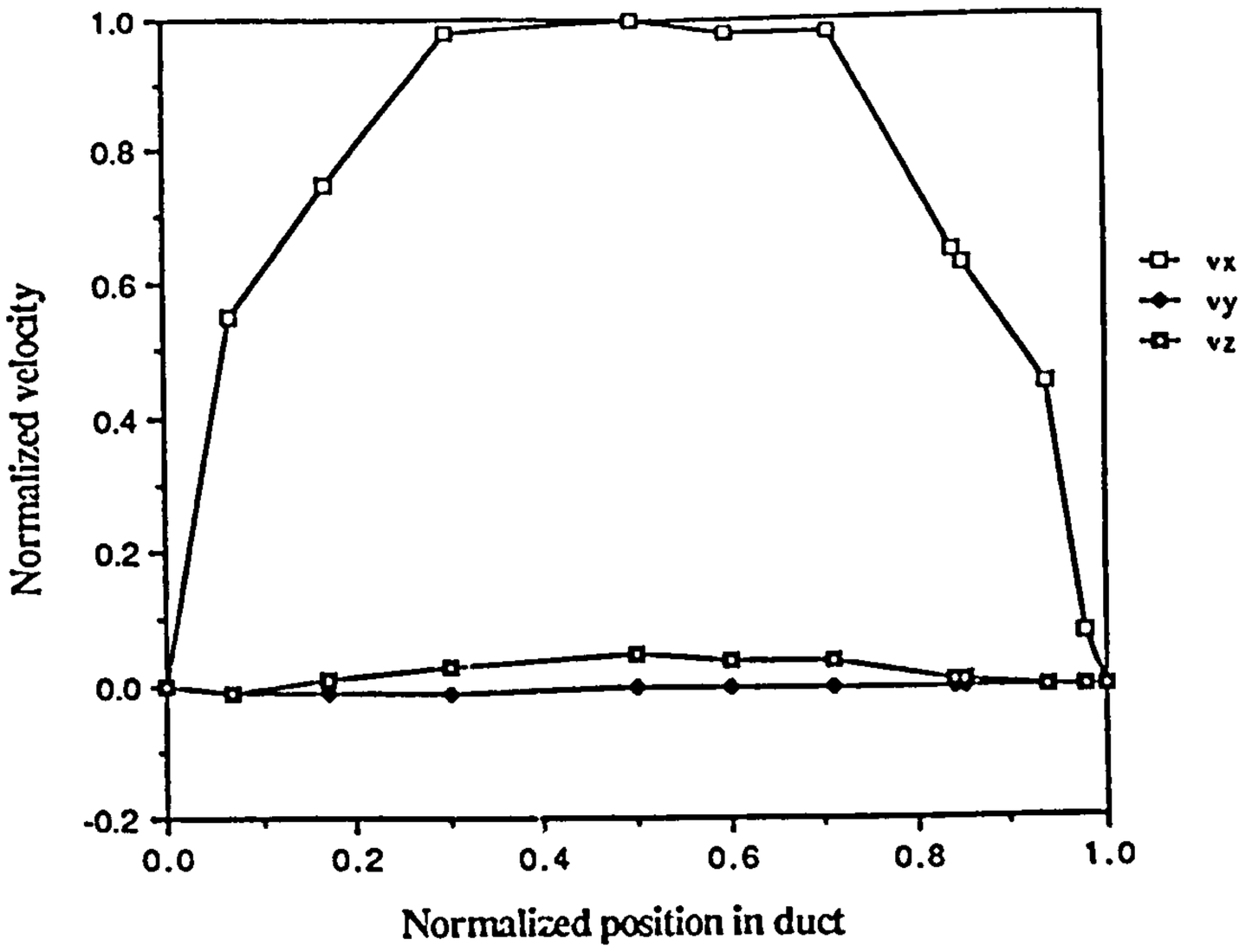

Figure 3.13. The steady-state distribution of velocity components for the vertical traverse of station I.

Figure 3.13 shows the steady-state velocity distribution for the vertical section of station I. As with experimental Figure 3.5, the predominant flow direction is in the x-direction but in this instance the velocity components v_y and v_z are trivial compared with v_x. The steady-state distribution for v_x is similar to that of Figure 3.5 in the centre of the duct but in the upper and lower quarters of the duct, the velocity falls steadily to zero, counter to experimental observation.

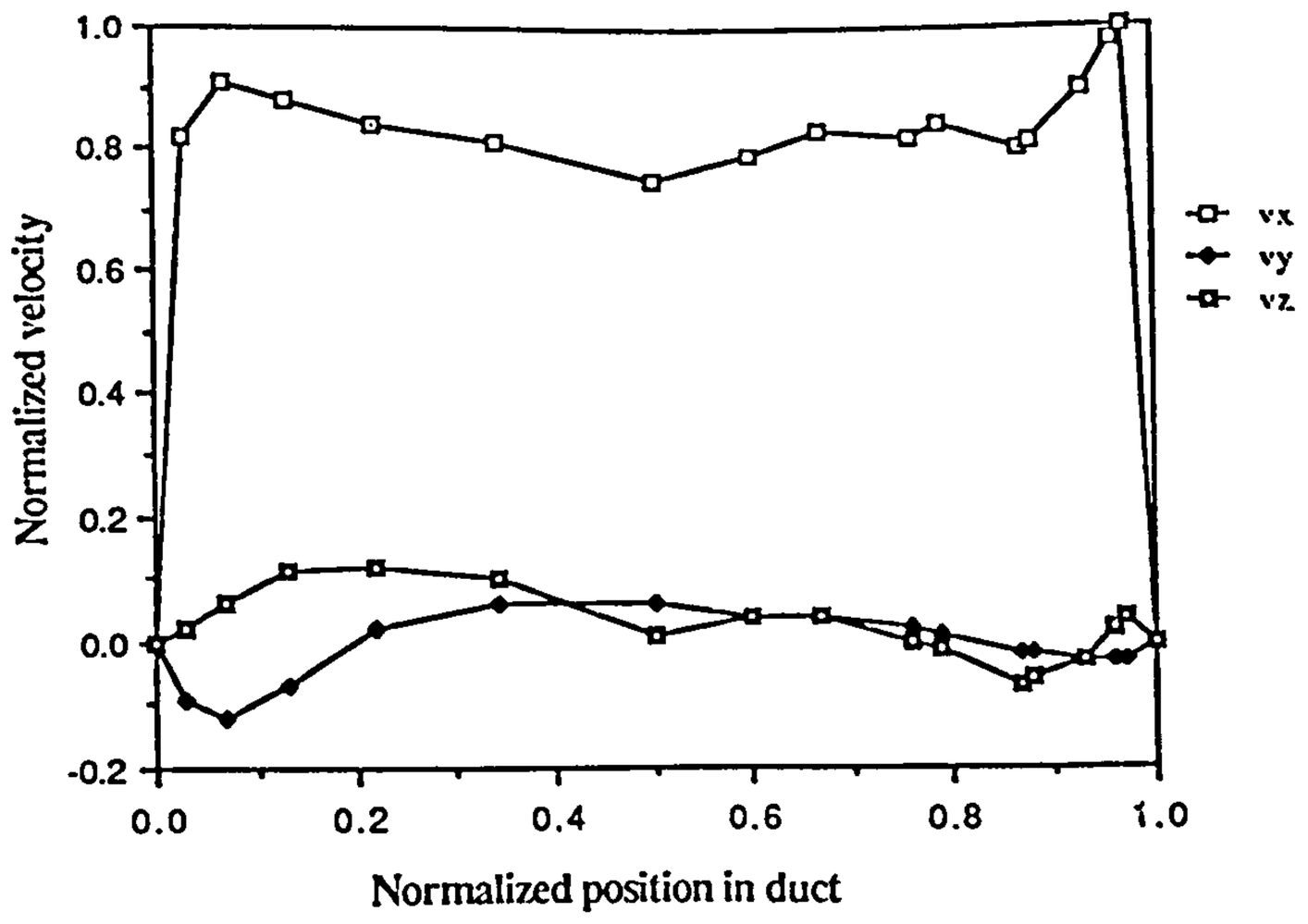

Figure 3.14. The distribution of velocity components for the vertical traverse of station I at the end of transient run no.1.

Figure 3.14 shows the velocities for the vertical section of station I at the end of transient run no.1, after the opening of port 3. The distribution for v_x is near-uniform across the duct, with v_y and v_z showing a slight swirl in the flow similar to Figure 3.5. Whilst there is a more marked increase in v_x when moving away from the wall in the near-wall region, when compared with the steady-state results of Figure 3.13, the normalized magnitude of v_x is lower than the experimental results of Figure 3.5.

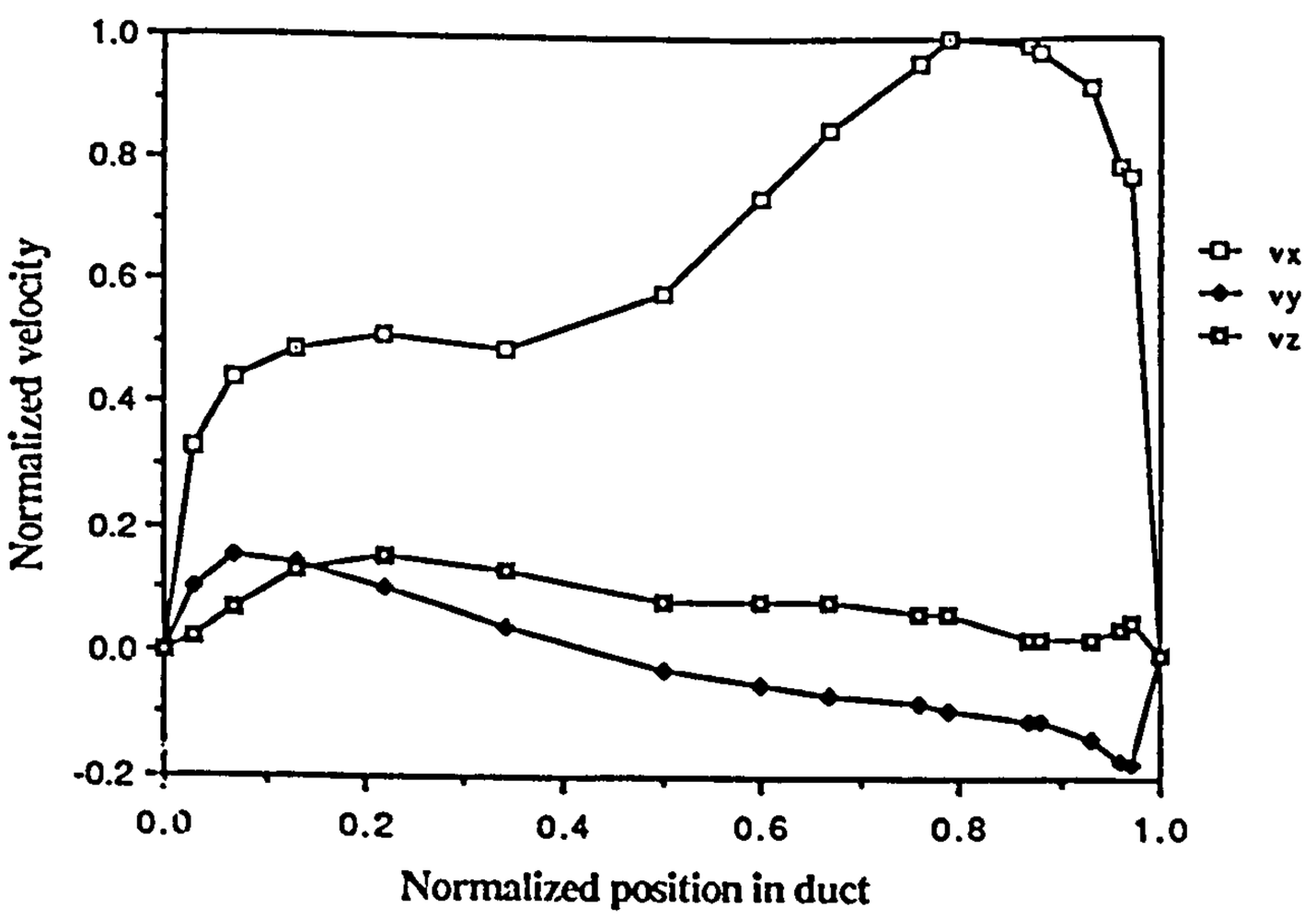

Figure 3.15. The distribution of velocity components for the vertical traverse of station I at the end of transient run no.2.

Figure 3.15 details events for the end of transient run no.2 after the closure of port 1. The profile for v_x shows it to be greater in the upper half of the duct in comparison with that in the lower portion. In that port 1 has just closed, from inspection of Figure 3.11, this results in the flow beneath side branch 1 turning away from the base of Face 2 to run along the upper surface of the main duct. Whilst the greater magnitude of v_x in the upper half of the duct, compared with that in the lower half, corresponds with experimental trends seen in Figure 3.5, quantitatively v_x is underestimated across the lower three-quarters of the duct. Again, the rise from zero velocity at the wall towards the freestream value occurs more gradually than in the experimental case.

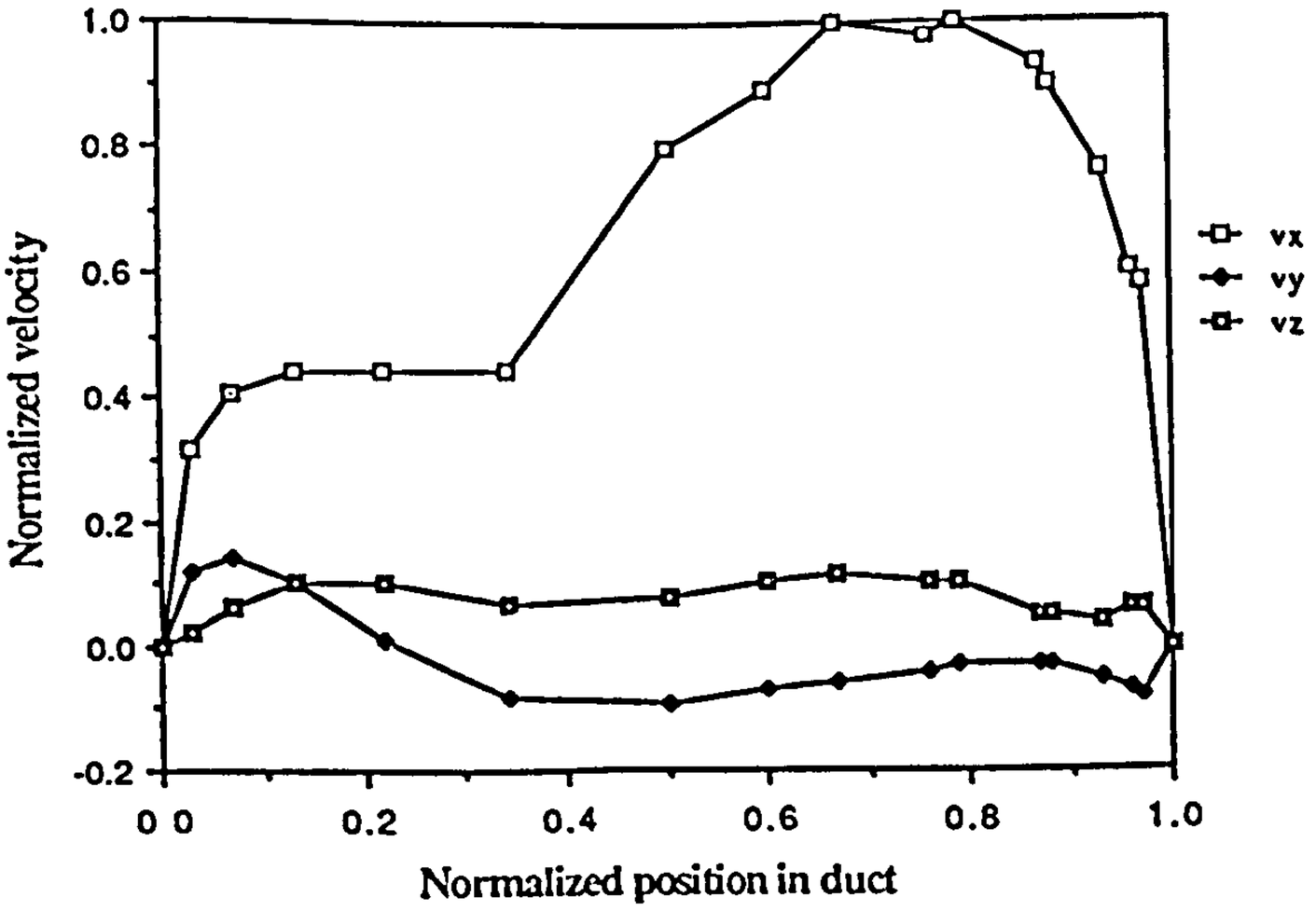

Figure 3.16. The distribution of velocity components for the vertical traverse of station I at the end of transient run no.3.

In Figure 3.16, velocities across the vertical section are shown after opening port 4, for transient run no.3. The general distribution of v_x is similar to Figure 3.15 but the magnitude of v_x in the region of the upper wall is reduced. However, that part of the flow where v_x is almost unity is broader. This suggests that as both port 3 and port 4 are now open, that the velocity in the core of the duct is rising as fluid is drawn towards port 4, beneath that being swept into port 3. In comparison with the experimental results of Figure 3.5, Figure 3.16 shows a deficit in v_x across much of the duct and too slow a rise towards the freestream velocity in the near-wall region, as was the case for Figure 3.15, depicting similar results for transient run no.2.

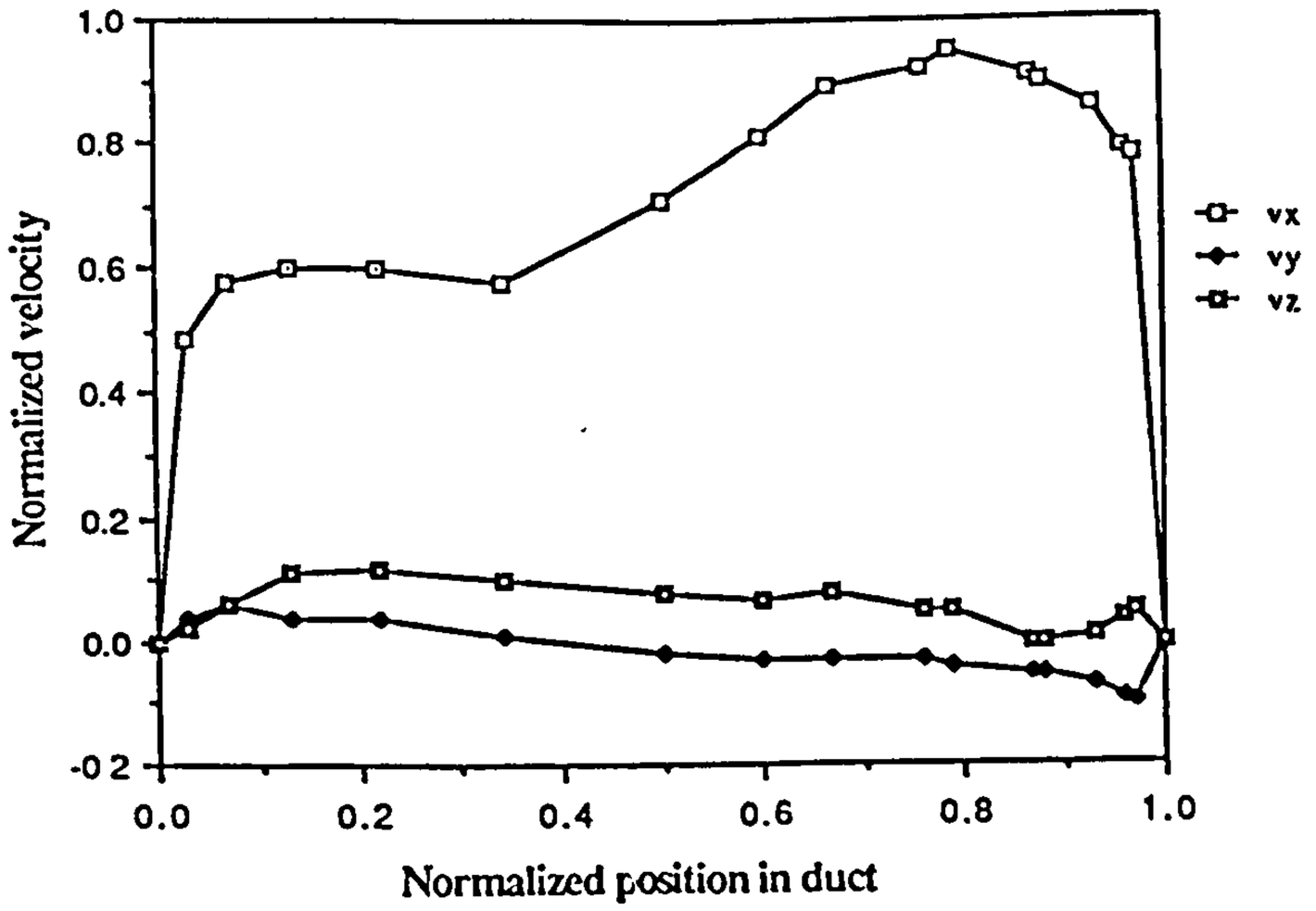

Figure 3.17. The distribution of velocity components for the vertical traverse of station I for the average of transient runs.

Figure 3.17 shows the average of the results shown in Figures 3.14 to 3.16. Whilst the combination of the transient runs performed does not comprise the complete cycle of induction events, it does give a limited, time-averaged description of the manifold flow. The averaged v_x profile is similar to that of Figure 3.5, with the maximum velocity recorded across the bulk of the upper portion of the duct, with lower velocity in the bottom half of the duct. However, the increase in velocity away from the near-wall region is more gradual for these averaged results. This suggests that the wall model is underestimating the local velocity, as may also be inferred from the steady-state results of Figure 3.13. The wall model of Haroutunian and Engelman (1991) uses Reichardt's law to determine velocity as a function of y^+. A low estimate of velocity would arise where the model was operated within the transitional sub-layer, for $y^+ < 30$.

Despite the generally low estimate for v_x of the averaged transient results of Figure 3.17, they bear closer resemblance to the experimental results of Figure 3.5 than either the steady-state results or those of individual time steps from the transient runs.

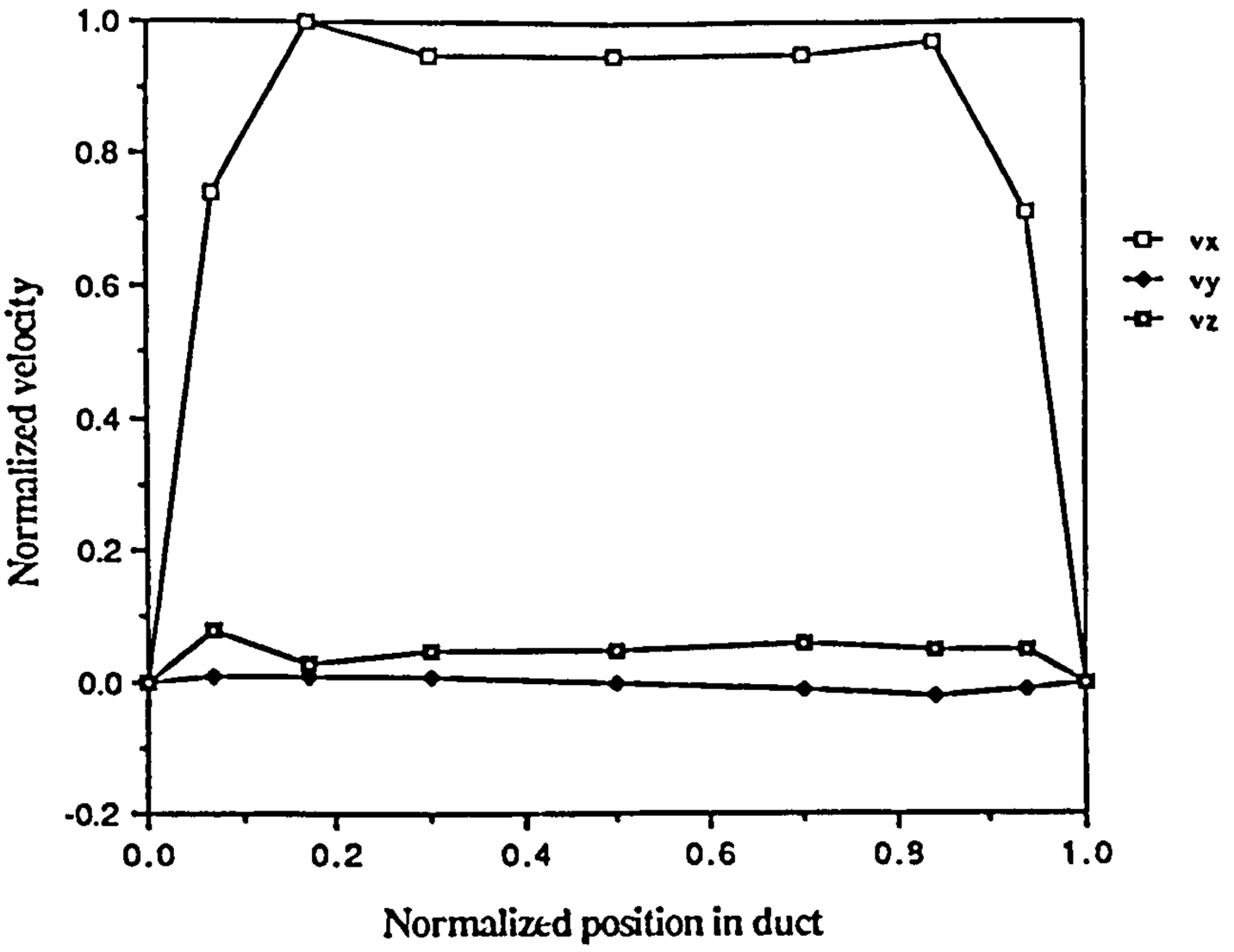

Figure 3.18. The steady-state distribution of velocity components for the horizontal traverse of station I.

Figure 3.18 shows the steady-state velocity distributions for the horizontal section at station I. Whilst experimental Figure 3.6 showed near uniform velocity across the duct, Figure 3.18 shows a reduction in v_x over a wide region on approach to the walls.

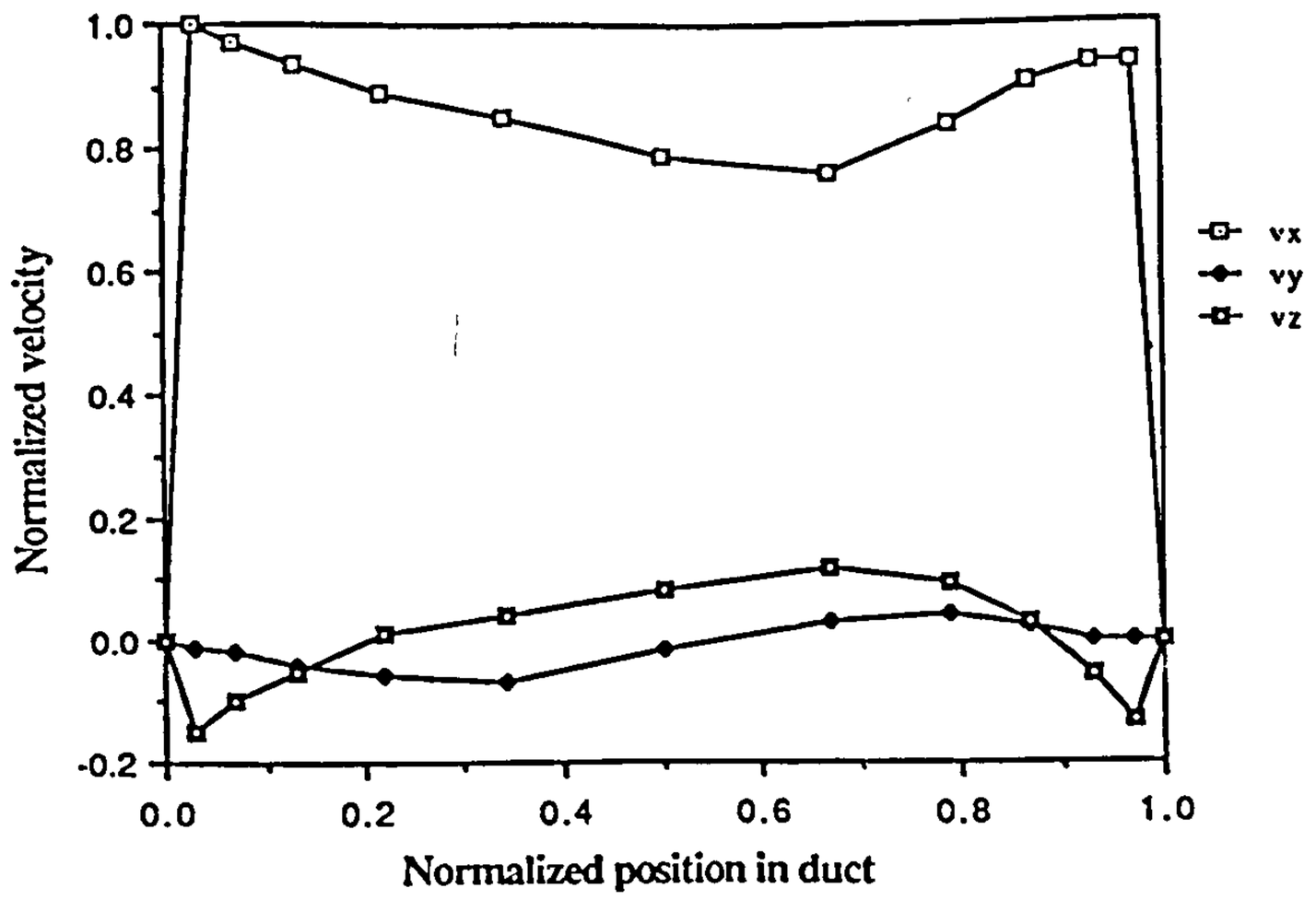

Figure 3.19. The distribution of velocity components for the horizontal traverse of station I for the average of the transient runs.

However, in Figure 3.19, showing the average of the transient results, the profile

for v_x is nearer to that of experiment, showing a normalized velocity near unity across the whole duct, as well as the slight reduction in v_x near the centre of the duct.

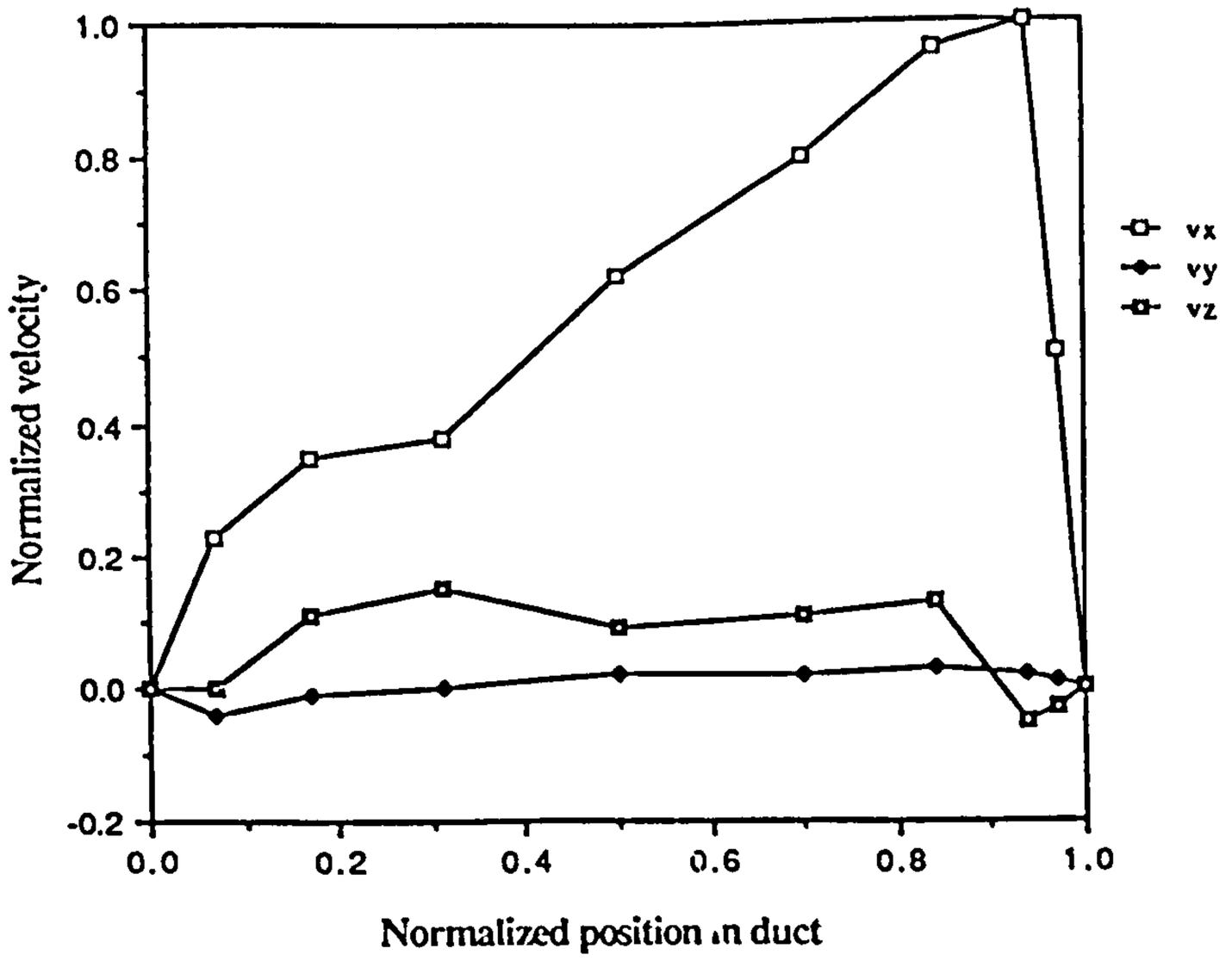

Figure 3.20. The steady-state distribution of velocity components for the vertical traverse of station II.

At station II, the velocities across the vertical section are shown for the steady-state model in Figure 3.20. Here there is a marked discepancy between results, with the computational prediction for v_x varying almost linearly from zero to unity towards the upper boundary of the duct. In the steady-state model, only one quarter of the mass flow will enter port 4 but the experimental results correspond to a system where all of the mass flow passes through port 4 for a quarter of the time. Whilst the experimental Figure 3.7 also shows a 'low' velocity across the lower quarter of the duct, in the upper portion of the duct, v_x is approximately uniform. As such, the steady-state model does not provide a good representation of the practical flow.

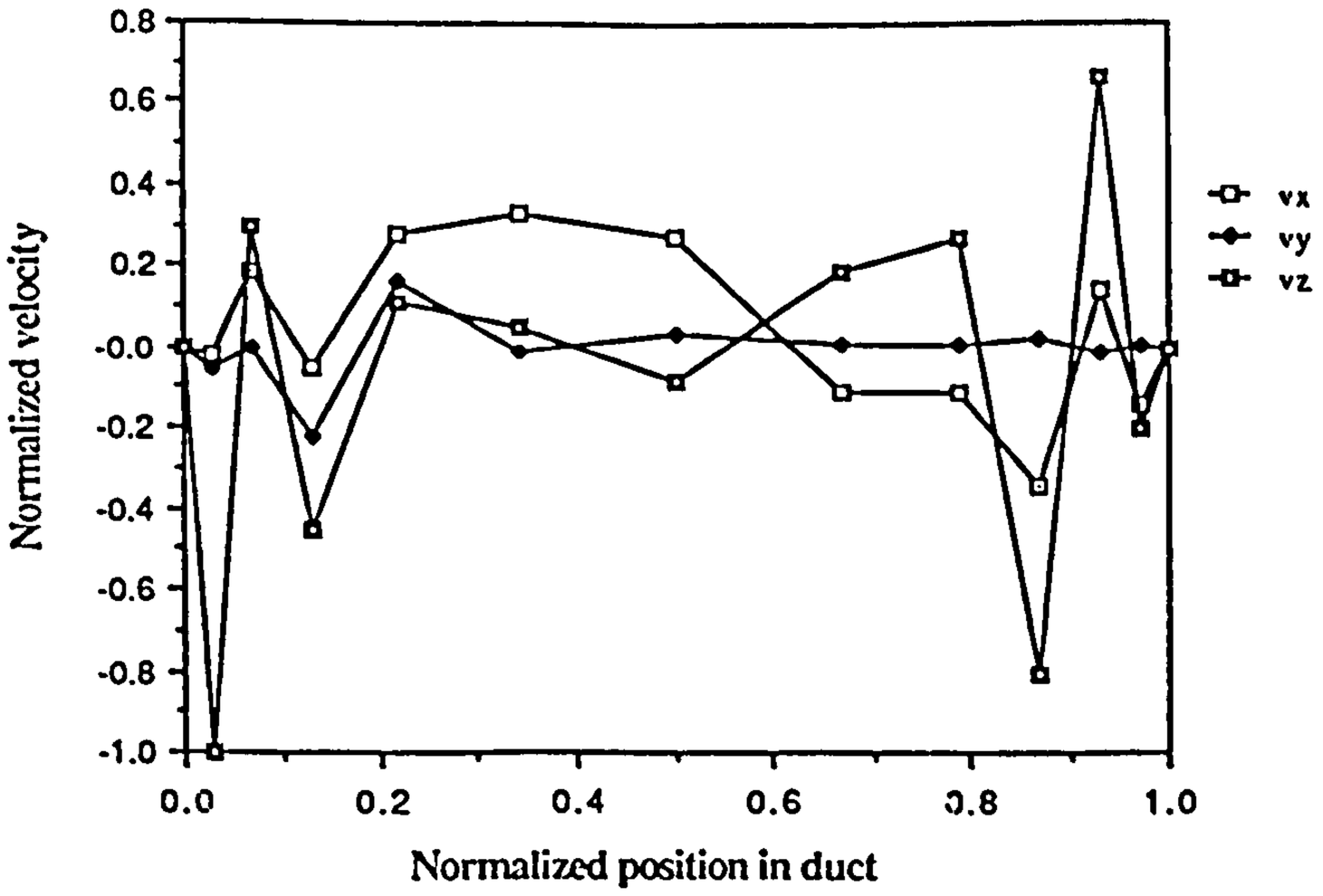

Figure 3.21. The distribution of velocity components for the vertical traverse of station II at the end of transient run no.1.

Figure 3.21 shows events for the vertical section of station II at the end of transient run no.1. Here, all three velocity components are of similar magnitude. At this time, port 4 is closed and from Figure 3.10, virtually no fluid is directed towards side branch 4. As such, these velocity distributions correspond to the movement of near-stagnating fluid. Similar results were gained for transient run no.2 and hence are not shown here.

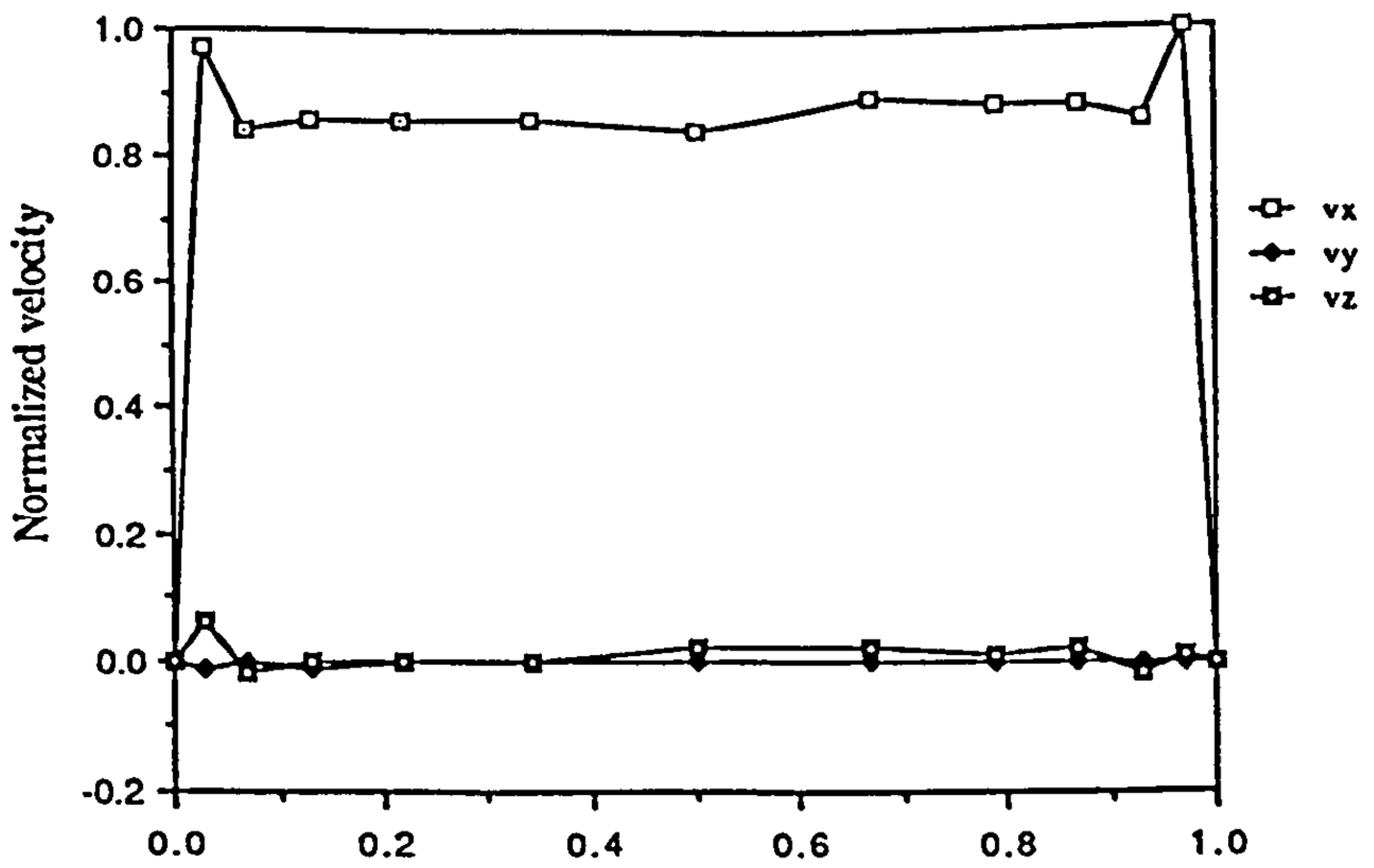

Figure 3.22. The distribution of velocity components for the vertical traverse of station II at the end of transient run no.3.

Figure 3.22 describes the corresponding velocity profiles for transient run no.3, after the opening of port 4. Whilst the distribution for v_x shows some similarity to experimental Figure 3.7, with near-uniform velocity across the majority of the duct, in the near-wall region the computational model deviates from observed trends.

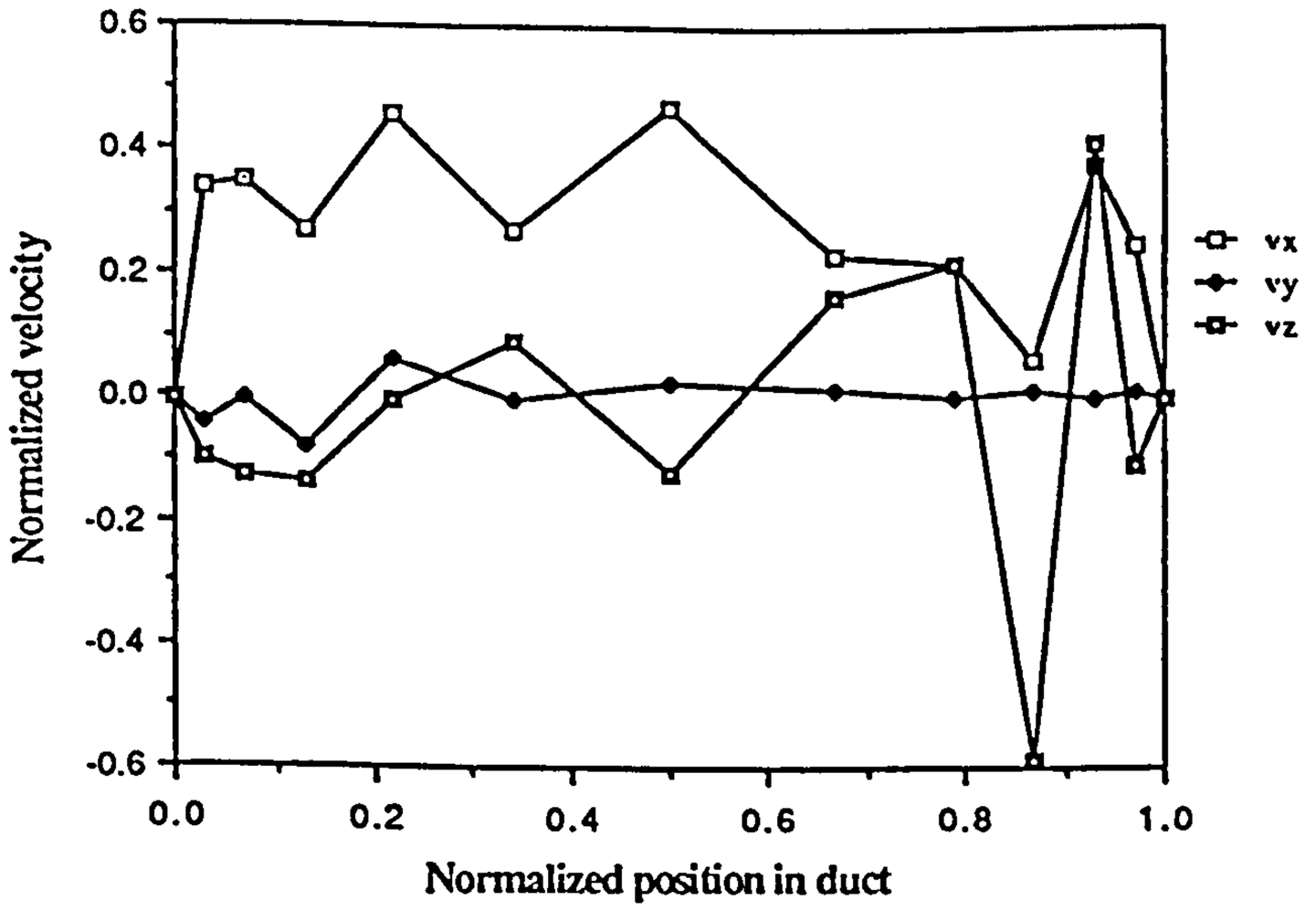

Figure 3.23. The distribution of velocity components for the vertical traverse of station II for the average of the transient runs.

The average of the transient results, as Figure 3.23, agrees less favourably with experimental results than previous averaged transient results although the reported main direction of flow is still the x-direction. In that the first two transient runs show near-zero values of v_x, the favourable reported results for the third transient run are somewhat diluted.

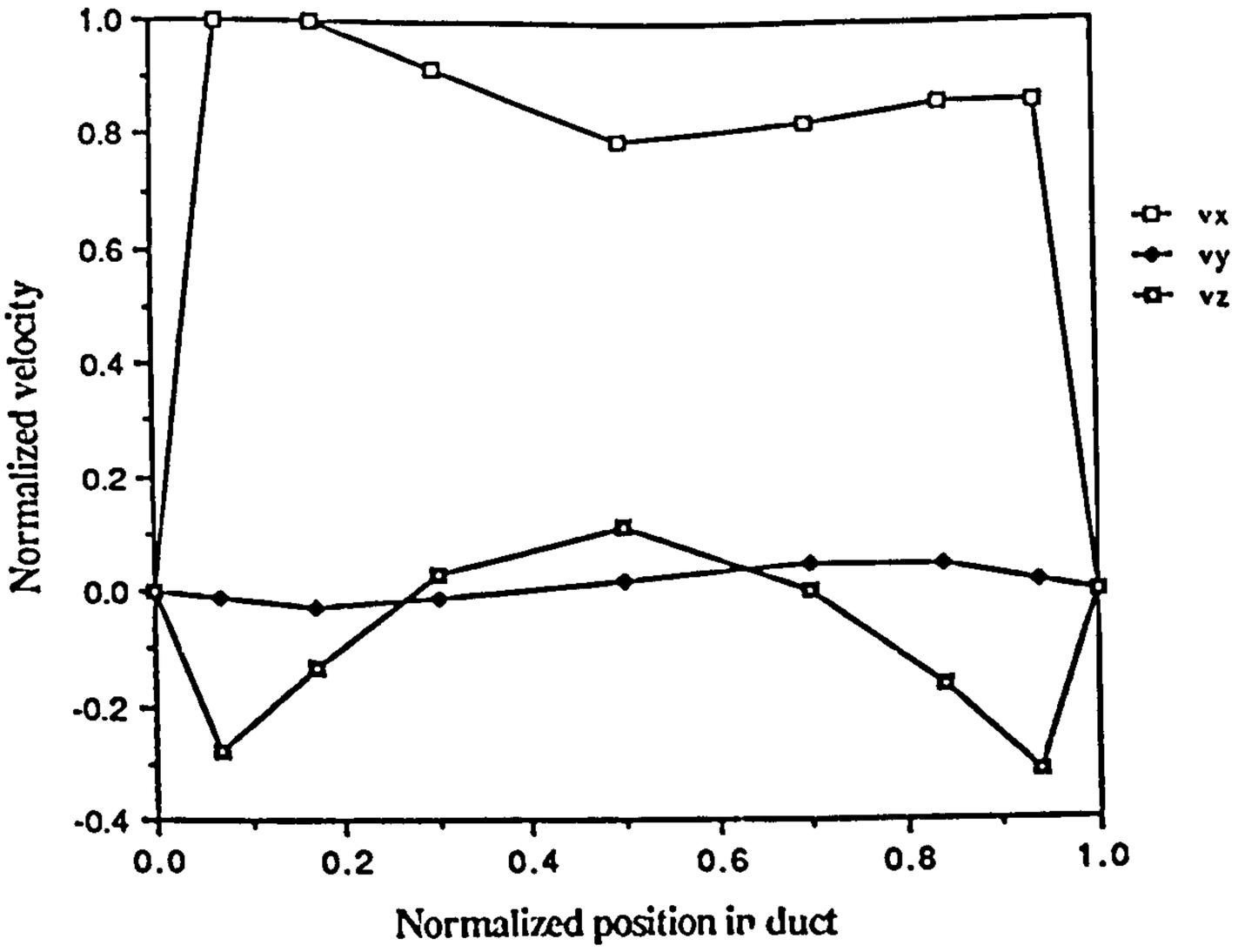

Figure 3.24. The steady-state distribution of velocity components for the horizontal traverse of station II.

The horizontal steady-state results at station II are shown in Figure 3.24 with some similarity in the v_x profile to the experimental results of Figure 3.8. However, where the experimental results showed v_x to be greatest in the rear quarter of the duct, the steady-state results predict the largest values of v_x near the front duct wall, with a slight, steady reduction in v_x towards the rear reaches of the duct.

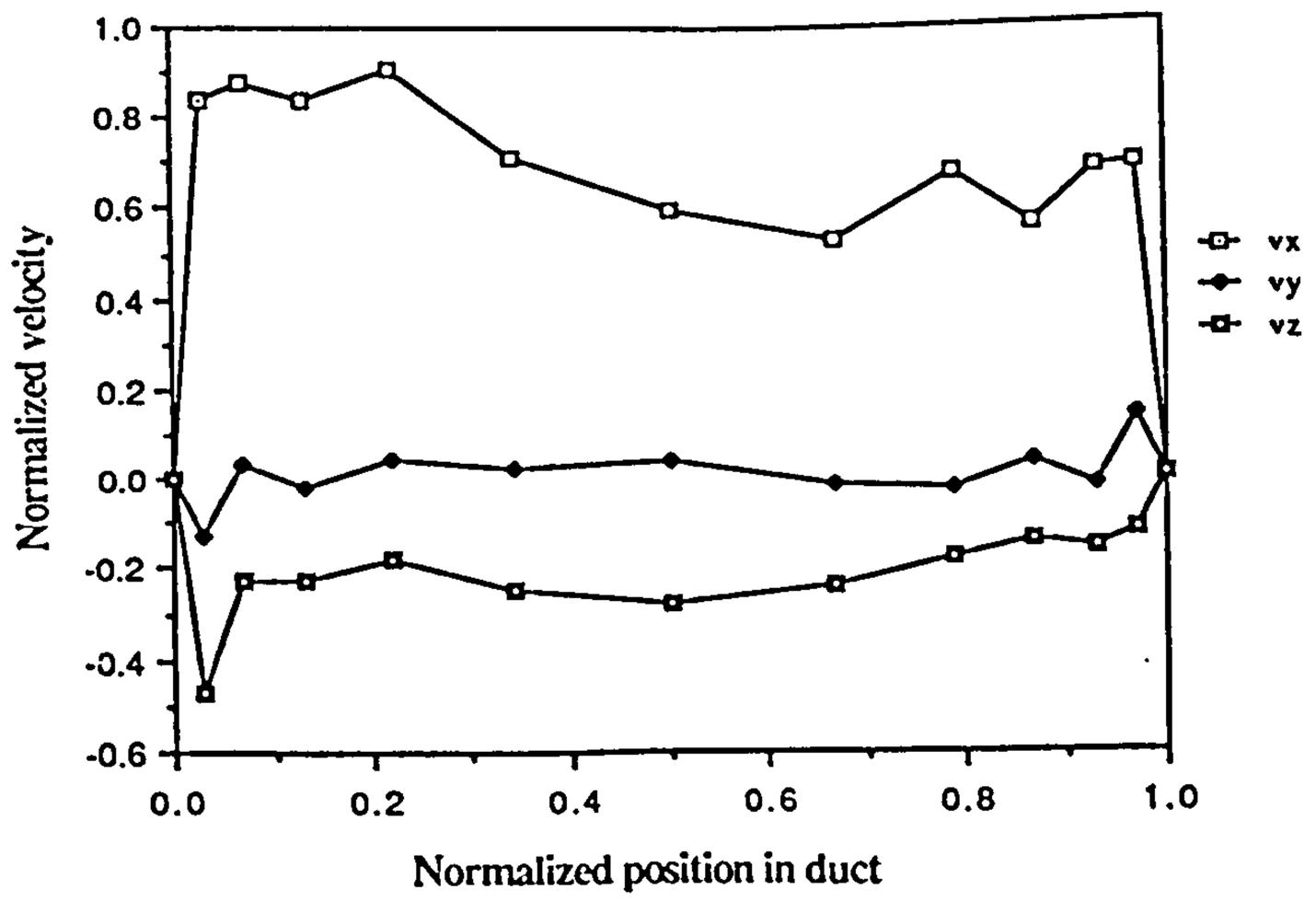

Figure 3.25. The distribution of velocity components for the horizontal traverse of station II for the average of the transient runs.

The average of the transient results, as Figure 3.25, shows some correspondance with Figure 3.8 but as with Figure 3.23, the effect of near-zero velocity for the first two transient runs reduces the average reported value of v_x.

3.3.2. The Transient Behaviour of y^+ and Pressure Gradient.

Consider now the pressure distributions corresponding to Figures 3.10 to 3.12. In the following discussion, all pressures will be presented in non-dimensionalised form, having been divided by $\frac{1}{2}\rho v^2$ (where v is the uniform velocity, prescribed at inlet to the manifold model). Figure 3.26 shows the pressure distribution some eight time steps after the opening of port 3.

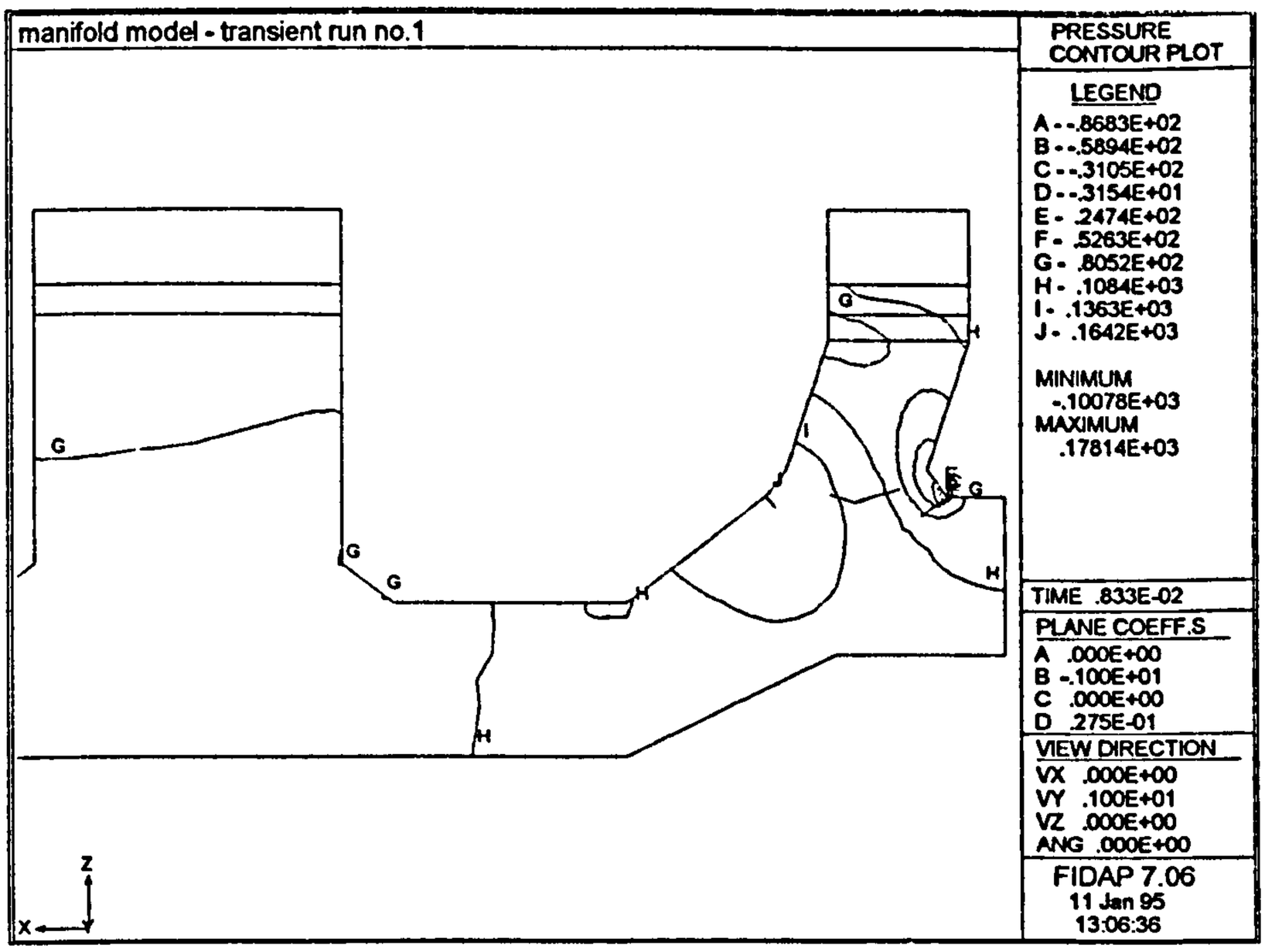

Figure 3.26. Pressure distribution for the final time step of transient run no.1.

Inspecting the pressure distribution shown above for the end of transient run no.1, there is a favourable pressure gradient before the inlet to side branch 1, with the pressure dropping from 1.47 to -0.06. The pressure then recovers up the surface of Face 1, regaining a value of 1.47 two-thirds of the way up that face, hence giving an adverse pressure gradient in the area where recirculation was observed in Figure 3.10. The contour at entrance to the final bend in the y-z plane of side branch 1 (and leading to port

1) indicates a pressure of 1.84.

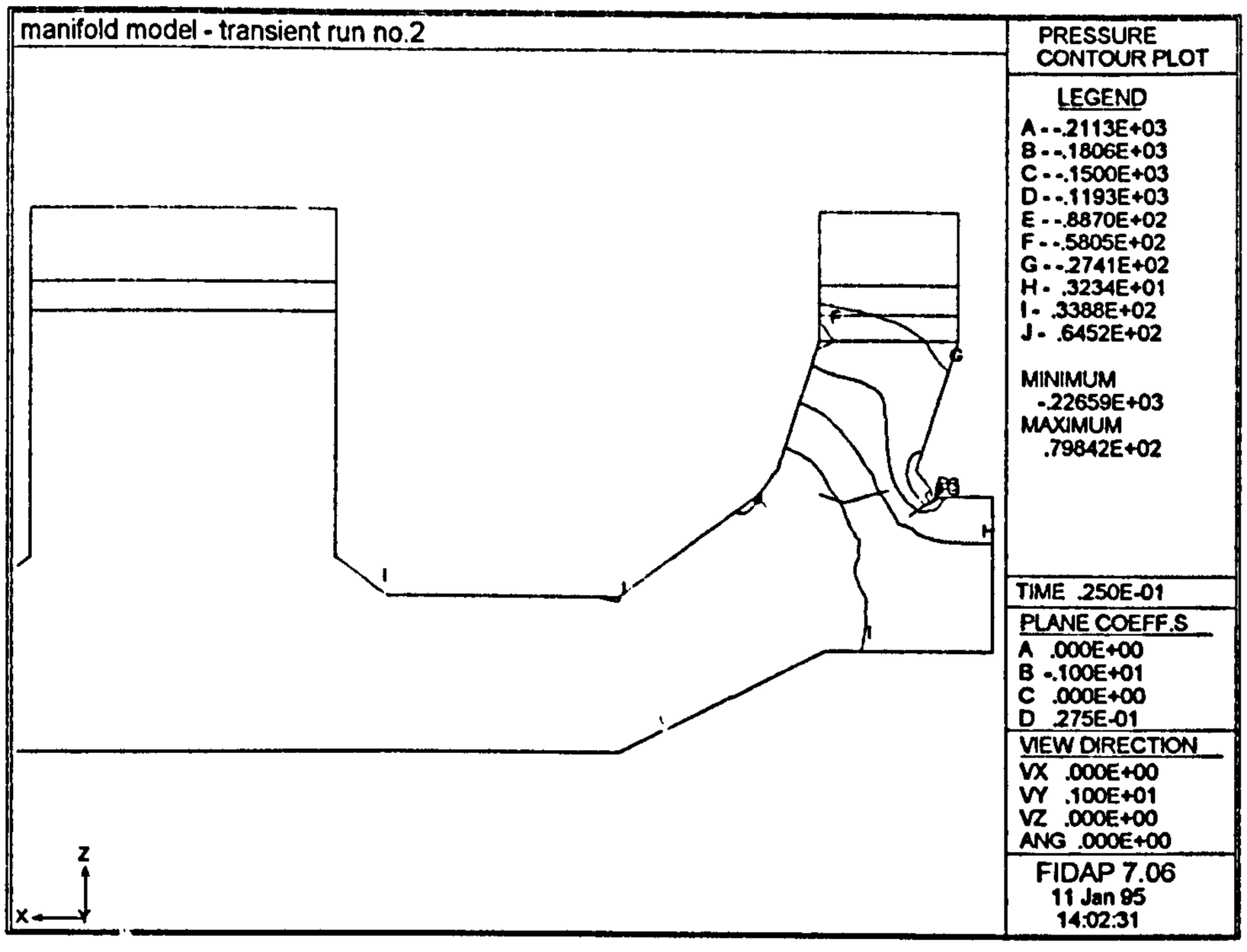

Figure 3.27. Pressure distribution for the final time step of transient run no.2.

Figure 3.27 gives the pressure distribution at the end of transient run no.2, at the start of which port 1 was closed. Whilst there is still a favourable pressure gradient at the upstream face of the inlet to side branch 1, the pressure now drops from -0.55 to -1.84. This implies that the pressure at the wall just before the foot of Face 1 has changed sign, even though a favourable pressure gradient has been maintained just upstream of the zone of recirculation. The pressure recovery on Face 1 occurs more rapidly here, with pressure reattaining the value prior to the branch inlet very soon after the fillet radius of Face 1. The contour at entrance to the bend of port 1 indicates a pressure of -0.55. In comparison with Figure 3.26, these results then indicate a dramatic change in local pressures, both in terms of magnitude and sign.

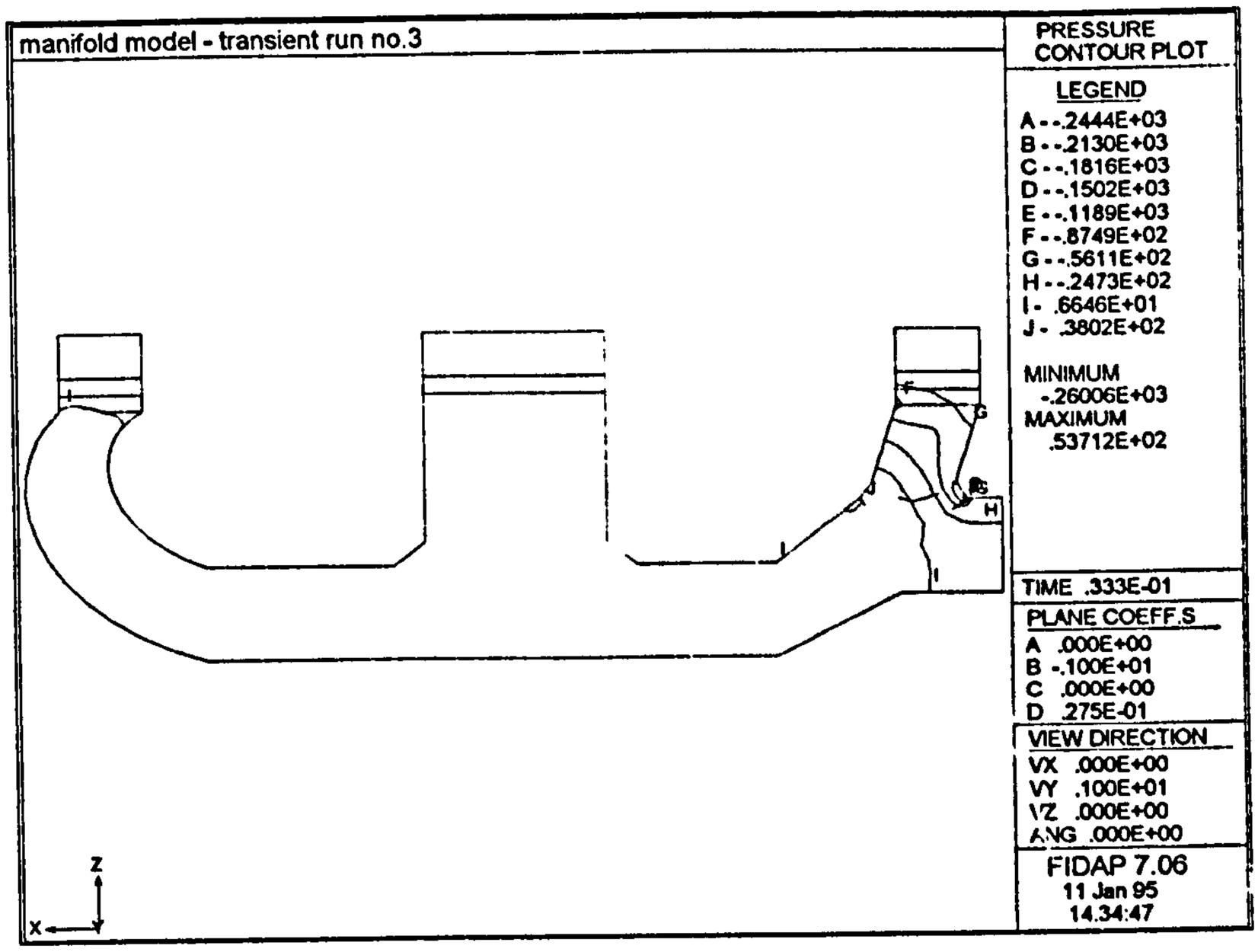

Figure 3.28. Pressure distribution for the final time step of transient run no.3.

The trends observed in comparing Figures 3.26 and 3.27 are continued in Figure 3.28. The pressure just upstream of Face 1 has now dropped to -0.92, with the region of favourable pressure gradient at the base of Face 1 now greatly reduced in size and the corresponding pressure recovery taking place across a smaller area of Face 1. The pressure contour at entrance to the bend leading to port 1 is now reduced to -0.92 also.

Taking the pressure distribution across Face 1 as an example, it can then be seen that the local pressures vary widely with time and at a given point, such as the leading edge of Face 1, the pressure was seen to go from a positive to a negative value in some 0.025s, indicating a marked variation in local pressure gradient at that point. Given that the pressure gradient is varying greatly in both space and time, there is then a clear need to account for this behaviour in the provision of a suitable wall law.

Figures 3.29 to 3.31 below detail the variation of y^+ across Face 1 over this time span.

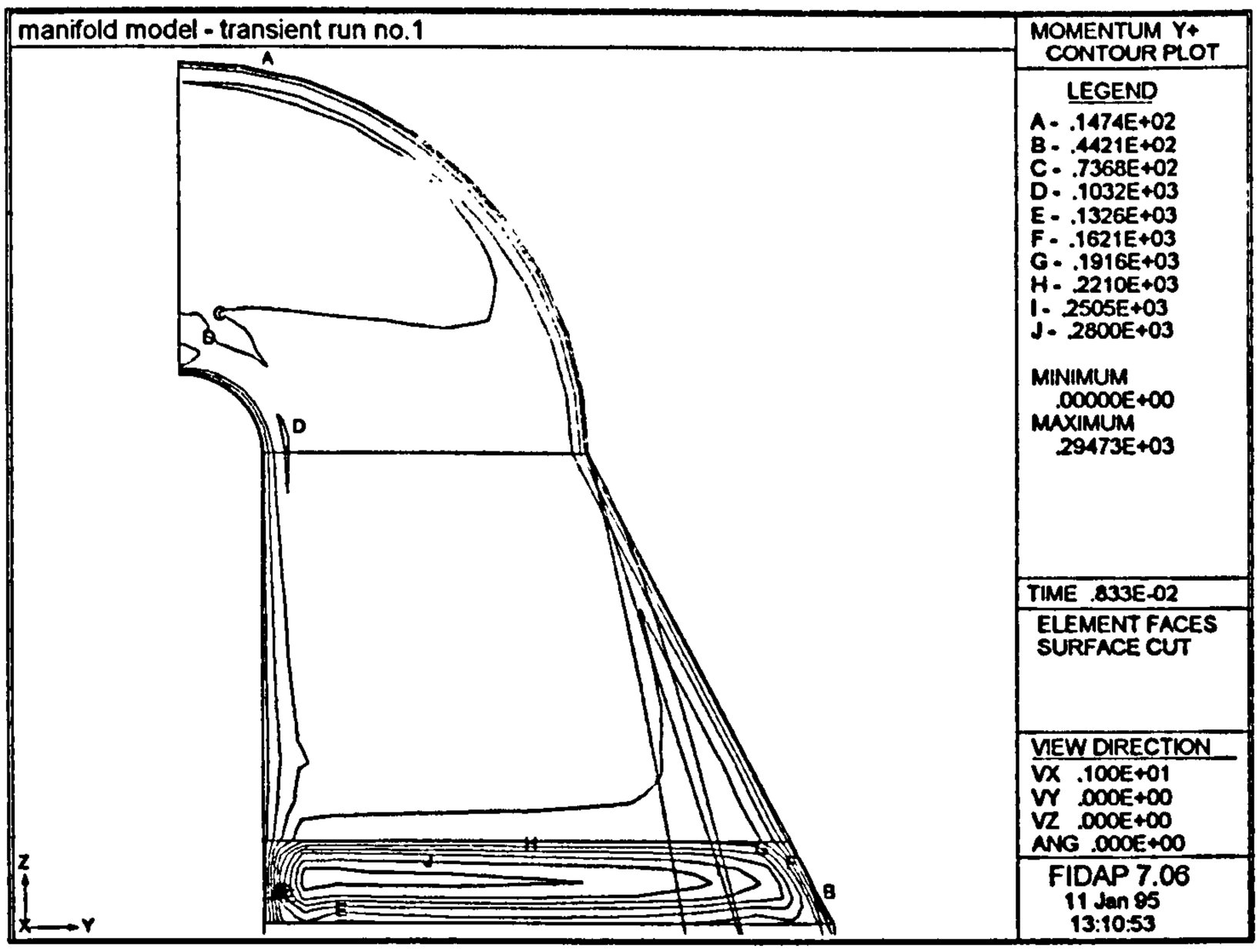

Figure 3.29. y^+ distribution across Face 1 at the end of transient run no.1.

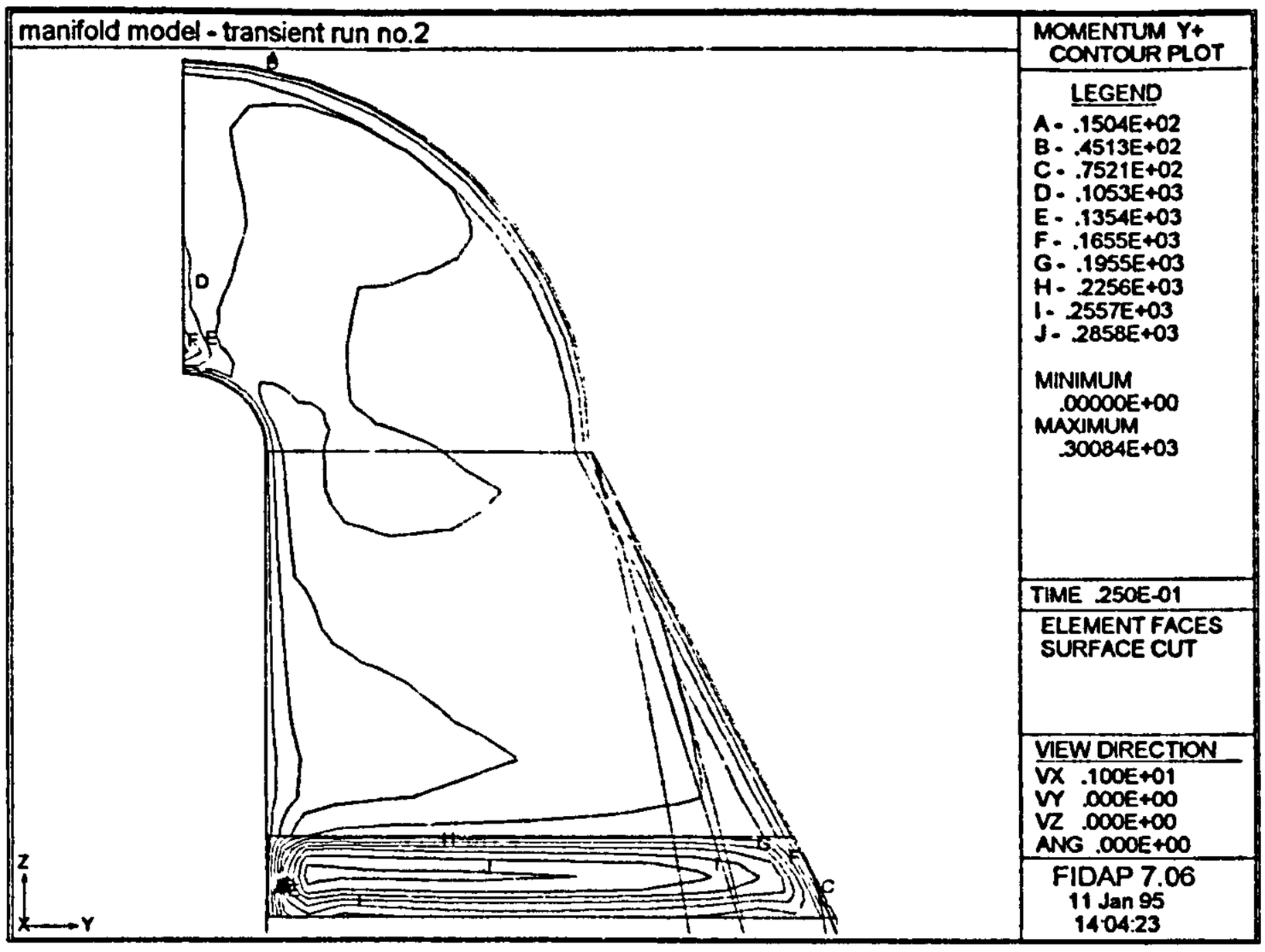

Figure 3.30. y^+ distribution across Face 1 at the end of transient run no.2.

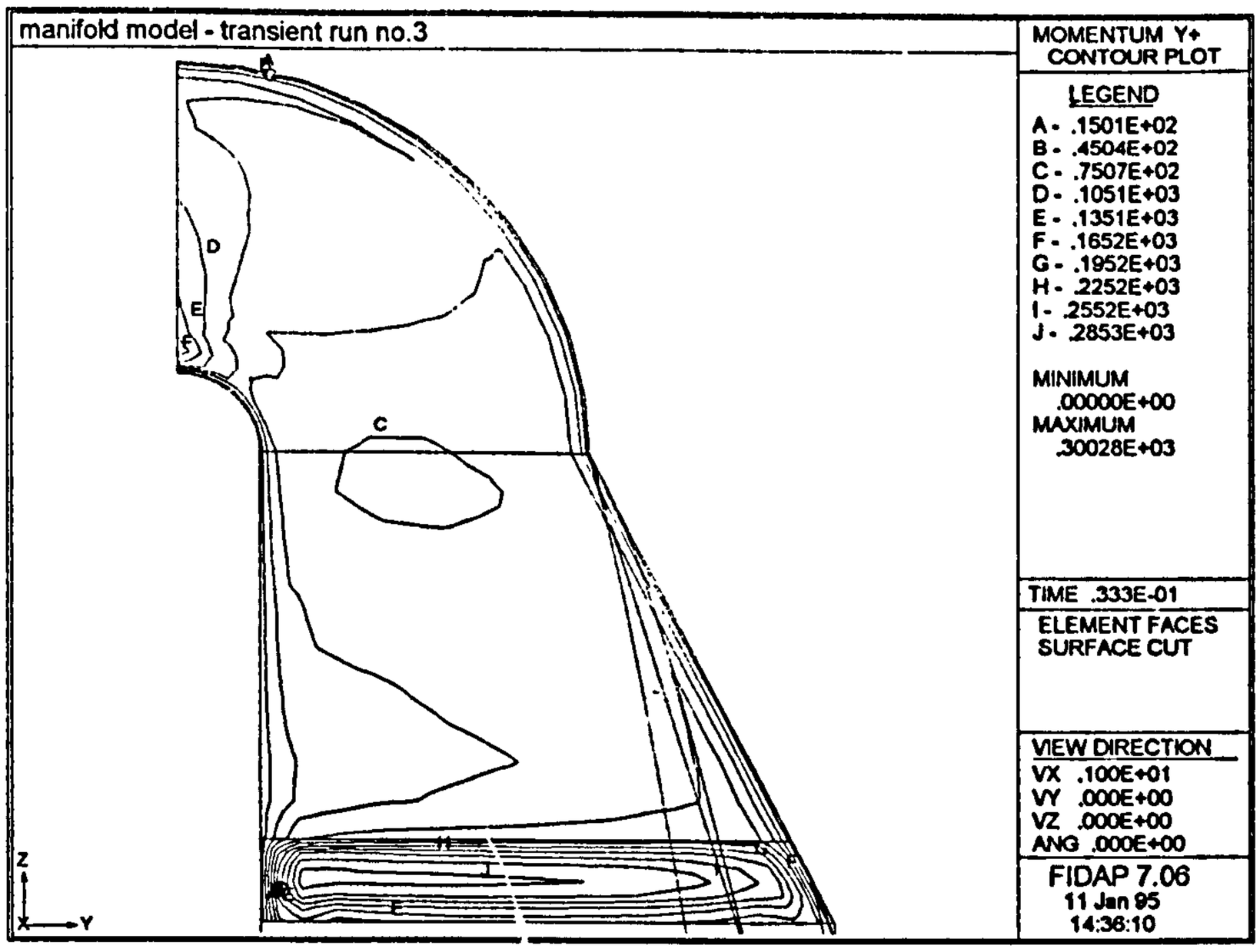

Figure 3.31. y^+ distribution across Face 1 at the end of transient run no.3.

At the end of transient run no.1, $y^+ \approx 15$ along the edges of Face 1 that join with the front and back faces of side branch 1. Such a value of y^+ falls below the minimum value at which the wall model of Haroutunian and Engelman (1991) is claimed to be valid. From the boundary representing the inlet port almost down to the lower, angled segment of Face 1, the bulk of Face 1, away from the periphery, has $y^+ \approx 73$, with values over the angled segment varying as $y^+ \approx 103 - 180$. Close to the inner radius of the final bend approaching port 1, there is a local peak in y^+ as $y^+ \approx 103$.

At the end of transient run no.2, conditions for y^+, as shown in Figure 3.30, are similar to that at the end of transient run no.1. However, the centre of the local peak on the inner radius of the bend before port 1 has now risen to $y^+ \approx 165$, with $y^+ > 100$ over the lower half of port 1. Likewise, Figure 3.31 shows a continuation of these trends.

The following figures detail the variation in y^+ across Face 3, being the upstream face of side branch 2/3 in the y-z plane, remembering that a recirculation zone was observed to develop with time next to this face.

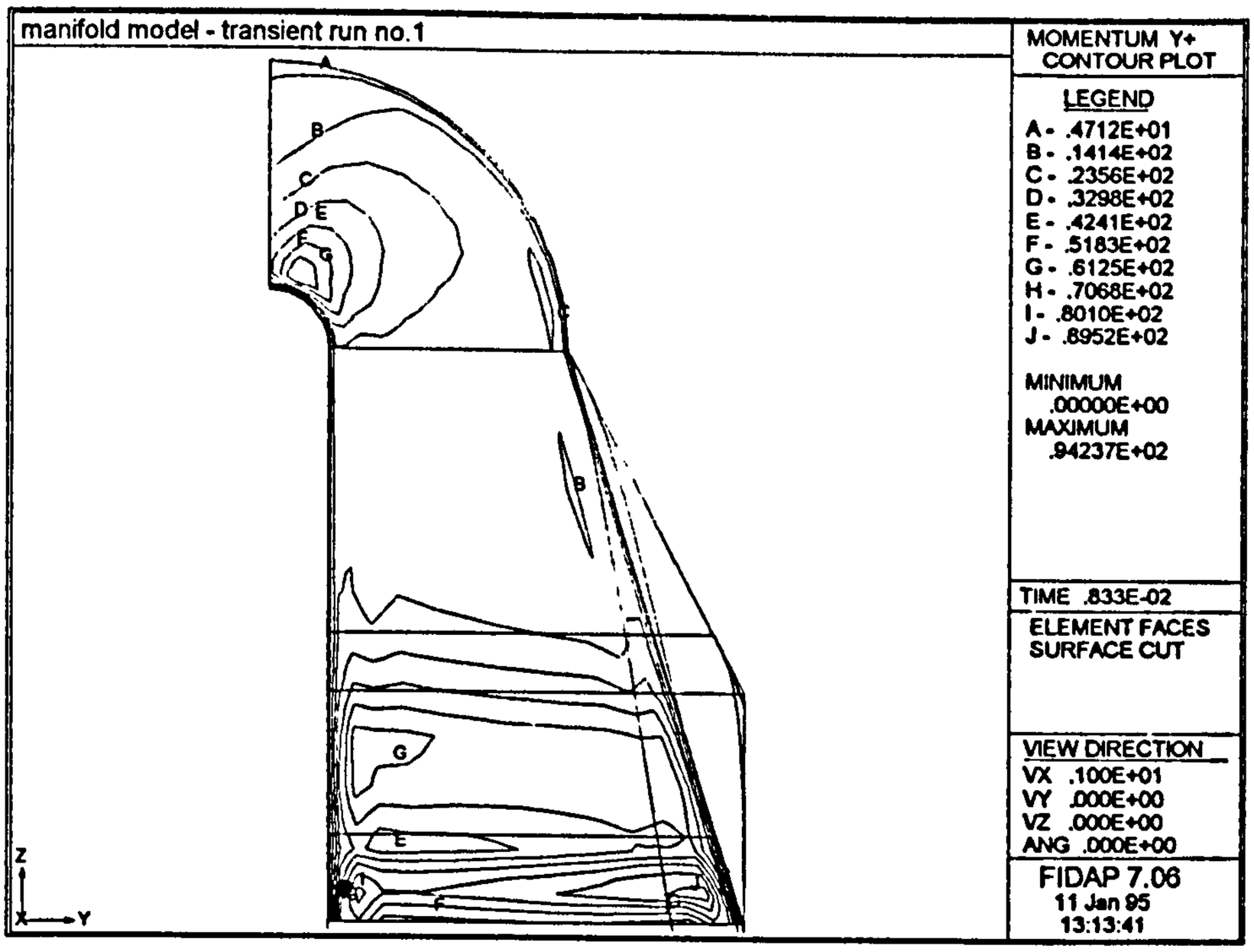

Figure 3.32. y^+ distribution across Face 3 at the end of transient run no.1.

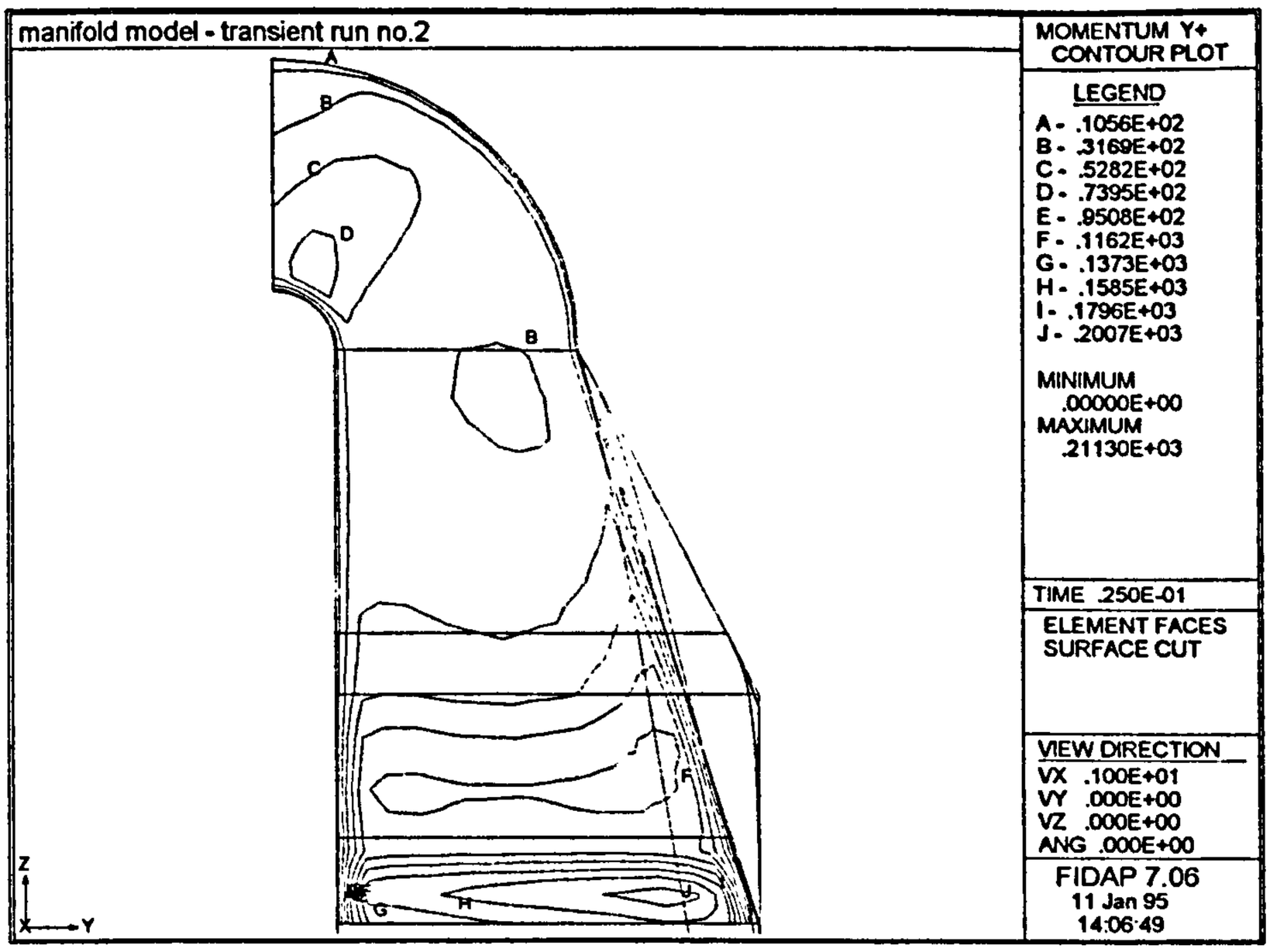

Figure 3.33. y^+ distribution across Face 3 at the end of transient run no.2.

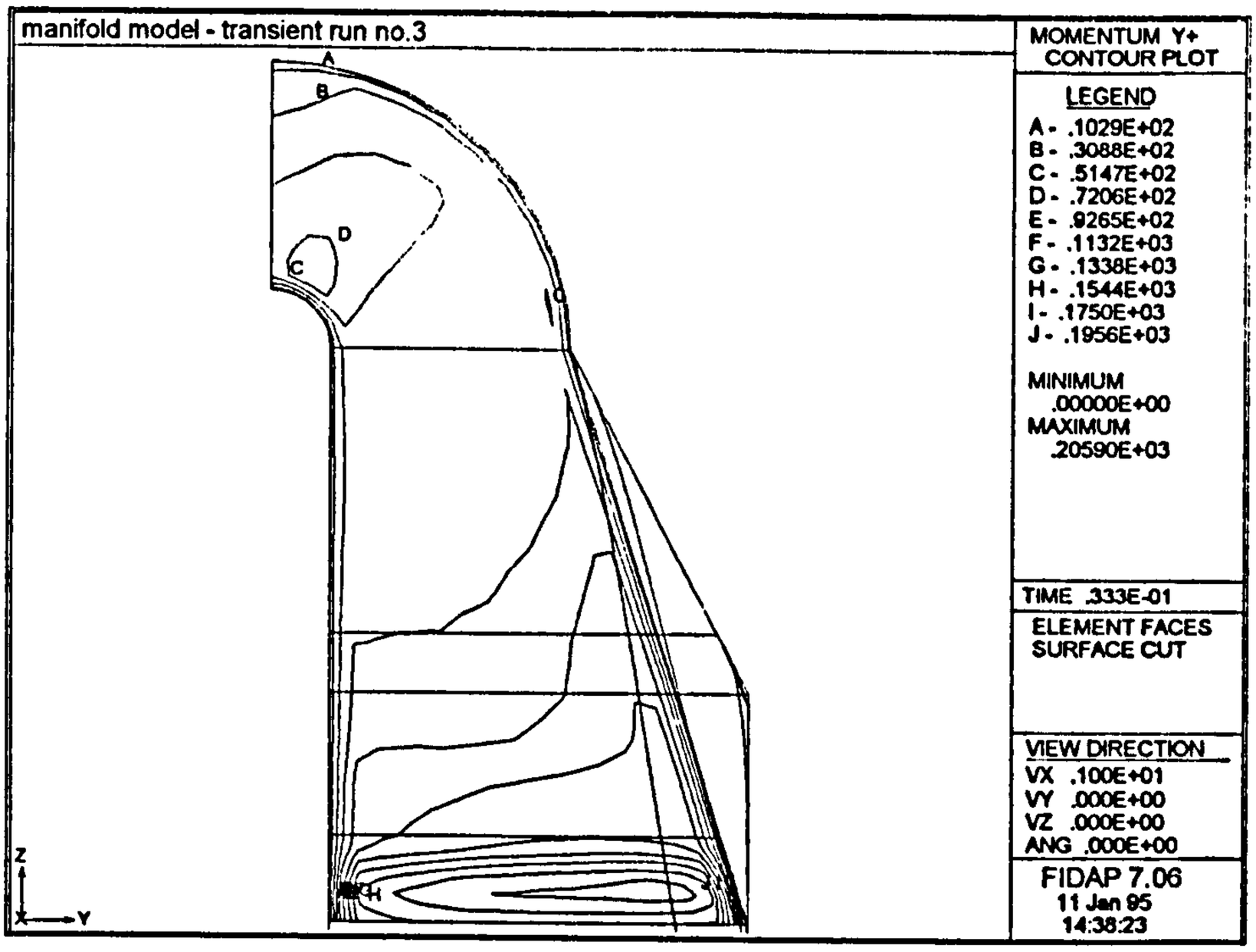

Figure 3.34. y^+ distribution across Face 3 at the end of transient run no.3.

In Figure 3.32, at the end of transient run no.1, during which port 3 was opened, $y^+ \approx 23$ across the upper two-thirds of Face 3, with a local peak of $y^+ \approx 61$ where the inner radius of the bend before port 2 meets the outlet boundary. In the lower portion of Face 3, $y^+ > 40$, with maximum values of $y^+ \approx 80$ across the lowest, angled segment of Face 3 (where it connects to the upper surface of the main duct).

At the end of transient run no.2, $y^+ > 100$ across the lower portion of Face 3, with maximum values of $y^+ \approx 200$ in the lowest, angled reaches. Across the upper two-thirds of Face 3, $y^+ > 50$ away from the peripheries, suggesting that the wall model is now valid in this region (pressure gradient arguments aside). The local peak at the base of the boundary representing port 2 now has the slightly greater value of $y^+ \approx 73$. At the end of transient run no.3, as shown in Figure 3.34, the general distribution of y^+ is similar to that of Figure 3.33.

A final comment on the problems with the model of Haroutunian and Engelman (1991) in regions of low velocity is made by consideration of Face 5, corresponding to the upstream boundary in the y-z plane of port 4.

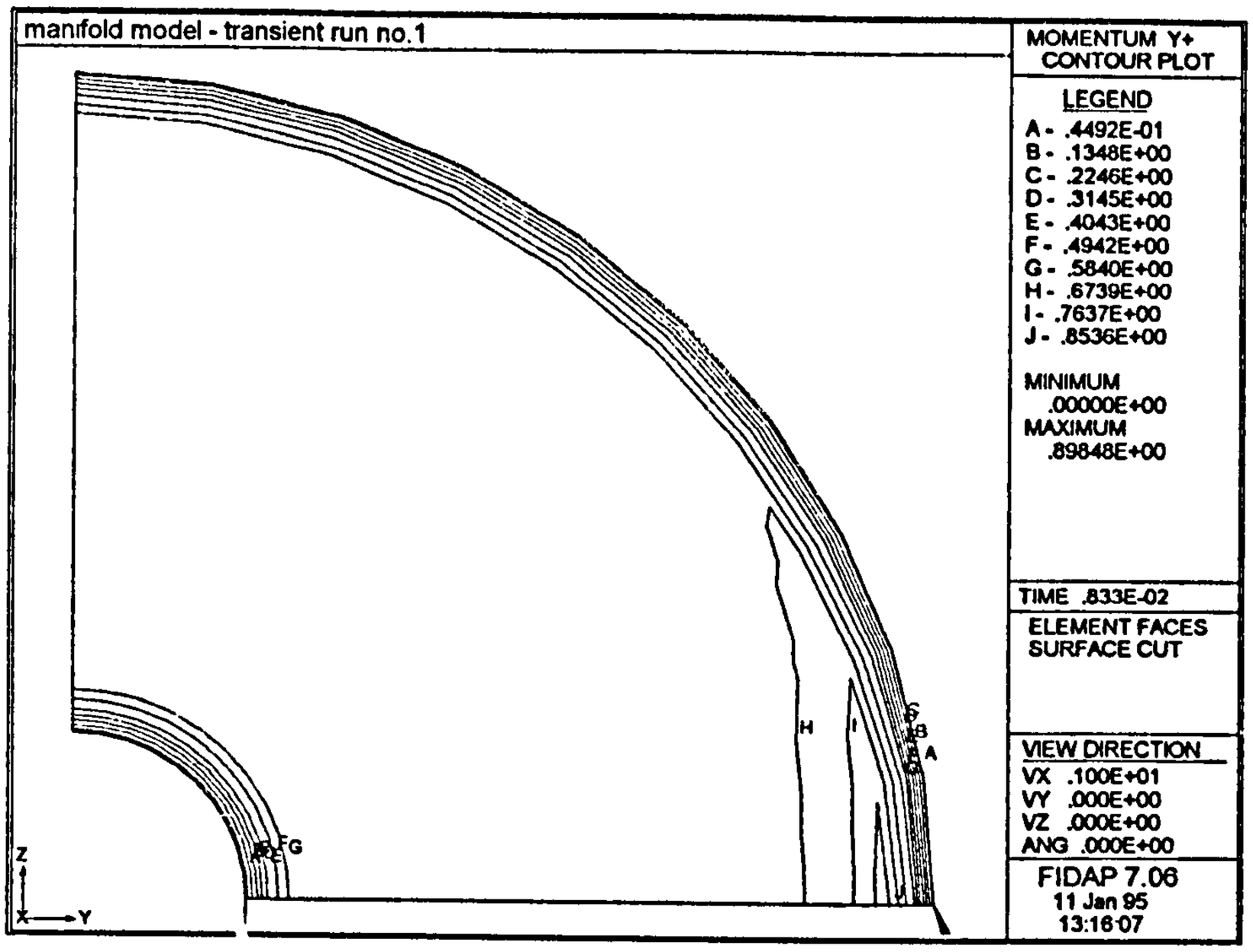

Figure 3.35. y^+ distribution across Face 5 at the end of transient run no.1.

At the end of transient run no.1, during which port 4 is closed, the y^+ values shown in Figure 3.35 are less than unity across the entirety of Face 5. Whilst this is consistent with the effective stagnation of the fluid under such conditions, at the end of transient run no. 3, y^+ is still less than 10 over Face 5 after opening port 4, as shown in Figure 3.36.

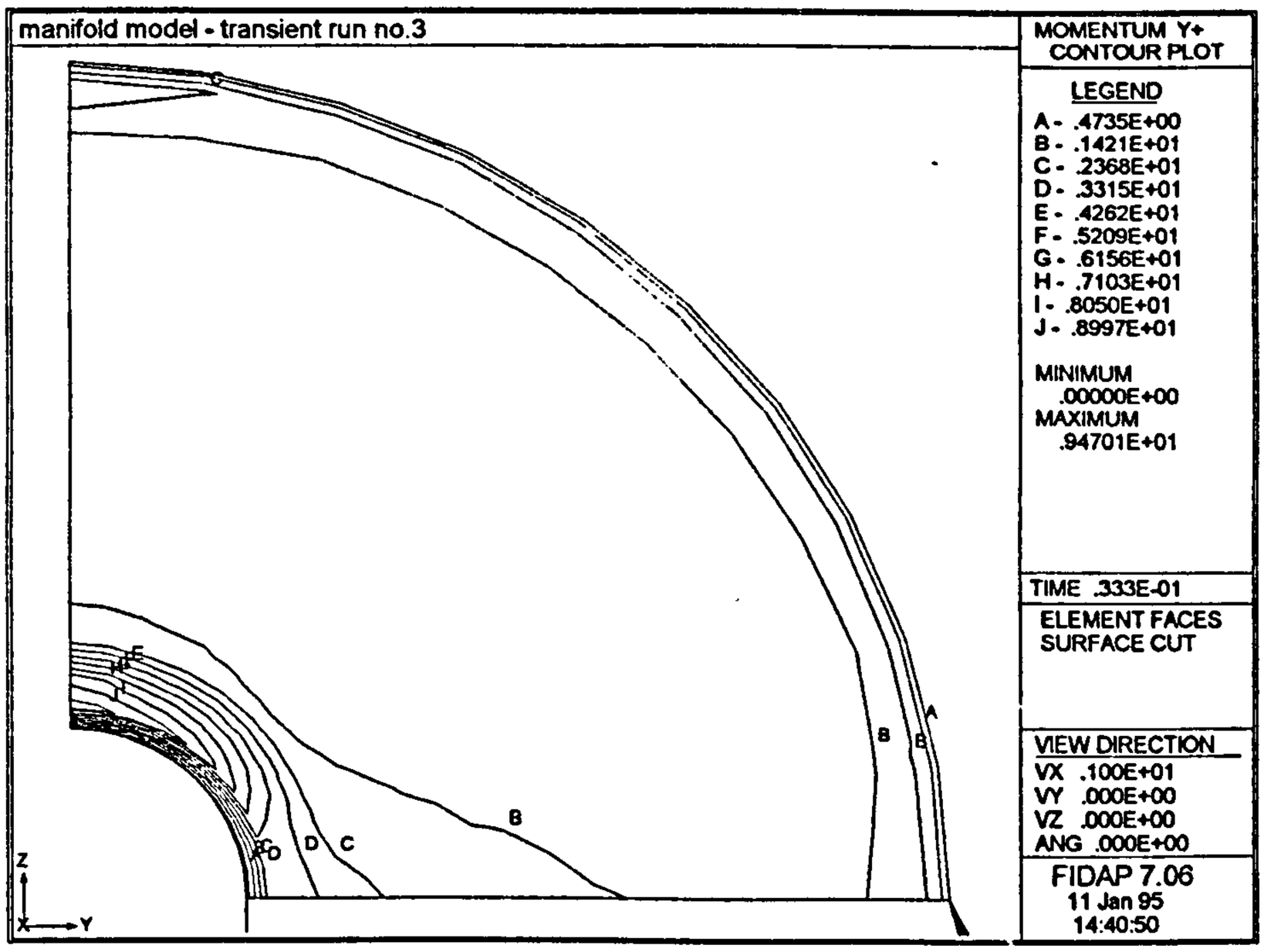

Figure 3.36. y^+ distribution across Face 5 at the end of transient run no.3.

3.4. Discussion of 3-d Computational Modelling.

When comparing the results of CFD modelling using 'traditional' wall models with experimental results, significant differences were observed. In the first instance, it had been suggested that a steady-state model of the manifold would bear some resemblance to the experimental results in that both gave a time-averaged description of the flow. However, examination of the steady-state results showed them to be deficient in the near-wall region. For example, at station I, the steady-state model results for the vertical traverse of the duct, Figure 3.13, deviated from the experimental Figure 3.5 both in magnitude across the freestream and in the predicted near-wall profile.

Likewise, the velocity profiles arising from individual time steps taken from transient runs showed marked differences in comparison with experimental results. Considering the vertical section at station I, Figure 3.14 for transient run no.1 differed in the magnitude of the freestream velocity from experimental Figure 3.5. After the closure of port 1 during transient run no.2, Figure 3.15 gave a poor description of the observed near-wall behaviour and significantly underpredicted freestream velocity across the greater part of the duct. Similar trends were also seen at the end of transient run no.3, in Figure 3.16. Such discrepancies appeared to be heightened in those instances where the general flow velocity was lowest. At station II, where local velocities were considerably lower than at station I even after the opening of port 4 at the start of transient run no.3, the computational results of Figures 3.20 to 3.23 related poorly to experimental Figure 3.7, especially in the near-wall region.

Comparing the steady-state and individual transient results, the separation bubbles observed in the steady case of Figure 3.9 were seen to move in both time and space during transient modelling under the influence of local, varying pressure gradients (see Figures 3.10 to 3.12). Given that the modelling method did not account for the pressure gradient and that the computational near-wall velocity profiles differed from experimental results, then these transient separation predictions must be viewed cautiously.

The closest correspondance with the experimental observations was provided by taking an average of the complete set of transient results at a given point. However, as the individual components of these averaged results deviated from those gained in practical experimentation, the averaged results were also poor in the near-wall region. For example, whilst Figure 3.17, showing the average of the transient vertical profiles at station I, bore greater resemblance to experimental Figure 3.5 than any of its constituent

profiles (being Figures 3.14 to 3.16), its near-wall predictions still did not meet with practical observations. Consequently, the CFD model was seen to be unable to replicate the results of simple laboratory experimentation. Whilst comparison with averaged transient results was shown to be more appropriate than with individual time steps, the lack of correspondance in the near-wall region showed the general modelling approach to be inadequate. Furthermore, since transient flow behaviour is a common feature of engineering problems, such shortcomings clearly require to be remedied.

The computational analysis of y^+ values and pressure gradients within the manifold then provided insight into the discrepancies between experimental and computational results. In Section 3.3.2, the results of transient modelling showed huge variations in local pressures, and hence in local pressure gradients, with time. This is shown clearly in the comparison of Figures 3.26 to 3.28, where the pressure gradients at the 'upstream' edges of the recirculation zones were seen to vary widely with time: the movement in the separation points was seen to correspond to these pressure changes.

Similarly, the y^+ values across the solid surfaces of the ducting were shown to be time-dependent. At Face 1 of side branch 1, Figures 3.29 to 3.31 showed marked variations in y^+, with significant regions of the modelled surface displaying y^+ values outside the operating range of the model of Haroutunian and Engelman (1991). Likewise, Figures 3.32 - 3.34 for Face 3 and Figures 3.35 and 3.36 for Face 5 showed problems in the observed range of y^+ values. For the model of Haroutunian and Engelman (1991), whilst they suggested coarsening of the mesh upon the occurence of extremely low values of y^+, for complex, time-dependent models to be conducted effectively, this would not be an appropriate solution having recognized y^+ itself to be a function of time. The experience of Section 2.4.2 was that a variety of 'traditional' wall laws were valid only for limited ranges of y^+; use of another of the commonly applied wall laws would not obviate this problem.

Taking an overview of the transient modelling results, they have been shown to offer poor correspondance with simple laboratory experimentation. The inability to reproduce even basic transient experimental data may be directly attributed to inadequacies in modelling of the near-wall region. Consequently, the need for an enhanced wall model, catering for pressure gradient effects and applicable over a wide range of y^+ values, has been demonstrated here experimentally, as well as having been argued from consideration of theory in Chapter 2.

3.5. Conclusions Arising from 3-d Computational Modelling.

The following conclusions may be drawn from the 'conventional' modelling of the inlet manifold:

i) The selection of appropriate CFD results is critical in seeking to draw a meaningful comparison with experimental data.

ii) The results from current CFD methods do not provide an adequate model of the near-wall region.

iii) Transient CFD results from 'conventional' models show marked variations in local pressure gradients and y^+ values with respect to both time and space; 'conventional' wall models take no account of such variations.

iv) The analysis of 'conventional' CFD model results for the inlet manifold supports the theoretical case of Section 2.7 for the development of a more robust wall model.

4. Computational Development.

The case proposing the theoretical need for a more robust wall model was laid out in Section 2.7 and the discussion of Section 3.4 demonstrated such a model to be necessary by comparison of experimental flow results with those provided by CFD. Of the boundary layer models of the wall law type reviewed, Coles' law of the wake appears to have the widest range of application, being valid from the outer edge of the viscous sub-layer to the freestream for a wide range of pressure gradients, including those that lead to separation. Notionally then, Coles' law should be a viable alternative to the widely used Reichardt's law as the influence of the local pressure gradient can be taken into account. Furthermore, if the flow variables close to the wall can be modelled more accurately by the proposed method, then a local reduction in mesh density might be afforded, in turning allowing larger flow systems to be modelled on a given computer system.

In setting out to use Coles' law in a computational environment, a number of practical points are of interest as

i) providing valid boundary conditions to the model,

ii) ensuring that the model is relevant locally,

iii) relating the computational points to their position within the simulated boundary layer and

iv) prescribing a link between Coles' wake parameter and the streamwise pressure gradient.

To develop such a Coles' law model, it is first necessary to determine suitable test cases by which its effectiveness may be gauged and then to describe those computational facilities deemed pertinent to its preparation as a result of preliminary investigations.

4.1. Proposed Test Cases.

In evaluating the effectiveness of C.F.D. codes and new modelling approaches, recourse is typically sought to a number of standard, or benchmark, tests. The flow characteristics of simple shear flows in two- and three-dimensional cases are readily replicated by most C.F.D. codes and so one of the criteria by which new methods are

judged is their ability to predict flow separation occurring in a variety of standard cases that have been rigorously studied in practical experiments.

With regard to demonstrating the usefulness of improved wall modelling techniques, in the guise of Coles' law, it is proposed to use two classic two-dimensional benchmark tests to assess the efficacy of the method. The pertinent two-dimensional cases are then thought to be

i) flow through an U-bend of tight curvature and
ii) flow over a backward facing step.

Whilst both cases are significant in their own right, being flow regimes that demonstrate marked separation experimentally, they may also be considered as basic geometric identities, common to a wide range of more complex flow domains. The inlet manifold test case considered in Chapter 3, for example, may be subdivided into a number of consecutive regions, some of which bear strong resemblance to these two-dimensional domains. As such, for a new model of the wall region to be of use in simulating complex flow geometries, its effectiveness should first be demonstrated with regard to fundamental flow configurations.

In both of the above examples, flow behaviour is governed by strong adverse pressure gradients, resulting in areas of recirculation that have been closely documented. As such, since the empirical basis of Coles' law takes account of the local pressure gradient and hence is valid up to the point of separation (Schofield, 1991), unlike the more traditional wall laws (such as Reichardt's law) which were prepared for boundary layers with zero pressure gradient, the Coles' law approach is expected to display a modelling advantage, in terms of computational demands and accuracy of results, over the more established methods. These benchmark tests will now be described, briefly, in turn.

4.1.1. The U-bend.

The first benchmark test to be considered is that of an U-bend of tight curvature. Here, whilst separation is generally considered to be undesirable in its leading to increased pressure losses, it may be advantageous where enhanced heat/mass and momentum transfer are required.

Separation in a turning channel typically depends upon the turn angle and the radius

of the bend, other factors being Reynolds number, turbulence intensity, length scales upstream of the bend and boundary layer thickness prior to the bend.

With regard to bends with large turn angles, strong separation downstream of the bend typically arises, due to the strong adverse pressure gradient arising from large curvature of the flow. For sharply turning flows, the system is thought to be governed by inviscid mechanisms and so simple models for viscosity and turbulence should provide good results. However, for bends with larger radius, the resulting pressure gradient will be more moderate and so separation will also depend upon turbulent and viscous transport mechanisms in the near-wall area. A balance of such mechanisms will determine whether separation occurs or not and so a more sophisticated turbulence model is generally required.

The benchmark test for a turning channel is then held to be the 180^0 U-bend, documented by the work of Sharma and Ostermier (1987) or that of Sandborn and Shin (1988). Such a problem is of practical interest, in being analogous to the internal passages of the Space Shuttle main engine. The geometry of this example is shown below as Figure 4.1.

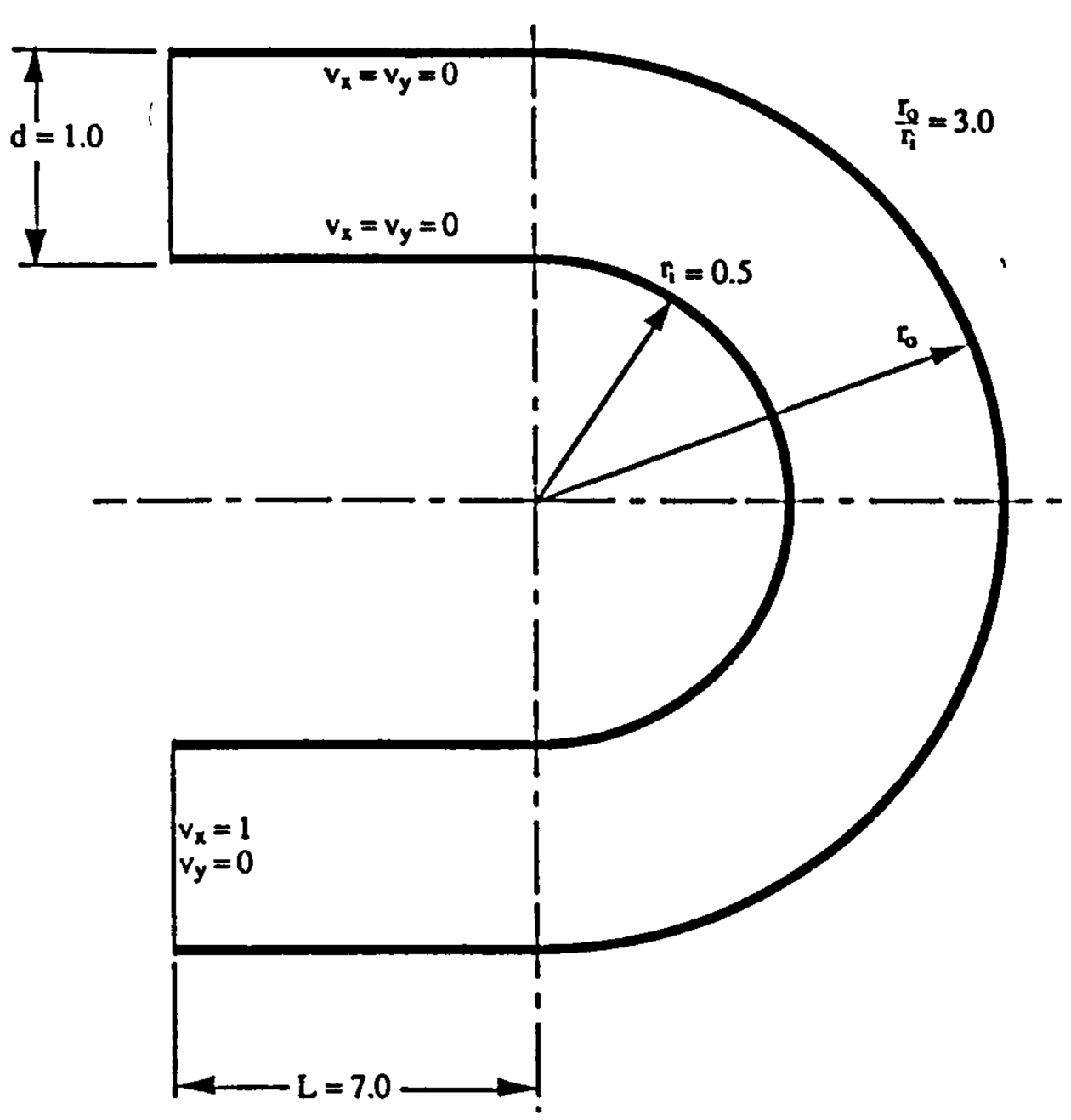

Figure 4.1. Cross-section of the U-bend of tight curvature.

The cross-section of the curved annular channel shown above has a duct width of

1.0, with the duct length upstream and downstream of the bend being 7.0. The radius of the inner wall of the bend is r = 0.5, with the ratio of outer to inner radii being 3.0. Flow enters the lower arm of the duct with an uniform inlet velocity of unity. No restrictions are placed on the outlet profile and all other boundaries are prescribed the 'no-slip' condition for velocity. By virtue of the symmetry of the flow domain, modelling may be reduced to an axi-symmetric study of the cross-section given as Figure 4.1.

4.1.2. The Backward Facing Step.

The backward facing step test case describes the two-dimensional, steady, turbulent, incompressible flow of fluid across a sudden expansion, as depicted in Figure 4.2 below.

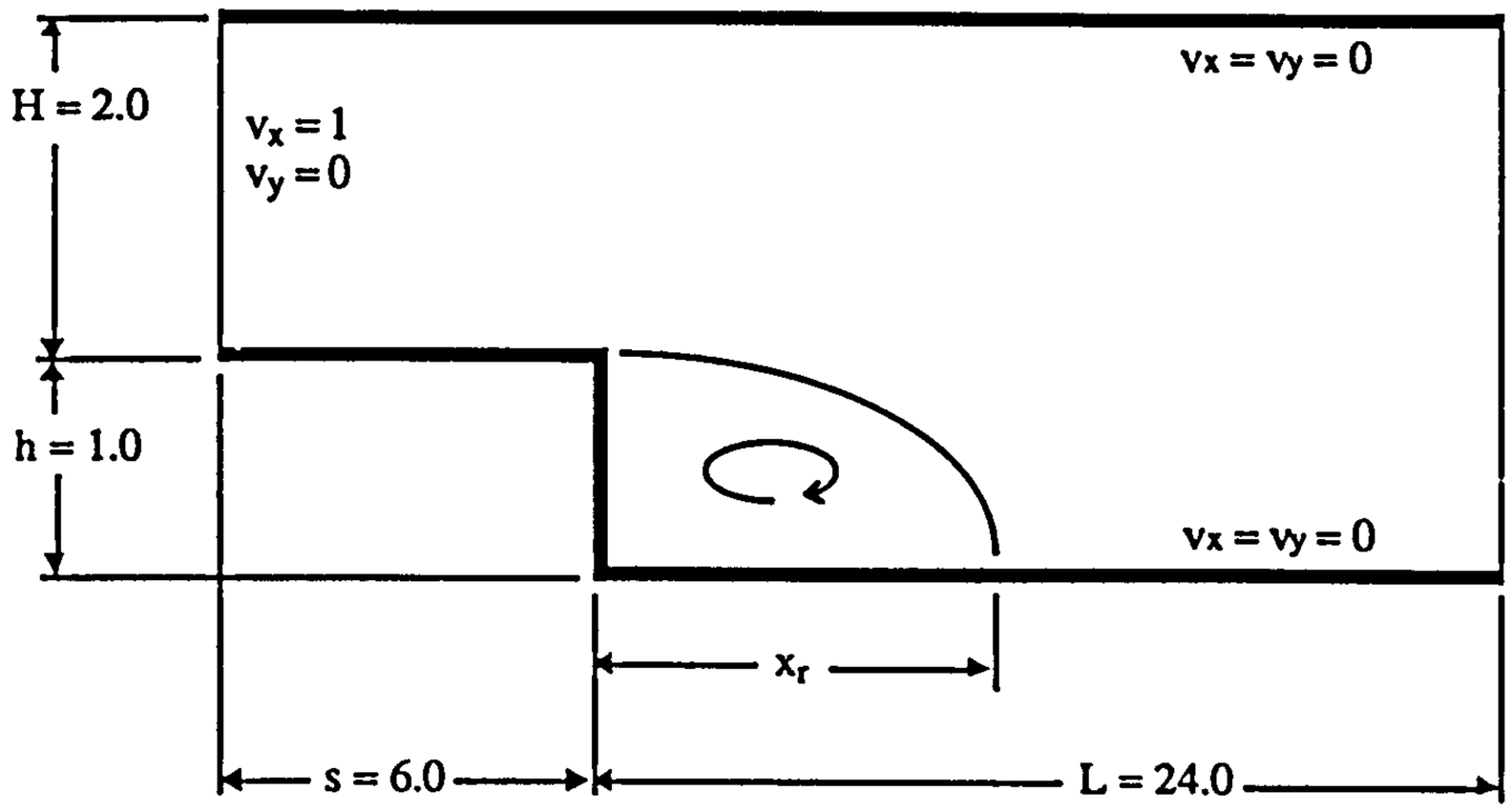

Figure 4.2. The geometry of the backward facing step.

The problem geometry details a duct of cross-section 3.0, reduced to a cross-section of height, H=2.0, at the inflow boundary, where an uniform velocity distribution ($v_x = 1.0$, $v_y = 0.0$) is imposed; this provides an abrupt step of height, h = 1.0. The inflow boundary is located six step heights upstream of the abrupt step, on the assumption that this distance allows for fully developed flow before the step is reached. Likewise, the outflow boundary is located some twenty-four step heights downstream of the step, to allow for re-establishment of fully developed flow after the recirculation zone, formed immediately in the wake of the step. No restrictions are imposed on the outflow boundary, whilst all other boundaries are set to the standard no-slip condition

($v_x = v_y = 0$).

Extensive experimental data is available for this problem (Kim, 1978); at low Reynolds number, an unique relationship exists between Reynolds number, the expansion ratio at the step and the normalized length of the recirculation zone, x_r/h, whilst for high Reynolds number, x_r is uniquely determined by the expansion ratio alone (Kaiktis et al., 1991).

The flow exists as a thin boundary layer at the entrance to the system, with low turbulence intensity in the main stream, hence presenting a challenge to the modelling technique to be used. In evaluating the numerical results, the length of the recirculation zone, x_r, is of principal interest. Experimentally, it is found that $x_r = (7.0 \pm 0.5)h$ (Kim, 1978).

4.2. Analytical Techniques.

The computational framework within which work was carried out was the FIDAP package. It is not intended to detail the mesh generation and solution techniques available in FIDAP (which are described exhaustively in the FIMESH manual (1994) and the FIPREP manual (1994) respectively). However, as this study hinges upon the prescription of an 'improved' wall model, the standard, high Reynolds number k-ε model and certain user-prescribed solution subroutines are of direct interest in developing a Coles' law model for computational use.

4.2.1. The High Reynolds Number k-ε Model.

In using a k-ε model to simulate bounded turbulent flows, in the regions close to the solid boundary, two main problems are encountered as

i) the resolution of sharply varying flow variables requiring the use of a disproportionately large number of mesh points, in turn leading to excessive computational expense and

ii) the very nature of the turbulence model used to describe the effects of viscosity on the turbulent field in the viscous sub-layer or, in other words, the effect of low Reynolds number on turbulence. Typically, k-ε models are only valid for high Reynolds number (as is the case with FIDAP) and so are inappropriate for

use in near-wall modelling.

On an historical basis, two approaches have been made to these difficulties as

i) a law of the wall technique, where wall functions are used to implement pertinent boundary conditions at the edges of the computational domain. However, this method becomes less relevant where there is pronounced departure from local one-dimensionality of flow (such as points of reattachment, separation and stagnation or where there are strong acceleration, retardation or body forces present) and

ii) less common but more sophisticated techniques, dispensing with the law of the wall concept and modelling the turbulent and mean flow fields all the way down to the wall. Variation of turbulent viscosity within the viscous sub-layer then requires to be modelled by some method such as

a) van Driest's mixing length model, with transition to the use of the standard k-ε model beyond the viscous sub-layer, or

b) use of a low Reynolds number variant of the k-ε model.

In either case, the technique will be both more universal and accurate than the prevalent law of the wall models but, in requiring very fine meshes to capture the sharply varying behaviour of the near-wall region, will again lead to excessive computational cost.

The FIDAP package uses an amalgam of these two main techniques to combine "the accuracy and universality of the latter with the cost-effectiveness of the former" (Haroutunian and Engelman, 1991). The computational domain is extended to the physical boundary and the full set of mean flow equations evaluated all the way to the wall. A single layer of 'special' elements is then used to model the near-wall region between the physical boundary and the fully turbulent freestream. These special elements use shape functions, based on universal near-wall flow profiles, to accurately predict the sharp variations in the mean flow variables across the near-wall region, where viscosity is important. The shape functions themselves are related to the characteristic Reynolds number of the locality and are adjusted automatically as simulation proceeds. Whilst the

standard k-ε model is used up to the outer edge of these special elements, the usual transport equations for k and ε (equations 2.13 to 2.15) are not valid beyond this point but are modelled by reference to the van Driest mixing length model instead.

This approach is transparent to the user, being invoked by assigning the special wall elements to the necessary boundaries and then specifying the correct boundary conditions (such as 'no slip' for impervious, stationary walls). FIDAP will then search all continuum elements within the computational domain for any element faces corresponding to the requested solid boundaries and then apply these special elements automatically.

These universal near-wall profiles, used to construct the shape functions of the special elements, result from consideration of the mean flow equations and from some simplifying assumptions, most notably that near-wall flow is predominantly parallel to the wall and is in local equilibrium and hence no transpiration or body forces need be considered. Under these conditions, both shear stress and mass flux across the sub-layer are very nearly constant and may be equated to their respective values at the wall. This assumption should be valid for most of the near-wall region, excepting points of reattachment, separation and stagnation or where there are strong non-equilibrium forces due to rapid variation in flow variables along the flow direction.

These assumptions then allow the mean flow equations to be manipulated to yield dimensionless velocity as a function of non-dimensionalised distance normal to the wall as

$$u^+ = \frac{v - v_w}{v^*} = f(y^+) \quad \text{and} \quad y^+ = \frac{\rho v^* \delta}{\mu}$$

FIDAP then uses Reichardt's law (equation 2.29) to model this relationship within the special elements.

Since the equations for k and ε may not be solved within the special element layer, a modelling scheme is required to simulate the variation of turbulent viscosity in this region. FIDAP uses a mixing length approach after Prandtl (1925) as

$$\mu_t = \rho l_m^2 \left[\left(\frac{\partial \bar{v}_x}{\partial x_y} + \frac{\partial \bar{v}_y}{\partial x_x} \right) \frac{\partial \bar{v}_x}{\partial x_y} \right]^{\frac{1}{2}} \qquad (4.1)$$

where the mixing length, l_m, for the case of smooth walls is taken from van Driest (1956) as

$$l_m = \kappa\delta(1-\exp(y^+/A)) \tag{4.2}$$

where A is an empirical constant, roughly equal to 26 for smooth walls with equilibrium near-wall flow, and y^+ is the dimensionless distance normal to the wall, expressed in terms of the kinetic energy at the edge furthest from the wall of the special wall element, k_t, as

$$y^+ = \rho\frac{(C_\mu^{1/2}k_t)^{1/2}y}{\mu} \tag{4.3}$$

The exponential term in van Driest's expression is then a viscous damping term, progressively suppressing the mixing length as y^+ tends to zero.

As k and ε, in the turbulence model, are only evaluated up to the outer border of the special elements, boundary conditions are required for kinetic energy and turbulent dissipation at this interface as

$$\frac{\partial k}{\partial n} = 0 \tag{4.4}$$

and

$$\varepsilon = \frac{(C_\mu^{1/2}k)^{3/2}}{\kappa\delta} \tag{4.5}$$

Again, local equilibrium is assumed and where k is constant, the turbulence length scale, $\frac{k^{3/2}}{\varepsilon}$, will vary linearly with normal distance from the wall, n. This 'Neumann' boundary condition for k is important: at the end of each iteration, the value of k is used to evaluate the characteristic turbulence velocity scale for the near-wall region as $k^{1/2}$. In turn, this will yield the local element Reynolds number, which is then used to control the form of the special shape functions.

From a practical point of view, the method is only valid if the viscous and

transitional sub-layers are fully contained by the special elements. If the sub-layer expands into the normal elements, then k and ε will be evaluated by the general, or freestream, technique in the low Reynolds number area. As such, where local element Reynolds number is markedly less than thirty, a *coarser* computational mesh should be employed adjacent to the wall.

4.2.2. Prescription of Boundary Conditions by Subroutine.

In seeking to model the near-wall region of a flow regime using Coles' law, then the wall model of Haroutunian and Engelman (1991) is to be dispensed with. It will then be necessary to supply a Coles' law model as a boundary condition to the simulated flow, between the solid surface and the freestream, as governed by the k-ε model. An effective Coles' law model will require a range of information; at a given point where Coles' law is to be evaluated, knowledge of the local geometry of the computational mesh and of local pressure and velocity gradients is necessary. Furthermore, such a model will need to interact with the solution as it proceeds and so a number of relevant subroutines, available within FIDAP may be seen as

i) subroutine USRINI, the variable derivative control subroutine, which requests that the solution procedure calulate the derivatives of selected solution variables,
ii) subroutine USRSKE, the source subroutine, which has access to the derivatives of solution variables and to geometric data describing the mesh and
iii) subroutine USRBCN, the boundary condition subroutine, which evaluates user-prescribed boundary conditions.

Since no one subroutine available within the solution procedure has access to all the information necessary to operate Coles' law, then a number of subroutines, each providing a portion of the required data, will be required to operate in unison to provide a viable Coles' law model. Once a given subroutine has accessed pertinent data, it should be possible to pass it to other subroutines involved in the Coles' law model by use of COMMONBLOCK statements, coded into the Fortran subroutines. The above mentioned subroutines will now be described in turn. (It should be noted that the following discussions relate to how the subroutines actually operate and not to those explanations provided by the FIDAP user manuals.)

Certain solution procedure subroutines, such as the source subroutine, have access to the arrays VARI and DVARI, which contain the solution variable values and their derivatives respectively. In order to keep computational time to a minimum, however, only those derivatives of the solution variables that are specifically requested by the user are evaluated. The solution variable derivatives that are required to be calculated may be defined by use of the variable derivative control subroutine.

A number of pointers exist for the possible degrees of freedom for the problem as shown in Table 4.1. below.

Degree of freedom	Pointer
v_x	kdu
v_y	kdv
v_z	kdw
k	kdk
ε	kde
p	kdp

Table 4.1. Showing the pointers denoting various degrees of freedom.

The variable derivative control subroutine then takes the form

```
subroutine USRINI(inivar)
include 'IMPLCT.COM'
include 'PARUSR.COM'
dimension inivar(*)
      .
      .
body of subroutine
      .
      .
return
```

The INCLUDE statements listed invoke COMMON files within the main body of FIDAP; these files declare the use of implicit double precision and define the pointers shown in Table 4.1. as PARAMETERs.

To request the calculation of the derivatives of a solution variable, then the appropriate entry in the INIVAR array is simply set to unity within the body of the subroutine. For example, should the user require the derivatives of the x-component of velocity to be calculated, then the body of the subroutine should contain

```
inivar(kdu) = 1
```

The notional purpose of the source subroutine is to specify the presence of a source term in the transport equations for kinetic energy and turbulent dissipation. As the source term is evaluated on a volumetric basis, the region to which it is to be applied must be a surface in 2-d or a volume in 3-d problems. The source subroutine then takes the form

```
      subroutine USRSKE(nelt,ne,ng,sorce,vari,dvari,ndfcd,ldofu,shp,
     c                  dsdx,xyzl,prop,time,npts,ndp,mndp,ierr,iopt,
     c                  visct,viscl,den,mdvsc)
      include 'IMPLCT.COM'
      include 'PARUSR.COM'
      dimension sorce(npts),visct(npts),viscl(9,npts),den(npts)
      dimension shp(mndp,npts),dsdx(mndp,npts,ndfcd),xyzl(npts,ndfcd)
      dimension prop(*),vari(npts,*),dvari(npts,ndfcd,*),ldofu(*)
      iopt=n
      do 10  i = 1, npts
            .
            .
            body of subroutine
            .
            .
            sorce(i) = v
10          continue
      zr0 = 0.D0
      return
```

Amongst the dummy arguments to the subroutine, those of principal interest are DVARI, IOPT, LDOFU, NDFCD, NELT, NPTS and VARI. (The statement given as zr0 = 0.D0 relates to FIDAP's error tracing system and must be included in the subroutine.)

Whilst the subroutine call in the solution procedure specifies whether a kinetic or a dissipation source is to be evaluated, the source type has to be defined within the subroutine as well; by setting IOPT to zero, the source type is understood to be kinetic energy, whilst a value of unity requests a dissipation source.

The subroutine evaluates the source term in the relevant transport equation for each individual element within the overall region to which the subroutine is applied. The argument NELT takes the name of the element currently under analysis as the subroutine sweeps through the region being studied. To be specific, the source term is calculated for each of the integration points present within each element considered. The number and distribution of integration points within an element is denoted by NPTS. For example, a linear, 2-d element will have four integration points as shown in Figure 4.3 below.

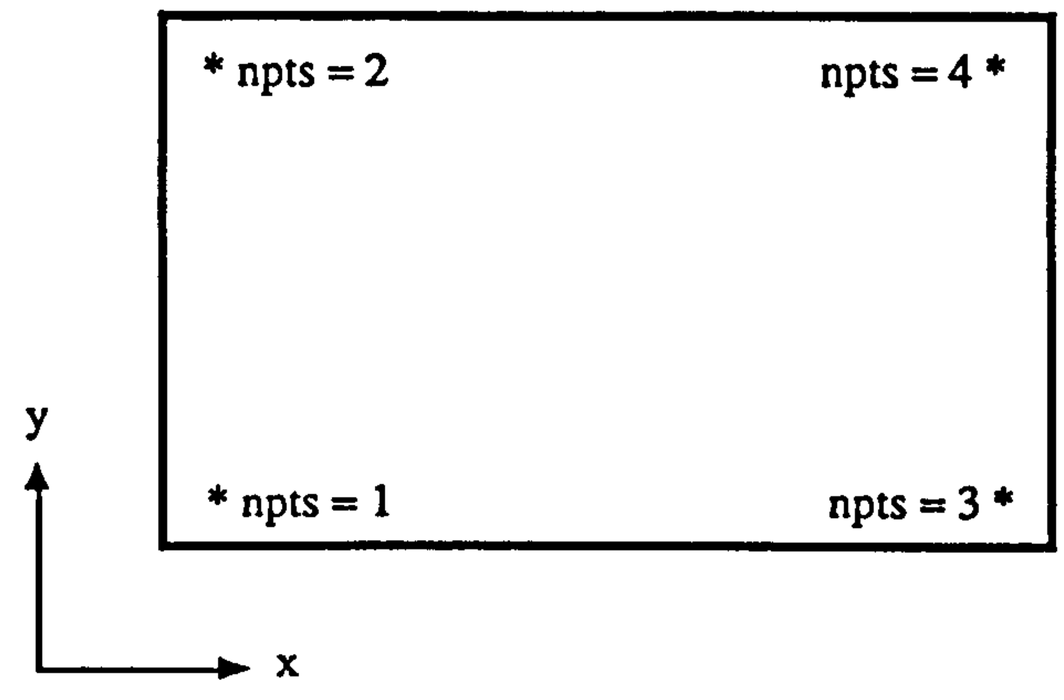

Figure 4.3. The distribution of integration points in a linear, 2-d element.

A simple flowchart for the operation of the subroutine may be seen as Figure 4.4 below.

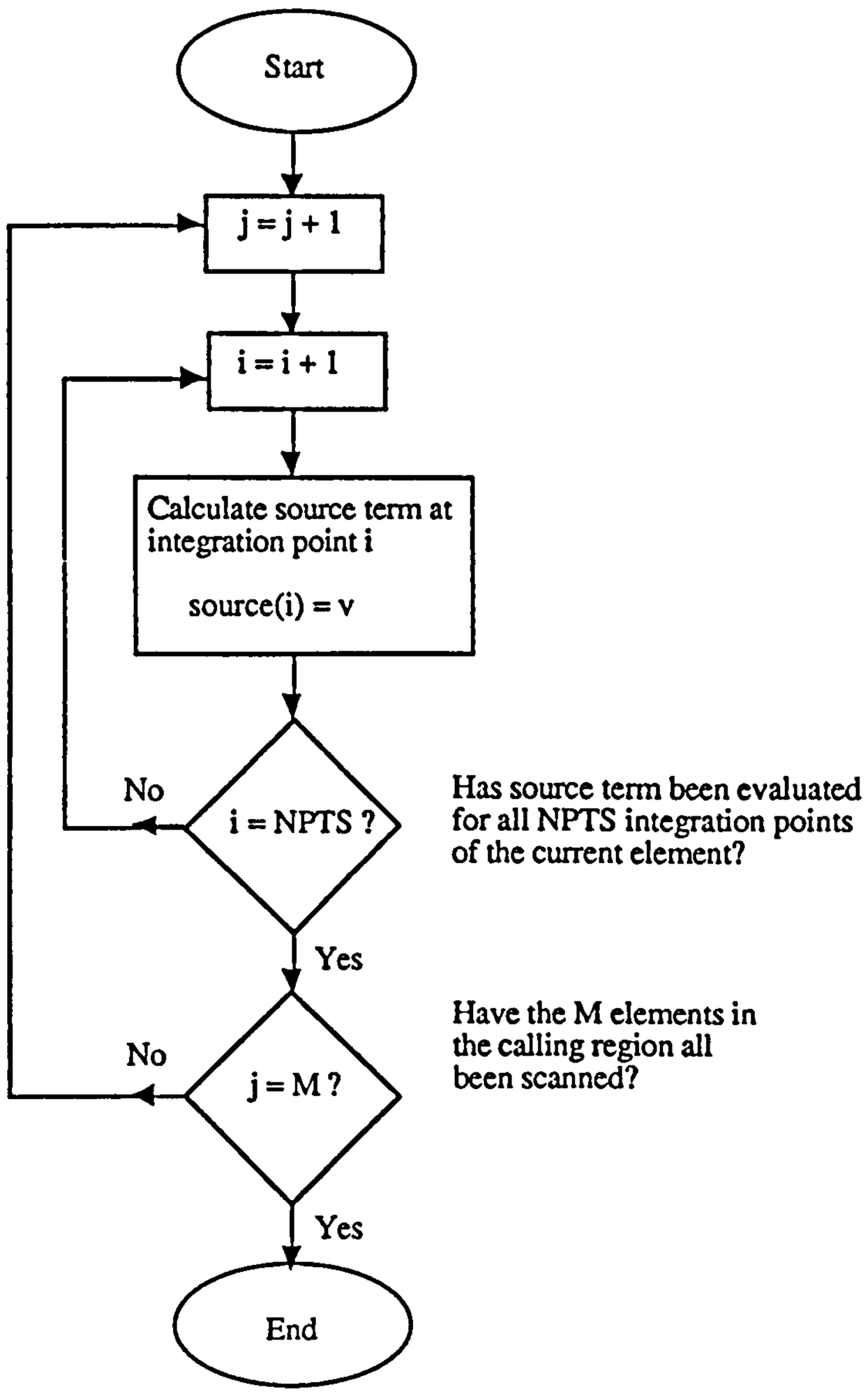

Figure 4.4. Simple flowchart for the source subroutine.

Note that the routine by which all elements contained within the calling region are accessed is invisible to the user and does not have to be overtly coded into the subroutine.

The subroutine must return a calculated value for the source term at each of the integration points for each element within the calling region as sorce(i) = v. Since the purpose of calling this subroutine, with regard to the implementation of Coles' law, is not to incorporate a source term into the model but to gain access to information available within the subroutine, then the source term should be set to zero uniformly as

sorce(i) = 0.0

The data which can be extracted from the source subroutine will now be considered.

The array XYZL contains the geometric co-ordinates of the integration points of each of the elements within the mesh. However, as the subroutine only analyses those elements contained within the calling region, care should be exercised when invoking this subroutine to ensure that all those elements of interest will be considered. The geometric co-ordinates are stored within the array as

```
xyzl ( npts, ndfcd )
```

where the first dimension, NPTS, denotes the integration point and the second dimension, NDFCD, specifies the co-ordinate type. NDFCD = 1 corresponds to the x co-ordinate, 2 to the y co-ordinate and 3 to the z co-ordinate. For example, the y co-ordinate at integration point 1 of an element is stored as

```
xyzl ( 1 , 2 )
```

All co-ordinates thus accessed will be related to the global Cartesian co-ordinate system used for problem solution.

LDOFU is a variable index array and is used as a pointer to specify the degree of freedom to be accessed within the VARI and DVARI arrays. The possible values of LDOFU are given in Table 4.1. So, for example, the x-component of velocity may be pointed to as

```
ldofu ( kdu )
```

The VARI array contains the values of solution variables at each integration point within each element of the entire mesh as

```
vari ( npts , * )
```

where the second dimension, *, is a floating argument corresponding to the total number

of active degrees of freedom in the problem. Thus, to access, say, the value of the x-component of velocity at integration point 1 of an element

```
vari ( 1 , ldofu ( kdu ) )
```

Care must be taken not to request values from VARI equating to degrees of freedom not active for the current problem.

The DVARI array contains the values of the solution variable derivatives at each integration point within the entire mesh as

```
dvari ( npts , ndfcd , * )
```

where the first dimension denotes the integration point, the second the derivative co-ordinate and the third is a floating argument corresponding to the total number of active degrees of freedom in the problem. For example, the derivative of the x-component of velocity with respect to y, namely $\frac{dv_x}{dy}$, at integration point 1 of an element could be accessed by

```
dvari ( 1 , 2 , ldofu ( kdu ) )
```

Again, caution should be exercised to ensure that only those solution variable derivatives that have been prepared by the use of the variable derivative control subroutine are requested.

Finally, the interactive subroutine for the evaluation of boundary conditions will be described. The boundary condition subroutine template then has the form

```
      subroutine USRBCN(val,node,idf,time,sol,ndof,numnp,ldofu,
     c                  constr)
      include 'IMPLCT.COM'
      include 'PARUSR.COM'
      dimension sol(*),id(numnp,ndof),constr(*),ldofu(*)
            .
            .
```

```
body of subroutine
        .
        .
val=v
zr0 = 0.D0
return
end
```

The subroutine is required to return a value for a specified degree of freedom for each node within the calling region. As such, the nature of the boundary condition subroutine is different to that of the source subroutine, in that its internal operation is by node and not by element. Thus a simple flowchart for the subroutine may be seen as Figure 4.5 below.

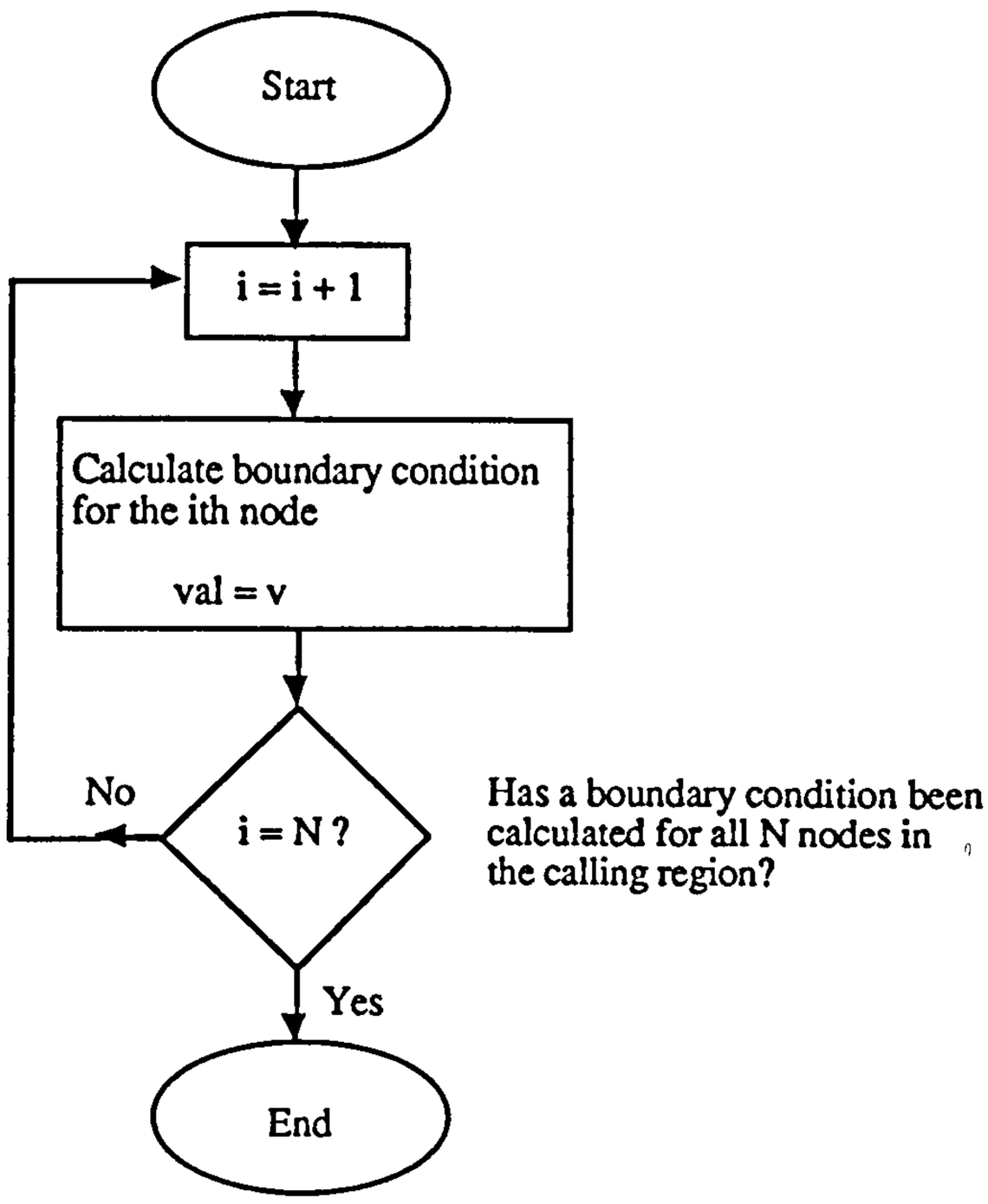

Figure 4.5. Simple flowchart for the boundary condition subroutine.

Note that the routine by which all nodes contained by the calling region are accessed is invisible to the user and does not have to be overtly coded into the subroutine.

Amongst the dummy arguments to the subroutine, those of principal interest are ID,

IDF, LDOFU, NDOF, NODE, NUMNP and SOL. The argument LDOFU functions as in the source subroutine. The argument NODE takes the name of the node currently under analysis as the subroutine sweeps through the region being studied. IDF is a pointer, defining the type of boundary condition to be calculated; its possible values are tabulated below.

Degree of freedom	IDF
v_x	1
v_y	2
v_z	3
k	4
ε	5
p	6

Table 4.2. Showing the possible values of the pointer, IDF.

Unlike the pointer IOPT in the source subroutine, IDF is set automatically by the command calling the subroutine. This is important - as FIDAP will only suffer the use of one subroutine of each possible type for a given problem, then IDF may be used as a discriminator to allow the one boundary condition subroutine supported by the problem to solve for more than one type of boundary condition.

SOL is the FIDAP solution vector, containing the values of currently active solution variables for each node within the entire mesh (unlike VARI in the source subroutine, which stores such information based upon integration points). ID is a degree of freedom connection array, storing information as

id (numnp , ndof)

where NUMNP is the total number of nodes in the mesh and NDOF the total number of active degrees of freedom. ID can be used to access solution information stored in SOL. For example, to access the current value of the x-component of velocity at

node 5 in the mesh

```
ieq = id ( 5 , ldofu ( kdu ) )
valx = sol ( ieq )
```

5. Development of Models for Wall Effects in 2-d.

In Section 4.1 the proposed test cases for the development of a Coles' law model were the U-bend with tight curvature and the backward facing step. These two flow domains constitute fundamental flow geometries, common to more complex domains such as the inlet manifold of Chapter 3. As such, in applying Coles' law to the U-bend and the backward facing step, its effectiveness in replicating basic flow features may be gauged, hence commenting on its potential use with regard to more elaborate flows. In either case, at the interface between the Coles' model and the k-ε turbulence model, used in the freestream, it is necessary to prescribe values for velocity, kinetic energy of turbulence and rate of turbulent dissipation of energy, namely to provide v, k and ε.

A successful model must not only offer these boundary conditions to the freestream but also test the local validity of Coles' law of the wake, as

$$\frac{\bar{v}}{v^*} = f\left(\frac{yv^*}{\nu}\right) + \frac{2\Pi}{\kappa} w\left(\frac{y}{\delta}\right) \qquad (5.1)$$

The function f in the above equation is expressed in terms of inner wall variables by equation 2.24 as

$$f\left(\frac{yv^*}{\nu}\right) = \frac{1}{\kappa} \ln y^+ + B \qquad \text{with } y^+ = \frac{yv^*}{\nu}$$

At each point where Coles' law is to be applied, the model will only be significant provided that $y^+ > 5$. In other words, the model should not be used to describe behaviour within the viscous sub-layer, in which a description of the flow is provided by equation 2.28 as

$$u^+ = y^+ \quad \text{or} \quad \frac{\bar{v}}{v^*} = \frac{yv^*}{\kappa}$$

The wake function, w, in equation 5.1 must then be considered. w, in providing a model for the excess velocity over and above that predicted by the simple log law equation of equation 2.24, relates the the boundary layer thickness, δ, to the point under consideration, at a distance, y, normal to the local solid boundary. This wake function is

given by equation 2.46 as

$$w\left(\frac{y}{\delta}\right) = \sin^2\left(\frac{\pi}{2}\eta\right) = 3\eta^2 - 2\eta^3 \qquad \text{with} \qquad \eta = \frac{y}{\delta}$$

Finally, in order to fully evaluate equation 5.1, it is necessary to describe the link between the wake parameter, Π, and the streamwise pressure gradient, $\frac{dp}{dx}$, at the edge of the boundary layer (i.e. at $y = \delta$).

5.1. A Basic Algorithm for Model Preparation in Two Dimensions.

To evaluate Coles' law, as described by equation 5.1 above, the model must first determine the location of the point of application in relation to the wall, then describe the local velocity gradient, $\frac{dv_x}{dy}$, in order to provide the wall friction velocity, v^*, and finally calculate the required properties, ν, k and ε, to link with the freestream model. As FIDAP can only support one boundary condition subroutine within the solution procedure, this subroutine must be capable of calculating ν, k or ε, subject to relevant subroutine calls from the main programme. A prototype algorithm for the operation of Coles' law is shown below.

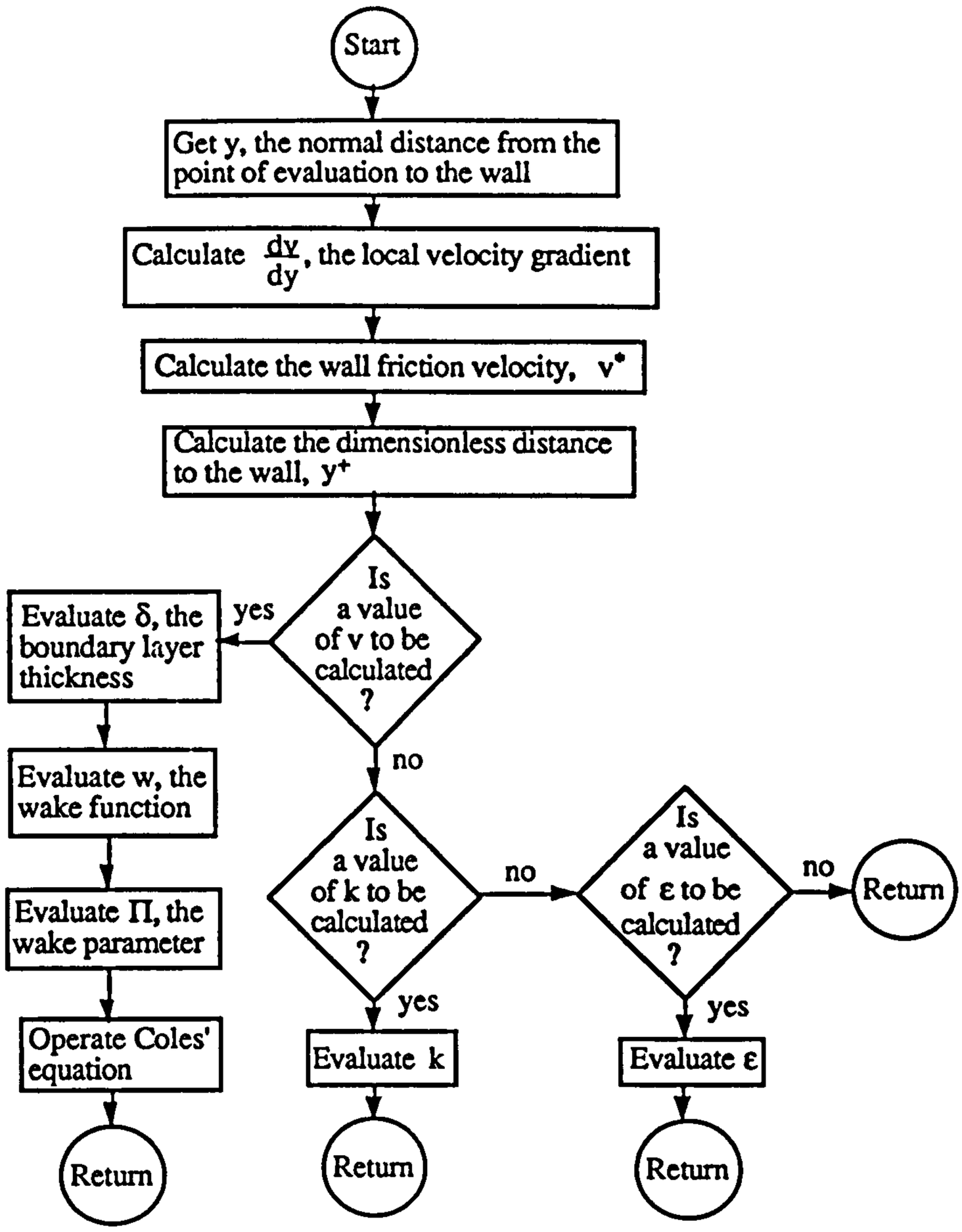

Figure 5.1. A basic algorithm for a 2-d Coles' law model, capable of calculating values for v, k and ε.

After considering the algorithm outlined above and on inspecting the geometries of the two test cases, as given by Figures 4.1 and 4.2, it is then proposed to apply the algorithm to the U-bend test case first: the U-bend, taken as an axi-symmetric model, consists of two non-intersecting solid surfaces, separated by a channel of constant width whereas the backward facing step has four sections of solid boundary, some of which intersect. At the point where these solid boundaries meet, some method was required to determine to which wall the point of intersection might be said to belong. As such, the simpler case of the U-bend was approached first in order to gain experience in manipulating Coles' law and in the practical use of those subroutines available for its

implementation.

5.1.1. Modelling k and ε Within the Coles'Law Model.

For the Coles' law model to successfully mate with the freestream, in the form of the k-ε turbulence model, it is necessary to predict values of k and ε at this interface. The method by which this is done in FIDAP, when using the 'standard' wall elements of Haroutunian and Engelman (1991) which operate Reichardt's law, is given in Section 4.2.1. A simpler method is initially proposed here, using empirical distributions for k and ε that are commonly used to predict values at inlet to a bounded flow (FIDAP7 Theory Manual, 1994).

A value of the kinetic energy of turbulence may be taken as

$$k = C_\mu^{1/2} \left\{ l_m \frac{dv_x}{dy} \right\}^2 \tag{5.2}$$

where C_μ is a modelling constant, equal to 0.09 for isothermal flow with no mass transfer (Rodi, 1975), and l_m is a mixing length.

The rate of turbulent dissipation is then given by

$$\varepsilon = C_\mu k^2 \left\{ l_m^2 \left| \frac{dv_x}{dy} \right| \right\}^{-1} \tag{5.3}$$

A simple model for the mixing length, l_m , appearing in the above two equations, is gained by recourse to Prandtl's mixing length theory (1925) as

$$l_m = \kappa y \tag{5.4}$$

It will then be seen that in operating this method, values of k for a point must be calculated prior to those required for ε as local values of ε are dependent upon their corresponding values of k.

5.1.2. Evaluation of the Boundary Layer Thickness.

In a discussion of Coles' work by Warsi (1993), a link between the local skin

friction, C_f, Reynolds number at the edge of the boundary layer, R_δ , and the boundary layer thickness, δ, is proposed. First consider the Reynolds number at the edge of the boundary layer, which Warsi (1993) gave as

$$R_\delta = \frac{v_\infty \delta \rho}{\mu} \tag{5.5}$$

where v_∞ is the freestream velocity.

Then for a boundary layer, with or without a pressure gradient, the local skin friction coefficient may be written as

$$C_f = \frac{2v^{*2}}{v_\infty^2} \tag{5.6}$$

Finally, to link C_f and R_δ , Warsi (1993) noted that

$$\frac{Re_\infty}{R_\delta} = 3.78\sqrt{\frac{C_f}{2}} - 25.0\left(\frac{C_f}{2}\right) \tag{5.7}$$

for the case of zero pressure gradient flow over a flat plate at high Reynolds number. Whilst this will not be truly valid for the U-bend, where a pressure gradient is present and the solid boundaries, in part, are curved, it does provide a useful first approximation in order to test the model's behaviour, remembering that for sharply turning flows, the flow regime is expected to be governed largely by inviscid mechanisms and thus that wall effects may be of limited importance.

After calculating C_f from equation 5.6 and substituting it into equation 5.7, then R_δ may be used in a reformulation of equation 5.5 to yield an estimate of δ.

Bearing in mind the reservations already voiced about the method, the choice of freestream velocity in equations 5.6 and 5.7 must also be considered. A sketch of the flow, predicted through the U-bend by the standard FIDAP model, is given below as Figure 5.2.

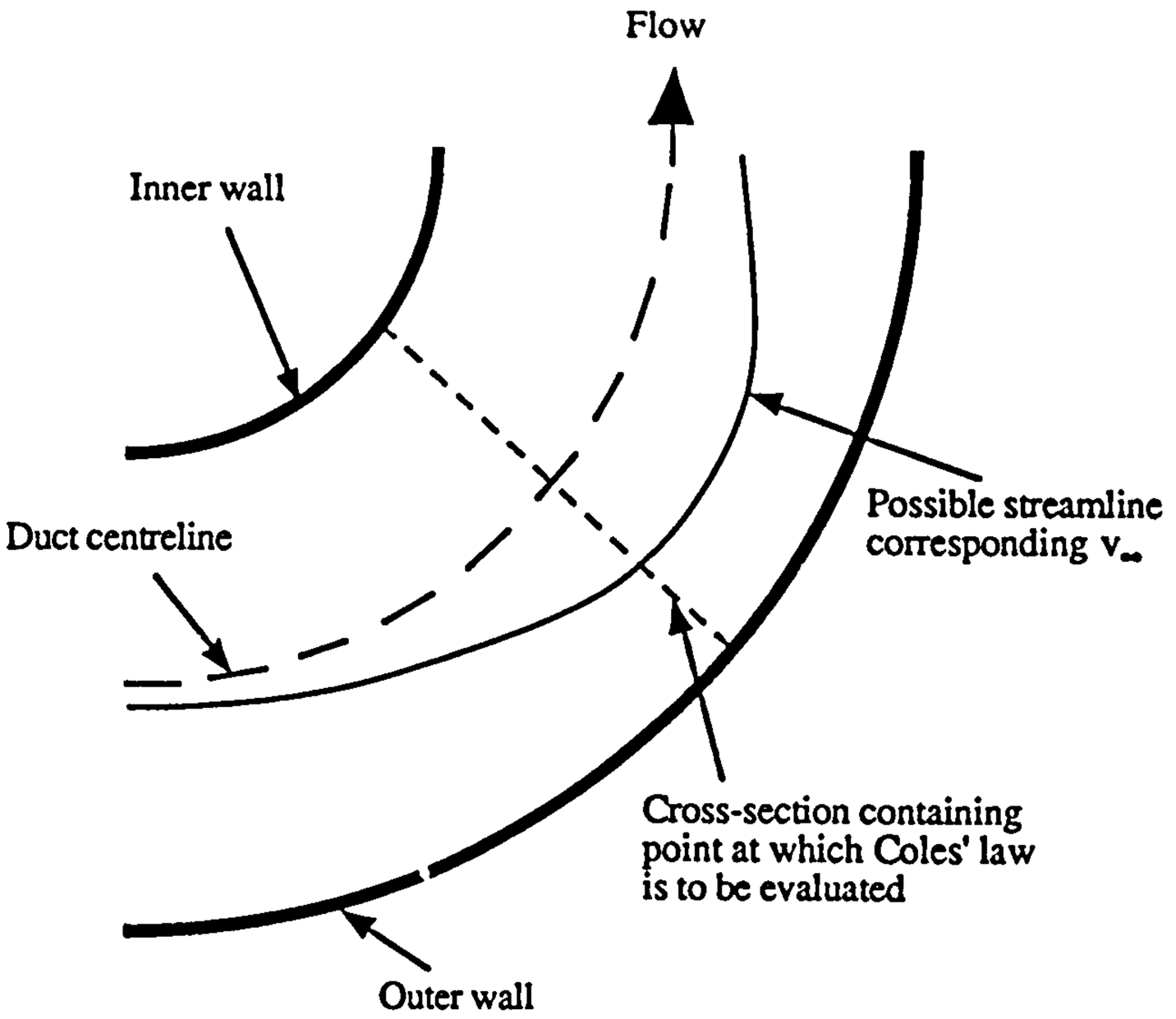

Figure 5.2. A sketch of the flow through a section of the U-bend.

For any given section, downstream of inlet, where Coles' law is to be evaluated, the freestream velocity, v_∞, will not necessarily correspond with the geometric centreline of the model. From inspection of the results of the standard FIDAP model however, the centreline velocity was typically found to be within 10% of the freestream value. Furthermore, the inclination of the centreline velocity to a tangent drawn through the centreline was typically less than 15°. Therefore, by taking v_∞ to equal the component of the centreline velocity tangential to the centreline, this would give a value of v_∞ to within 15% of the true value. Whilst this method was then adopted for use with the proposal for δ outlined above, it was not generic but problem specific.

5.2. The U-bend Model.

The 'standard' FIDAP model of the U-bend, provided by the FIDAP library of examples and listed in Appendix A3 as ex29.FDREAD, was run both to establish a basis for comparison of results and to gain knowledge of the distribution of element and node numbers throughout the computational mesh, which are given by the logical space diagram as Figure 5.3 below.

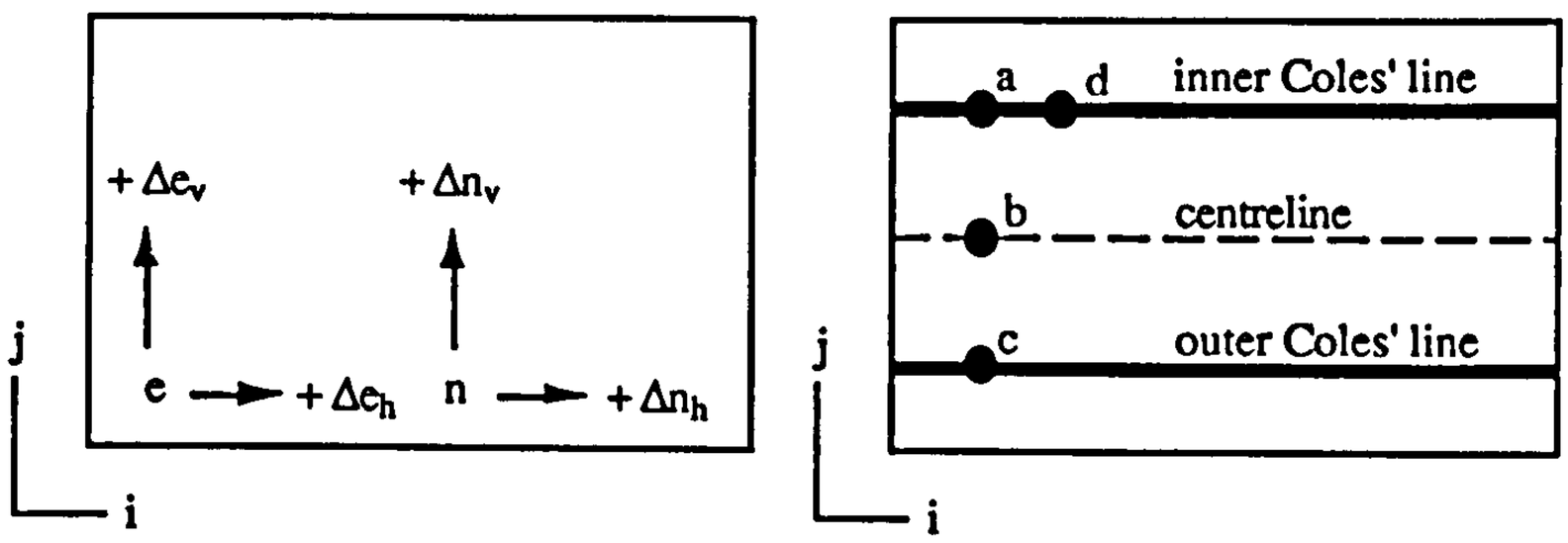

Key

● node

e element number

n node number

For a mesh with N nodes across the duct width,

$$b = a - \left(\frac{N-2}{2}\right) = c + \left(\frac{N-2}{2}\right)$$

$$d = a + \Delta n_h$$

Figure 5.3. Showing the general layout of element and node numbers and of Coles' lines throughout the model.

Inspecting Figure 5.3, then moving horizontally across the logical mesh, a nodal increment of Δn_h is seen between successive nodes and between successive elements, an increment of Δe_h is observed. Likewise, when traversing the logical mesh vertically, the corresponding nodal and elemental increments are Δn_v and Δe_v respectively. For simplicity, the lines along which Coles' law is to be applied, at the border of the k-ε model, will be referred to from now on as "Coles' lines".

Certain important nodes and elements are highlighted in Figure 5.4 below, which will be of use in detailing the workings of the U-bend model.

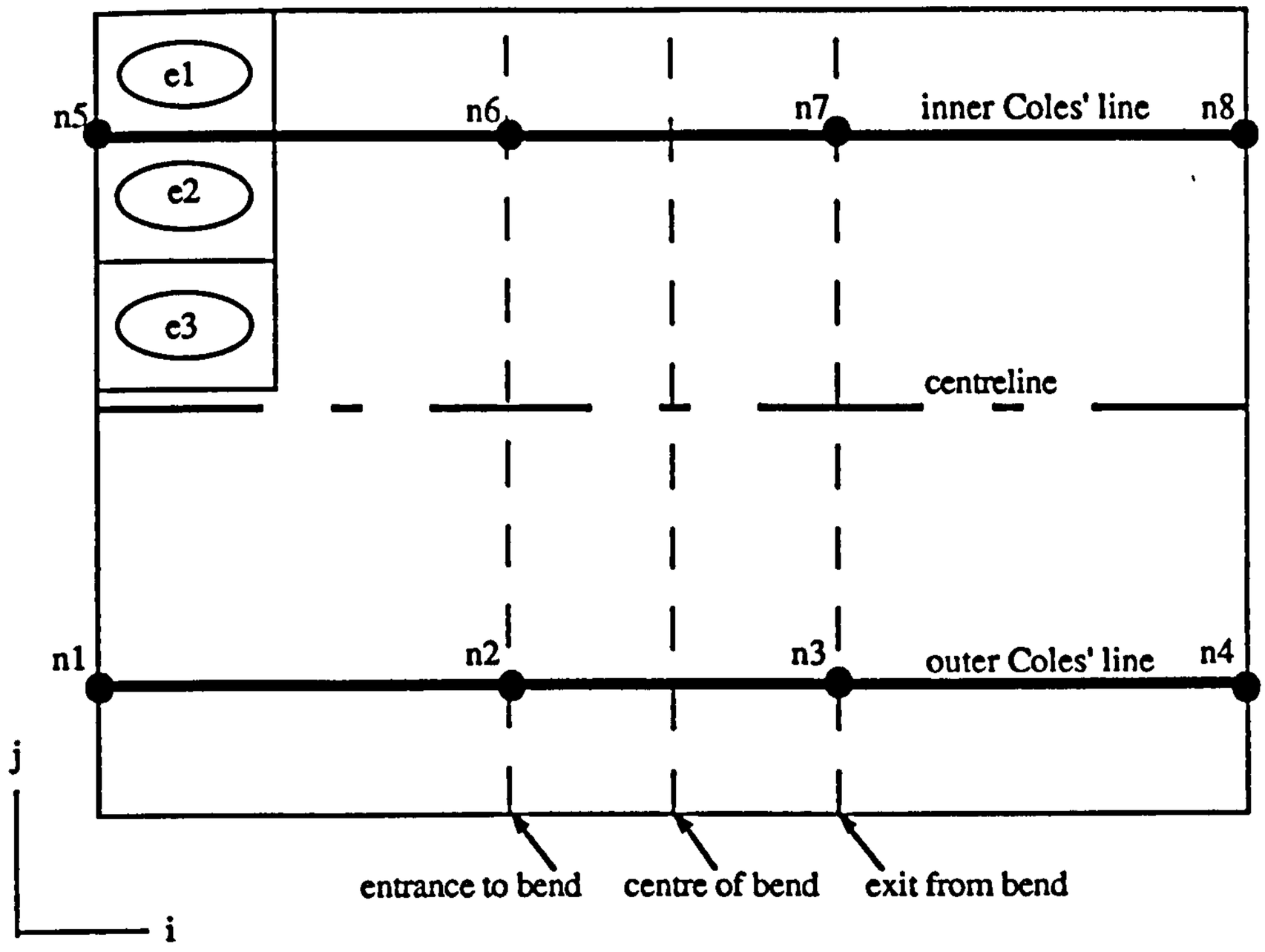

Key

● node

n node number

e element, with number

Figure 5.4. Logical diagram of the U-bend, showing certain important nodes and elements.

From consideration of the above diagrams, the nodal regions across which the Coles' law model operated may be listed in order below as Table 5.1.

Property to be calculated	Location in mesh	Defining nodes
v_x	entire inner Coles' line	n5 - n8
v_y	curved portion of inner Coles' line	n6 - n7
k	entire inner Coles' line	n5 - n8
ε	entire inner Coles' line	n5 - n8
v_x	entire outer Coles' line	n1 - n4
v_y	curved portion of outer Coles' line	n2 - n3
k	entire outer Coles' line	n1 - n4
ε	entire outer Coles' line	n1 - n4

Table 5.1. Specification of the mesh regions invoking a Coles' law model of the U-bend.

The input file for this model, peeg.FDREAD, is listed in Appendix A3.

5.2.1. An Algorithm for a Coles' Law Model of the U-bend.

Some information required by the boundary condition subroutine, such as geometric data and derivatives of solution variables, was only available within the source subroutine. Since the source subroutine orders data in terms of element and integration point numbers whilst the boundary condition subroutine operates on node numbers, the relationship between element and node numbering (shown in Figure 5.3) was of importance in model construction.

A generic algorithm for the implementation of Coles' law was given as Figure 5.1 but the differing nature by which the boundary condition and source subroutines operate, coupled with the form of analysis adopted, required the model to be largely 'hard-wired' to the problem in hand. The analysis of the U-bend with regard to Coles' law can then be broken down into a number of parts as

i) find the elemental thickness, separating the Coles' line from the solid boundary,
ii) evaluate the inclination of the sector of the mesh under consideration to the

horizontal,

iii) find the local velocity, tangential to the solid surface and hence the local velocity gradient,

iv) evaluate the shear stress at the wall, the wall friction velocity and y^+,

v) calculate values of v, k or ε as required and

vi) where a value for v is required, evaluate the wake function and wake parameter, gain v from Coles' law and return its value in global co-ordinates.

Inspecting the logical representation of the U-bend, as Figure 5.3, it would be easy to forget the real geometry of the problem and to oversimplify the problem. Coles' equation should yield the velocity at a point in the boundary layer parallel to the solid boundary. Where that boundary is curved, then the computed value will require to be converted to the global co-ordinate system, in which the solution procedure requires boundary conditions to be provided.

The analysis then hinges upon the correct determination of the velocity gradient at the given point where Coles' law is to be applied. The location of the Coles' line was defined as the outer edge of the first elemental layer abutting the solid boundary, giving the Coles' model the same depth as the wall model of Haroutunian and Engelman (1991) (where the first layer of elements into the flow are special wall elements). Figure 5.5 below outlines the method by which the local velocity gradient was assessed.

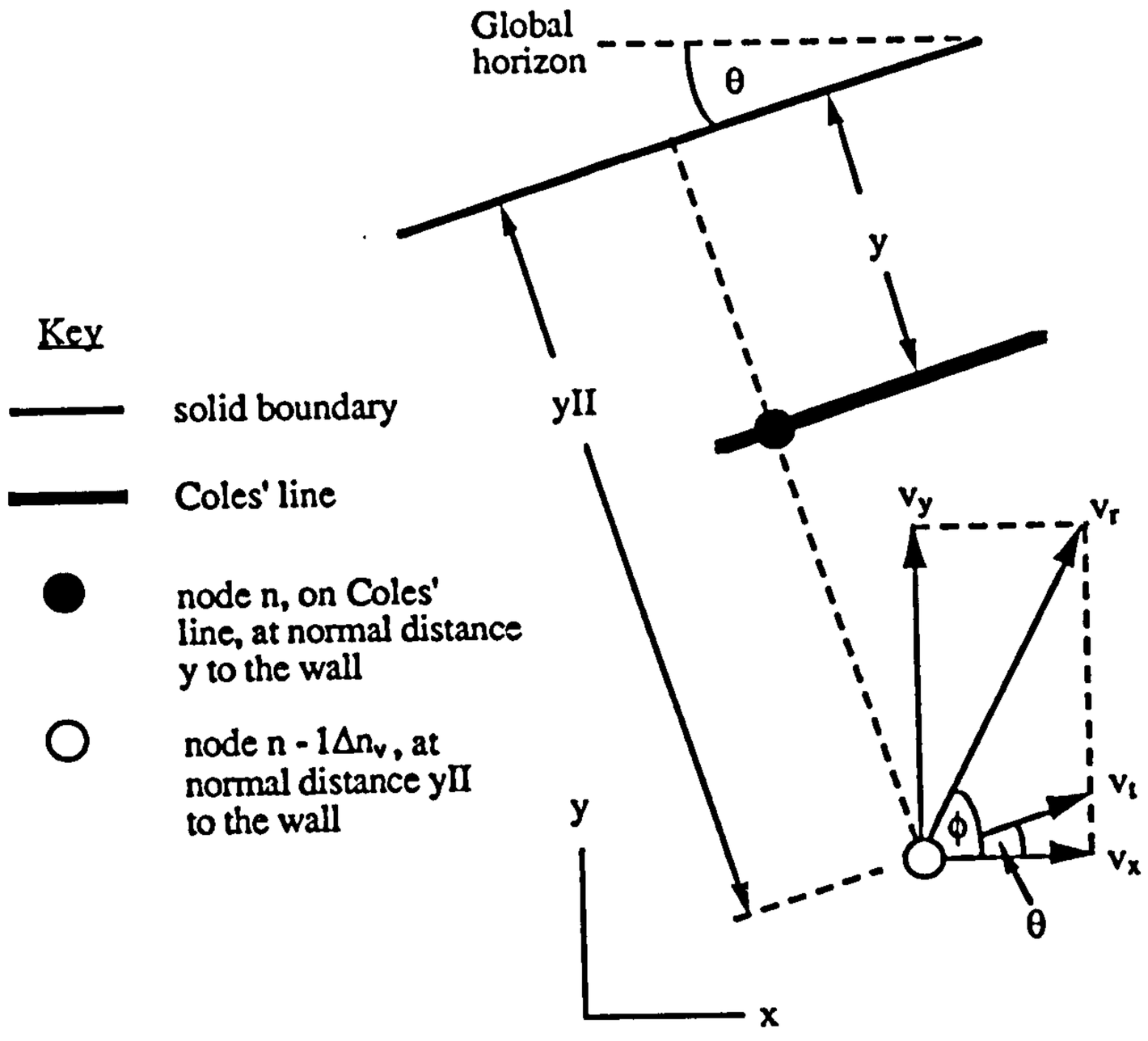

Figure 5.5. Calculation of the local velocity gradient.

Figure 5.5 shows a node on a Coles' line, at a distance, y, normal to the solid boundary. At this point in the mesh, the solid boundary (and hence the Coles' line) is inclined to the horizontal at an angle, θ. Extending the normal line from the wall through the node on the Coles' line out to the next elemental layer from the surface, a node is found at a normal distance, yII, from the wall. At this node, the global velocity components, v_x and v_y, provide a resultant velocity, v_r, at an angle, ϕ, to the horizontal. By taking the component of the resultant velocity tangential to the solid boundary, v_t, then an approximation to the local velocity gradient is given by

$$\frac{dv}{dy} = \frac{v_t}{yII} \qquad (5.8)$$

This assumes that the velocity gradient varies approximately linearly within the near-wall region, which might be reasonable where yII is small. That the velocity gradient was taken as the first node out into the mesh beyond the Coles' line was a result of the need to allow the Coles' model to integrate with the k-ε model; an earlier model taking the velocity gradient at the node on the Coles' line itself by a similar method, lead to the Coles' model being largely self-referencing and isolated from the continuum that it

bordered.

In order to obtain the distance yII then, in the source subroutine, the Cartesian co-ordinates were considered for each integration point for each element within the first three elemental layers adjacent to either solid boundary. For the instance of the inner wall, for example, this information was stored in arrays, xi and yi, as

x co-ordinates

xi (element no., integration point no.) = xyxl (coordinate pointer, integration point no.)

y co-ordinates

yi (element no., integration point no.) = xyxl (coordinate pointer, integration point no.)

where xyzl is the original array of geometric co-ordinates within the source subroutine. These arrays of geometric co-ordinates were then made available to the boundary condition subroutine by use of the COMMONBLOCK 'distancei'.

Now, as the element thickness normal to the wall was invariant throughout the mesh, then the normal distances y and yII were evaluated once at the mesh inlet and then assumed constant for all nodes downstream, as shown in Figure 5.6 below.

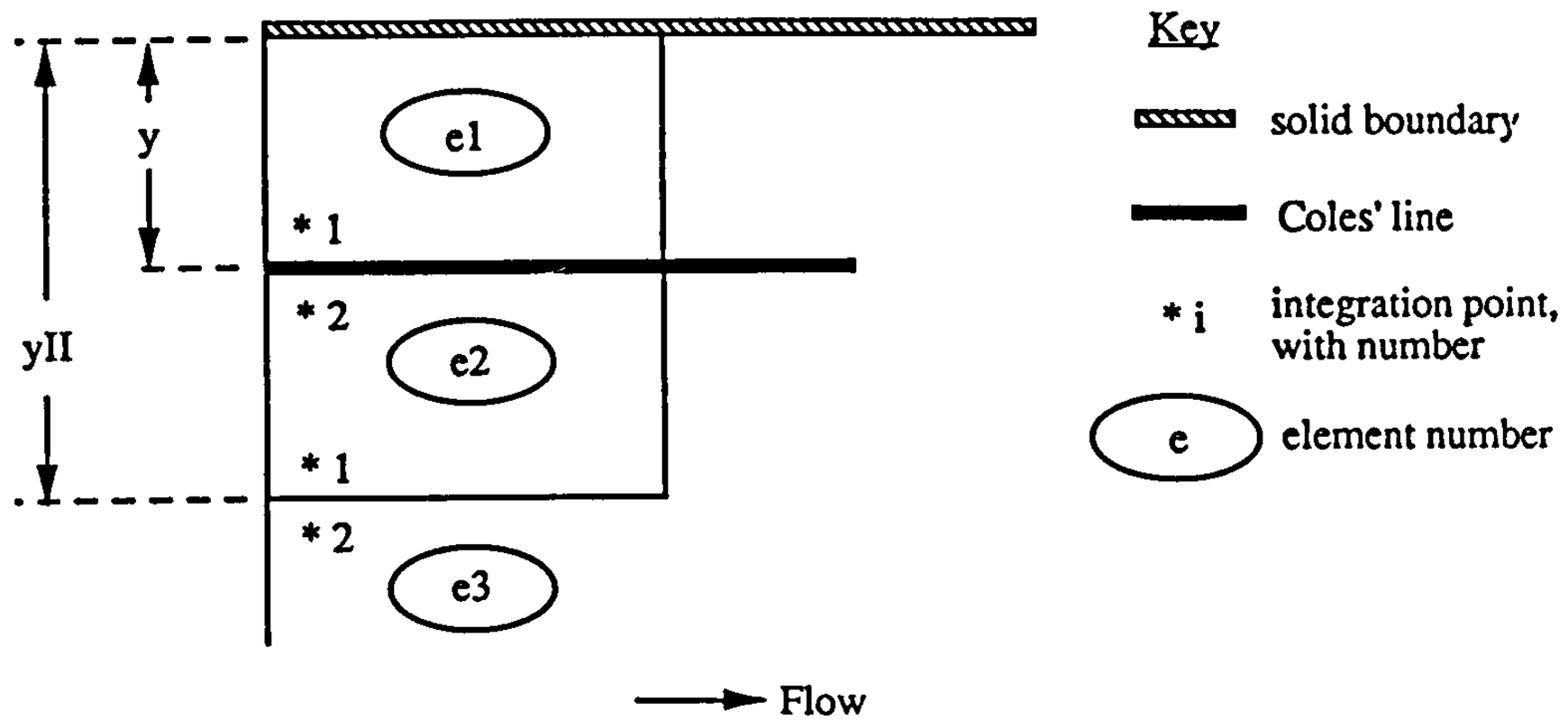

Figure 5.6. Calculation of elemental thicknesses at inlet to the model inner wall.

At inlet to the U-bend, the location of the inner wall was known to be (x_I,y_I) and so

the perpendicular distance from the inner Coles' line to the solid boundary, y, was

$$y = y_I - \frac{yi(e2,2) + yi(e1,1)}{2}$$

and similarly, yII was given by

$$yII = y_I - \frac{yi(e2,1) + yi(e3,2)}{2}$$

Now the calculation of the local velocity gradient, $\frac{dv}{dy}$, may be illustrated by considering a node, n, on the inner Coles' line, at a point where the Coles' line is inclined to the horizontal at an angle, θ, as shown in Figure 5.7 below.

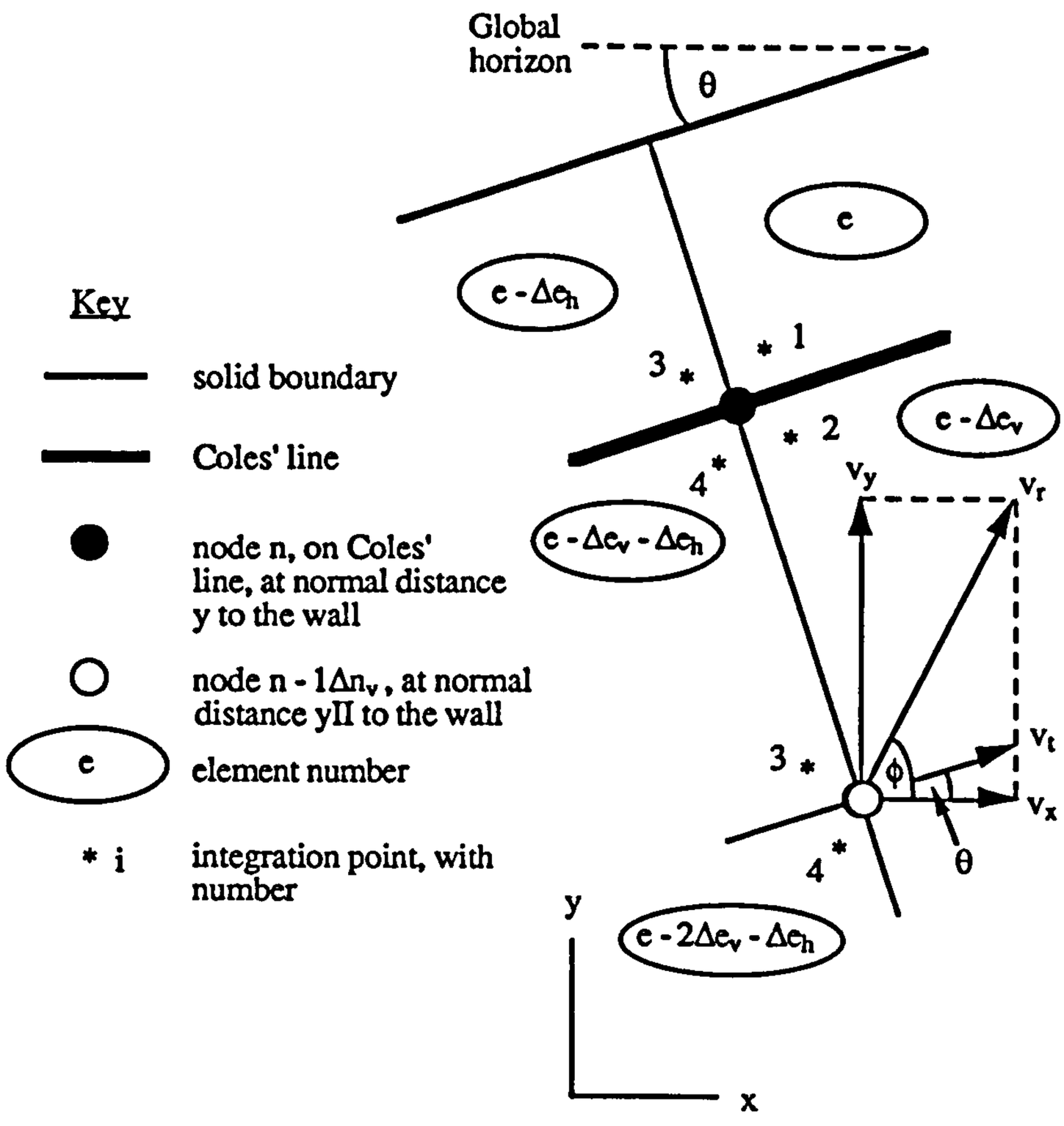

Figure 5.7. Extraction of the local velocity gradient from the computational mesh.

Inspecting the above diagram, then the local inclination of the mesh to the horizontal at node n is given by

$$\theta = \tan^{-1}\left|\frac{dy}{dx}\right| \qquad (5.9)$$

where $dy=\{yi(e,1)+yi(e - \Delta e_v,2)\}-\{yi(e - \Delta e_h,3)+yi(e - \Delta e_v - \Delta e_h,4)\}$

and $dx=\{xi(e,1)+xi(e - \Delta e_v,2)\}-\{xi(e - \Delta e_h,3)+xi(e - \Delta e_v - \Delta e_h,4)\}$

The velocity component, v_t, used to evaluate the local velocity gradient is taken from the next node out into the mesh normal to the Coles' line, being node, $n\text{-}1\Delta n_v$ (see Figure 5.3).

At node $n\text{-}1\Delta n_v$, in Figure 5.7, have

$$v_x = \text{sol}\ (\ n\text{-}1,\ \text{ldofu(kdu)}\ )$$

and $$v_y = \text{sol}\ (\ n\text{-}1,\ \text{ldofu(kdv)}\ )$$

Thus, the resultant velocity , v_r , is given by

$$v_r = \sqrt{v_x^2 + v_y^2} \qquad (5.10)$$

and the angle of flow, ϕ, is

$$\phi = \tan^{-1}\left|\frac{v_y}{v_x}\right| \qquad (5.11)$$

Then the required tangential velocity component, v_t , is given by

$$v_t = v_r \cos\ (\ \theta - \phi\ ) \qquad (5.12)$$

The local velocity gradient is then yielded as

$$\frac{dv}{dy} = \frac{v_t}{yII}$$

However, for the above procedure to work throughout the model, the values of θ and ϕ were required to be given as global values as

$$0 \leq \theta \leq \pi$$
$$0 \leq \phi \leq 2\pi$$

remembering that the Fortran language requires angles to be given in radians.

Since the equations 5.9 and 5.11, providing θ and ϕ respectively, returned values between 0 and $\frac{\pi}{2}$, they had to be transformed to global angles, as detailed in Table 5.2 below.

dx	dy	θ
>0	0	0
>0	>0	θ
0	>0	$\frac{\pi}{2}$
<0	>0	$\pi-\theta$
<0	0	π

v_x	v_y	ϕ
>0	0	0
>0	>0	ϕ
0	>0	$\frac{\pi}{2}$
<0	>0	$\pi-\theta$
<0	0	π
<0	<0	$\pi+\phi$
0	<0	$\frac{3\pi}{2}$
>0	<0	$2\pi-\phi$

Table 5.2. Setting global values of θ and ϕ.

A similar process was used to gain $\frac{dv}{dy}$ for the outer wall and also to capture the 'centreline' velocity, v_∞.

Having gained a value for $\frac{dv}{dy}$, the shear stress at the wall was then given by

$$\tau_0 = \mu \frac{dv}{dy} \tag{5.13}$$

where μ is the dynamic viscosity of the fluid.

The wall friction velocity is then

$$v^* = \sqrt{\frac{|\tau_0|}{\rho}} \tag{5.14}$$

In comparison with equation 2.21, the equation for v^* above takes the modulus of τ_0 (Rashid, 1993). The shear stress at the wall, in practice, has both magnitude and direction - a positive value of τ_0 would arise when the flow was in the direction of decreasing x (towards the x origin).

y^+ may then be calculated, using equation 2.27 as

$$y^+ = \frac{yv^*}{\nu}$$

As such, the modulus of τ_0 is required not just to validate the square root in equation 5.14 but also to provide a meaningful value for y^+ - a negative value of y^+ would imply that the boundary layer was penetrating the solid boundary, which is clearly facile.

A first approximation to the wake parameter, Π, was taken from Warsi (1993). Once the centreline velocity, v_∞, has been evaluated, then the Reynolds number of the freestream is given by

$$Re = \frac{v_\infty d\rho}{\mu} \tag{5.15}$$

where d is taken as the diameter of the channel.

Then for the case of a boundary layer over a flat plate, for $Re < 5000$

$$\Pi = 0.55\left\{1 - \exp\left(-0.243\sqrt{\frac{Re}{425} - 1} - 0.298\left(\frac{Re}{425} - 1\right)\right)\right\} \tag{5.16}$$

and where $Re > 5000$ then

$$\Pi = 0.55 \tag{5.17}$$

As with the initial method of evaluating δ, given in Section 5.1.2, this method was

chosen to provide a simple first estimate of Π, sufficient to validate the general structure of the model. Clearly, later models would require to take account of the local pressure gradient, $\frac{dp}{dx}$, when predicting Π.

In fact, the method taken from Warsi to calculate the boundary layer thickness, δ, did not work. The approach consistently gave values for δ that were two orders of magnitude greater than the channel width. This was considered to result from the use of equation 5.7, which, on closer inspection, was only valid for the boundary layer on a flat plate with zero pressure gradient - a flow regime too far removed from the one in hand to be of benefit.

Thus another simplification to the problem was made so as to set $\delta = y$ in the wake function of equation 2.46. Whilst allowing the general running of preliminary models to be assessed, this is clearly an arrogant assumption. In saying $\delta = y$ uniformly throughout the model, boundary layer growth is suppressed.

Coles' law may now be operated at the node, the result being a velocity tangential to the Coles' line at the node considered in Figure 5.7. However, as the solution procedure requires boundary conditions to be provided within a Cartesian framework, then depending on whether values of v_x or v_y were required, one of the following transformations was performed

$$v_x = v_{Coles} \cos \theta \tag{5.18}$$

$$v_y = v_{Coles} \sin \theta \tag{5.19}$$

where v_{Coles} was the result provided by the Coles' law equation, repeated below as

$$v = v^* \left\{ \frac{\ln y^+}{\kappa} + B + \frac{2\Pi}{\kappa} \right\}$$

Note that the wake function has been omitted here, being reduced to unity by the assumption that $\delta = y$.

Now the above equation will always yield a positive value for v since v^* and y^+ are always positive by definition. Hence, in order to provide values of v_x and v_y that indicate the direction of flow within the channel, the sign of the local velocity gradient was inspected, as depicted by Figure 5.8 below.

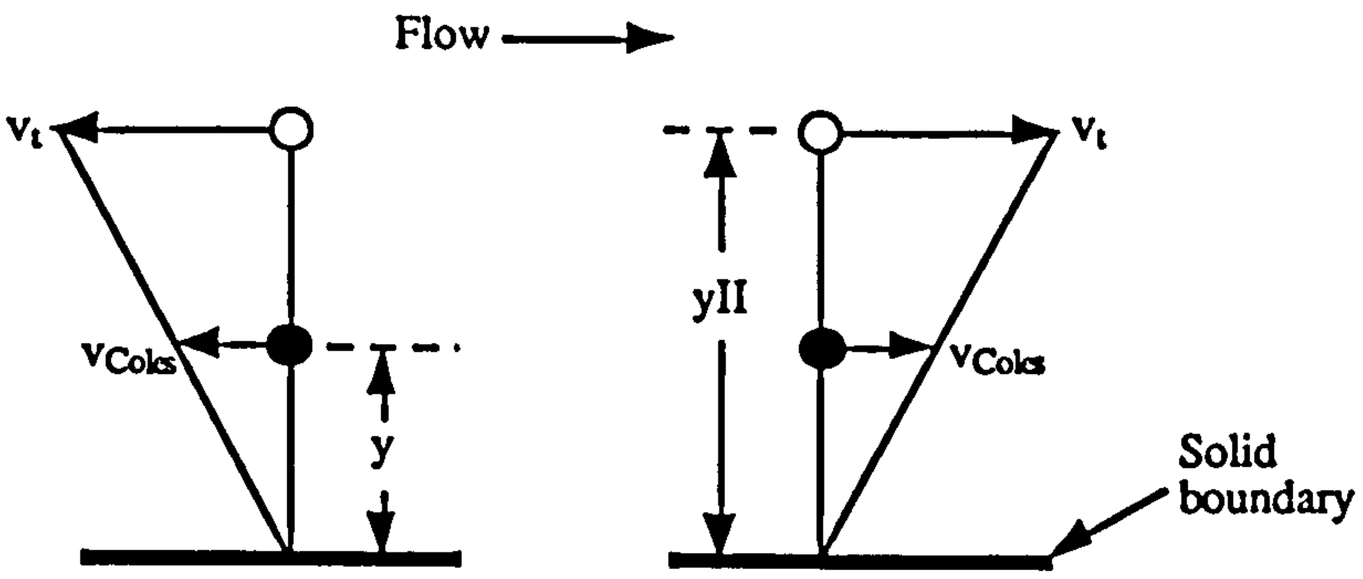

$\frac{dv_x}{dy}$ -ve $\frac{dv_x}{dy}$ +ve

Figure 5.8. Comparing the result of Coles' equation with the local velocity gradient.

As such, the model was subdivided into a number of zones in order to decide on the sign of the result of Coles' equation, as shown in Figure 5.9 below.

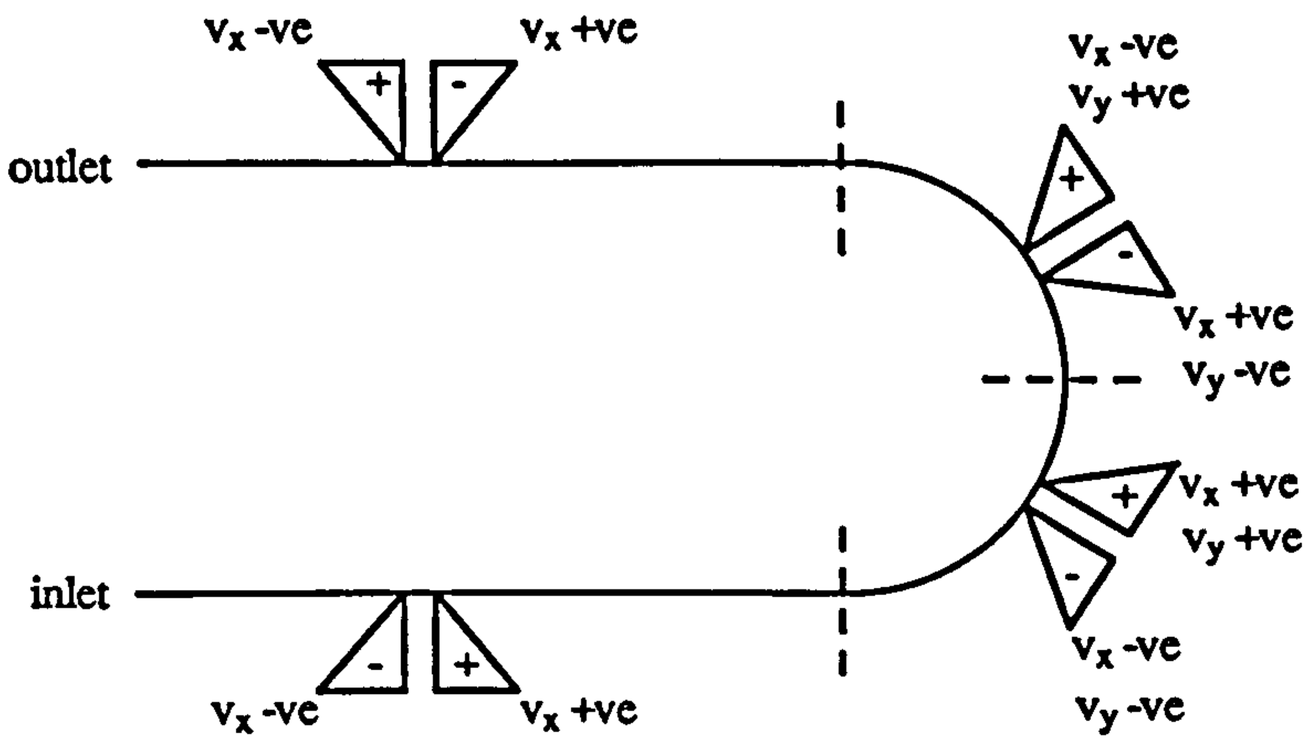

Key

+/- velocity gradient, with sign

v_x , v_y velocity component from Coles' law, with correct sign

Figure 5.9. Valid prescription of the signs of v_x and v_y, based upon the sign of the local velocity gradient.

5.2.2. Initialization of the U-bend Model.

Finally, the prescription of initial conditions to the model will be considered briefly. When preparing the model input file for solution, the Coles' model subroutines are invoked when scanning the initial condition statements of the input file. This implementation of the Coles' model prior to the onset of the solution process results in the internal arrays of the model subroutines being filled with invalid data, hence corrupting the subsequent solution. To prevent this problem, a counter was used to monitor the number of times that the subroutines were accessed. This counter could then be used to prevent operation of the Coles' law model before the proper solution process got underway. Inspecting Table 5.1, then, say for the inner Coles' line, this counter should be caused to increment by

i) the current node number being n = n5, denoting the first node at inlet to the model and

ii) the current node number being n = n6, denoting the first node at entrance to the bend proper.

In the former case, this would correspond to the calculation of v_x , k and ε along the entire inner Coles' line, whilst the latter case would arise from the calculation of v_y for the inner curved section of the U-bend. The value of this counter, called 'start', is tabulated below as Table 5.3.

Iteration number		i=1	i=2	i=n
Value of "start" at	onset of iteration	i+42	i+42+14(i-1)	i+42+14(n-1)
	end of iteration	i+42+9i	i+42+14(i-1)+9(i-1)	i+42+23(n-1)

Table 5.3. Values of the counter 'start' for successive iterations.

The initial conditions to the solution are shown below in Figure 5.10 in logical format.

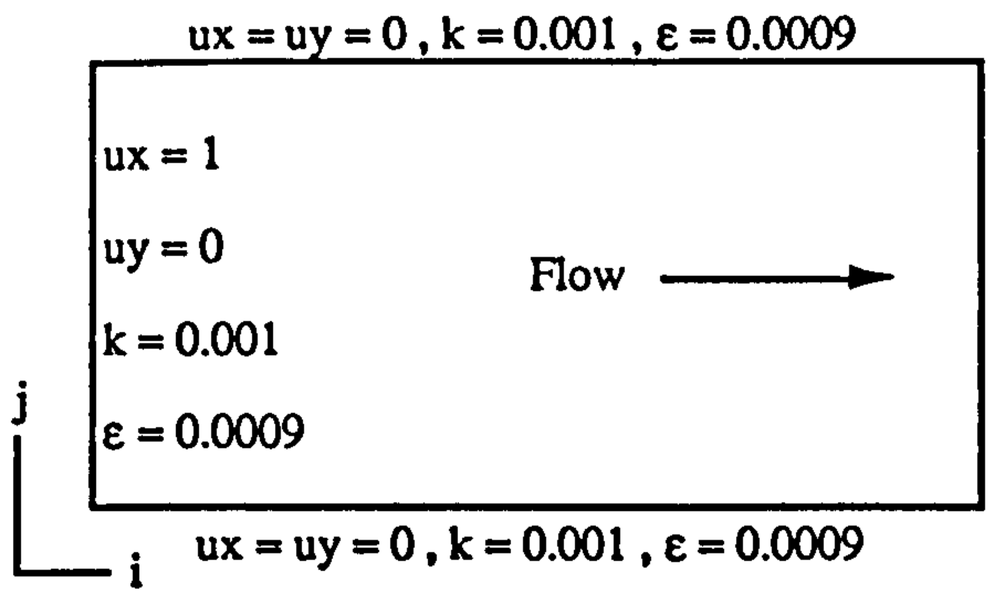

Figure 5.10. Initial conditions for analysis of the U-bend.

The initial conditions at boundary to the model were set within the model input file. In addition to these initial conditions, the initial conditions along the Coles' lines were also set within the boundary condition subroutine. By forcing $v_x = v_y = 0$, $k = 0.001$ and $\varepsilon = 0.0009$ along both Coles' lines for the first six iterations (until start ≥ 127), then the k-ε model of the freestream was initiated before the Coles' model began to operate, hence providing meaningful values of $\frac{dv}{dy}$, the local velocity gradient, to the Coles' model.

The set of subroutines forming the Coles' law model of the U-bend are listed as template 'blammo.f' in Appendix A3, which also contains an algorithm flowchart of this subroutine template.

5.3. The Backward Facing Step Model.

As with the analysis of the U-bend, outlined in Section 5.2, study of flow over the backward facing step, described in Section 4.1.2, is based upon the generic algorithm of Figure 5.1. However, as with the U-bend model, that for the backward facing step was necessarily dedicated to the flow regime in hand.

In approaching the simpler case of the U-bend first, where the Coles' lines did not intersect, a number of valuable lessons were learnt with regard to the calculation of the wake parameter, Π, the artificial fixing of the boundary layer thickness as $\delta = y$, the use of the local velocity gradient in determining the flow direction at the Coles' line and also in the prescription of initial conditions within the subroutine.

Modelling of the backward facing step was then proposed in two distinct phases as

i) a simple model, following the guidelines drawn from the experience gained from the U-bend and introducing the idea of relaminarisation where y^+ is less than five at the Coles' line and

ii) an improved model, with more rigorous treatment of the wake function and wake parameter, based upon consideration of the boundary layer thickness and the local pressure gradient.

5.3.1. Description of the Computational Mesh for the Backward Facing Step.

The computational mesh describing the backward facing step was that of the standard FIDAP example (listed in Appendix A3 as input file 'ex19.FDREAD'), hence allowing for direct comparison of the results from the Coles' model with those provided by the standard model.

In attempting to apply those techniques already developed to the backward facing step, it was discovered that whilst the boundary condition commands in the model input file required the use of 'external' node numbers, as observed in the post-processed results, when in the boundary condition subroutine, nodes must be referenced by 'internal' node numbers. These internal node numbers are those used by the solution procedure to prosecute the flow solution and may be related to their external counterparts on inspection of the output files relating to the solution. The difference in node naming arises from the solution procedure renaming nodes to optimise the bandwidth of the matrices used in the solution. Whilst for the U-bend model its internal and external node numbers were identical, this was not the case for the backward facing step model. The distribution of element and internal and external node numbers throughout the mesh is shown as Figure 5.11 below.

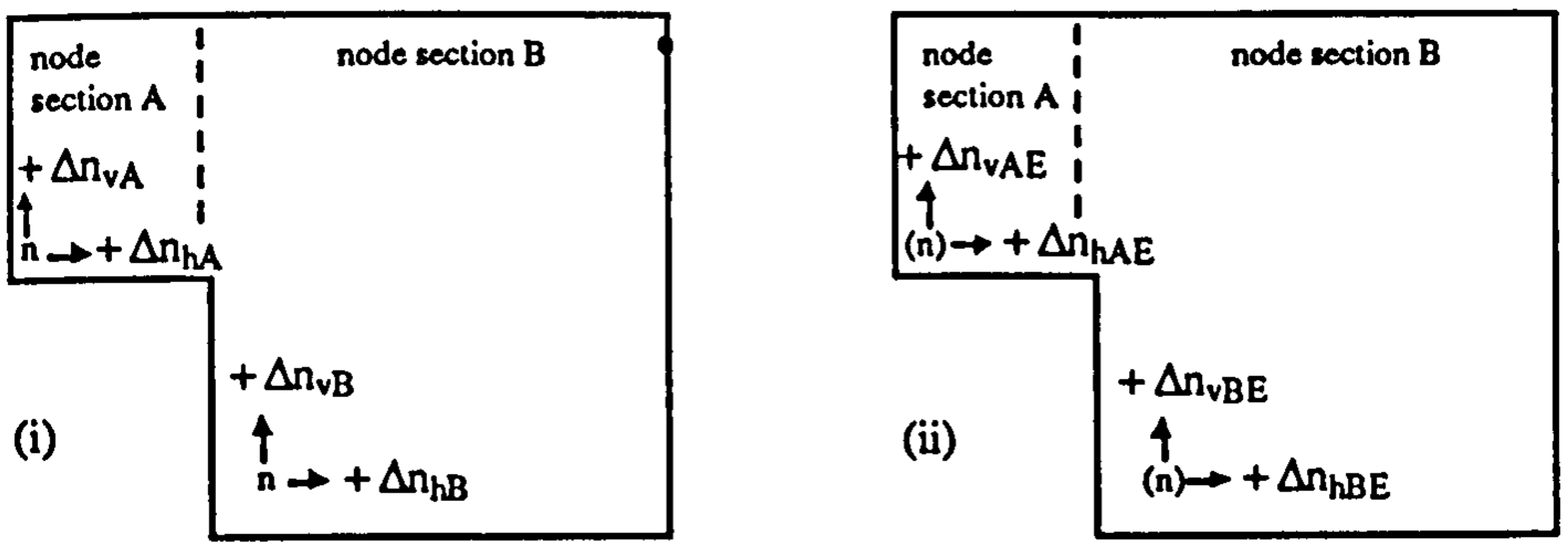

Figure 5.11. General overview of element and node numbering within the backward facing step model.

Inspecting Figure 5.11, it will be seen that there is a discontinuity in both element and node numbering across the face of the mesh. With regard to element numbering, in element section A, the horizontal and vertical increments in element number are seen as Δe_{hA} and Δe_{vA} respectively, with Δe_{hB} and Δe_{vB} being the corresponding increments in element section B.

The internal node numbers throughout the mesh, being those of principal interest in seeking to construct a viable computational model within the various subroutine templates, are also shown in Figure 5.11. For node section A, the horizontal and vertical increments in *internal* node number are Δn_{hA} and Δn_{vA}, with Δn_{hB} and Δn_{vB} being the corresponding increments in node section B. Each of these nodal increments for the internal numbering scheme has a corresponding increment in the external scheme, denoted by the extra suffix 'E' in the relevant portion of Figure 5.11 above.

Figure 5.12 below sketches the Coles' lines for the mesh, showing the points at which they intersect for the lower surfaces. Nodes and elements of interest in delineating the behaviour of the computational model are also shown. For the purpose of calculating v_∞, the centreline velocity used in the estimation of the wake parameter was held to be the

horizontal line bisecting the inlet section of the model (again a similar argument to that in Figure 5.2 might be made as to the choice of centreline).

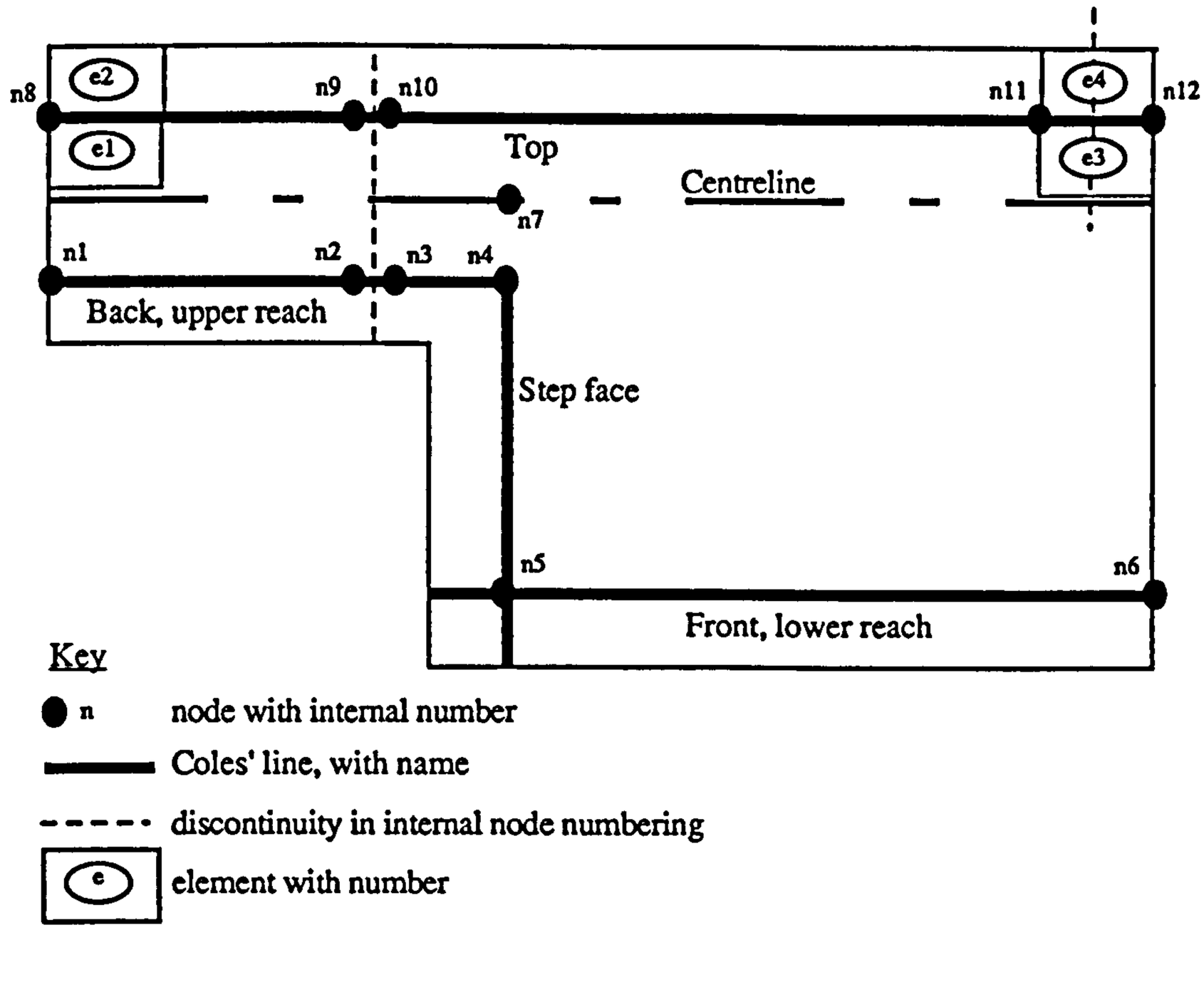

Figure 5.12. Coles' lines, elements and nodes of interest for the backward facing step model.

After inspecting Figures 5.11 and 5.12, the necessary groups of nodes analysed by Coles' law model within the boundary condition subroutine are given in Table 5.4 below.

Coles' line name	Properties to be calculated	Internal node numbers for use in the boundary condition subroutine template
top	v_x , k and ε	n8 - n9 in increments of Δn_{hA} then n10 - n11 in increments of Δn_{hB} then n12
back upper reach	v_x , k and ε	n1 - n2 in increments of Δn_{hA} then n3 - n4 in increments of Δn_{hB}
step face	v_y , k and ε	n5 - n4 in increments of Δn_{vB}
front lower reach	v_x , k and ε	n5 - n6 in increments of Δn_{hB}

Table 5.4. The operating regions of the backward facing step model.

All subsequent references to node numbers will be understood to be for internal node numbers unless otherwise specified. The backward facing step models will now be described in turn.

5.3.2. A Basic Coles' Law Model of the Backward Facing Step.

In essence, the basic Coles' law model for the backward facing step was akin to that of the U-bend; where those techniques had to be modified, a description will now be given.

As will be remembered from Section 5.2.1, the Coles' lines were placed at a depth of one element into the flow, as prompted by the practice of the wall element model of Haroutunian and Engelman (1991), used in 'standard' FIDAP models. As such, for any given Coles' line, the normal distance from the Coles' line to its attendant solid boundary, namely y, was invariant along the length of that Coles' line. Consequently, where values of y for each Coles' line were established in the source subroutine, they needed to be calculated only at the start of a given line. The overall model then possessed four different

y values corresponding to the four Coles' lines. These y values were then used, as before, in computing y^+ at each node and would also be of potential use in a better model for the wake function, w.

With regard to the calculation of the local velocity gradient, however, the whole basis by which $\frac{dv}{dy}$ was gained was now reviewed. On consideration of the general subroutine capabilities as discussed in Section 4.2.2, it was seen that $\frac{dv}{dy}$ could be provided by FIDAP itself. The source subroutine makes available all derivatives of the active degrees of freedom for the solution, provided that a request for their calculation is made within the variable derivative control subroutine.

This method may be illustrated by considering the accessing of $\frac{dv_x}{dy}$ along the top Coles' line, as shown in Figure 5.13.

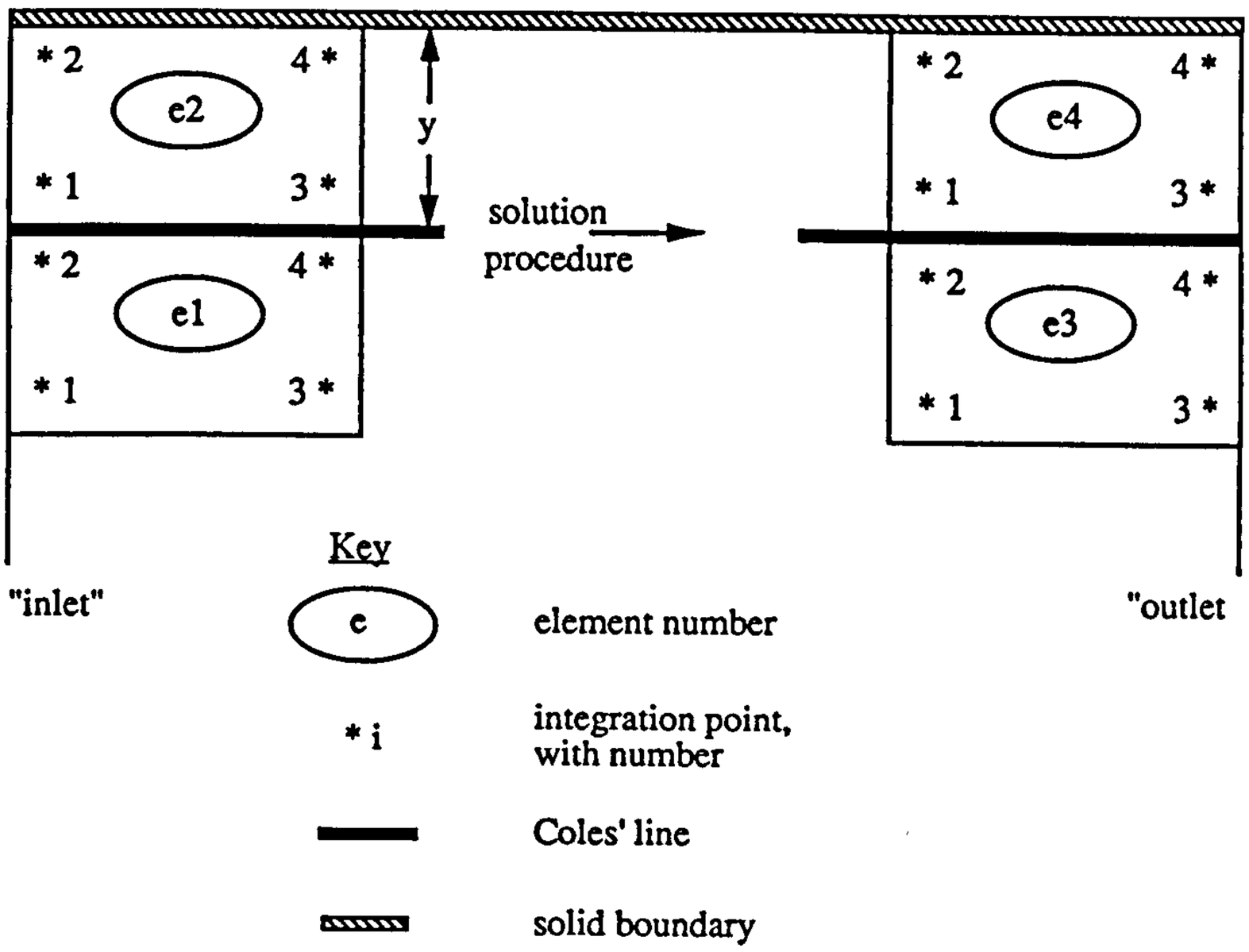

Figure 5.13. Access to $\frac{dv_x}{dy}$ for the top Coles' line.

Calculation of $\frac{dv_x}{dy}$ within the source subroutine was then requested by the following statement within the variable derivative control subroutine as

inivar (kdu) = 1

Values of $\frac{dv_x}{dy}$ were then computed at all integration points throughout the mesh. With regard to the top Coles' line, those values of interest lay within the region bounded by elements e1 to e4, being the elements on either side of that Coles' line. These values were then stored in arrays slopet1, for the elements above the Coles' line, and slopet2, for those below. Initially, it was attempted to access velocity gradients from the current iteration, remembering that the solution procedure invokes the subroutines at the end of the current iteration, in order to prepare boundary conditions for the next iteration. This, however, did not provide a stable solution and so a storage system was developed whereby the velocity gradients from the current iteration were put into a dummy array for use by the next iteration: as such, a given iteration always used values for $\frac{dv_x}{dy}$ from the previous iteration as

```
slopet1 ( nelt , i ) = storet1 ( nelt , i )
storet1 ( nelt , i ) = dvari ( i , 2 , ldofu ( kdu ) )
```

for the ith integration point of the element nelt abutting the top Coles' line.

The arrays of gradients available for current use, as slopet1 and slopet2, were then transferred to the boundary condition subroutine by the COMMONBLOCK 'tlayer'.

The boundary condition subroutine then had access to velocity gradients on either side of the Coles' line, stored in arrays with the dimensions of element number and integration point. To convert these results to the velocity gradient at a given node, the average of the values of the velocity gradient at the integration points surrounding that node was taken. In order to perform this conversion, the relationship between element and node numbering along the Coles' line was studied, offering a generic algorithm. In the case of the top Coles' line, away from the nodes at inlet and outlet, then the method is shown by Figure 5.14.

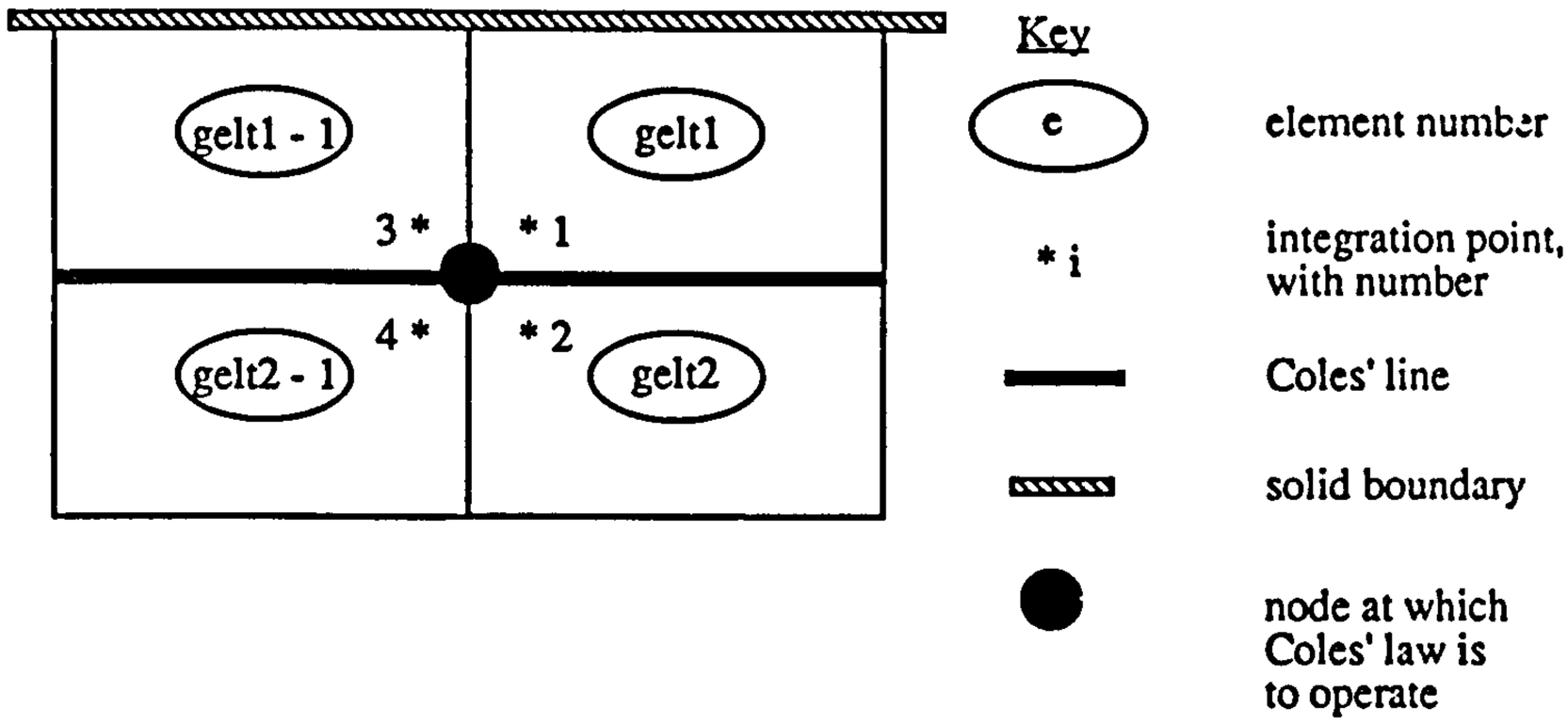

Figure 5.14. Calculation of $\frac{dv_x}{dy}$ at a node on the top Coles' line.

From the above diagram, $\frac{dv_x}{dy}$ at the node on the Coles' line is given by

$$\frac{dv_x}{dy} = \frac{\text{slopet1(gelt1,1)} + \text{slopet1(gelt1-1,3)} + \text{slopet2(gelt2,2)} + \text{slopet2(gelt2-1,4)}}{4}$$

and so the task was then reduced to one of relating the element numbers, gelt1 and gelt2, to the node number, n. On inspecting Figures 5.11 and 5.12 and excepting nodes n8 and n12 at the extremities, then for nodes ($n8 + 1\Delta n_{hA}$) to n9 (along which section the nodal increment is Δn_{hA}), then a relationship appears as

$$\text{imp} = \frac{n + 1}{\Delta n_{hA}} + 1$$

with gelt1 = e2 + imp

and gelt2 = e1 + imp

and for the balance of the top Coles' line, from node n10 to node n11 (between which there is a nodal increment of Δn_{hB}), then the relationship becomes

$$\text{imp} = \frac{n - n10}{\Delta n_{hB}}$$

with gelt1 = (e2 + $10\Delta e_{hA}$) + imp

and $\quad gelt2 = (e1 + 10\Delta e_{hA}) + imp$

A similar process is used at the extremities of the Coles' line, bearing in mind that for an end node, there will be only two adjacent integration points. This procedure was adopted in calculating $\frac{dv_x}{dy}$ along all Coles' lines (n.b. in the case of the 'step face' line, the required velocity gradient was $\frac{dv_y}{dx}$, gained in a like fashion).

A tactical problem arose at node n4, where the Coles' lines for the back upper reach and for the step face intersect, and at node n5, where the Coles' line for the step face crosses that for the front lower reach. In both instances, one node serves two Coles' lines and, depending upon which Coles' line is currently active, either $\frac{dv_x}{dy}$ must be selected for an horizontal Coles' line or $\frac{dv_y}{dx}$ for a vertical one.

This selection was governed by consideration of the variable pointer, idf, and the use of two pointers, called 'flag' and 'npole', the operation of which is shown in the truth table below.

Coles' line name	Property to be calculated	idf	Value of "npole" at		Velocity gradient at node n4	Value of "flag" at		Velocity gradient at node n5
			start of subroutine call	end of subroutine call		start of subroutine call	end of subroutine call	
top	vx	1	0	0	dvx/dy	0	0	dvx/dy
	k	4	0	0	dvx/dy	0	0	dvx/dy
	e	5	0	0	dvx/dy	0	0	dvx/dy
back upper reach	vx	1	0	1	dvx/dy	0	0	dvx/dy
	k	4	1	2	dvx/dy	0	0	dvx/dy
	e	5	2	3	dvx/dy	0	0	dvx/dy
step face	vy	1	3	3	dvy/dx	0	1	dvy/dx
	k	4	3	3	dvy/dx	1	2	dvy/dx
	e	5	3	0	dvy/dx	2	3	dvy/dx
front lower reach	vx	1	0	0	dvx/dy	3	3	dvx/dy
	k	4	0	0	dvx/dy	3	3	dvx/dy
	e	5	0	0	dvx/dy	3	0	dvx/dy

Table 5.5. Selection of local velocity gradients.

For example, for node n5, if flag=3 at the start of the present subroutine call, then $\frac{dv_x}{dy}$ is used, as the subroutine is currently being called by the front lower reach Coles'

line. At the end of the third consecutive subroutine call for the front lower reach, flag is reset to zero upon the condition idf = 5 being satisfied. When node n5 is next activated, when the subroutine is analyzing the step face, $\frac{dv_y}{dx}$ is selected since flag is less than three at the start of all subroutine calls pertinent to this Coles' line (for v, k and ε).

Having obtained the velocity gradient, then τ_0, v^* and y^+ were calculated as before. The centreline velocity, v_∞, corresponding to a given node was obtained by a similar process to that used for the U-bend model. In retrieving v_∞ for the nodes along the step face, the definition of 'centreline' or 'freestream' became much more arbitrary as the boundary layer incumbent upon the step face was normal to all the other boundary layers lying along the other solid boundaries. Given that the step face was expected to bound the recirculating pocket of fluid, then no obvious choice for v_∞ lay in a plane parallel to the step. v_∞ was used in the simple Coles' model for the estimation of the wake parameter in order to validate the general structure of the model for the backward facing step - subsequent models were to evaluate the wake parameter formally upon consideration of the local pressure gradient. As such, for the purposes of the simple Coles' model, it was proposed that along the entire step face Coles' line, that v_∞ be taken as the velocity at that node on the 'major' centreline, vertically above the step face Coles' line.

Initially then, for v_∞ along the step face, v_x at node n7 was taken (see Figure 5.12.) but this lead to a rapidly diverging solution. This arose by virtue of the comparitive magnitudes of v_x at node n7 and the values of v_y to be returned by the subroutine along the step face. Along the centreline, v_x is significantly greater than both v_y at the centreline and the typical v_y values near to the step face in the standard FIDAP model. This was remedied by taking v_∞ as the value of v_y at node n7 for this Coles' line.

Where the subroutines were called to compute k and ε, the procedure was as for the U-bend, being based upon the method outlined in Section 5.1.1. In the event of the subroutines being called to evaluate v_x (for the top, back upper reach and front lower reach Coles' lines) or v_y (for the step face), then the wake parameter was derived from the method of Section 5.2.1.

In returning velocities to the main program, the fact that the Coles' equation is essentially positive, and hence does not indicate the direction of flow, again required to be considered. Notionally, the sign of the local velocity gradient may be imposed on the result of Coles' equation at a node as

$$v = \text{sign}\left(v_{Coles} , \frac{dv}{dy}\right) \qquad (5.20)$$

but in the instance of the top Coles' line, this approach had to be modified by taking the opposite sign to that of the local velocity gradient; for the top Coles' line, $\frac{dv}{dy}$ is seen to increase in the direction of diminishing y co-ordinate.

An improvement over the U-bend model was the slightly more precise use of Coles' law, which should not be used within the viscous sub-layer, where y^+ is less than five. Before returning a nodal velocity to the main program, the model inspected the value of y^+ at that node, given that y^+ has the form of Reynolds number. Should y^+ be less than five, then instead of calculating the velocity using Coles' law, it was gained from a rearrangement of equation 2.28 as

$$\overline{v} = \frac{yv^{*2}}{\nu} \tag{5.21}$$

5.3.3. Initialization of the Basic Model of the Backward Facing Step.

The initial conditions for the solution are shown in Figure 5.15 below.

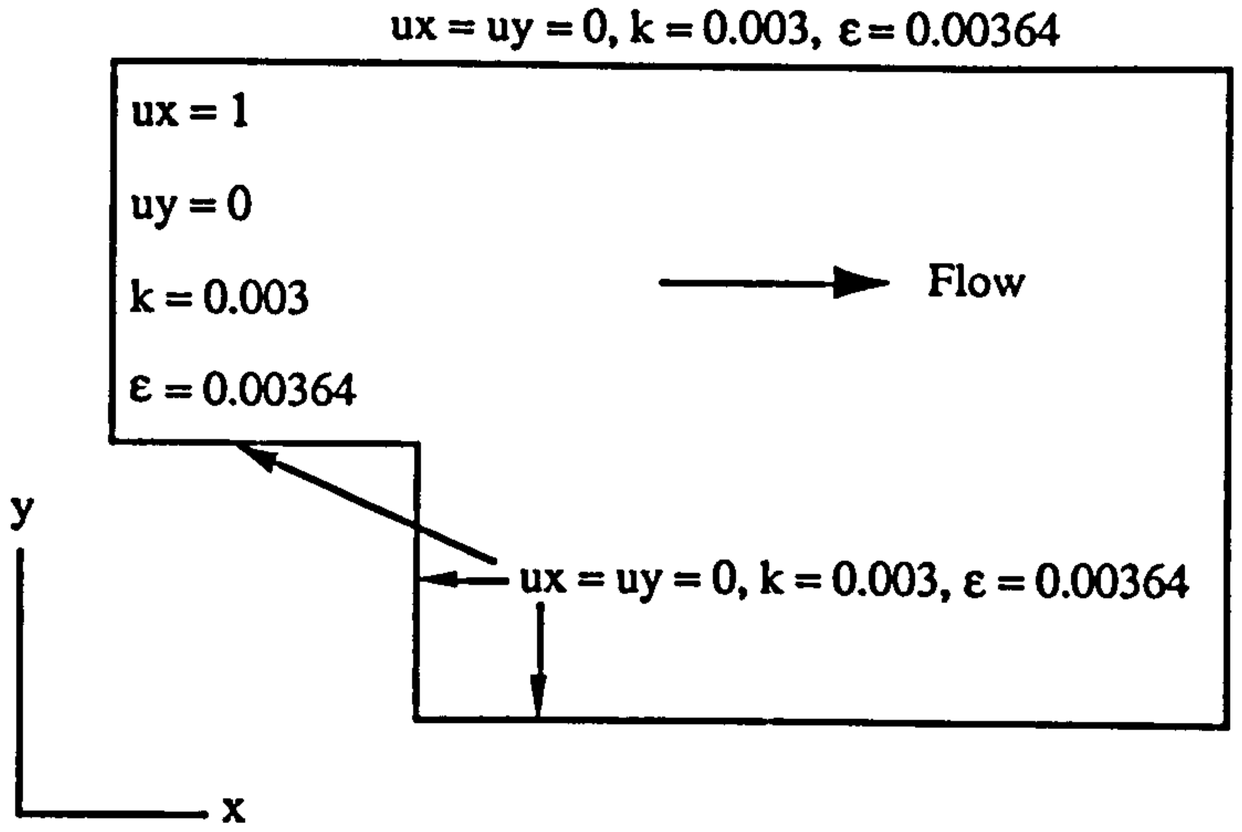

Figure 5.15. Prescription of initial conditions for the backward facing step.

As with the U-bend model, the backward facing step model did not begin operation at solution iteration number one but was delayed until the second iteration to ensure that it had a favourable environment to commence within. In this case, the 'start' counter was triggered by one specified node within each Coles' line (such as node n1 for the back upper reach), providing a sequence of counter events as Table 5.6. below.

Iteration number		i=1	i=2	i=n
Value of	onset of iteration	i+37	i+37+12(i-1)	i+37+12(n-1)
"start" at	end of iteration	i+37+11i	i+37+12(i-1)+11(i-1)	i+37+21(n-1)

Table 5.6. Detailing the values of the counter 'start' for successive iterations.

Within the subroutine then, until the second iteration, when start = 49, the subroutine returned $v_x = v_y = 0$, $k = 0.003$ and $\varepsilon = 0.00364$ throughout the Coles' model.

Appendix A3 then contains the following information pertaining to the basic Coles' law model of the backward facing step: the input file, tat2.FDREAD: the subroutine template, erasure.f: an algorithm flowchart of erasure.f.

5.3.4. Improved Evaluation of the Wake Parameter and Wake Function for the Backward Facing Step.

To date, all models discussed have had very simple descriptions of the wake parameter, Π, and the wake function, w. Whilst Π was based upon an empirical relationship with the freestream Reynolds number for a flat plate with zero pressure gradient, w was forced to unity by the blanket prescription of $\delta = y$.

In a discussion of the practical use of Coles' law, White (1991) notes an empirical relationship between Π and Clauser's equilibrium parameter, β, developed by Das (1987, 1988). After studying a range of flows with both favourable and adverse pressure gradients, Das observed that the following empirical relationship provided a good approximation to the variation of β with Π as

$$\beta = -0.4 + 0.76\,\Pi + 0.42\,\Pi^2 \qquad (5.22)$$

Recalling equation 2.31 as

$$\beta = \frac{\delta^*}{\tau_0}\frac{dp_\infty}{dx}$$

then a direct link is established between the wake parameter and the streamwise pressure gradient at the edge of the boundary layer, $\frac{dp_\infty}{dx}$. Given that the pressure gradient can be accessed by use of the DVARI array in the source subroutine (much as $\frac{dv}{dy}$ was gained), then the problem is reduced to finding δ^*, the displacement thickness of the boundary layer.

The displacement thickness, described by the general equation 2.32, may be rewritten for a fluid of constant density as

$$\delta^* = \int_0^\delta \left(1 - \frac{\bar{v}}{v_\infty}\right) dy \qquad (5.23)$$

where δ is the boundary layer thickness and v_∞ the freestream velocity at the edge of the boundary layer. For use to be made of this relationship, the boundary layer thickness has to be evaluated properly. A sketch of the boundary layer at a point in the mesh is then shown as Figure 5.16 below.

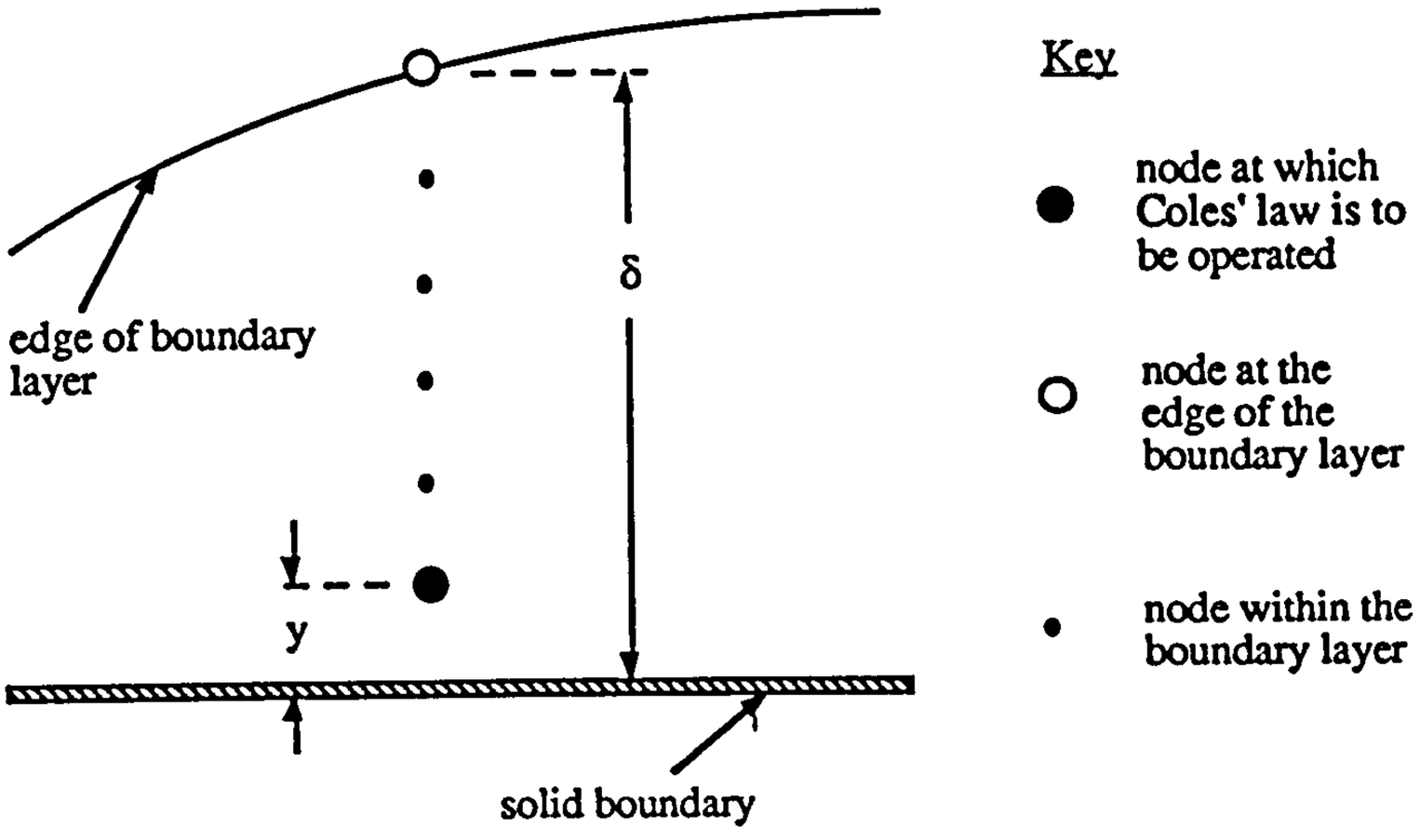

Figure 5.16. Nodes within the boundary layer.

Now at the edge of the boundary layer,

$$v = v_\infty$$

and so $$\frac{dv_x}{dy} = 0 \qquad (5.24)$$

As such, if the velocity gradient were inspected at successive nodes out into the flow until a node satisfying equation 5.24 was reached, then the geometric location of that node would yield the boundary layer thickness, δ.

Returning to equation 5.23 and Figure 5.16, knowing δ and the spatial separation of the nodes within the boundary layer, then the integral in equation 5.23 could be replaced by a summation process to yield δ^*.

An algorithm for the prediction of the wake parameter and the wake function would then take the following form as

i) inspecting successive nodes out from the Coles' line, test for $\frac{dv_x}{dy} = 0$,

ii) set δ to the y co-ordinate of the node satisfying (i) above,

iii) operate equation 5.23 in a modified form as a summation across the boundary layer to give δ^*,

iv) for the node at $y = \delta$, gain $\frac{dp_\infty}{dx}$ from information provided by the source subroutine,

v) calculate β from equation 2.31,

vi) calculate Π from equation 5.22 and

vii) set the wake function, using equation 2.46.

5.3.5. Development of a Model to Evaluate the Wake Function and Wake Parameter.

The modelling of the wake function, w, and the wake parameter, Π, can be seen to depend upon establishing the thickness of the boundary layer, δ. Once δ has been established, the displacement thickness and the desired wake properties may be determined. The proposed method for estimating δ requires the inspection of a number of flow variables along a line of nodes normal to the solid boundary and passing through the node at which Coles' law is to be operated, as depicted by Figure 5.16. Upon closer inspection of Figure 5.16, in conjunction with Figure 5.11, a general relationship between the node on the Coles' line and the elements on either side of the line of inspection can be seen as Figure 5.17 below.

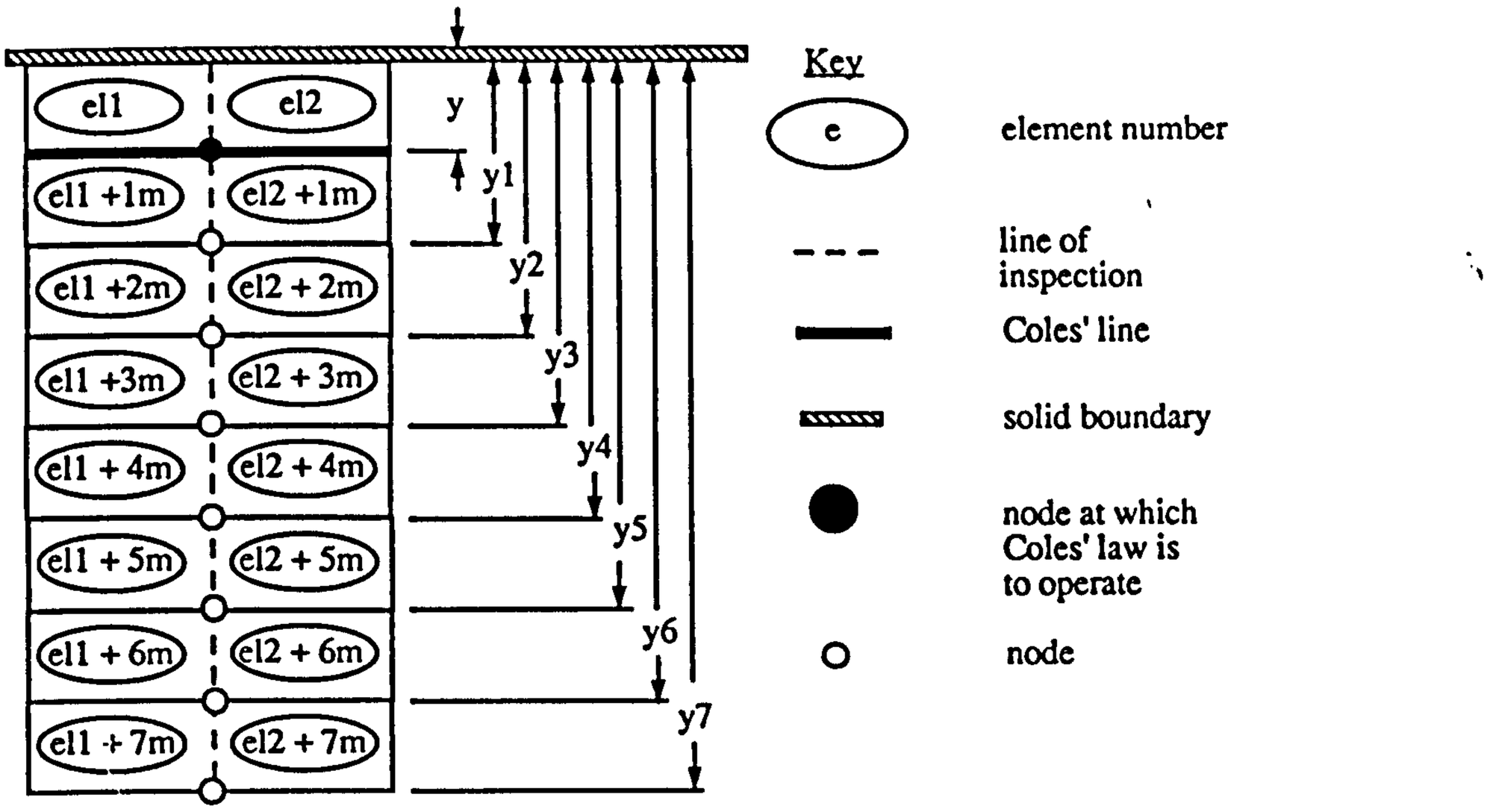

Figure 5.17. Showing a column of elements about a node on a Coles' line.

For a given portion of a Coles' line, there will be a regular increase in element number, when moving away from the wall in a normal direction, from one element to the next. Furthermore, the names of the elements to either side of a given node on a Coles' line can be rigorously defined for that node, such relationships having been already made use of in the algorithm for determining the local velocity gradient at a node, as shown by Figure 5.14. The location of each of the elements within the column of Figure 5.17 can then be calculated, once the names of the basal elements are known.

For example, comparing Figure 5.17 with Figure 5.14, for the top Coles' line, for nodes (n8 + $1\Delta n_{hA}$) to n9 (along which section the nodal increment is Δn_{hA}) then

$$el1 = gelt1\text{-}1 = e2 + imp - 1$$
$$\text{and} \quad el2 = gelt1 \quad = e1 + imp$$

Then inspecting Figure 5.11, the increment in element number, m, when moving from element to element, away from the wall is

$$m = -\Delta e_{vA}$$

Similar relationships can be mooted for the balance of the top Coles' line and also for its end points.

Thus, the analysis of the column of elements in order to determine the boundary layer thickness can proceed by considering the various geometric co-ordinates and flow variables at the integration points of those elements and hence, by implication, at the nodes along the line of inspection. Figure 5.6 demonstrated how nodal locations might be calculated and Figure 5.14 detailed how the local velocity gradient might be determined for a node upon studying its surrounding integration points. After inspecting the converged solution for the standard FIDAP model of the backward facing step, it was observed that the boundary layer typically lay within the first eight layers of elements adjacent to a given solid boundary. Thus, within the source subroutine, the normal distance from the wall to each of the nodes in the first eight elemental layers was calculated and stored in arrays, such as yt(i) for ith node on the top line of inspection. yt(1) was then the y co-ordinate of the node on the Coles' line (and hence the value of y used for computing y^+) and y(8) the location of the furthest node away from the wall to be inspected.

To simplify the transfer of this data from the source subroutine to the boundary condition subroutine, when specifying values for el1, el2 and m for a node, a unique pointer, 'line', was set to identify which Coles' line was currently under analysis. 'line' values are given in Table 5.7 below.

Name of Coles' line	Value of pointer "line"
back upper reach	1
front lower reach	2
step face	3
top	4

Table 5.7. Prescription of 'line' values.

The value of 'line' for a node on the Coles' line was then used to transfer the relevant array of node co-ordinates from the source subroutine into a local array in the boundary condition subroutine. For example, for a node on the top Coles' line, line = 4 and so the local array y(i) of the boundary condition subroutine is given the values contained by the yt(i) array of the source subroutine. (At this juncture it was realised that the pointer 'line' could have been used to select the correct local velocity gradient for use at nodes n4 and n5, where two Coles' lines intersect. This would offer a more elegant discriminant than the pointers 'flag' and 'npole', already in use.)

Having determined the nodal locations of those nodes along the line of inspection, the search for the boundary layer thickness then proceeded by consideration of the flow properties at successive nodes along the line of inspection. Whilst it was suggested that the local velocity gradient be inspected at successive nodes, saying that edge of the boundary had been reached once the local velocity gradient fell below an arbitrary tolerance, this caused problems in the comparison of two very small numbers. It was found to be much simpler to compare the values of the velocity in the boundary layer at successive nodes to one another, as shown by Figure 5.18.

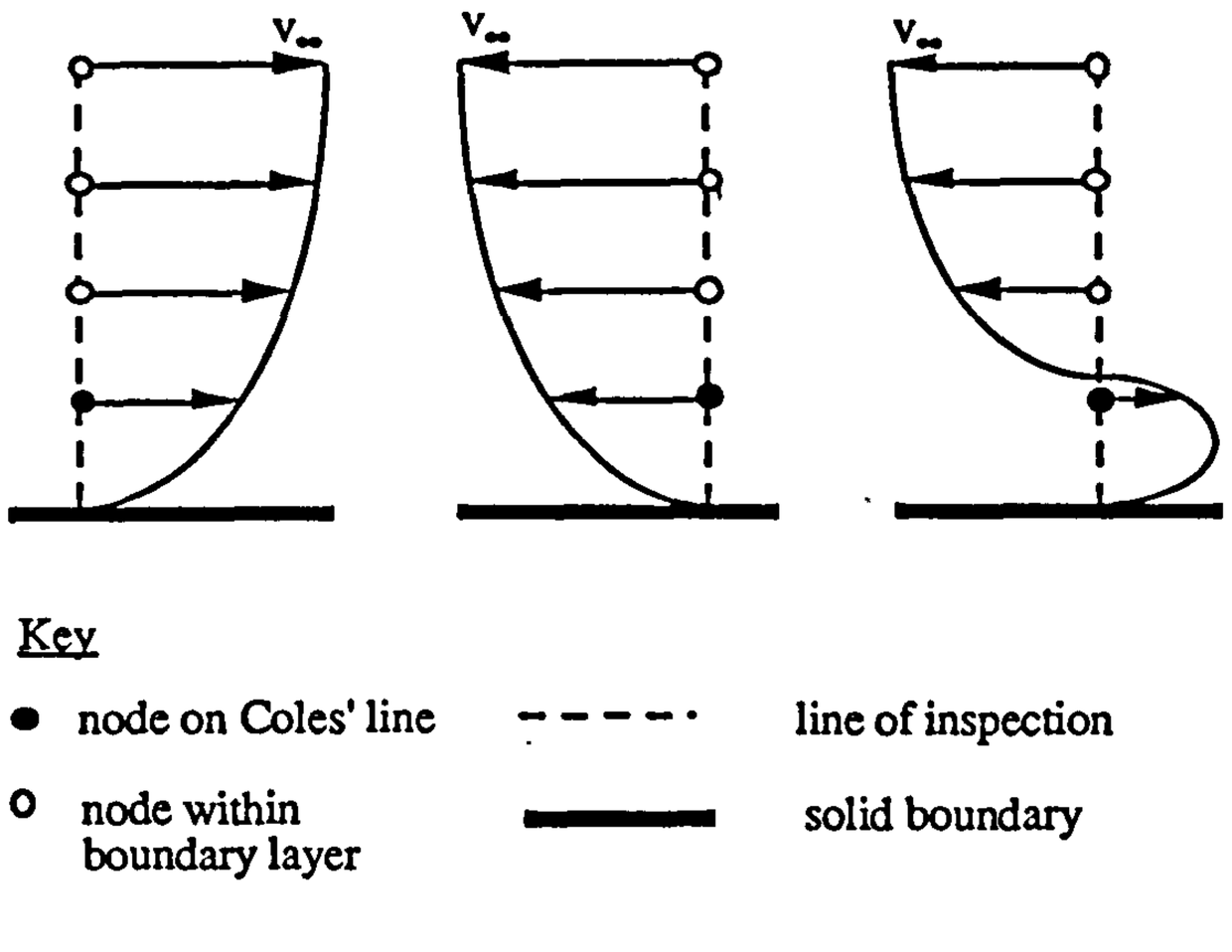

Figure 5.18. Variation of velocity within typical boundary layer profiles.

The velocities at each node on the line of inspection may be stored as an array, vo(i). Then for a given node, i, the velocity at that node, vo(i), may be compared with the next node, vo(i+1). If vo(i+1) has a different sign or is smaller in magnitude than vo(i), then the edge of the boundary layer is said to have been reached, such that $\delta = y(i)$. A

further condition was added to this method of testing for δ, by allowing δ to be set if vo(i) was equal to or greater than 90% of vo(i+1). This avoided the possible problem of comparing two small and almost equal numbers.

Having established δ, then equation 5.23 for δ^*, the displacement thickness, may be rewritten as a summation as

$$\delta^* = \sum_{j=1}^{j=i} \left(1 - \frac{|vo(j)|}{|vo(i)|}\right)(y(j) - y(j-1)) \qquad (5.25)$$

where i is the pointer to the node at the edge of the boundary layer, vo(i) is the freestream velocity and {y(j) - y(j-1)} the thickness of an elemental strip, as shown in Figure 5.19 below.

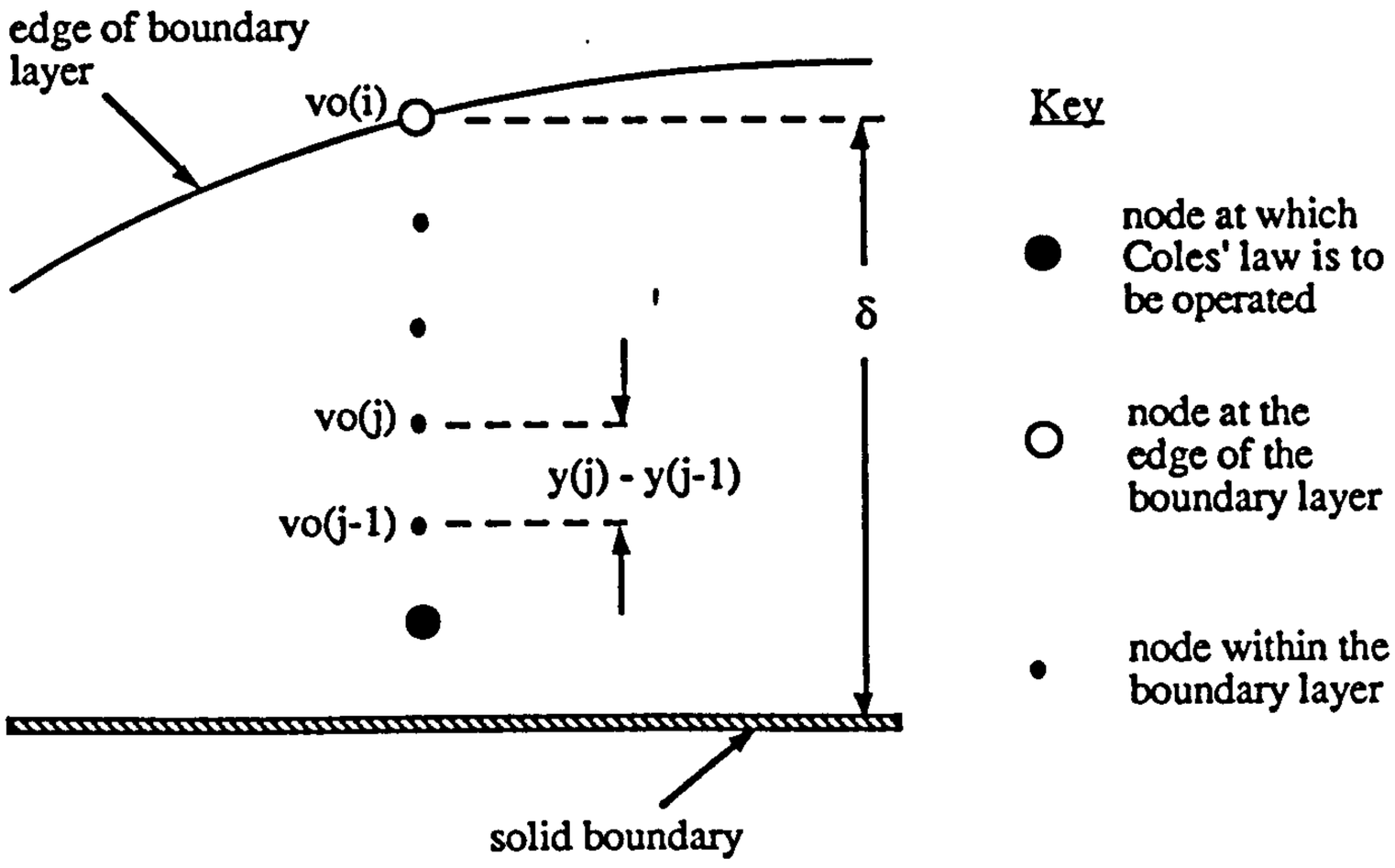

Figure 5.19. Nomenclature of equation 5.25.

By taking the modulus of the nodal velocities in equation 5.25, the model was able to take account of reversing flow. However, should the boundary layer thickness correspond to the first node out from the wall (i.e. to the Coles' line) then the model collapsed as when j = i = 1, the summation gave $\delta^*=0$.

This problem was overcome by interpolating between each node in the column to gain values of velocity and distance normal to the wall at the midpoints between

successive nodes. The expanded velocity array,ve(i), and the expanded location array, ye(i), were used in equation 5.25. Since by linear interpolation

$$ve(i) = \frac{vo(1) + vo(0)}{2} \quad \text{with} \quad vo(o) = 0, \text{ the slip velocity}$$

then δ^* cannot equal zero because vo(1) will always have a real value, such that $0 \leq |ve(1)| \leq |ve(2)|$.

Having calculated δ, then the wake function, w, could be computed from equation 2.46 but to evaluate the wake parameter, Π, from equation 5.22, then Clauser's equilibrium constant, β, had to be gained first as equation 2.31. This required knowledge of both δ^* and the streamwise pressure gradient, $\frac{dp_\infty}{dx}$.

Notionally, $\frac{dp_\infty}{dx}$ can be accessed from the DVARI array in the source subroutine but as this facility had not yet been coded into the latest release of FIDAP, it had to be calculated 'manually' by considering the pressure values at the integration points, available in the VARI array. In order to access the pressures at the integration points, however, the solution had to be run with pressure as a degree of freedom, necessitating the use of a slower solution procedure. To ensure consistency between the results from different models, all computational experiments for the backward facing step were then solved for pressure as an active degree of freedom. As such, the streamwise pressure gradient was evaluated at the node i, deemed to be at the edge of the boundary layer, as shown in Figure 5.20.

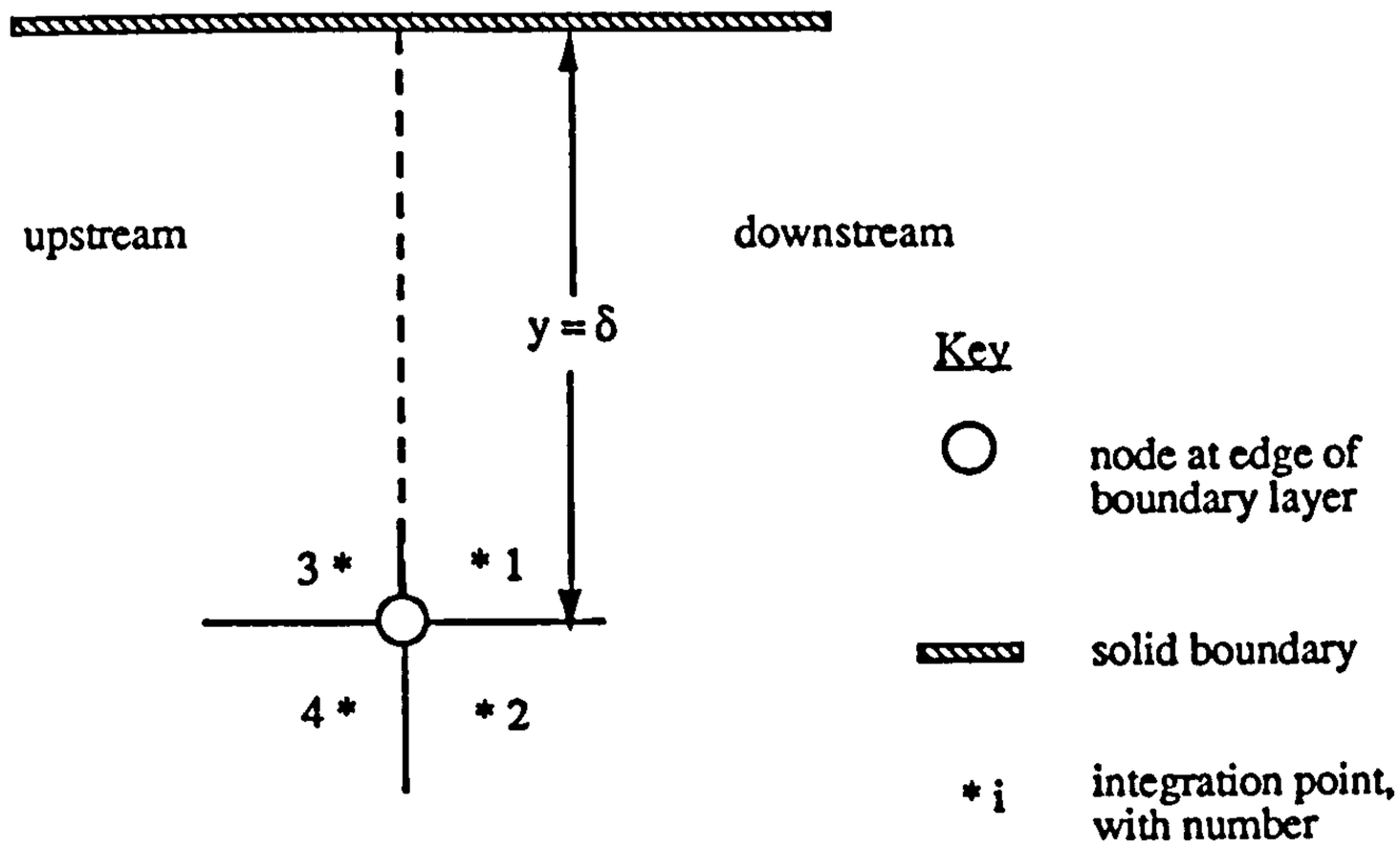

Figure 5.20. Showing the evaluation of $\frac{dp_\infty}{dx}$ at $y = \delta$.

From Figure 5.20 then

$$dp = \frac{p_1 + p_2}{2} - \frac{p_3 + p_4}{2}$$

$$\text{and} \quad dx = x_1 - x_4 \quad \text{or} \quad dx = x_2 - x_3$$

where p_1 is the pressure at integration point 1, x_1 is the x co-ordinate of integration point 1 and so on.

Finally then, knowing δ^* and $\frac{dp_\infty}{dx}$, the wake parameter, Π, was evaluated using equation 5.22. In practice, the basic Coles' law model of Section 5.3.2 was run for iterations 2 to 29, after which the full model as described was implemented. This allowed the pressure field to stabilise somewhat before the onset of the improved model. Even allowing for this, the local pressure gradients in the immediate vicinity of the upper and lower extremities of the step face were so large as to predict excessive values of β and hence of Π. This resulted in the predicted velocities at this point on the step face Coles' line being several orders of magnitude greater than at any of the surrounding nodes. As this caused the solution to diverge, an arbitrary upper limit on β was imposed on the step face, to obviate this problem.

Furthermore, when inspecting the initial results of the improved model, it was observed that $y^+ < 5$ for considerable portions of the Coles' lines - as this would result in the local velocity being calculated from $u^+ = y^+$, then in order to force the evaluation of Coles' law, the input file was rewritten to offer a coarser computational mesh.

The input file, andy.FDREAD, is listed in Appendix A3, as is the subroutine template for the model, circus.f, and its accompanying algorithm flowchart.

6. Results and Discussion of Two-dimensional Modelling.

6.1. Basic Results of U-bend Modelling.

The experimental work of Sandborn and Shin (1988) is taken as the reference by which to assess the results of U-bend modelling by the standard FIDAP method (using the wall model of Haroutunian and Engelman (1991)) and the simple Coles' law model, described in Section 5.2.

6.1.1. Principal Features of Flow in the U-bend.

Sandborn and Shin (1988) conducted an experimental study of water flow in an 180° turnaround rectangular duct for Re 70,000 - 500,000. Their work identified a number of main features for two-dimensional flow in a turnaround duct which may be summarized as

i) a separation bubble on the inner wall from 150° around the bend, extending to one duct width beyond the bend exit and with a maximum radial extent of 0.2 duct widths,
ii) large acceleration of the flow along the inner wall from the bend entrance up to a point 90° around the bend,
iii) an adverse pressure gradient along the outer wall in the early part of the bend, only causing separation for low Reynolds number, with pressure at the outer wall approximately constant from 50 - 130° around the bend,
iv) the development of a thin boundary layer on the outer wall downstream of the bend exit and
v) equalisation of pressure across the duct some two duct widths downstream of the bend exit, with overall pressure distribution largely independent of Reynolds number.

The key features of the separating flow for the U-bend are shown overleaf as Figure 6.1

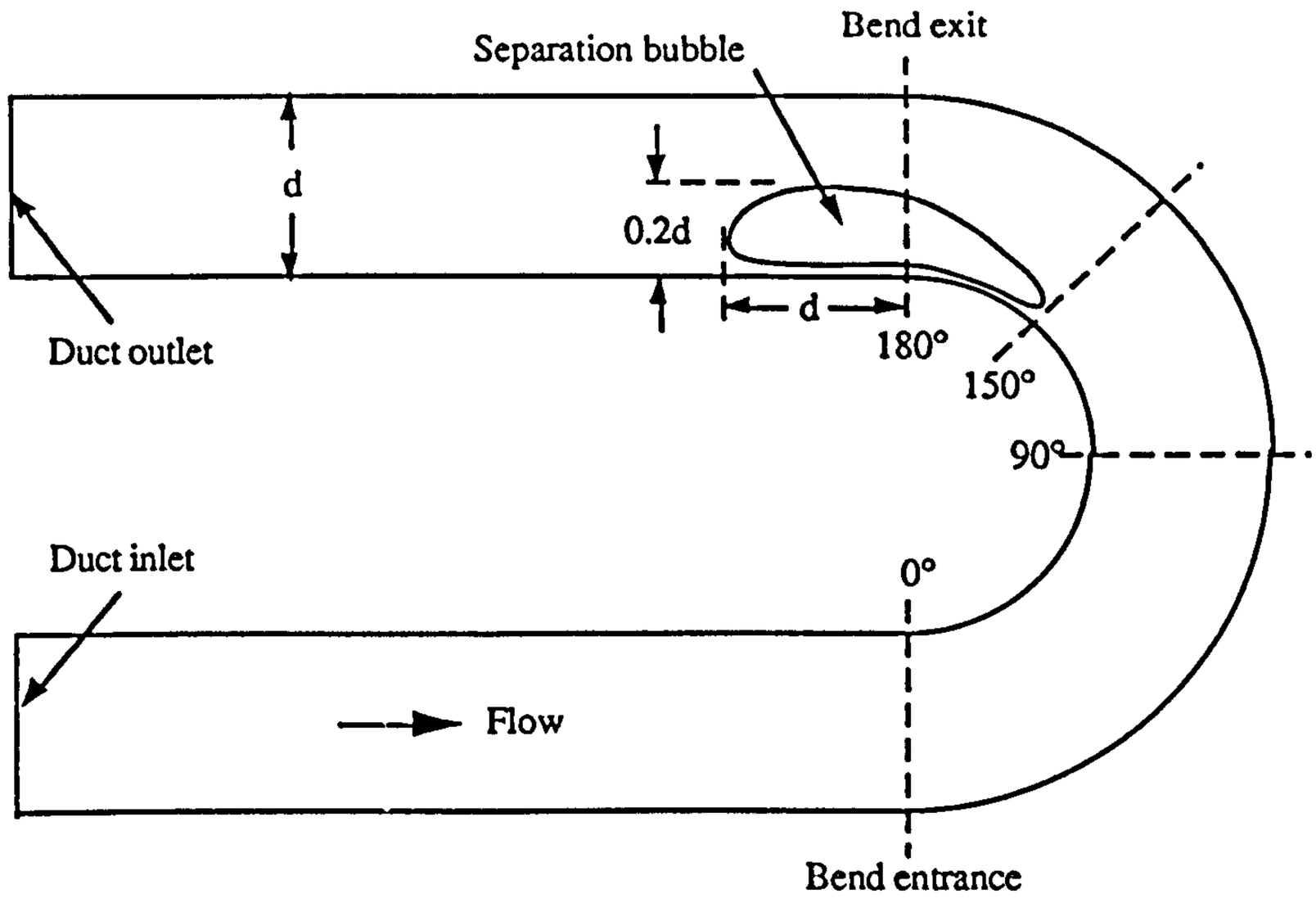

Figure 6.1. Principal features of flow in the U-bend, after Sandborn and Shin (1988).

6.1.2. U-bend Results for the Wall Model of Haroutunian and Engelman (1991).

The computational mesh used for both the standard FIDAP model and the simple Coles' law model of the U-bend is shown as Figure 6.2 below.

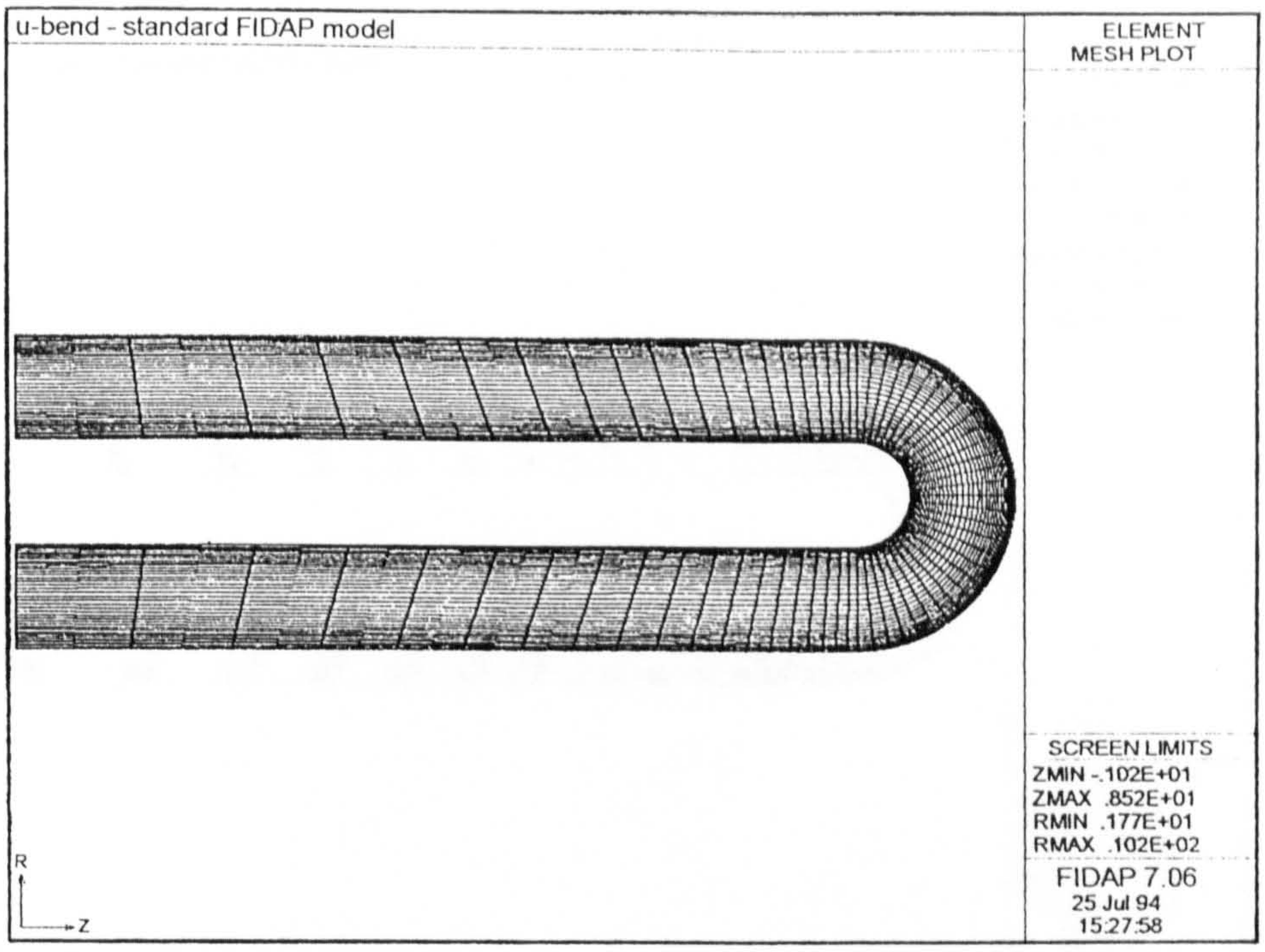

Figure 6.2. Computational mesh used for analysis of the U-bend.

On inspecting Figure 6.2, it will be seen that the mesh is graduated across the width of the duct to provide finer meshing towards the solid boundaries. Finer meshing is also used for the turning section of the duct, particularly around the inner surface of the bend where separation is expected to commence. Whilst mesh-dependent 'improvements' in the flow predictions of a given modelling scheme may arise from adjustments to local mesh density, all computational models of the U-bend used the mesh shown as Figure 6.2 above. As such, any difference in results between the models may be attributed to the wall model used and not to mesh density effects. (Likewise, one common mesh was used for all backward facing step models.)

The flow has a nominal Reynolds number of 100,000 based upon an uniform inlet velocity of 1.0 m/s; uniform distributions of $k = 0.001$ and $\varepsilon = 0.0009$ are used for kinetic energy and turbulent rate of dissipation respectively and a no-slip velocity condition is prescribed for the solid boundaries. The segregated solver, as described in Section 2.3.2, was used to implement the solution for all U-bend models. The main features of the flow through the U-bend may be shown by considering the results of the standard FIDAP model.

Figure 6.3 below is a velocity vector plot for flow through the U-bend.

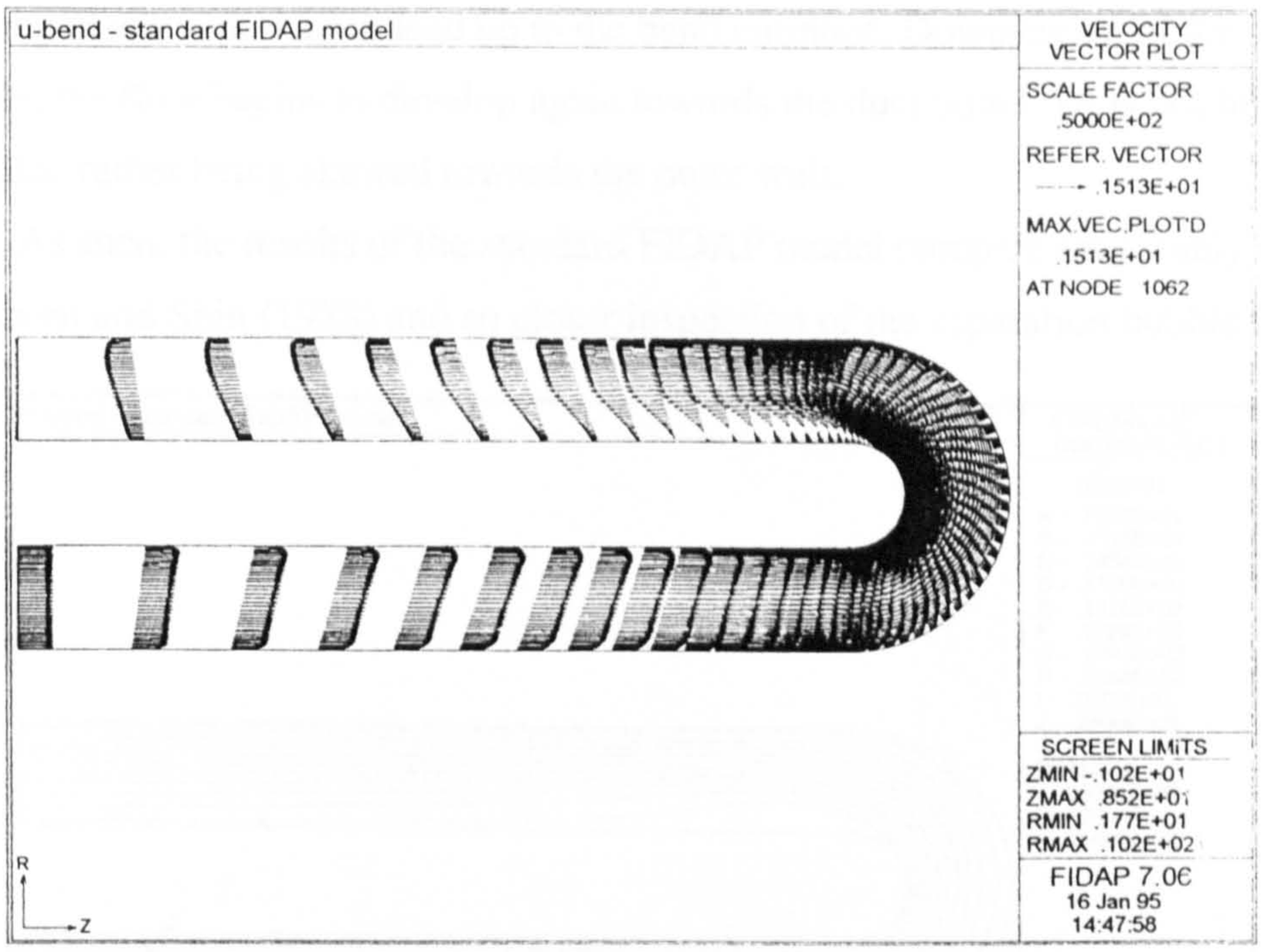

Figure 6.3. Velocity vectors for flow through the U-bend, as predicted by the standard FIDAP model.

Inspecting Figure 6.3, it can be seen that the standard FIDAP model predicts a separation bubble. The separation point is just before the exit of the bend, on the inner wall, and the separation bubble extends downstream of the bend exit for approximately two duct widths.

The uniform velocity profile at inlet tends towards fully developed flow as flow proceeds downstream, with an accompanying growth of turbulent boundary layers on both inner and outer walls. The rapid turning of the flow at inlet to the bend wipes the turbulent boundary layer off the inner surface. The large acceleration in the flow on the inner surface, almost up to 90° around the bend, leads to the flow effectively turning away from the outer wall at the start of the bend. As such, for the first half of the bend, a favourable pressure gradient is predicted on the inner wall whilst an adverse pressure gradient will be present on the outer wall. This situation is reversed in the second half of the bend where the flow along the inner wall is decelerating and that along the outer wall accelerates.

Whilst the adverse pressure gradient on the outer wall in the first half of the bend does not lead to separation, that along the inner wall towards the bend exit does result in separation. On the outer wall, the turbulent boundary layer is thin downstream of the bend

in comparison with that on lead up to the bend entrance. Downstream of the separation bubble, the flow begins to develop again towards the duct outlet but is not fully developed at outlet, rather being skewed towards the outer wall.

As such, the results of the standard FIDAP model compare favourably with those of Sandborn and Shin (1988) and so closer inspection of the separation bubble is warranted.

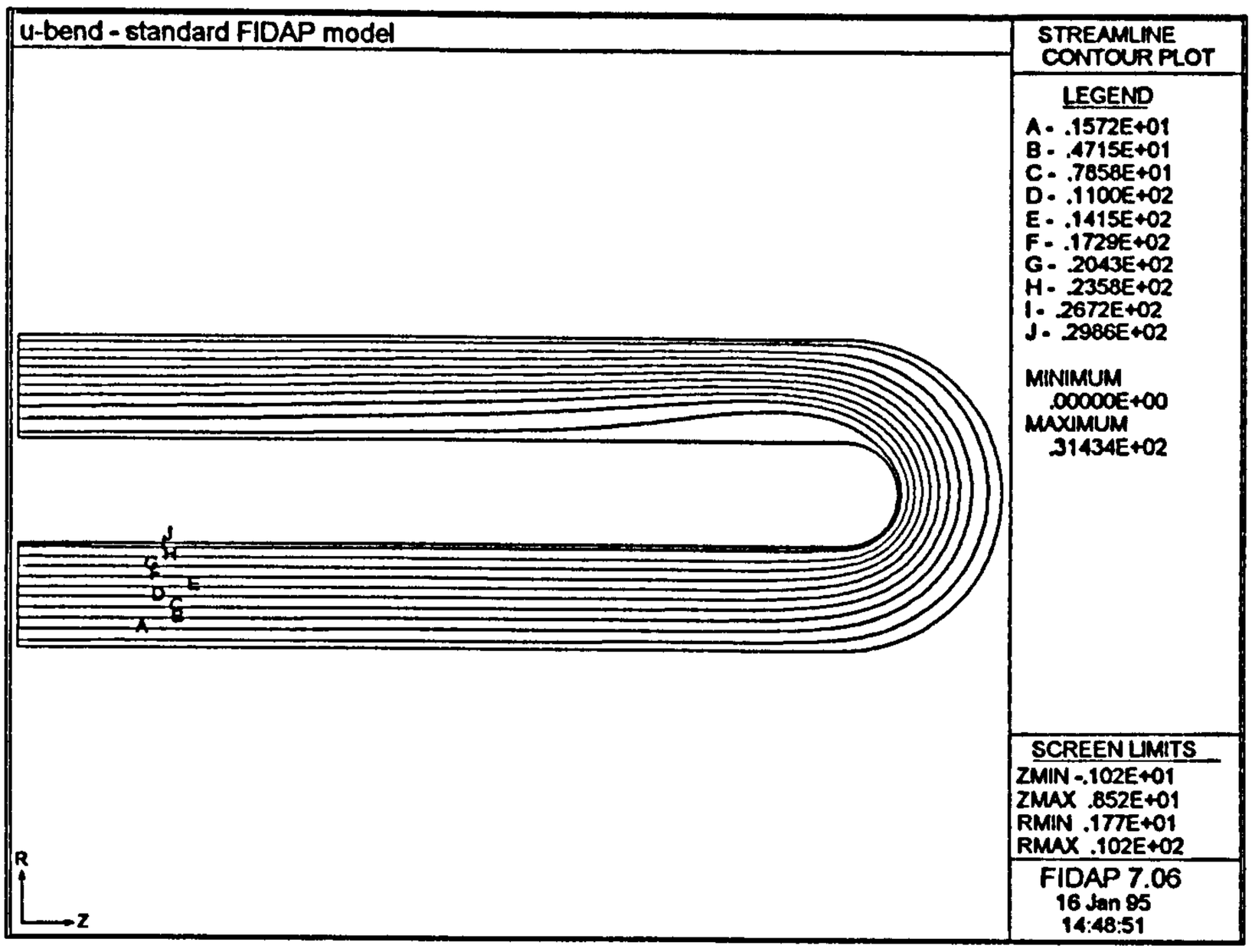

Figure 6.4. Streamline contour plot for flow flow through the U-bend, as predicted by the standard FIDAP model.

The streamline contour plot of Figure 6.4 shows the separation bubble to begin before the bend exit and to extend some two duct widths downstream of the bend exit, having a maximum radial extent of roughly 0.25 duct widths. This is shown in greater detail by Figure 6.5, showing a magnified detail of Figure 6.3.

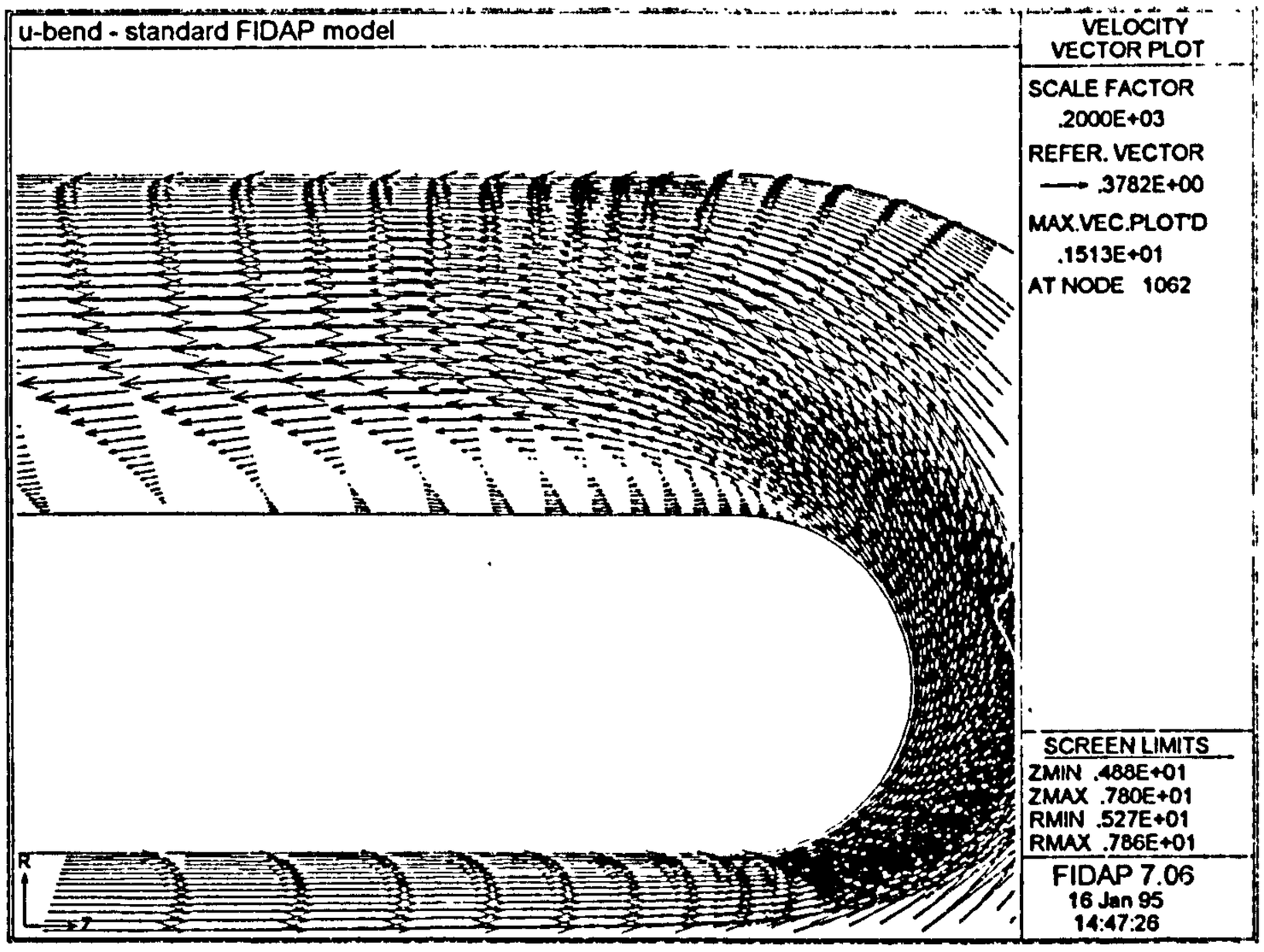

Figure 6.5. Showing magnified velocity vectors in the region of the latter half of the bend, as predicted by the standard FIDAP model.

By defining the extent of the separation bubble as that portion of the flow where velocity vectors adjacent to the wall run counter to the prevalent, or core, flow, then from Figure 6.5, the separation bubble commences at 155° around the bend and ends 2.1 duct widths downstream of the bend exit. At its thickest point, the separation bubble has a maximum radial extent of 0.23 duct widths.

Whereas the flow was turned away from the outer wall on inlet to the bend, at exit from the bend, the core flow, in passing over the top of the separation bubble, is diverted away from the inner wall and impacts upon the outer wall. At this point on the outer wall, just downstream of the bend exit, the outer wall turbulent boundary layer is just beginning to develop and, as noted earlier, is uncommonly thin.

A simple definition for the point of separation is that point on the solid boundary where the shear stress is zero, i.e. where $\tau_0 = 0$. Figure 6.6 presents a stress boundary plot for the inner wall of the U-bend.

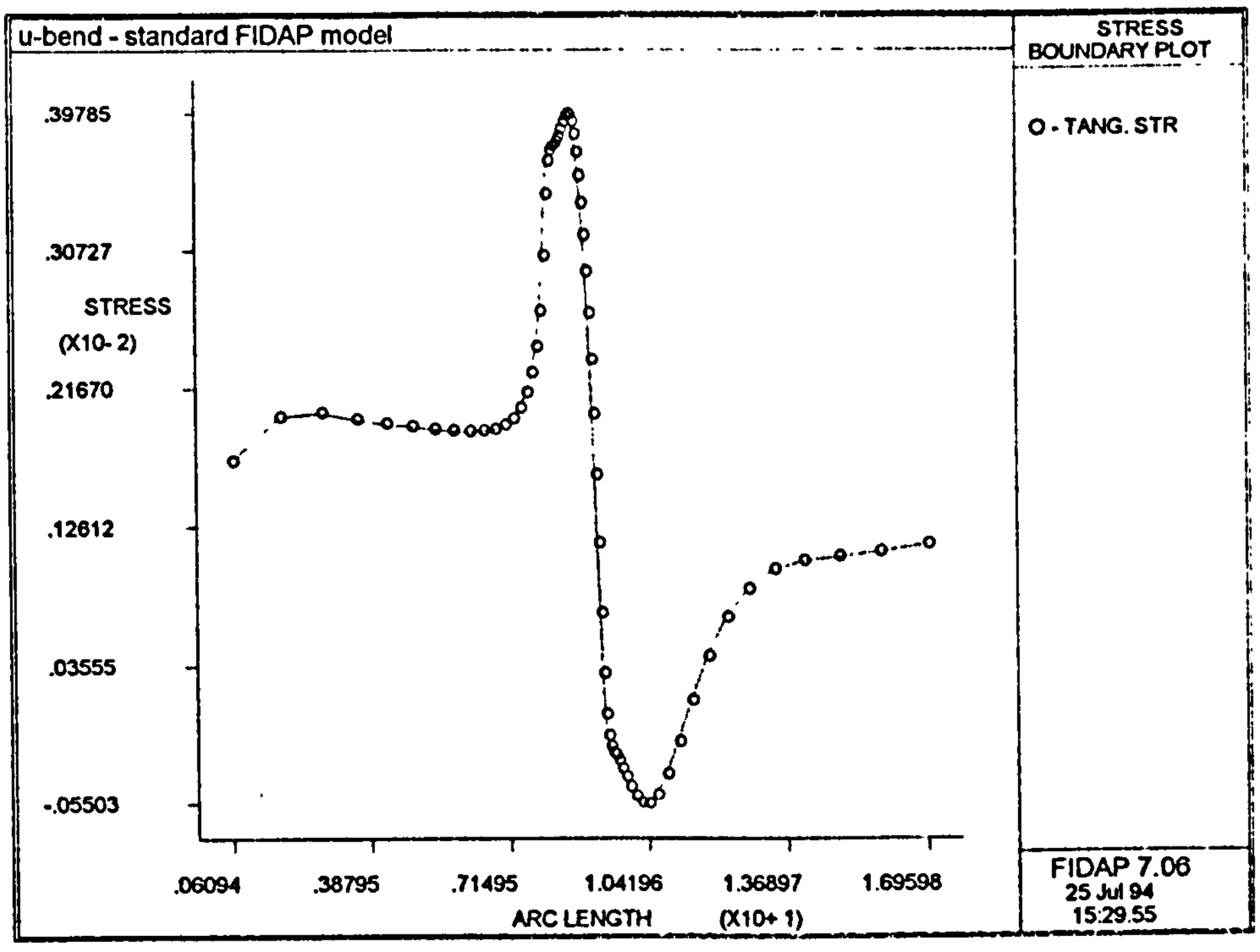

Figure 6.6. A stress boundary plot for the inner wall of the U-bend, as predicted by the standard FIDAP model.

Inspecting Figure 6.6, then observe that $\tau_0 = 0$ at 152°, which shows fair agreement with the corresponding estimate taken from Figure 6.5.

From the results so far considered for the U-bend, the standard FIDAP model appears to compare well with the work of Sandborn and Shin (1988). Given that the flow is thought to be governed by inviscid mechanisms, then these favourable results might arise from the FIDAP code providing a good model of the core flow (via the k-ε turbulence model) rather than from any benefits accruing from the wall model of Haroutunian and Engelman (1991), used in the standard FIDAP model. (Note that it is not intended to infer that the FIDAP turbulence model is valid right down to the wall but merely to question how limited an effect the presence of solid boundaries has in this case.)

6.1.3. U-bend Results in the Absence of Any Prescribed Wall Law.

To assess the influence of boundary layer modelling on the general flow characteristics of the U-bend, the standard FIDAP model was modified such that no wall model was used. The simple boundary conditions $k = \varepsilon = 0$ were prescribed along the

solid walls, replacing the boundary layer model of Haroutunian and Engelman (1991). Whilst this model is an over-simplification of the physics of the flow, it should demonstrate the necessity of providing a wall law for use with the standard high Reynolds number k-ε model. The result of this experiment is shown as Figure 6.7 below.

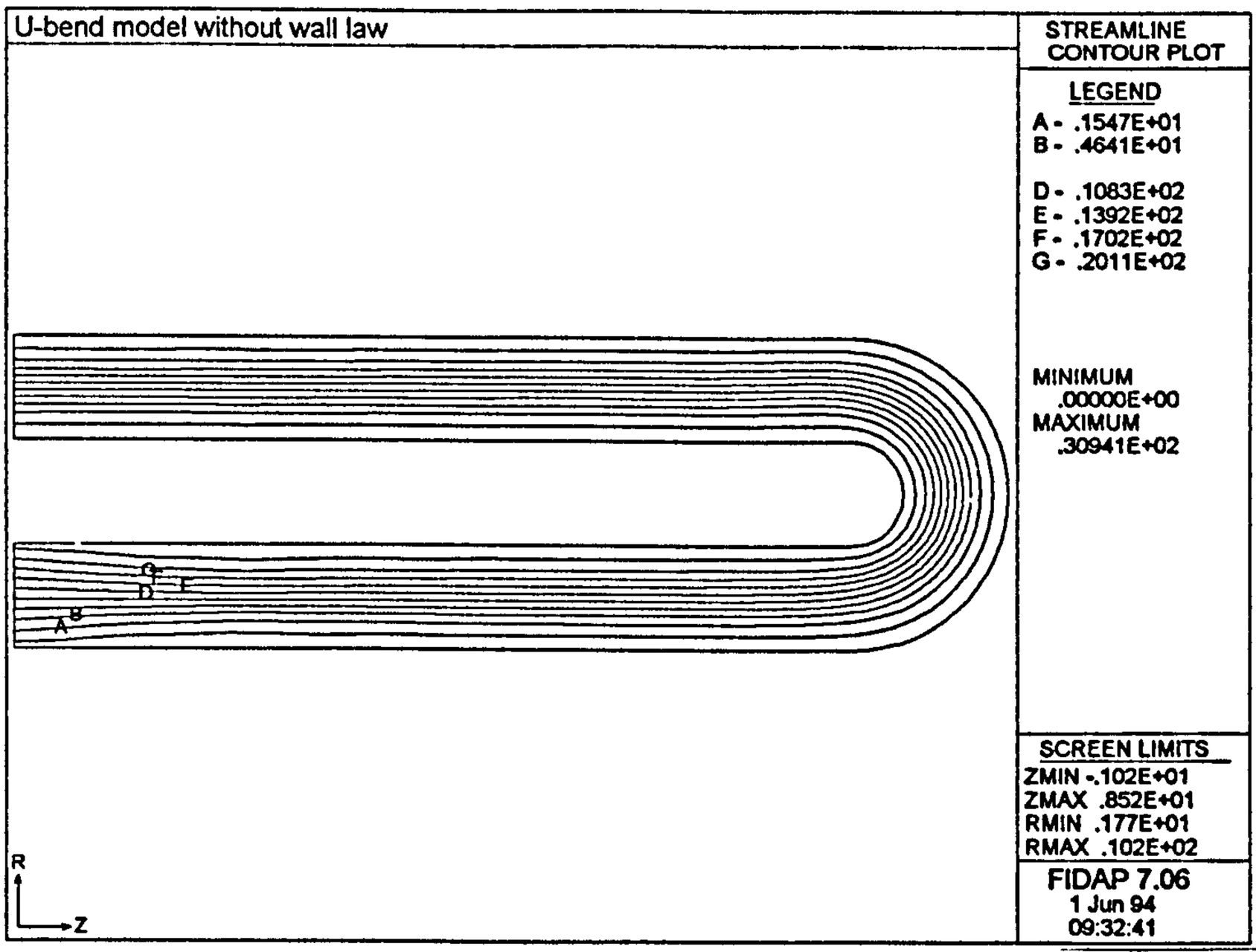

Figure 6.7. Showing the streamline distribution for the U-bend, predicted by operating FIDAP without any wall law model at the bounds of the flow.

Whilst the magnitude and distribution of streamlines in Figure 6.7 are notionally similar to that of Figure 6.4, where special wall elements were used, this model without a wall law does not predict any separation. Consequently, whilst the general flow may be momentum-driven, wall effects are still important: to what degree they influence the flow may be shown by considering the results arising from the application of Coles' law to the U-bend.

6.1.4. U-bend Results for the Simple Coles' Law Model.

The following results were provided by the final version of the simple Coles' law model of the U-bend, as described in Section 5.2.1. An overview of the results of the simple Coles' law model may be gained from Figure 6.8 below.

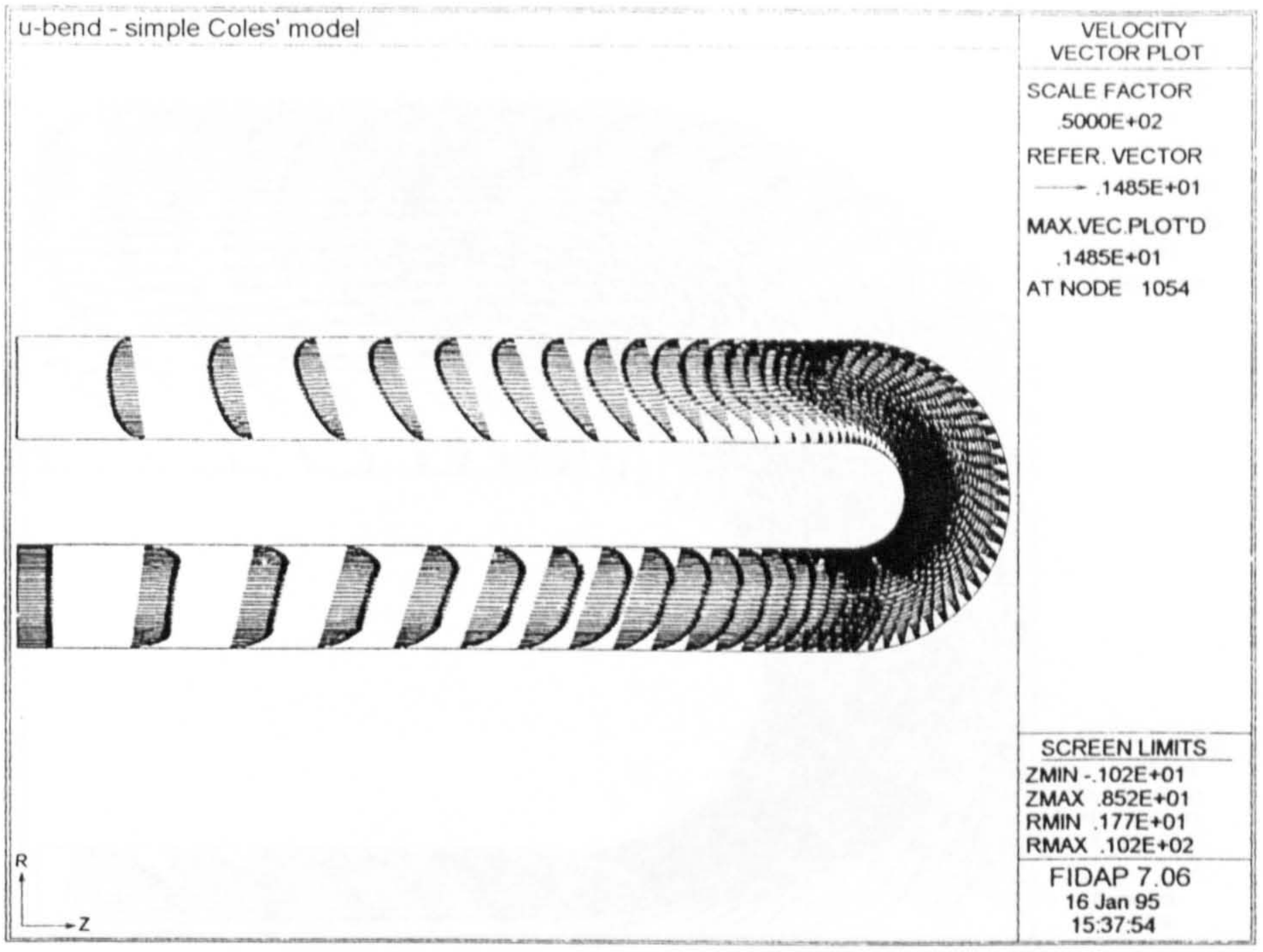

Figure 6.8. A velocity vector distribution for flow through the U-bend, as provided by the simple Coles' law model.

On first inspection, Figure 6.8 shows strong resemblance to Figure 6.3, the corresponding results from the standard FIDAP model. However, in detail, there are a number of important differences, which will now be outlined.

From the duct inlet, downstream towards the bend entrance, the flow tends towards full development but with a thicker boundary layer than the standard FIDAP model. Again, upon entering the bend, the flow is turned away from the outer surface and the acceleration of the flow around the inner surface of the bend leads to the onset of separation in the latter half of the bend, although this separation commences earlier than for the standard case.

After the bend exit, the duration of the separation bubble is shorter than before and on the outer surface, the developing boundary layer, whilst initially thin in comparison with that before the bend inlet, becomes established sooner than in the standard FIDAP model. Downstream of the separation bubble, the redeveloping flow is more uniformly distributed across the duct cross-section towards the duct outlet and shows less skewing towards the outer surface.

The separation bubble predicted by the simple Coles' law model may be seen better in Figure 6.9 below.

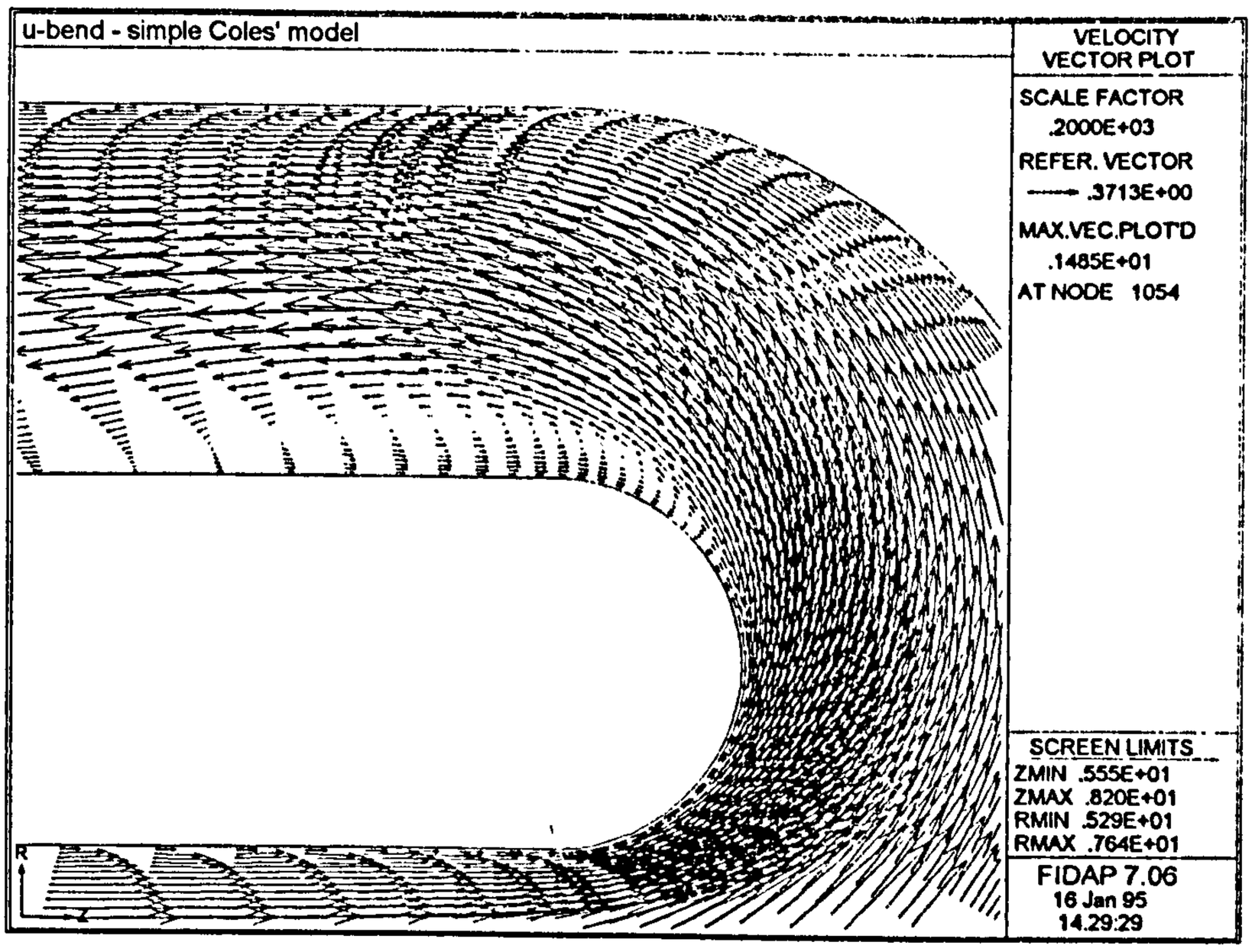

Figure 6.9. Showing magnified velocity vectors in the region of the exit to the bend, as predicted by the simple Coles' law model.

From the above figure, the separation bubble is seen to begin at 140° around the inner surface of the bend and to extend 1.4 duct widths downstream of the bend exit, having a maximum radial extent of 0.24 duct widths. Whilst the extent of the separation bubble beyond the bend exit is closer to Sandborn and Shin's prediction (1988), the onset of separation occurs some 10° earlier than expected.

In comparison with the standard FIDAP model results of Figure 6.5, the velocity vectors immediately adjacent to the solid boundaries are up to 80% lower on the approach to the inner bend entrance, 40% lower on exit from the bend along the outer wall and approximately 50% lower between the separation bubble and the inner wall. It can also be seen that as the flow is turned away from the inner wall on approach to the bend exit, that it does not collide so markedly with the outer wall near the bend exit. This also corresponds to a more rapid re-establishment of the turbulent boundary layer on the outer wall beyond the bend exit, for the case of the simple Coles' law model.

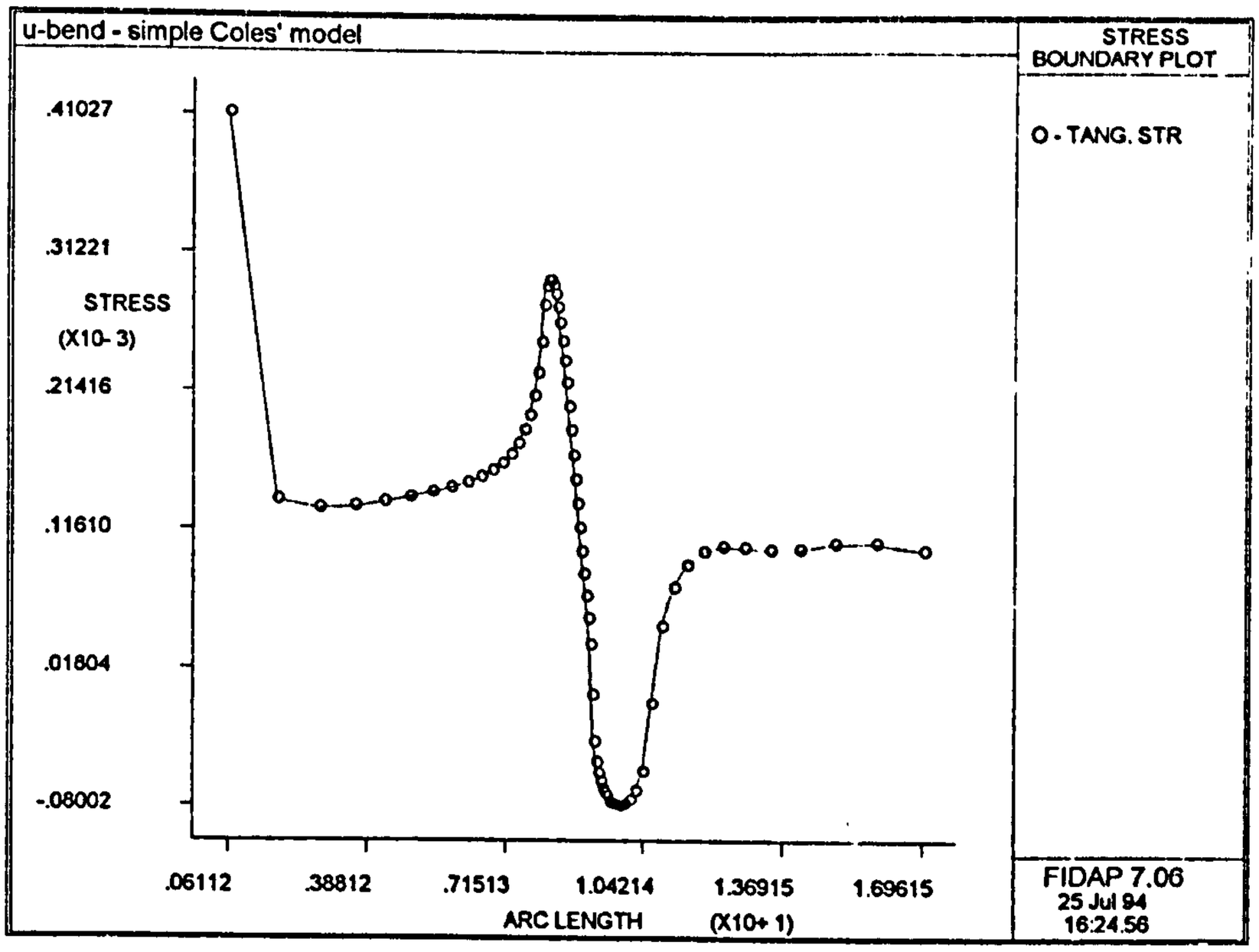

Figure 6.10. Showing a stress boundary plot for the inner wall of the U-bend, predicted by the simple Coles' law model.

The point of separation may also be gauged from Figure 6.10, showing the stress distribution along the inner surface of the duct. From this figure, it can be seen that $\tau_0 = 0$ at 141°, which compares well with the prediction taken from Figure 6.9. Note that whilst the tangential stress distribution is similar in form to that of Figure 6.6 for the standard FIDAP model, the tangential stress is approximately an order of magnitude less for the case of the simple Coles' law model.

As was noted earlier, the turbulent boundary layer developing between the duct inlet and the bend entrance on both inner and outer walls was noticeably thicker for the simple Coles' law model than for that predicted by the standard FIDAP model. To compare the boundary layers of the two computational models, the first ten mesh cross-sections downstream of the duct inlet were considered; beyond this point the turning of the flow away from the outer wall, arising from the presence of the bend, became significant. δ was taken to be that point at which the local nodal velocity was 90% or more of the estimated freestream velocity. The results of this comparison are shown as Table 6.1 below.

Length along duct, L (m)	δ from standard FIDAP model (m)	δ from simple Coles' model (m)
1.07	0.04	0.08
2.02	0.07	0.10
2.83	0.08	0.14
3.54	0.08	0.16
4.16	0.10	0.18
4.71	0.11	0.18
5.20	0.13	0.18
5.60	0.13	0.18
5.96	0.13	0.19
6.28	0.14	0.21

Table 6.1. Comparing boundary layer thicknesses downstream of the duct inlet, along the outer wall, for δ observed from the standard FIDAP and simple Coles' law models.

Whilst such a comparison must be made with reservation, since the graphical estimate of δ from the computational results is necessarily open to interpretation, at successive mesh cross-sections downstream of the duct inlet, the boundary layer of the simple Coles' law model is some 40-80% greater than that seen for the standard FIDAP model.

6.2. Analysis of the Behaviour of the Simple Coles' Law Model, as Applied to the U-bend.

Whilst it has been shown in Section 6.1 that the simple Coles' law model replicates the significant features of the flow through the U-bend, as documented by Sandborn and Shin (1988), the implementation of this model will now be discussed more closely.

6.2.1. Comparison of Boundary Layer Profiles.

Coles' law, in a simplified form, was stated in Section 5.2.1 as

$$v = v^*\left(\frac{\ln y^+}{\kappa} + B + \frac{2\Pi}{\kappa}\right) \qquad (6.1)$$

after assuming that the wake function, w, could be set to unity. Notionally then, Coles' law should predict a larger local velocity than that from Reichardt's law since some account is made of the local pressure gradient, even in this simplified form. Consider Reichardt's law below (Haroutunian and Engleman, 1991) as equation 2.29 as

$$u^+ = \frac{v}{v^*} = \frac{1}{\kappa}\ln(1 + 0.4y^+) + 7.8\left\{1 - \exp\left(-\frac{y^+}{11}\right) - \frac{y^+}{11}(-0.33y^+)\right\}$$

This is an experimental fit to the law of the wall which, expressed in inner variables as equation 2.24, may be shown as

$$u^+ = \frac{v}{v^*} = \frac{1}{\kappa}\ln y^+ + B$$

Comparing equations 6.1 and 2.24, the pressure gradient term, $\frac{2\Pi}{\kappa}$, being additive to the basic law of the wall, should predict an enhanced estimate of local velocity, provided a local pressure gradient exists. As this was not seen to be the case in comparing the results of the standard FIDAP and simple Coles' law models, then the principal variables of the above equations, namely u^+ and y^+, should be considered afresh, as given by equations 2.26 and 2.27 respectively as

$$u^+ = \frac{v}{v^*}$$

and

$$y^+ = \frac{y\, v^*}{\nu}$$

Further, v^* in equation 2.26 was expressed as equation 5.14 for computational purposes as

$$v^* = \sqrt{\frac{|\tau_o|}{\rho}}$$

Given that y, ρ and ν are common to both models in calculating v^* and hence in gaining u^+ and y^+, then the difference in the estimates of the local velocity immediately adjacent to the solid boundaries must be attributed to the determination of v^*.

In that v^* is dependent on the variation of shear stress at the wall, consider again

Figures 6.6 and 6.10 showing the stress distribution for the standard FIDAP and simple Coles' law models in turn for the inner wall. From these figures, it will be remembered that the tangential stress at the boundary was an order of magnitude lower for the case of the simple Coles' law model, although the form of the stress distribution was similar. The values yielded by the simple Coles' law model are lower than those from the standard FIDAP model: at the bend entrance the Coles' law stress estimate is some 7% of that given by the standard FIDAP model, rising to 10% at bend exit. As such, the wall friction velocity predicted by Reichardt's law in the wall model of Haroutunian and Engelman (1991) would be necessarily larger than that for the simple Coles' law model.

The simple Coles' law model calculated v^* from the shear stress at the wall and in turn from the velocity gradient near the wall as

$$\frac{dv}{dy} = \frac{v_t}{yII} \qquad (5.8)$$

whence $$\tau_o = \mu \frac{dv}{dy} \qquad (5.13)$$

So the velocity predicted by the simplified Coles' law model as equation 6.1 is dependent upon the local velocity gradient (equation 5.8), in turn related back to the velocity in the elemental layer adjacent to the Coles' law model. From comparisons noted earlier, in Section 6.1, between Figures 6.5 and 6.9, the velocity adjacent to the wall, as predicted by Coles' law, is from 40-80% lower than that of the standard FIDAP model. The substitution of this lower velocity into equation 5.8 for $\frac{dv}{dy}$ would lead to the Coles' law prediction of v^* being 63-89% lower than that for the standard FIDAP model, when τ_0 was used to calculate v^* from equation 5.14. Consequently, as v^* acts as a multiplicative constant to the right hand side of both equations 6.1 and 2.29 then this would account for the low velocity predicted by the Coles' law model, subject to further consideration of the other principal variable in these equations, namely y^+.

Values for y^+ along the inner duct wall are presented for both models as Figures 6.11 and 6.12 below.

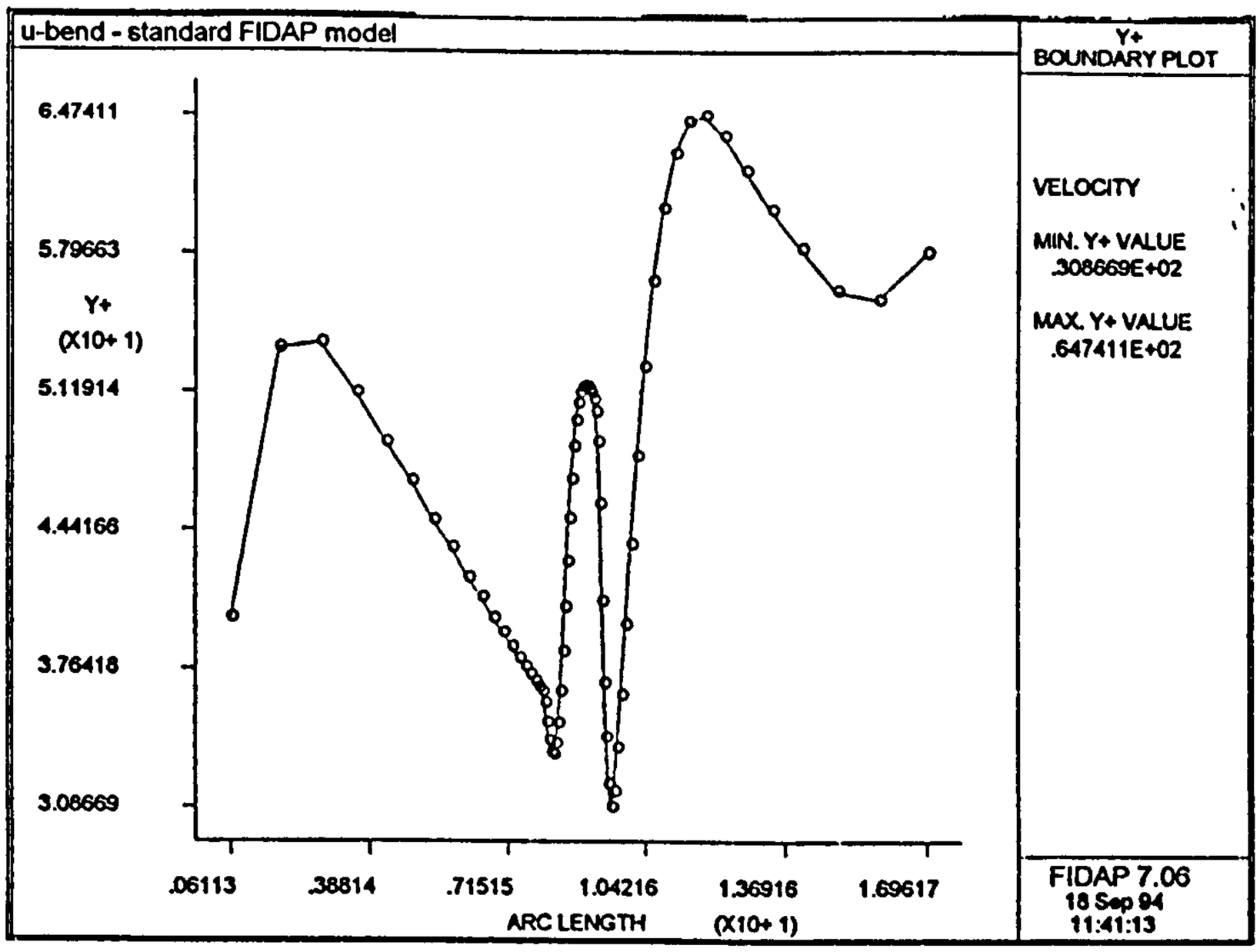

Figure 6.11. The y^+ distribution along the inner wall of the U-bend, predicted by the standard FIDAP model.

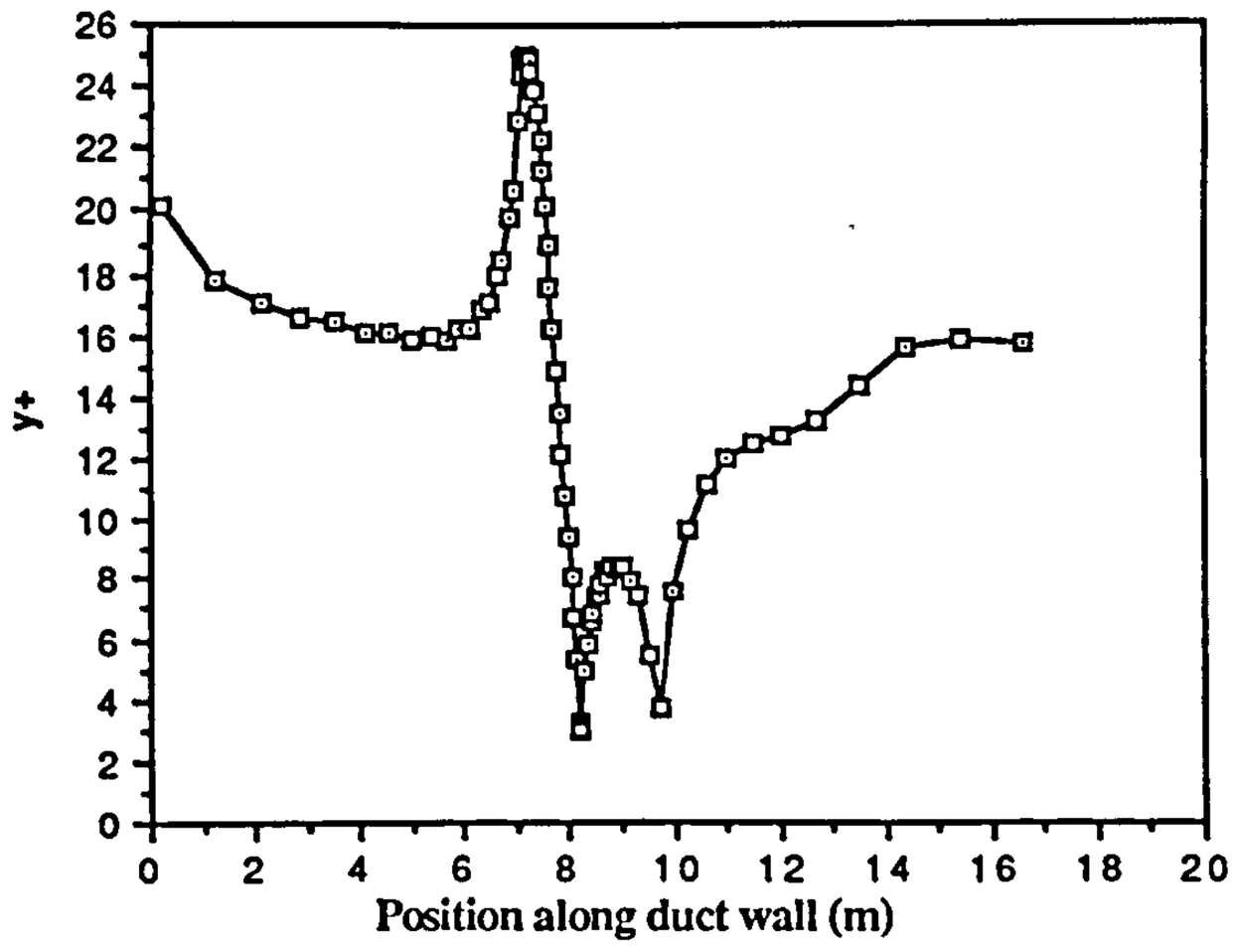

Figure 6.12. The y^+ distribution along the inner wall of the U-bend, predicted by the simple Coles' law model.

The y^+ values along the inner wall for the standard FIDAP model, as Figure 6.11, are typically $y^+ < 5$, excepting the latter part of the duct after the bend exit. This suggests

that the k-ε turbulence model was being operated close to or inside the viscous sublayer, for which its use is unsuitable and hence a coarser mesh should strictly be used in the near-wall region. This may be considered to be a shortcoming of this model solution, presented as it is as an example of good modelling in the FIDAP7 Examples manual (1994). Be this as it may, the two minima in the y^+ curve of Figure 6.11 represent the points of separation and reattachment of the separation bubble to the inner wall. Whilst it is expected that $y^+ = 0$ at such a point since $\tau_0 = 0$ at a point of singularity, this would only be observed in the results if, say, a separation point were to coincide exactly with a geometric mesh point; where separation occurs close to a mesh point, values of τ_0, v^* and hence y^+ will necessarily be small but finite at that mesh point.

This idea is bourne out by Figure 6.12, where the second point of minimum y^+ occurs at an earlier point along the length of the wall for the Coles' law model than for the standard model, corresponding with the shorter separation bubble observed in this case. Note also that outside the region representing the separation bubble, y^+ is typically three times greater for the simple Coles' law model than for the Haroutunian and Engelman model (1991), despite the Coles' law model having lower implied values of v^*.

For the inner wall, outside the separation bubble, if $y^+ = 5$ is taken as a representative value for the standard FIDAP model, then substituting $y^+ = 5$ into Reichardt's law, equation 2.29, and taking $\kappa = 0.41$ then gain $v = 8.83v^*$. Likewise, by taking $y^+ = 15$ as representative along the inner wall of the simple Coles' law model, then with $B = 5.0$ and Π estimated as 0.55 (since $Re > 5000$ by observation along the entire centreline of the duct for the simple Coles' law model) then from equation 6.1, gain $v = 14.29v^*$. However, taking a notional value of $v^*_{std} = 1$ for the standard FIDAP model, then the effective value of v^* for the simple Coles' law model is 70% lower than this as $0.3v^*_{std}$ and so the simple model really yields $v = 4.29v^*_{std}$ and thus the estimate of nodal velocity provided by Coles' law is approximately 50% of that from the standard model. The influence of v^* in equation 6.1 may be further illustrated by considering the effect that a doubling in the value of v^* has on the predicted velocity. Taking $y = 0.015m$ and $\nu = 1x10^{-5}m^2/s$, then by setting $v^*_{std} = 2$ in equation 6.1, the calculated velocity increases by 113%. Consequently, the marked effect that v^* has on the velocity prediction shows that the correct determination of v^* is critical to the operation of Coles' law.

In the event that v^* is lower when calculated by the Coles' law model, then the greater value of y^+ for this model, in comparison with the standard FIDAP model, is initially surprising. However, whilst y^+ is calculated directly from v^*, via equation 2.27,

for the simple Coles' law model, this was not the case for the standard FIDAP model where y^+ was taken as

$$y^+ = \frac{y\left(C_\mu^{1/2} k_t\right)^{1/2}}{\nu} \qquad (4.3)$$

where k_t is the kinetic energy of turbulence at the edge of the special wall element furthest from the wall i.e. at a distance y from the solid boundary. Consequently, y^+ for the standard FIDAP model is not related explicitly to wall conditions; the expression of Haroutunian and Engelman (1991) for y^+ builds upon a number of implicit assumptions regarding boundary layer behaviour and the relationship between the wall friction velocity and the turbulent field.

Turning to the apparent thickness of boundary layers as predicted by the simple Coles' law model, this model was used to enforce the nodal velocity at the first node in the fluid continuum away from the solid boundary by implimenting Coles' law as a boundary condition at the edge of the fluid continuum. Whilst this model interacted with the freestream (the k-ε turbulence model) since the velocity gradient was evaluated in terms of the velocity at the second layer of nodes within the continuum away from the wall, the enforced boundary condition still gave underestimates of velocity at the edge of the freestream, when compared with the results of the standard FIDAP model. Consequently, as the velocity along the innermost portion of the boundary layer was 'low', then the velocity of the outer boundary layer where local velocity matches the freestream velocity, at $y = \delta$, would only be achieved at a greater distance from the solid boundary.

6.2.2. The Effect of Incorrect Prescription of Boundary Conditions.

Further light may be shed on the general behaviour of the simple Coles' law model by considering some of the early and 'unsuccessful' versions of this model. In Figure 5.9, the valid prescription of the nodal velocity to be returned by the boundary condition subroutine, as Cartesian components v_x and v_y, is detailed. Dependent upon the location of the current node being examined by the subroutine within the overall mesh, there is a clear relationship between the sign of the velocity component and the sign of the velocity gradient, $\frac{dv}{dy}$. In an earlier and incorrect approximation to this relationship, the velocity

arising from the operation of Coles' law was simply given the sign of the velocity gradient, without accounting for the location of the node within the computational mesh. The behaviour of this primitive model is shown in Figure 6.13 below.

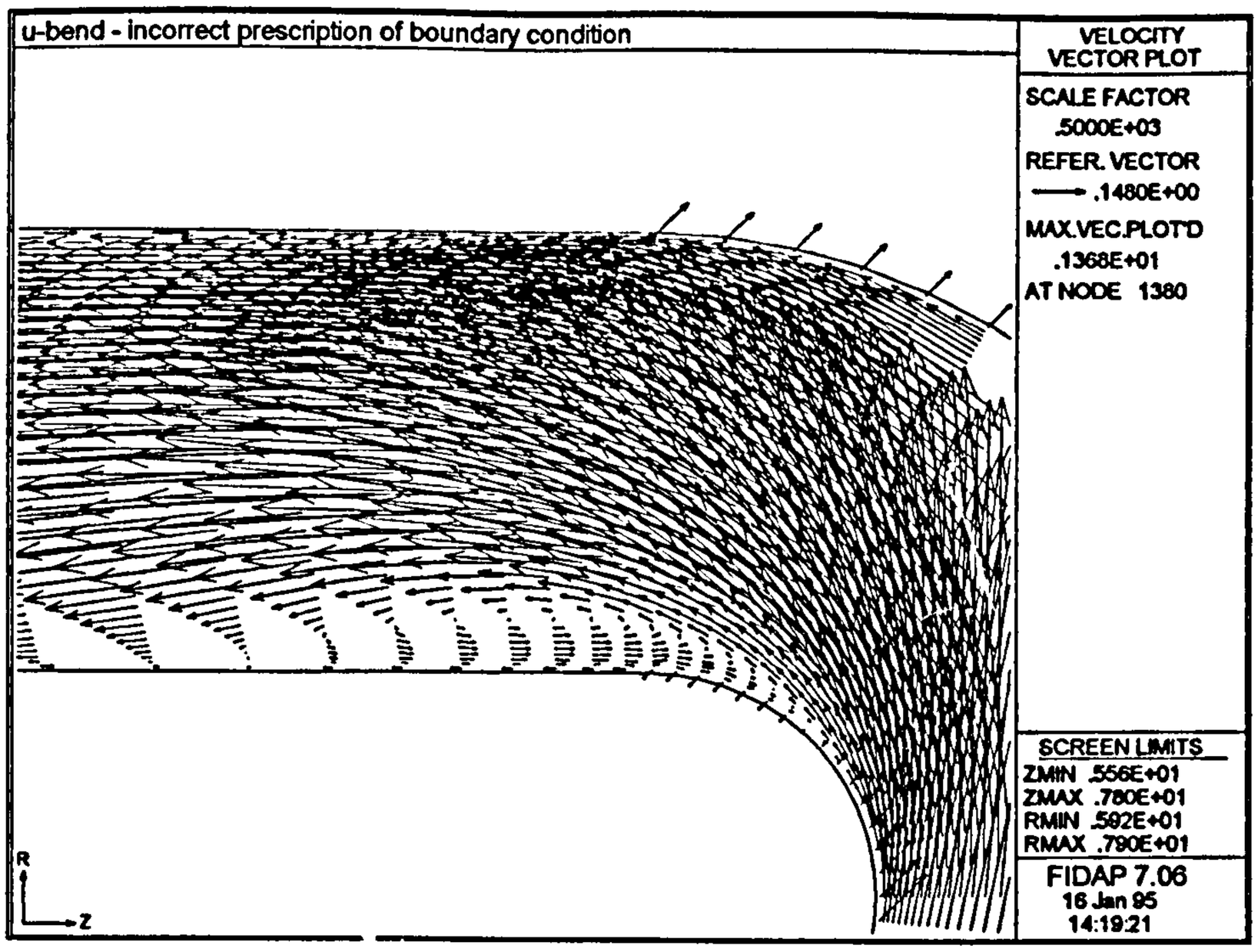

Figure 6.13. A magnified view of velocity vectors in the region of the bend exit for the U-bend, as predicted by a simple Coles' law model with inappropriate velocity sign conventions.

As can be seen from Figure 6.13, many of the desired features of flow through the U-bend are still replicated by this model. However, whilst recirculation is demonstrated, the model has a number of shortcomings: the sense of velocity between the separation bubble and the inner wall of the duct is wrong in that it runs counter to the bulk of the separation bubble: this counter-running stream beneath the separation bubble results in a considerable lengthening of the bubble, well beyond that length which might be reasonably expected: around the outer wall of the bend, the resultant velocity adjacent to the wall is colliding with the wall, rather than running along it tangentially. Despite these serious departures from the work of Sandborn and Shin (1988), separation is still predicted, thus suggesting that the major influence on the flow distribution around the duct is the momentum of that flow and that the wall effects have a secondary role. All the same, on remembering Figure 6.7, where no separation was predicted as a result of ignoring wall effects, the fine details of the flow must then be determined by accurate

description of the viscous effects in the near-wall region.

Again substituting for $y^+ = 15$ into equation 6.1, then the weighting of each of the terms in the simple Coles' law model may be seen as

$$v = v^*\left\{\frac{\ln y^+}{\kappa} + B + \frac{2\Pi}{\kappa}\right\} = v^*\{6.61 + 5.00 + 2.68\}$$

Now the second right hand term, B, is constant, whilst the first and third terms should vary with velocity and pressure gradients respectively. Given that the third term, $\frac{2\Pi}{\kappa}$, returning a value of 2.68 in this working, is a generous estimate of the pressure term since $y < \delta$ from the experience of Figures 6.3 and 6.8, then the variation of Π here is important. In that the simple model of the pressure term relates Π to the Reynolds number of the freestream, via equations 5.15-5.17, then from the method used, Π will only deviate from 0.55 (and hence $\frac{2\Pi}{\kappa}$ from 2.68) when the centreline Reynolds number drops below 5000. Inspection of Figure 6.8 shows this not to occur anywhere in the model and, consequently, the third term in equation 6.1 is essentially static.

As such, variation in the nodal velocity predicted by this simple model is dependent purely on the first term in equation 6.1 and ultimately upon the method by which the local velocity gradient is calculated. The model, as it stands, computes the velocity gradient via equation 5.8, taking it to be a linear distribution from the solid boundary out to a node in the continuum at a normal distance yII, where the local velocity is v_t. In that yII is the separation of the second nodal layer from the wall then this linear distribution is held to extend some distance out into the flow, probably well beyond the viscous sub-layer. An earlier model had attempted to set

$$\frac{dv}{dy} = \frac{v_{Coles}}{y}$$

where y is the normal distance from the Coles' line to the wall and v_{Coles} is the local velocity at the node on the Coles' line, thus claiming a linear velocity gradient over a smaller portion of the boundary layer. However, this method failed in that the solution persistently diverged, this being attributed to the velocity gradient and the velocity at a given node being effectively expressed in terms of each other - the solution became incestuous and did respond to development of the flow in the core of the duct.

Nevertheless, whilst the method employed for calculating $\frac{dv}{dy}$ in the final simple Coles' model lead to moderately successful results for the U-bend, this part of the model was clearly both influential and, to some degree, deficient.

6.2.3. Consideration of Other Modelling Schemes Applied to U-bend Flow.

Prior to considering the results of modelling of the backward facing step, the effectiveness of the Coles' law model of the U-bend may be gauged by comparison with a number of reported U-bend models using a variety of modelling schemes. The importance of implementing a good model of the near-wall region was highlighted by a series of papers presented at the WUA-CFD Second World Conference in Applied Computational Fluid Dynamics, Basel, 1994. One of the test cases, set by the conference as 'benchmark problem no.1', bears similarity to the U-bend situation analysed here as a round inlet pipe feeding into an annular section which turns through 180°. At inlet to this benchmark problem, experimental values of Reynolds number, the turbulence intensity and the mean velocity profile were specified, with results given as pressure coefficients for the inner and outer surfaces of the duct. The flow was considered to be isothermal, incompressible, fully turbulent and steady and all models submitted were axi-symmetric. As with the U-bend analysed in this work, since separation was expected after the bend, choice of turbulence modelling methods for the benchmark problem was important. Of the several worked solutions submitted to conference, each used a different modelling code - whilst most made use of some form of the k-ε turbulence model, not all predicted flow separation. Once more, this suggests that model implimentation can have significant bearing on computational results.

Jones and Hope (1994) analysed the benchmark problem using three differing techniques as the standard k-ε model, the RNG k-ε model and a Reynolds stress model. Their standard k-ε model gave no recirculation, merely showing that such models cannot mimic near-wall behaviour (as was expected and shown by Figure 6.7 here). Whilst the RNG k-ε and Reynolds stress models predicted separation, the size and position of the separation bubble varied widely. They reported no results for pressure coefficients in their paper.

Ginter, Heitele and Ruprecht (1994) also used three different modelling approaches, in this case being a low Reynolds number, laminar approximation to the given problem, a

standard k-ε model utilizing the standard law of the wall and finally a two-layer turbulence model. This latter model used the k-ε model for the high Reynolds number freestream, with an one-equation k model and analytically prescribed ε (from a length scale formula) for the near-wall region. Whilst the model least close to the problem specification, being for laminar flow, showed recirculating flow, the two turbulent models failed to do so. Both predicted high values of kinetic energy in the curvature region but also gave high turbulent rates of dissipation, which they cited as suppressing any tendency to separation. Notionally, a two-layer model of this type should perform well, possibly better than the more common k-ε and law of the wall combination, provided close attention is paid to mesh density and switching between model layers in the near-wall region.

Deb, Diner and Ray (1994) used the standard k-ε model in conjunction with an adaptive grid to interactively concentrate the mesh in 'trouble' areas upon inspection of local solution error estimates during the course of the solution. Their results showed a very small pocket of recirculating fluid after the bend, suggesting that the common law of the wall wedded to a fine computational mesh was inappropriate. This was also seen from the results of Göhner (1994), whose adaptive mesh gave a separation bubble excessively far downstream of the bend outlet.

Finally, Engelman (1994) applied the standard FIDAP wall methodology (Haroutunian and Engelman (1991)), as used for one of the U-bend models in this study, to the benchmark problem provided by the conference. Recirculation was predicted at and after the bend outlet, with good comparison between results for pressure coefficients on the outer bend and those experimental values quoted. On the inner surface of the bend, however, there was significant discrepancy in the results for pressure coefficient at the apex of the bend.

In general, all of the models summarised above used different inlet conditions for k and ε, each having interpreted the prescribed turbulence intensity at inlet differently. More significantly though, across a wide range of wall modelling techniques there was little concensus in the results, many of which had trouble reproducing the desired flow behaviour. This strengthens the argument alluded to earlier that the implementation of a modelling concept is as important as the physics of the model itself. That the simple Coles' law model gave a fair account of the U-bend in this work suggests that the basic framework of this model is sound, even though some reservations as to its fine details have been expressed. As such, in the early analysis of the backward facing step, this simple Coles' law model was first applied as a basis upon which to extend modelling to

account more fully for pressure and velocity gradient effects.

6.2.4. Summary of Observations Arising from U-bend Modelling.

Taking an overview of the results arising from study of the U-bend, the principal observations may be summarized as:

i) In the absence of a wall model, the standard high Reynolds number k-ε model does not predict separation.

ii) Both the standard FIDAP and the simple Coles' law models of the U-bend offer good general flow predictions in comparison with the benchmark work of Sandborn and Shin (1988). However, the predictions of thickness of the separation bubble and its extent downstream of the bend exit for the simple Coles' law model are closer to the experimental results of Sandborn and Shin (1988) than the corresponding standard FIDAP results.

iii) The velocity in the near-wall region predicted by the simple Coles' model is lower than the corresponding standard FIDAP results.

iv) The wake parameter in the simple Coles' law model is essentially constant. Therefore, the principal variables in the Coles' law model are v^* and y^+ and, ultimately, τ_0, the shear stress at the wall.

v) The lower values of τ, the post-processed shear stress at the wall, for the simple Coles' law model do not fully account for the deficit in near-wall velocity.

vi) The greater y^+ values of the simple Coles' law model do not correlate with its lower values of v^* in comparison with the inferred values of v^* from the standard FIDAP model. This discrepancy arises from the different methods by which the two models evaluate y^+.

vii) Consideration of U-bend models with incorrectly assigned boundary conditions

shows the momentum of the core flow to have a significant effect on recirculation events.

viii) A review of other recent U-bend modelling approaches showed that modelling results are dependent upon model implementation. Consequently, the valid encoding of a particular modelling scheme is as influential as the physics of that model.

ix) The simple Coles' law model of the U-bend, in having given a good description of the flow, offers a viable framework from which to develop a full model of Coles' law of the wake.

6.3. Basic Results of Backward Facing Step Modelling.

The results arising from the three backward facing step models presented in Section 5.3 will now be considered; a standard model of the backward facing step was created, along with a basic Coles' law model, described in Section 5.3.2 and analogous to the simple Coles' law model of the U-bend, and also an enhanced Coles' law model of the backward facing step, detailed in Section 5.3.4.

6.3.1. Description of Principal Flow Features for the Backward Facing Step.

The efficacy of the computational models of the backward facing step may be judged in comparison with the experimental work of Kim (1978), the salient points of which will now be described. The wind-tunnel test section of Kim had similar dimensions to the backward facing step of Figure 4.2, upon which the mesh for computational modelling was based.

Kim determined that the size of the separated zone "depends on a balance between backward flow and flow 'entrained' by the free shear layer and pulled forward". The non-dimensionalized recirculation length, x_r , was seen to be independent of the ratio of step height to overall duct width. The pressure distribution up to reattachment was independent of step height but beyond this point was determined by duct width.

The key regions of the separation-reattachment process according to Kim are identified in Figure 6.14 below.

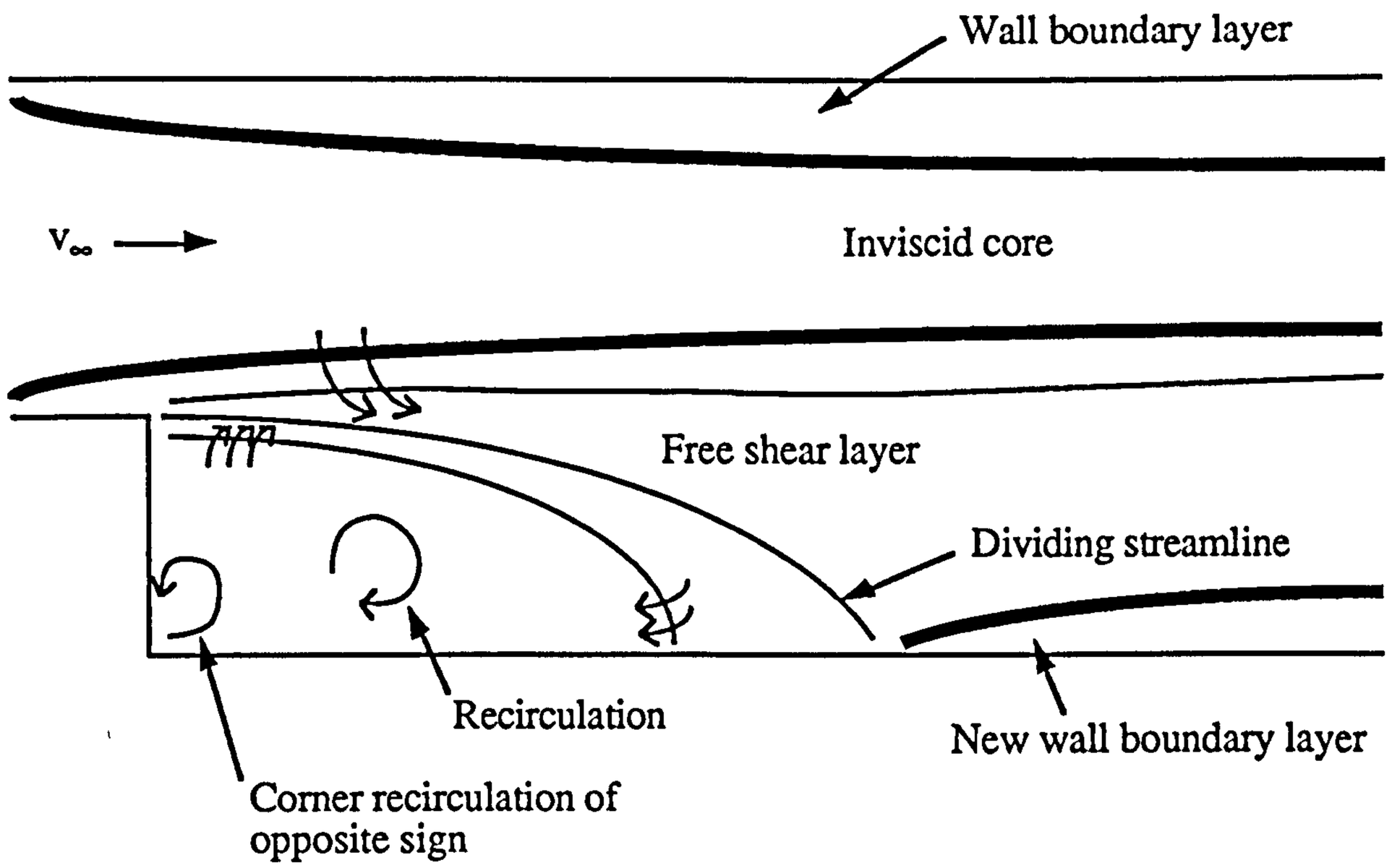

Figure 6.14. Key features of flow over a backward facing step, after Kim (1978).

Only a small part of the separation bubble was seen to be steady, equal to about one step height, halfway along the length of the bubble. Most of the region was unstable, especially near reattachment, where the recirculation length was seen to vary continuously about a mean value as $x_r = (7\pm1)h$, where h is the height of the step. The large unsteady fluctuations near reattachment suggested that large eddies in the approaching shear layer moved alternately back and forth, causing the instantaneous reattachment point to move around within the fluctuating band, rather than splitting in two at the reattachment zone. Furthermore, the instantaneous value of x_r did not correspond to a straight line across the span of the test section, although it was a straight line in the mean. Kim tentatively suggested a three-dimensional spanwise structure to the flow near reattachment but did not investigate this feature closely.

For a number of ratios of step height to duct width, Kim found the general flow characteristics to be both invariant and largely independent of Reynolds number, stating that $x_r = (7\pm1)h$ was universally valid, provided that flow was either turbulent at the point of separation or that the transition to turbulent flow occurred close to that point. Kim favoured the term 'reattachment zone' rather than 'reattachment point', suggesting that entrainment in the mixing layer did not occur at an uniform rate but rather fluctuated as x_r

seemed directly related to entrainment rate: as entrainment rose, x_r became shorter (hence for laminar flow, x_r would be significantly longer than for turbulent flow).

The fluid inside the recirculation is rather unsteady and turbulent. Fluid entrained in the recirculation zone then carries turbulent energy into the adjacent mixing layer and so the shear stress in the separated shear layer is higher than for a plane mixing layer.

The static pressure decreases beyond the step to a point $x/h = 4$, then rapidly increases throught the reattachment zone, with the final pressure depending upon the boundary geometry. The pressure decrease near the step before its rising through the reattachment zone is consistent with the observation of reseparation of the reversed flow, remembering that an adverse pressure gradient is necessary for flow separation.

In the region beyond reattachment, where the pressure rises, the velocity profile becomes flatter. As there is less momentum flux for a given mass flux, then the pressure must rise to balance the momentum loss, assuming that τ_0 is not significant in this region.

Within the separation bubble, the reversed velocities are seen to be 10-20% of the freestream value, with a maximum value of 25% of v_∞ and a sharp velocity gradient near the surface. After reattachment, the velocity profile tends to that of an ordinary turbulent boundary layer. However, whilst the inner part of the flow adjusts quickly , the outer portion of the new boundary layer develops less quickly; at $x/h = 16$, the profile below $y/\delta \leq 0.05$, where $v/v_\infty = 0.65$, is the same as the boundary layer before separation but the balance of the boundary layer has a wake-like form. Kim suggested that the outer boundary layer here was more strongly influenced by large turbulent eddies having longer life than the small eddies near the surface. As these large eddies carry 'memory' of the free shear layer, the outer zone of the new boundary layer takes longer to attain the structure of an ordinary boundary layer. The profile of the middle of the boundary layer deviates below the 'universal' wall law, unlike that of the 'no-step' wall which follows the log-law.

Kim observed that scaling by v^* on the 'step-side' wall was inappropriate as the velocity profile only adjusted rapidly to changes in v^*, such as those at reattachment, close to the wall. The mixing length after reattachment was also larger than expected - as part of the separated shear layer (having a larger value of mixing length than usual near a solid boundary) is brought close to the surface through reattachment, the turbulent length scale can be very large close to the surface, decreasing rapidly to zero at the surface, leading to a low velocity gradient near the surface and hence the dip in the velocity profile below the log-law. This deficit is not seen immediately downstream of reattachment but

develops later; coupled with a value of v^* close to zero in the region, then scaling by v^* is poor, with no overlap layer being observed in the developing boundary layer.

Finally, Kim noted that whilst the common law of the wall did not describe the flow adequately, that a version of Coles' law adapted for flow reversal provided a good description of the boundary layer, except in the immediate vicinity of the step.

6.3.2. Backward Facing Step Results for the Standard FIDAP Model of Haroutunian and Engelman (1991).

The geometry of the backward facing step was shown in Figure 4.2 and the resulting computational mesh is given as Figure 6.15 below.

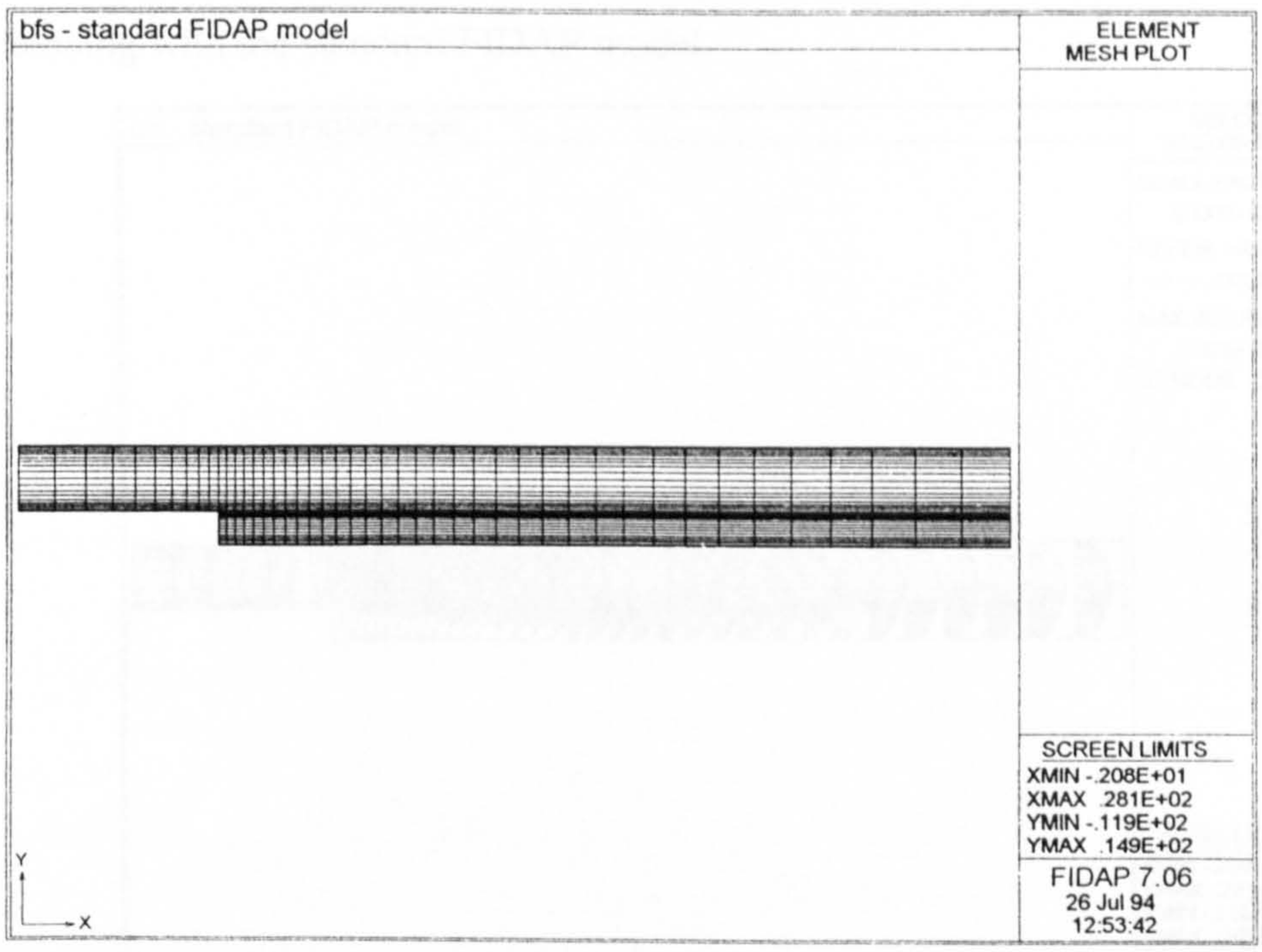

Figure 6.15. The computational mesh used for modelling the backward facing step.

The mesh is graded to provide finer meshing in the near-wall region and is a modified form of the original mesh provided as a FIDAP example. The original mesh gave $y^+ \leq 5$ along most of the walls in the Coles' law solution and hence the boundary velocity was solved by equation 5.21, setting $u^+ = y^+$, rather than using Coles' law. In order to force the widespread solution of Coles' law along the Coles' lines, the original mesh was coarsened slightly to increase the calculated value of y^+. This mesh was then

used for all modelling conducted in order to provide compatibility of results.

The original FIDAP example was run using the successive substitution solver but in wanting to access pressure information at the element integration points, the segregated solver had to be used for the enhanced Coles' law model in order to provide pressure as a degree of freedom in the solution procedure. Again desiring compatibility, where possible, between the different models, it was decided to use the segregated solver in each case. To see whether this would affect the quality of results, the standard FIDAP model was run with both solvers and the results compared; as no discernible difference was noted, then the segregated solver was used for all subsequent models.

Uniform distributions at inlet were specified as $v_x = 1m/s$, $v_y = 0m/s$, $k = 0.003$ and $\varepsilon = 0.00364$, hence giving a nominal Reynolds number of $Re = 45000$, corresponding to the value of Reynolds number at which the practical experiments of Kim (1978) were conducted. The basic modelling results will now be viewed in turn, commencing with the standard FIDAP model.

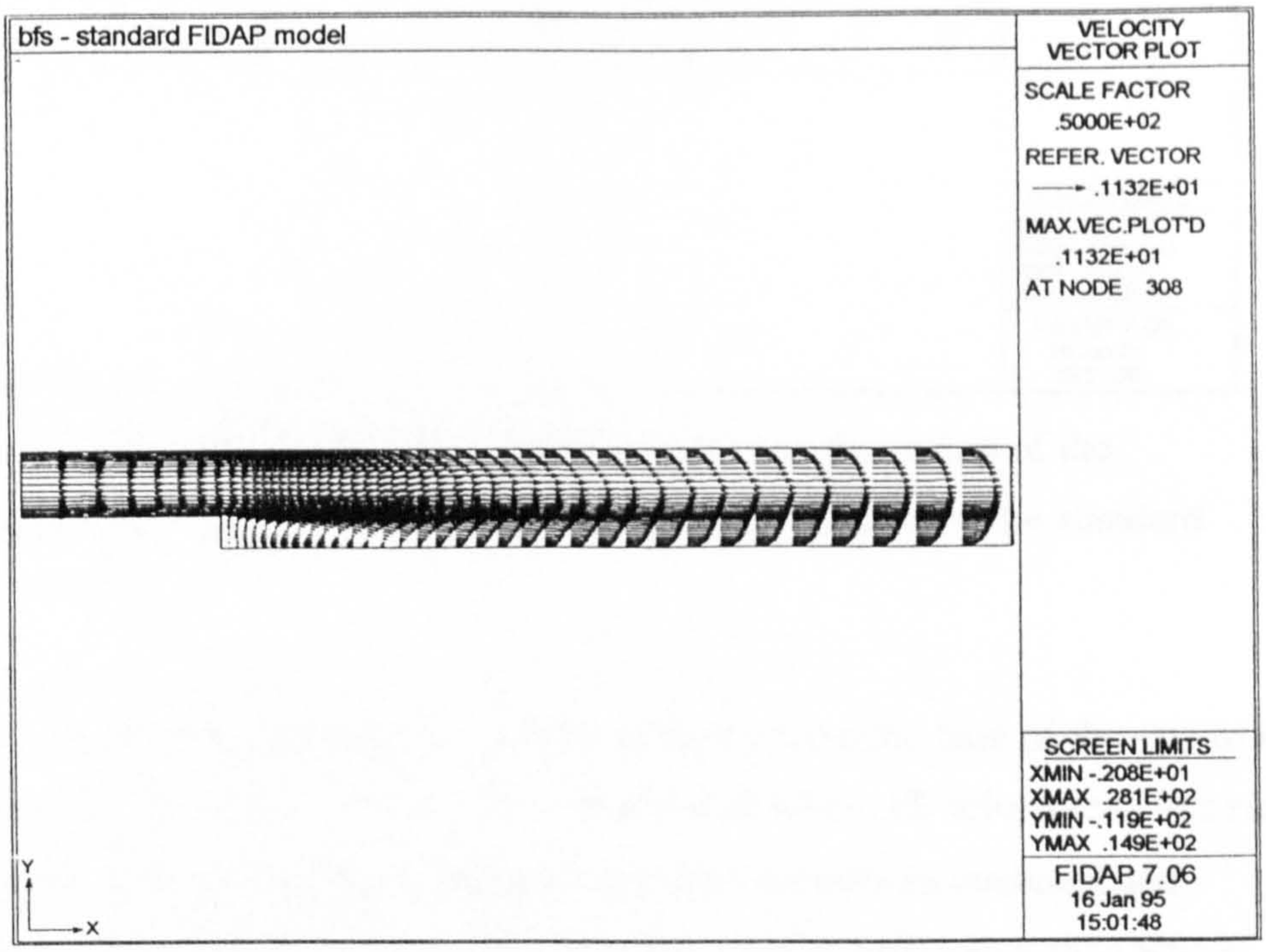

Figure 6.16. A velocity vector distribution for flow over the backward facing step, predicted by the standard FIDAP model.

Inspecting the above figure, the general flow features observed by Kim are seen; the flow possesses an inviscid, tapering core downstream of inlet, with a separation bubble forming behind the step face. Between the inviscid core and the separation bubble, there

exists a free shear layer which springs off the apex of the step. A turbulent boundary layer is seen to develop along the top surface of the duct, with a slight boundary layer beginning to develop on the front lower reach of the duct after reattachment. At outlet, the flow is not seen to be fully developed. The nature of the separation bubble is seen more clearly in Figure 6.17 below.

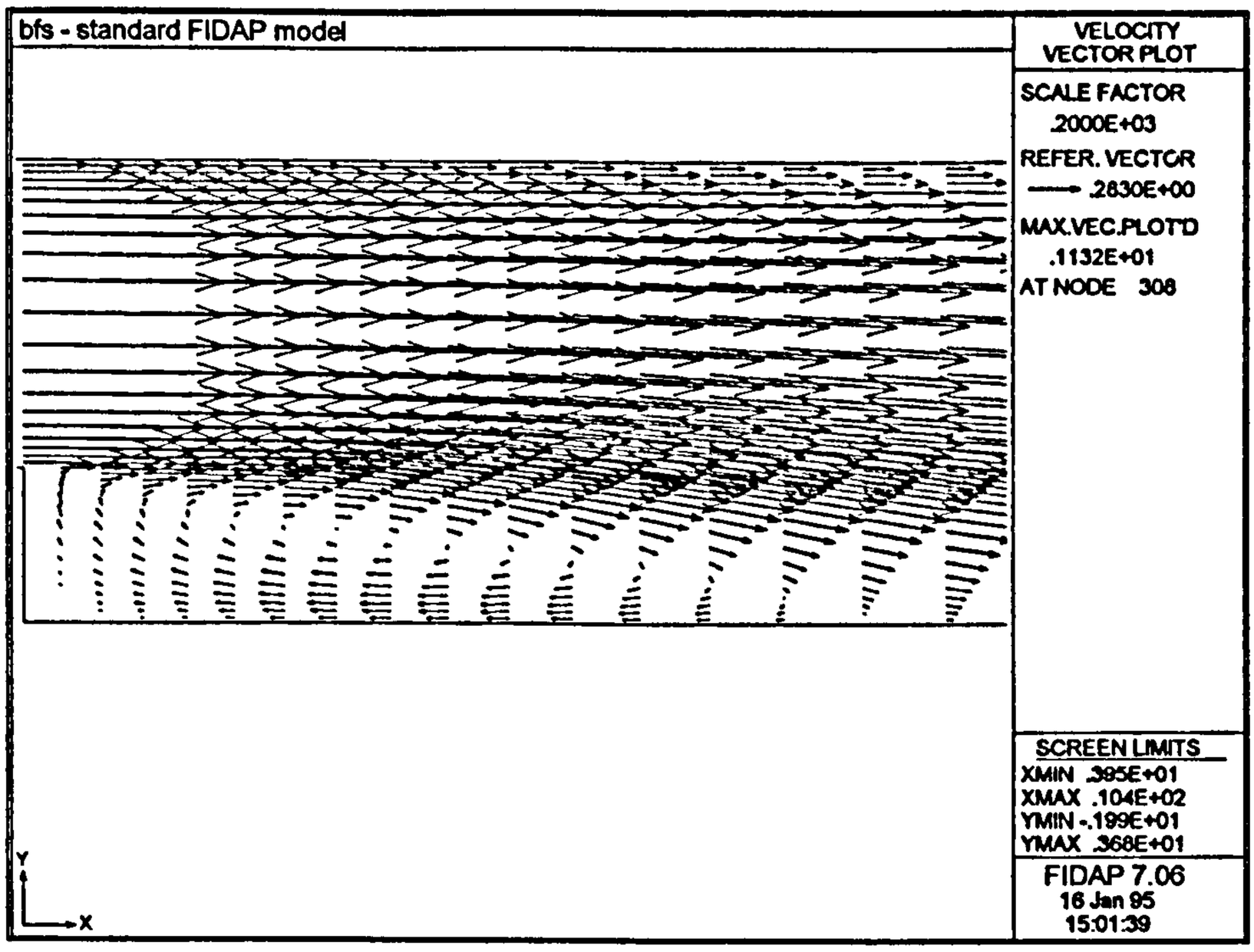

Figure 6.17. A magnified view of velocity vectors in the region of the separation bubble of the backward facing step, as predicted by the standard FIDAP model.

Taking the recirculation length, x_r, as the distance from the base of the step to that mesh cross-section normal to the front lower reach wall where all velocity vectors run in the same direction as those in the freestream core, then the non-dimensionalised recirculation length is $x_r = 5.4$. Note that this value is some 23% lower than Kim's observations but is in keeping with the general tendency of k-ε turbulence models to underestimate x_r (Rodi, 1991). The velocity immediately adjacent to the wall is low in comparison with that in the subsequent two or three elemental layers running parallel to the lower front reach wall. Midway along the base of the separation bubble then, between the wall and the centre of the bubble there is the semblance of a developing velocity profile, which is not noted between the centre of the bubble and the free shear layer that

lies above it. As the reversed flow approaches the step face, the flow turns upwards towards the apex of the step, close to which it turns abruptly to run beneath the free shear layer. As such, the velocities observed at the base of the step are very small in comparison with those elsewhere in the separation bubble. Furthermore, no secondary separation of the flow is seen at the base of the step, thus showing a marked deviation in results from those of Kim.

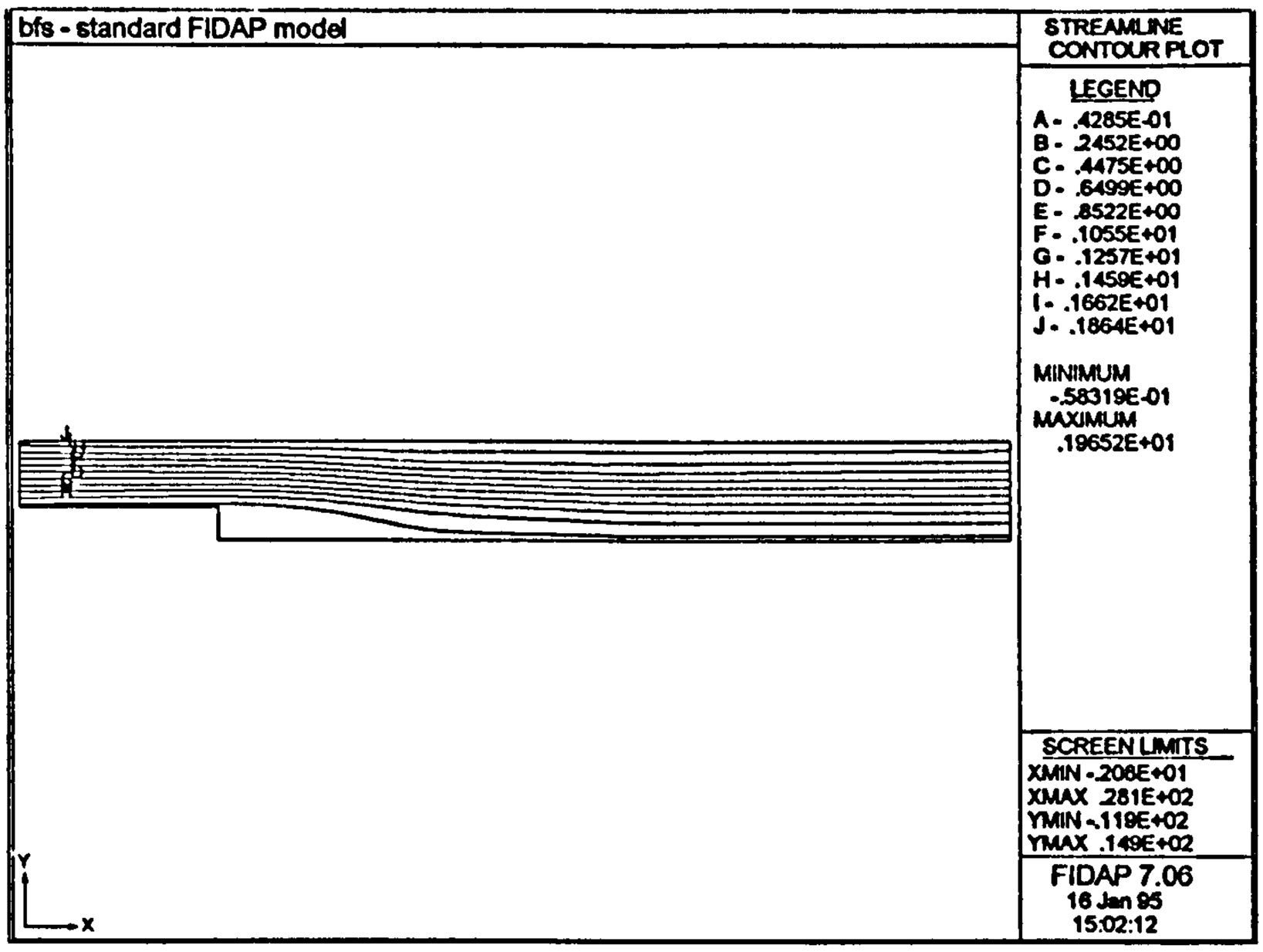

Figure 6.18. A streamline distribution for flow over the backward facing step, predicted by the standard FIDAP example.

The streamline distribution, taken from the standard FIDAP example, reaffirms the location of the separation bubble behind the step whilst showing that no reseparation of the reversed flow occurs at the base of the step.

6.3.3. Backward Facing Step Results Arising from the Simple Coles' Law Model.

The simple Coles' law model will be inspected now, firstly by observing the general velocity vector distribution throughout the duct.

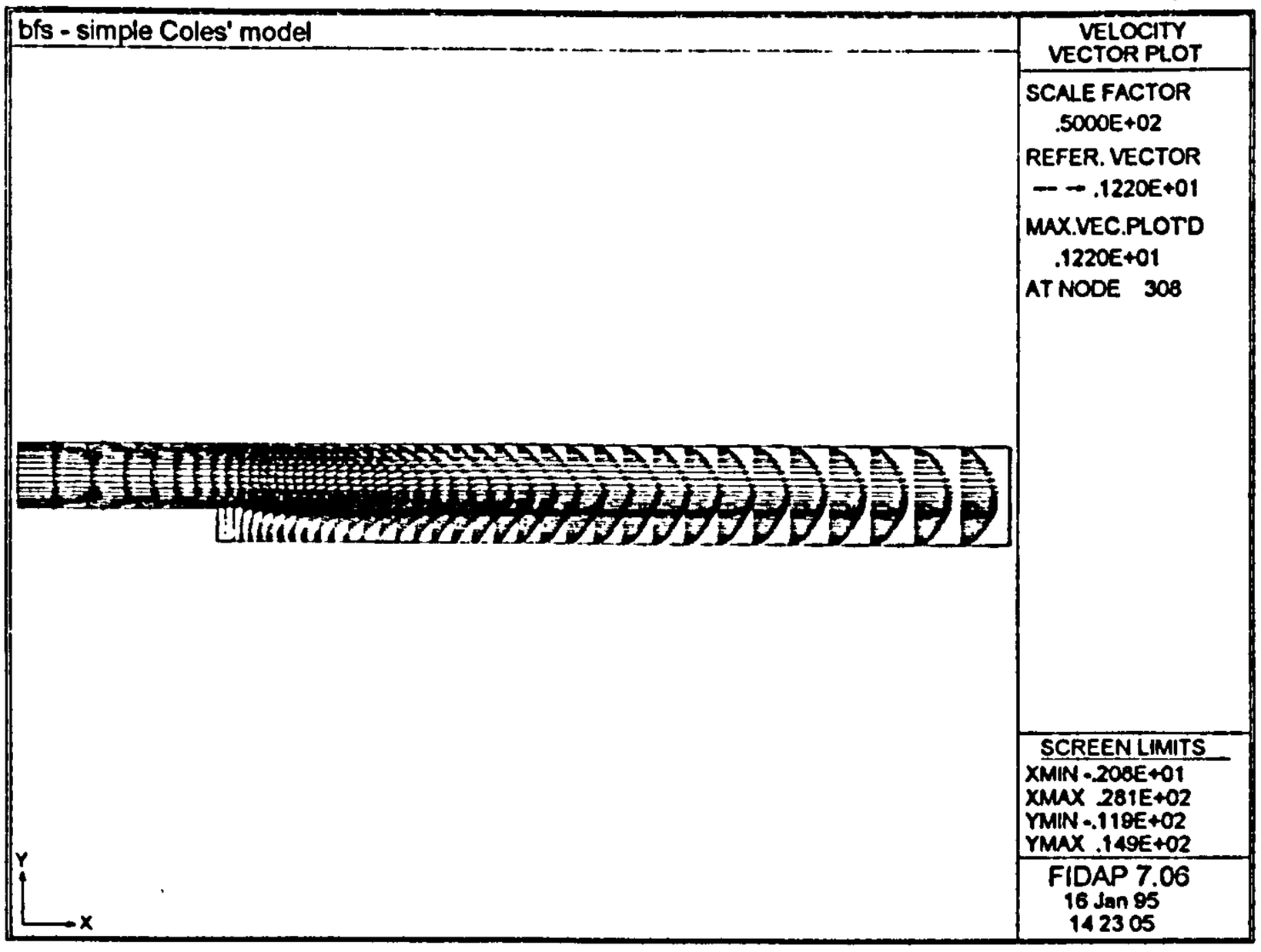

Figure 6.19. Velocity vector distribution over the backward facing step, as predicted by the simple Coles' law model.

The general velocity distribution arising from the simple Coles' law model is very similar to that of Figure 6.16, for the standard FIDAP model. Along the back upper reach and top walls, however, the resultant velocity along the Coles' line is seen to have alternately positive and negative y components at successive nodes, suggesting some form of numerical oscillation in the solution, remembering that along the Coles' lines, whilst the tangential velocity component was evaluated by Coles' law, the normal velocity component was set by the general FIDAP model. As with Figure 6.16, the boundary layer along the top wall appears to thicken temporarily in the region corresponding to the reattachment zone on the front lower reach wall. Again the flow at outlet is not fully developed but shows skewing towards the free shear layer. The boundary layers in general also seem somewhat thicker than for the standard FIDAP model.

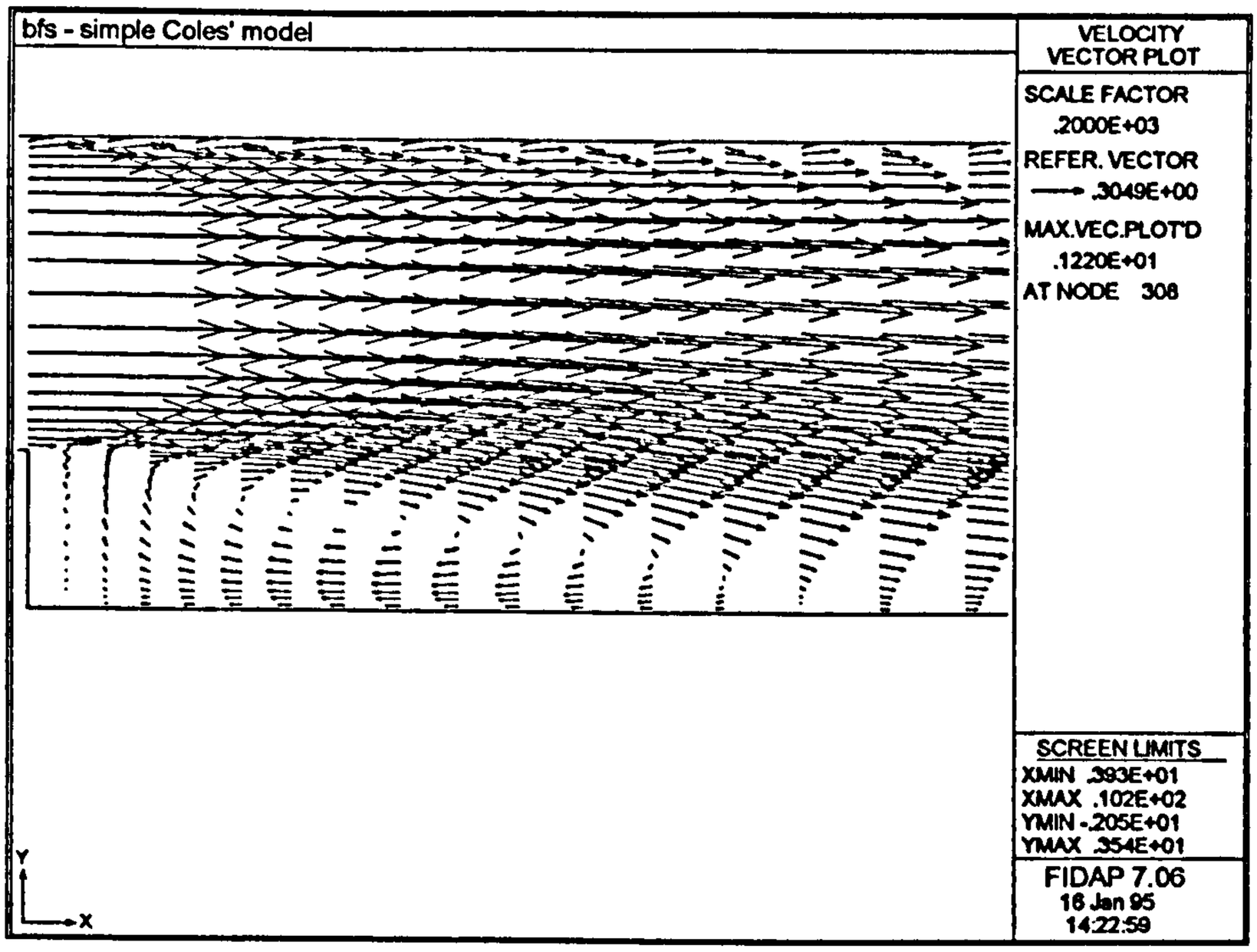

Figure 6.20. A magnified view of velocity vectors in the region of the separation bubble of the backward facing step, predicted by the simple Coles' law model.

The simple Coles' law model predicts $x_r = 5.5$, slightly in excess of the standard FIDAP model. The velocity beneath the separation bubble is lower than for the standard case, as is also true along the step face. Note the oscillation in the direction of the resultant velocity along the step face, as is also shown clearly along the top wall. Again the velocity profile at the mid-section of the separation bubble shows increasing velocity away from the front lower reach wall although at a more gradual rate. Once more, the presence of reseparation of the reversed flow is not predicted at the base of the step.

6.3.4. Basic Results for the Backward Facing Step, as Predicted by the Enhanced Coles' Law Model.

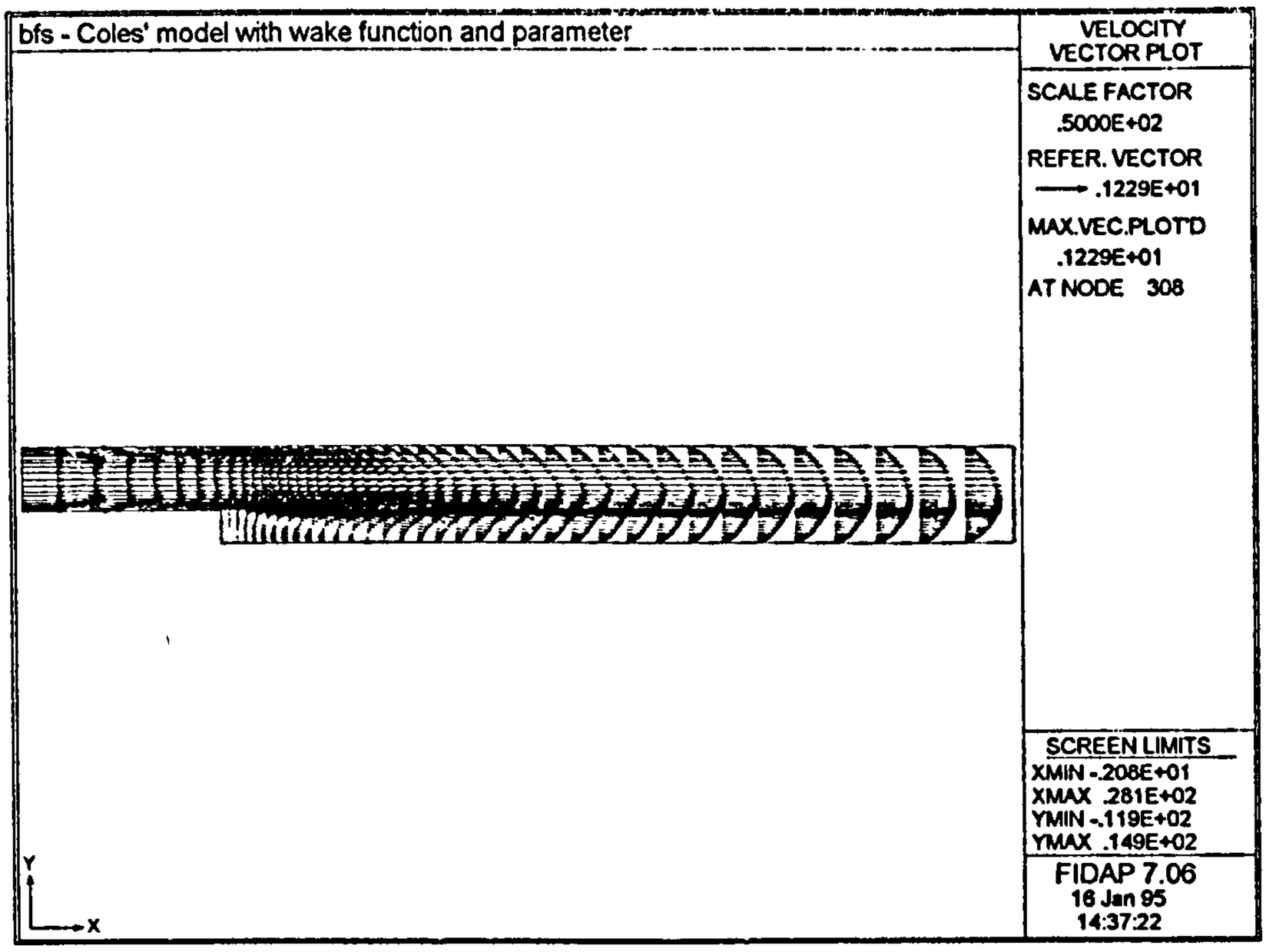

Figure 6.21. Velocity distribution over the backward facing step, predicted by the enhanced Coles' law model.

The velocity distribution for the enhanced Coles' law model bears great resemblance to that for the simple Coles' law model of Figure 6.19, showing all the general flow features of the standard model as Figure 6.16. However, the outlet velocity profile is less developed than for the simple model, showing increased skewing towards the free shear layer. Also, the oscillation in the y-component of the resultant velocities along the back upper reach and top walls is again observed.

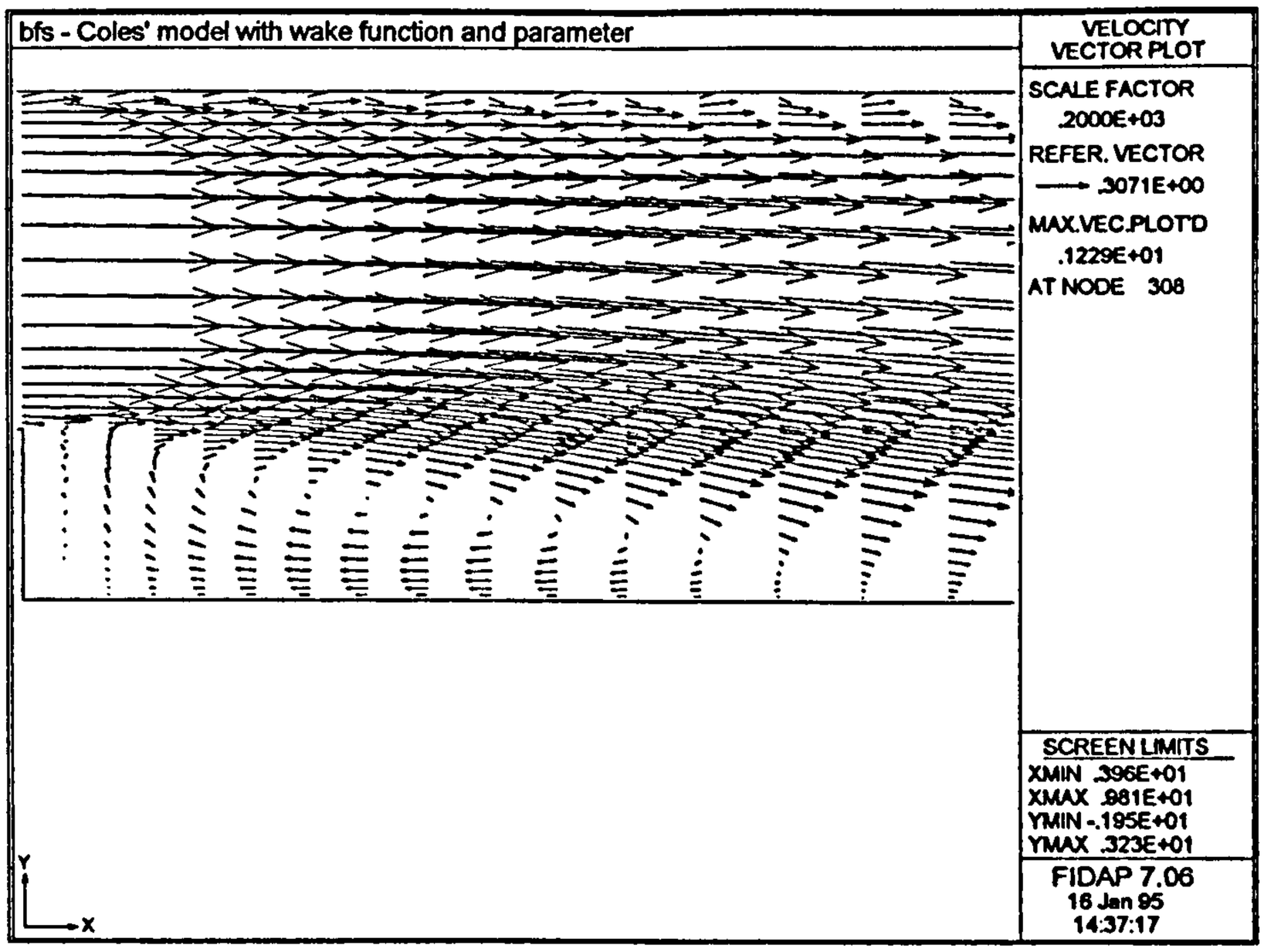

Figure 6.22. A magnified view of velocity vectors in the region of the separation bubble of the backward facing step, predicted by the enhanced Coles' law model.

The enhanced Coles' law model predicts $x_r = 5.4$, identical to the standard FIDAP model. As with the simple Coles' law model, the direction of the velocity up the step face is seen to oscillate to and fro. In that the distribution and magnitude of streamlines for the two Coles' law models are so similar to that shown in Figure 6.18, they will not be presented here.

6.3.5. Comparison of Results from the Standard FIDAP and the Simple and Enhanced Coles' Law Models.

The velocities predicted by the Coles' law models along the Coles' lines may now be considered and compared with those of the standard model at corresponding stations. Interest here is concentrated on the response along the front lower reach, where the reattachment zone exists. The following three figures detail the velocities predicted adjacent to the front lower reach.

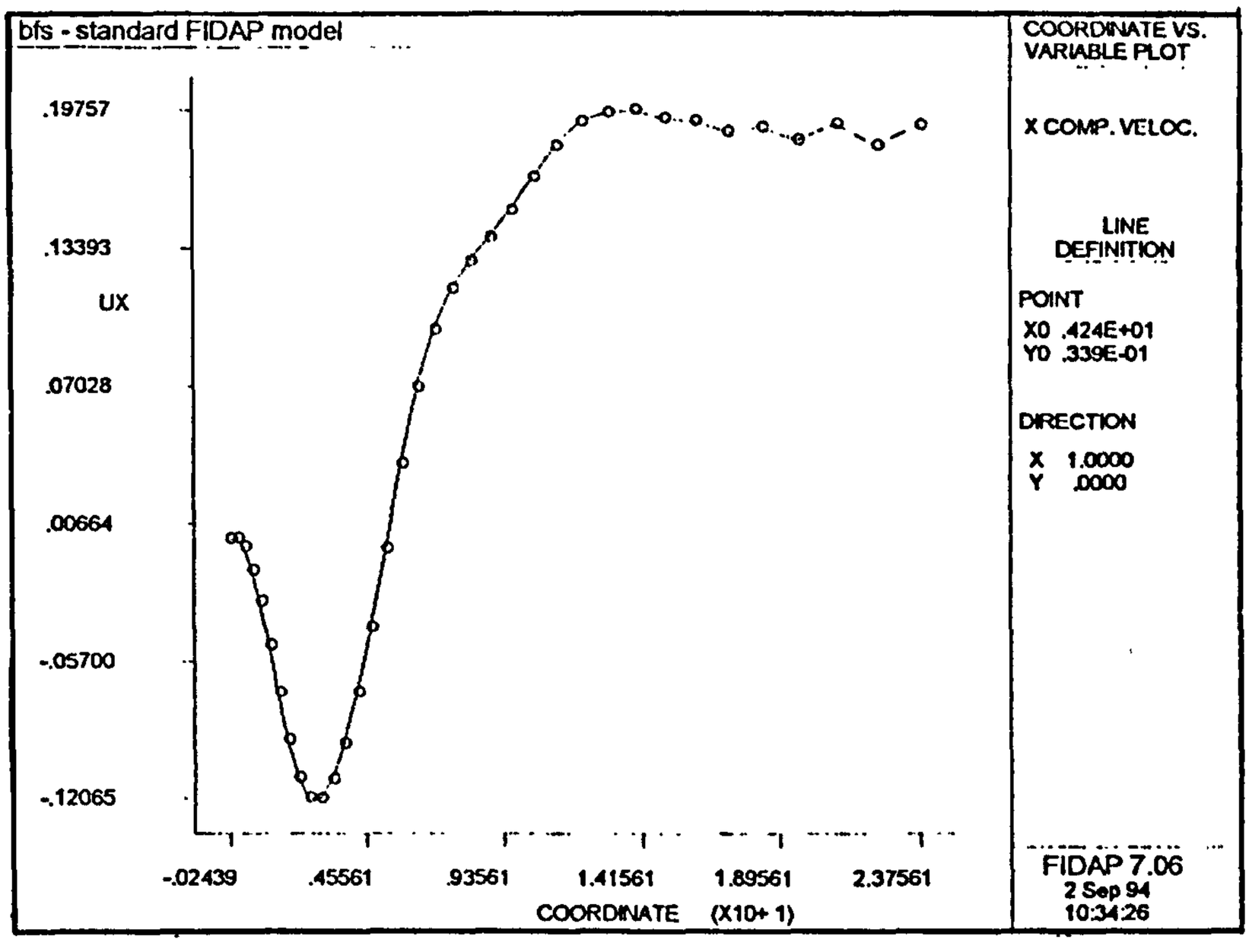

Figure 6.23. The x-component of velocity along the front lower reach, predicted by the standard FIDAP model.

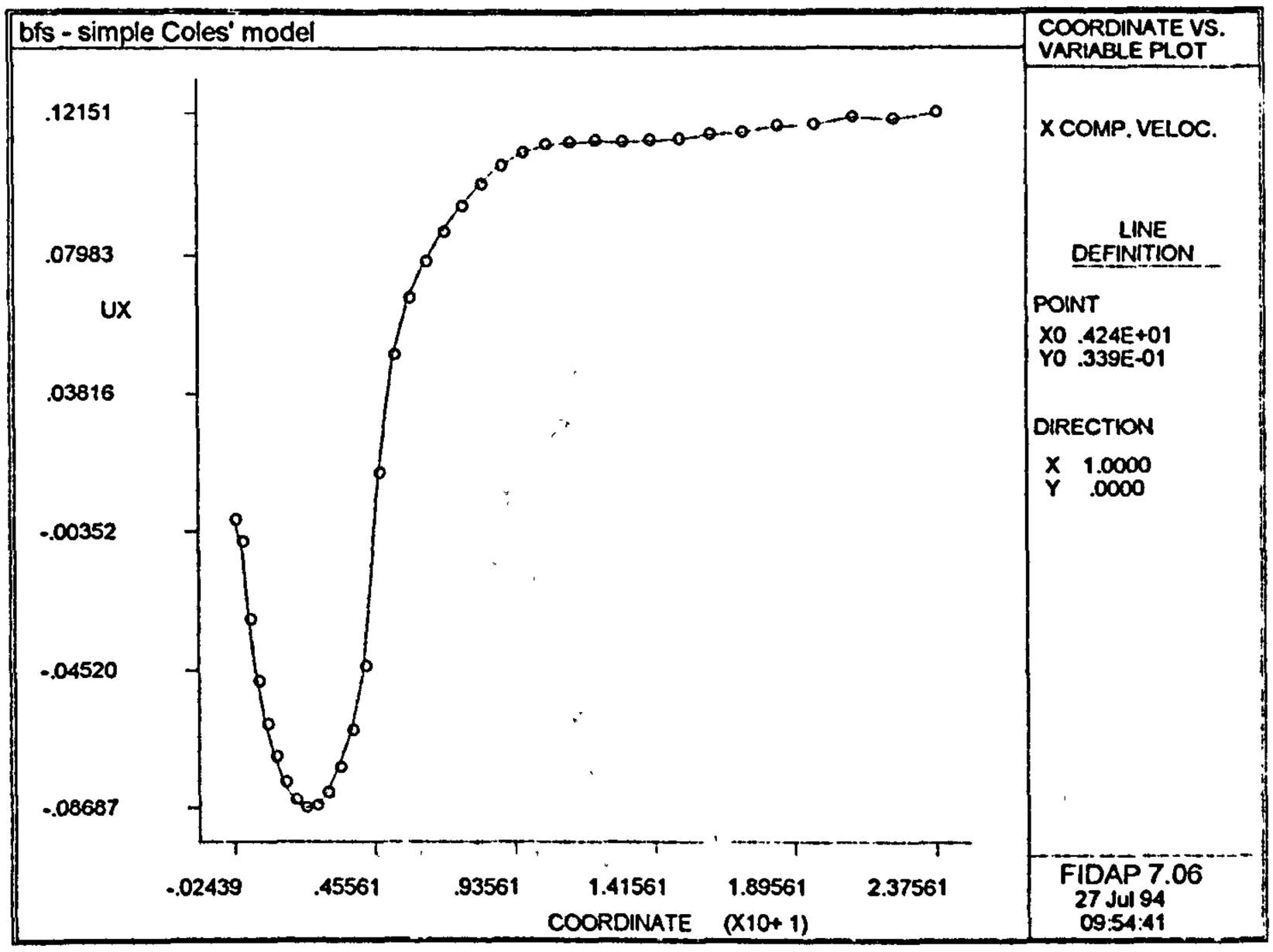

Figure 6.24. The x-component of velocity along the front lower reach, predicted by the simple Coles' law model.

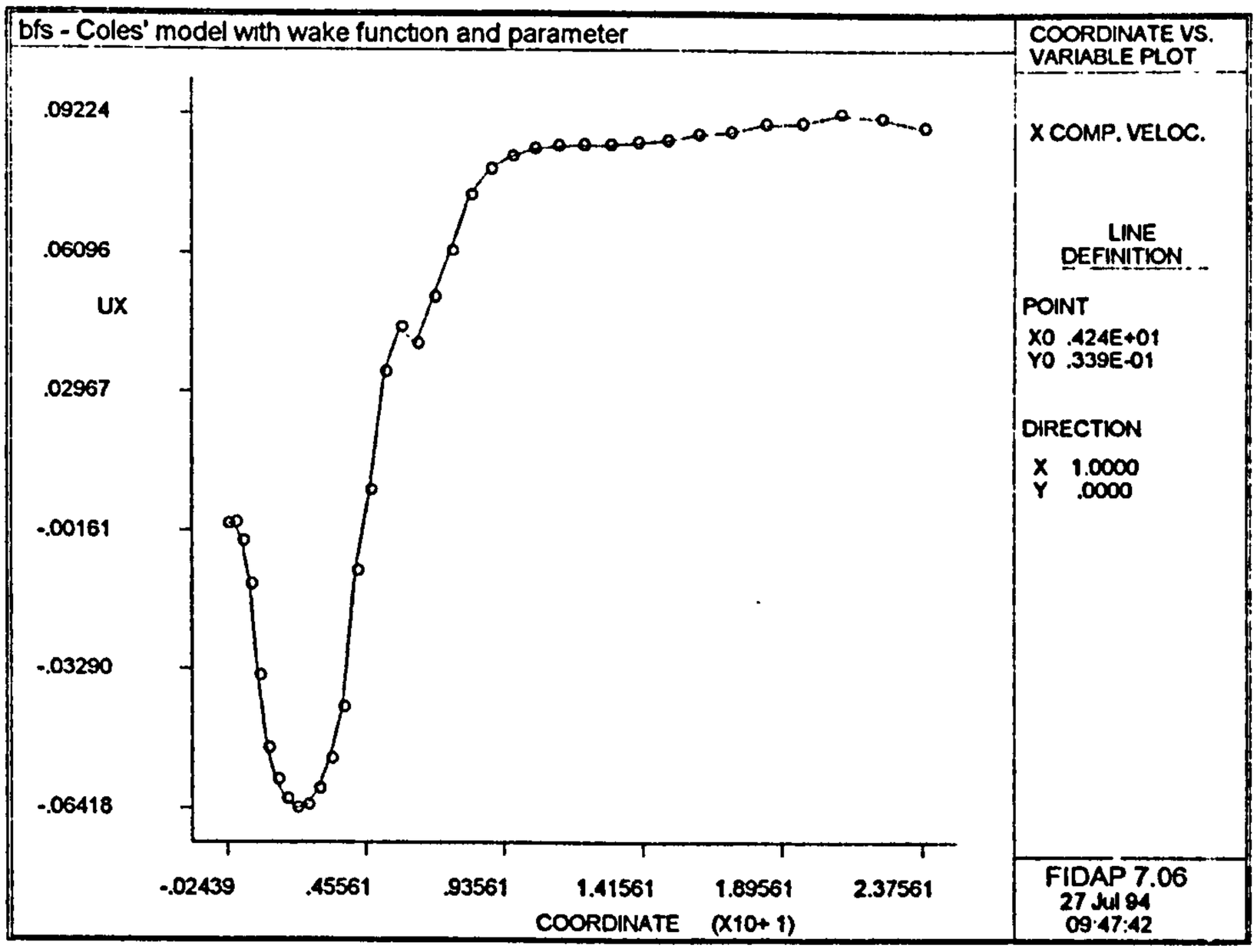

Figure 6.25. The x-component of velocity along the front lower reach, predicted by the enhanced Coles' law model.

In each case, the form of the velocity distribution along the front lower reach is similar; the negative velocity up to x ≈ 5m beyond the base of the step corresponds to the region of reversed flow, with the maximum reversed velocity occuring at the midpoint of the separation bubble. There is a rapid rise in velocity across the reattachment zone, leading to an approximately constant velocity downstream towards the duct exit.

For the standard FIDAP model, Figure 6.23, the maximum reversed velocity on the Coles' line is about 12% of the freestream velocity and so from Figure 6.17, the maximum reversed velocity in the separation bubble as a whole is roughly 25% v_∞, corresponding to Kim's findings.

For the simple Coles' law model, the reported velocities are lower, amounting to 8% v_∞ at the midpoint of the separation bubble and hence 33% lower than the standard model. At the duct outlet, the velocity is 36% lower than the standard FIDAP model.

As already intimated, the velocities returned by the enhanced Coles' law model are lower still - the maximum reversed velocity on the Coles' line is only 6% v_∞, with the velocity at exit to the duct being 52% less than for the standard FIDAP model.

Having observed that both Coles' law models return lower velocities as boundary conditions to the fluid continuum in comparison with the standard FIDAP model, then the

principal equations of each model may be reviewed to determine the possible reasons for this deficit.

For the standard FIDAP model of Haroutunian and Engelman (1991), the velocity at the outer edge of the special wall elements is evaluated by Reichardt's law (equation 2.29) as

$$v = v^*\left\{\frac{1}{\kappa}\ln(1 + 0.4y^+) + 7.8\left[1 - \exp\left(-\frac{y^+}{11}\right) - \frac{y^+}{11}(-0.33y^+)\right]\right\}$$

and for the simple Coles' law model, the velocity on the Coles' line is equation 6.1 as

$$v = v^*\left\{\frac{\ln y^+}{\kappa} + B + \frac{2\Pi}{\kappa}\right\}$$

whereas the enhanced Coles' law model, in accounting for boundary layer thickness and pressure gradient effects more fully, is seen as

$$v = v^*\left\{\frac{\ln y^+}{\kappa} + B + \frac{2\Pi}{\kappa}\, w\left(\frac{y}{\delta}\right)\right\} \qquad (6.2)$$

$$\text{with} \quad w\left(\frac{y}{\delta}\right) = 3\eta^2 - 2\eta^3 \quad : \quad \eta = \frac{y}{\delta} \qquad (2.46)$$

Notionally, an expression of Coles' law would be expected to predict higher velocity than Reichardt's law in those instances where there was a local pressure gradient. As Reichardt's law is an experimental fit to Prandtl's law of the wall (equation 2.24) expressed in inner variables, then it does not account for the local pressure gradient. Having shown that contrary to expectations, the Coles' law models predict lower velocities, then upon inspection of the above equations, it is again necessary to consider the behaviour of the wall friction velocity, v^*. In each of the principal equations, v^* acts to multiply the whole right hand side of the equations shown.

From the investigation of the behaviour of the simple Coles' law model as applied to the U-bend, it is known that the term Π will be essentially constant and further that the assumption that w equals unity is an overestimate of the effect of boundary layer thickness. Laying aside, at present, any thought of the variation in Π for the enhanced Coles' law model, then the function w in equation 6.2, as evaluated by equation 2.46, is likely to be less than unity, hence giving the third right hand term of the Coles' law model

a lower value in the enhanced case, remembering that the enhanced model gave lower velocities than the simple model. However, before considering the trade off between Π and w for the two Coles' law models, the principal variables v^* and y^+ should first be inspected.

From equation 5.14, v^* was shown to be proportional to the root of the shear stress at the wall and for y^+, in the instance of the Coles'-law-type models, to be directly proportional to v^*. The tangential stress along the front lower reach boundary may then be used to study v^*.

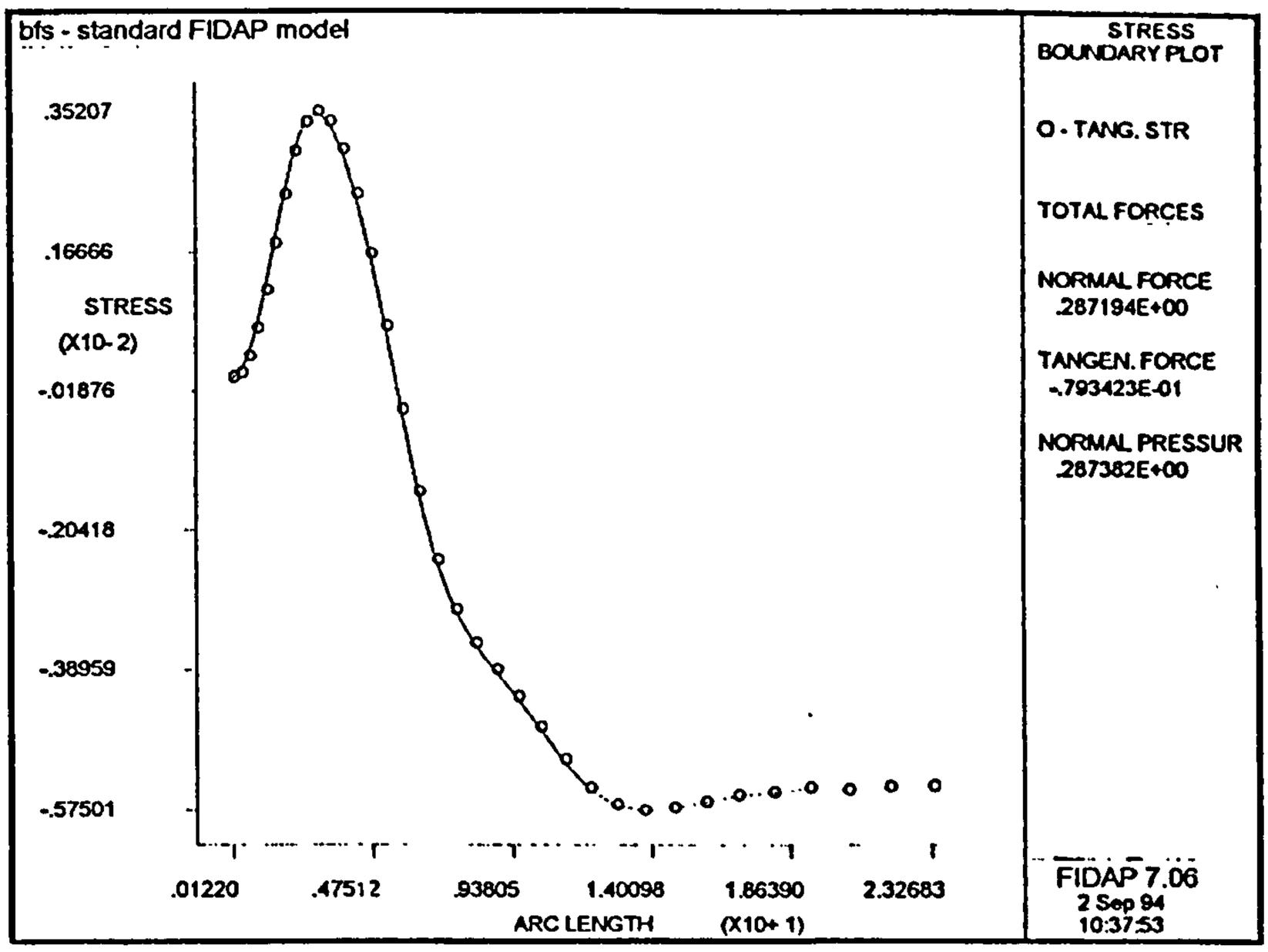

Figure 6.26. The boundary stress disribution along the front lower reach of the backward facing step, predicted by the standard FIDAP model.

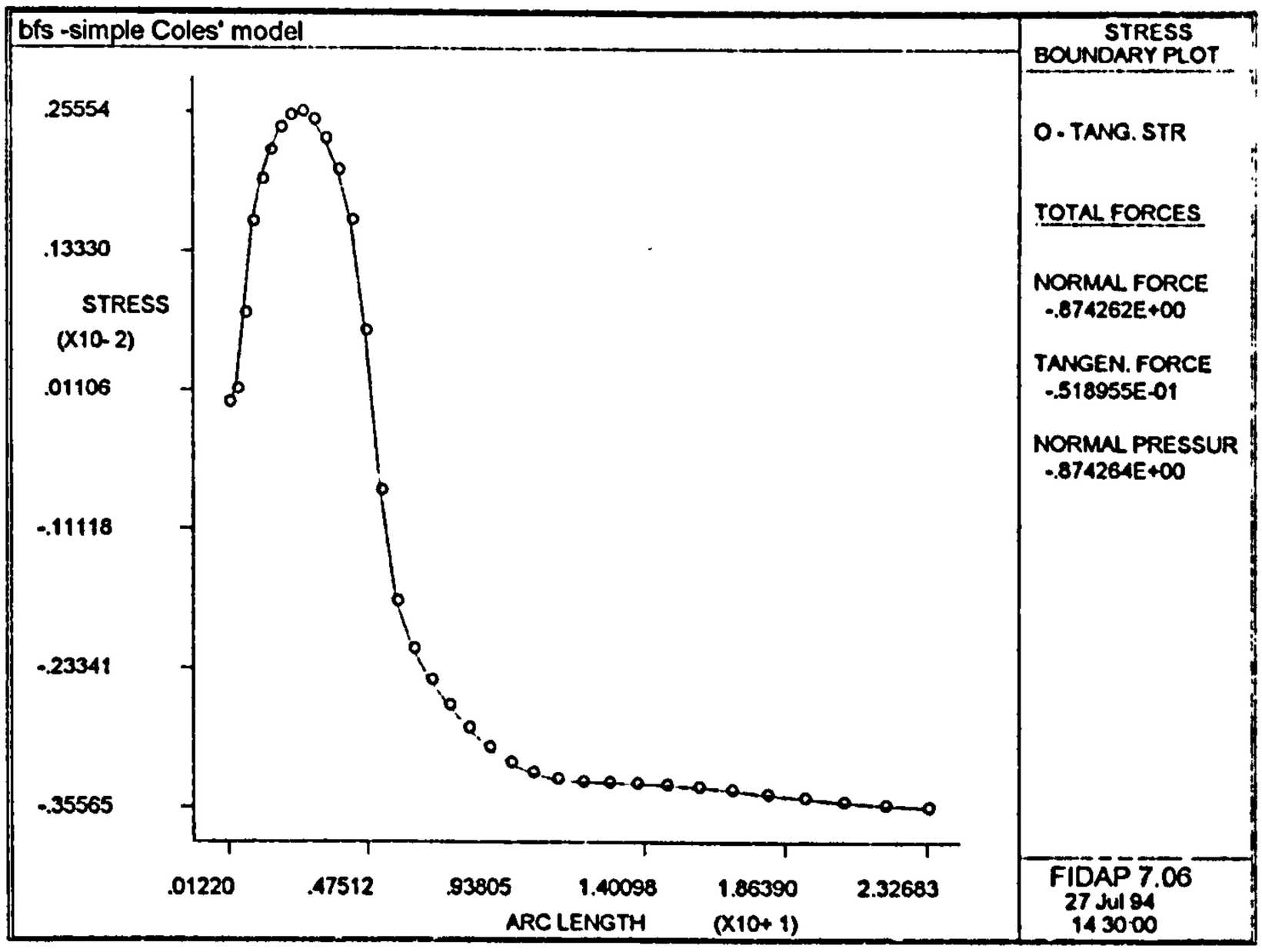

Figure 6.27. The boundary stress disribution along the front lower reach of the bacward facing step, predicted by the simple Coles' law model.

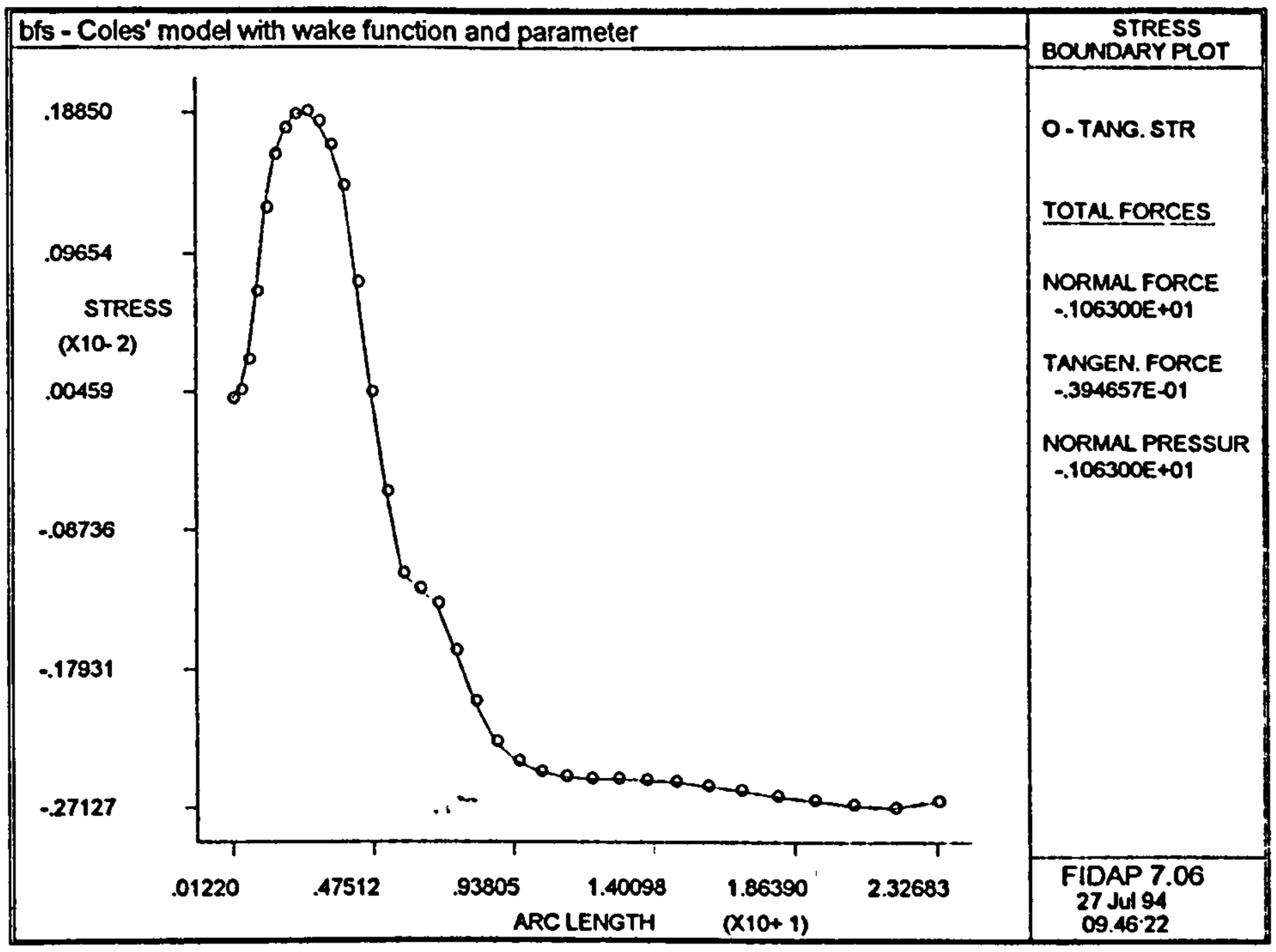

Figure 6.28. The boundary stress distribution along the front lower reach of the backward facing step, predicted by the enhanced Coles' law model.

The tangential stress distribution of the standard model has similar form, but opposite sign to its corresponding velocity distribution for v_x as Figure 6.23, with the

peak in positive stress coinciding with the maximum reversed velocity at the edge of the separation bubble. The difference in sign between the distributions of the two variables is accounted for by the tangential stress acting to oppose the fluid motion. The similar peak in tangential stress for the simple Coles' law model, as Figure 6.27, is 30% lower than the standard model, which would predict a 55% deficit in v^* from equation 5.14. Likewise, the enhanced Coles' law model of Figure 6.28 shows a maximum tangential stress 45% lower than the standard case, which would yield a 70% deficit in v^*.

Given that v^* is 55% lower for the simple Coles' law model and up to 70% less for the enhanced model compared with the standard case, then the fact that the velocity predictions via Coles' law are between 40-60% lower on average than those of Reichardt's law is only partially accounted for. The other 'main' variable in equations 2.29, 6.1 and 6.2 is y^+, being shown below for the front lower reach of each model in turn.

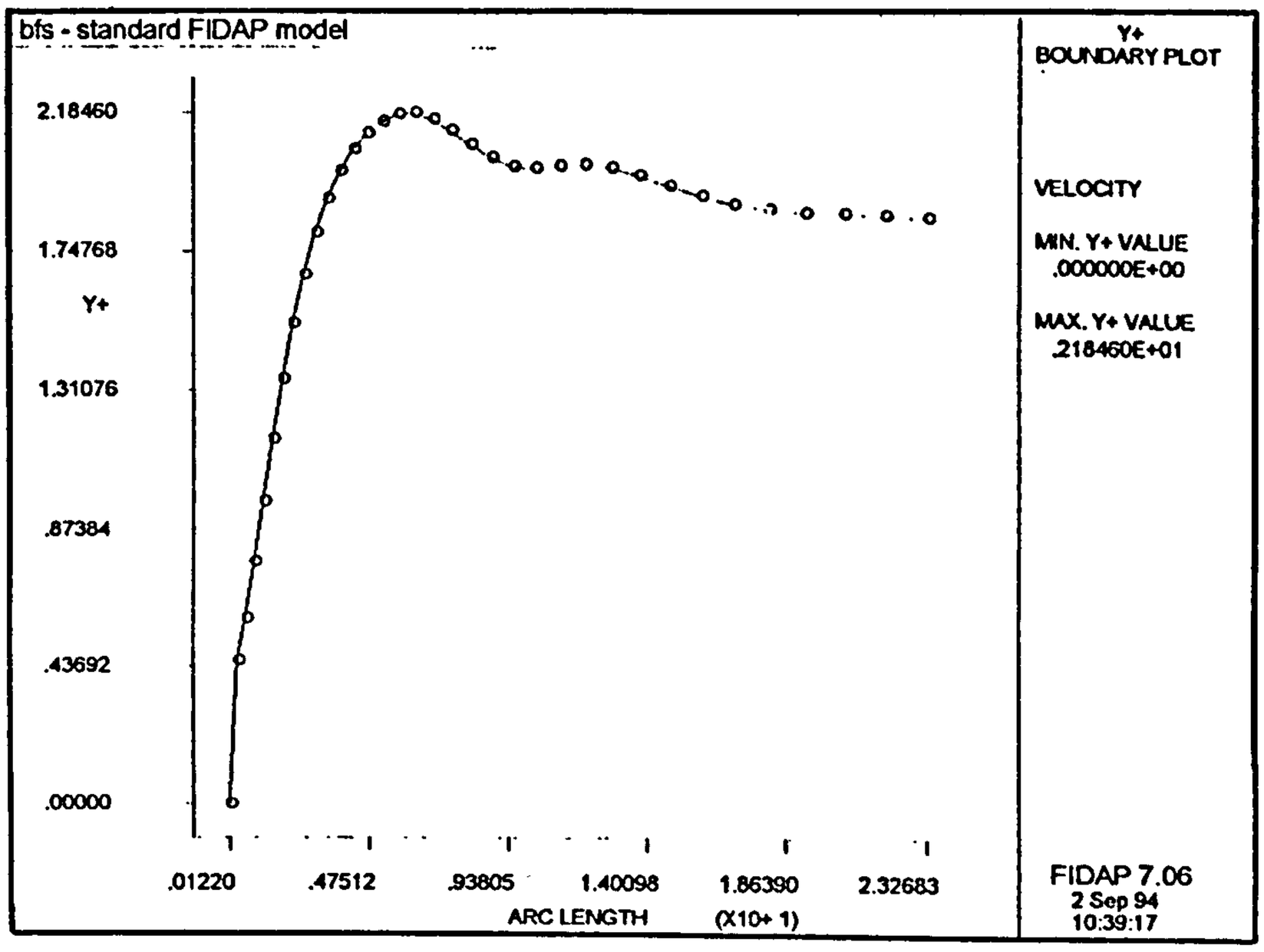

Figure 6.29. The y^+ distribution along the front lower reach of the backward facing step, predicted by the standard FIDAP model.

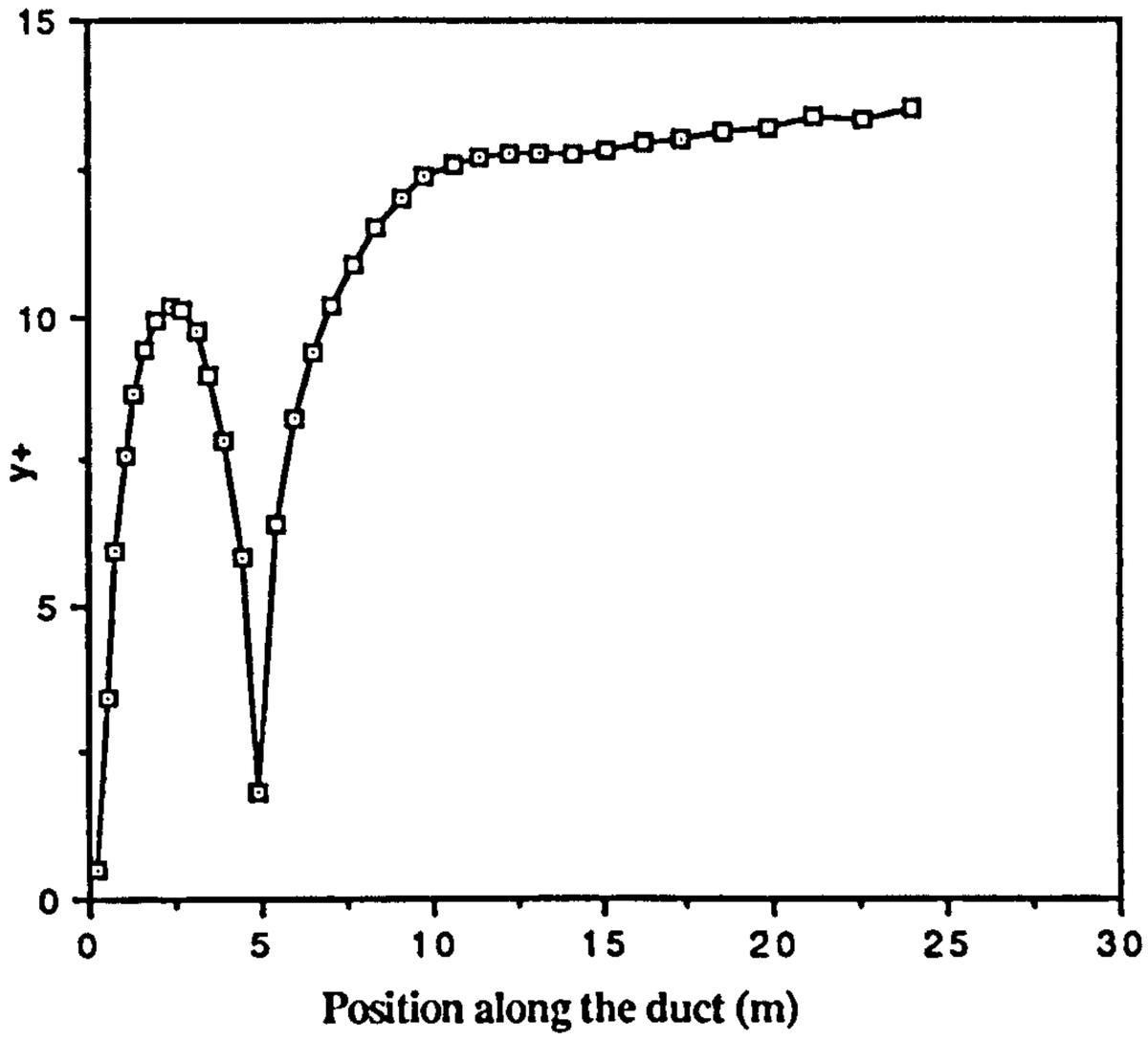

Figure 6.30. The y^+ distribution along the front lower reach of the backward facing step, predicted by the simple Coles' law model.

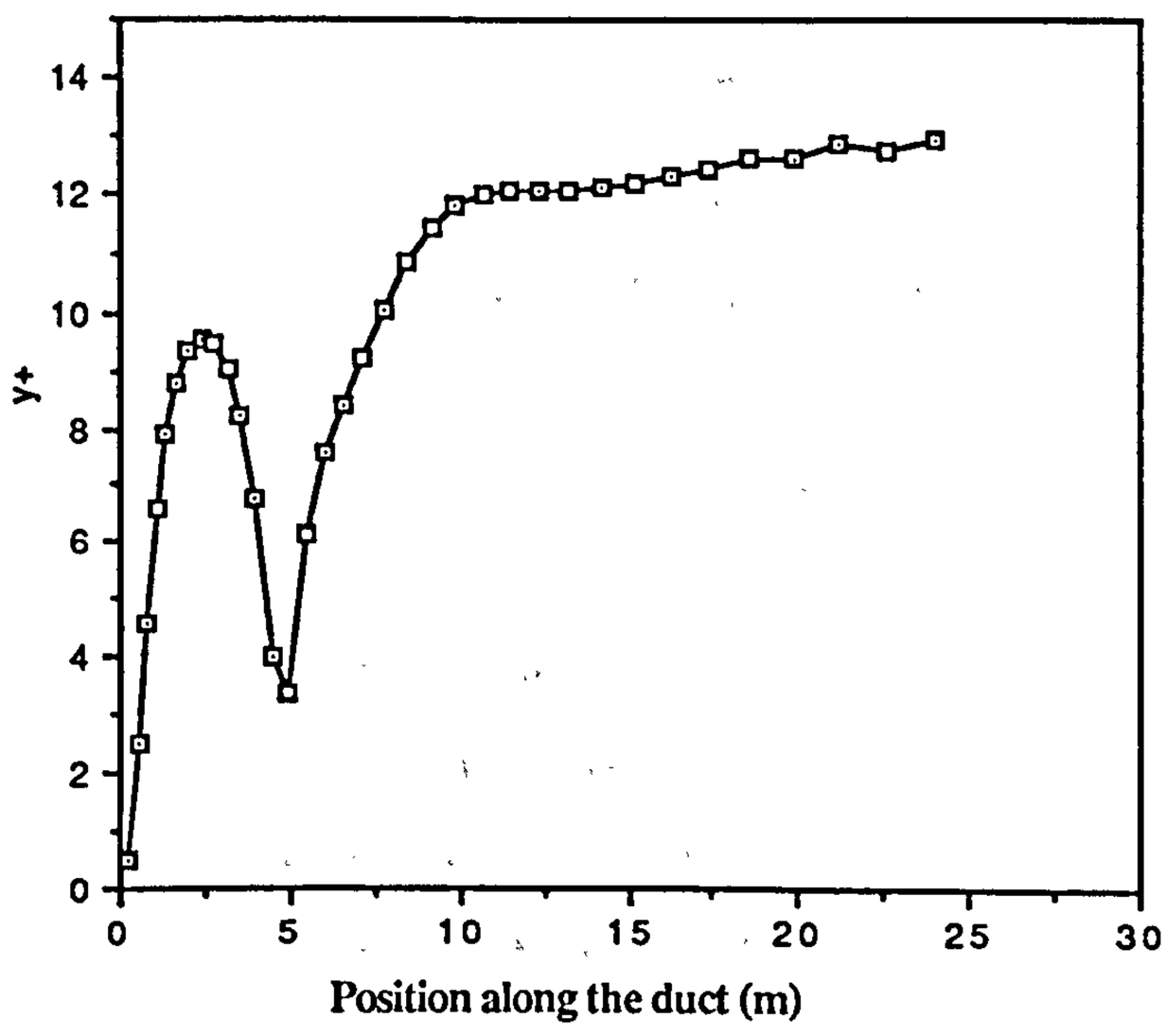

Figure 6.31. The y^+ distribution along the front lower reach of the backward facing step, predicted by the enhanced Coles' law model.

The standard FIDAP model, Figure 6.29, gives values of $y^+ < 5$ along the entire front lower reach wall, suggesting that even with the coarsened mesh, Reichardt's law is

being operated too close to the vicous sub-layer. The y^+ values for the Coles' law models are approximately seven times greater than for the standard model, thus demonstrating that in coarsening the mesh, these models were forced to operate Coles' law across most of the region shown rather than $u^+ = y^+$ where $y^+ \leq 5$, as would have been the case otherwise. Both Coles' law models show a local minimum in y^+ corresponding to the point in the relevant tangential stress distribution where $\tau \approx 0$ at the wall.

The low values of y^+ in comparison with the Coles' law methodology is again attributed to the difference in methods by which y^+ is evaluated. Whilst the Coles' law models take y^+ as a function of v^* and hence relate it to conditions at the wall, the Haroutunian and Engelman model (1991) relates y^+ to the kinetic energy of turbulence at the top of the special wall elements.

In order to see the effect that the low values of v^* coupled with higher y^+ values common to the Coles' law models (in comparison with the method of Haroutunian and Engelman (1991)) has on the predicted velocity, consider the front lower reach.

Taking the point of maximum reversed velocity along the front lower reach Coles' line, then for the standard FIDAP model, $y^+ = 2.2$ from Figure 6.29. Substituting for y^+ into equation 2.29, then $v = 3.97v^*$. For the simple Coles' law model at a similar point, $y^+ = 10$ from Figure 6.30. As with the simple Coles' law model of the U-bend, Π was constant throughout the model as $\Pi = 0.55$ and so from equation 6.1 gain

$$v = v^*\left\{\frac{\ln y^+}{\kappa} + B + \frac{2\Pi}{\kappa}\right\} = v^*\{5.61 + 5.00 + 2.68\} = 13.29v^*$$

To evaluate equation 6.2 in a like fashion for the enhanced Coles' law model, knowledge of both Π and w is required. Appendix A4 lists a range of variables, calculated within the circus subroutine, for the front lower reach Coles' line. From Appendix A4, for the point of maximum reversed velocity along the front lower reach Coles' line, observe $y^+ = 9.5$, $\Pi = 0.13e^{-7}$ and $y = \delta = 0.74e^{-1}$m whence

$$v = v^*\left\{\frac{\ln y^+}{\kappa} + B + \frac{2\Pi}{\kappa} w\left(\frac{y}{\delta}\right)\right\} = v^*\left\{5.49 + 5.00 + 6.34e^{-8}\right\} = 10.49v^*$$

Taking a notional value of $v^*_{std} = 1$ for the standard FIDAP model, then the effective value of v^* for the simple Coles' law model is 55% lower as $0.45v^*_{std}$ and so the simple

model yields $v = 5.98v^*_{std}$. This result suggests that the simple Coles' model should predict a velocity in this region some 50% greater than that of the standard model; however, the simple model actually underpredicted the local velocity by 28%, when comparing the relevant Figures 6.24 and 6.23. Likewise, the 70% deficit predicted in y^* for the enhanced Coles' model leads to a standardized velocity as $v = 3.14v^*_{std}$. As such, the enhanced Coles' model should predict velocities in this region that are some 20% lower than the standard FIDAP model. This runs counter to the experience of Figure 6.25 where the enhanced model actually predicted velocities approximately 54% lower than the standard case of Figure 6.23.

To account for this discrepancy between the observed velocity deficits and those estimated by consideration of variations in v^* and y^+ between the models, the wall model of Haroutunian and Engelman (1991) must be assessed once more.

The standard FIDAP model sets

$$y^+ = \frac{y\left(C_\mu^{1/2}k_t\right)^{1/2}}{\nu} \tag{4.3}$$

whereas the Coles' models employ

$$y^+ = \frac{yv^*}{\nu} \tag{2.27}$$

Haroutunian and Engelman claim that $\left(C_\mu^{1/2}k_t\right)^{1/2}$ may be used to replace v^* as it provides "a more fundamental (and hence more universal) turbulent velocity scale of $k^{1/2}$ .... which has been found to hold in the fully turbulent near-wall region under conditions where the turbulent field is in local equilibrium". However, the physical assumptions necessary for this substitution are only implicitly detailed in the paper of Haroutunian and Engelman (1991). That this relationship is only offered for regions in local equilibrium suggests that it may become inappropriate under adverse flow conditions, where streamwise variations in pressure gradient, for example, distort that local equilibrium. Again, it is worth reitterating the weakness in using Reichardt's law - although it is an excellent fit to experimental velocity profiles for the viscous sub-layer, the transitional sub-layer and the fully turbulent outer layer, it too is only valid where local equilibrium in the flow exists.

Inspection of the y^+ values for the various models discussed here, in conjunction with equations 2.27 and 4.3 seems to imply that

$$\frac{y(C_\mu^{1/2}k_t)^{1/2}}{\nu} < \frac{yv^*}{\nu}$$

and hence that $v^* > (C_\mu^{1/2}k_t)^{1/2}$.

However, from the argument developed earlier, this does not appear to be the case, with the inferred values of v^* for the standard model being significantly greater than those predicted by consideration of shear stress plots at the wall for the Coles' models.

Taking the example of the front lower reach, Figure 6.32 presents the distribution of kinetic energy of turbulence along the top of the special wall elements for the standard model, being k_t in equation 4.3.

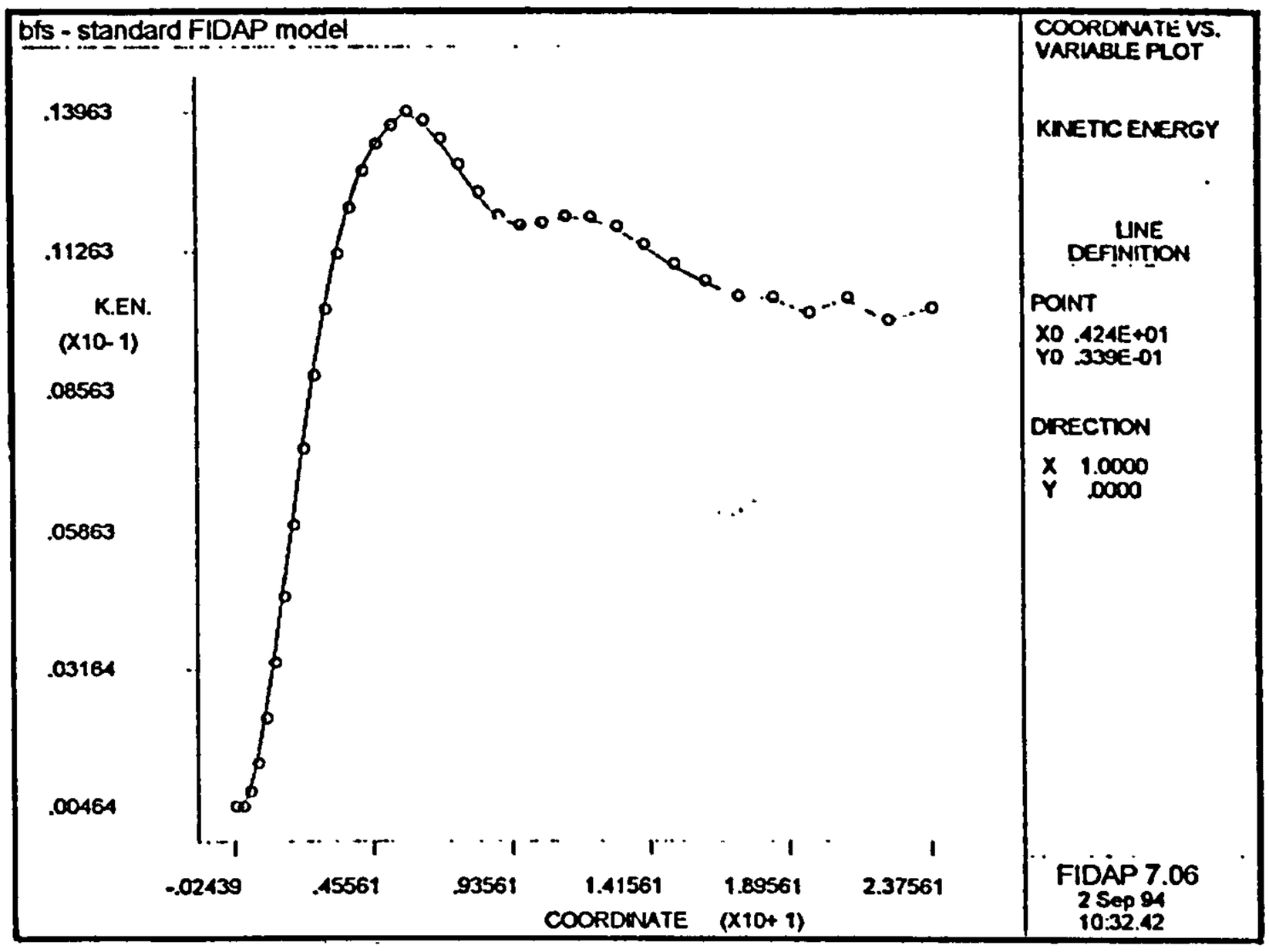

Figure 6.32. Distribution of kinetic energy of turbulence along the lower front reach for the standard FIDAP model.

From the above figure, the peak value in kinetic energy occurs beneath the separation bubble as $k = 0.013963$ and taking $C_\mu = 0.09$ then $(C_\mu^{1/2}k_t)^{1/2} = 0.0647$. At a similar point in Figure 6.29, the standard model then gives $y^+ = 2.18$. The corresponding results from the enhanced Coles' law model (listed in the table of Appendix A4) show that

$v^* = 0.0039$ with $y^+ = 6.1$. As such, $\left(C_\mu^{1/2} k_t\right)^{1/2}$ is greater than v^*, even though the reported values of y^+ suggest otherwise.

On close inspection of Haroutunian and Engelman's explanation of equation 4.3, it emerges that y is taken to be the "average height of the element above the wall" and so the value of y used in equation 4.3 will be approximately half that used in equation 2.27. Whilst this may account for the low reported values of y^+ for the standard model, the greater nodal velocity resulting from Reichardt's law is still unresolved. The final answer is thought to lie in the actual implementation of Reichardt's law. This relationship, shown as equation 2.29, is actually modified within the wall elements by the local value of Reynolds number. Reichardt's law is operated by a scheme of shape functions which are governed by the number of nodes within the element and weighted with regard to Reynolds number.

With regard to the claim that $v^* = \left(C_\mu^{1/2} k_t\right)^{1/2}$, it is difficult to test this relationship further. In that the Coles' law models evaluate k along the Coles' lines in a different manner to the standard FIDAP method of Haroutunian and Engelman (1991) (see Sections 5.1.1 and 4.2.1 respectively), the Coles' models cannot be used at present to compare v^* calculated in terms of the shear stress at the wall with that based upon k_t.

6.4. Analysis of the Behaviour of the Coles' Law Model, as Applied to the Backward Facing Step.

6.4.1. Consideration of Velocity Gradient Evaluation.

In adapting the simple Coles' law model to the task of analysing the backward facing step, the principal adjustment lay in the method by which the velocity gradient was evaluated. Having identified shortcomings in the simple technique for calculating the velocity gradient and having shown that data could be successfully transferred from the source subroutine to the boundary condition subroutine, it was realised that use could be made of the local velocity gradients calculated by the general solution procedure and available within the source subroutine. As such, the simple Coles' law model of the backward facing step transferred the velocity gradients at the integration points of all the elements available within the source subroutine to the boundary condition subroutine where they were to be used. At a given node then, the nodal velocity gradient was taken

as the average of those values recorded at the surrounding integration points. Whilst it was thought that this method would more closely capture the nature of the sharply varying velocity gradients in the near-wall region, evidence presented earlier regarding the values of v^*, which depend upon the local velocity gradients, would suggest that this did not yield values of v^* any closer to those of the standard FIDAP model.

The new method for evaluating the local velocity gradient used the same assumption as that for the U-bend model - the velocity gradient was taken to vary linearly with distance from the wall out to that point in the flow where it was evaluated, at the relevant Coles' line. By taking the velocity gradient as the average of those values at the integration points on either side of the Coles' line, the method took some account of the variation in velocity at the edge of the region governed by the k-ε model as well as that within the area controlled by the Coles' model. Experience of the early workings of the U-bend model showed this to be important as the first model for $\frac{dv_x}{dy}$ failed where no allowance was made for variations in the velocity on the freestream side of the Coles' line affecting that on the wall side.

All the same, whilst this encouraged the use of a velocity gradient model operating at an average distance y from the wall, in hindsight this could have been used to provide an estimate of the velocity gradient nearer to the wall. If the velocity gradient were assumed to decrease assymptotically on approach to the wall, then a weighted estimate could be provided for $\frac{dv_x}{dy}$, using the value recorded at the Coles' line to comment on that closer to the wall. In thus returning an elevated estimate of the velocity gradient, the ensuing values of v^*, y^+ and ultimately v would be increased. However, without further study of the experimental variation of $\frac{dv_x}{dy}$ in the near-wall region, this would be, at best, a numerical tuning exercise, seeking to boost the predictions for shear stress at the wall, which are an order of magnitude lower than those arising from the standard FIDAP model at present.

The other main difference in the operation of the simple Coles' model, when comparing the backward facing step and U-bend applications, lay in the region over which Coles' law was operated. Coles' law is not strictly valid within the viscous sub-layer and so the Coles' models of the backward facing step inspected the calculated value of y^+, operating equation 5.21 wherever $y^+ \leq 5$.

6.4.2. The Effect of Incorrect Prescription of Boundary Conditions.

Before turning to those extensions to the Coles' law model provided to cater for the incorporation of pressure gradient effects into the scheme, it is worth considering some early, faulty models of the backward facing step.

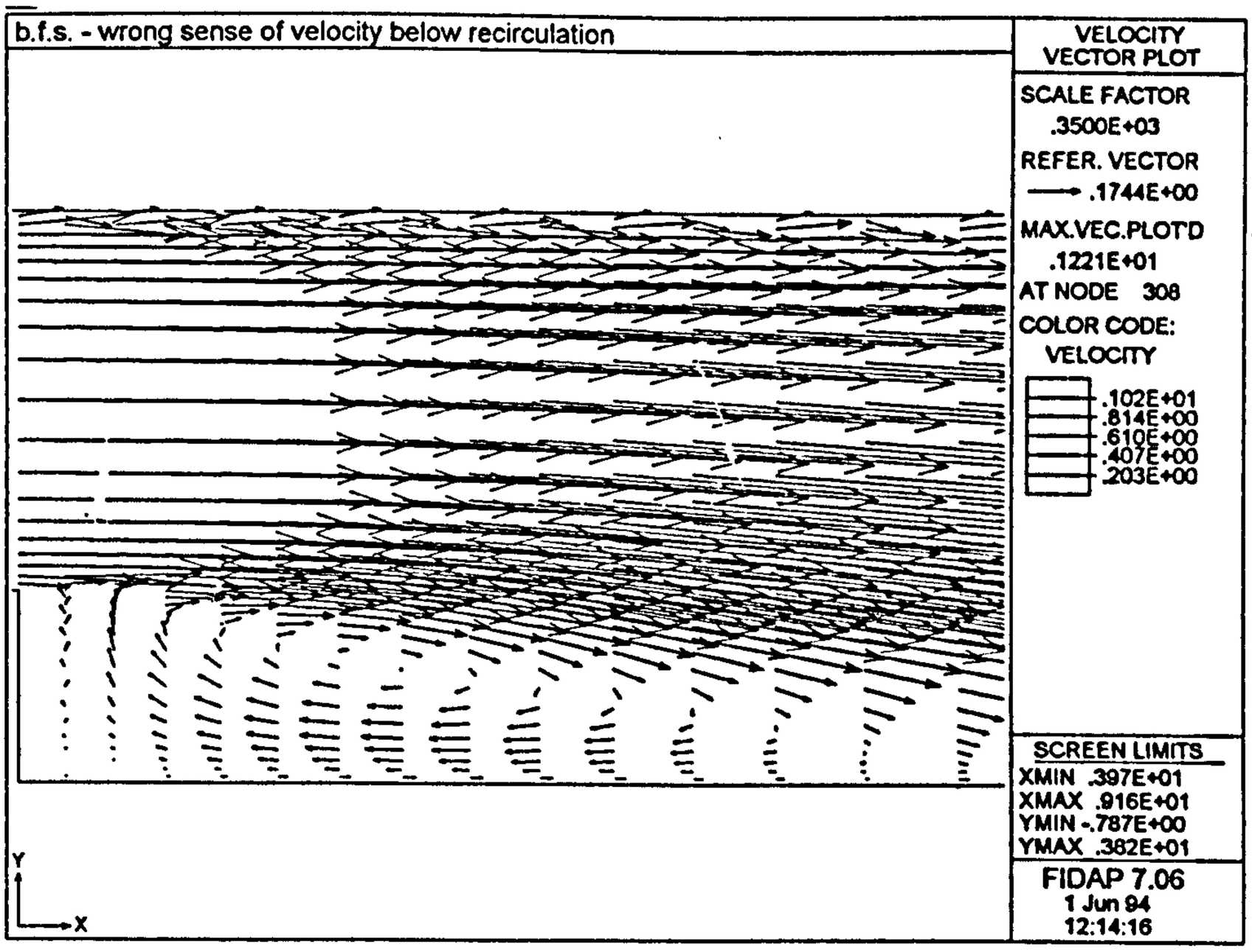

Figure 6.33. Early model of the backward facing step with no allowance for the sign of the velocity gradient.

As noted in the discussion of Figure 6.13 for the U-bend, since Coles' law provides the magnitude of the velocity in the boundary layer but does not comment directly on its direction, the plain application of Coles' law can predict flow in a direction counter to practical observation. In Figure 6.33, this early model of the backward facing step made no allowance for the sign of the local velocity gradient. As such, the nodal velocity returned by the erasure subroutine was systematically positive in relation to the global, Cartesian co-ordinate set. The flow along the underside of the separation bubble therefore ran against that prevailing in the bulk of the recirculating pocket. Notionally, this could be corrected by allocating to the velocity prediction the sign of the velocity gradient at that point, as was done for Figure 6.34 below.

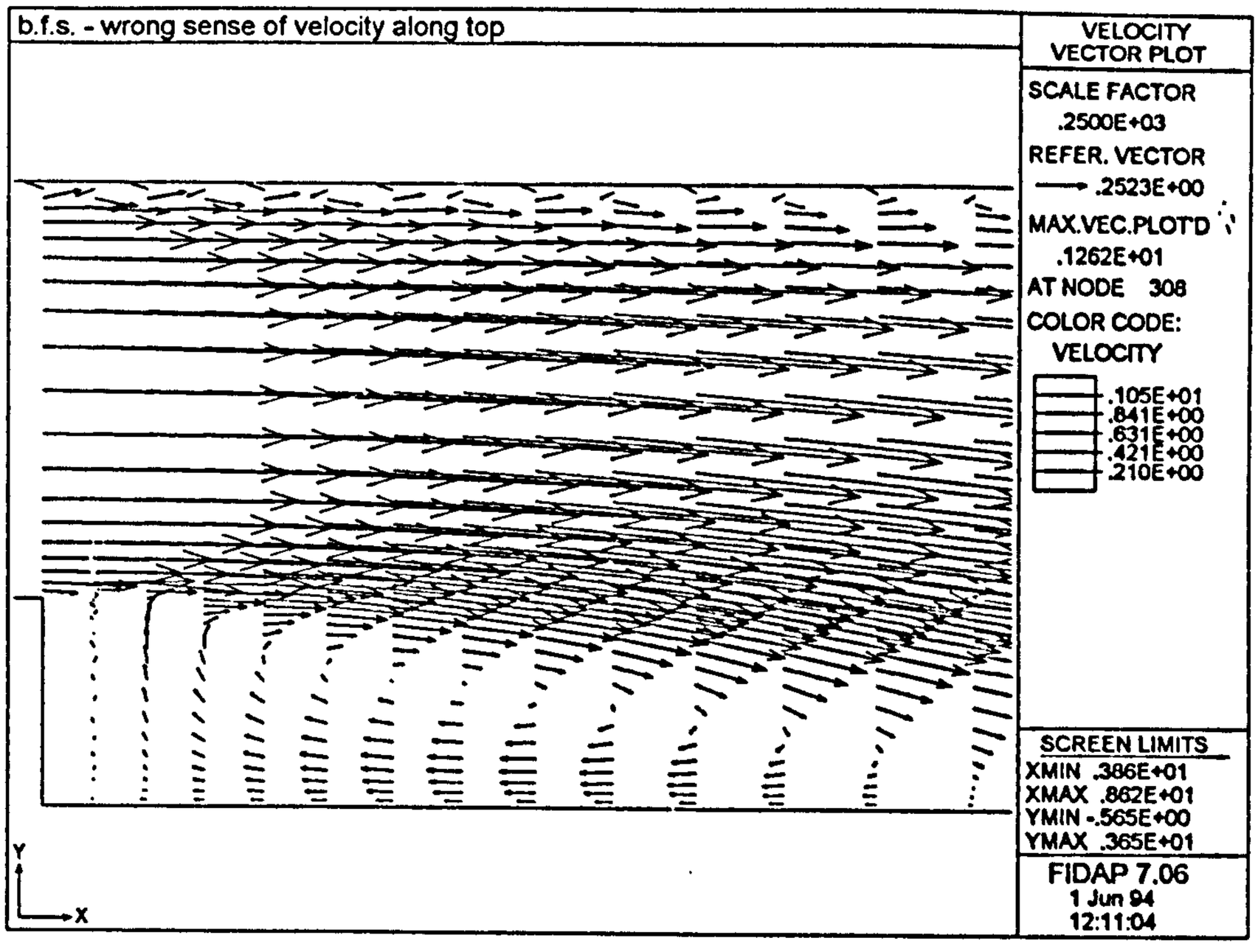

Figure 6.34. Coles' model taking the sign of the Coles' line velocity as that of the local velocity gradient.

Whilst the sense of the velocity beneath the separation bubble is now in keeping with experimental evidence, along the top Coles' line, there is local reversal of flow. This arose from the method by which the solution procedure expresses velocity gradients in terms of the global co-ordinate set. For the top wall, the velocity gradient for 'positive' flow (in the direction of increasing x-co-ordinate) will increase when moving away from the wall, in the direction of diminishing y-co-ordinate. Whilst $\frac{dv_x}{dy}$ is positive in local terms, on a global basis, it will be negative since dy is negative when moving away from the top wall out into the fluid continuum. As such, the subroutine required to specify the sign of the nodal velocity along the top Coles' line as opposite to that of the local velocity gradient. Whilst this final modification to the simple Coles' model of the backward facing step provided a plausible velocity field, it meant that as with the U-bend model, the interpretation of Coles' law was zonal in its method, with the model application having to be dedicated to the geometry considered.

With regard to the general flow predictions of the above two models, Figure 6.33 gave $x_r = 4.9$ and Figure 6.34 $x_r = 4.5$. The predictions for recirculation length here are not very good, being 32% lower on average than the findings of Kim. Now in the absence of any wall model, the k-ε will not predict separation, as was shown in Figure

6.7 for the U-bend model. Consequently, the presence of a separation bubble in these two models, however poor, can but be attributed to the operation of the wall model. The k-ε model cannot account for near-wall viscous effects but, beyond the viscous and transition sub-layers, becomes increasingly appropriate with rising Reynolds number. As such, where *some* form of provision is made for the viscosity adjacent to the wall, beyond this region, the response of the 'freestream' model is to predict recirculation in response to the adverse pressure gradient behind the step expansion.

The quality of the predicted recirculation is still dependent upon a sensible boundary model. Note that the poorest estimate of x_r is given by the model where the flow direction is incorrect above the core flow, along the top Coles' line, and not when flow is reversed beneath the separation bubble. Comparing the velocities along the top and front lower reach Coles' lines of Figures 6.33 and 6.34, Δv (the difference in reported velocity at a given node) is greatest along the top Coles' line. This suggests that the length of the recirculation zone is affected by the momentum of the core flow: indeed Kim observed x_r to be inversely proportional to the entrainment rate between the separation bubble and the free shear layer above it. In Figure 6.34, the flow reversal in the boundary layer along the top wall provides a thicker boundary layer, skewing the flow away from the upper wall of the duct towards the separation bubble. As the velocity across the free shear layer is then increased, so the separation bubble is shortened. This then implies that the momentum of the core flow is an important factor in determining the length of recirculation, with the influence of the wall being less significant than previously supposed.

6.4.3. Modelling of the Law of the Wake.

The lower velocities in the near-wall region, when comparing the Coles' law models to the standard FIDAP example, necessarily imply that the momentum flux across the boundary layer is less for the Coles' law models. As with the U-bend model, this is observed in the increased thickness of the boundary layer, when comparing Figures 6.21 and 6.16 for the enhanced Coles' and standard FIDAP models.

This 'artificial' thickening of the boundary layer will compromise the evaluation of Coles' wake function, w. In equation 2.46 for the enhanced Coles' model, the wake function is related to the ratio of y to δ. The simplifying assumption that $y = \delta$ in the simple model was known to be false. Leaving aside the variation of Π, the wake

parameter, for the moment, the setting $\delta = y$ infers that the node currently being evaluated lies at the very edge of the boundary layer, giving the largest possible value to w. However, in the enhanced model, where an attempt was made to formally evaluate δ, the uncommonly thick boundary layer would result in an underestimate of the wake function since y/δ would be low.

The method for obtaining the boundary layer thickness was illustrated in Figures 5.17 to 5.19 of Section 5.3.5. Whilst at the edge of the boundary layer, $\frac{dv_x}{dy} = 0$ as equation 5.24, this valid relationship was abandoned in favour of the simpler comparison of nodal velocities at successive nodes normal to the wall at the given point on the Coles' line. In searching for the result, $\frac{dv_x}{dy} = 0$, it would have been necessary in Fortran to use the result $\left|\frac{dv_x}{dy}\right| < tol$ to identify the edge of the boundary layer where tol was an arbitrary tolerance, of small but finite value. At the edge of the boundary layer then, this would have lead to the comparison of two very small and almost equal numbers and hence have been dependent upon the precision with which such small numbers, close in magnitude to zero, are held as binary figures within computer memory. Desiring to avoid the potential discrepancies attendant upon such practice, the local velocities were inspected instead.

At any node within the boundary layer, the modulus of the nodal velocity will be greater than that of its accompanying velocity gradient and so a comparison of successive nodal velocities, in considering larger numbers, should be more robust. In actuality, the form of the velocity profiles in the near-wall region presented a problem. Inspecting Figure 6.21 say, for the enhanced Coles' model, the profile rises rapidly from zero at the wall across the first two or three elemental layers but then continues to rise steadily almost to the centre of the duct. The specification of the freestream velocity under these conditions is not immediately obvious and the decision to set δ at that location where the nodal velocity was greater than 90% of that at the previous node is, at best, arbitrary. Arguably, a finer tolerance could be used but this would again result in the comparison of two almost equal numbers.

Within the separation bubble, the selection of v_∞ central to this method is likewise obscure. Whilst v_∞ might be defined here as the velocity of the free shear layer above the separation bubble, in terms of the general structure of the Coles' model at present, use of such a maxim would be tenuous. Given the current dependence of the model on the geometry of the problem, no generic algorithm for the selection of the free shear velocity (or the freestream velocity for that matter) is immediately obvious.

The variation of calculated boundary layer thickness along the front lower reach is presented as Figure 6.35.

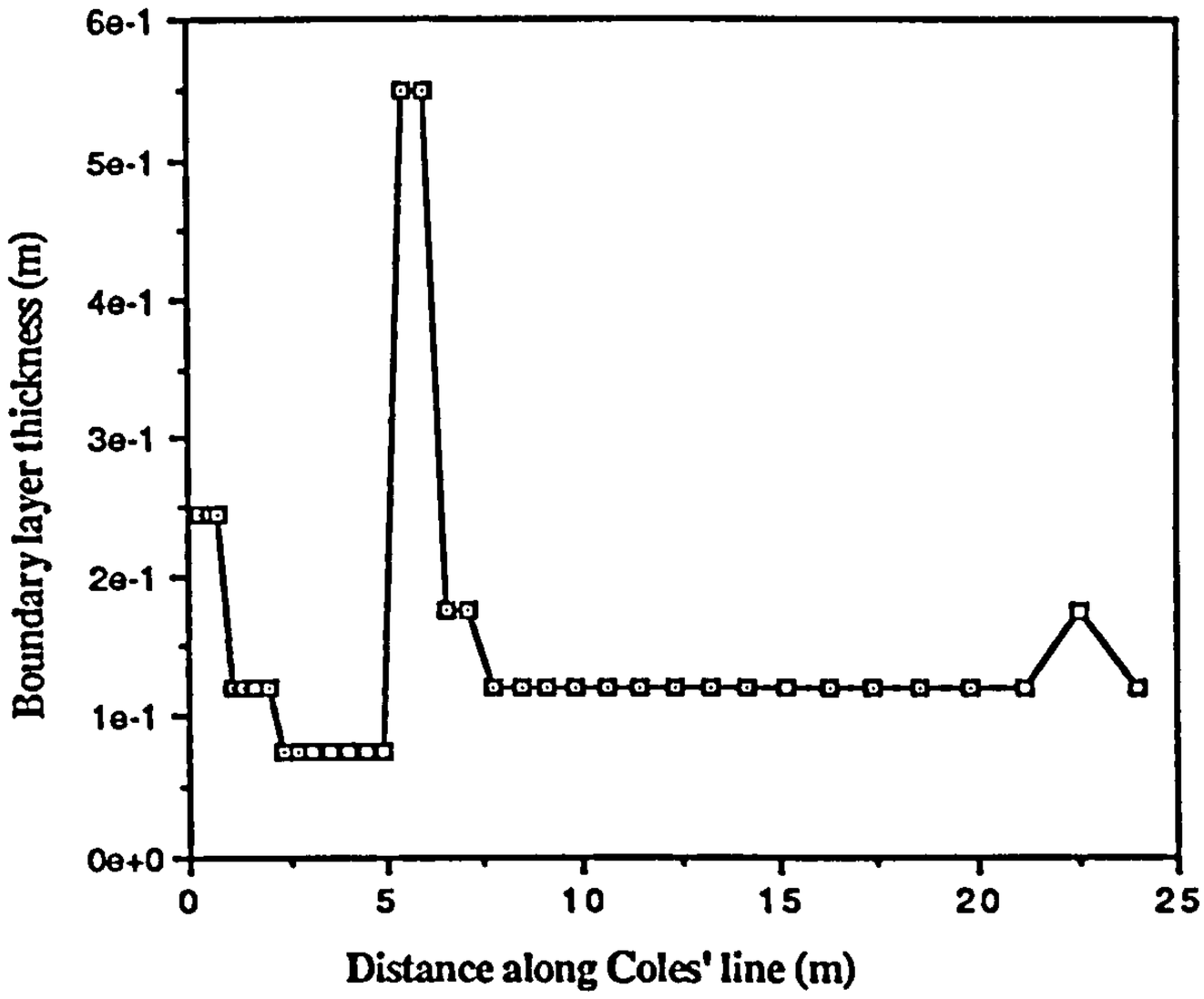

Figure 6.35. The variation of δ along the front lower reach of the enhanced Coles' law model.

Inspecting the above figure, the result of the method used to estimate δ is clearly crude. At the extremities of the separation bubble, where the velocity at the Coles' line is very small (see Figure 6.22), the greatest values of δ are seen. At these points, the increase in velocity between successive nodes, when moving away from the wall, suggests a linear velocity profile. Elsewhere along the Coles' line, where the nodal velocity is greater, the shape of the boundary layer profile is more rounded, hence satisfying the test for δ closer to the surface. Excepting these local peaks in δ, the predictions for boundary layer thickness, instead of showing growth in boundary layer thickness, as is observed experimentally and also partly seen in Figure 6.21, demonstrate δ to be largely constant across the face of the front lower reach. In that this result is nonsensical, the present method for evaluating δ is clearly deficient. With regard to the predicted values of δ shown, in comparison with the y value for the front lower reach, the resulting ratio y/δ suggests that Coles' law is being operated here for the inner region of the boundary layer.

The largely constant value for δ will then provide a near constant value of displacement thickness along the lower front reach. Now the displacement thickness is used in calculating β, via equation 2.31, in turn used to evaluate the wake parameter, Π, by the method of Das (1987, 1988) as equation 5.22; these expressions are repeated below as

$$\beta = \frac{\delta^*}{\tau_o}\frac{dp_\infty}{dx} \qquad (2.31)$$

and $$\beta = -0.4 + 0.76\Pi + 0.42\Pi^2 \qquad (5.22)$$

As access to local pressure gradients within the DVARI array of the source subroutine is not available at present within FIDAP, the local pressure gradient at the estimated edge of the boundary layer was calculated by the method of Figure 5.20. The variation in pressure gradient for the edge of the boundary layer adjacent to the lower front reach Coles' line is shown in Figure 6.36 below.

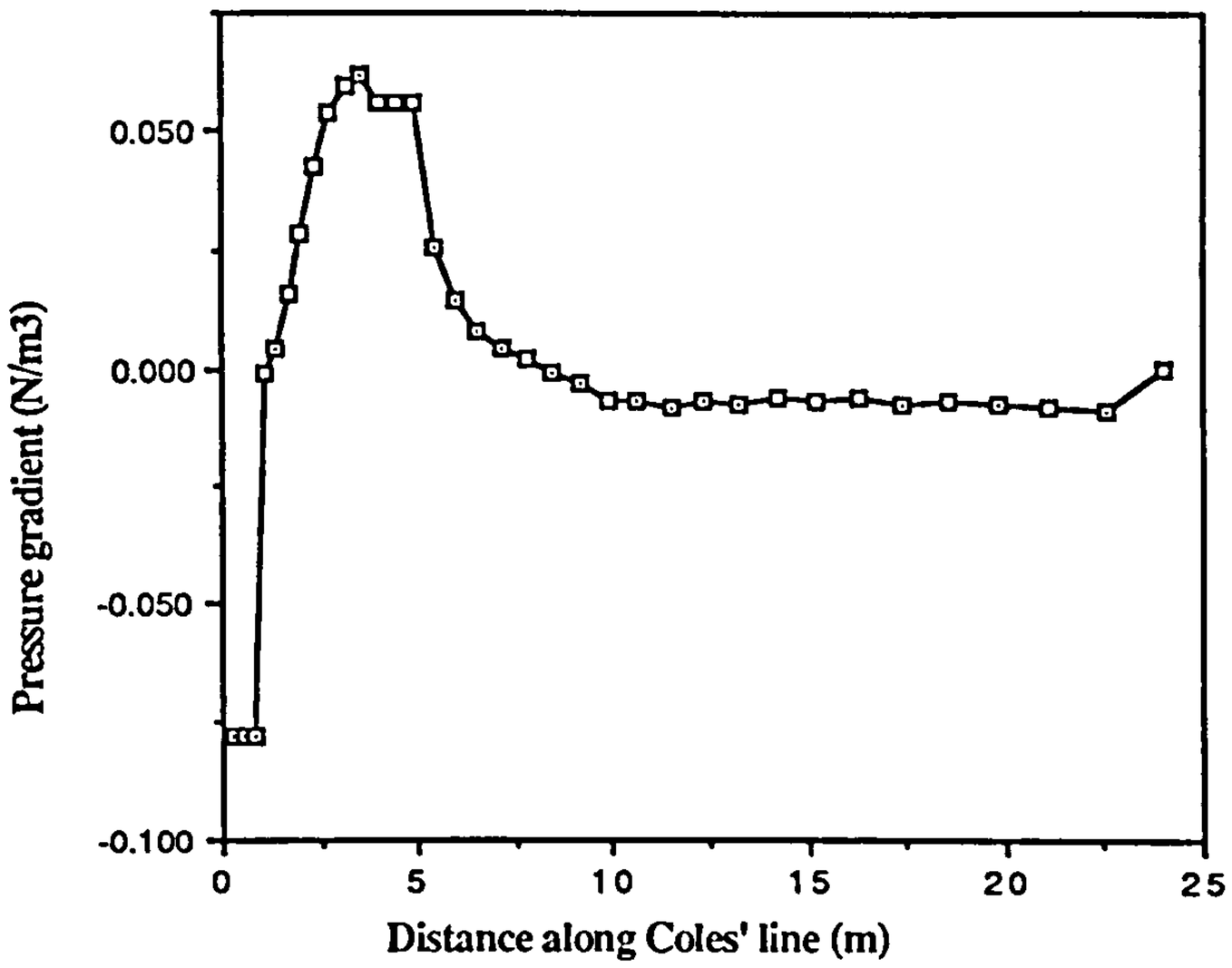

Figure 6.36. Pressure gradient distribution along the front lower reach Coles' line of the enhanced Coles' law model.

The above figure, detailing the local pressure gradient at the estimated edge of the boundary layer is in accord with the velocity distribution (Figure 6.21) for the same

model. There is a positive (adverse) pressure gradient across the major part of the Coles' line beneath the separation bubble - in the immediate vicinity of the step face though, the pressure gradient is negative. However, this local negative gradient cannot be considered favourable since the flow is reversed in that region and so the gradient must be deemed adverse. Whilst this agrees with the observations of Kim, this 'adverse' gradient does not lead to reseparation of the reversing flow, although there is near-stagnation locally on approach to the very base of the step. After reattachment at x = 5.5m or so, there is a very mild negative (favourable) pressure gradient towards the duct exit, as the boundary layer of the reattached flow develops in that direction.

Whilst the pressure gradients of Figure 6.36 appear correct qualitatively, they may be questioned quantitatively. From the point of reattachment to the duct exit, a steady decrease in pressure is implied but the gradients of the above figure are surprisingly small. From Figure 5.20, the pressure gradient is taken as the change in pressure divided by the change in co-ordinate for the integration points lying to either side of the node identified as nearest to the supposed edge of the boundary layer. Within any one element, the solution method used provides a constant pressure at each integration point throughout that element. Thus for the very fine mesh of the backward facing step, both dp and dx will be small quantities and so the result appears to be a low estimate for $\frac{dp}{dx}$.

Now from equation 2.31, Clauser's equilibrium parameter can be seen to be a balance between the displacement thickness multiplied by the pressure gradient and the shear stress at the wall. Figure 6.37 details the calculated value of β along the front lower reach.

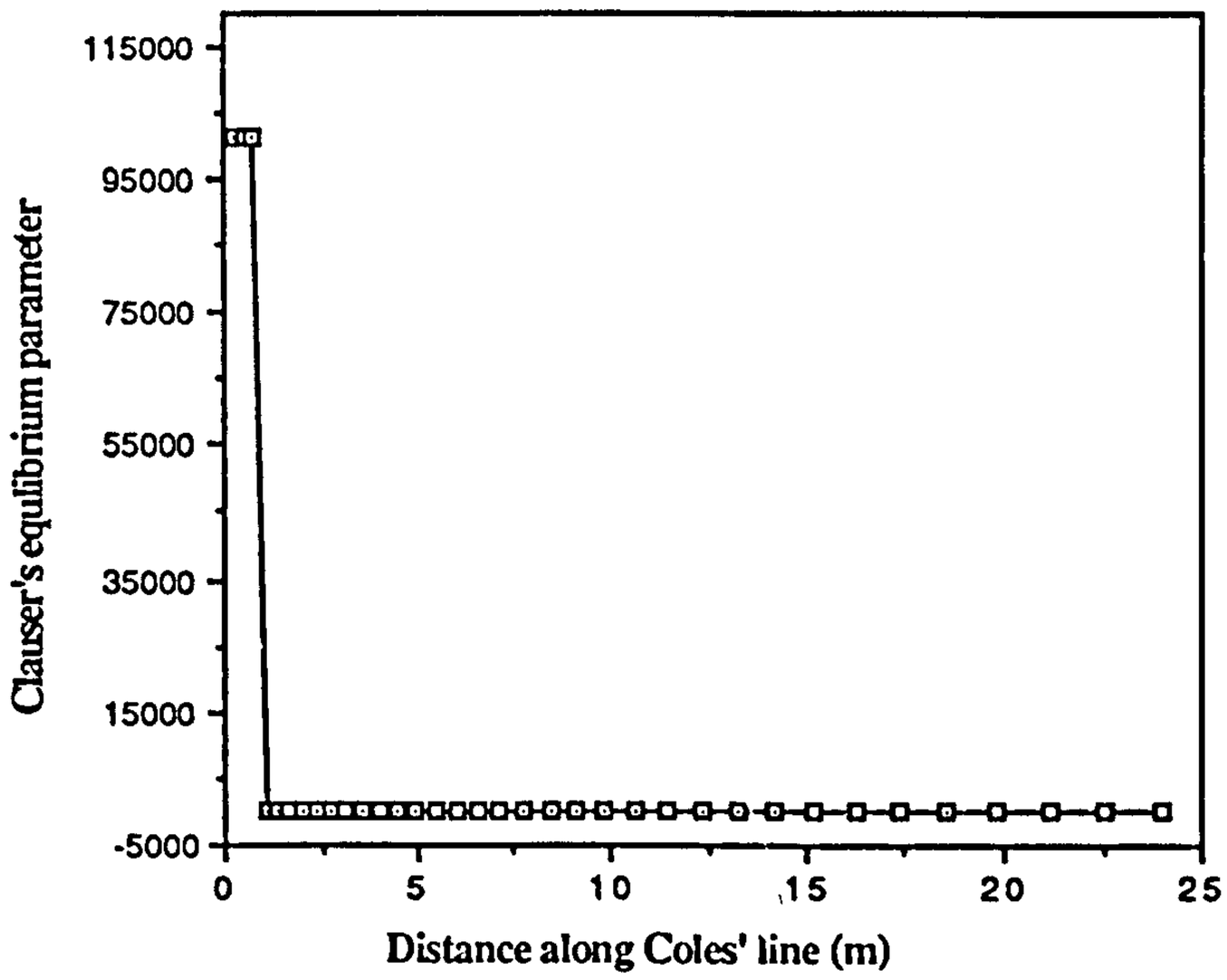

Figure 6.37. The variation of Clauser's equilibrium parameter along the front lower reach of the enhanced Coles' law model.

Excepting the extremities of the separation bubble, β has the value $\beta = -0.4$. For the β - Π correlation of Das, equation 5.22, in the limit as Π tends to zero under an increasingly favourable pressure gradient, then β tends to -0.4. As such, since a negative value of Π has no meaning here, $\beta = -0.4$ denotes the most negative value that Clauser's equilibrium parameter can assume under a favourable pressure gradient. Along the section of the Coles' line experiencing forward flow, where the pressure gradient is mildly negative, β is forced to -0.4 by this requirement that Π cannot become negative. However, within the separation bubble, the fact that $\beta = -0.4$ runs counter to expectations. As the pressure gradient here is positive, β should likewise be positive.

This discrepancy may be explained by studying the values for shear stress at the wall, τ_0, internal to the circus subroutine, as Figure 6.38 below.

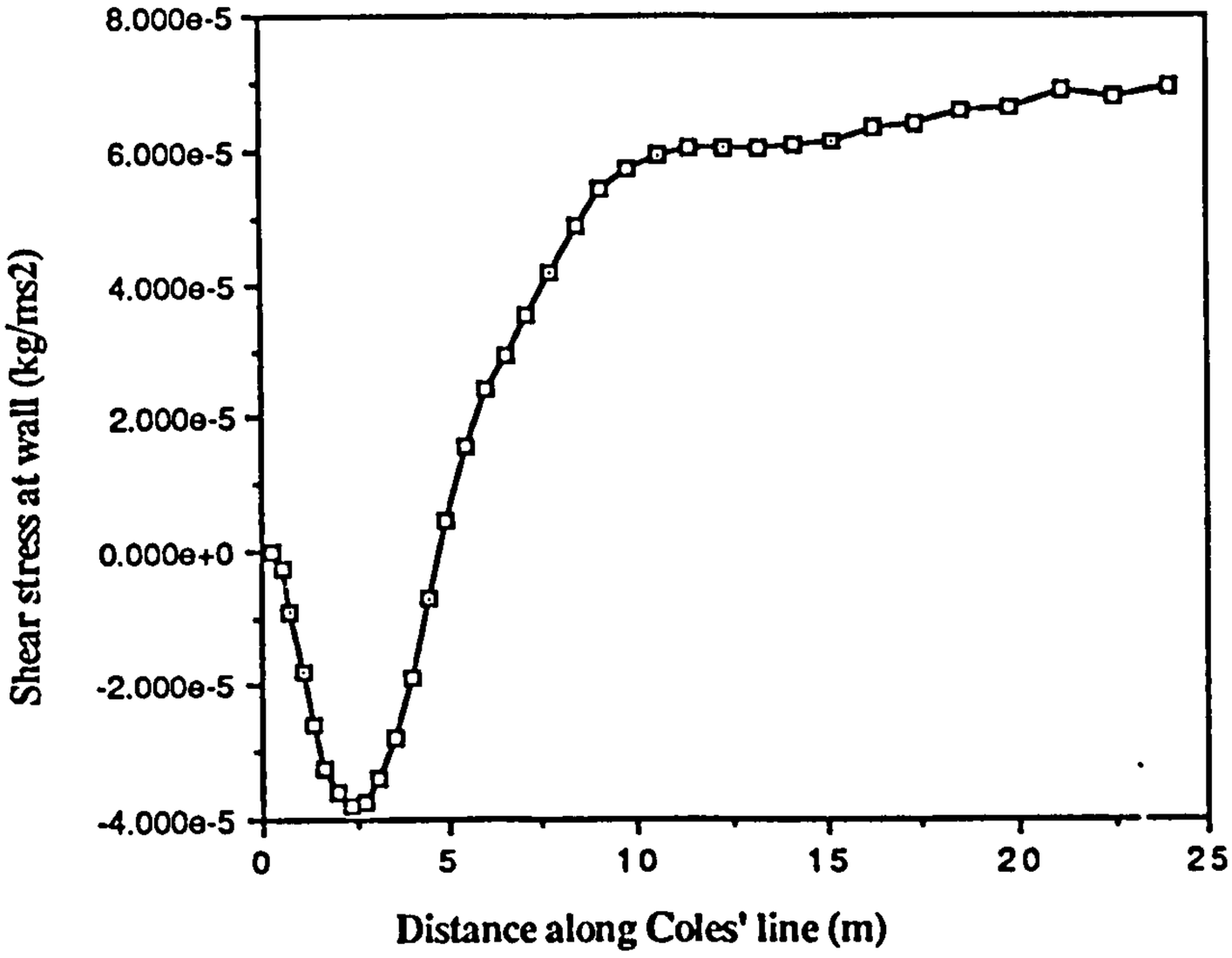

Figure 6.38. Shear stress at the wall for the front lower reach Coles' line of the enhanced Coles' model, as calculated within the model subroutines.

Up to x = 5.5m, in the region corresponding to the separation bubble, the value of τ_0 calculated within, and used by, the model subroutine is negative. The post-processed results for stress at this boundary, Figure 6.28, show τ as positive in this region. The results of Figure 6.28 are coherent in that the wall shear stress should have opposite sign to the local velocity. This *error* in the model can be traced to the definition of τ_0 - equation 5.13 does not account for the shear stress acting so as to oppose prevalent fluid motion.

In the simple Coles' model, equation 5.13 caused no problem as its only use was in determining the wall friction velocity, v^*, for which the modulus of the wall shear stress was required. As such, in preparing that part of the model, the sign of τ_0 was never considered and when seeking to use τ_0 to determine β, this aspect of the relationship between τ_0 and $\frac{dv_x}{dy}$ was overlooked. The outcome of this error is plain: β was forced to accept an inappropriate and negative value throughout much of the model, hence giving a value of Π close to zero.

For the example considered here, only in the immediate vicinity of the step base, where $\frac{dp}{dx}$ (as calculated) was significantly negative, did β deviate markedly from -0.4

(and Π by implication from virtually zero). At the base of the step, a comparatively large value of δ was seen, as already discussed. For the very low velocity in this region, the shear stress at the wall, as calculated within the model subroutine, was two orders of magnitude lower than anywhere else on the front lower reach, excepting those values corresponding to the zone of reattachment (see tabulated values in Appendix A4). The end result of this combination of factors was an estimate for β of over 100,000 and hence an excessive value for Π. Despite the tendency of the typically low y/δ ratio to suppress wake effects in the enhanced model, the prediction for Π here was sufficiently great to distort the solution process. As mentioned in Section 5.3.5, this lead to a local peak in velocity at the Coles' line which destabilised the solution process. During model development, this was circumvented by arbitrary prescription of an upper limit on β, on the erroneous assumption that the problem arose from extremely high pressure gradients at the extremities of the step face, observed during the early stages of the work. Consequently, the real cause of the problem was not realised during model development.

As has already been mentioned, the enhanced Coles' law model systematically predicted velocities at the Coles' line lower than those for the simple Coles' law model. It is now apparent that this was caused by deficiencies in the methods by which w *and* Π were evaluated. w was largely invariant as a result of the crudity of the test used to detect the edge of the boundary layer, whilst Π was almost universally set to virtually zero because of a fundamental error in the definition of τ_0. As with the simple Coles' law model, the enhanced model effectively ran a law-of-the-wall scheme but in this instance without the benefit of any supplementary law-of-the-wake, accommodating the local pressure gradient.

Notionally, this error in the model could be corrected by modifying equation 5.13 to provide the correct direction for the shear stress as

$$\tau_o = - \mu \frac{dv}{dy}$$

Incorporating this correction into the enhanced Coles' law model, the velocity field in the region of the step can be seen as Figure 6.39 below.

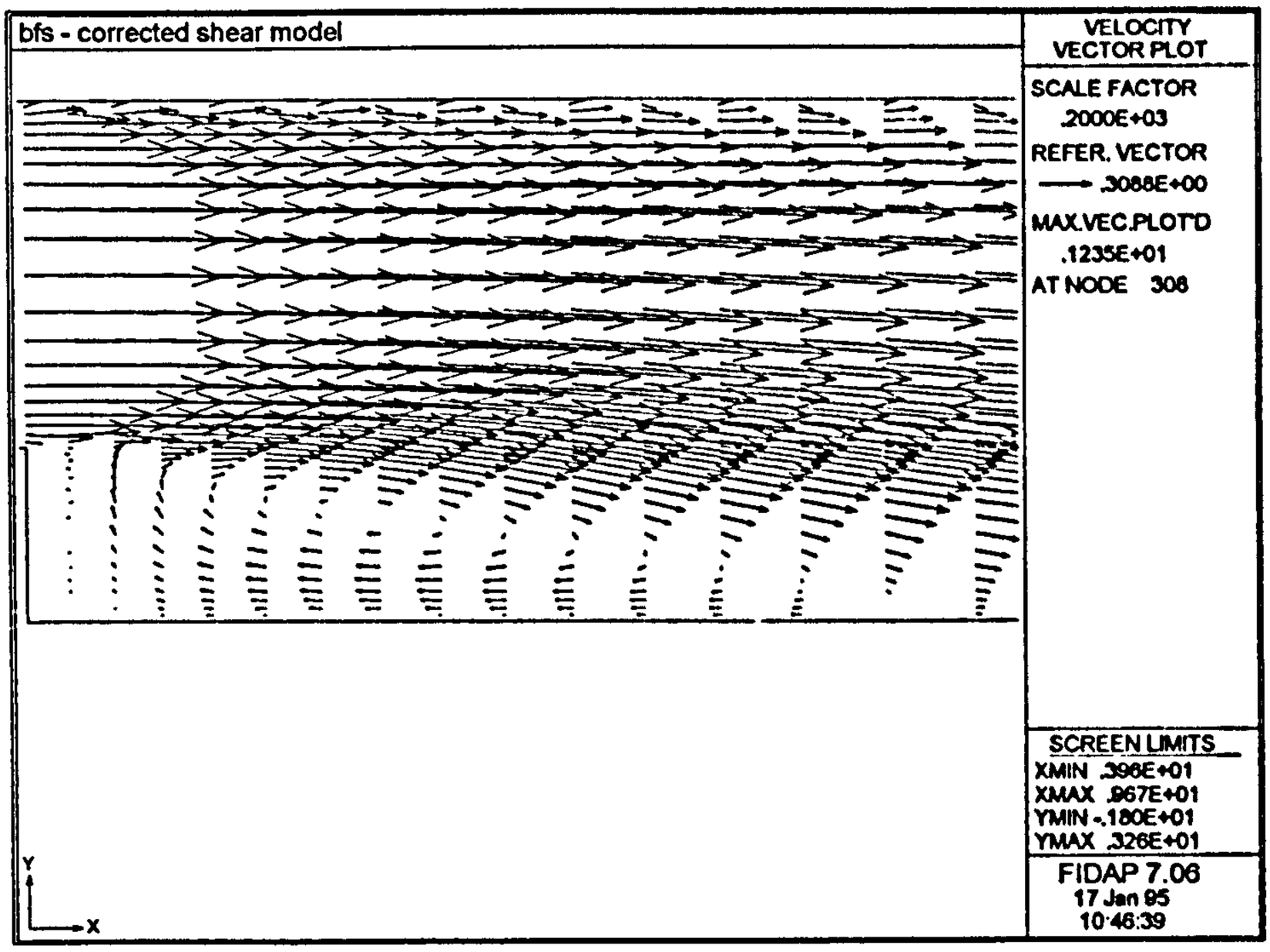

Figure 6.39. Magnified view of velocity vectors in the region of the separation bubble, predicted by the enhanced Coles' law model with corrected shear stress evaluation.

Inspecting the above figure, the prediction for recirculation length is now $x_r = 5.5$, which seems to be a slight improvement over the original enhanced model result of $x_r = 5.4$. Beyond the point of reattachment and along the top Coles' line, the predicted velocities appear to be marginally lower than before (in comparison with Figure 6.22). However, excepting the extremities of the separation bubble, the Coles' line velocity within the bubble is much reduced, as shown by Figure 6.40.

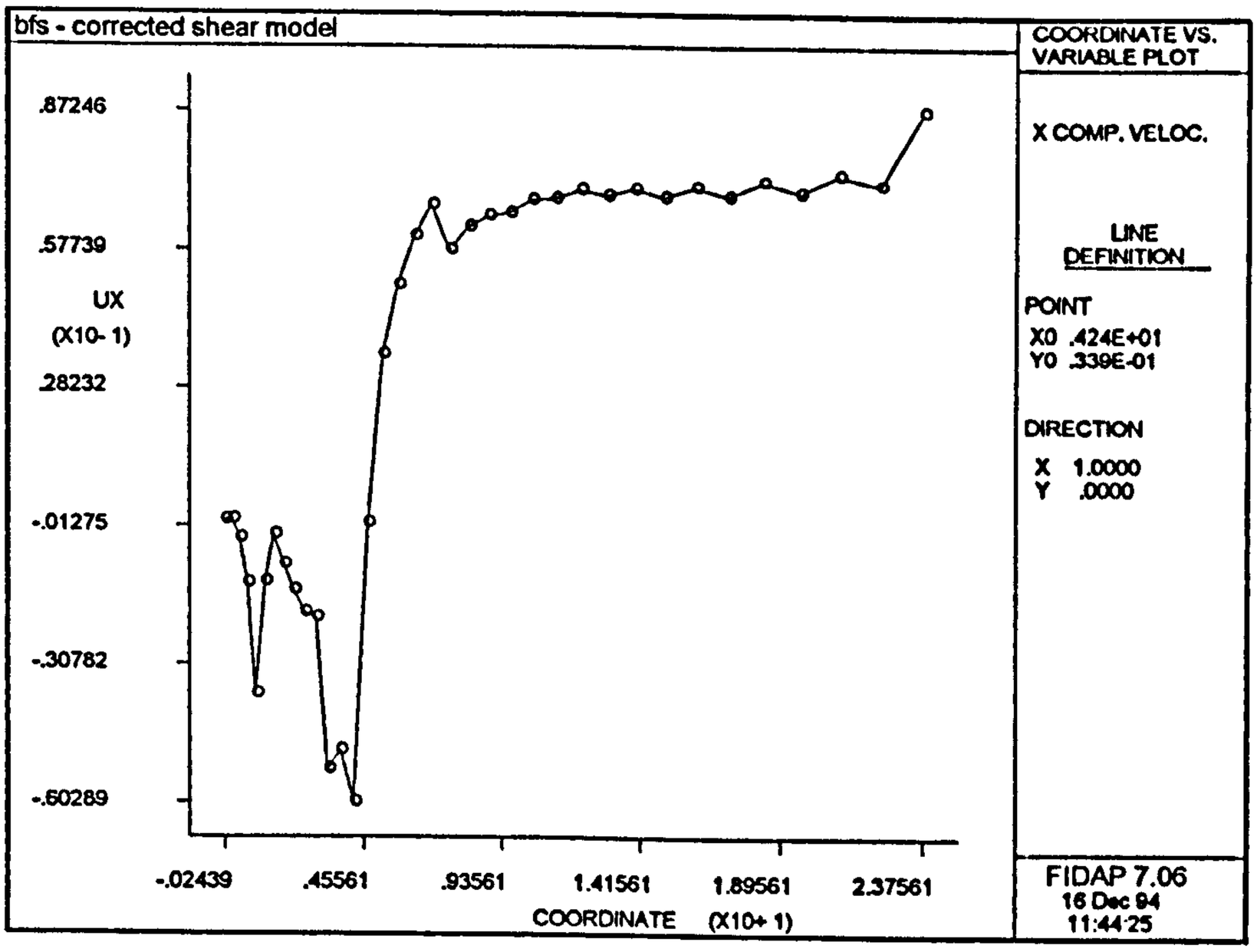

Figure 6.40. Distribution of v_x along the front lower reach Coles' line for the corrected enhanced Coles' law model.

Comparing the above figure with the original results for the enhanced model of Figure 6.25, the corrected prediction for velocity is 6% lower at the extremities of the bubble, rising to an almost 90% deficit mid-way along the base of the separation bubble.

Note also that there is no longer a graduated variation in velocity along the length of the Coles' line beneath the separation bubble, with velocity oscillating between estimates close to zero and near those of the original enhanced model. Beyond the point of reattachment, the predicted velocities are some 18% lower than before. Remembering the marked influence that τ_o has on both v^* and y^+, the boundary stress distribution for the 'corrected' model is shown below.

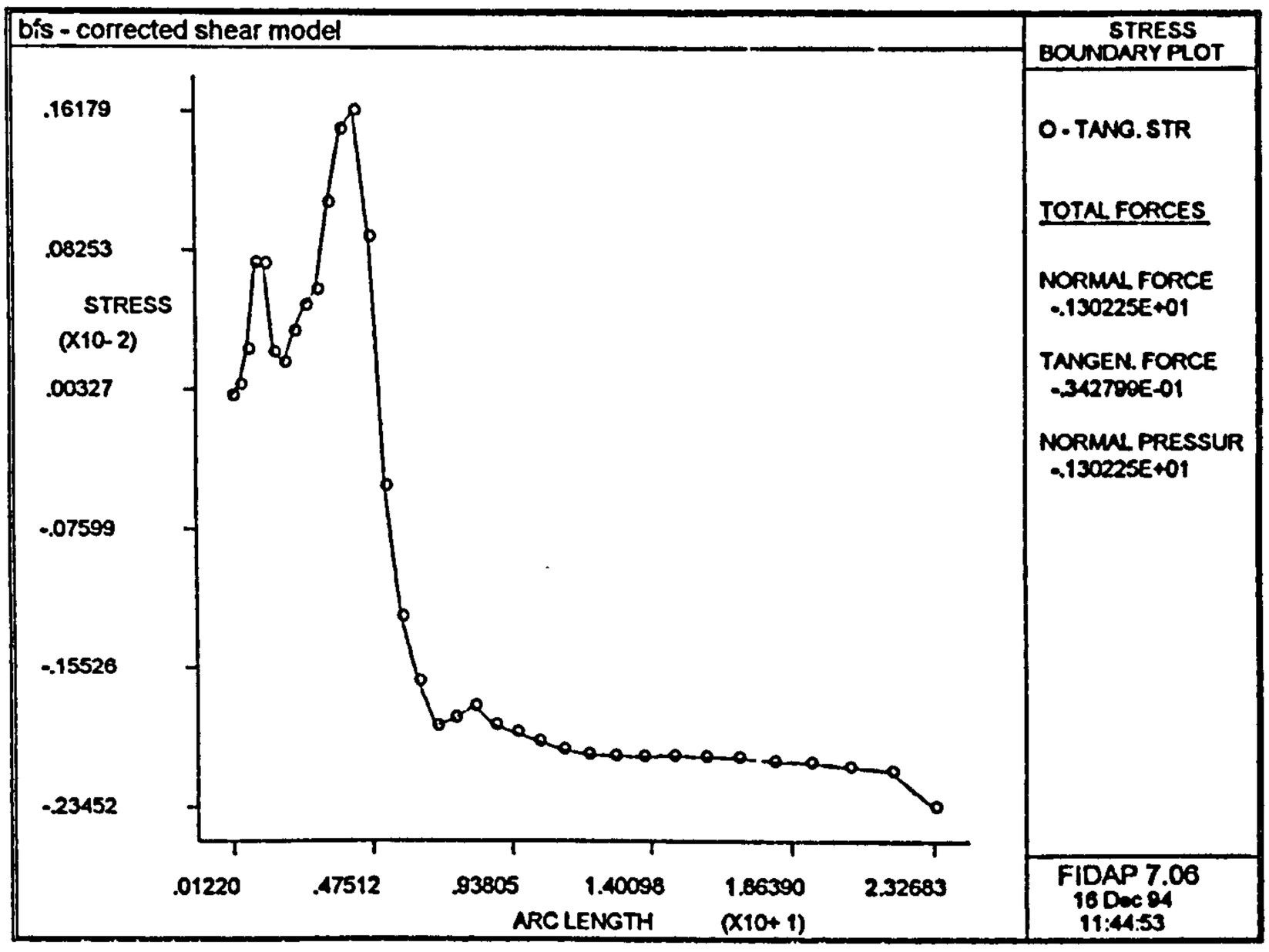

Figure 6.41. Boundary stress plot for the lower front reach of the corrected enhanced Coles' model.

Comparing Figure 6.41 with the original stress distribution of Figure 6.28, outside the separation bubble, τ is some 15% lower than before. As such, v^* and y^+ will be correspondingly reduced, leading to the observed small reduction in velocity.

Within the region of reversed flow however, there is a scatter in the results for τ which corresponds to the oscillations in velocity seen in Figure 6.40. The very small values of τ midway along the base of the separation bubble will lead to very low values of v^* and y^+ and hence almost negligible velocity. The cause of this local reduction in τ must lie in the corrections made to the calculation of τ_o in the model subroutine and thus on the operation of β and Π.

From Figure 6.39, the reversed 'boundary' layer for the separation bubble has a similar form to that of the original enhanced model (Figure 6.22). In consequence, the predictions for δ, and thus δ^*, will be similar. Along the lower front reach, δ will be largely constant, providing a low estimate of w and an approximately constant value of δ^*.

In equation 2.31, for Clauser's equilibrium parameter, with little change in δ^* and $\frac{dp}{dx}$ between the two enhanced models, any variation in β between the two models is then

determined by τ_o. For the original model, since τ_o incorrectly had the wrong sign, the signs of $\frac{dp}{dx}$ and τ_o were opposite along the entire Coles' line, forcing β to a negative, favourable value everywhere and hence Π tended to zero.

Having ammended the shear stress equation, then within the separation bubble, τ_o and $\frac{dp}{dx}$ will have the same sign and so β becomes positive for reversing flow and Π will increase above zero, as required by theory. This should manifest itself in an increased estimate of local velocity for the corrected model. Inspecting Figures 6.39 and 6.40, no such improvement was observed. Since δ will be roughly equal for the two models, then any rise in Π above zero here is not being masked by a corresponding decrease in the wake function.

As with the original enhanced model, an arbitrary upper limit for β had to be enforced. At the extremities of the separation bubble, where $\frac{dp}{dx}$ was locally large and τ_o small, an excessive estimate for β provided a value for Π that distorted the local velocity field and lead to failure of the solution process. Consequently, the method for evaluating Π appears to be sensitive to the precise balance between the pressure gradient and the shear stress at the wall.

Away from the extremities of the separation bubble, where τ_o varies widely from node to node within the reversed flow, so does the reported velocity. The gradual reduction in the magnitude of the pressure gradient and corresponding general rise in τ moving away from the step means that β falls and thus Π is not great enough to cause the solution to fail. However, the scatter in nodal velocities here will arise from this balance between $\frac{dp}{dx}$ and τ_o, suggesting that equation 2.31 for β is very sensitive to local changes in flow conditions.

Comparing τ_o internal to the model subroutine (Figure 6.38) with the corresponding post-processed results of Figure 6.28, not only was the sign wrong, it was also some three orders of magnitude lower. Assuming this trend to continue for the corrected model, then the very small values for τ seen in the reversed flow region of Figure 6.41 will correspond to values of τ_o within the subroutine approximating to zero, hence suppressing local velocity, regardless of the increase in the wake parameter. The mutual sensitivity of the wake parameter model and that for shear stress at the wall is unresolved to date and clearly requires further attention.

6.4.4. Consideration of Turbulence Modelling in the Boundary Layer.

The provisions for k and ε at the interface between the Coles' model and the main fluid continuum will now be discussed. In Figure 6.32, the distribution for k along the front lower reach Coles' line was presented for the standard FIDAP model. The corresponding results for the enhanced Coles' law model are shown below as Figure 6.42.

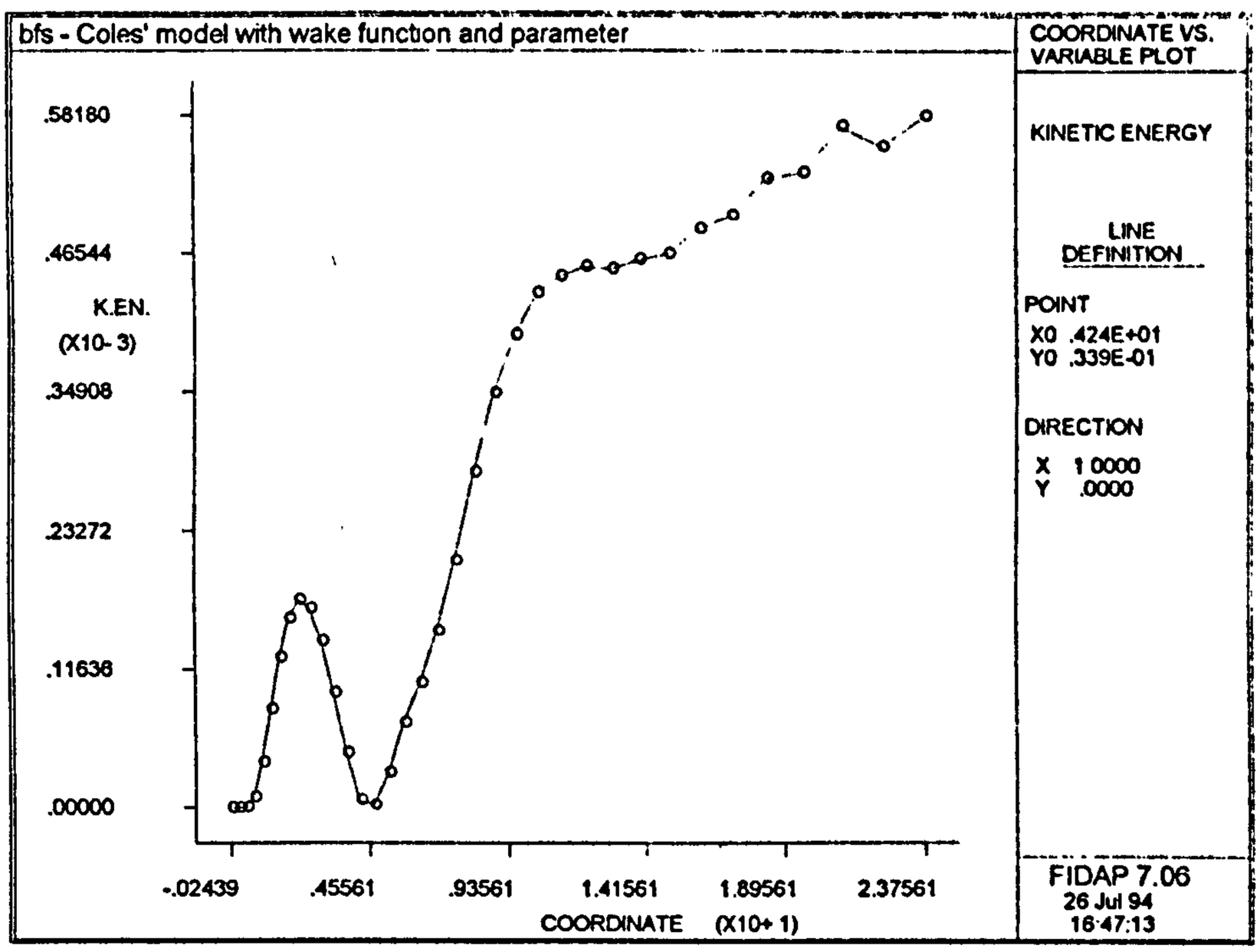

Figure 6.42. Distibution of kinetic energy of turbulence along the lower front reach of the enhanced Coles' law model.

From a comparison of Figures 6.32 and 6.42, the form of the distribution for k in the enhanced Coles' model is unlike that of the standard FIDAP model of Haroutunian and Engelman (1991), as well as being roughly two orders of magnitude lower. Given that the corresponding values for ε in either model are dependent on the value of k at any point in the wall models, then the distributions for ε are likewise dissimilar, as shown below.

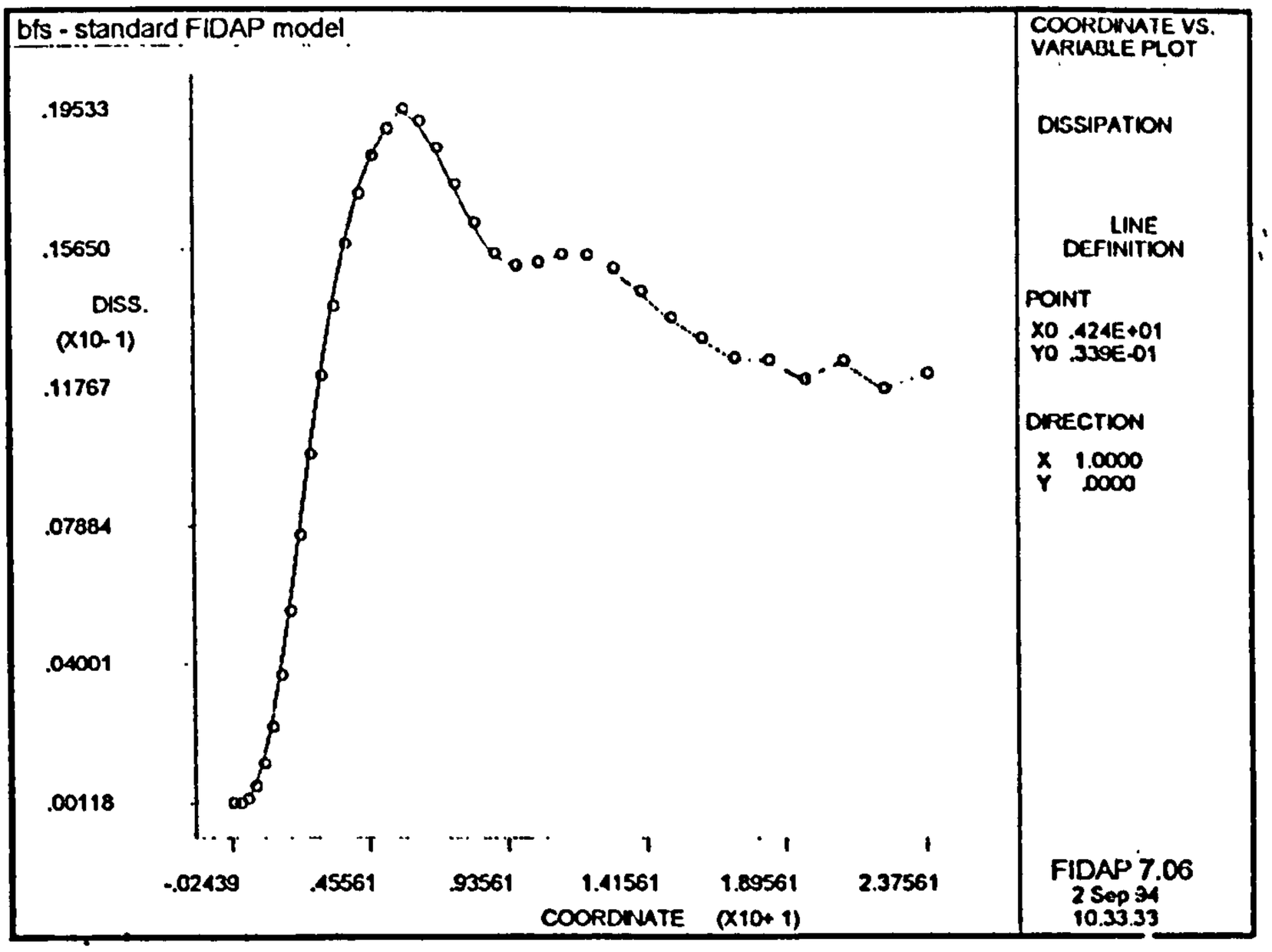

Figure 6.43. Distribution of turbulent rate of dissipation along the lower front reach for the standard FIDAP model.

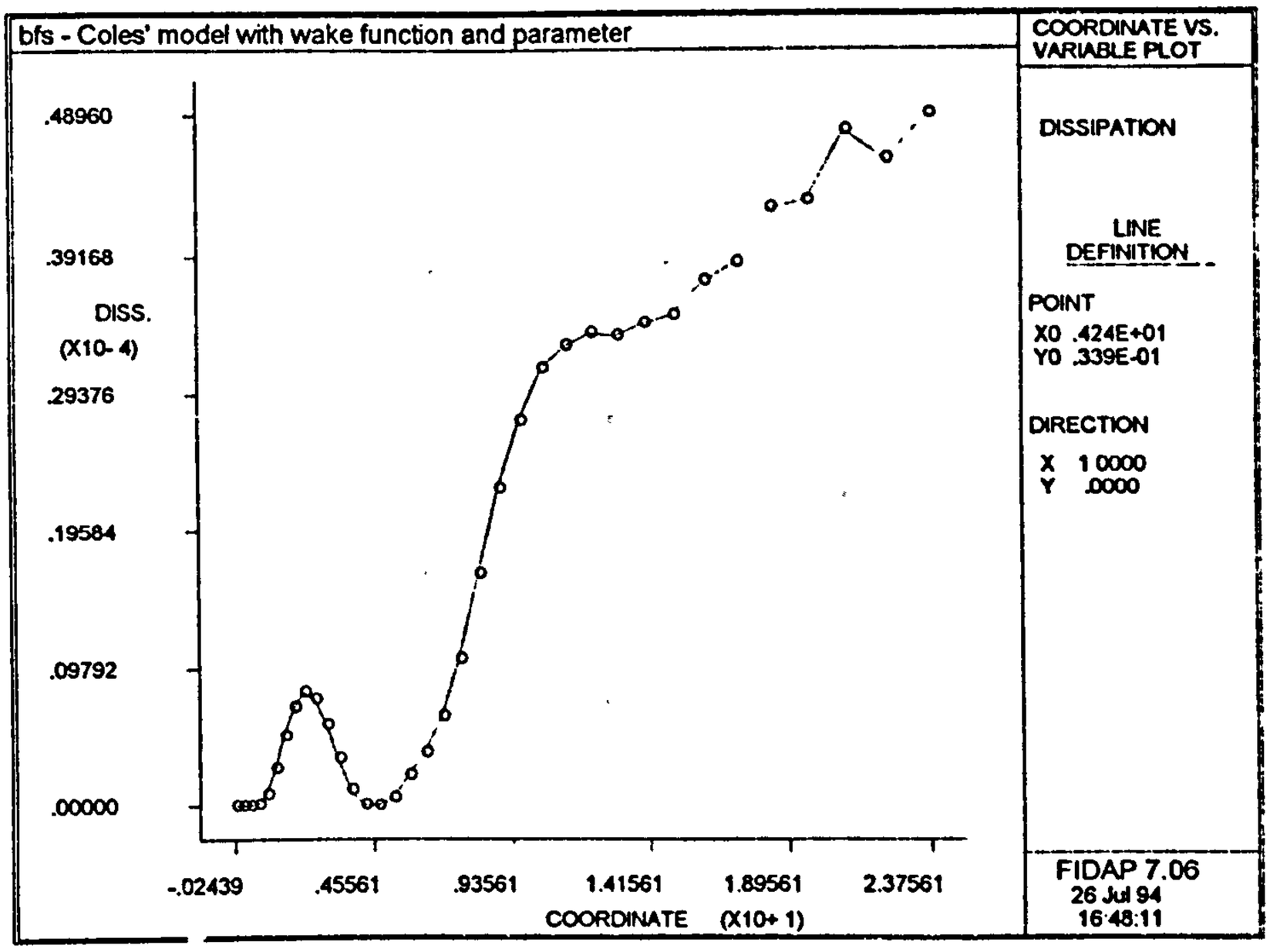

Figure 6.44. Distribution of turbulent rate of dissipation along the lower front reach for the enhanced Coles' model.

In the standard FIDAP model of Haroutunian and Engelman (1991) of these

boundary conditions, as detailed in Section 4.2.1, the modelling assumption for k is taken as zero gradient in k across the span of the special element normal to the wall, equation 4.4. By implication then, k is constant across the element and the boundary acts like a mirror at the edge of the continuum. This value of k at the wall is then used as the turbulence length scale of equation 4.5 to predict ε at that point.

By contrast, the boundary conditions for k and ε in the Coles' models, as described in Section 5.1.1, use simple empirical relationships that were originally prepared to comment on the turbulent field at inlet to a bounded flow. k is expressed in terms of the local velocity gradient and a mixing length, as equation 5.2. ε is then a function of the estimate of k at that point, the mixing length and the velocity gradient.

These boundary values of k and ε for the Coles' models, whilst known to be a simplification, were originally used for the simple Coles' model of the U-bend as a first approximation to k and ε, allowing the general structure of the Coles' law model to be validated. Setting aside the oversight of equation 5.4, where the mixing length used in equations 5.2 and 5.3 is invariant with y^+ (counter to the observations of Prandtl and von Karman (White, 1991)), the basic limitation of the method is that no account of the turbulent field near the wall is made. The k-ε boundary conditions at the Coles' line do not consider the levels of k and ε in the adjacent freestream model.

For the Coles' law model of the backward facing step, it was sought to remedy this shortcoming by applying boundary conditions for k and ε using the method employed in the FIDAP wall elements of Haroutunian and Engelman (1991). As such, instead of prescribing k and ε (based on the local velocity gradient) at the Coles' line, the freestream turbulence model was operated at that point. The Coles' model then calculated k and ε at the wall, based upon the corresponding value of k at the Coles' line. Whilst this duplicated the approach of the special wall elements in principal, in practice it provided facile solutions to the flow. Figures 6.45 and 6.46 below show the velocity field for this experiment at solution iterations just before and just after the implementation of this 'improved' boundary model for k and ε.

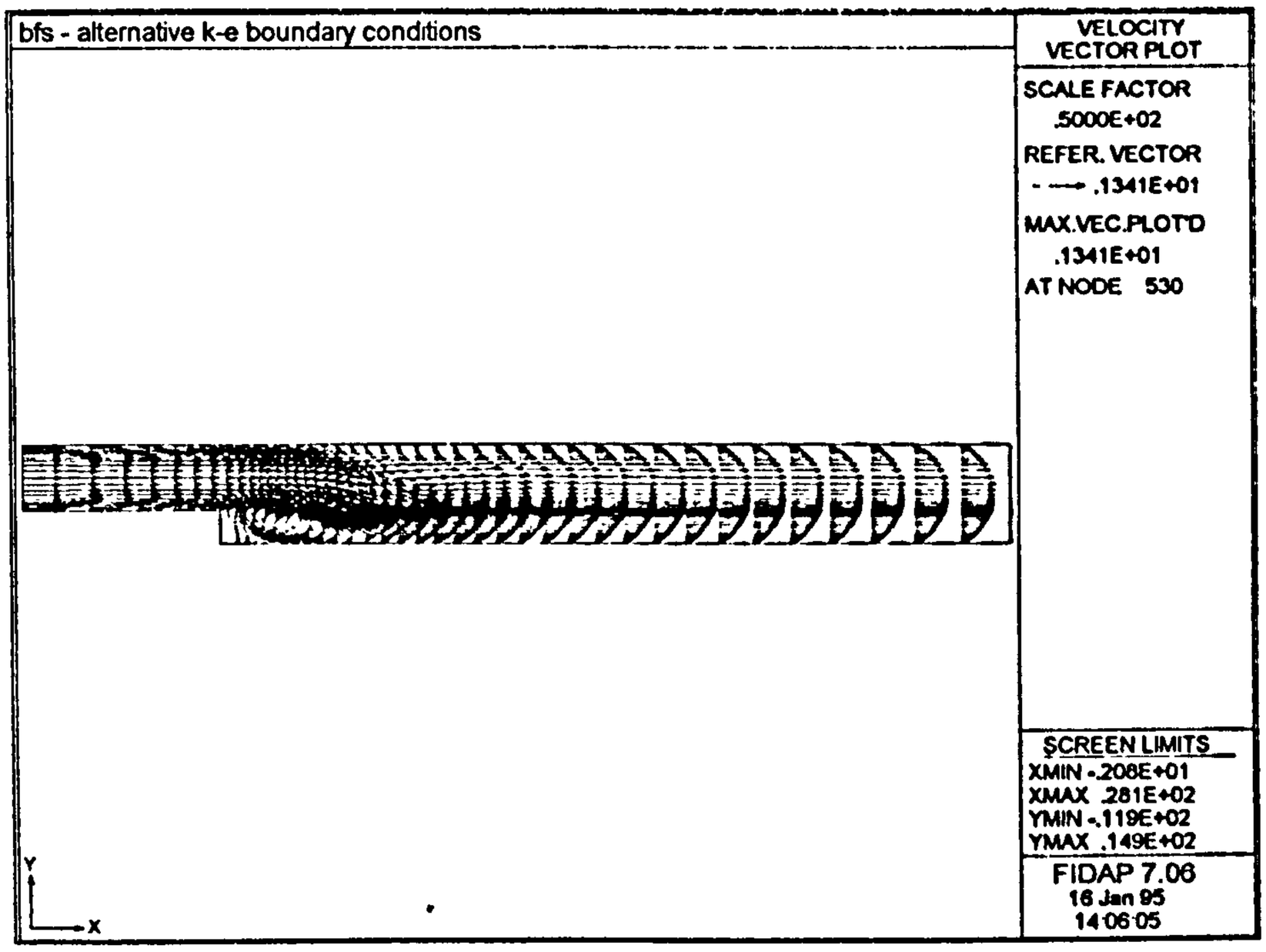

Figure 6.45. Velocity field for the Coles' law model using the FIDAP turbulence model at the wall, just prior to its implementation.

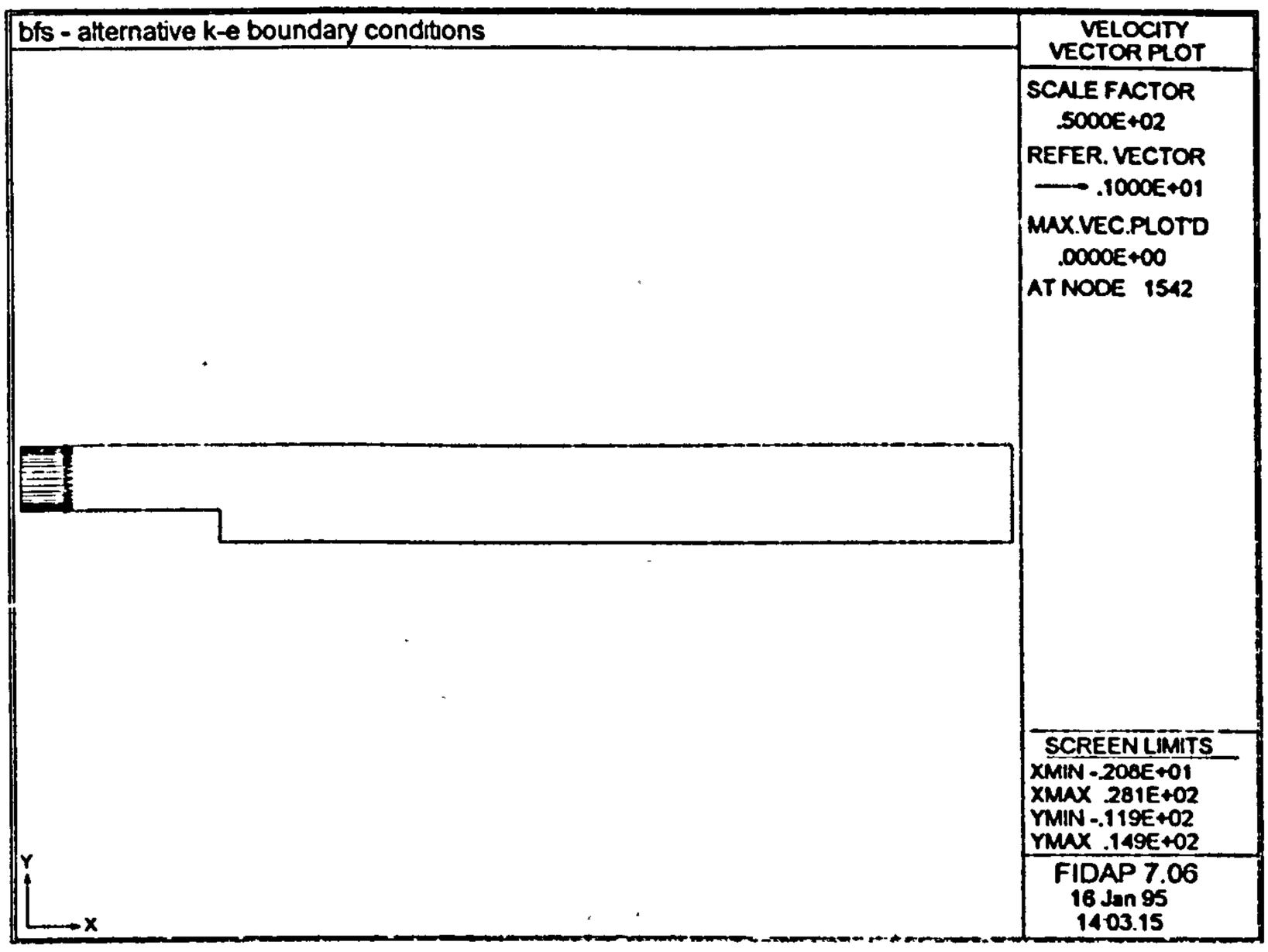

Figure 6.46. Velocity field for the Coles' law model using the FIDAP turbulence model at the wall, just after to its implementation.

The above figures represent the state of the velocity field for two iterations early in

the overall solution process. At the onset of the solution process, early experience of subroutine usage had lead to the use of counters to govern the actual iteration at which the Coles' model commenced useful operation. These counters prevented the Coles' model accessing the contents of the solution arrays VARI, DVARI and SOL before they 'filled' with data pertinent to the genuine flow solution. Remembering this, the new boundary conditions for k and ε did not come into effect for several iterations, before which their values were uniformly set across all boundaries to the initial conditions provided for the onset of solution.

In that the model converged on a spurious solution very rapidly after that iteration at which the new model for k and ε was first activated, it is likely that the failure of the model was caused by the abrupt change in the levels of k and ε occuring at that iteration. The step change in k and ε at the boundary to the continuum was a necessary outcome of the method by which the Coles' law model commenced. As such, whilst the original boundary conditions for k and ε were considered deficient, they were used for all of the other Coles' model experiments discussed earlier.

6.4.5. The Effect of Mesh Density on Modelling Results.

In seeking to compare the results of Coles' law models directly with those arising from the model of Haroutunian and Engelman (1991), the computational meshes used throughout this study were the standard 'example' meshes, available within the FIDAP library of examples. Consequently, no comment was then offered on the sensitivity of the Coles' law approach with respect to computational mesh density in the near-wall region. In discussing the behaviour of the simple and enhanced Coles' law models of the backward facing step, it was shown that both schemes effectively operated a modified law of the wall model: in the former case, the simple Coles' law model of equation 6.1 had a constant wake component, whilst in the latter instance, the enhanced model of equation 6.2, wake effects were depressed by errors in the wake parameter model, using equations 2.31 and 5.22. Nevertheless, mesh dependency of the solution is still a matter of interest and may be considered by inspection of Figure 6.47 below.

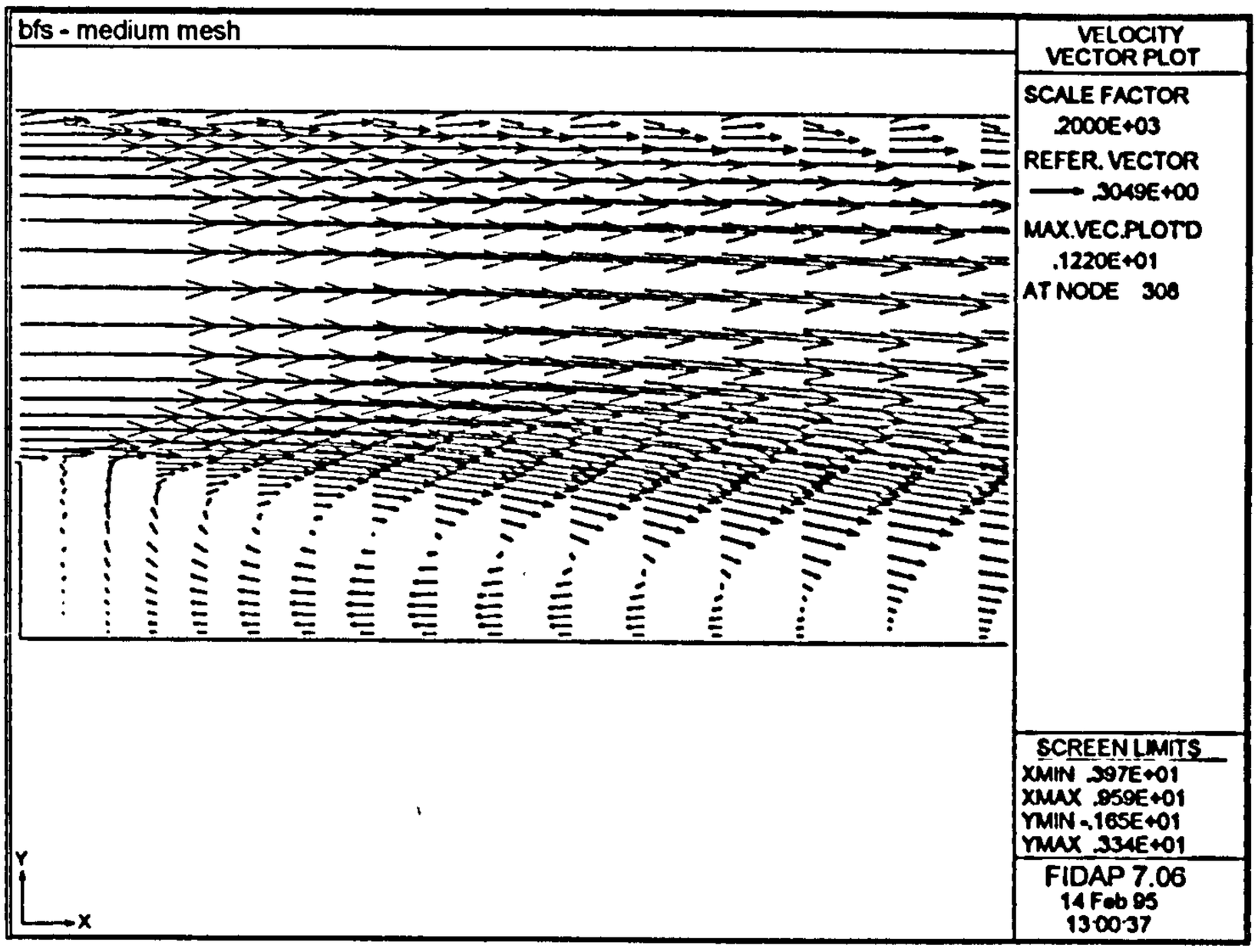

Figure 6.47. Simple Coles' law model of the backward facing step using a medium grade mesh.

In the above figure, the simple Coles' law model was operated with modified mesh density in the near-wall region, such that the elemental layer abutting the solid surfaces of the duct was twice the thickness of that used in the previous solution of Figure 6.20. Consequently, the medium grade mesh had a larger value for y when evaluating y^+ in equation 6.1, such that the Coles' line was situated within the wake region of the boundary layer. The resulting estimate for the recirculation length given by the medium grade mesh was $x_r = 5.3$, which bears reasonable comparison with that of the original, finely graded mesh of Figure 6.20, which predicted $x_r = 5.5$. Since the simple Coles' law model is effectively an expression of the law of the wall, given in terms of inner variables, then as y^+ increases, the quality of velocity profile predictions would be expected to fall: the law of the wall formula after Prandtl (equation 2.24) is an earlier and cruder fit to experimental near-wall data than either the models of Reichardt (equation 2.29) or of Spalding (equation 2.30). Consequently, as the effective distance between the Coles' line, where the wall model is invoked, and the solid boundary is increased, the quality of velocity profile predictions at that point would be expected to diminish. This observation is supported by a marked deterioration in the estimated recirculation length following a further doubling of the thickness of the first layer of elements adjacent to the

solid boundaries of the model. In Figure 6.48 below, the separation of the Coles' lines from the wall is four times that of Figure 6.20, with a corresponding reduction in the recirculation length as $x_r = 5.0$.

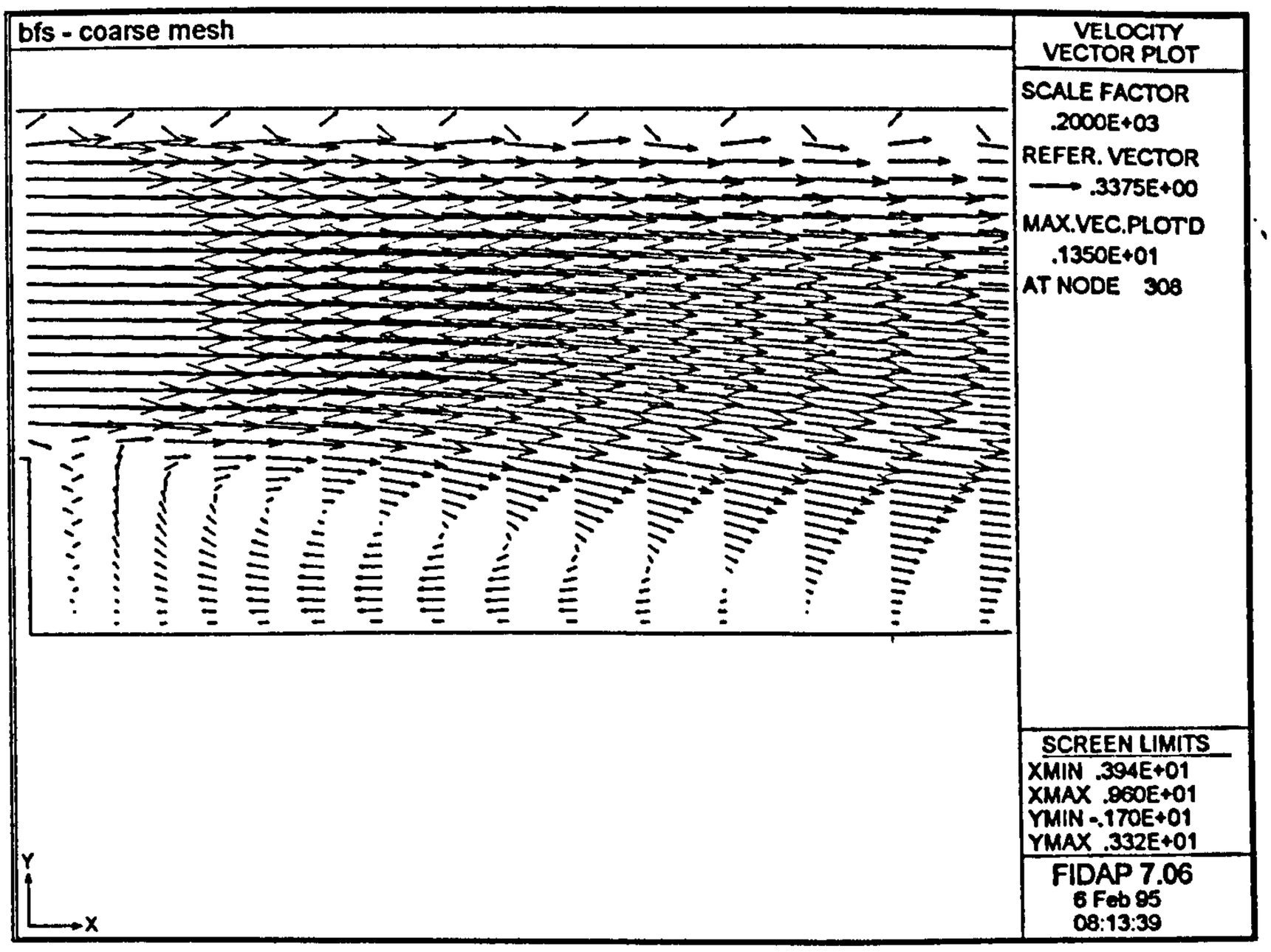

Figure 6.48. Simple Coles' law model of the backward facing step using a coarse grade mesh.

6.4.6. Summary of Observations Arising from Backward Facing Step Modelling.

Taking an overview of the results arising from study of the backward facing step, the principal observations may be summarized as:

i) The CFD models of the backward facing step offer a fair description of the flow in comparison with the work of Kim (1978), underpredicting recirculation length by some 20% (in keeping with the work of Rodi (1991)). As such, the Coles' law models provide a viable alternative to the 'traditional' wall modelling approach of Haroutunian and Engelman (1991).

ii) The Coles' law models predict lower near-wall velocities than the standard FIDAP model. As with the U-bend models, this deficit in local velocity is related to low

predictions of shear stress at the wall for the Coles' law models.

iii) The lower predictions for near-wall velocity of the Coles' models are not fully accounted for by the 'low' values of shear stress at the wall. As with the U-bend model, the discrepancy in results is influenced by the difference in methods by which the modelling schemes evaluate y^+.

iv) The 'low' Coles' law predictions of shear stress at the wall were related to the method by which the near-wall velocity gradient was calculated - the approach to this for the Coles' models was considered to be an over-simplification of the physics of the problem.

v) Consideration of early backward facing step models with incorrectly applied boundary conditions showed the momentum of the core flow to have a marked effect on recirculation length.

vi) The evaluation of the boundary layer thickness, and hence of the wake function, was only partially effective.

vii) The model of the wake parameter was incorrect. The fault was traced to an error in the evaluation of the shear stress at the wall. As such, the enhanced Coles' law model did not fully evaluate pressure gradient effects.

viii) In seeking to correct the model for the wake parameter, the β-Π relationship of Das (1987, 1988) was shown to be sensitive to the local value of shear stress at the wall.

ix) The boundary conditions for k and ε for the Coles' models were overly simplistic - attempts to rectify this in using an approach similar to that of Haroutunian and Engelman (1991) were unsuccessful.

x) The Coles' law model was shown to have limited dependence upon near-wall mesh density - the local mesh density could be significantly reduced before adversely affecting flow predictions.

7. General Discussion - an Overview of Conducted Studies.

At the outset of this study, CFD was forwarded as an alternative to, or a complementary tool for use with, practical experimentation for the design and development of wall-bounded flows, such as the inlet manifold detailed in Chapter Three. The majority of CFD schemes use the popular high Reynolds number k-ε model in conjunction with a wall law for general modelling purposes. However, the widely used wall models of Reichardt (1951) and of Spalding (1961) were prepared for equilibrium flows, in the absence of marked pressure gradients. In that many practical engineering flows are transient, such wall models are unable to mimic the physics of those flows.

Possible alternatives to this approach within a CFD framework, such as second moment models or low Reynolds number variants of the k-ε scheme are of limited practical use because of their need for finely graded meshes in the near-wall region. Furthermore, the low Reynolds number k-ε models typically contain fundamental flaws in their modelling assumptions (Patel et al, 1985).

In a review of momentum integral analyses, a number of potential wall models were considered with regard to the preparation of a more robust wall law. The works of Clauser (1954, 1956) and of Schofield (1981) were seen to offer advantages for the analysis of pressure-driven flows but to be limited in their range of application. The law of the wake, developed by Coles in 1956, was then identified as offering a sound basis for the modelling of such flows. Whilst the original law of the wake was only valid up to the point of near-separation, subsequent work by Kline et al (1983) and by Das (1987, 1988) has extended its usage into regions of reversed flow.

7.1. Investigation of Wall Model Behaviour Using Prevalent CFD Techniques.

Having reviewed a range of modelling approaches to bounded turbulent flows, the need for a wall model applicable to pressure-driven flows was identified from a theoretical standpoint. In order to determine whether current CFD techniques were deficient for such flows in practice, a typical transient engineering flow was analysed using contemporaneous methods. The work conducted shows that state of the art CFD models do not give suitable results for transient flows.

When comparing CFD with experimental results, two issues arise as how to compare results and the subsequent analysis of chosen results. In this work, the flow through an inlet manifold was identified as an exemplary problem. Since CFD is used in industry as an alternative to practical developmental experimentation, it was attempted to duplicate the results of the manifold using CFD. To this end, a practical study of the manifold flow was conducted using rudimentary laboratory techniques in common usage commercially.

The experimental velocity profiles of Figures 3.5-3.8 were taken using a simple flow angle meter and thus gave a time-averaged description of the flow, in that the response of the metering equipment was significantly greater than the time scale of individual events occurring within the inlet manifold.

In presenting CFD results for comparison with experimental data, three main options arose as steady-state, time-dependent and averaged time-dependent analyses. The steady-state analysis offered a time-averaged flow simulation upon the assumption that in having all four ports of the manifold model 'open', that this approximated to the practical behaviour of the manifold over a period of time. The time-dependent approach provided a sequence of model solutions to individual manifold events, such as opening or closing of inlet ports, which combined to simulate the complete cycle of manifold events. Finally, the averaged time-dependent results gave a time-averaged analysis of the individual time-dependent solutions.

Regardless of the type of CFD analysis chosen, the predictions in the near-wall region were very poor. The vertical velocity profiles at station I may be taken to be indicative of the CFD results. Using the velocity distributions of experimental Figure 3.5 as a benchmark, the steady-state results of Figure 3.13 deviated widely in the near-wall region. Likewise, the time-dependent results of Figures 3.14-3.16 gave poor near-wall predictions and underestimated the magnitude of the freestream velocity. Whilst the aggregate of the time-dependent results, as shown in Figure 3.17, offered the nearest approximation to Figure 3.5 of the three analyses offered, it still gave too slow a rise in velocity away from the wall, with freestream results being similarly poor.

Consequently, by attempting to replicate experimental results by a number of different approaches, the shortcomings in computational results were not attributed to the given modelling technique used *per se* but rather taken to be a function of state of the art CFD. With respect to current, commercial CFD packages, no consideration of such problems was observed in conducting a literature survey. Furthermore, where wall effects

have been mentioned in recent papers on CFD applications, such as those of Baxendale (1993) and Taklanti (1993), neither the effect of local pressure gradients on near-wall velocity distributions nor the behaviour of pressure gradients in transient flows were appraised.

The k-ε model, in conjunction with the law of the wall, is generally considered to offer a cost-effective tool in CFD (Haroutunian and Engelman, 1991) but if such a framework is to applicable to adverse and transient flows, then a new approach to modelling in the near-wall region is patently needed. Subsequent analysis of the time-dependent results highlighted this need. The 'conventional' CFD results for the manifold made use of the wall model of Haroutunian and Engelman (1991), in turn based upon the works of van Driest (1956) and of Reichardt (1951). This model makes no allowance for the deviation from near-wall equilibrium observed in the results that it generated here. Figures 3.26-3.28 demonstrated the existence of marked pressure gradients within the manifold, moving in time and space. Furthermore, the y^+ distribution, of Face 1 of the manifold for example (Figures 3.29-3.31), was seen to be a function of time. In that the working limits for y^+ of the Haroutunian and Engelman model (1991) were exceeded in different parts of the manifold at different times, then in conjunction with the pressure effects noted, the inability of the manifold model to match experimental results is accounted for.

Consequently, having first demonstrated the need for a more robust wall model theoretically, conventional CFD modelling also supported this argument. The use of Coles' law for such a modelling tool was then investigated, being a scheme prepared for adverse flow conditions across a wide range of y^+.

7.2. Selection of Test Cases.

In order to obtain a reliable implementation of a chosen wall model, it is necessary to select a good benchmark against which to validate modelling results. With regard to the implementation of Coles' law, test cases were identified as the U-bend and the backward facing step. Both of these examples existed as flows that have been thoroughly documented and for which high quality experimental data is available.

Whilst the inlet manifold was useful as a tool for demonstrating the real need for a comprehensive and suitable wall model, it was not advocated as a test case for the use of Coles' law. The experimental data gained from the inlet manifold was sufficient to the

needs of assessing current wall model behaviour. However, given the problems discussed in Section 7.1 regarding the matching of computational and experimental data, the inlet manifold results were not considered a proper benchmark for Coles' law. To offer the manifold as a test case for Coles' law, detailed transient data for the near-wall region would be a prerequisite: the gathering of such data would be a specialised task, being beyond the intended scope of the current work.

The proposed test cases constitute fundamental geometric identities for which excellent experimental data is readily available. Since the U-bend and backward facing step may be viewed as examples of the typical 'building blocks' from which more complex flow regimes are constructed, including the inlet manifold of Chapter Three, then a wall model successfully describing their behaviour would, by inference, offer a powerful tool for modelling complex domains. As such, modelling of the U-bend and the backward facing step via Coles' law was sufficient to the needs of this project.

7.3. Discussion of Modelling with Coles' Law.

7.3.1. U-bend Results.

At the outset of this comparison of standard FIDAP and Coles' law models, it is worth reitterating the fact that the Coles' lines along which Coles' law was operated were sited at the same distance from the wall as the outer edge of the FIDAP special wall elements. This allowed for direct comparison of the velocities predicted by Coles' law with those of the modified Reichardt model used by FIDAP.

The standard against which all the U-bend models were judged was the experimental work of Sandborn and Shin (1988). The standard FIDAP model reproduced the main flow features identified by Sandborn and Shin but differed in detail. The onset of separation in the standard model occured slightly later round the bend than expected, with a considerable excess in the length of the recirculation bubble.

At this point in the overall study, remembering that for an U-bend of tight curvature, the flow is thought to be dominated by inviscid mechanisms, the FIDAP model was modified and operated using no wall model whatsoever. In that this experiment showed no recirculation in the flow at all, the need for a wall model was demonstrated; a good model of the core flow, such as the k-ε turbulence model here, is insufficient.

The simple Coles' model again gave a good general description of the flow but

predicted separation too early around the inner bend of the duct. However, a shorter separation bubble was observed, much closer in length to that predicted by Sandborn and Shin than the standard model. With regard to general features of the flow then, the Coles' model was considered somewhat superior to the standard FIDAP model.

The main object of either model was to predict the local velocity at each node adjacent to the wall and separated from it at a distance, y. In a comparison of the velocity predictions of the two models as Figures 6.5 and 6.9, the velocity arising from Coles' law was lower than the standard case. The low velocity at the wall also lead to the excessively thick boundary layer in comparison with the standard model, as seen in Table 6.1. By suppressing the velocity near the wall, the rising velocity moving up through the boundary layer would not attain the same value as that of the freestream so close to the wall as the standard model.

The lower velocities predicted by Coles' law were initially surprising, given that higher values were expected under adverse conditions in comparison with the standard FIDAP model. On inspecting the main equations of the two models, the principal variables were seen to be v^* and y^+, since Π and w were found to be essentially constant for the Coles' law model. Now y^+ is proportional to v^*, which in turn is proportional to the square root of the shear stress at the wall.

On viewing the post-processed shear stress distributions for both models, Figures 6.6 and 6.10, τ for the Coles' model was seen to be an order of magnitude lower, hence implying that v^* was lower for the Coles' model. However, counter to this observation, y^+ values for the Coles' model were higher than those of the standard model, when comparing Figures 6.12 and 6.11. The low values of y^+, despite high inferred v^*, for the standard model in comparison with those of the Coles' model were attributed to the different method by which the wall elements of Haroutunian and Engelman (1991) define y^+. All the same, by inserting the results for y^+ and inferred v^* for each model into their respective governing equations, the deficit in the velocities predicted by Coles' law was apparently accounted for.

7.3.2. Backward Facing Step Results.

For the backward facing step test case, the numerical solutions were set against the work of Kim (1978). All three models, being the standard FIDAP model, the simple and the enhanced Coles' models, reproduced the majority of the main flow features.

However, the models all underpredicted the length of the recirculation zone behind the step expansion by roughly 20% (as observed common for k-ε models by Rodi (1991). Furthermore, the secondary recirculation at the base of the step, observed by Kim, was not seen, although the enhanced Coles' model did show a local rise in pressure gradient away from the base of the step, which would provide an adverse pressure gradient to the reversed flow in that region.

Again, as with the U-bend results, in comparing the Coles' models with the standard FIDAP model, the velocities along the Coles' lines were lower, and the observed boundary layers thicker. For the simple Coles' law model this was partly expected as it was an adaptation of the original U-bend model to the case of the backward facing step, prepared in order to provide a sound structure within which Coles' law could be applied more fully. For the case of the enhanced Coles' law model, however, these lower local velocities required investigation.

The inferred values of v^* from the post-processed results for shear stress were again considered, along with the values of y^+ for all three models. Once more, the low values of inferred v^* suggested that y^+ for the Coles' models should be lower than the corresponding standard results, contrary to the observed results for y^+ of Figures 6.29-6.31. Furthermore, when inserting the predicted values for v^* and the observed values of y^+ into the relevant modelling equations, the estimates for velocity thus gained did not match the velocity deficits seen when comparing Coles' law results with the standard model.

It was then necessary to consider the FIDAP model of Haroutunian and Engelman (1991) more closely. Haroutunian and Engelman constructed the wall modelling elements of FIDAP with a modified form of Reichardt's law. The turbulent scale v^* was replaced by $\left(C_\mu^{1/2}k_t\right)^{1/2}$ in evaluating y^+. Whilst no evidence was offered for their claim that the two functions were approximately equal provided the flow was in local equilibrium, they did observe that k_t, the kinetic energy at the top of the wall element, would be a more fundamental scale than v^*. One advantage of their method is that it avoids the problems arising near separation , when v^* tends to zero. Against this, it must be remembered that Prandtl and von Karman noted the boundary layer to be affected by wall conditions - the modified expression for y^+ does not explicitly account for this.

From the observed results for y^+, it was inferred that $\left(C_\mu^{1/2}k_t\right)^{1/2} < v^*$, counter to the argument based on observation of the post-processed shear stress in Figures 6.26-6.28. To resolve this discrepancy, the values of these two functions were evaluated for a

point on the lower front Coles' line and $(C_\mu^{1/2}k_t)^{1/2}$ from the standard model was seen to exceed v^* from the Coles' model. Whilst this partially accounted for the greater estimate of v based on study of the local shear stress, the low standard y^+ results were traced to the use of y/2 in the FIDAP wall evaluation of y^+. The greater values of local velocity for the standard model, in comparison with the Coles' models, were finally attributed to the weighting scheme used within the special wall elements, where Reichardt's law was modified by the local value of Reynolds number.

Unfortunately, the difference in the methods by which k was evaluated at the Coles' lines for the Coles' models precluded the use of Coles' results to study the claim that $v^* = (C_\mu^{1/2}k_t)^{1/2}$. However, the reported requirement for local equilibrium of the flow of this relationship means that, in theory, it is no more defensible than Reichardt's law when in the presence of an adverse pressure gradient.

7.3.3. Consideration of Model Implementation.

In devising and encoding Coles' law algorithms, the nature of the programming environment precluded the development of a generic wall model. The complete range of data pertinent to the wall model was divided between a number of solution subroutines. The basis upon which these subroutines processed data varied between subroutines such that the transfer of data between subroutines was mesh-dependent. Given that mesh descriptors, such as element and node numbers, varied in their distributions across the meshed region (and further differed between the solution procedure and the post-processed results), then the Coles' law model was not only non-generic but also zonal in application with regard to any given test case. The need to return boundary conditions in a global Cartesian format compounded the tendency of the model subroutines to being zonal; specification of calculated boundary conditions was then a function of the geometry of the problem. Consequently, whilst it was possible to evaluate Coles' law as an alternative to 'traditional' wall laws, the current work did not lead to a generic prototype wall model, even though the Coles' law models were based upon a generic algorithm.

A measure of confidence was gained in the implementation of the simple Coles' model, when considering its results in comparison with the proceedings of the Basel conference (1994), where a number of modelling schemes were applied to a similar U-bend test case. In that widely differing flow predictions were reported, with several modelling schemes offering little or no sign of separation, then the close correspondance

of the simple Coles' model with Kim's findings showed the general structure of the model to be valid.

However, for the simple Coles' model, where the wake function was set to unity, and the crude model for the wake parameter showed Π to be invariant throughout the model, then the variation in local velocity was governed by v^* and y^+ alone. This then meant that the principal variable in the simple Coles' model was the local velocity gradient, $\frac{dv}{dy}$.

The simple model of Coles' law, in having effectively fixed values of Π and w, was reduced to being an expression of the traditional law-of-the-wall, to which an 'arbitrary' constant had been added. Be this as it may, the general predictions of the simple model for both the U-bend and the backward facing step compared favourably with experimental data and the standard FIDAP model. The low estimates for velocity provided by the simple models were then a result of the estimate of the local velocity gradient.

From the analysis of the enhanced Coles' model, τ_o in Figure 6.38 (the value of shear stress at the wall calculated within the circus subroutine) was much lower than the corresponding post-processed results for shear stress at the boundary, τ, of the same model (Figure 6.28). Further, the values of τ from the enhanced Coles' model were less than those of the standard FIDAP model as Figure 6.26. This is direct reflection upon the method by which $\frac{dv}{dy}$ was calculated within the Coles' models. The 'improved' method by which $\frac{dv}{dy}$ was estimated , when adapting the simple Coles' model to the case of the backward facing step, showed no great advantage over the original approach, used in the U-bend. The greater values of shear stress at the boundary seen by post-processing of the velocity field imply that FIDAP calculates the local shear from the available velocity gradients in a different fashion to the Coles' models.

The low estimate of τ_o is then thought to arise from the assumption that it varies linearly from the wall out to the edge of the first elemental layer. In the absence of further information on the distribution of the velocity gradient in the near-wall region, this dubious assumption was adhered to rather than resorting to *ad hoc* numerical tuning of the model which might offer 'improved' results.

Turning to the enhanced model, the law-of-the-wake component of the velocity distribution was to be evaluated formally. Given the greater thickness of the Coles' model boundary layers in comparison with the standard model, a high value of δ was expected, hence providing a small estimate for w, the wake function. However, the simplified test

used to identify the edge of the boundary layer, lead to a prediction of δ smaller than expected. All the same, δ in Figure 6.35 was typically less than 0.25 over much of the Coles' line inspected, suggesting that Coles' law was typically being operated at a point within the inner region of the boundary layer. The main problem with the model for δ was the method by which the freestream velocity was identified. The test for the successive increase in nodal velocity normal to the wall being less than 10% worked poorly within the shapes of boundary layer encountered. As such, the value for δ was almost constant over large reaches of the Coles' line, implying no development of the boundary layer throught the model.

The comparatively large value of δ at separation and reattachment showed that the test was even poorer near to recirculation. In this instance the problem lies in the choice of an appropriate reference velocity, with the velocity within the neighbouring free shear layer being a possible candidate. However, for the current structure of the general model, the method for distinguishing between various zones in the flow that would be required to detect free shear velocity is difficult to imagine.

The singular downfall of the wake component of the model lay in the calculation of the wake parameter, Π. Whilst the value of w was low (away from the points of separation and reattachment), in keeping with the point of evaluation being in the inner boundary layer, the value of Π was almost universally near zero. As such, the enhanced model did not offer the expected advantages of Coles' law in the presence of pressure gradients. As the product Π.w was lower for the enhanced model, then the predicted velocity for the enhanced model was less than for the simple Coles' model.

The result $\Pi \approx 0$ arose from the incorrect sign allocated to the shear stress at the wall. The sign of τ_o was the same as that of the local velocity and so τ_o was negative for adverse (positive) pressure gradient. Similarly, for forward flow under a negative pressure gradient, τ_o was erroneously positive. As the signs of τ_o and $\frac{dp}{dx}$ were almost invariably opposite (when comparing Figures 6.38 and 6.36), then β was forced to take a negative value and Π tended to zero. The exception to this was at the base of the step face where the reversed flow gave an incorrect, negative value of τ_o whilst $\frac{dp}{dx}$ was negative, corresponding to the localised fall in pressure away from the step base. In this region then, the typically low value of τ_o in conjunction with a large value of $\frac{dp}{dx}$ gave an

excessive estimate of β and hence of Π. This then had to be curtailed to prevent breakdown of the solution.

An attempt was made to rectify this problem but this did not meet with success. The relationship for β was seen to be very sensitive to the precise balance between $\frac{dp}{dx}$ and τ_o in the reversed flow region. Whilst the exact nature of the problem was not identified, that it arose in the region of reversed flow where τ_o would be low (even if not underestimated as for all the Coles' models) is significant.

Insight into the nature of the U-bend and backward facing step flows was also provided by the overtly incorrect applications of the Coles' law models, where the local velocities ran counter to experience. Whilst the prescription of no wall law in Figure 6.7 showed the k-ε model to be incapable of predicting separation on its own, where a boundary layer model was provided, separation under adverse pressure gradient ensued. That this was also true for boundary layer models predicting flow against the body of the separation bubble suggests that the momentum of the core flow is as important as the near-wall viscous effects in leading to separation. This idea was bolstered by observation of an incorrect backward facing step model, where flow was reversed along the top Coles' line as Figure 6.34. This lead to greater thickening of the upper boundary layer and hence skewing of the core flow towards the free shear layer. As the momentum within the free shear layer increased, so did the entrainment with the separation bubble and so the recirculation length was further reduced below expectations.

Implementation of a wall law is not only a programming exercise but also requires understanding of the physics involved, as demonstrated by problems in current low Reynolds number k-ε modelling (Patel et al, 1985) and in the papers of the recent Basel conference (1994). Taking an overview of model results arising from the operation of Coles' law, the developed algorithms provided a good description of the selected test cases. The predictions of separation events for the U-bend and the backward facing step provided a viable alternative to the 'traditional' model of Haroutunian and Engelman (1991): furthermore, in seeking to incorporate pressure gradient effects into the near-wall modelling scheme used in conjunction with the freestream model, the applicability of the standard high Reynolds number k-ε turbulence model to transient flow has been improved. The robustness of the Coles' law model developed here was further demonstrated in the mesh density experiments of Figures 6.47-6.48, where coarsening of local mesh density was still seen to offer reasonable flow predictions.

8. Conclusions.

i) The use of the standard, high Reynolds number k-ε model was identified as a cost-effective tool for the analysis of turbulent, wall-bounded flows, subject to sensible prescription of boundary conditions.

ii) Theoretical consideration of prevalent wall models showed them to be unsuitable for the analysis of pressure-driven or transient flows.

iii) The selection of appropriate CFD results for comparison with experimental data was shown to be critical to their valid interpretation.

iv) Current CFD techniques, when compared with experimental data, do not offer a suitable model in the near-wall region. Transient modelling results show pressure gradient and y^+ to be time-dependent.

v) Coles' law was identified as offering a potentially more robust wall model.

vi) In comparison with both experimental data and the standard FIDAP model of Haroutunian and Engelman (1991), the Coles' law models provided good general flow predictions.

vii) The method by which wall models are implemented markedly affects computational results.

viii) The simple U-bend model was effectively an application of the classic law-of-the-wall, to which a constant, extra term had been added.

ix) Given the favourable response of the simple U-bend model in comparison with experiment and the standard FIDAP model, it provided a viable framework within which to develop a complete model of Coles' law.

x) Analysis of the simple Coles' law model showed it to reduce to the application of the

classic law-of-the-wall, to which a constant, extra term had been added. However, in predicting the general flow of the U-bend at least as well as the standard FIDAP model and also in comparison with a range of U-bend analyses using a variety of wall models, the simple Coles' model was seen to offer a viable framework within which to develop a complete model of Coles' law.

xi) In the absence of a significant estimate of the wake component of Coles' law, the predicted velocity was seen to hinge upon the estimate of the local shear stress at the wall and hence upon the determination of the velocity gradient. By comparison of shear stress values within the model subroutine with post-processed boundary stresses for the same model, the velocity gradient model was shown to be deficient.

xii) The differing approach in the estimation of y^+ between the Coles' law and standard FIDAP models made detailed comparison of local velocities between the models somewhat involved. However, in seeking to improve the Coles' model, greater concern is experienced for the accurate evaluation of the local velocity gradient. The validity of the substitution of $\left(C_\mu^{1/2}k_t\right)^{1/2}$ for v^* in the equation for y^+ is questionable in its suitability for pressure driven flows. Whilst the altered equation for y^+ in the FIDAP model is somewhat peripheral to the desired end goal of a more robust wall model, the necessary preparation of more suitable boundary conditions for k and ε would allow the relationship between v^* and $\left(C_\mu^{1/2}k_t\right)^{1/2}$ to be tested.

xiii) The wake component of the enhanced Coles' model was flawed. The low estimate for the wake function (away from duct inlet and from the separation bubble) was reasonable, given the close proximity of the Coles' lines to the walls. However, the model was somewhat crude, with the value of δ not increasing proportionately with observed boundary layer growth.

The error in the evaluation of wall shear stress and hence of Clauser's equilibrium parameter caused the wake parameter of the enhanced model to be largely negligible. The correction of this fault had the greatest effect within the reversed flow: in regions of forward flow under favourable pressure gradient, β was correctly favourable in the faulty model but for the wrong reasons. Within the separation bubble, the β - Π model of Das was seen to be very sensitive to the precise balance between pressure gradient and shear stress. Whilst the shear stress was underestimated, future improvements to the Coles'

model will have to concentrate on the response of β to variations in τ_o.

xiv) The implementation of early Coles' models with aberrant flow directions showed that the momentum of the core flow riding over the separation bubble had a marked effect on flow behaviour, with wall conditions being less significant than previously supposed.

xv) In summing up this work, in comparison with the aims laid out in Section 2.5, the need for a more robust wall law was clearly shown by studies of a transient, three-dimensional flow. Definite progress was also made towards the development of just such a wall model.

9. Recommendations for Further Work.

The improvements necessary for the continued development of the Coles' law model are laid out briefly below:

i) first and foremost, the correct description of the velocity gradients in the near-wall region,

ii) the use of velocity gradients in the detection of the boundary layer thickness,

iii) the mixing length equation in the model for k and ε at the edge of the Coles' model is faulty but these conditions require to be replaced by a more significant model anyway,

iv) investigation of the claim made by Haroutunian and Engelman (1991) that $v^* = \left(C_\mu^{1/2} k_t\right)^{1/2}$, which would be possible once having satisfied (iii) above,

v) investigation of possible *reductions* in model dependency on problem geometry, with a view to developing a generic Coles' law wall model,

vi) analysis of the problem in the β - Π relationship for reversed flow. Extension of the modelling system to embrace the wake velocity approach of Kline, Bardina and Strawn (1983) might be merited, where the wake velocity function remains positive and finite across the region of separation and finally

vii) exploration of the effect of applying the Coles' model to a series of elemental layers adjacent to the wall, observing the increased influence of the wake as y^+ thus rises.

Bibliography.

Baxendale, A.J. (1993).*The Role of Computational Fluid Dynamics in Exhaust System Design and Development.* Warrendale: Society of Automotive Engineers, S.A.E. paper 931072, 25-37.

Bird, R.B., Stewart, W.E. and Lightfoot, E.N. (1966) *Transport Phenomena*. New York: John Wiley and Sons.

Boussinesq, J. (1877) Theorie de l'ecoulement tourbillant. *Mem. pres. Acad. Sci*, **23**, 46.

Clauser, F.H. (1954). Turbulent boundary layers in adverse pressure gradients. *Journal of the Aeronautical Sciences*, **21**, 91-109.

Clauser, F.H. (1956). The turbulent boundary layer. *Advances in Applied Mechanics*, **4**, 1-51.

Coles, D. (1956). The law of the wake in the turbulent boundary layer. *Journal of Fluid Mechanics*, **1**, 191-226.

Coles, D.E. and Hirst, E.A. (1968). Computation of turbulent boundary layers - 1968. In: *Proceedings of the AFORS-IFP Stanford conference Stanford University, Stanford, California*, **2**.

Das, D.K. (1987). A numerical study of turbulent separated flows. *American Soceity of Mechanical Engineers Forum on Turbulent Flows*, **FED vol 51**, 85-90.

Das, D.K. (1988). A simple theory for calculating turbulent boundary layers under arbitrary pressure gradients. *International Journal of Engineering Fluid Mechanics*, **1**, 83-99.

Deb, M., Diner, A.I. and Ray, I. (1994). Benchmark problem no.1. In: *9th Annual*

Conference of the International Hightech-Forum - Basel World CFD User Days 1994, Basel, 1-5 May, 1994. Basel: World User Asscosciation in Applied Computational Fluid Dynamics.

Dengel, P. and Fernholz, H.H. (1990). An experimental investigation of an incompressible turbulent boundary layer in the vicinity of separation. *Journal of Fluid Mechanics*, **212**, 615-636.

Driver, D.M. and Seegmiller, H.L. (1985). Features of reattaching turbulent shear layer in divergent channel flow. *American Institute of Aeronautics and Astronautics Journal*, **23**, 163-171.

Emmons, H.W. (1970). Critique of Numerical Modeling of fluid mechanics phenoma. *Annual Review of Fluid Mechanics*, **2**, 15-36.

Engelman, M. (1994). WUA-CFD test case 1/93. In: *9th Annual Conference of the International Hightech-Forum - Basel World CFD User Days 1994, Basel, 1-5 May, 1994*. Basel: World User Asscosciation in Applied Computational Fluid Dynamics.

FIDAP7 Examples Manual. (1994). Chicago: Fluid Dynamics International Inc.

FIDAP7 FIMESH Manual. (1994). Chicago: Fluid Dynamics International Inc.

FIDAP7 FIPOST Manual. (1994). Chicago: Fluid Dynamics International Inc.

FIDAP7 Theory Manual. (1994). Chicago: Fluid Dynamics International Inc.

Ginter, F., Heitele, M. and Ruprecht, A. (1994). WUA-CFD benchmark 1/93. In: *9th Annual Conference of the International Hightech-Forum - Basel World CFD User Days 1994, Basel, 1-5 May, 1994*. Basel: World User Asscosciation in Applied Computational Fluid Dynamics.

Göhner, U. (1994). Benchmark solutions of the FLOTRAN^{R} program. In: *9th Annual*

Conference of the International Hightech-Forum - Basel World CFD User Days 1994, Basel, 1-5 May, 1994. Basel: World User Asscosciation in Applied Computational Fluid Dynamics.

Haroutunian, V. (1991). Turbulent Flows With FIDAP Seminar Notes, *FIDAP User Conference, Paris, May 1991*. Chicago: Fluid Dynamics International Inc.

Haroutunian,V. and Engelman, M.S. (1991). On modeling wall-bound turbulent flows using specialized near-wall finite elements and the standard k-ε turbulence model. In: *FED - Vol 117, Advances in Numerical Simulation of Turbulent Flows: The First ASME-JSME Fluids Engineering Conference, Portland, Oregon, 23-27 June 1991*. New York: American Society of Mechanical Engineers, 97-104.

Hinze, J.O. (1975). *Turbulence*. 2nd ed. New York: McGraw-Hill.

Jones, I.P. and Hope, C.B. (1994). Axi-symmetric isothermal turbulent flow in a narrowing bend. In: *9th Annual Conference of the International Hightech-Forum - Basel World CFD User Days 1994, Basel, 1-5 May, 1994*. Basel: World User Asscosciation in Applied Computational Fluid Dynamics.

Jones, W.P. and Launder, B.E. (1972). The prediction of laminarization with a two-equation model of turbulence. *International Journal of Heat and Mass Transfer*, **15**, 301-314.

Kaitkis, L., Karniadakis, G.E. and Orszag, S.A. (1991). Onset of three-dimensionality, equilibria and early transition in flow over a backward facing step. *Journal of Fluid Mechanics*, **231**, 501-528.

Kim, J.J. (1978). *Investigation of Separation and Reattachmant of a Turbulent Shear Layer Flow Over a Backward Facing Step*. Stanford: Ph.D. thesis, Stanford University.

Kleinstein, G. (1967). Generalized law of the wall and eddy-viscosity model for wall

boundary layers. *American Institute of Aeronautics and Astronautics*, 5(8), 1402-1407.

Kline, S.J., Bardina, J.G. and Strawn, R.C. (1983). Correlation of the detachment of two-dimensional turbulent boundary layers. *American Institute of Aeronautics and Astronautics*, 21(1), 68-73.

Launder, B.E. (1984). Second-moment closure: methodology and practice. In: *Turbulence Models and their Applications*, 2. Paris: Eyrolles.

Launder, B.E. and Shima, N. (1989). Second-moment closure for the near-wall sublayer: development and application. *American Institute of Aeronautics and Astronautics Journal*, 27(10), 1319-1325.

Launder, B.E. and Spalding, D.B. (1972). *Mathematical Models of Turbulence.* London: Academic Press.

Launder, B.E. and Spalding, D.B. (1974). The numerical computation of turbulent flows. *Computer Methods in Applied Mechanics and Engineering*, 3(3), 269-289.

Leschziner, M.A. (1989). Application of second-moment closure in complex flows. In: *Proceedings of the International Forum on Mathematical Modelling of Processes in Engineering Systems, Sarajevo, March 1989*. Sarajevo: IFMMPES.

Lindgren, E.R. (1965). *Experimental Study on Turbulent Pipe Flows of Distilled Water.* Oklahoma State University: Civil Engineering Department, Report 1AD621071.

Mellor, G.L. and Gibson, D.M. (1966). Equilibrium turbulent boundary layers. *Journal of Fluid Mechanics*, 24, 225-253.

Patel, V.C., Rodi, W. and Scheuerer, G. (1985). Turbulence models for near-wall and low Reynolds number flows: a review. *American Institute of Aeronautics and Astronautics Journal*, 23(9), 1308-1319.

Perry, A. and Schofield, W.H. (1973). Mean velocity and shear stress distributions in

turbulent boundary layers. *The Physics of Fluids*, **16**, 2068-2074.

Prandtl, L. (1925).Über die ausgebildete Turbulenz. *Z. Angew Mech*, **5**, 136-139.

Prandtl, L. (1933). In: *Collected Works, (1961)*. **1-3**, Berlin: Springer.

Rashid, T.M. (1993). *Computational Modelling of Dynamic Wind Effects Relating to Compliant Offshore Structures*. Hatfield: University of Hertfordshire.

Reichardt, H. (1951). Vollständige Darstellung der turbulenten Gesschwindigkeitsverteilung. *Z.A.M.M.*, **31**, 208-219.

Rodi, W. (1975). A note on the empirical constant in the Kolmogorov-Prandtl eddy-viscosity expression. *Transactions of the A.S.M.E. Journal of Fluid Engineering*, **97**(3), 386-389.

Rodi, W. (1991). Examples of turbulence model applications. In: *von Karman Institute for Fluid Dynamics Lecture Series 1991-92, 18-21 March 1991*. Brussels: vKI, 1-28.

Sandborn, V.A., and Shin, J.C. (1988). Water flow measurements in a 180 degree turn-around rectangular duct. In: *Proceedings of the 6th SSME CFD Workshop, NASA Marshall Space Flight Centre, Huntsville, Alabama, 26-28 April 1988*. Huntsville: SSME.

Schlichting, H. (1979). *Boundary Layer Theory*. 7th ed. New York: McGraw-Hill.

Schofield, W.H. (1981). Equilibrium boundary layers in a moderate to strong adverse pressure gradient. *Journal of Fluid Mechanics*, **113**, 91-122.

Schofield, W.H. (1986). Two-dimensional separating turbulent boundary layers. *American Institute of Aeronautics and Astronautics*, **24**, 1611-1620.

Sharma, L.K. and Ostermier, B.J. (1987). In: *Proceedings of the 5th SSME CFD*

Workshop, NASA Marshall Space Flight Centre, Huntsville, Alabama, 21-23 April 1987. Huntsville: SSME.

Spalart, P.R. (1988). Direct simulation of a turbulent boundary layer up to Re = 1400. *Journal of Fluid Mechanics*, **187**, 61-98.

Spalding, D.B. (1961). A single formula for the law of the wall. *Journal of Applied Mechanics*, **28**, 455-458.

Taklanti, A. (1993). Numerical simulation of internal flows in the automotive industry. In: Murthy, T.K.S. and Brebbia, C.A. (eds). *Supercomputing in Fluid Flow*. Southampton: Computational Mechanics Publishers, 331-351.

Tennekes, H. and Lumley, J.L. (1972). *A First Course in Turbulence*. Cambridge, Massachusetts: The M.I.T. Press.

van Driest, E.R. (1956). On turbulent flow near a wall. *Journal of the Aeronautical Sciences*, **23**, 1007-1011.

von Karman, T. (1930). Mechanische Ahnlicchkeit and Turbulenz. *Nach. Ges. Wiss. Gottingen, Math. Phys. Klasse*, **58**.

Wahls, R.A., Burnwell, R.W. and DeJarnette, F.R. (1989). Defect stream function, law of the wall/wake method for compressible turbulent boundary layers. *American Institute of Aeronautics and Astronautics Journal*, **28**(1), 1432-1439.

Warsi, Z.U.A. (1993). *Fluid Dynamics - Theoretical and Computational Approaches*. Boca Raton: CRC Press Inc., 505-509.

White, F.M. (1991). *Viscous Fluid Flow*. 2nd ed. New York: McGraw-Hill, 394-495.

Wieghardt, K. (1943). *Über die Wandschubspannung in turbulenten Reibungs-schichten bei veränderlichem Aussendruck.*. Göttingen: U & M.

Appendix A1. Experimental Measurement of Flow Within the Inlet Manifold.

A1.1. Preparation and Use of a Flow Angle Meter.

In wanting to take a number of discrete velocity distribution samples along the length of the main duct of the manifold, the type of processed test results required must first be considered. To draw direct comparison with FIDAP results, the experiment should yield velocity distributions for v_x, v_y and v_z. A simple probe of the Pitot-static type, whilst yielding the total flow velocity at a point, would not provide data relating to the individual velocity components as it would not assess the local flow angle, being the angle between the local velocity vector and the main, longitudinal x-axis of the duct. As such, a probe was required that could measure both total flow velocity and flow angle. Given that the flow to be measured was three-dimensional, the flow angle would then have both horizontal and vertical components, deemed yaw and pitch respectively. Furthermore, for one intended probe to be able to measure horizontal *and* vertical velocity distributions across the section the duct, the probe calibration for yaw and pitch for, say, a velocity sample taken vertically across the duct, would have to serve as pitch and yaw calibrations for a corresponding horizontal traverse of the duct at the same station. As such, the probe used may be best described as a flow angle meter and is depicted in Figure A1.1 below.

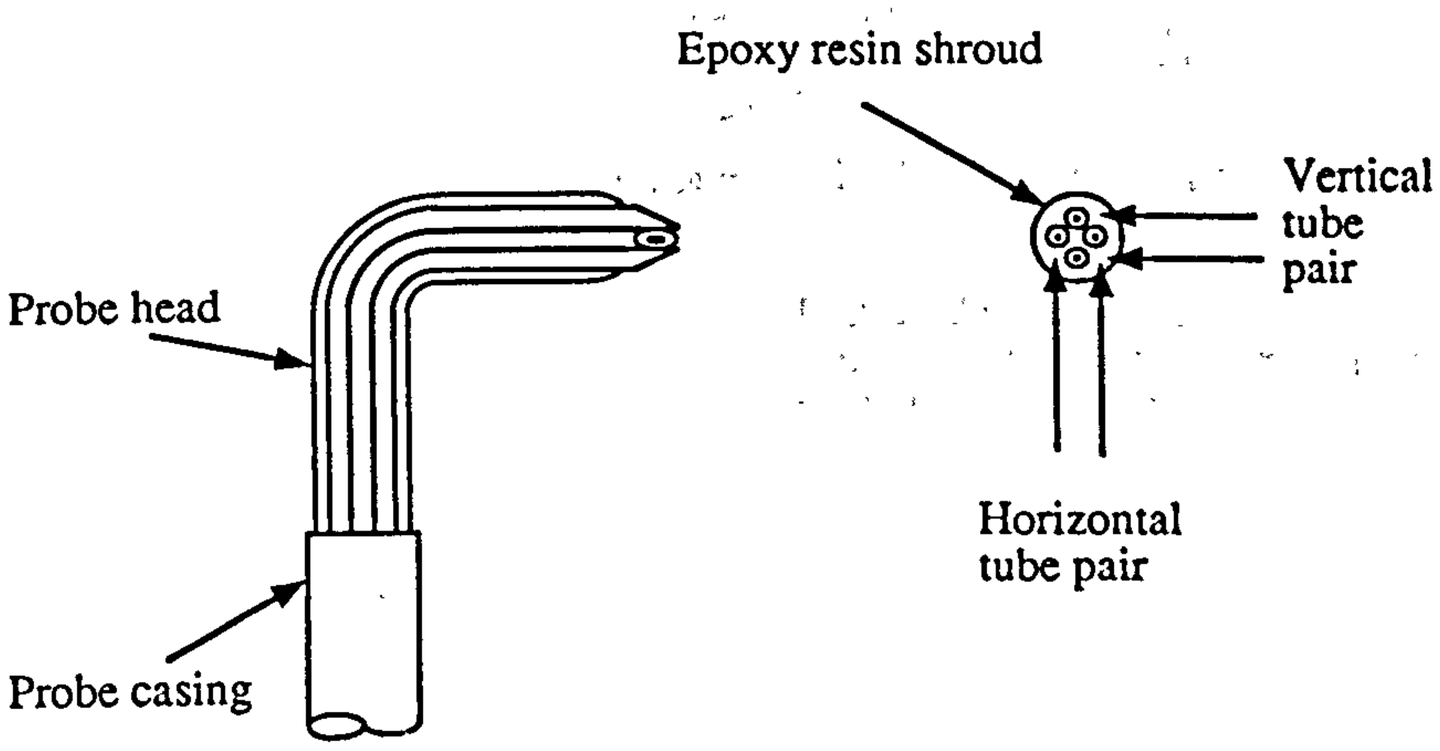

Figure A1.1. Showing the construction of the flow angle meter.

Ideally, the probe should be as slight as is practicable in order that it not disturb the

passage of the flow being measured. The duct cross-section at stations I and II was approximately 60x70mm and the finest, steel capillary tubing that was available had internal and external diameters of 0.6 and 0.8mm respectively. As such, four of these capillary tubes could be mounted in a brass tubing sheath of 3.2mm external diameter, providing the simplest form of combined pitch and yaw meter possible.

The brass sheath secured the capillary tubes in relation to one another and also acting as a sliding mount for traversing the probe across the duct. That section of the probe that stood proud of the sheath was held together and 'streamlined' by a shroud of epoxy resin that served to smooth the exterior of the probe as presented to the flow.

The probe, as described, was capable of evaluating θ_h and θ_v, the horizontal and vertical components of the flow angle, θ. The tip of each capillary tube was at an angle of 30° to its major axis, as shown in Figure A1.1, so that the pitch and yaw components of the meter were designed to act exclusively. In order to measure the total velocity of the flow, a form of Pitot-static arrangement was required. In order to provide a probe of slender section in comparison with the duct cross-section, there was space for neither a formal stagnation nor a static tapping at the probe head. The method by which these results were then obtained is detailed in Figure A1.2 below, showing the method by which the probe was mounted in the inlet manifold duct.

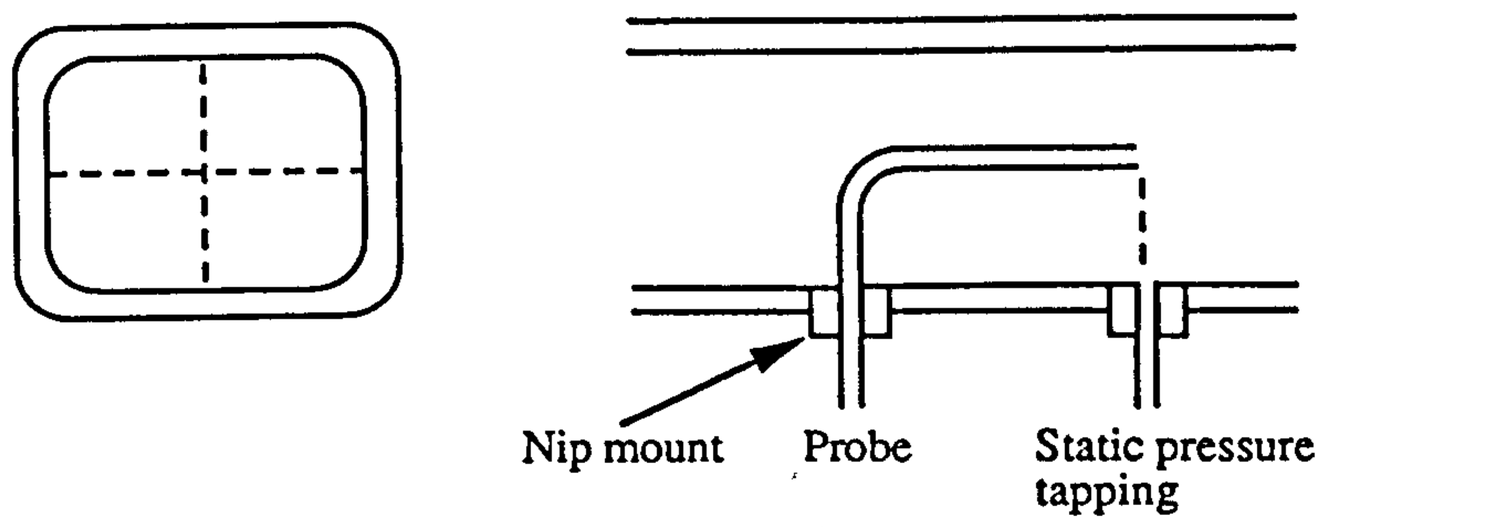

Transverse cross-section of manifold, showing probe path

Longitudinal section of manifold, showing relative position of probe and static pressure tapping

Figure A1.2. Showing the mounting of the flow angle meter in the manifold duct.

Figure A1.2 shows transverse and longitudinal sections of the manifold for stations I and II. The longitudinal section shows the probe in situ for vertical traversing of the duct. The probe can move freely normal to the duct wall and be secured at any given position by tightening a nip mount at the wall. This mount consisted of a hollow stud

threaded into the manifold wall. The probe sheath could move freely with respect to the stud and be clamped down by use of a locknut that forced an olive ring to pinch the sheath. This locknut had to be tightened carefully to allow for secure location of the probe without crushing of the probe sheath.

At a distance upstream of the probe mounting point equal to the streamwise length of the probe, a static pressure tapping was drilled in the manifold wall. As the static tapping was in the same plane as the tip of the probe, static pressure readings were taken on the assumption that at any point downstream of the manifold entrance, the static pressure was then constant across the entire cross-section of the duct at that point. The stagnation pressure reading was then obtained by assuming it to equal the average of the pressure readings taken from the four capillary tubes comprising the probe tip.

The transverse cross-section of the manifold, shown in Figure A1.2, shows the horizontal and vertical paths along which the probe traversed the manifold. The experiment then gave one horizontal and one vertical velocity profile at station I and at station II along the length of the manifold.

In order to calibrate the flow angle meter, it was placed in an open-jet, recirculating wind tunnel, as shown in Figure A1.3 below.

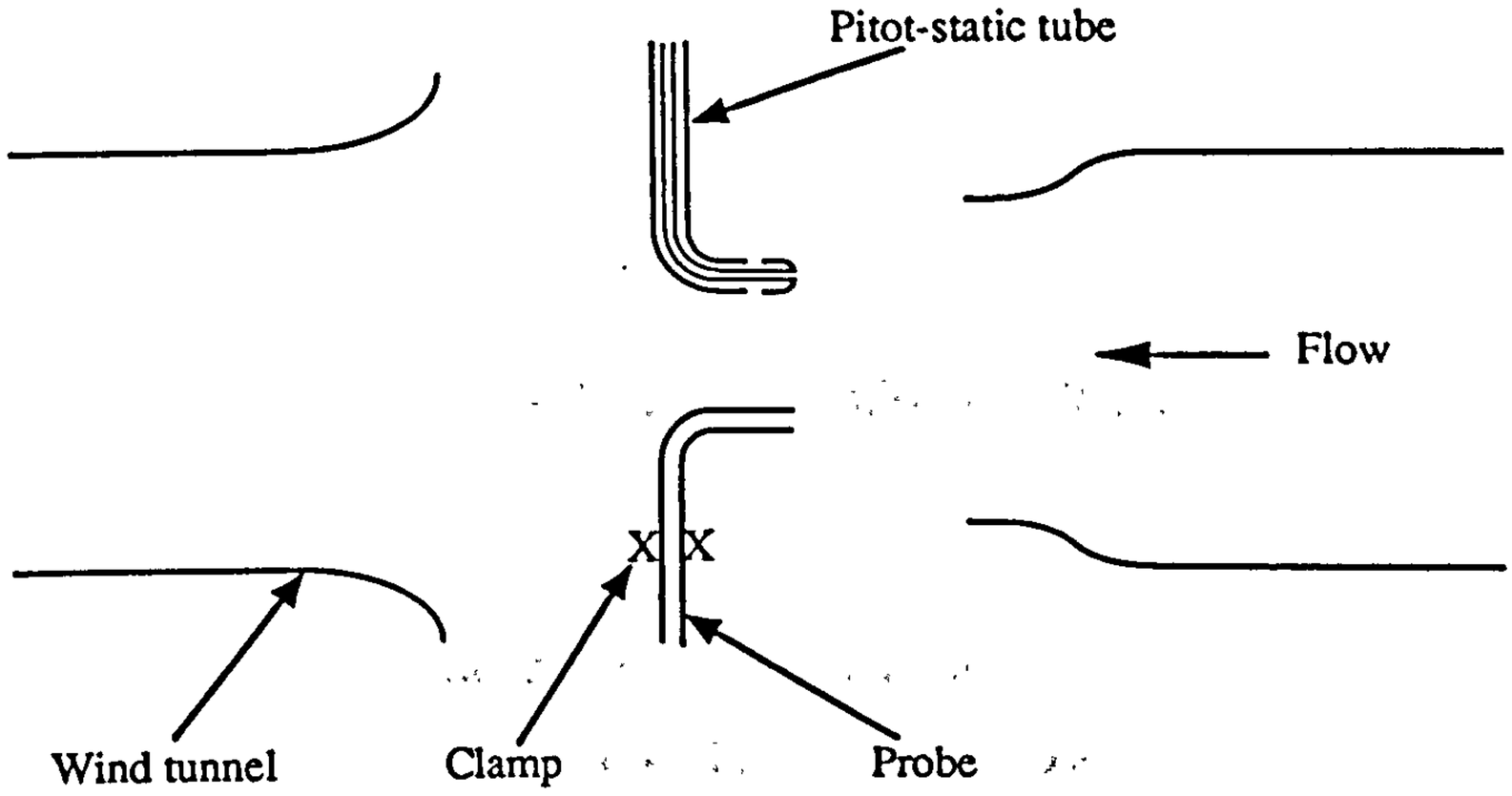

Figure A1.3. Showing the flow angle meter mounted in a wind tunnel for calibration purposes.

The probe was held in position in the wind tunnel by a simple clamp that allowed the inclination of the probe to the flow to be set to the desired value. The horizontal and vertical tube pairs of the probe were connected to an air-on-water U-tube manometer bank. The inclination of the manometer bank to the horizontal could be varied to provide signal amplification. A separate Pitot-static tube was also mounted in the flow to measure

its dynamic pressure.

The flow angle meter was calibrated in both the horizontal and vertical planes by setting the probe at a known angle to the flow and then reading, for each tube pair, the difference in head across the tube pair as recorded at the manometer bank. For each reading, the dynamic head from the Pitot-static tube was also recorded.

The inclination of the probe to the flow was measured by use of a protractor scale fixed to the clamp holding the probe in position in the flow. For both horizontal and vertical calibration of the flow angle meter, results were taken in 5° steps for probe inclinations from -45° to +45° normal to the flow. The sign convention used to denote the flow angle, for both calibration and subsequent practical use, is given by Figure A1.4.

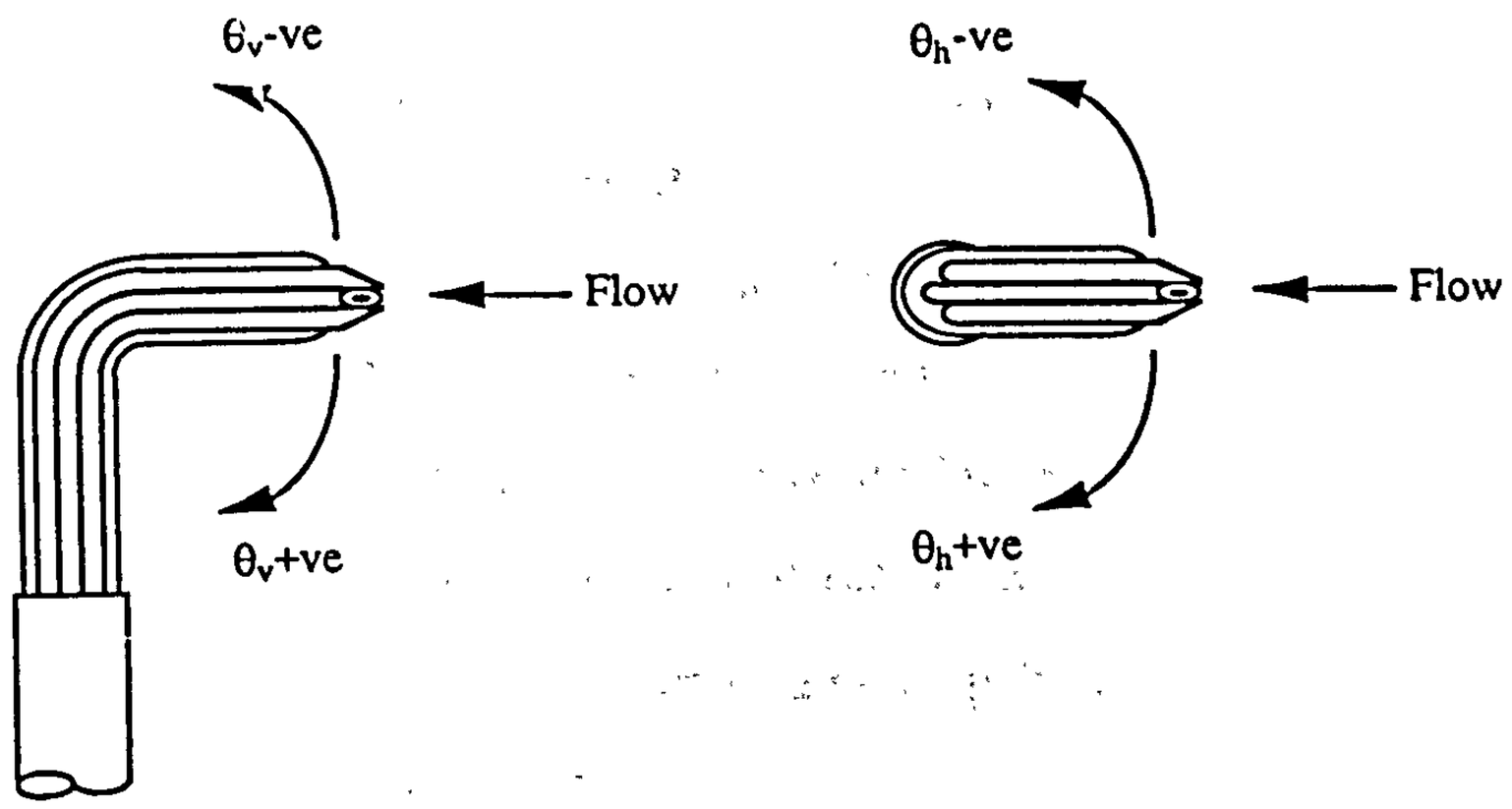

Figure A1.4. Flow angle sign convention in relation to the main, longitudinal x-axis of the inlet manifold.

Having thus calibrated the flow angle meter by recording its response when inclined at known angles to the flow, it could then be used to analyse the flow in the inlet manifold. In this instance, for each given step in the probe's passage across the duct, it had the same nominal inclination to the flow; at all times, the longitudinal axis of the probe head was held parallel to the main axis of the inlet manifold.

Velocity profiles were then taken, both horizontally and vertically at each station, by traversing the duct in 5mm steps. Initially, trouble was experienced in trying to take readings that could be repeated or even read: the readings at the manometer bank were found to fluctuate both rapidly and wildly about a given point. Considering the transient nature of the flow under consideration and the measurement technique used, the response

time of a pressure tapping-manometer combination should yield a time-averaged measurement of the true, transient flow. The instability in the readings was then held to arise from the too quick a response from the manometer columns and hence to be caused by insufficient signal damping. This problem was then solved by introducing extra damping to the system in the form of glass capillary links at inlet to each manometer leg. Each glass link consisted of a glass rod, roughly 20mm in length, through which was drilled a hole of comparable internal diameter to that of the probe's capillary tubing. These glass links then acted as fluid capacitors.

A1.2. Processing of Results.

Before presenting the results of the probe calibration, the methods by which the results were analysed will be detailed.

Consider first the readings taken in calibrating the flow angle meter. For the flow angle meter of Figure A1.1, the horizontal tube pair correspond to a pressure head reading, Δh_h, at the manometer bank, the vertical tube pair to Δh_v and the dynamic pressure head across the Pitot-static tube is read as Δh_{dyn}.

The pressure difference, Δp, across a given pair of tubes is related to the head recorded at the manometer, Δh, by

$$\Delta p = \rho_m g \Delta h$$

where ρ_m is the density of the manometer fluid.

For a given flow angle, θ, a non-dimensionalized pressure coefficient, C_p, may be written as

$$C_p = \frac{\Delta p \text{ across a tube pair}}{\text{dynamic pressure}}$$

where dynamic pressure = p_o-p = stagnation pressure - static pressure, as given by the Pitot-static tube.

$$\text{So} \quad C_p = \frac{\rho_m g \Delta h}{\rho_m g \Delta h_{dyn}} = \frac{\Delta h}{\Delta h_{dyn}}$$

and the horizontal and vertical pressure coefficients may be written as

$$C_{ph} = \frac{\Delta h_h}{\Delta h_{dyn}} \qquad : \qquad C_{pv} = \frac{\Delta h_v}{\Delta h_{dyn}}$$

As the pressure coefficient is a ratio comparing two pressure heads read from the same manometer bank, the inclination of the manometer bank (used to amplify the readings for ease of inspection) does not need to be taken into account.

By preparing pressure coefficients for each prescribed flow angle, when these coefficients are plotted against flow angle, a calibration graph is obtained. When the probe is used to measure a practical flow, by calculating the horizontal and vertical pressure coefficients at a point in that flow, they can be used in conjunction with the calibration graphs to provide the flow angle, θ.

For such a flow angle meter, for moderate flow angles of up to $\pm$ 45°, an approximately linear relationship between C_p and θ would be expected. Furthermore, for an accurately machined device, when calibrating the meter in one plane, say the horizontal, the corresponding response of the vertical tube pair to movement in the horizontal plane should be negligible, giving $C_{pv} = 0$ as C_{ph} varies with θ. (The converse should be true as well.)

Now consider the use of the flow angle meter to measure the total flow velocity, v_t. For a Pitot-static tube,

$$v_t = \sqrt{\frac{2(p_o - p)}{\rho_a}} \qquad \text{and} \qquad p_o - p = \rho_m g \Delta h_{dyn}$$

where ρ_a is the density of the fluid flow being measured.

$$\text{So} \quad v_t = \sqrt{\frac{2\rho_m g \Delta h_{dyn}}{\rho_a}}$$

The above result will hold true for a well machined Pitot-static tube for small flow angles of up to ± 15° or so. In this instance, the inclination of the manometer bank, ϕ, is important. For a given amplified reading of Δh_{dyn} for a given value of ϕ, the corrected dynamic head will be $\Delta h_{dyn} \sin\phi$ and so the total flow velocity is given by

$$v_t = \sqrt{x \Delta h_{dyn}} \qquad \text{where} \qquad x = \frac{2\rho_m g \sin\phi}{\rho_a}$$

Having calculated C_{ph}, C_{pv} and v_t and used the calibration graphs to obtain θ_h and θ_v, the velocity components v_x, v_y and v_z may be obtained simply, as shown in Figure A1.5 below.

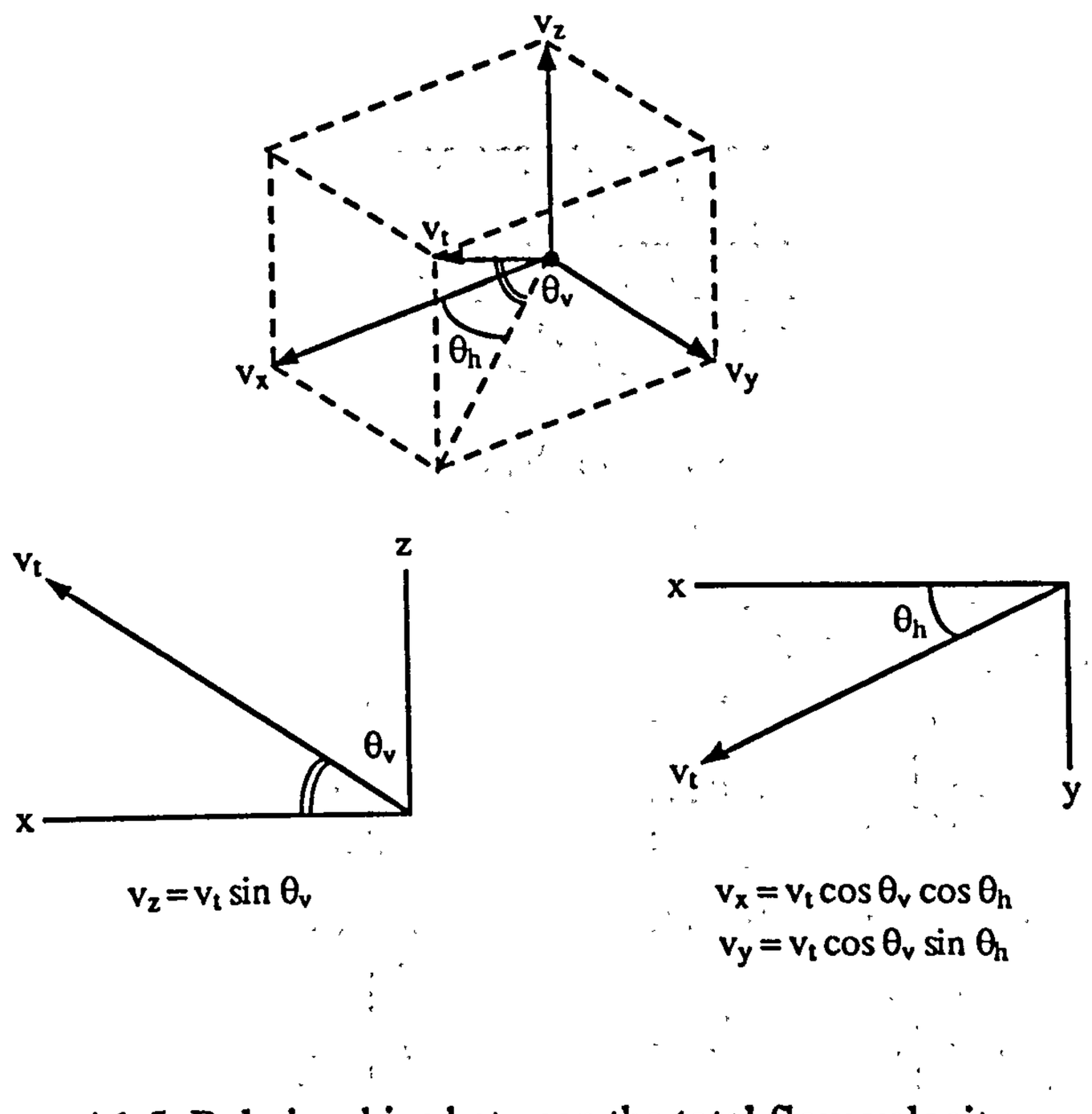

Figure A1.5. Relationships between the total flow velocity, v_t, and its components v_x, v_y and v_z.

Note that the transformations given in Figure A1.5 and the sign conventions for flow angle given in Figure A1.4 lead to values for v_x, v_y and v_z in keeping with FIDAP's

sign convention.

A1.3. Tabulated Calibration and Test Results for the Inlet Manifold.

Note that in the following tables, unless otherwise specified, the following units are used

i) all manometer readings, Δh_h, Δh_v and Δh_{dyn} in inches,

ii) v, v_x, v_y and v_z in m/s,

iii) θ_h and θ_v in degrees and

iv) C_{ph} and C_{pv} are dimensionless.

Table A1.1. Manometer readings for the horizontal calibration of the flow angle meter.

Angle of inclination	Manometer readings											
	South		North		West		East		Stagnation		Static	
	Up	Down	Up	Down	Up	Down	Up	Down	Up	Down	Up	Down
45	29.30		32.15		15.50		40.80		26.20		15.40	
40	27.00	26.95	29.30	29.00	15.95	16.45	39.20	38.70	26.40	26.50	15.80	16.30
35	25.75	25.60	26.40	25.85	16.30	16.75	37.60	37.00	26.60	26.65	16.10	16.45
30	24.60	24.40	24.35	23.80	17.00	17.10	35.35	34.85	26.70	26.80	16.55	16.60
25	23.45	23.45	23.20	23.20	17.45	17.50	32.55	32.50	26.85	26.90	16.70	16.70
20	22.90	22.90	23.20	23.20	18.00	18.05	30.90	30.75	26.90	26.95	16.80	16.75
15	22.20	22.40	23.20	23.35	18.50	19.00	29.20	28.95	26.95	27.00	16.70	16.80
10	22.20	22.10	23.30	23.30	20.00	20.10	27.40	27.10	27.00	27.00	16.85	16.80
5	22.00	22.00	23.20	23.15	21.60	21.60	25.35	25.30	27.00	27.00	16.85	16.80
0	21.95	21.95	23.40	23.20	23.15	23.25	23.30	23.15	27.00	27.00	16.95	16.85
-5	21.95	22.00	23.30	23.20	24.90	25.05	21.45	21.25	27.00	27.05	17.00	16.80
-10	21.80	21.80	23.30	23.25	26.60	26.75	19.95	19.80	27.00	27.05	17.00	16.85
-15	21.45	21.45	23.55	23.55	28.40	28.40	18.65	18.75	27.00	27.00	16.60	16.80
-20	21.45	21.50	23.90	24.00	30.60	30.50	17.85	18.00	27.00	27.00	16.60	16.75
-25	21.90	21.90	24.50	24.50	32.50	32.40	17.35	17.50	26.90	26.90	16.55	16.70
-30	22.45	22.40	25.30	25.30	34.00	34.20	17.20	17.05	26.80	26.80	16.70	16.60
-35	23.10	23.05	26.35	26.35	35.80	35.95	16.85	16.75	26.70	26.70	16.60	16.50
-40	23.90	24.00	27.80	27.90	37.60	37.70	16.60	16.55	26.60	26.60	16.45	16.40
-45	26.20		29.30		38.90		16.40		26.45		16.30	

Table A1.2. Processed test results of the horizontal calibration of the flow angle meter.

Angle of inclination	Δh_v	Δh_h	Δh_{dyn}	C_{pv}	C_{ph}
45	-2.85	-25.30	10.80	-0.26	-2.34
40	-2.18	-22.75	10.40	-0.21	-2.19
35	-0.45	-20.73	10.35	-0.04	-2.01
30	0.42	-18.05	10.18	0.04	-1.78
25	0.25	-15.05	10.18	0.02	-1.48
20	-0.30	-12.80	10.15	-0.03	-1.27
15	-0.98	-10.32	10.23	-0.95	-1.01
10	-1.15	-7.20	10.18	-0.12	-0.71
5	-1.18	-3.73	10.18	-0.12	-0.37
0	-1.35	-0.13	10.10	-0.13	0.00
-5	-1.28	3.63	10.13	-0.13	0.36
-10	-1.48	6.70	10.10	-0.15	0.68
-15	-2.10	9.70	10.30	-0.21	0.95
-20	-2.48	12.63	10.33	-0.24	1.23
-25	-2.60	15.03	10.28	-0.25	1.46
-30	-2.88	16.98	10.15	-0.28	1.67
-35	-3.28	19.08	10.15	-0.32	1.88
-40	-3.90	21.08	10.18	-0.38	2.07
-45	-3.10	22.50	10.15	-0.31	2.22

Table A1.3. Manometer readings for the vertical calibration of the flow angle meter.

Angle of inclination	Manometer readings											
	South		North		West		East		Stagnation		Static	
	Up	Down	Up	Down	Up	Down	Up	Down	Up	Down	Up	Down
45	15.95		44.5		32.40		31.10		25.95		15.8	
40	16.20	16.70	41.70	40.75	30.60	30.00	28.80	28.40	26.15	26.25	16.00	16.60
35	16.40	16.90	39.00	38.50	28.80	28.65	26.45	26.65	26.35	26.40	16.25	16.75
30	16.65	17.10	36.40	35.85	27.15	26.95	24.50	24.65	26.55	26.55	16.50	16.95
25	17.00	17.40	33.85	33.70	25.15	25.15	23.00	23.30	26.70	26.70	16.65	17.05
20	17.50	17.85	31.70	31.45	24.55	24.50	22.50	22.65	26.80	26.80	17.00	17.15
15	19.30	18.40	29.20	29.15	24.60	24.55	22.25	22.35	26.85	26.85	17.10	17.20
10	19.00	19.15	27.45	27.35	24.75	24.60	21.90	22.00	26.90	26.90	17.15	17.20
5	20.00	20.10	25.50	25.40	24.35	24.30	21.65	21.75	26.95	27.00	17.20	17.25
0	21.25	21.40	23.45	23.35	24.15	24.05	21.60	21.80	27.00	27.00	17.25	17.30
-5	22.60	22.80	21.75	21.70	23.90	23.85	21.80	22.00	27.00	27.00	17.25	17.35
-10	24.00	24.10	20.50	20.50	23.70	23.70	21.90	22.00	27.00	27.00	17.20	17.35
-15	25.40	25.55	17.50	19.60	23.75	23.75	21.95	22.05	27.00	27.00	17.20	17.35
-20	26.95	27.00	18.75	18.80	24.10	24.10	22.00	22.10	26.95	26.95	17.25	17.30
-25	28.60	28.65	18.05	18.20	24.75	24.80	22.30	22.40	26.90	26.90	17.15	17.25
-30	30.40	30.35	17.55	17.70	25.60	25.60	23.00	23.10	26.80	26.80	17.10	17.20
-35	32.05	32.15	17.25	17.30	26.70	26.80	24.00	24.05	26.70	26.65	17.00	17.05
-40	33.80	33.70	17.00	17.05	28.45	28.35	25.10	25.00	26.55	26.60	16.90	16.95
-45	34.75		16.90		30.00		26.40		26.45		16.80	

Table A1.4. Processed test results of the vertical calibration of the flow angle meter.

Angle of inclination	Δh_v	Δh_h	Δh_{dyn}	C_{pv}	C_{ph}
45	-28.55	1.30	10.15	-2.81	0.13
40	-23.78	1.70	9.90	-2.50	0.18
35	-22.10	2.18	9.87	-2.24	0.22
30	-19.25	2.48	9.83	-1.96	0.25
25	-16.58	2.00	9.85	-1.69	0.20
20	-13.90	1.95	9.73	-1.43	0.20
15	-10.83	2.28	9.70	-1.12	0.24
10	-8.33	2.73	9.73	-0.86	0.28
5	-5.40	2.63	9.75	-0.55	0.27
0	-2.08	2.40	9.73	-0.22	0.25
-5	0.98	1.98	9.70	0.10	0.21
-10	3.55	1.75	9.73	0.37	0.18
-15	6.93	1.75	9.73	0.72	0.18
-20	8.24	2.05	9.68	0.86	0.22
-25	10.27	2.43	9.70	1.06	0.25
-30	10.75	2.55	9.65	1.32	0.27
-35	14.83	2.73	9.65	1.54	0.29
-40	16.73	3.35	9.65	1.74	0.35
-45	17.85	3.60	9.65	1.85	0.37

Table A1.5. Ambient conditions for the velocity profile experiments.

	Station			
	I		II	
	Horizontal	Vertical	Horizontal	Vertical
Engine speed (rpm)	1241	1218	1230	1229
Atmospheric pressure (mmHg)	767.75	761.50	766.75	765.40
Ambient temperature (°C)	21.0	23.5	24.0	24.0
Manometer inclination (degrees)	20	20	20	20
Air density (kg/m^3)	1.20	1.20	1.19	1.19
Water density (kg/m^3)	997.96	998.20	997.25	997.25
x in $v=\sqrt{x\Delta h_{dyn}}$	141.43	141.43	142.86	142.86

Table A1.6.Manometer readings for the horizontal velocity profile experiment conducted at station I.

Probe position	Manometer reading					
	South	North	West	East	Average	Static wall
	Up Down	Up Down	Up Down	Up Down	Up Down	Up Down
0	4.40 4.60	5.30 5.50	5.40 5.50	4.10 4.30	4.80 4.98	6.30 6.30
1	4.60 4.60	5.40 5.40	5.40 5.40	4.20 4.20	4.90 4.90	6.10 6.10
2	4.10 4.10	5.00 5.00	5.00 5.00	3.90 3.90	4.50 4.50	6.10 6.10
3	4.60 4.40	5.40 5.20	5.30 5.15	4.35 4.20	4.91 4.74	6.50 6.05
4	4.60 4.60	5.45 5.45	5.30 5.30	4.50 4.50	4.96 4.96	6.30 6.30
5	4.80 4.80	5.65 5.65	5.45 5.45	4.75 4.75	5.16 5.16	6.10 6.10
6	4.80 4.60	5.50 5.50	5.30 5.20	4.80 4.70	5.10 5.00	6.20 6.30
7	4.30 4.40	5.40 5.50	5.05 5.15	4.65 4.70	4.85 4.94	6.30 6.35
8	4.45 4.45	5.25 5.25	4.80 4.80	4.50 4.50	4.75 4.75	6.00 6.00
9	4.50 4.50	5.00 5.10	4.50 4.60	4.40 4.40	4.60 4.65	6.00 5.90
10	4.50 4.50	5.20 5.20	4.55 4.55	4.60 4.60	4.71 4.71	5.90 5.90
11	4.50 4.50	4.80 4.80	3.95 3.95	4.30 4.30	4.39 4.39	5.70 5.70

Table A1.7. Processed test results of the horizontal velocity profile experiment conducted at station I.

Probe position	Δh_v	Δh_h	C_{pv}	θ_v	C_{ph}	θ_h	Δh_{dyn}	v	v_x	v_y	v_z
0	-0.90	1.25	0.83	14.3	-0.60	5.5	1.51	14.62	14.12	1.36	3.60
1	-0.80	1.20	1.00	17.0	-0.67	6.0	1.20	13.03	12.39	1.30	3.81
2	-0.90	1.10	0.69	12.0	-0.56	5.0	1.60	15.04	14.66	1.28	3.12
3	-0.80	0.95	0.67	11.5	-0.56	4.8	1.45	14.31	13.97	1.16	2.85
4	-0.85	0.80	0.60	10.0	-0.63	6.0	1.34	13.77	13.49	1.44	2.39
5	-0.85	0.70	0.74	13.0	-0.90	11.0	0.94	11.53	11.02	2.14	2.59
6	-0.80	0.50	0.42	7.5	-0.67	6.5	1.20	13.02	12.83	1.46	1.70
7	-1.10	0.43	0.30	5.3	-0.77	8.0	1.43	14.22	14.02	1.97	1.30
8	-0.80	0.30	0.24	4.5	-0.64	6.0	1.25	13.30	13.19	1.39	1.04
9	-0.55	0.15	0.12	2.0	-0.42	2.3	1.33	13.69	13.67	0.54	0.48
10	-0.70	-0.05	-0.04	-1.0	-0.59	5.5	1.19	12.97	12.91	1.24	-0.22
11	-0.30	-0.35	-0.27	-5.0	-0.23	-0.5	1.31	13.61	13.55	-0.12	-1.19

Table A1.8.Manometer readings for the vertical velocity profile experiment conducted at station I.

Probe position	Manometer reading											
	South		North		West		East		Average		Static wall	
	Up	Down	Up	Down	Up	Down	Up	Down	Up	Down	Up	Down
0	4.05	4.05	2.60	2.60	3.25	3.25	1.90	1.90	2.95	2.95	4.40	4.40
1	4.05	4.05	2.90	2.90	3.40	3.40	1.90	1.90	3.06	3.06	4.30	4.30
2	4.05	4.05	3.30	3.30	3.60	3.60	2.70	2.70	3.41	3.41	4.60	4.60
3	4.10	4.10	3.90	3.90	3.90	3.90	3.80	3.80	3.93	3.93	5.50	5.50
4	4.90	4.90	4.40	4.40	4.30	4.30	4.60	4.60	4.55	4.55	6.20	6.20
5	5.40	5.40	5.00	5.00	4.70	4.70	5.35	5.35	5.11	5.11	6.60	6.60
6	5.55	5.55	5.35	5.35	4.90	4.90	5.90	5.90	5.45	5.45	7.00	7.00
7	6.45	6.45	6.00	6.00	5.55	5.55	6.85	6.85	6.21	6.21	7.65	7.65
8	6.65	6.65	6.20	6.20	5.50	5.50	7.20	7.20	6.39	6.39	8.20	8.20
9	6.80	6.80	6.40	6.40	5.65	5.65	7.50	7.50	6.59	6.59	8.35	8.35

Table A1.9. Processed test results of the vertical velocity profile experiment conducted at station I.

Probe position	Δh_v	Δh_h	C_{pv}	θ_v	C_{ph}	θ_h	Δh_{dyn}	v	v_x	v_y	v_z
0	1.45	1.35	1.00	23.00	0.93	16.00	1.45	14.28	12.64	-3.62	5.58
1	1.15	1.50	0.93	22.00	1.21	20.00	1.24	13.20	11.50	-4.19	4.94
2	0.75	0.90	0.63	16.50	0.76	13.00	1.19	12.93	12.08	-2.79	3.67
3	0.20	0.10	0.13	7.50	0.06	1.00	1.57	14.86	14.73	-0.26	1.94
4	0.50	-0.30	0.30	10.50	-0.18	-3.00	1.65	15.23	14.95	0.05	2.78
5	0.40	-0.65	0.27	10.00	-0.44	-7.50	1.49	14.47	14.13	1.86	2.51
6	0.20	-1.00	0.13	7.50	-0.65	-11.00	1.55	14.76	14.36	2.79	1.93
7	0.45	-1.30	0.31	11.00	-0.90	-15.00	1.44	14.23	13.49	3.61	2.72
8	0.45	-1.70	0.25	9.50	-0.94	-16.00	1.81	15.95	15.12	4.34	2.63
9	0.40	-1.85	0.23	9.00	-1.05	-17.00	1.76	15.73	14.86	4.54	2.46

Table A1.10.Manometer readings for the horizontal velocity profile experiment conducted at station II.

Probe position	Manometer reading											
	South		North		West		East		Average		Static wall	
	Up	Down	Up	Down	Up	Down	Up	Down	Up	Down	Up	Down
0	4.00	4.00	3.40	3.40	3.70	3.70	3.30	3.30	3.60	3.60	5.60	5.60
1	4.00	4.00	3.15	3.15	3.40	3.40	2.90	2.90	3.36	3.36	5.30	5.30
2	4.00	4.00	3.30	3.30	3.50	3.50	3.20	3.20	3.50	3.50	5.30	5.30
3	4.00	4.00	3.00	3.00	3.10	3.10	3.00	3.00	3.28	3.28	5.00	5.00
4	4.00	4.00	2.90	2.90	2.90	2.90	2.90	2.90	3.18	3.18	5.00	5.00
5	4.00	4.00	2.80	2.80	2.80	2.80	2.90	2.90	3.13	3.13	4.95	4.95
6	4.00	4.00	2.70	2.70	2.65	2.65	2.75	2.75	3.03	3.03	4.55	4.55
7	4.00	4.00	2.10	2.50	2.10	2.50	2.20	2.55	2.60	2.89	4.15	4.55
8	4.00	4.00	2.55	2.55	2.60	2.60	2.70	2.70	2.96	2.96	4.65	4.65
9	4.00	4.00	3.25	3.45	3.30	3.50	3.40	3.65	3.49	3.65	5.40	5.70
10	4.00	4.00	4.70	4.70	4.70	4.70	4.90	4.90	4.58	4.58	6.80	6.80
11	4.00	4.00	4.90	4.90	4.85	4.85	5.05	5.05	4.70	4.70	7.00	7.00

Table A1.11. Processed test results of the horizontal velocity profile experiment conducted at station II.

Probe position	Δh_v	Δh_h	C_{pv}	θ_v	C_{ph}	θ_h	Δh_{dyn}	v	v_x	v_y	v_z
0	0.60	0.40	0.20	3.5	0.30	-10.0	2.00	16.90	16.61	-2.93	1.03
1	0.85	0.50	0.26	5.0	0.44	-13.0	1.94	16.65	16.16	-3.73	1.45
2	0.70	0.30	0.17	3.0	0.39	-12.0	1.80	16.04	15.67	-3.33	0.84
3	1.00	0.10	0.06	1.0	0.58	-16.0	1.72	15.68	15.07	-4.32	0.27
4	1.10	0.00	0.00	0.0	0.60	-16.0	1.82	16.12	15.49	-4.44	0.00
5	1.20	-0.10	-0.05	-0.5	0.66	-16.5	1.82	16.12	15.45	-4.58	-0.14
6	1.30	-0.10	-0.07	-1.0	0.86	-20.0	1.52	14.74	13.85	-5.04	-0.26
7	1.70	-0.08	-0.05	-0.8	2.07	-24.0	1.61	15.14	13.83	-6.15	-0.20
8	1.45	-0.10	-0.06	-1.0	0.86	-20.0	1.69	15.54	14.60	-5.31	-0.27
9	0.65	-0.13	-0.06	-0.8	0.33	-11.0	1.98	16.82	16.50	-3.20	-0.22
10	-0.70	-0.20	-0.09	-1.5	-0.32	0.5	2.22	17.81	17.80	0.16	-0.47
11	-0.90	-0.20	-0.09	-1.5	-0.39	2.0	2.30	18.13	18.12	0.63	-0.47

Table A1.12.Manometer readings for the vertical velocity profile experiment conducted at station II.

Probe position	Manometer reading											
	South		North		West		East		Average		Static wall	
	Up	Down	Up	Down	Up	Down	Up	Down	Up	Down	Up	Down
0	7.55	7.55	4.85	4.85	5.05	5.05	4.70	4.70	5.54	5.54	6.85	6.85
1	4.90	4.90	4.55	4.55	4.75	4.75	4.50	4.50	4.68	4.68	6.85	6.85
2	5.00	5.00	4.50	4.50	4.65	4.65	4.55	4.55	4.68	4.68	6.60	6.60
3	4.55	4.55	4.00	4.00	4.15	4.15	4.10	4.10	4.20	4.20	6.10	6.10
4	4.45	4.45	3.80	3.90	3.90	4.00	4.00	4.10	4.04	4.11	6.10	6.10
5	4.10	4.10	3.40	3.40	3.40	3.40	3.60	3.60	3.63	3.63	5.50	5.50
6	3.80	3.80	3.35	3.35	3.30	3.30	3.55	3.55	3.50	3.50	5.30	5.30
7	3.85	3.85	3.10	3.10	3.05	3.05	3.30	3.30	3.33	3.33	5.20	5.20
8	3.85	3.85	3.00	3.00	3.00	3.00	3.10	3.10	3.24	3.24	5.00	5.00
9	3.85	3.85	3.30	3.00	3.30	3.00	3.40	3.05	3.46	3.23	5.30	5.10

Table A1.13. Processed test results of the vertical velocity profile experiment conducted at station II.

Probe position	Δh_v	Δh_h	C_{pv}	θ_v	C_{ph}	θ_h	Δh_{dyn}	v	v_x	v_y	v_z
0	2.7	0.35	2.06	41.0	0.27	-5.0	1.31	13.68	10.29	-0.90	8.97
1	0.35	0.25	0.16	8.0	0.12	-2.5	2.17	17.61	17.59	-0.77	2.45
2	0.50	0.10	0.26	10.0	0.05	-1.0	1.92	16.56	16.30	-2.88	2.88
3	0.55	0.05	0.29	10.5	0.03	-0.5	1.90	16.48	16.20	-0.14	3.00
4	0.60	-0.10	0.30	10.5	-0.05	0.5	2.03	17.01	16.72	0.15	3.10
5	0.70	-0.20	0.37	11.0	-0.11	1.5	1.87	16.34	16.03	0.42	3.12
6	0.45	-0.25	0.25	9.5	-0.14	2.0	1.80	16.04	15.81	0.55	2.65
7	0.75	-0.25	0.40	12.0	-0.13	2.0	1.87	16.34	15.97	0.56	3.40
8	0.85	-0.10	0.48	14.0	-0.06	0.5	1.76	15.86	15.38	0.14	3.83
9	0.70	-0.08	0.38	12.3	-0.04	0.5	1.86	16.28	15.90	0.14	3.44

A1.4. Calibration Results for the Flow Angle Meter.

The calibrations of the flow angle meter, for horizontal and vertical pressure coefficients versus flow angle are presented graphically below.

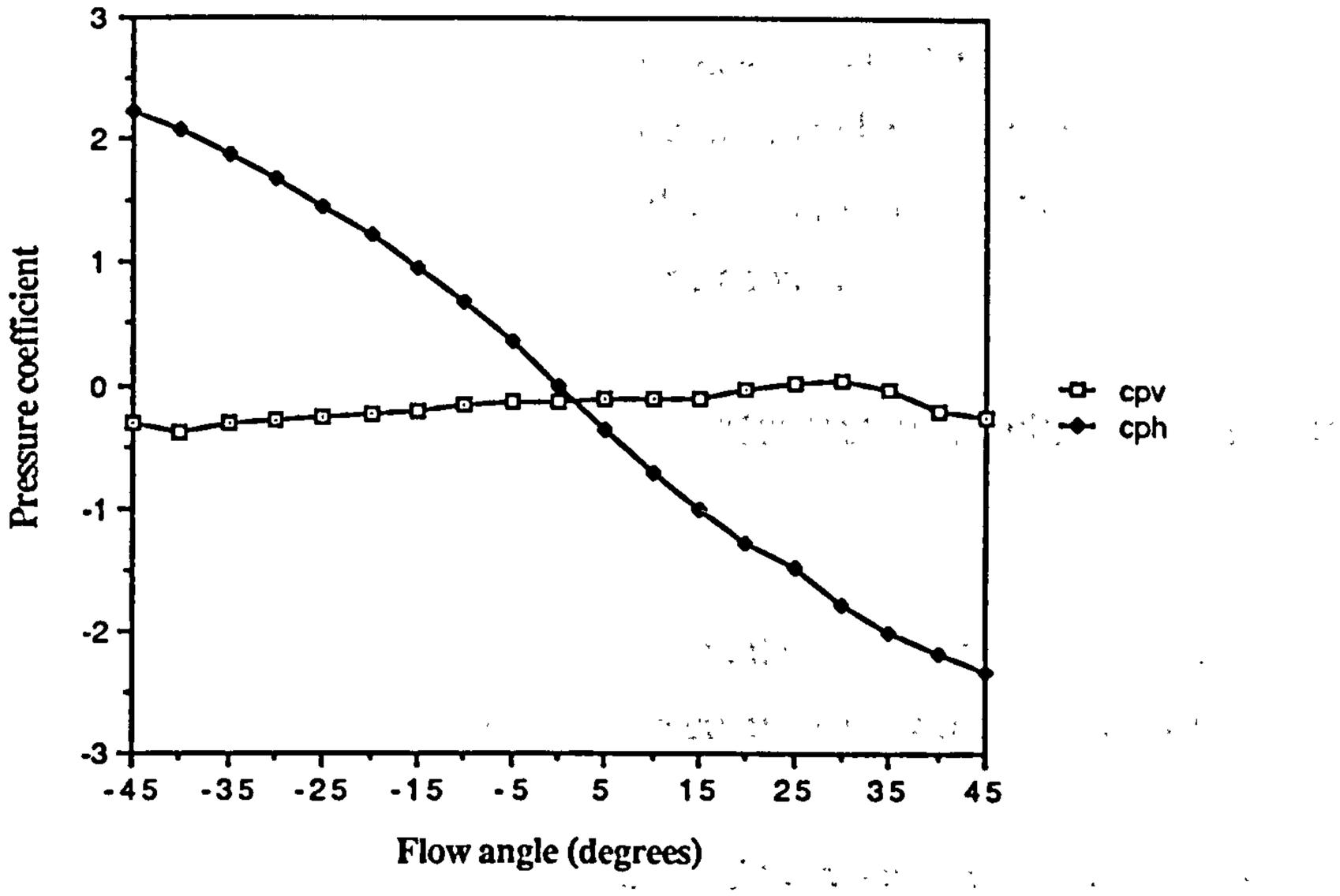

Figure A1.6. Showing horizontal pressure coefficient against the horizontal component of the flow angle, C_{ph} vs. θ_h.

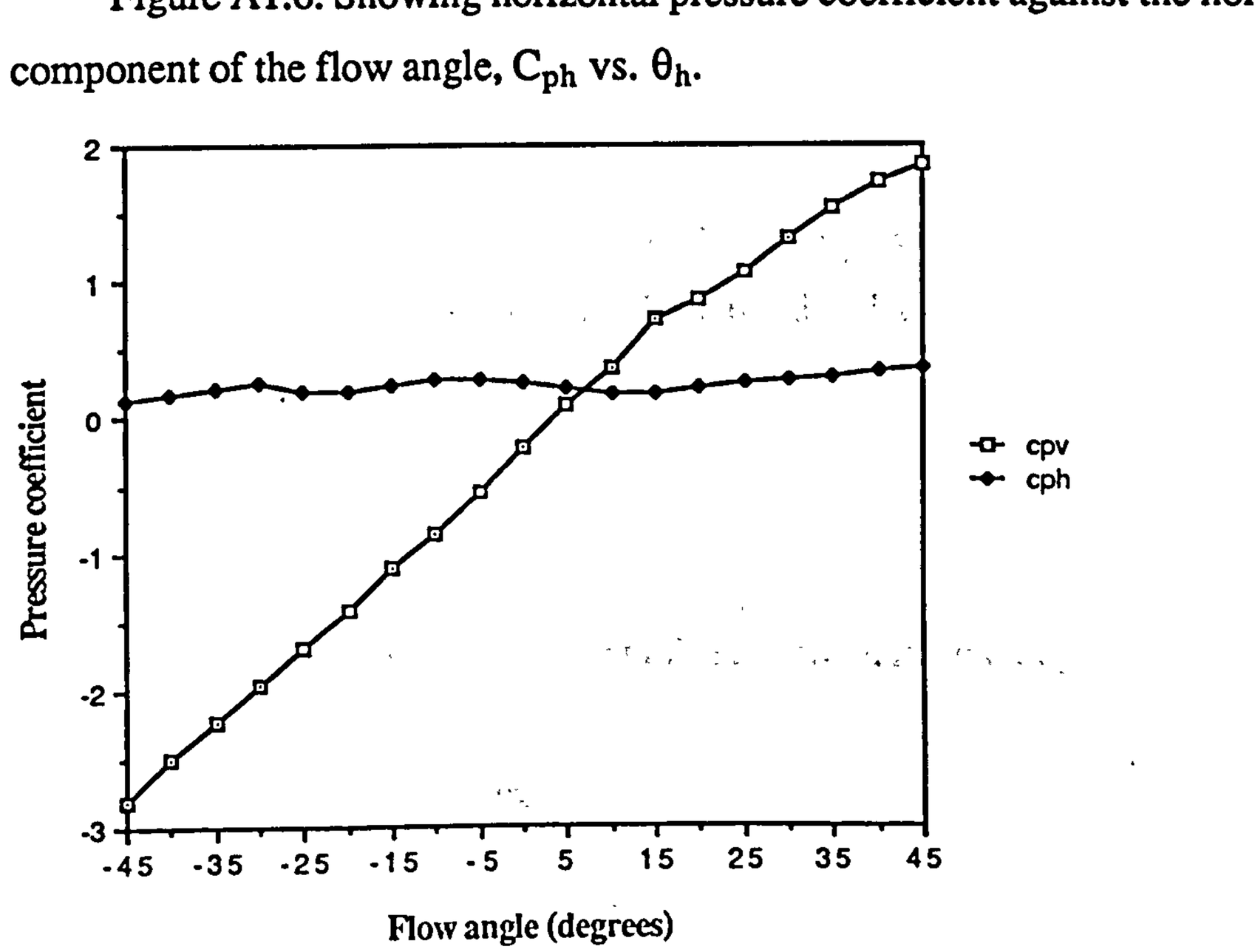

Figure A1.7. Showing vertical pressure coefficient against the vertical component of the flow angle, C_{pv} vs. θ_v.

The calibration results are also tabulated in Section A1.3 of Appendix A1.

Inspecting either of the calibration graphs, it can be readily seen that the response of the flow angle meter is nearly linear for a fair range of flow angle. Also, as predicted, the interaction of, say, the horizontal component of the meter to normal flow angle variation is negligible. (Similarly, a variation in θ_h causes only minor fluctuation in C_{pv} about zero.) The slight kinks in the above figures may be reasonably attributed to slight imperfections in the manufacture of the probe, such as the angled tips of the two sets of tube pairs not being quite normal to one another.

A1.5. Estimation of the Nominal Streamwise Velocity Along the Main Duct of the Manifold.

The manifold considered is that at inlet to a four cylinder, four stroke engine. So, during one complete revolution of the crankshaft, two cylinders will undergo an induction stroke.

If the engine speed is N rev/min and the volume of each cylinder is V then the volumetric flowrate through the manifold is given by

$$q = \frac{2VN}{60} \text{ m}^3/\text{s}$$

provided that volumetric efficiency is blithely assumed to be 100%.

Now for a given cross-section of the manifold, of breadth, b, and height, h, then the cross-sectional area for flow is

$$A = bh$$

Thus the streamwise velocity at this section, v, is given by

$$v = \frac{q}{A} = \frac{2VN}{60\,bh} \text{ m/s}$$

Now if $N = 1220$ rpm,

$b = 70$ mm,

$h = 60$ mm and

$V = 1l = 1x10^{-3}m^3$

Then $$v = \frac{2 \times 1x10^{-3} \times 1220}{60 \times 70x10^{-3} \times 60x10^{-3}} = 9.72 \text{ m/s}$$

Appendix A2. Development of a Computational Model of the Inlet Manifold.

A2.1. Development of a Computational Mesh for the Inlet Manifold.

The inlet manifold described in Figures 3.1-3.3 of Section 3.2.1 will now be detailed. The inlet manifold can be subdivided into three main sections, as shown below.

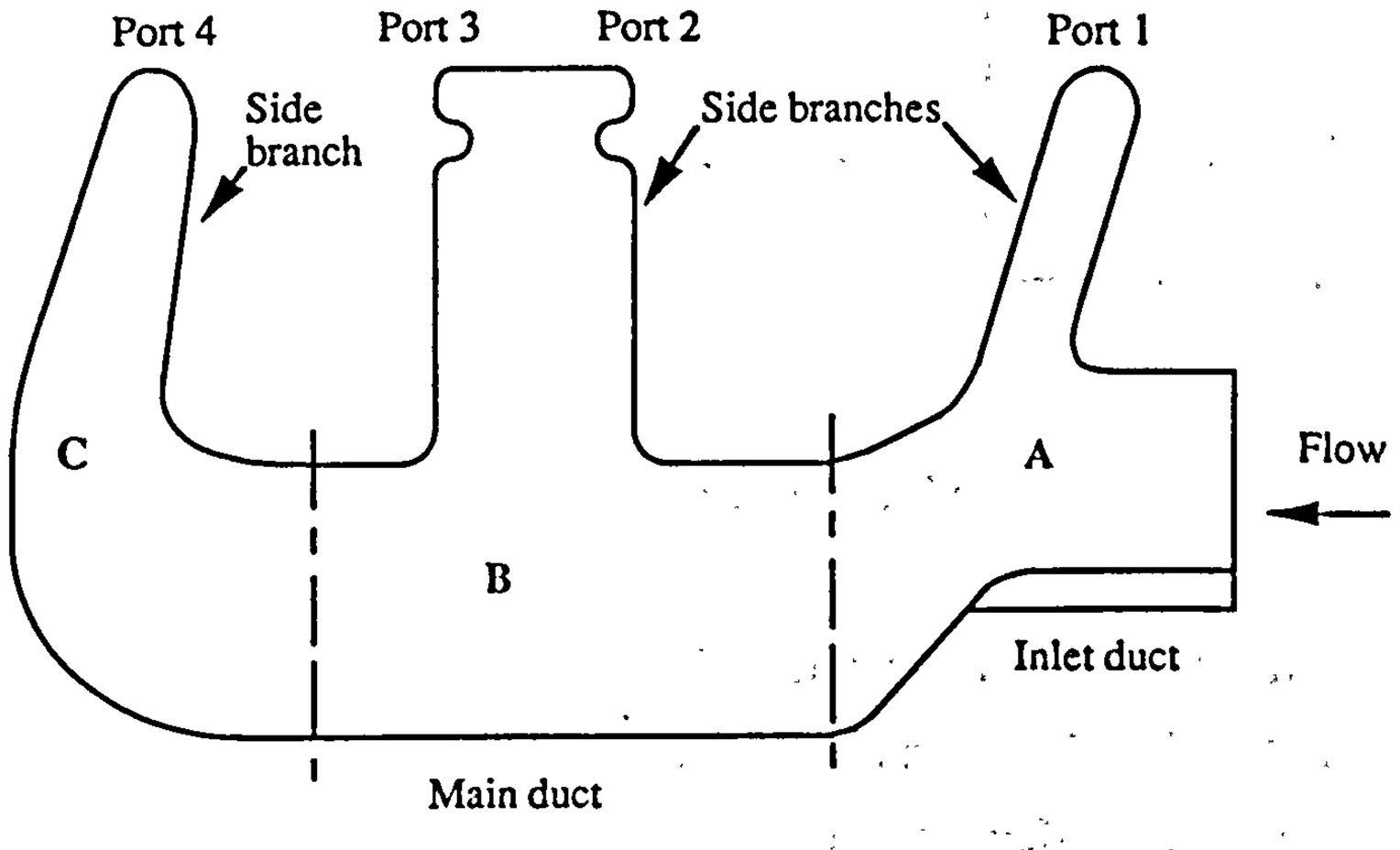

Figure A2.1. Thumbnail sketch of the inlet manifold in elevation.

The main features (and principal dimensions with regard to meshing) of these three sections will now be considered in turn, making use of a number of further thumbnail sketches.

Section A of the manifold comprises the inlet to the flow domain and a side branch, linking to port one of the engine, as shown in Figure A2.2 below.

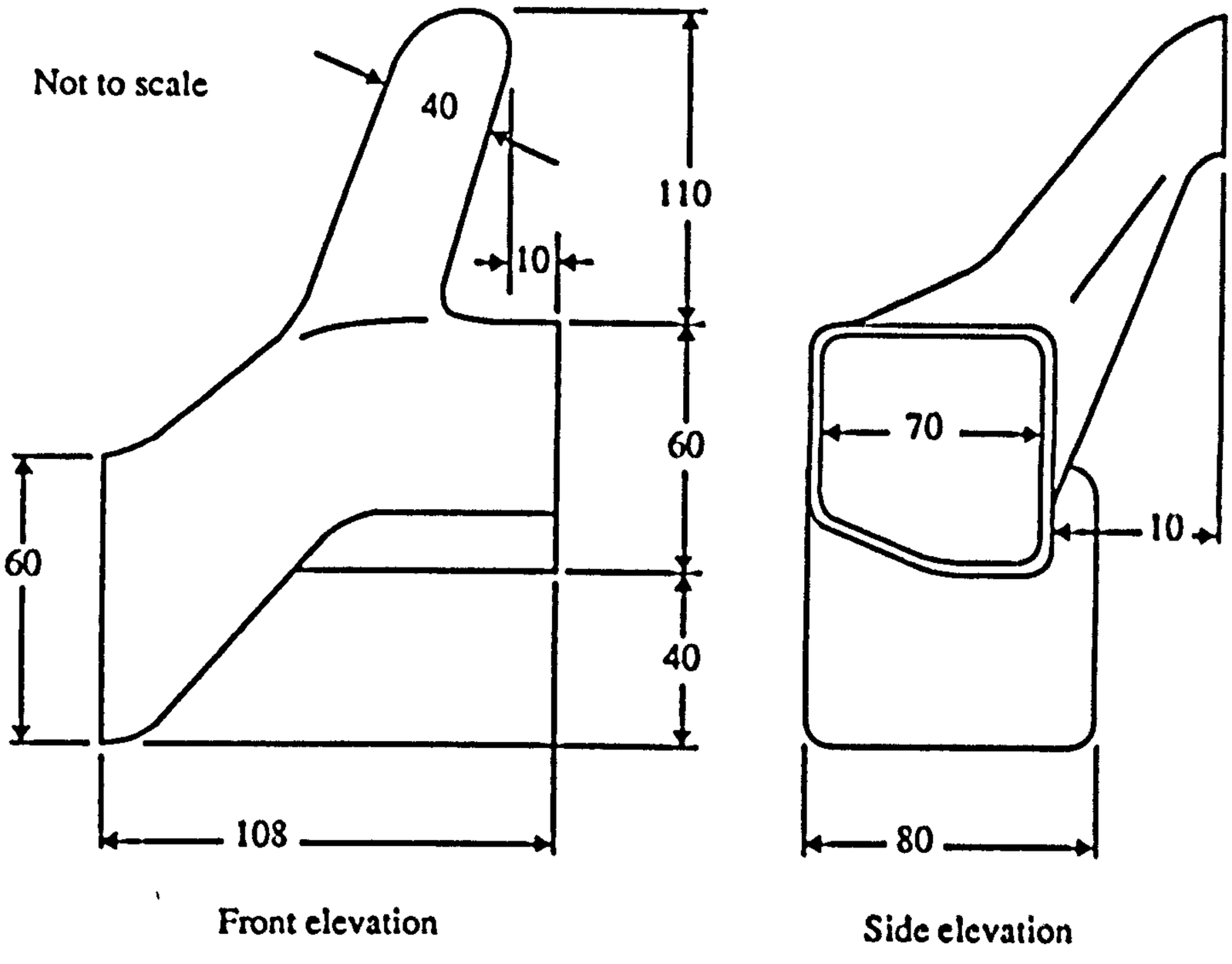

Figure A2.2. Section A of the inlet manifold.

The five-sided duct at inlet is raised some 40mm above the main run of the rectangular section duct which forms the lower reach of section B of the manifold. The side branch, connecting to engine port one, is essentially of rectangular cross section, blending to an oval cross-section at the port. The whole side branch slopes back toward the plane of the inlet, as seen in elevation.

The side view of the branch shows that it slopes away from the inlet duct, blending smoothly with the main duct halfway along the upper and right-hand walls of the inlet duct, as seen in side view. The inlet duct merges smoothly with the main duct, at which point the main duct is seen to be some 10mm wider than at inlet, as seen in the side elevation. Again, it must be emphasised that all cross-sections of the manifold have fillet radii (rounded corners) of 5mm radius.

Section B of the manifold, consisting of the main duct and side branch to ports two and three, is shown in Figure A2.3 below.

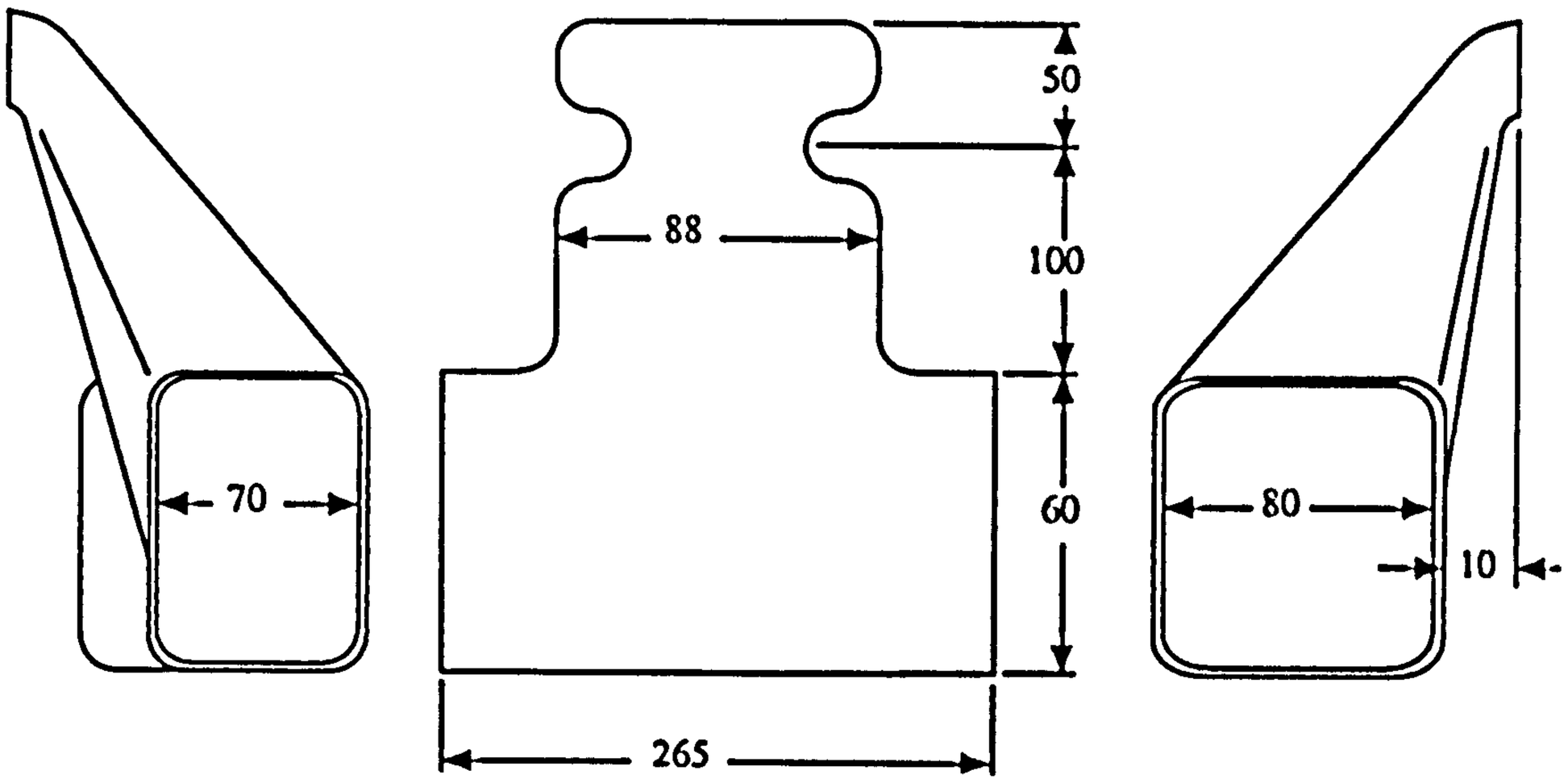

Side elevation Front elevation Side elevation

Not to scale

Figure A2.3. Section B of the inlet manifold.

Midway along the rectangular main duct of section B, the manifold branches off to connect with inlet ports two and three of the engine. From the side view sketches above, it can be seen that the wedge-shaped side branch blends with the top of the front of the main duct and also halfway down its rear vertical face. Furthermore, the main duct tapers abruptly from 80mm to 70mm in breadth at the rear vertical face, midway along its length. The side branch, rectangular in cross-section, draws in to a waist before blending to oval section at the ports.

Section C is basically a plain side branch, connecting the main duct to port four, as shown in Figure A2.4 below.

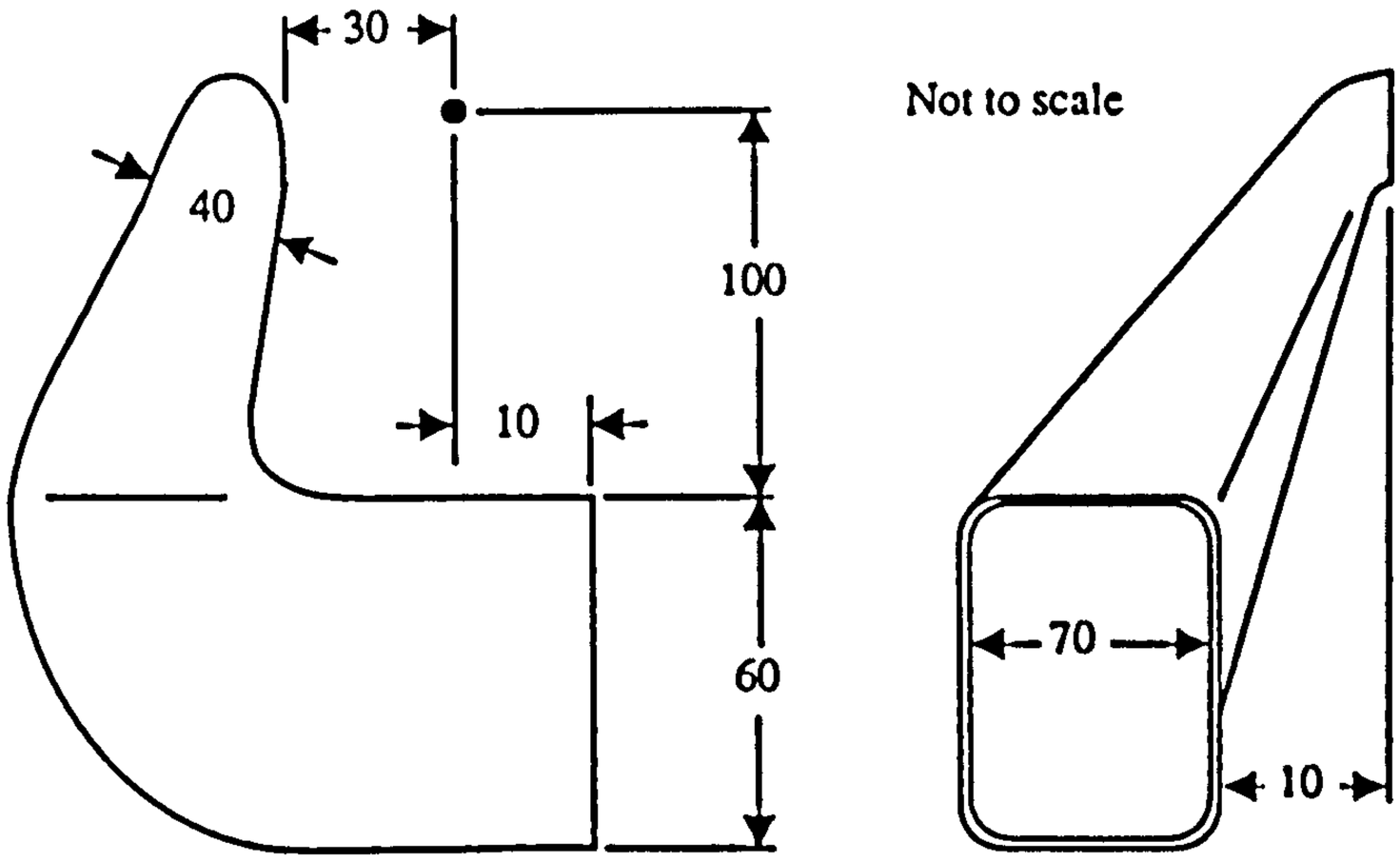

Figure A2.4. Section C of the inlet manifold.

Section C exists as a series of complex curves in rectangular cross-section. The main duct first turns through 90° before sloping back towards inlet (in elevation). This results in the ridge seen at the front of the duct where the upper front edge of the duct meets the wedge shaped side branch. At the rear, the side branch blends with the main duct halfway up its vertical face. Again, the rectangular cross-section of the side branch becomes ovular at the port.

Having considered the main features of each section of the manifold, the simplifications used in generating a corresponding computational mesh will now be considered. With regard to mesh generation then, the basis of the model can be seen as two tee-sections and a plain channel, as shown in Figure A2.5.

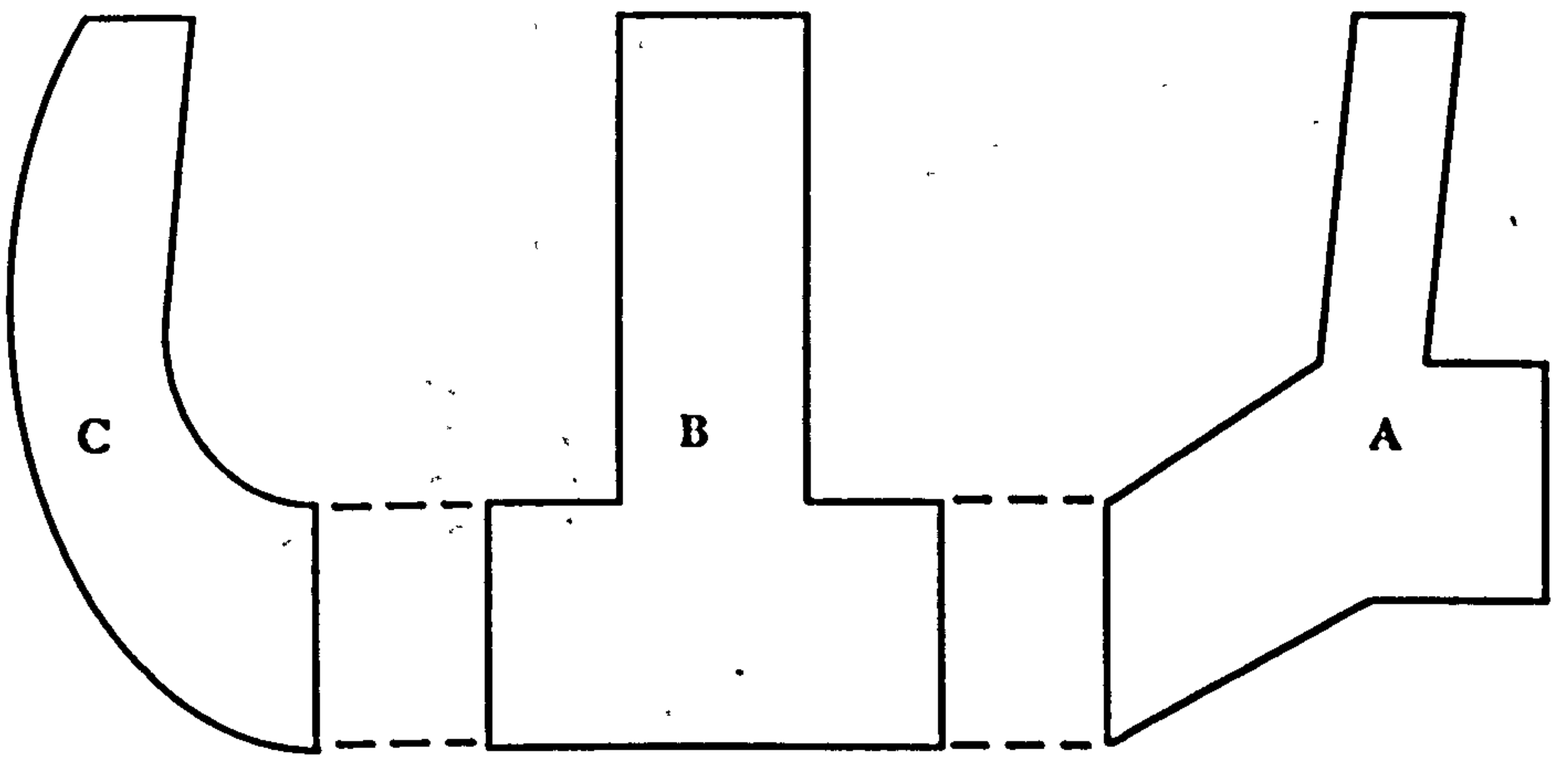

Figure A2.5. Simplified elevation of the manifold.

For the mesh generation system used, any given section of the mesh is required to

exist as a curvilinear region. Whilst mesh generation techniques are fully discussed in the FIMESH manual (FIDAP, 1994), in essence, this flow domain, existing as a curvilinear region in geometric space (represented by Cartesian co-ordinates), is simultaneously modelled by a rectilinear region in logical space (represented by the co-ordinates i, j and k). The logical space model merely serves to define inter-element connectivity but the requirement that it should consist of rectilinear regions means that it cannot replicate triangular prisms. Figure A2.6 then shows a valid model for a tee-section in both geometric and logical space.

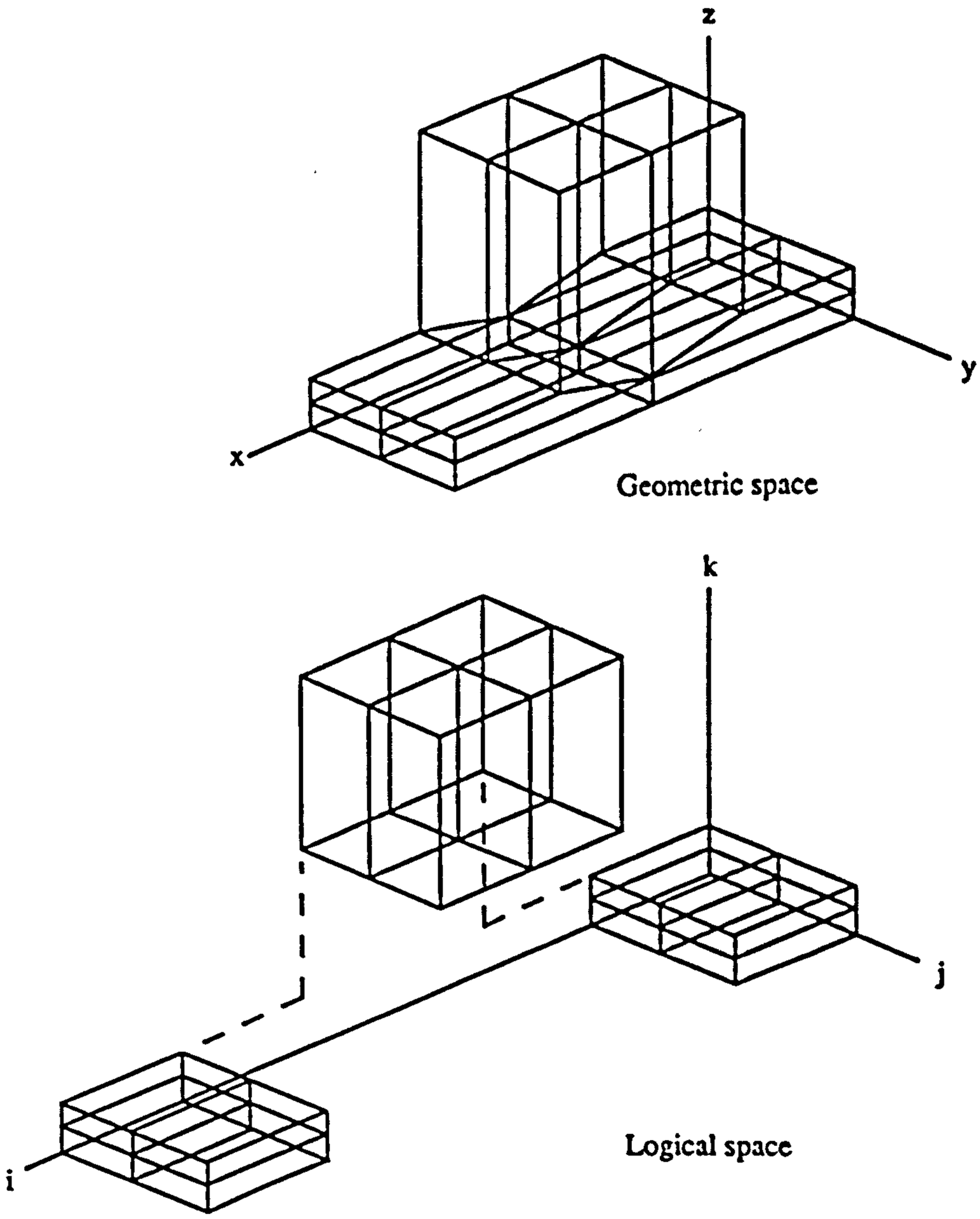

Figure A2.6. Showing the wire frame of a tee-section, capable of providing mesh grading in three directions.

Where a given surface of the tee-section of Figure A2.6 is seen to be divided between two mutally perpendicular logical planes, the presence of finer mesh elements is

confined to the near-wall region by use of the MERGE facility. The mutally perpendicular near-wall regions are modelled as two discrete logical regions, even though they have a common, connecting face in geometric space. The two mesh regions are graded individually in logical space and then 'merged' together in geometric space.

Whilst Figure A2.6 offers a method of restricting finer mesh elements to the proximity of the solid boundaries, two significant problems arise in comparison with the real geometry of the manifold as

i) treatment of the duct cross-sections, which typically exist as rounded-off rectangles and

ii) modelling the real surface of the junctions between the side branches and the main duct.

Whilst the former problem relates to the number of nodal points in the mesh (and hence to the computational power available), the latter is more fundamental in nature as it touches upon the requirement for the model to consist of rectilinear blocks in logical space.

Figure A2.7 below compares the meshes for a simple rectangular cross-section and for one with rounded corners.

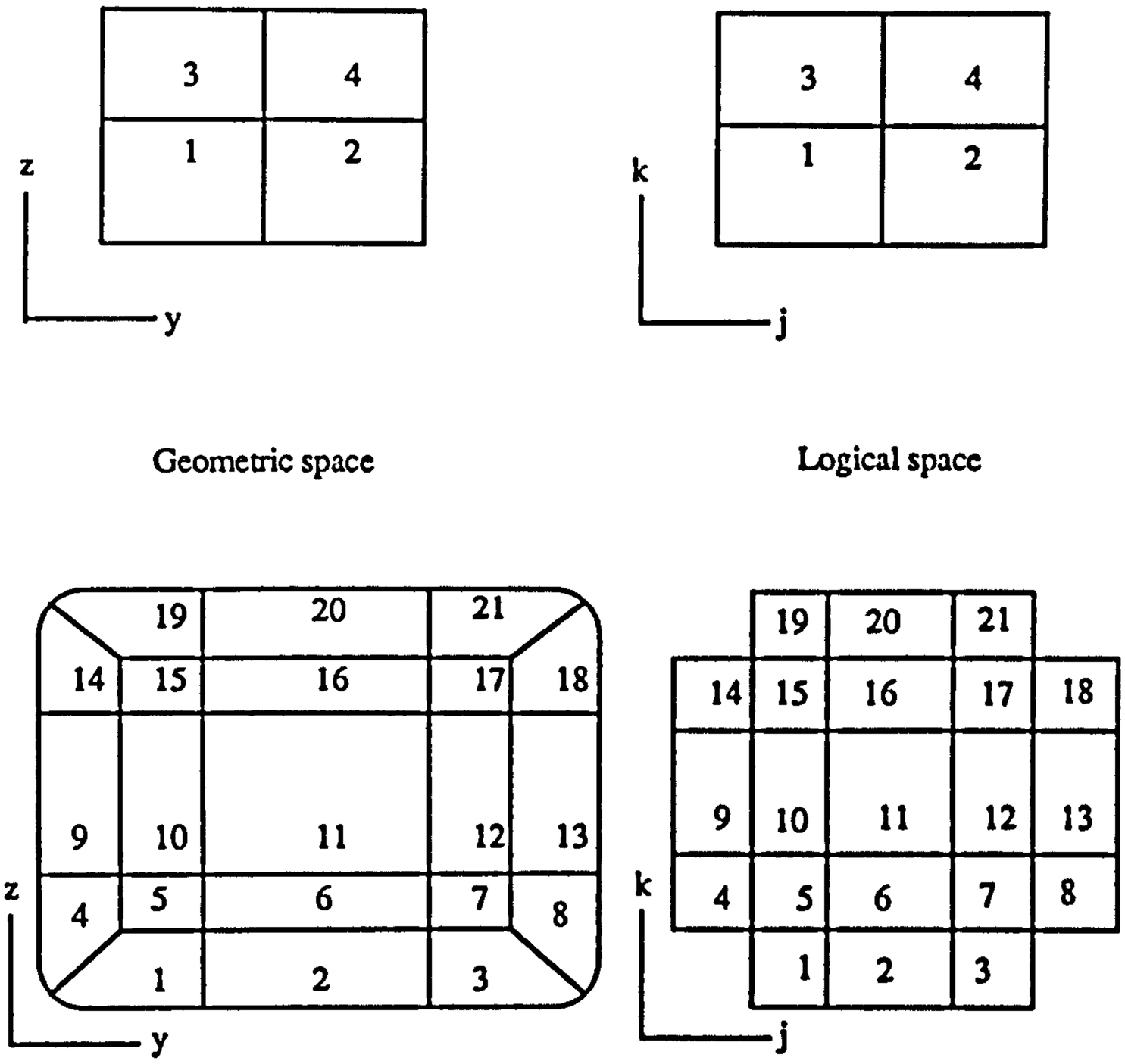

Figure A2.7. Two possible methods of meshing the main duct cross-section.

Straight away, it can be seen that the more elegant, curved-corner mesh requires roughly five times as many elements, and hence almost four times as many nodes, as the simple rectangular mesh section. For a model of the complexity of the inlet manifold, computational restrictions meant that a direct choice had to be made between the following:

i) use of a graded mesh, with finer elements close to the walls and
ii) use of a more realistic duct cross-section, with rounded corners.

Since one of the principal concerns of this study is to assess the response of current near-wall modelling techniques to the variation in y^+ and pressure gradient with time, it was decided that the facility of grading the mesh toward its boundaries was more important than rounding off the duct cross-section (where the corner radius was typically one tenth of the duct width).

Now the more serious problem of how to join the side branches of the model to the main duct may be considered. Having elected to construct the model from simple, rectangular mesh sections, then a 'squared-off' form of one of the tee-sections, say for

section B, would appear as Figure A2.8 below.

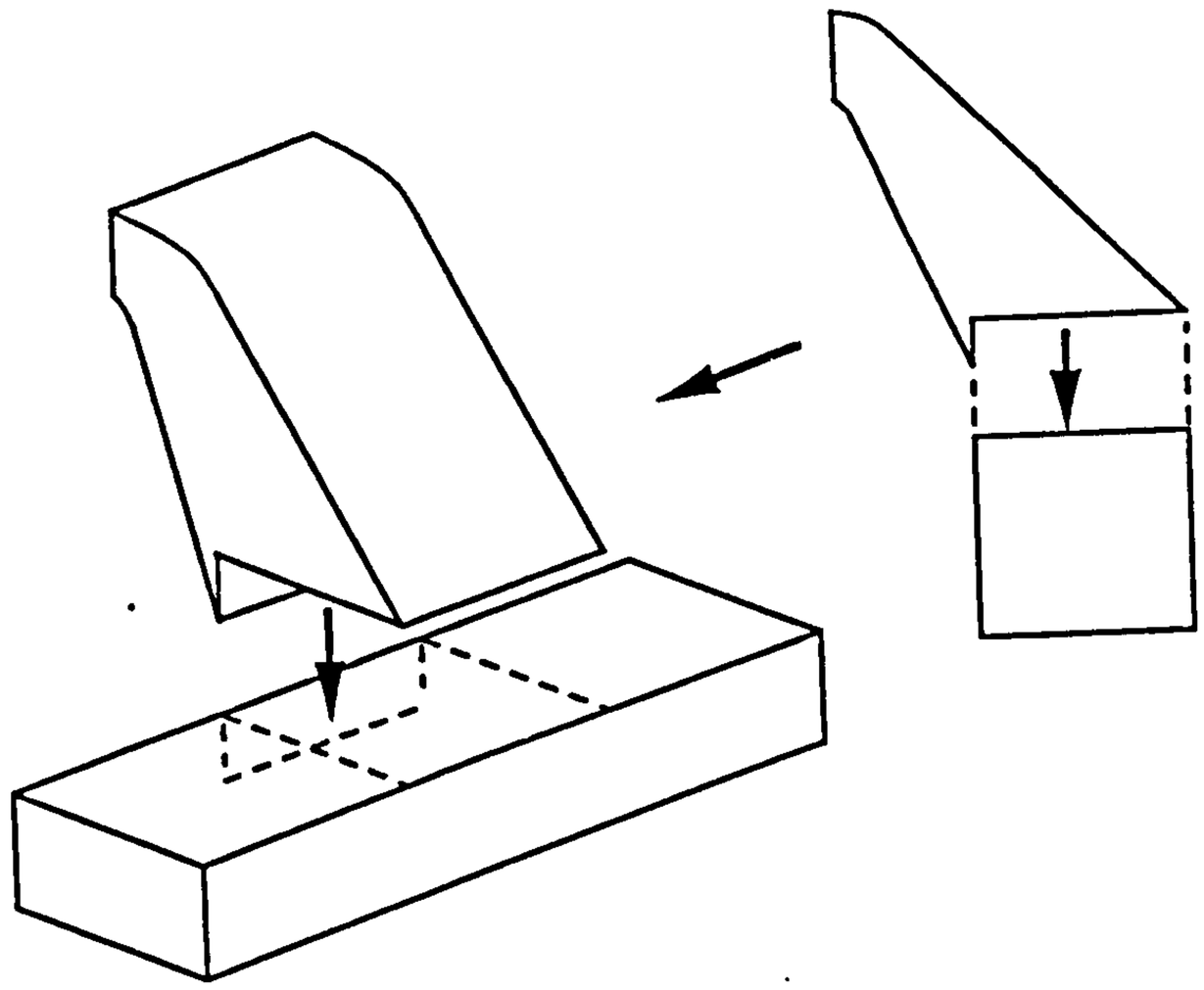

Figure A2.8. Simple exploded view of section B.

As seen in Figure A2.8 above, where the side branch mates with the main duct, there exists a triangular lip. In sub-dividing section B into curvilinear blocks to generate a valid mesh, as outlined in Figure A2.6, this triangular lip cannot be rationalised as a curvilinear block in real space and hence as a rectilinear block in logical space. Indeed, where other sub-divisions of the duct cross-section were attempted (remembering that a graded mesh is required), the result was merely to shuffle this triangular prism about the region. As far as could be determined, this triangular prism was a direct result of the choice of a simple rectangular form for the duct cross-section.

Since the simple cross-section had been chosen to allow for reasonable mesh density, given the computational power available, it was reluctantly decided to abandon this triangular prism and to model the side branches with rear faces flush with the main duct.

As such, these decisions caused a number of other features of the actual manifold not to exist in the model: the oval port outlets were substituted by rectangular ones and the inlet duct reduced to a rectangular cross-section of constant area. Even so, the major dimensions of the manifold were retained, with particular attention paid to maintaining similar cross-sectional areas for flow wherever possible.

A2.2. Model Construction.

In the previous section, the geometry of the inlet manifold was discussed, with regard to those approximations to its actual geometry necessary to prepare a suitable computational mesh. It was proposed that the model be constructed from rectangular cross-section ducts, in three discrete but adjoining sections. As such, each section possessed its own local co-ordinate system and, once designed, by relating these local co-ordinate systems to one another, the sections were joined together to form one contiguous whole. The general layout of the model can then be seen as Figure A2.9 below.

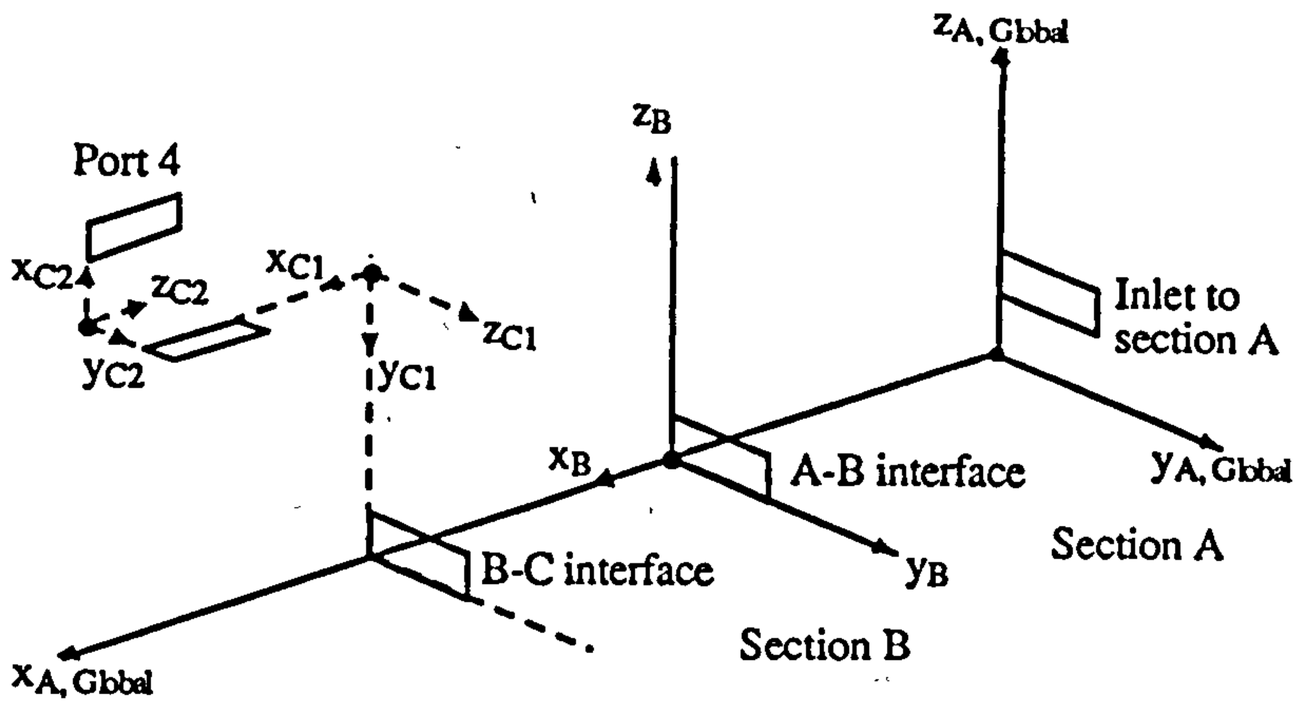

Figure A2.9. Showing the relationship between the local section co-ordinate systems and the global co-ordinate system.

Sections A and B were modelled on the tee-section design given as Figure A2.6. The side branch of the tee-section then served as the side branch of the model section, linking the manifold main duct to the relevant engine inlet port. These side branches then had constant width in the x-direction and had tapering depth in the y-direction, to offer the wedge-like shape of the actual side branches. In each case, the wedge portion of the side branch was linked to its engine inlet port by use of the ARC facility to create a curved duct of rectangular cross-section. A side elevation of the resulting side branch is shown in Figure A2.10 below.

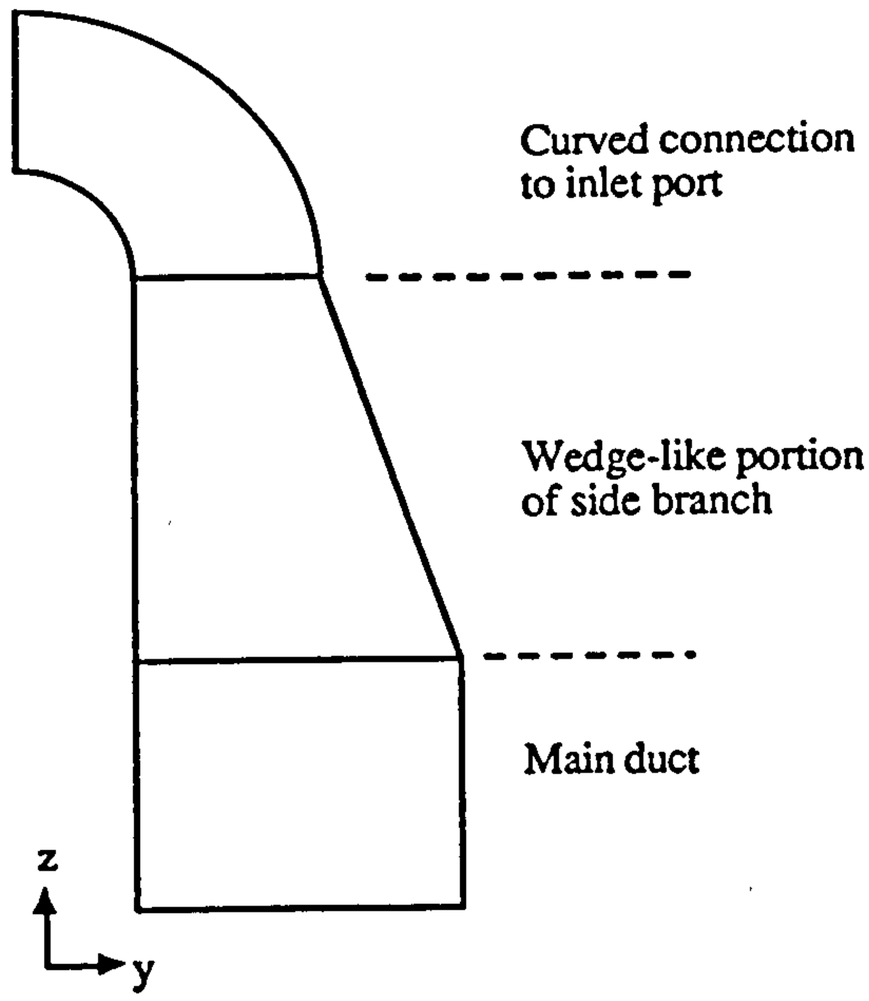

Figure A2.10. Side elevation of the tee-section used to model the side branches.

Section C, linking the main manifold duct to engine inlet port 4, was required to simulate a rectangular cross-section duct, tapering from 70x60mm at its inlet to 40x40mm at the port face, in a complex curve. The simplest method by which this could be achieved was in the use of the BLEND facility, whereby a region of the mesh may be created between two previously specified end planes. Three-dimensional blending is only offered in the x-y plane and so use was made of COORDINATE commands to provide appropriate local axes for the end planes defining the region to be blended. This technique is shown in Figure A2.11 below.

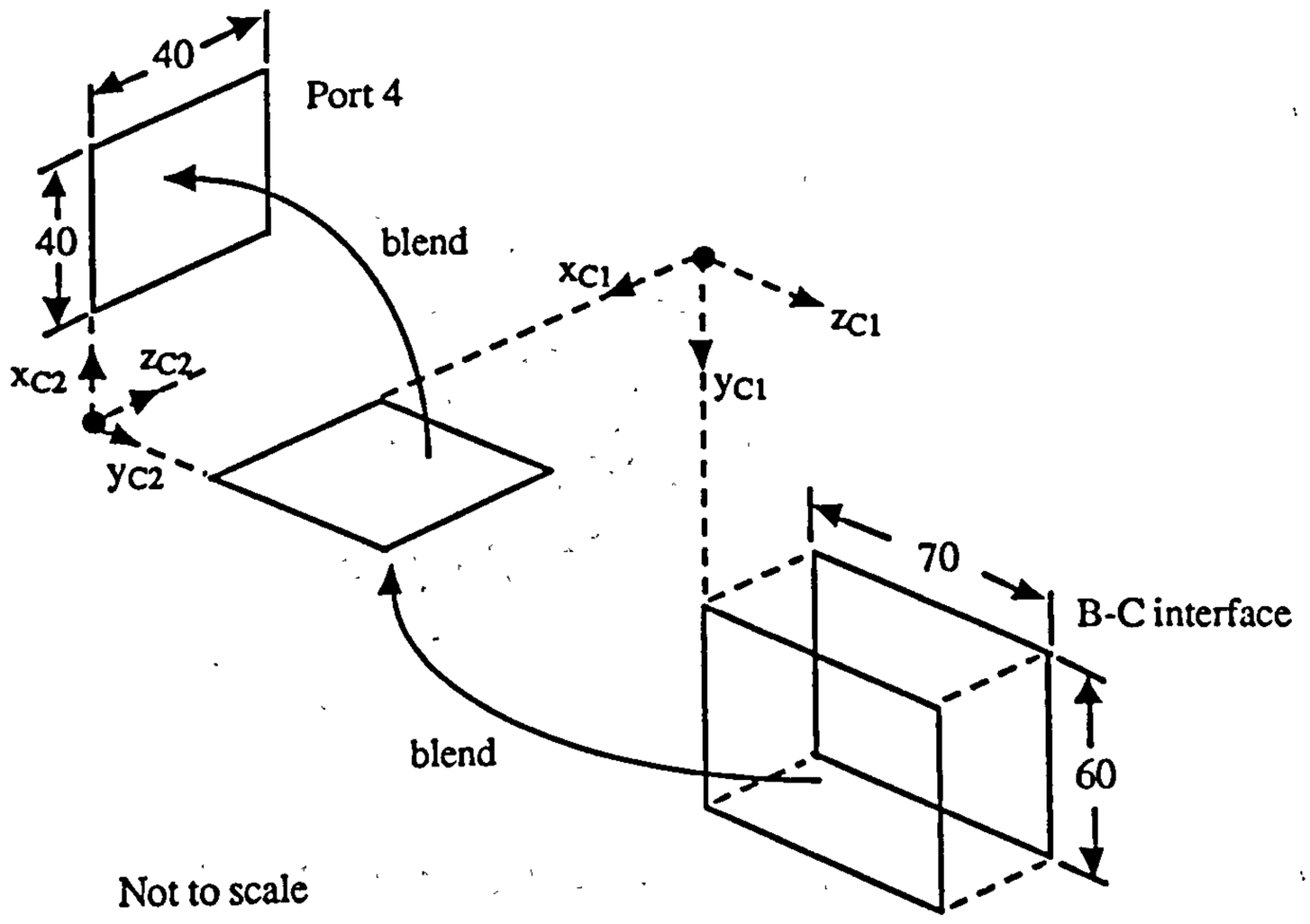

Figure A2.11. Showing the method of construction of section C.

On considering the manifold model, employing the technique of Figure A2.6 for the tee-sections, by presenting a sudden, right-angle turn to the flow, the roots of the tee-sections would be likely to predict separation in the flow that might not be present in the real manifold. As such, this portion of the model was redesigned to allow for more gentle turning of the flow, as shown in Figure A2.12 below.

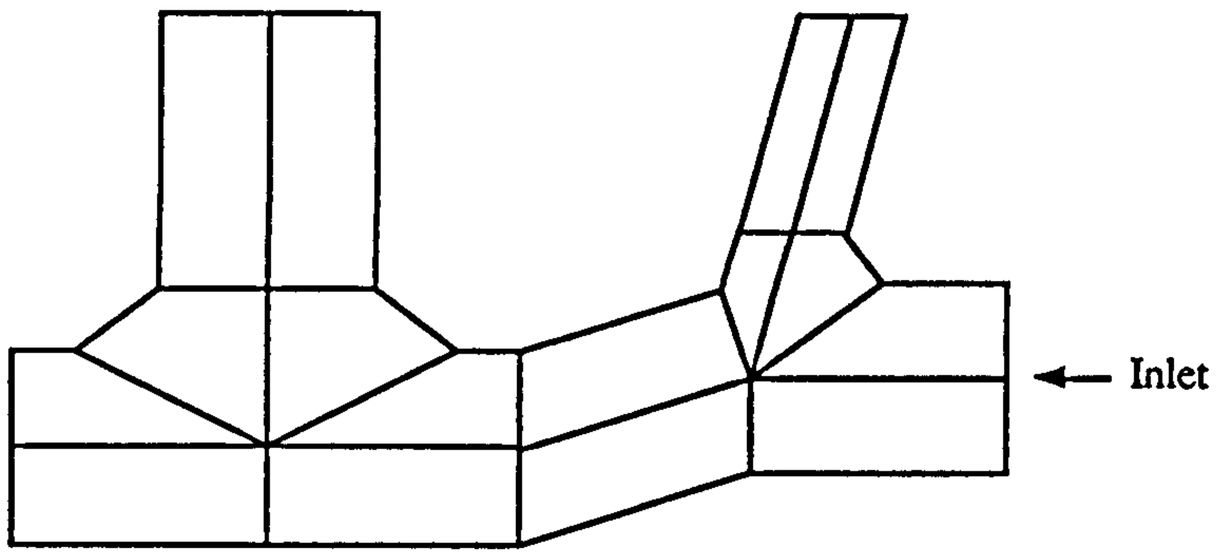

Figure A2.12. Showing a wire-frame proposal for better tee-sections in sections A and B of the model (in front elevation).

The above improved tee-sections were incorporated into the model and, as desired, provided a better approximation to the interface between the side branches and the main duct. However, the resulting front face of each side branch was grooved: this problem is considered in Figure A2.13 below, showing tee-section B.

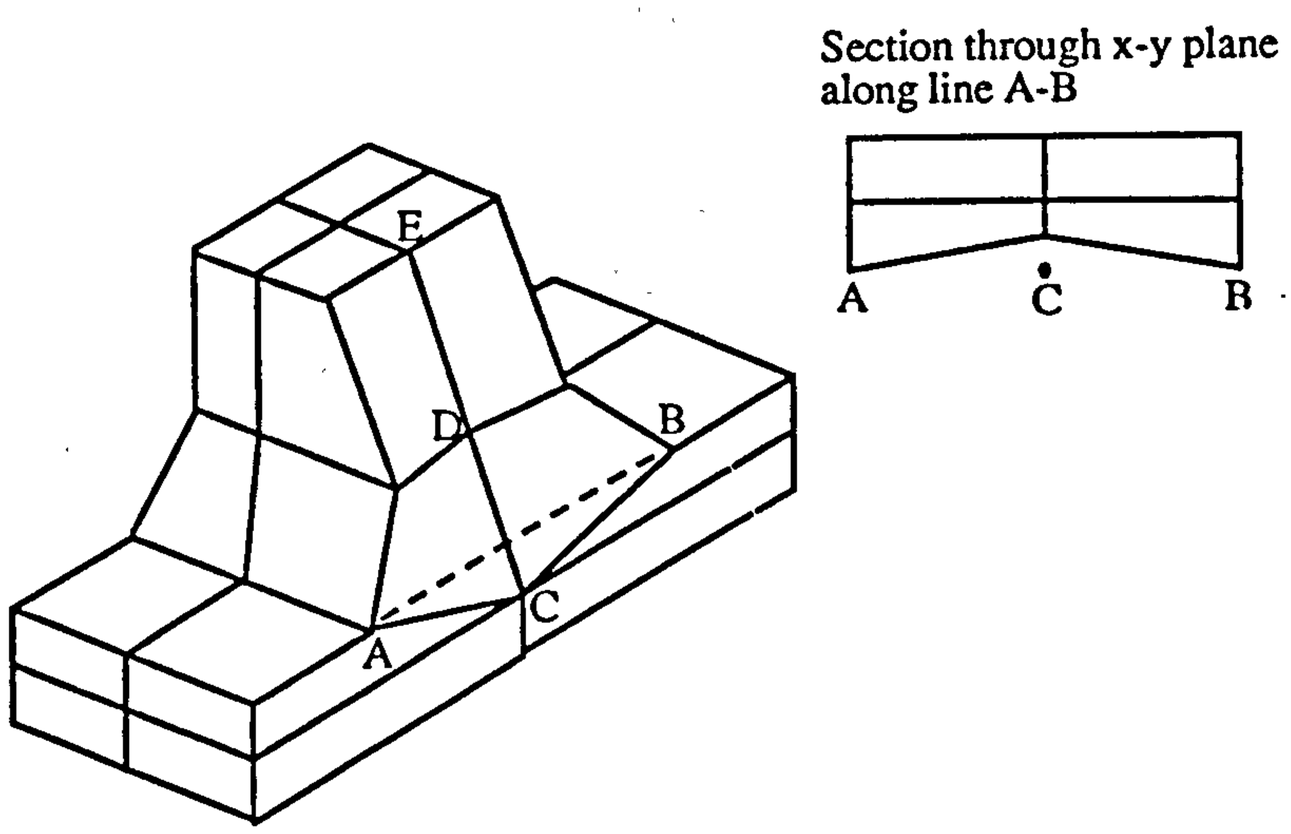

Figure A2.13. Showing the vee-shaped groove running up the face of tee-section B.

The mesh line C-D-E, representing the centreline of the front face of the side branch, is seen to run behind the vertical line dropped through point C. Ideally, the front face centreline should rise vertically from point C to intersect the line A-B, being the upper front edge of the main duct. The desired form of the face A-C-B-D is shown in Figure A2.14 below.

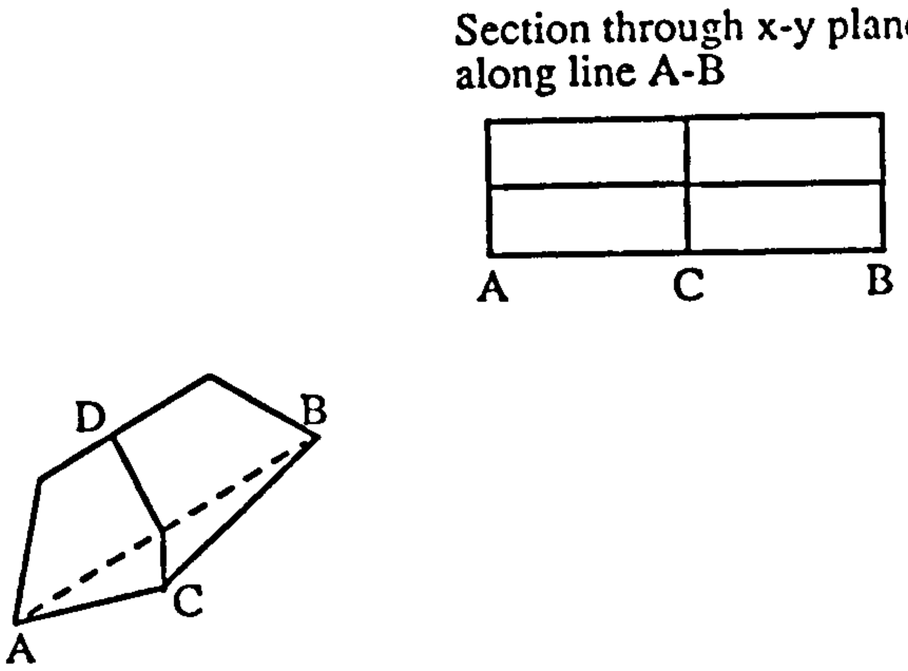

Figure A2.14. Showing an improved side branch frontage.

Inspecting Figure A2.14, it will be realised that the proposed face A-C-B-D consists of two subordinate, five-sided faces, contrary to FIDAP's requirement of rectangular prisms for three-dimensional elements. This problem was circumvented by defining the line C-D with CURVE, taking advantage of the 'dot-to-dot' nature of the CURVE command, in its constructing curves from straight lines between those points specified by its corresponding data card.

The final version of the model geometry, as demonstrated by the turbulent, steady-state input file barf.FDREAD, which is listed in Appendix A2, is then shown in detail in geometric space as Figure A2.15 below. Figure A2.16 then provides a velocity distribution at inlet and outlet to the model.

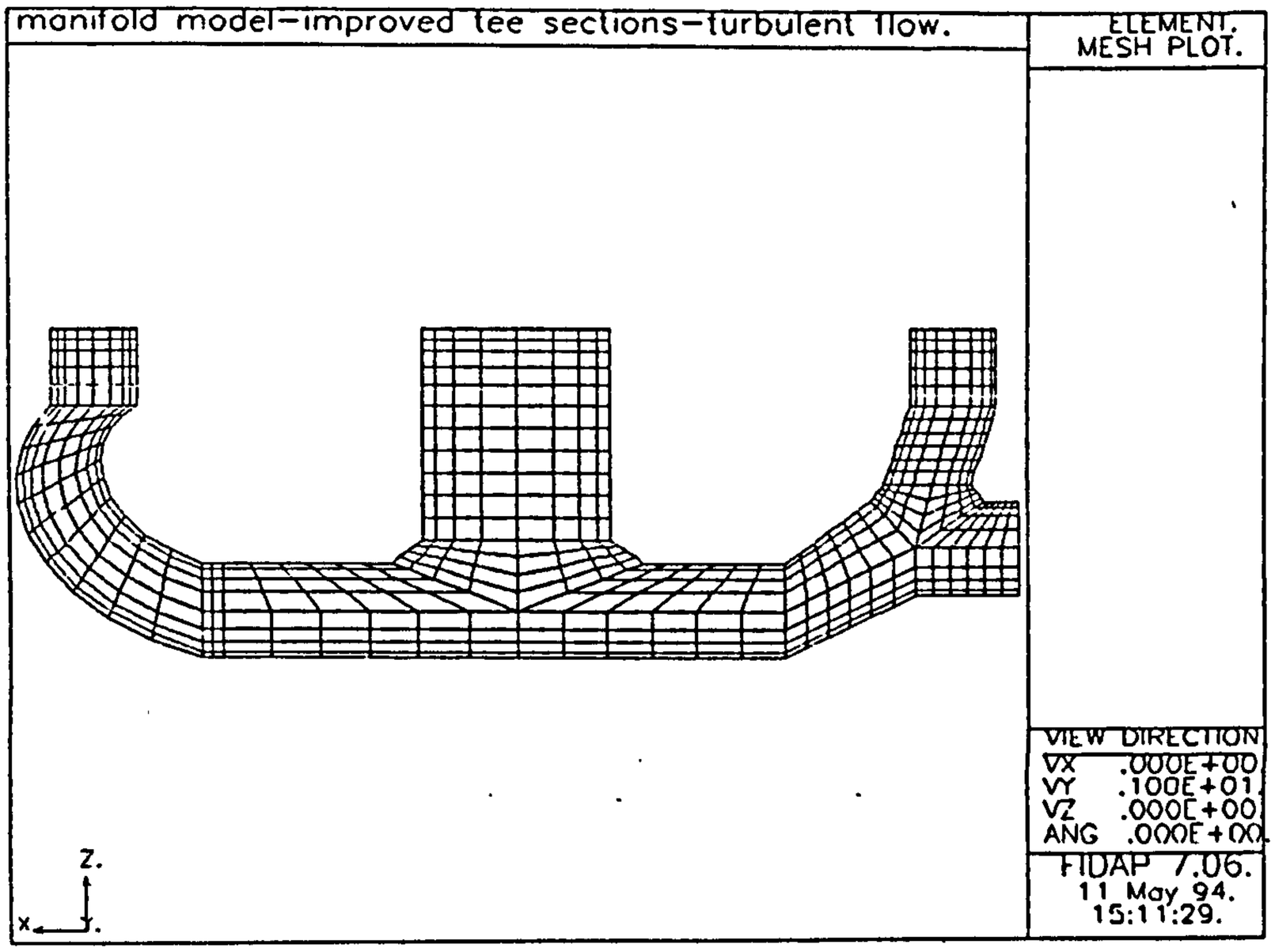

Figure A2.15a. Computational mesh for the turbulent, steady-state manifold model - geometric representation in front elevation.

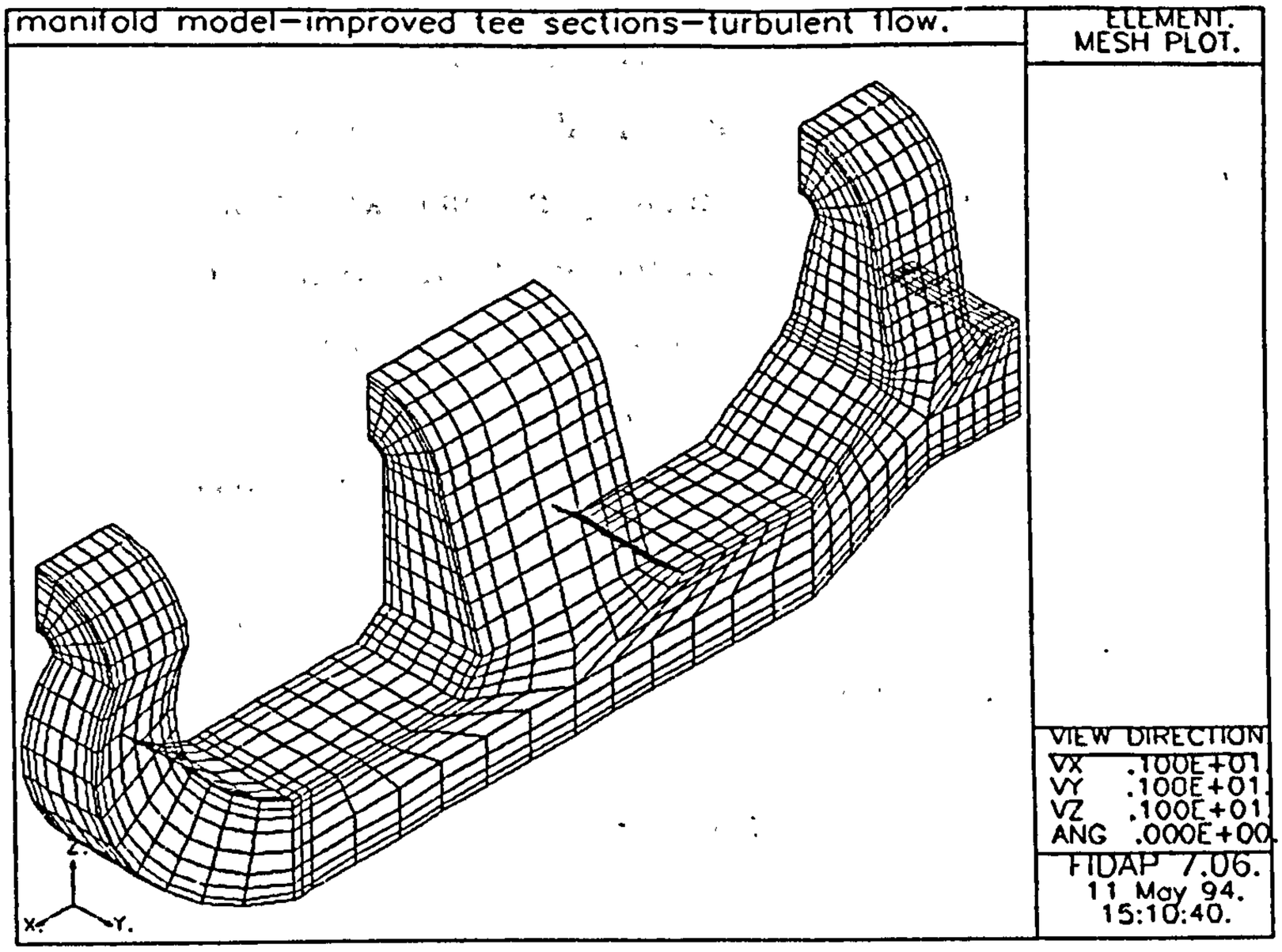

Figure A2.15b. Computational mesh for the turbulent, steady-state manifold model - isometric geometric representation.

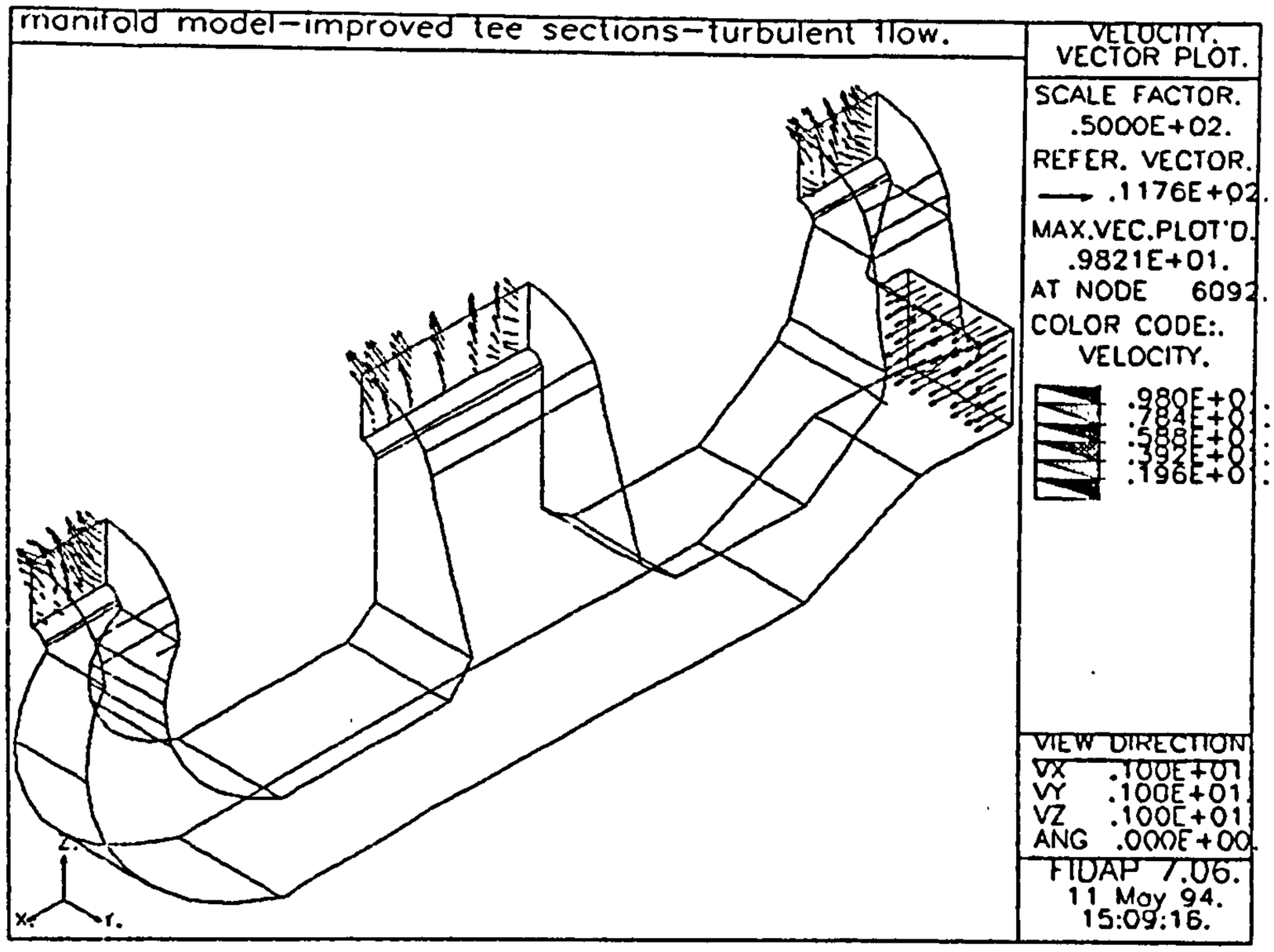

Figure A2.16. A velocity vector plot of the manifold model.

The above figures show the model to have no hidden false surfaces, not to 'leak' and to have side branch faces that are largely true.

This version of the manifold mesh was then expanded to provide a denser mesh and used for all subsequent work in this study. Whilst the model still had some shortcomings, which will be detailed shortly, for the purposes of this work, they were not rectified. The model, as detailed, contained some 19,000 nodes, which was found to be close to the capacity of the computer used for model simulation for time-dependent analysis. More elegant meshes could have been prepared for steady-state analyses but these would have been trivial, in that any results thus obtained could not be compared with transient results from simpler meshes. However, these model limitations will now be touched upon briefly, before turning to the uses that this computational mesh was put to.

The model inlet exists as a rectangular section, as opposed to the five-sided duct of the real manifold. A modified inlet section could be used as Figure A2.17 below.

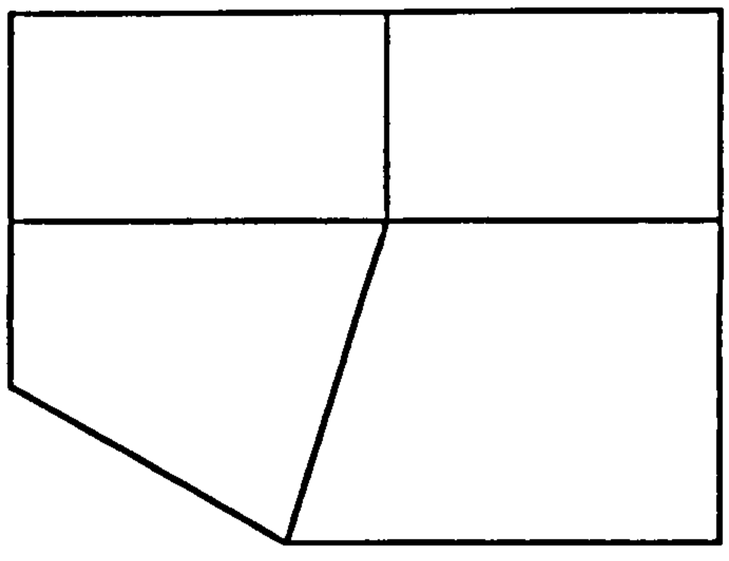

Figure A2.17. Possible improved cross-section for model inlet.

Such a section could be run along the inlet duct to join the rectangular cross-section of the main duct beneath the side branch to port 1. However, at this point a curved section would be required for the two ducts to be joined together smoothly. This would require more complex meshing locally and hence would increase the number of nodes necessary for the model.

Finally, the links between the side branches and their engine inlet ports could be improved, as shown in Figure A2.18 below.

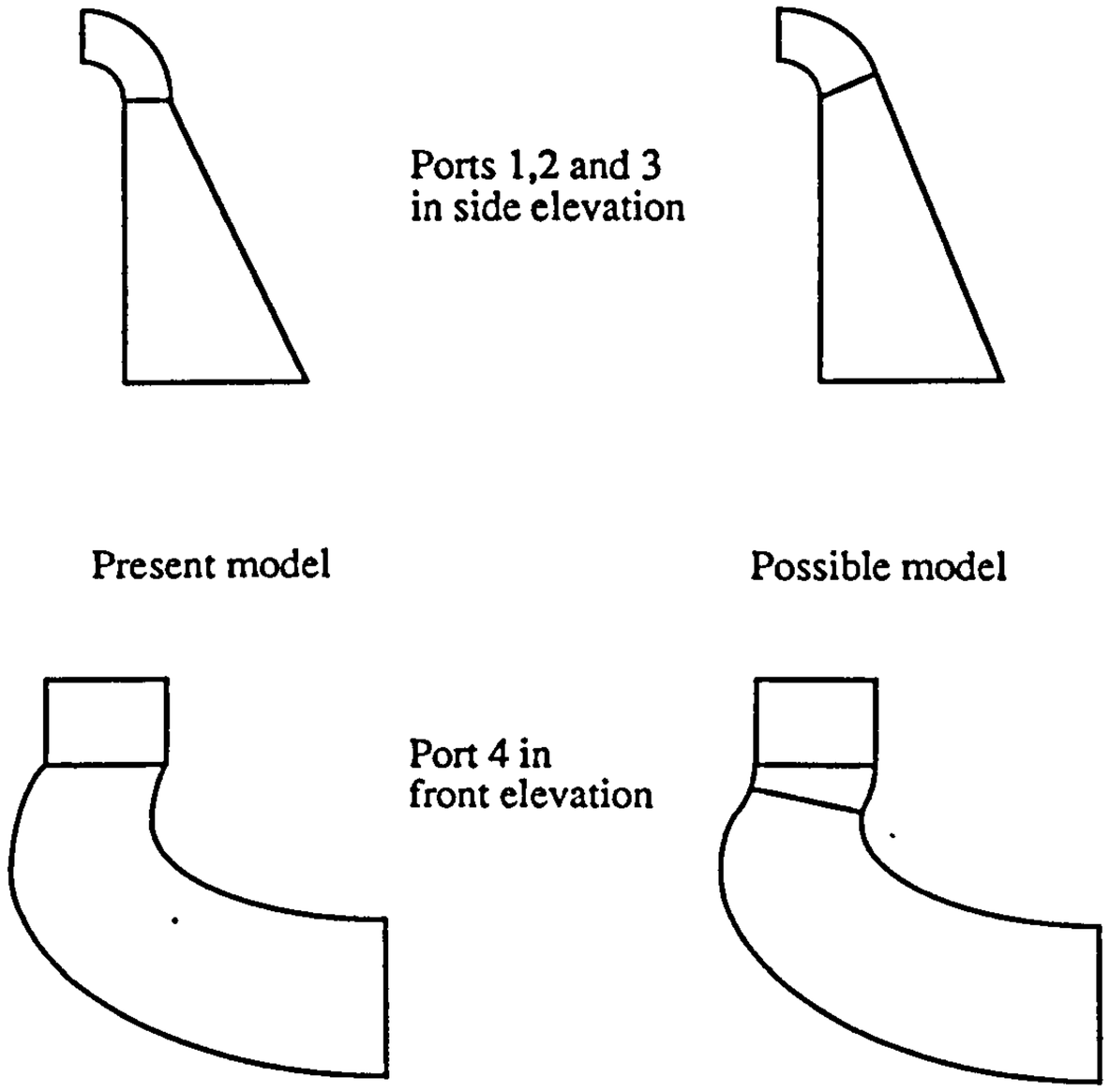

Figure A2.18. Showing details of potential porting improvements.

With regard to ports 1, 2 and 3, connected to tee-sections A and B, by tilting the end plane of the wedge-shaped body of the tee, the front face of the tee could be made to

be tangential to the arcs forming the port entrance, as shown in Figure A2.18. Also, by forming the duct between the outlet of section B and port 4 from three blended sections instead of two, the joint between the port and the duct could be made less abrupt. Again, whilst this is possible to do, with the nodal limitations for time-dependent study, it was elected not to perform these repairs.

Figure A2.19. Input file, barf.FDREAD: the inlet manifold model.

```
/ INPUT FILE FOR MANIFOLD MODEL -
/ STEADY-STATE CASE
title
manifold model
fimesh(3-d,imax=23,jmax=5,kmax=11)
expi
1 0 7 0 11 0 15 0 21 0 27 0 31 0 35 0 41 0 43 0 53 0 59
expj
1 0 5 0 9
expk
1 0 5 0 9 0 13 0 19 0 25
/ model section A
points(cartesian)
1 1 1 1 0 0 40
2 1 3 1 0 35 40
3 1 5 1 0 70 40
4 1 1 3 0 0 70
5 1 3 3 0 35 70
6 1 5 3 0 70 70
7 1 1 5 0 0 100
8 1 3 5 0 35 100
9 1 5 5 0 70 100
10 3 1 1 48 0 40
11 3 3 1 48 35 40
12 3 5 1 48 70 40
13 3 1 3 48 0 70
14 3 3 3 48 35 70
15 3 5 3 48 70 70
16 3 1 5 16 0 100
17 3 3 5 16 35 100
18 3 5 5 16 70 100
19 3 1 9 10 0 160
20 3 3 9 10 20 160
21 3 5 9 10 40 160
22 3 1 11 10 -10 170
23 3 3 11 10 -10 190
24 3 5 11 10 -10 210
25 5 1 9 30 0 160
2
6 5 3 9 30 20 160
27 5 5 9 30 40 160
28 5 1 11 30 -10 170
29 5 3 11 30 -10 190
30 5 5 11 30 -10 210
31 7 1 5 68 0 100
32 7 3 5 68 35 100
33 7 5 5 68 70 100
34 7 1 9 50 0 160
35 7 3 9 50 20 160
36 7 5 9 50 40 160
37 7 1 11 50 -10 170
38 7 3 11 50 -10 190
39 7 5 11 50 -10 210
40 9 1 1 108 0 0
41 9 3 1 108 35 0
42 9 5 1 108 70 0
43 9 1 3 108 0 30
44 9 3 3 108 35 30
45 9 5 3 108 70 30
46 9 1 5 108 0 60
47 9 3 5 108 35 60
48 9 5 5 108 70 60
49 5 1 5 48 0 70
50 5 3 5 48 35 70
51 5 5 5 48 70 70
52 7 1 1 48 0 40
53 7 3 1 48 35 40
54 7 5 1 48 70 40
55 7 1 3 48 0 70
56 7 3 3 48 35 70
57 7 5 3 48 70 70
58 0 0 0 50 -10 160
59 0 0 0 30 -10 160
60 0 0 0 10 -10 160
150 3 1 7 22 0 110.3923
151 3 3 7 22 32.401925 110.3923
152 3 5 7 22 64.80385 110.3923
153 5 1 7 39.92154 0 110.3923
154 5 3 7 39.92154 110.3923
155 5 5 7 39.92154 64.80385 110.3923
156 7 1 7 62 0 110.3923
157 7 3 7 62 32.401925 110.3923
158 7 5 7 62 64.80385 110.3923
line
1 2 1.4
2 3 0.7
4 5 1.4
5 6 0.7
7 8 1.4
8 9 0.7
10 11 1.4
11 12 0.7
13 14 1.4
14 15 0.7
16 17 1.4
17 18 0.7
19 20 1.4
20 21 0.7
22 23 1.4
23 24 0.7
49 50 1.4
50 51 0.7
25 26 1.4
26 27 0.7
28 29 1.4
29 30 0.7
52 53 1.4
53 54 0.7
55 56 1.4
56 57 0.7
31 32 1.4
32 33 0.7
34 35 1.4
35 36 0.7
37 38 1.4
38 39 0.7
40 41 1.4
41 42 0.7
43 44 1.4
44 45 0.7
46 47 1.4
47 48 0.7
1 4 1.4
4 7 0.7
2 5 1.4
5 8 0.7
3 6 1.4
6 9 0.7
10 13 1.4
13 16 0.7
11 14 1.4
14 17 0.7
12 15 1.4
15 18 0.7
52 55 1.4
55 31 0.7
53 56 1.4
56 32 0.7
54 57 1.4
57 33 0.7
40 43 1.4
43 46 0.7
41 44 1.4
44 47 0.7
42 45 1.4
45 48 0.7
1 10
4 13
7 16
2 11
5 14
8 17
3 12
6 15
9 18
49 16 0.7
19 25 1.4
22 28 1.4
50 17 0.7
20 26 1.4
23 29 1.4
51 18 0.7
21 27 1.4
24 30 1.4
49 31 0.7
25 34 0.7
28 37 0.7
50 32 0.7
26 35 0.7
29 38 0.7
51 33 0.7
27 36 0.7
30 39 0.7
52 40
55 43
31 46
53 41
56 44
32 47
54 42
57 45
33 48
16 150
17 151
18 152
49 153
50 154
31 156
32 157
33 158
150 19
151 20
152 21
153 25
154 26
155 27
156 34
157 35
158 36
150 151 1.4
151 152 0.7
153 154 1.4
154 155 0.7
156 157 1.4
157 158 0.7
150 153 1.4
153 156 0.7
151 154 1.4
154 157 0.7
152 155 1.4
155 158 0.7
arc
19 22 60
20 23 60
21 24 60
25 28 59
```

```
26 29 59
27 30 59
34 37 58
35 38 58
39 36 58
curve
51 155 6
46 70 80
44 70 90
42 70 100
41.480385 68.7009625 102.598075
40.96077 67.401925 105.19615
40.44116 66.1028875 107.794225
surface
1 13
1 12
1 6
15 10
15 4
15 3
4 16
4 9
18 13
18 7
18 6
16 34
16 33
16 21
36 31
36 19
36 18
19 37
19 24
39 34
39 22
39 21
52 43
52 42
52 57
45 40
45 55
45 54
55 46
55 33
48 43
48 31
48 57
merge
10 15 52 57
16 15 16 51
31 57 31 51
3-d
1 15
4 18
16 36
19 39
52 45
55 48
/ inlet conditions to manifold model
bcnodc(ux)
1 9 9.42
bcnodc(uy)
1 9 0
bcnodc(uz)
1 9 0
bcnodc(kinetic)
1 9 0.015
bcnodc(dissipation)
1 9 0.33068
/ no-slip boundary conditions for section A
bcnodc(velocity)
1 13
4 16
16 34
19 37
52 43
55 46
3 15
6 18
18 36
21 39
54 45
57 48
1 12
52 42
7 18
31 48
18 19
21 22
33 34
36 37
/ modcl section B
coordinatc(system=2.oldsystem=1.cartesian)
40
points(system=2.cartesian)
61 11 1 1 126 0 0
62 11 3 1 126 35 0
63 11 5 1 126 70 0
64 11 1 3 126 0 30
65 11 3 3 126 35 30
66 11 5 3 126 70 30
67 11 1 5 67 0 60
68 11 3 5 67 35 60
69 11 5 5 67 70 60
70 11 1 9 82 0 160
71 11 3 9 82 20 160
72 11 5 9 82 40 160
73 11 1 11 82 -10 170
74 11 3 11 82 -10 190
75 11 5 11 82 -10 210
76 13 1 9 126 0 160
77 13 3 9 126 20 160
78 13 5 9 126 40 160
79 13 1 11 126 -10 170
80 13 3 11 126 -10 190
81 13 5 11 126 -10 210
82 15 1 5 185 0 60
83 15 3 5 185 35 60
84 15 5 5 185 70 60
85 15 1 9 170 0 160
86 15 3 9 170 20 160
87 15 5 9 170 40 160
88 15 1 11 170 -10 170
89 15 3 11 170 -10 190
90 15 5 11 170 -10 210
91 17 1 1 265 0 0
92 17 3 1 265 35 0
93 17 5 1 265 70 0
94 17 1 3 265 0 30
95 17 3 3 265 35 30
96 17 5 3 265 70 30
97 17 1 5 265 0 60
98 17 3 5 265 35 60
99 17 5 5 265 70 60
100 13 1 5 126 0 30
101 13 3 5 126 35 30
102 13 5 5 126 70 30
103 15 1 1 126 0 0
104 15 3 1 126 35 0
105 15 5 1 126 70 0
106 15 1 3 126 0 30
107 15 3 3 126 35 30
108 15 5 3 126 70 30
109 0 0 0 170 -10 160
110 0 0 0 126 -10 160
111 0 0 0 82 -10 160
160 11 1 7 82 0 75
161 11 3 7 82 32.75 75
162 11 5 7 82 65.5 75
163 13 1 7 126 0 75
164 13 3 7 126 32.75 75
165 13 5 7 126 65.5 75
166 15 1 7 170 0 75
167 15 3 7 170 32.75 75
168 15 5 7 170 65.5 75
linc
61 62 1.4
62 63 0.7
64 65 1.4
65 66 0.7
67 68 1.4
68 69 0.7
70 71 1.4
71 72 0.7
73 74 1.4
74 75 0.7
100 101 1.4
101 102 0.7
76 77 1.4
77 78 0.7
79 80 1.4
80 81 0.7
103 104 1.4
104 105 0.7
106 107 1.4
107 108 0.7
82 83 1.4
83 84 0.7
85 86 1.4
86 87 0.7
88 89 1.4
89 90 0.7
91 92 1.4
92 93 0.7
94 95 1.4
95 96 0.7
97 98 1.4
98 99 0.7
61 64 1.4
64 67 0.7
62 65 1.4
65 68 0.7
63 66 1.4
66 69 0.7
103 106 1.4
106 82 0.7
104 107 1.4
107 83 0.7
105 108 1.4
108 84 0.7
91 94 1.4
94 97 0.7
92 95 1.4
95 98 0.7
93 96 1.4
96 99 0.7
40 61
43 64
46 67
41 62
44 65
47 68
42 63
45 66
48 69
100 67 0.7
70 76 1.4
73 79 1.4
101 68 0.7
71 77 1.4
74 80 1.4
102 69 0.7
72 78 1.4
75 81 1.4
100 82 0.7
76 85 0.7
79 88 0.7
101 83 0.7
77 86 0.7
80 89 0.7
102 84 0.7
78 87 0.7
81 90 0.7
103 91
106 94
82 97
104 92
107 95
83 98
105 93
108 96
84 99
67 160
68 161
69 162
100 163
101 164
82 166
83 167
84 168
160 70
161 71
162 72
163 76
164 77
165 78
166 85
167 86
168 87
160 161 1.4
161 162 0.7
163 164 1.4
164 165 0.7
166 167 1.4
167 168 0.7
160 163 1.4
163 166 0.7
161 164 1.4
164 167 0.7
162 165 1.4
```

```
165 168 0.7
arc
70 73 111
71 74 111
72 75 111
76 79 110
77 80 110
78 81 110
85 88 109
86 89 109
87 90 109
curve(system=2,cartesian)
102 165 6
126 70 40
126 70 50
126 70 60
126 68.875 63.75
126 67.750 67.75
126 66.625 71.25
surface
40 64
40 63
66 61
66 43
66 42
43 67
69 64
69 46
69 45
67 85
67 84
67 72
87 82
87 70
87 69
70 88
70 75
90 85
90 73
90 72
103 94
103 93
103 108
96 91
96 106
96 105
106 97
106 84
99 94
99 82
99 108
merge
67 66 67 102
82 108 82 102
61 66 103 108
3-d
40 66
43 69
67 87
70 90
103 96
106 99
/ no-slip boundary conditions for section B
bcnode(velocity)
40 64
43 67
67 85
70 88
103 94
106 97
42 66
45 69
69 87
72 90
105 96
108 99
40 63
103 93
46 69
82 99
67 72
70 75
82 87
85 90
/ model section C
points(system=2,cartesian)
139 0 0 0 275 0 160
coordinate(system=3,rotation,oldsystem=2,cylindrical)
139 1 -90
points(system=3,cylindrical)
112 19 1 1 160 90 0
113 19 3 1 160 90 35
114 19 5 1 160 90 70
115 19 1 3 130 90 0
116 19 3 3 130 90 35
117 19 5 3 130 90 70
118 19 1 5 100 90 0
119 19 3 5 100 90 35
120 19 5 5 100 90 70
121 21 1 1 70 0 0
122 21 3 1 70 0 20
123 21 5 1 70 0 40
124 21 1 3 50 0 0
125 21 3 3 50 0 20
126 21 5 3 50 0 40
127 21 1 5 30 0 0
128 21 3 5 30 0 20
129 21 5 5 30 0 40
140 0 0 0 70 0 -10
coordinate(system=4,rotation,oldsystem=3,cylindrical)
140 2 -90 3 -90
points(system=4,cylindrical)
130 23 1 1 10 0 0
131 23 3 1 30 0 0
132 23 5 1 50 0 0
133 23 1 3 10 0 20
134 23 3 3 30 0 20
135 23 5 3 50 0 20
136 23 1 5 10 0 40
137 23 3 5 30 0 40
138 23 5 5 50 0 40
line
91 112
92 113
93 114
94 115
95 116
96 117
97 118
98 119
99 120
112 113 1.4
113 114 0.7
115 116 1.4
116 117 0.7
118 119 1.4
119 120 0.7
112 115 1.4
115 118 0.7
113 116 1.4
116 119 0.7
114 117 1.4
117 120 0.7
121 122 1.4
122 123 0.7
124 125 1.4
125 126 0.7
127 128 1.4
128 129 0.7
121 124 1.4
124 127 0.7
122 125 1.4
125 128 0.7
123 126 1.4
126 129 0.7
130 131 1.4
131 132 0.7
133 134 1.4
134 135 0.7
136 137 1.4
137 138 0.7
130 133 1.4
133 136 0.7
131 134 1.4
134 137 0.7
132 135 1.4
135 138 0.7
surface
91 114
114 99
99 118
118 91
112 120
121 129
130 138
3-d
91 120
blend(system=3,cylindrical)
112 120 121 129
blend(system=4,cylindrical)
121 129 130 138
/ no-slip boundary conditions for section C
bcnode(velocity)
91 114
114 99
99 118
118 91
112 123
112 127
120 123
120 127
121 132
121 136
129 132
129 136
/ declaration of continuum elements
elements(brick,nodes=8,all,entity="fluid")
/ declaration of wall elements
elements(boundary.face.entity="back1")
1 13
4 16
elements(boundary.face.entity="back2")
16 34
19 37
elements(boundary.face.entity="back3")
52 43
55 46
elements(boundary.face.entity="front1")
3 15
6 18
elements(boundary.face.entity="front2")
18 36
21 39
elements(boundary.face.entity="front3")
54 45
57 48
```

```
elements(boundary.face,entity="bot1")
1 12
elements(boundary.face,entity="bot3")
52 42
elements(boundary.face,entity="top1")
7 18
elements(boundary.face,entity="top3")
31 48
elements(boundary.face,entity="side1")
18 19
21 22
elements(boundary.face,entity="side3")
33 34
36 37
elements(boundary.face,entity="back4")
40 64
43 67
elements(boundary.face,entity="back5")
67 85
70 88
elements(boundary.face,entity="back6")
103 94
106 97
elements(boundary.face,entity="front4")
42 66
45 69
elements(boundary.face,entity="front5")
69 87
72 90
elements(boundary.face,entity="front6")
105 96
108 99
elements(boundary.face,entity="bot4")
40 63
elements(boundary.face,entity="bot6")
103 93
elements(boundary.face,entity="top4")
46 69
elements(boundary.face,entity="top6")
82 99
elements(boundary.face,entity="side4")
67 72
70 75
elements(boundary.face,entity="side6")
82 87
85 90
elements(boundary.face,entity="bot7")
91 114
elements(boundary.face,entity="front7")
114 99
elements(boundary.face,entity="top7")
99 118
elements(boundary.face,entity="back7")
118 91
elements(boundary.face,entity="bot8")
112 123
elements(boundary.face,entity="back8")
112 127
elements(boundary.face,entity="front8")
120 123
elements(boundary.face,entity="top8")
120 127
elements(boundary.face,entity="bot9")
121 132
elements(boundary.face,entity="back9")
121 136
elements(boundary.face,entity="front9")
129 132
elements(boundary.face,entity="top9")
129 136
/ports I - IV
bcnode(velocity)
/24 37
/75 79
/81 88
/130 138
elements(boundary.face,entity="portage")
24 37
75 79
81 88
130 138
end
fiprep
/ specification of problem and solution types
problem(3-d,turbulent,nonlinear)
pressure(penalty=1.e-6)
execution(newjob)
solution(segregated=700,cgs=5000,cr=5000,accf=0.8)
options(upwinding=0.8)
/ element declarations
entity(name="fluid",fluid)
entity(name="top1",wall)
entity(name="top3",wall)
entity(name="top4",wall)
entity(name="top6",wall)
entity(name="top7",wall)
entity(name="top8",wall)
entity(name="top9",wall)
entity(name="bot1",wall)
entity(name="bot3",wall)
entity(name="bot4",wall)
entity(name="bot6",wall)
entity(name="bot7",wall)
entity(name="bot8",wall)
entity(name="bot9",wall)
entity(name="back1",wall)
entity(name="back2",wall)
entity(name="back3",wall)
entity(name="back4",wall)
entity(name="back5",wall)
entity(name="back6",wall)
entity(name="back7",wall)
entity(name="back8",wall)
entity(name="back9",wall)
entity(name="front1",wall)
entity(name="front2",wall)
entity(name="front3",wall)
entity(name="front4",wall)
entity(name="front5",wall)
entity(name="front6",wall)
entity(name="front7",wall)
entity(name="front8",wall)
entity(name="front9",wall)
entity(name="side1",wall)
entity(name="side3",wall)
entity(name="side4",wall)
entity(name="side6",wall)
entity(name="portage",plot)
/ declaration of fluid properties and initial conditions
icnodes(velocity,stokes,entity="fluid")
icnodes(kinetic,constant=0.015,entity="fluid")
icnodes(dissipation,constant=0.33068,entity="fluid")
viscosity(k.e.,clip=1.e6,const=1.7e-5)
density(constant=1.226)
renumber
scale(x=0.001,y=0.000785,z=0.00075)
end
create(fisolv)
end
```

Figure A2.20. Modifications to the input file, barf.FDREAD: solution procedures for transient models of the inlet manifold.

```
/ MODIFICATIONS TO MANIFOLD INPUT FILE
/ FOR TRANSIENT RUN no 1
/ ***** alterations in fimesh module *****
title
manifold model - transient run no. 1
/ports I - IV
bcnode(velocity)
/24 37
75 79
/81 88
130 138
/ ***** alterations in fiprep module *****
/ specification of problem and solution types
problem(3-d,turbulent,nonlinear,transient)
execution(restart)
solution(segregated=2050,velconv=0.0075,cgs=5000,cr=5000,accf=0.8)
timeintegration(backward,nsteps=8,tstart=0.0,tend=0.008336,dt=0.001042,fixed)
postprocess(nblocks=1)
2 8 3
```

```
/ MODIFICATIONS TO MANIFOLD INPUT FILE
/ FOR TRANSIENT RUN no.2
/ ***** alterations in fimesh module *****
title
manifold model - transient run no.2
/ports I - IV
bcnode(velocity)
24 37
75 79
/81 88
130 138
/ ***** alterations in fiprep module *****
/ specification of problem and solution types
problem(3-d,turbulent,nonlinear,transient)
execution(restart)
solution(segregated=2050,velconv=0.0075,cgs=5000,cr=5000,accf=0.8)
timeintegration(backward,nsteps=8,tstart=0.008336,tend=0.025008,dt=0.001042,fixed)
postprocess(nblocks=1)
2 16 7
```

```
/ MODIFICATIONS TO MANIFOLD INPUT FILE
/ FOR TRANSIENT RUN no.3
/ ***** alterations in fimesh module *****
title
manifold model - transient run no.3
/ports I - IV
bcnode(velocity)
24 37
75 79
/81 88
/130 138
/ ***** alterations in fiprep module *****
/ specification of problem and solution types
problem(3-d,turbulent,nonlinear,transient)
execution(restart)
solution(segregated=2050,velconv=0.0075,cgs=5000,cr=5000,accf=0.8)
timeintegration(backward,nsteps=8,tstart=0.025008,tend=0.0333440,dt=0.001042,fixed)
postprocess(nblocks=1)
2 8 3
```

Appendix A3. Algorithm Flowcharts and Subroutine Listings for Two-dimensional Coles' Law Models.

The FIDAP input files, algorithm flowcharts and subroutine listings detailing the Coles' law models of the U-bend and the backward facing step will now be listed in turn. A description of the workings of these models is given in Chapter Five.

Figure A3.1. Input file, ex29.FDREAD: the standard FIDAP model of the U-bend.

```
/ INPUT FILE FOR U-BEND -
/ STANDARD fidap MODEL
title
u-bend - standard FIDAP model
fimesh(2-d,imax=5,jmax=3)
expi
/1  2  3  4  5
 1 20 35 50 70
expj
/1  2  3
 1 21 41
point
/N  I J K  X     Y
 1  1 1 1 -1.    4.5
 2  1 2 1 -1.    5.0
 3  1 3 1 -1.    5.5
 4  2 1 1  7.    4.5
 5  3 1 1  8.5   6.0
 6  4 1 1  7.    7.5
 7  5 1 1 -1.    7.5
 8  5 3 1 -1.    6.5
 9  4 3 1  7.    6.5
10  3 3 1  7.5   6.0
11  2 3 1  7.    5.5
12  5 2 1 -1.    7.0
13  2 2 1  7.    5.0
14  3 2 1  8.0   6.0
15  4 2 1  7.    7.0
30  0 0 0  7.    6.0
line
 1  2  1.05
 3  2  1.05
 8  12  1.05
 7  12  1.05
 4  13  1.1
11  13  1.1
10  14  1.1
 5  14  1.1
 9  15  1.1
 6  15  1.1
 1  4  .875
 3  11  .855
 7  6  .875
 8  9  .855
arc
 4  5  30
 5  6  30
11 10  30
10  9  30
surface
1 8
bcnode(ux)
1 3 1.
bcnode(uy)
1 3 0.
bcnode(velocity)
1 7 0.
8 3 0.
bcnode(kinetic)
1 3 .001
bcnode(dissipation)
1 3 .0009
elements(quadrilateral,nodes=4,all,entity="blob")
elements(boundary,face,entity="horn")
1 7
8 3
number
2 1
end
fiprep
problem(nonlinear,turbulent,axi-symmetric)
pressure(mixed,discontinuous)
execution(newjob)
density(constant=1)
icnode(kinetic,constant=.001,entity="blob")
icnode(dissipation,constant=.0009,entity="blob")
viscosity(k.e.,clip=1.e6,constant=1.e-5)
solution(segregated=300,pprojection)
options(upwinding)
dataprint(nodes=2,elements=1)
entity(name="blob",fluid)
entity(name="horn",wall)
ENDend
create(fisolv)
endEND
```

```
/ INPUT FILE FOR U-BEND -
/ SIMPLE COLES' MODEL
title
u-bend - simple Coles' model
fimesh(2-d,imax=5,jmax=3)
expi
/1  2  3  4  5
 1 20 35 50 70
expj
/1  2  3
 1 21 41
point
/N  I J K  X     Y
 1  1 1 1 -1.    4.5
 2  1 2 1 -1.    5.0
 3  1 3 1 -1.    5.5
 4  2 1 1  7.    4.5
 5  3 1 1  8.5   6.0
 6  4 1 1  7.    7.5
 7  5 1 1 -1.    7.5
 8  5 3 1 -1.    6.5
 9  4 3 1  7.    6.5
10  3 3 1  7.5   6.0
11  2 3 1  7.    5.5
12  5 2 1 -1.    7.0
13  2 2 1  7.    5.0
14  3 2 1  8.0   6.0
15  4 2 1  7.    7.0
30  0 0 0  7.    6.0
line
 1   2   1.05
 3   2   1.05
 8  12   1.05
 7  12   1.05
 4  13   1.1
11  13   1.1
10  14   1.1
 5  14   1.1
 9  15   1.1
 6  15   1.1
 1   4   .875
 3  11   .855
 7   6   .875
 8   9   .855
arc
 4  5  30
 5  6  30
11 10  30
10  9  30
surface
1 8
bcnode(ux)
1 3 1.
bcnode(uy)
1 3 0.
bcnode(velocity)
1 7 0.
8 3 0.
bcnode(kinetic)
1 3 .001
1 7 0.
8 3 0.
bcnode(dissipation)
1 3 .0009
1 7 0.
8 3 0.
elements(quadrilateral,nodes=4,all,entity="domain")
elements(boundary,face,entity="outerwall")
1 7
elements(boundary,face,entity="innerwall")
8 3
elements(boundary,face,entity="oatlet")
7 8
elements(boundary,face,entity="inlet")
1 3
number
2 1
end
fiprep
problem(nonlinear,turbulent,axi-symmetric)
pressure(mixed,discontinuous)
execution(newjob)
density(constant=1)
icnode(kinetic,constant=.001,entity="domain")
icnode(dissipation,constant=.0009,entity="domain")
source(kinetic,entity="domain",subroutine)
bcnode(ux,nodes,fsubroutine)
40 2869 41
0
bcnode(uy,nodes,fsubroutine)
819 2049 41
0
bcnode(uy,nodes,constant=0.0)
40 778 41
0
bcnode(uy,nodes,constant=0.0)
2090 2869 41
0
bcnode(kinetic,nodes,fsubroutine)
40 2869 41
0
bcnode(dissipation,nodes,fsubroutine)
40 2869 41
0
bcnode(ux,nodes,fsubroutine
2 2831 41
0
bcnode(uy,nodes,fsubroutine
781 2011 41
0
bcnode(uy,nodes,constant=0.0)
2 740 41
0
bcnode(uy,nodes,constant=0.0)
2052 2831 41
0
bcnode(kinetic,nodes,fsubroutine)
2 2831 41
0
bcnode(dissipation,nodes,fsubroutine)
2 2831 41
0
viscosity(k.e.,clip=1.e6,constant=1.e-5)
solution(segregated=400,pprojection)
options(upwinding)
dataprint(nodes=2,elements=1)
entity(name="domain",fluid)
entity(name="outerwall",plot)
entity(name="innerwall",plot)
entity(name="oatlet",plot)
entity(name="inlet",plot)
end
create(fisolv)
end
```

Figure A3.2. Input file, peeg.FDREAD: the simple Coles' law model of the U-bend.

Figure A3.3. Algorithm flowchart, blammo.f: the simple Coles' law model of the U-bend.

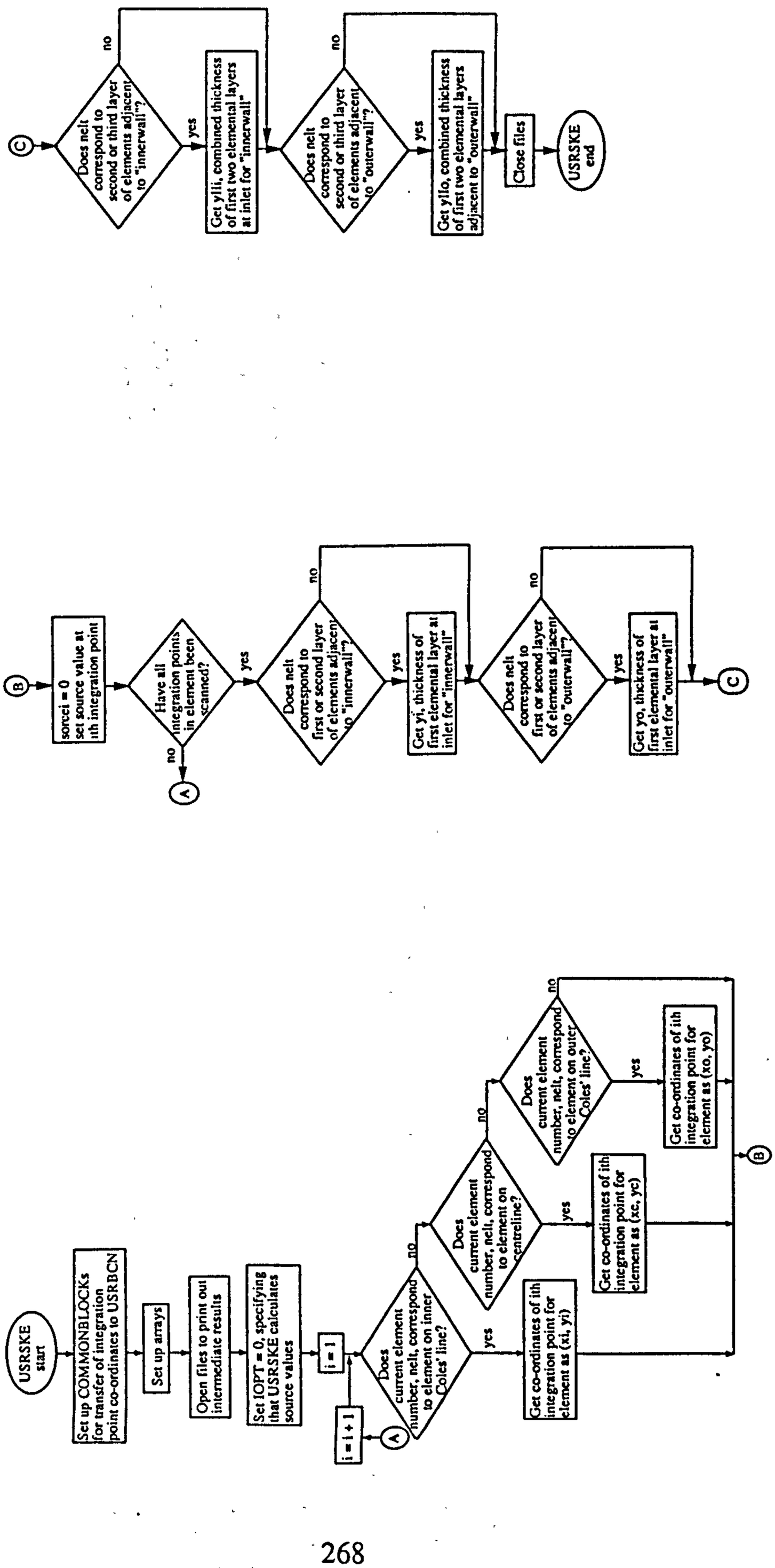

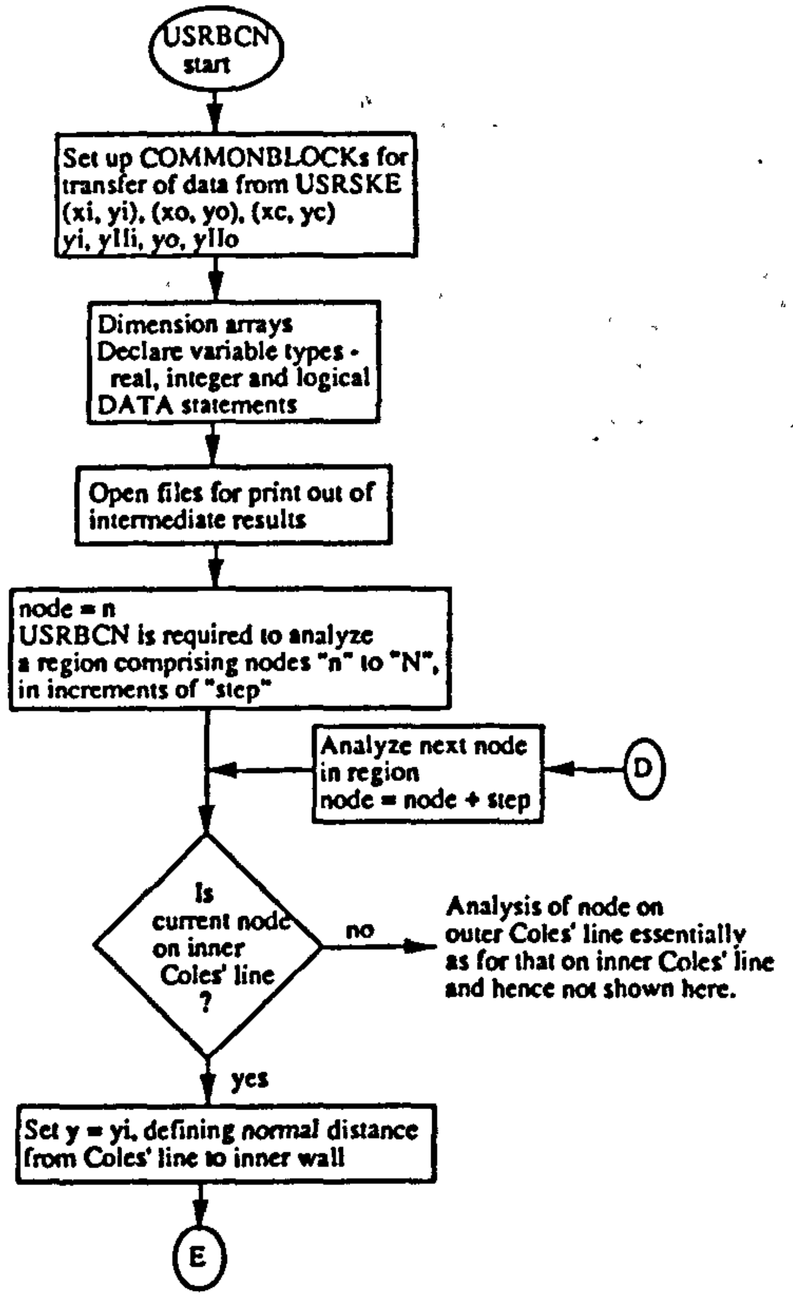
USRBCN
start
Set up COMMONBLOCKs for transfer of data from USRSKE
(xi, yi), (xo, yo), (xc, yc)
yi, yIIi, yo, yIIo
Dimension arrays
Declare variable types - real, integer and logical
DATA statements
Open files for print out of intermediate results
node = n
USRBCN is required to analyze a region comprising nodes "n" to "N", in increments of "step"
Analyze next node in region
node = node + step
D
Is current node on inner Coles' line ?
no
Analysis of node on outer Coles' line essentially as for that on inner Coles' line and hence not shown here.
yes
Set y = yi, defining normal distance from Coles' line to inner wall
E

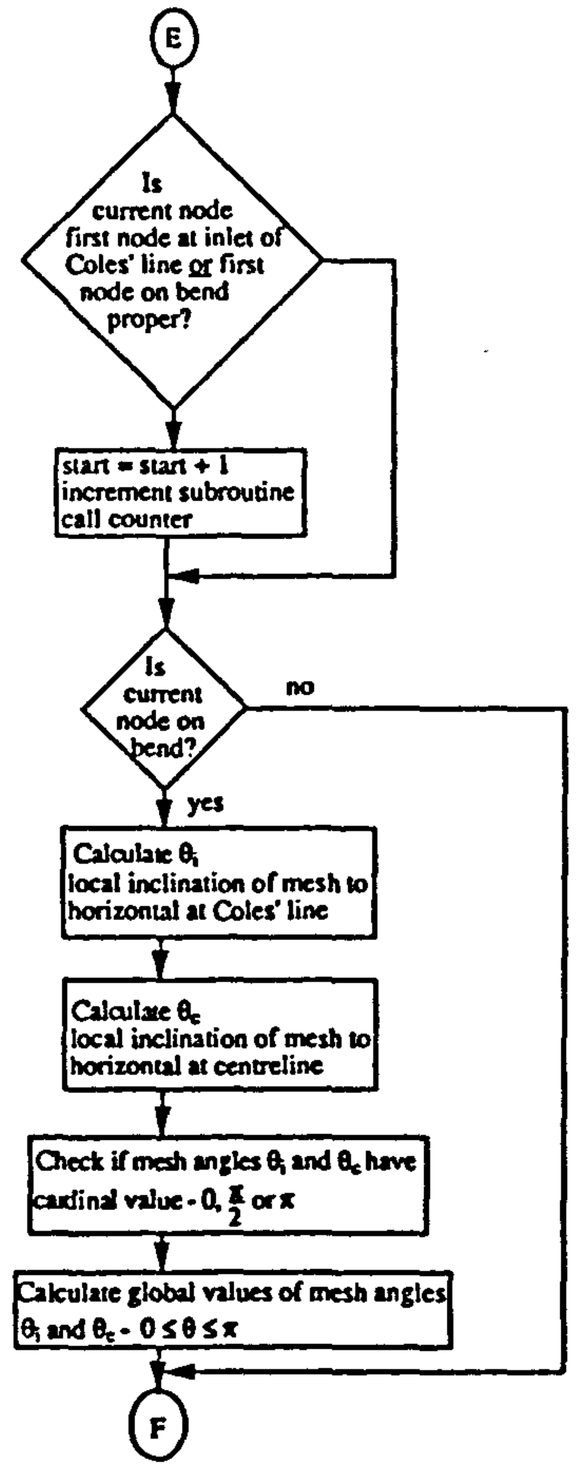
E
Is current node first node at inlet of Coles' line or first node on bend proper?
start = start + 1
increment subroutine call counter
Is current node on bend?
no
yes
Calculate θ_i
local inclination of mesh to horizontal at Coles' line
Calculate θ_c
local inclination of mesh to horizontal at centreline
Check if mesh angles θ_i and θ_c have cardinal value - 0, $\frac{\pi}{2}$ or π
Calculate global values of mesh angles θ_i and θ_c - $0 \leq \theta \leq \pi$
F

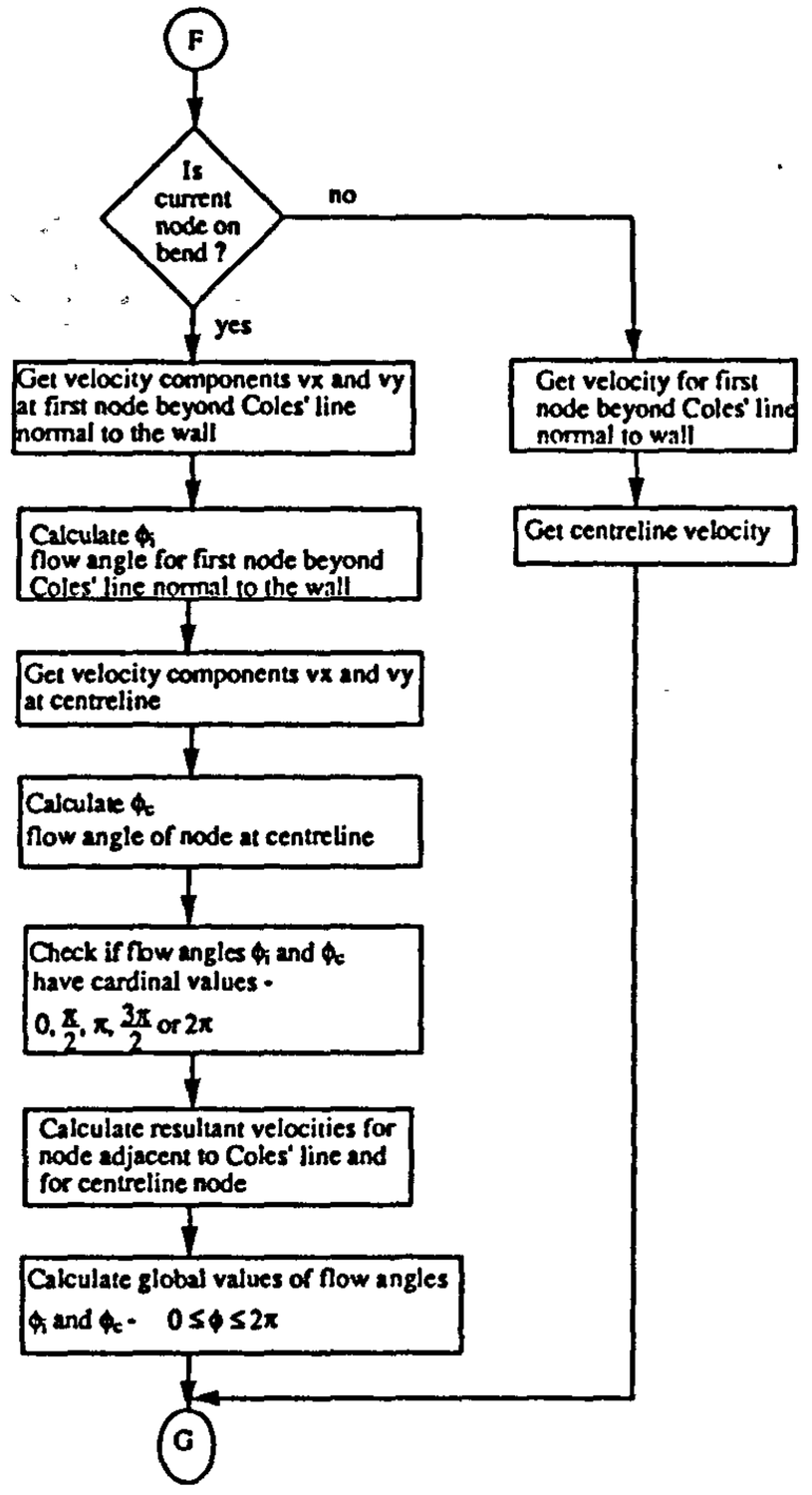
F
Is current node on bend ?
no
yes
Get velocity components vx and vy at first node beyond Coles' line normal to the wall
Get velocity for first node beyond Coles' line normal to wall
Calculate ϕ_i flow angle for first node beyond Coles' line normal to the wall
Get centreline velocity
Get velocity components vx and vy at centreline
Calculate ϕ_c flow angle of node at centreline
Check if flow angles ϕ_i and ϕ_c have cardinal values - $0, \frac{\pi}{2}, \pi, \frac{3\pi}{2}$ or 2π
Calculate resultant velocities for node adjacent to Coles' line and for centreline node
Calculate global values of flow angles ϕ_i and ϕ_c - $0 \leq \phi \leq 2\pi$
G

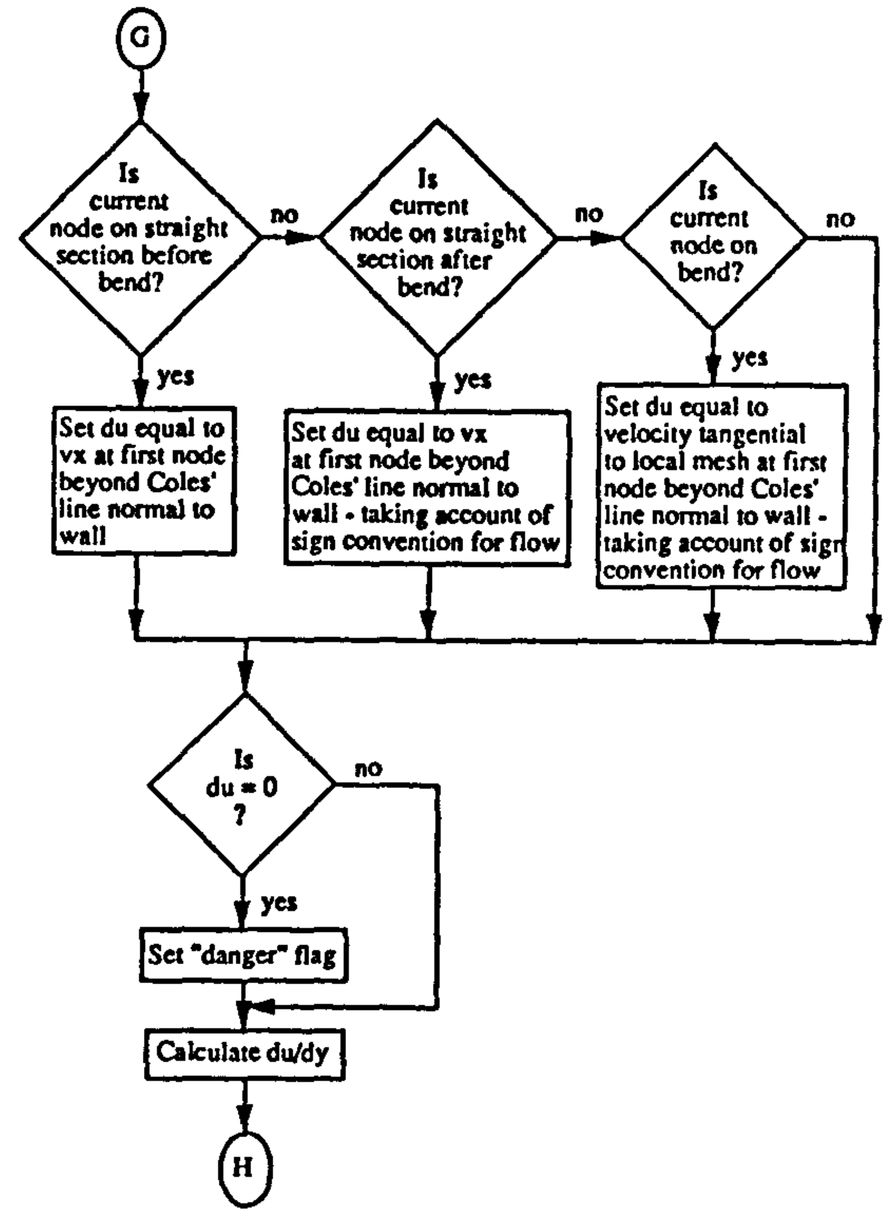
G
Is current node on straight section before bend?
no
Is current node on straight section after bend?
no
Is current node on bend?
no
yes
yes
yes
Set du equal to vx at first node beyond Coles' line normal to wall
Set du equal to vx at first node beyond Coles' line normal to wall - taking account of sign convention for flow
Set du equal to velocity tangential to local mesh at first node beyond Coles' line normal to wall - taking account of sign convention for flow
Is du = 0 ?
no
yes
Set "danger" flag
Calculate du/dy
H

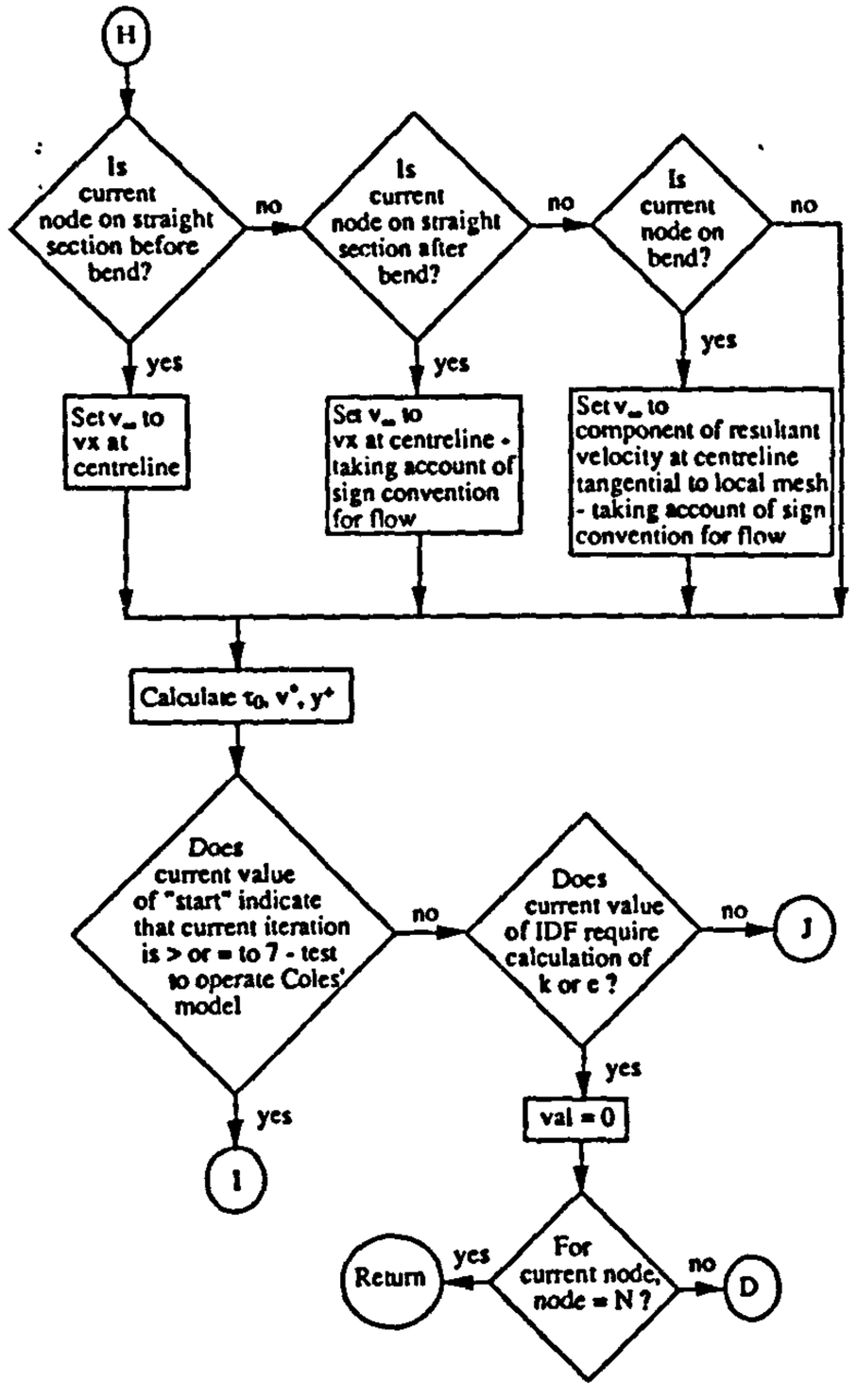
H
Is current node on straight section before bend?
no
Is current node on straight section after bend?
no
Is current node on bend?
no
yes
yes
yes
Set v_m to vx at centreline
Set v_m to vx at centreline - taking account of sign convention for flow
Set v_m to component of resultant velocity at centreline tangential to local mesh - taking account of sign convention for flow
Calculate τ0, v*, y+
Does current value of "start" indicate that current iteration is > or = to 7 - test to operate Coles' model
no
Does current value of IDF require calculation of k or e ?
no
J
yes
yes
I
val = 0
Return
yes
For current node, node = N ?
no
D

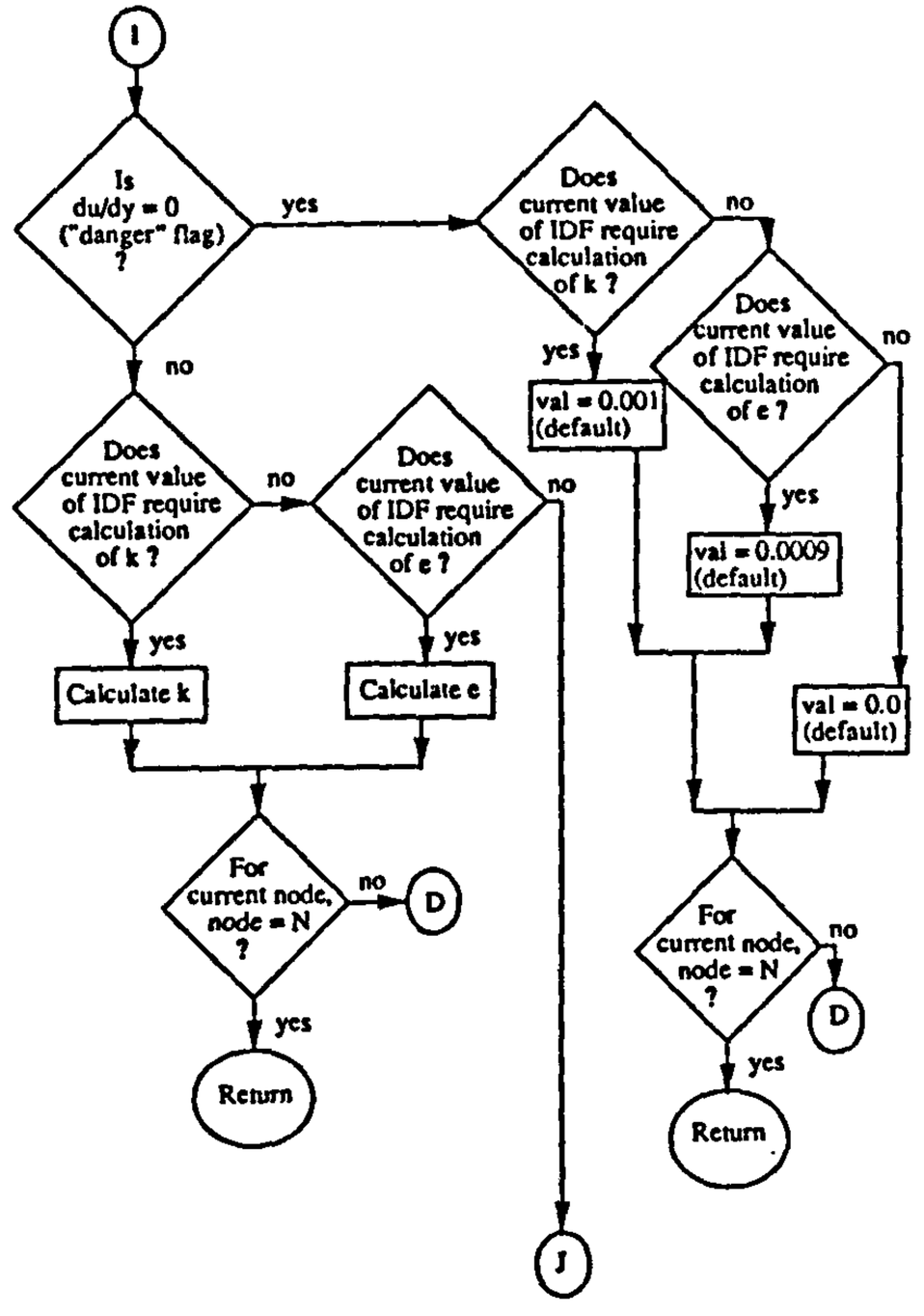
I
Is du/dy = 0 ("danger" flag) ?
yes
Does current value of IDF require calculation of k ?
no
yes
val = 0.001 (default)
Does current value of IDF require calculation of e ?
no
yes
val = 0.0009 (default)
no
val = 0.0 (default)
Does current value of IDF require calculation of k ?
no
Does current value of IDF require calculation of e ?
no
yes
yes
Calculate k
Calculate e
For current node, node = N ?
no
D
yes
Return
J
For current node, node = N ?
no
D
yes
Return

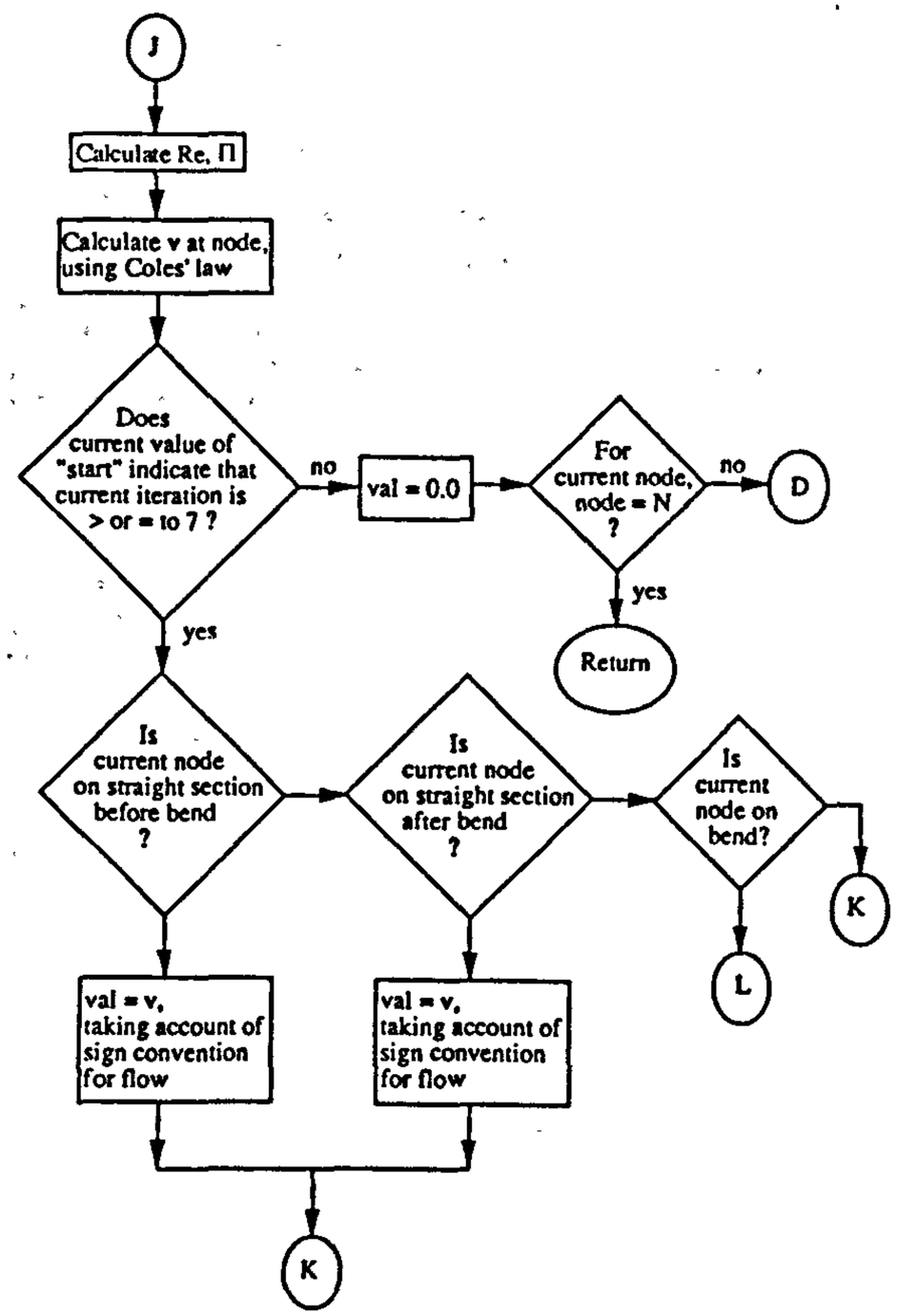
J
Calculate Re, Π
Calculate v at node, using Coles' law
Does current value of "start" indicate that current iteration is > or = to 7 ?
no
val = 0.0
For current node, node = N ?
no
D
yes
Return
yes
Is current node on straight section before bend ?
Is current node on straight section after bend ?
Is current node on bend?
K
L
val = v, taking account of sign convention for flow
val = v, taking account of sign convention for flow
K

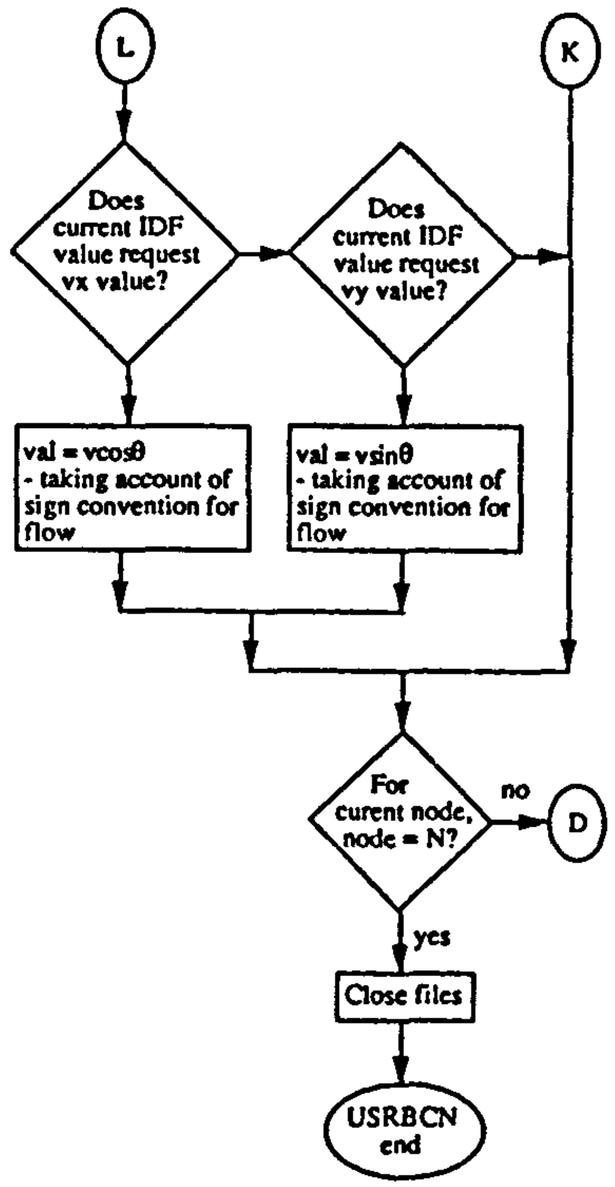
L
K
Does current IDF value request vx value?
Does current IDF value request vy value?
val = vcosθ - taking account of sign convention for flow
val = vsinθ - taking account of sign convention for flow
For curent node, node = N?
no
D
yes
Close files
USRBCN end

```
      SUBROUTINE USRSKE (NELT,NE,NG,SORCE,VARI,DVARI,NDFCD,LDOFU,SHP,
     1                   DSDX,XYZL,PROP,TIME,NPTS,ndp,MNDP,IERR,IOPT,
     2                   visct,viscl,den,mdvsc)
C
C     USER DEFINED SOURCES FOR KINETIC ENERGY OR DISSIPATION
C
C     NELT  = GLOBAL ELEMENT NUMBER
C     NE    = LOCAL ELEMENT NUMBER
C     NG    = GROUP NUMBER
C     SORCE = TURBULENT KINETIC ENERGY OR DISSIPATION (RETURNED VALUES)
C     VARI  = ARRAY OF SOLUTION VARIBLES AT INTEGRATION POINTS
C     DVARI = GRADIENTS OF SOLUTION VARIABLES AT INTEGRATION POINTS
C     LDOFU = pointer array for accessing vari and dvari information
C     XYZL  = X,Y,Z COORDINATES
C     SHP   = ELEMENT SHAPE FUNCTIONS
C     DSDX  = SHAPE FUNCTION DERIVATIVES IN THE X,Y,Z DIRECTION
C     PROP  = USER DEFINED PARAMETERS
C     MNDP  = FIRST DIMENSION OF SHAPE FUNCTION MATRICES
C     TIME  = TIME
C     NPTS  = NUMBER OF POINTS
C     IOPT = 0   ENERGY EQUATION
C     IOPT = N   TRANSPORT EQUATION FOR SPECIES N (0<N<16)
C     VISCT = TURBULENT VISCOSITY
C     VISCL = LAMINAR VISCOSITY
C     MDVSC = NUMBER OF COMPONENTS OF VISCOSITY ARRAY
C     IOPT = 0   KINETIC ENERGY SOURCES
C     IOPT = 1   DISSIPATION SOURCES
C
      INCLUDE 'IMPLCT.COM'
      INCLUDE 'PARUSR.COM'
c     ****** beware the Ides of March **********************
      common/distancei/ whyi,xi(2623:2760,4),yi(2623:2760,4)
      common/distanceo/ whyo,xo(1:138,4),yo(1:138,4)
      common/centre/ xc(1312:1449,4),yc(1312:1449,4)
      common/distII/yIIi,yIIo
      DIMENSION SORCE(NPTS),visct(npts),viscl(9,npts),den(npts)
      DIMENSION SHP(MNDP,NPTS),DSDX(MNDP,NPTS,NDFCD),XYZL(NPTS,NDFCD)
      DIMENSION PROP(*),VARI(NPTS,*),DVARI(NPTS,NDFCD,*),LDOFU(*)
      logical alive
c     ****** file handling *************
      inquire(file='ubend1',exist=alive)
      if(.not.alive)then
        open(9,file='ubend1',status='new',form='formatted')
      else
        open(9,file='ubend1',status='old',form='formatted')
      endif
      iopt=0
c     ****** obtain Gaussian point co-ordinates ******
      do 10 i=1,npts
        sorce(i)=0.
        if((nelt.ge.2623).and.(nelt.le.2760))then
c         ****** inner *******
          xi(nelt,i)=xyzl(i,1)
          yi(nelt,i)=xyzl(i,2)
        elseif((nelt.ge.1312).and.(nelt.le.1449))then
c         **** centreline ****
          xc(nelt,i)=xyzl(i,1)
          yc(nelt,i)=xyzl(i,2)
        elseif((nelt.ge.1).and.(nelt.le.138))then
c         ****** outer *******
          xo(nelt,i)=xyzl(i,1)
          yo(nelt,i)=xyzl(i,2)
        endif
10      continue
c     ******* obtain y values ***************
c     *** first element layer ***
      if(nelt.eq.2623)then
        gauhgi2=xyzl(2,2)
      elseif(nelt.eq.2692)then
        gauhgi1=xyzl(1,2)
        whyi=abs(5.5-((gauhgi1+gauhgi2)/2.))
      endif
      if(nelt.eq.1)then
        gauhgo1=xyzl(2,2)
      elseif(nelt.eq.70)then
        gauhgo2=xyzl(1,2)
        whyo=abs(4.5-((gauhgo1+gauhgo2)/2.))
      endif
c     *** second layer ***
      if(nelt.eq.2554)then
        gaughi3=xyzl(2,2)
      elseif(nelt.eq.2623)then
        gaughi4=xyzl(1,2)
        yIIi=abs(5.5-((gaughi3+gaughi4)/2.))
      endif
      if(nelt.eq.70)then
        gaugho3=xyzl(2,2)
      elseif(nelt.eq.139)then
        gaugho4=xyzl(1,2)
        yIIo=abs(4.5-((gaugho3+gaugho4)/2.))
      endif
      if(nelt.eq.2760)then
        write(9,*)'whyi',whyi,'whyo',whyo,'go1',gauhgo1,'go2',
     c            gauhgo2
        write(9,*) 'yIIi',yIIi,'yIIo',yIIo
      endif
      close(9)
      RETURN
      END
c
      SUBROUTINE USRBCN (VAL,NODE,IDF,TIME,SOL,ID,NDOF,NUMNP,LDOFU,
     1                   CONSTR)
      INCLUDE 'IMPLCT.COM'
      INCLUDE 'PARUSR.COM'
c     ******** remember the postcode ********************
      common/distancei/ whyi,xi(2623:2760,4),yi(2623:2760,4)
      common/distanceo/ whyo,xo(1:138,4),yo(1:138,4)
      common/centre/ xc(1312:1449,4),yc(1312:1449,4)
```

Figure A3.4. Subroutine listing, blammo.f: the simple Coles' law model of the U-bend.

```
      common/distII/yIIi,yIIo
      DIMENSION SOL(*),ID(NUMNP,NDOF),CONSTR(*),LDOFU(*)
      dimension cay(3000),storei(40:2869),uistx(40:2869)
     c,vistx(40:2869),uisty(819:2049),visty(819:2049)
      dimension storeo(2:2831),uostx(2:2831),vostx(2:2831),
     cuosty(781:2011),vosty(781:2011)
      dimension ucst(21:2850),vcst(21:2850),vel(3000),dudy(3000)
      integer start
      integer flag
      integer danger
      real phii,phic,phio,pang
      logical alive,kickin
c     ********** problem dependent things ******************
      data visk,destny,gnew,dia/1.e-5,1.,1.e-5,1.0/
      data bee,voncam,seemew,pang/4.9,0.41,0.09,3.1415927/
      inquire(file='ubend1',exist=alive)
c     ****** file handling *************
      if(.not.alive)then
        open(9,file='ubend1',status='new',form='formatted')
      else
        open(9,file='ubend1',status='old',form='formatted')
      endif
      inquire(file='ubend2',exist=kickin)
      if(.not.kickin)then
        open(10,file='ubend2',status='new',form='formatted')
      else
        open(10,file='ubend2',status='old',form='formatted')
      endif
c     ****** set pointers ******************
c     ****** flag=1 - inner bend **********
c     ****** flag=2 - outer bend **********
c     ****** idf=1 ux *********************
c     ****** idf=2 uy *********************
c     ****** idf=4 k **********************
c     ****** idf=5 e **********************
      if((node.eq.40).or.(node.eq.819))then
        flag=1
        start=start+1
      elseif((node.eq.2).or.(node.eq.781))then
        flag=2
        start=start+1
      endif
c     ****** evaluate theta **********************
      if(flag.eq.1)then
        why=whyi
        if((node.ge.819).and.(node.le.2049))then
c         ****** theta - inner and cl. ********
          imp=(node-40)/41
          nelti=2692+imp
          neltc=1381+imp
          topi=((yi(nelti,1)+yi(nelti-69,2))-
     c          (yi(nelti-1,3)+yi(nelti-70,4)))
          boti=((xi(nelti,1)+xi(nelti-69,2))
     c          -(xi(nelti-1,3)+xi(nelti-70,4)))
          topc=((yc(neltc,1)+yc(neltc-69,2))-
     c          (yc(neltc-1,3)+yc(neltc-70,4)))
          botc=((xc(neltc,1)+xc(neltc-69,2))
     c          -(xc(neltc-1,3)+xc(neltc-70,4)))
          if(topi.eq.0.)then
            if(boti.lt.0.)then
              thetai=pang
            else
              thetai=0.
            endif
          else
            thetai=atan(abs(topi/boti))
          endif
          if(topc.eq.0.)then
            if(botc.lt.0.)then
              thetac=pang
            else
              thetac=0.
            endif
          else
            thetac=atan(abs(topc/botc))
          endif
        endif
      elseif(flag.eq.2)then
        why=whyo
        if((node.ge.781).and.(node.le.2011))then
c         ****** theta - outer and cl. ********
          imp=(node-2)/41
          nelto=70+imp
          neltc=1381+imp
          topo=((yo(nelto,1)+yo(nelto-69,2))-
     c          (yo(nelto-1,3)+yo(nelto-70,4)))
          boto=((xo(nelto,1)+xo(nelto-69,2))
     c          -(xo(nelto-1,3)+xo(nelto-70,4)))
          topc=((yc(neltc,1)+yc(neltc-69,2))-
     c          (yc(neltc-1,3)+yc(neltc-70,4)))
          botc=((xc(neltc,1)+xc(neltc-69,2))
     c          -(xc(neltc-1,3)+xc(neltc-70,4)))
          if(topo.eq.0.)then
            if(boto.lt.0.)then
              thetao=pang
            else
              thetao=0.
            endif
          else
            thetao=atan(abs(topo/boto))
          endif
          if(topc.eq.0.)then
            if(botc.lt.0.)then
              thetac=pang
            else
              thetac=0.
            endif
          else
            thetac=atan(abs(topc/botc))
          endif
        endif
      endif
c     ****** set theta for cardinals **
c     ****** theta - centreline (cl.) *
      if(botc.eq.0.)then
        if(topc.gt.0.)then
          thetac=pang/2.
        endif
      elseif(botc.gt.0.)then
        if(topc.eq.0.)then
          thetac=0.
        elseif(topc.gt.0.)then
          thetac=thetac
        endif
      elseif(botc.lt.0.)then
        if(topc.gt.0.)then
          thetac=pang-thetac
        elseif(topc.eq.0.)then
          thetac=pang
        endif
      endif
      if(flag.eq.1)then
c       ****** theta - inner bend ***
        if(boti.eq.0.)then
          if(topi.gt.0.)then
            thetai=pang/2.
          endif
        elseif(boti.gt.0.)then
          if(topi.eq.0.)then
            thetai=0.
          elseif(topi.gt.0.)then
            thetai=thetai
          endif
        elseif(boti.lt.0.)then
          if(topi.gt.0.)then
            thetai=pang-thetai
          elseif(topi.eq.0.)then
            thetai=pang
          endif
        endif
      elseif(flag.eq.2)then
c       ****** theta - outer bend ***
        if(boto.eq.0.)then
          if(topo.eq.0.)then
            thetao=pang/2.
          endif
        elseif(boto.gt.0.)then
          if(topo.eq.0.)then
            thetao=0.
          elseif(topo.gt.0.)then
            thetao=thetao
          endif
```

```
      elseif(boto.lt.0.)then
        if(topo.gt.0.)then
          thetao=pang-thetao
        elseif(topo.eq.0.)then
          thetao=pang
        endif
      endif
    endif
c   ****** evaluate phi **********************
    if(flag.eq.1)then
c   *** extract velocities from present I ***
c   *** to set Coles' b.c.'s for next I *****
c     *** inner Colesline ***
      ieqcu=id(node-1,ldofu(kdu))
      ieqcv=id(node-1,ldofu(kdv))
      uiu=sol(ieqcu)
      viv=sol(ieqcv)
c     *** centreline ***
      ieqcu=id(node-19,ldofu(kdu))
      ieqcv=id(node-19,ldofu(kdv))
      ucst(node-19)=sol(ieqcu)
      vcst(node-19)=sol(ieqcv)
      ucu=ucst(node-19)
      vcv=vcst(node-19)
      if((node.ge.819).and.(node.le.2049))then
c       ****** phi - inner bend and bend cl. *
        if(viv.eq.0.)then
          if(uiu.ge.0.)then
            phii=0.
          else
            phii=pang
          endif
        elseif(uiu.eq.0.)then
          if(viv.gt.0.)then
            phii=pang/2.
          else
            phii=3*pang/2.
          endif
        else
          phii=atan(abs(viv/uiu))
        endif
        if(vcv.eq.0.)then
          if(ucu.ge.0.)then
            phic=0.
          else
            phic=pang
          endif
        elseif(ucu.eq.0.)then
          if(vcv.gt.0.)then
            phic=pang/2.
          else
            phic=3*pang/2.
          endif
        else
          phic=atan(abs(vcv/ucu))
        endif
      endif
c     ****** resultants - inner bend and inner cl. *
      uir=sqrt(uiu*uiu+viv*viv)
      ucr=sqrt(ucu*ucu+vcv*vcv)
    elseif(flag.eq.2)then
c   *** extract velocities from present I ***
c   *** to set Coles' b.c.'s for next I ***
c     *** outer Colesline ***
      ieqcu=id(node+1,ldofu(kdu))
      ieqcv=id(node+1,ldofu(kdv))
      uou=sol(ieqcu)
      vov=sol(ieqcv)
c     *** centreline ***
      ieqcu=id(node+19,ldofu(kdu))
      ieqcv=id(node+19,ldofu(kdv))
      ucst(node+19)=sol(ieqcu)
      vcst(node+19)=sol(ieqcv)
      ucu=ucst(node+19)
      vcv=vcst(node+19)
      if((node.ge.781).and.(node.le.2011))then
c       ****** phi - outer bend and bend cl. *
        if(vov.eq.0.)then
          if(uou.ge.0.)then
            phio=0.
          else
            phio=pang
          endif
        elseif(uou.eq.0.)then
          if(vov.gt.0.)then
            phio=pang/2.
          else
            phio=3*pang/2.
          endif
        else
          phio=atan(abs(vov/uou))
        endif
        if(vcv.eq.0.)then
          if(ucu.ge.0.)then
            phic=0.
          else
            phic=pang
          endif
        elseif(uou.eq.0.)then
          if(vcv.gt.0.)then
            phic=pang/2.
          else
            phic=3*pang/2.
          endif
        else
          phic=atan(abs(vcv/ucu))
        endif
      endif
c     ****** resultants - outer bend and outer cl. *
      uor=sqrt(uou*uou+vov*vov)
      ucr=sqrt(ucu*ucu+vcv*vcv)
    endif
c   ****** set phi values to global *******
c   ****** phi - inner bend ***************
    if(viv.eq 0.0)then
      if(uiu.gt.0.0)then
        phii=0.0
      elseif(uiu.lt.0.0)then
        phii=pang
      endif
    elseif(uiu.eq.0.0)then
      if(viv.gt.0.0)then
        phii=pang/2.
      elseif(viv.lt.0.0)then
        phii=3.*pang/2.
      endif
    elseif(uiu.gt.0.0)then
      if(viv.gt.0.0)then
        phii=phii
      elseif(viv.lt.0.0)then
        phii=2.*pang-phii
      endif
    elseif(uiu.lt.0.0)then
      if(viv.gt.0.0)then
        phii=pang-phii
      elseif(viv.lt.0.0)then
        phii=pang+phii
      endif
    endif
c   ****** phi - outer bend *****
    if(vov.eq.0.0)then
      if(uou.gt.0.0)then
        phio=0.0
      elseif(uou.lt.0.0)then
        phio=pang
      endif
    elseif(uou.eq.0.0)then
      if(vov.gt.0.0)then
        phio=pang/2.
      elseif(vov.lt.0.0)then
        phio=3.*pang/2.
      endif
    elseif(uou.gt.0.0)then
      if(vov.gt.0.0)then
        phio=phio
      elseif(vov.lt.0.0)then
        phio=2.*pang-phio
      endif
    elseif(uou.lt.0.0)then
      if(vov.gt.0.0)then
        phio=pang-phio
      elseif(vov.lt.0.0)then
```

```
          phio=pang+phio
        endif
      endif
c     ******* phi - centreline (cl.) **
      if(vcv.eq.0.0)then
        if(ucu.gt.0.0)then
          phic=0.0
        elseif(ucu.lt.0.0)then
          phic=pang
        endif
      elseif(ucu.eq.0.0)then
        if(vcv.gt.0.0)then
          phic=pang/2.
        elseif(vcv.lt.0.0)then
          phic=3.*pang/2.
        endif
      elseif(ucu.gt.0.0)then
        if(vcv.gt.0.0)then
          phic=phic
        elseif(vcv.lt.0.0)then
          phic=2.*pang-phic
        endif
      elseif(ucu.lt.0.0)then
        if(vcv.gt.0.0)then
          phic=pang-phic
        elseif(vcv.lt.0.0)then
          phic=pang+phic
        endif
      endif
c     ****** convert to tangential co -ords *****
      if(flag.eq.1)then
        if(node.lt.819)then
c       *** inner inlet st. ***
          uit=uiu
        elseif(node.gt.2049)then
c       *** inner outlet st. ***
          if(uiu.lt.0.)then
            uit=abs(uiu)
          elseif(uiu.gt.0.)then
            uit=-uiu
          else
            uit=0.
          endif
        else
c       *** inner bend ***
          uit=uir*cos(thetai-phii)
          if(thetai.lt.(pang/2.))then
            if(((phii.ge.0.).and.(phii.le.(thetai+(pang/2.))))
     c       .or.((phii.le.(2.*pang)).and.(phii.ge.(2.*pang-
     c       ((pang/2.)-thetai)))))then
              uit=abs(uit)
            else
              uit=-abs(uit)
            endif
          elseif(thetai.ge.(pang/2.))then
            if((phii.ge.(thetai-(pang/2.))).and.(phii.le.
     c       (thetai+(pang/2.))))then
              uit=abs(uit)
            else
              uit=-abs(uit)
            endif
          endif
        endif
c       ****** set inner bend du/dy **************************
        if(uit.eq.0.0)then
          danger=1
        else
          danger=0
        endif
        duidt=uit/yIIi
        dudy(node)=duidt
      elseif(flag.eq.2)then
        if(node.lt.781)then
c       *** outer inlet st. ***
          uot=uou
        elseif(node.gt.2011)then
c       *** outer outlet st. ***
          if(uou.lt.0.)then
            uot=abs(uou)
          elseif(uou.gt.0.)then
            uot=-uou
          else
            uot=0.
          endif
        else
c       *** outer bend ***
          uot=uor*cos(thetao-phio)
          if(thetao.lt.(pang/2.))then
            if(((phio.ge.0.).and.(phio.le.(thetao+(pang/2.))))
     c       .or.((phio.le.(2.*pang)).and.(phio.ge.(2.*pang-
     c       ((pang/2.)-thetao)))))then
              uot=abs(uot)
            else
              uot=-abs(uot)
            endif
          elseif(thetao.ge.(pang/2.))then
            if((phio.ge.(thetao-(pang/2.))).and.(phio.le.
     c       (thetao+(pang/2.))))then
              uot=abs(uot)
            else
              uot=-abs(uot)
            endif
          endif
        endif
c       ****** set outer bend du/dy **************************
        if(uot.eq 0)then
          danger=1
        else
          danger=0
        endif
        duodt=uot/yIIo
        dudy(node)=duodt
      endif
      if(((idf.eq.1).and.(node.lt.819))
     c.or.((idf.eq.2).and.(node.lt.781)))then
c       *** centreline inlet st. ***
        uct=ucu
      elseif(((idf.eq.1).and.(node.gt.2049))
     c.or.((idf.eq.2).and.(node.gt.2011)))then
c       *** centreline outlet st. ***
        if(ucu.lt.0.)then
          uct=abs(ucu)
        elseif(ucu.gt.0.)then
          uct=-ucu
        else
          uct=0.
        endif
      else
c       *** centreline bend ***
        uct=ucr*cos(thetac-phic)
        if(thetac.lt.(pang/2.))then
          if(((phic.ge.0.).and.(phic.le.(thetac+(pang/2.))))
     c     .or.((phic.le.(2.*pang)).and.(phic ge.(2.*pang-
     c     ((pang/2.)-thetac)))))then
            uct =abs(uct)
          else
            uct=-abs(uct)
          endif
        elseif(thetac.ge.(pang/2.))then
          if((phic.ge.(thetac-(pang/2.))) and.(phic.le.
     c     (thetac+(pang/2.))))then
            uct=abs(uct)
          else
            uct=-abs(uct)
          endif
        endif
      endif
      vinf=uct
c     ****** y+ and friends *************************
      shear0=visk*dudy(node)
c     *** *** ***  remember physical senses  *** *** *
      shrmod=abs(shear0)
      walfrc=sqrt(shrmod/destny)
      whypls=(why*walfrc)/gnew
c     *********** k-e database substream ***************
      emel=voncam*why
      if(start.ge.127)then
c       *** activate Coles analysis beyond I7 ***
        if(danger.eq.1)then
c         *** protection against du/dy=0 ***
          if(idf.eq.4)then
            val = 0.001
```

```
      return
     elseif(idf.eq.5)then
      val=0.0009
      return
     endif
    else
c    *** evaluate k and e ***
     if(idf.eq.4)then
      cay(node)=sqrt(seemew)*emel*dudy(node)*emel*dudy(node)
      val=cay(node)
      if((node.eq.2).or.(node.eq.40))then
c      *** inlet b.c. protection ***
       val=0.001
      endif
      return
     elseif(idf.eq.5)then
      epsil=seemew*cay(node)*cay(node)
c       /(emel*emel*abs(dudy(node)))
      val=epsil
      if((node.eq.2).or.(node.eq.40))then
c      *** inlet b.c. protection ***
       val=0.0009
      endif
      return
     endif
    endif
    else
c    *** analysis inactive before I7 ***
     if((idf.eq.4).or.(idf eq 5))then
      val=0.0
      return
     endif
    endif
c    ********** Reynolds number and big pie **********
    reyno=(destny*dia*(vinf))/visk
    cofric=(2.*walfrc*walfrc)/(vinf*vinf)
    reydel=reyno/((3.78*sqrt(cofric/2.))-12.5*cofric)
    if(reyno.le.5000.)then
     zedone=abs((reyno/425.)-1.)
     bigpi=0.55*(1.-exp((-0.243*sqrt(zedone))-(0.298*zedone)))
    else
     bigpi=0.55
    endif
    delta=(reydel*visk)/(destny*vinf)
c    ****** calculate Coles' velocity ***********************
    vel(node)=walfrc*((log((why*walfrc)/gnew)/voncam)+bee
c       +(2.*bigpi)/voncam)
c    ****** convert Coles' velocity to global co-ords *******
c    ************************************************************
c    ****** return calculated, global velocities **
    if(flag.eq.1)then
c    *** inner Colesline ***
     if(start.ge.127)then
c     *** activate Coles' analysis beyond I7 ***
     if((node.lt.819).and.(node.gt.40))then
c     *** inlet st. ***
      val=sign(vel(node),dudy(node))
     elseif(node.gt.2049)then
c     *** outlet st. ***
      sync=-dudy(node)
      val=sign(vel(node),sync)
     elseif((node.ge.819).and.(node.le.2049))then
      if(idf.eq.1)then
c      *** bend ux component ***
       valc=vel(node)*cos(thetai)
      elseif(idf.eq.2)then
c      *** bend uy component ***
       valc=vel(node)*sin(thetai)
      endif
c     *** sign adjustment for bend ***
      if(thetai.le.(pang/2.))then
       val=sign(vale,dudy(node))
      elseif(thetai.gt.(pang/2.))then
       bane=-dudy(node)
       if(idf.eq.1)then
        val=sign(valc,bane)
       elseif(idf.eq.2)then
        val=sign(vale,dudy(node))
       endif
      endif
     endif
     else
c     *** analysis inactive before I7 ***
      val=0.0
     endif
     if(node.eq.40)then
c     *** protect inlet b.c. ***
      val=1.0
     endif
    elseif(flag.eq.2)then
c    *** outer Colesline
     if(start.ge.127)then
c     *** activate Coles' analysis beyond I7 ***
      if((node.lt.781).and.(node.gt.2))then
c      *** inlet st. ***
       val=sign(vel(node),dudy(node))
      elseif(node.gt.2011)then
c      *** outlet st. ***
       syne=-dudy(node)
       val=sign(vel(node),syne)
      elseif((node.ge.781).and.(node.le.2011))then
       if(idf.eq.1)then
c       *** bend ux component ***
        valc=vel(node)*cos(thetao)
       elseif(idf.eq.2)then
c       *** bend uy component ***
        vale=vel(node)*sin(thetao)
       endif
c      *** sign adjustment for bend ***
       if(thetao.le.(pang/2.))then
        val=sign(vale,dudy(node))
       elseif(thetao.gt.(pang/2.))then
        bane=-dudy(node)
        if(idf.eq.1)then
         val=sign(vale,bane)
        elseif(idf.eq.2)then
         val=sign(vale,dudy(node))
        endif
       endif
      endif
     else
c     *** analysis inactive before I7 ***
      val=0.0
     endif
     if(node.eq.2)then
c     *** protect inlet b.c. ***
      val=1.0
     endif
    endif
c    *** printout block ***
    if((start.ge.169).and.(start.le.178))then
     if(flag.eq.1)then
      if((node.eq.40).or.(node.eq.81).or.(node.eq.
c      778).or.(node.eq.2090).or.(node.eq 2828).or
c      .(node.eq.2869))then
       write(10,*) 'start',start
       write(10,*) ' '
       write(10,*) 'node',node
       write(10,*) 'uiu',uiu,'uit',uit
       write(10,*) 'ucu',ucu,'uct',uct
       write(10,*) 'vinf',vinf
       write(10,*) 'duidt',duidt
       write(10,*) 'dudy',dudy(node)
       write(10,*) 'vel',vel(node),'val',val
       write(10,*) 'shear0',shear0,'shrmod',shrmod
       write(10,*) 'walfrc',walfrc,'y+',whypls
       write(10,*) 'Re',reyno,'bigpi',bigpi
       write(10,*) ' '
      elseif((node.eq.819).or.(node.eq.860).or.(node.
c      eq.1393).or.(node.eq.1434).or.(node.eq.1475).o
c      r.(node.eq.2008).or.(node.eq.2049))then
       write(10,*) 'start',start
       write(10,*) ' '
       write(10,*) 'node',node
       write(10,*) 'uiu',uiu,'viv',viv
       write(10,*) 'ucu',ucu,'vcv',vcv
       write(10,*) 'uir',uir,'ucr',ucr
       write(10,*) 'uit',uit
       write(10,*) 'uct',uct,'vinf',vinf
       write(10,*) 'thetai',thetai,'phii',phii
       write(10,*) 'thetac',thetac,'phic',phic
       write(10,*) 'duidt',duidt
```

```
            write(10,*) 'dudy',dudy(node)
            write(10,*) 'cos',cos(thetai),'sin',sin(thetai)
            write(10,*) 'vel(node)',vel(node)
            write(10,*) 'vale',vale,'val',val
            write(10,*) 'shear0',shear0,'shrmod',shrmod
            write(10,*) 'walfrc',walfrc,'y+',whypls
            write(10,*) 'Re',reyno,'bigpi',bigpi
            write(10,*) ' '
          endif
        elseif(flag.eq 2)then
          if((node.eq.2).or.(node.eq 43).or.(node.eq.
     c     740).or.(node.eq.2052).or.(node.eq 2790).or
     c     .(node.eq.2831))then
            write(10,*) 'start',start
            write(10,*) '    '
            write(10,*) 'node',node
            write(10,*) 'uou',uou,'uot',uot
            write(10,*) 'ucu',ucu,'uct',uct
            write(10,*) 'vinf',vinf
            write(10,*) 'duodt',duodt
            write(10,*) 'dudy',dudy(node)
            write(10,*) 'vel',vel(node),'val',val
            write(10,*) 'shear0',shear0,'shrmod',shrmod
            write(10,*) 'walfrc',walfrc,'y+',whypls
            write(10,*) 'Re',reyno,'bigpi',bigpi
            write(10,*) ' '
          elseif((node.eq.781).or.(node.eq 822).or.(node.
     c     eq.1355).or.(node.eq.1396).or.(node.eq.1437).o
     c     r.(node.eq.1970).or.(node.eq.2011))then
            write(10,*) 'start',start
            write(10,*) '    '
            write(10,*) 'node',node
            write(10,*) 'uou',uou,'vov',vov
            write(10,*) 'ucu',ucu,'vcv',vcv
            write(10,*) 'uor',uor,'ucr',ucr
            write(10,*) 'uct',uct,'vinf',vinf
            write(10,*) 'uot',uot
            write(10,*) 'thetao',thetao,'phio',phio
            write(10,*) 'thetac',thetac,'phic',phic
            write(10,*) 'duodt',duodt
            write(10,*) 'dudy',dudy(node)
            write(10,*) 'cos',cos(thetao),'sin',sin(thetao)
            write(10,*) 'vel(node)',vel(node)
            write(10,*) 'vale',vale,'val',val
            write(10,*) 'shear0',shear0,'shrmod',shrmod
            write(10,*) 'walfrc',walfrc,'y+',whypls
            write(10,*) 'Re',reyno,'bigpi',bigpi
            write(10,*) ' '
          endif
        endif
      endif
c     ********** bedtime ************************************
      close(10)
      close(9)
      return
      end
```

Figure A3.5. Input file, ex19.FDREAD: the standard FIDAP model of the backward facing step.

```
/ INPUT FILE FOR BACKWARD FACING STEP -
/ STANDARD fidap MODEL
title
bfs - standard FIDAP model
fimesh(2-d,imax=5,jmax=9)
expi
1 0 1 1 0 46
expj
1 0 9 0 17 0 27 0 37
points(cartesian)
1 1 9 1 -2 3
2 3 9 1 4 3
3 5 9 1 28 3
4 1 7 1 -2 2
5 1 5 1 -2 1
6 3 5 1 4 1
7 3 3 1 4 0.5
8 3 1 1 4 0
9 5 1 1 28 0
line
5 4 6 3
4 1 6 4
6 7 3 3
7 8 3 4
1 2 4 4
2 3 6 3
8 9 6 3
cdrive
1 5 1 3
6 8 8 9
bcnode(ux)
1 5 1
5 6 0
6 8 0
8 9 0
3 1 0
bcnode(uy)
1 5 0
5 6 0
6 8 0
8 9 0
3 1 0
bcnode(kinetic)
1 5 0.003
bcnode(dissipation)
1 5 0.00364
number
2 1
elements(quad,nodes=4,all,entity="channel")
elements(boundary,face,entity="sides")
5 6
6 8
8 9
3 1
end
fiprep
problem(nonlinear,turbulent)
execution(newjob)
icnode(ux,constant=1.,entity="channel")
icnode(kinetic,constant=0.003,entity="channel")
icnode(dissipation,constant=0.00364,entity="channel")
viscosity(k.e.,clip=1.e6,constant=1.0e-3)
solution(segr=900,cr=5000,cgs=5000,accf=0.5)
options(upwinding)
entity(name="channel",fluid)
entity(name="sides",wall)
renumber
end
create(fisolv)
end
```

```
/INPUT FILE - BACKWARD FACING STEP, SIMPLE COLES' MODEL
/ AND ENHANCED COLES' MODEL
title
bfs - simple Coles' model
/bfs - Coles' model with wake function and parameter
fimesh(2-d,imax=5,jmax=9)
expi
1 0 11 0 46
expj
1 0 9 0 17 0 27 0 37
points(cartesian)
1 1 9 1 -2 3
2 3 9 1 4 3
3 5 9 1 28 3
4 1 7 1 -2 2
5 1 5 1 -2 1
6 3 5 1 4 1
7 3 3 1 4 0.5
8 3 1 1 4 0
9 5 1 1 28 0
line
5 4 6 3
4 1 6 4
6 7 3 3
7 8 3 4
1 2 4 4
2 3 6 3
8 9 6 3
cdrive
1 5 1 3
6 8 8 9
/ **** leave ux,uy alone along top surface
bcnode(ux)
1 5 1
5 6 0
6 8 0
8 9 0
3 1 0
bcnode(uy)
1 5 0
5 6 0
6 8 0
8 9 0
3 1 0
bcnode(kinetic)
1 5 0.003
3 1
5 6
6 8
8 9
bcnode(dissipation)
1 5 0.00364
3 1
5 6
6 8
8 9
number
2 1
elements(quad,nodes=4,all,entity="channel")
elements(boundary,face,entity="back")
5 6
elements(boundary,face,entity="step ")
6 8
elements(boundary,face,entity="front")
8 9
elements(boundary,face,entity="top")
3 1
end
fiprep
problem(nonlinear,turbulent)
execution(newjob)
pressure(mixed=1.0e-12)
/icnode(velo,read,all)
/icnode(kinetic,read,all)
/icnode(dissipation,read,all)
icnode(ux,constant=1.,entity="channel")
icnode(kinetic,constant=0.003,entity="channel")
icnode(dissipation,constant=0.00364,entity="channel")
viscosity(k.e.,clip=1.e6,constant=1.0e-3)
solution(segr=1350,cr=5000,cgs=5000,accf=0.5)
options(upwinding)
source(kinetic,entity="channel",subroutine)
/*** top *****
bcnode(ux,nodes,fsubroutine)
20 209 21
246 1541 37
0
/*** top *****
bcnode(kinetic,nodes,fsubroutine)
20 209 21
246 1541 37
0
/*** top *****
bcnode(dissipation,nodes,fsubroutine)
20 209 21
246 1541 37
0
/**** back *****
bcnode(ux,nodes,fsubroutine)
2 170 21
191 265 37
0
/**** back *****
bcnode(kinetic,nodes,fsubroutine)
2 170 21
191 265 37
0
/**** back *****
bcnode(dissipation,nodes,fsubroutine)
2 170 21
191 265 37
0
/**** step *****
bcnode(uy,nodes,fsubroutine)
249 265 1
0
/**** step *****
bcnode(kinetic,nodes,fsubroutine)
249 265 1
0
/**** step *****
bcnode(dissipation,nodes,fsubroutine)
249 265 1
0
/**** front *****
bcnode(ux,nodes,fsubroutine)
249 1507 37
0
/**** front *****
bcnode(kinetic,nodes,fsubroutine)
249 1507 37
0
/**** front *****
bcnode(dissipation,nodes,fsubroutine)
249 1507 37
0
entity(name="channel",fluid)
entity(name="back",plot)
entity(name="step",plot)
entity(name="front",plot)
entity(name="top",plot)
renumber
end
create(fisolv)
end
```

Figure A3.6. Input file, tat2.FDREAD: the simple Coles' law model of the backward facing step. (This input file also served as andy.FDREAD, the enhanced Coles' law model of the backward facing step.)

Figure A3.7. Algorithm flowchart, erasure.f: the simple Coles' law model of the backward facing step. (This flowchart also describes the enhanced Coles' law model of the backward facing step, circus.f - where circus.f differs from erasure.f, the flowchart outline is printed boldly for circus.f operations.)

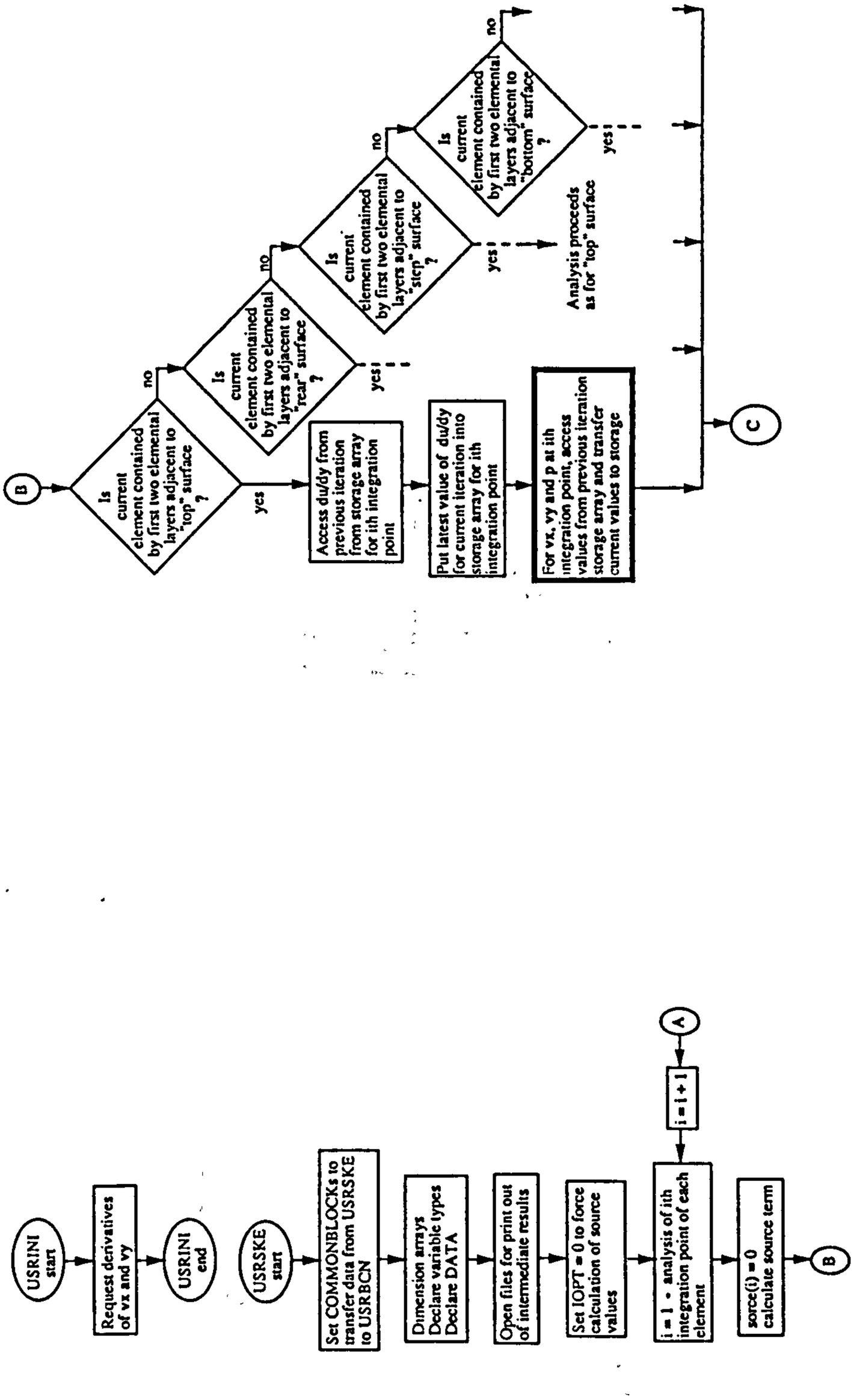

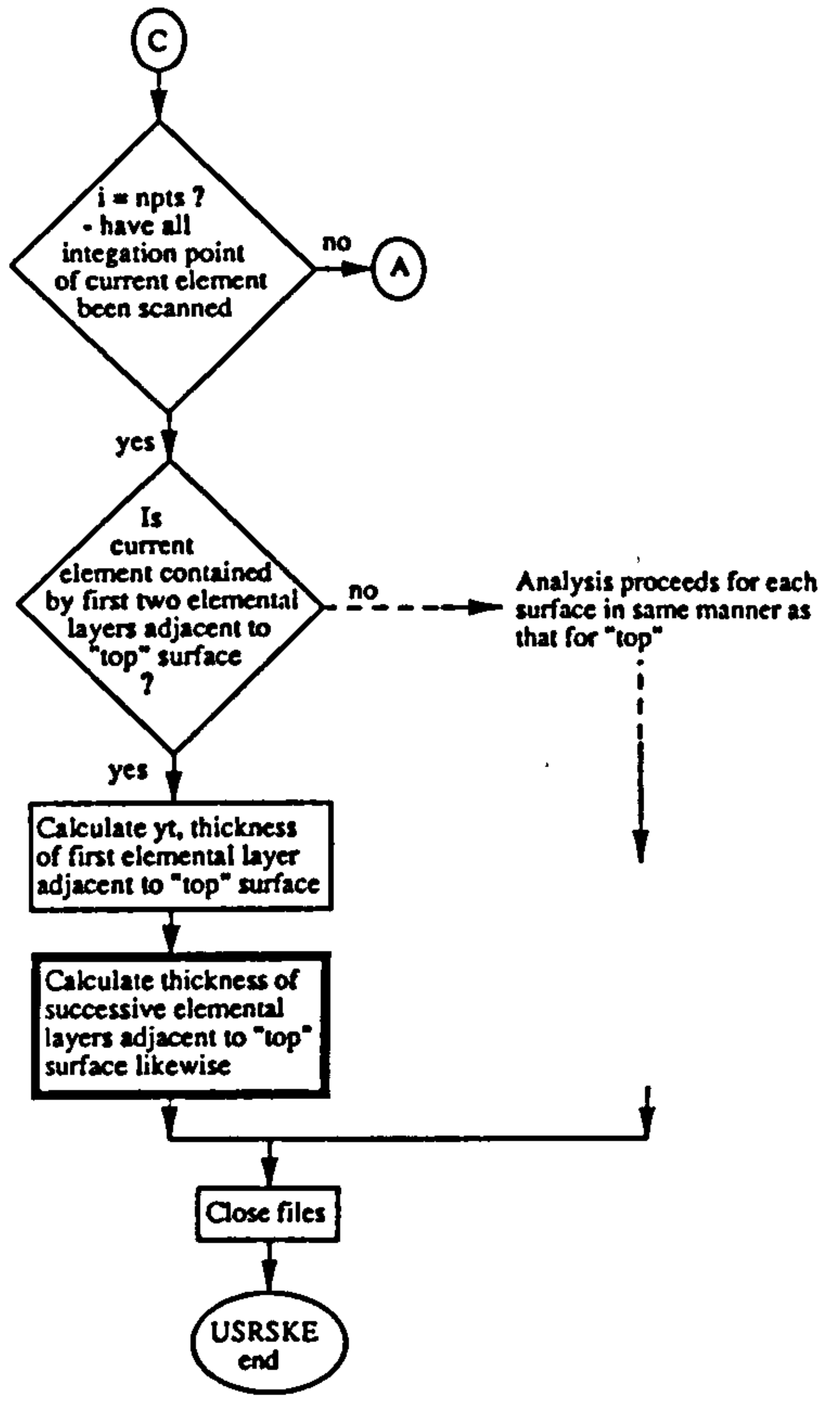
C
i = npts ? - have all integation point of current element been scanned
no
A
yes
Is current element contained by first two elemental layers adjacent to "top" surface ?
no
Analysis proceeds for each surface in same manner as that for "top"
yes
Calculate yt, thickness of first elemental layer adjacent to "top" surface
Calculate thickness of successive elemental layers adjacent to "top" surface likewise
Close files
USRSKE end

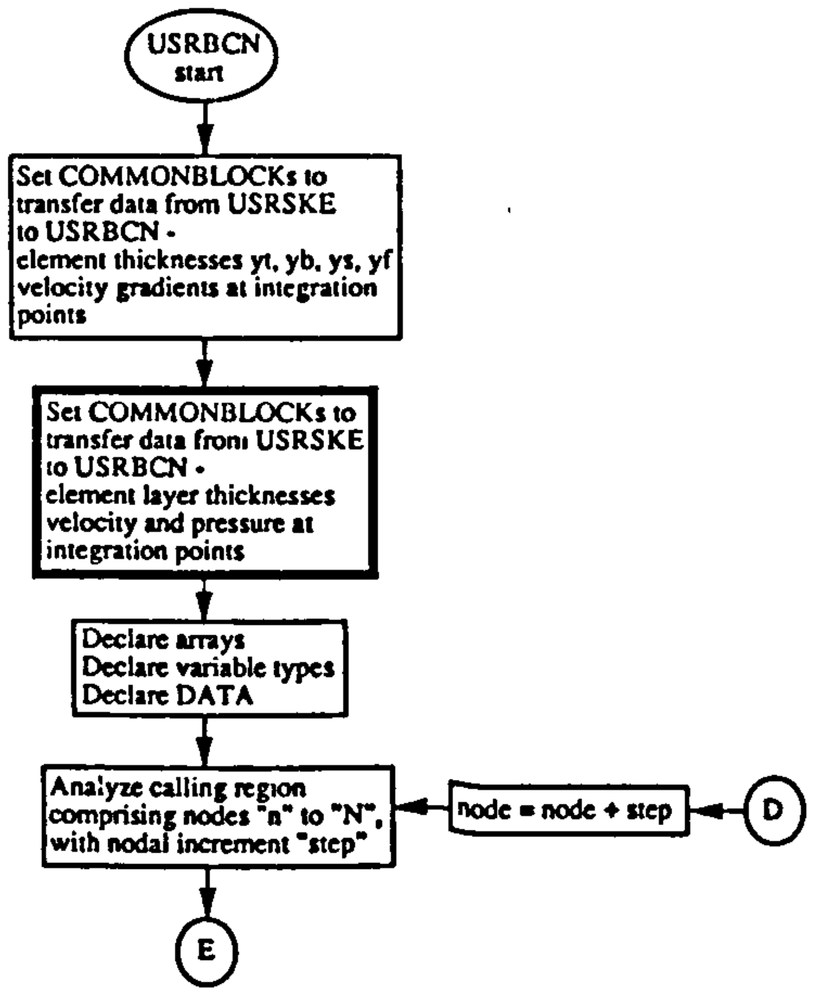
USRBCN start
Set COMMONBLOCKs to transfer data from USRSKE to USRBCN - element thicknesses yt, yb, ys, yf velocity gradients at integration points
Set COMMONBLOCKs to transfer data from USRSKE to USRBCN - element layer thicknesses velocity and pressure at integration points
Declare arrays
Declare variable types
Declare DATA
Analyze calling region comprising nodes "n" to "N", with nodal increment "step"
node = node + step
D
E

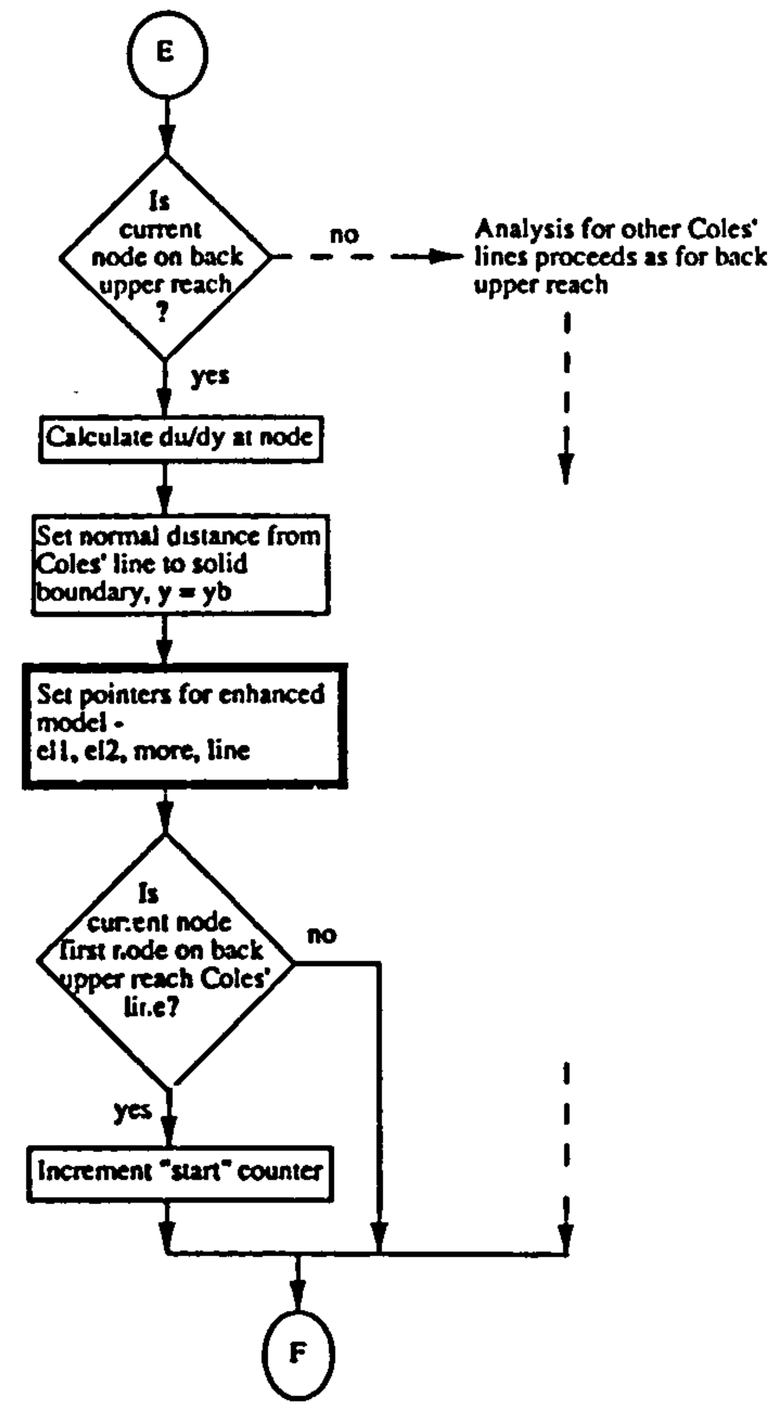
E
Is current node on back upper reach ?
no
Analysis for other Coles' lines proceeds as for back upper reach
yes
Calculate du/dy at node
Set normal distance from Coles' line to solid boundary, y = yb
Set pointers for enhanced model - el1, el2, more, line
Is current node first node on back upper reach Coles' line?
no
yes
Increment "start" counter
F

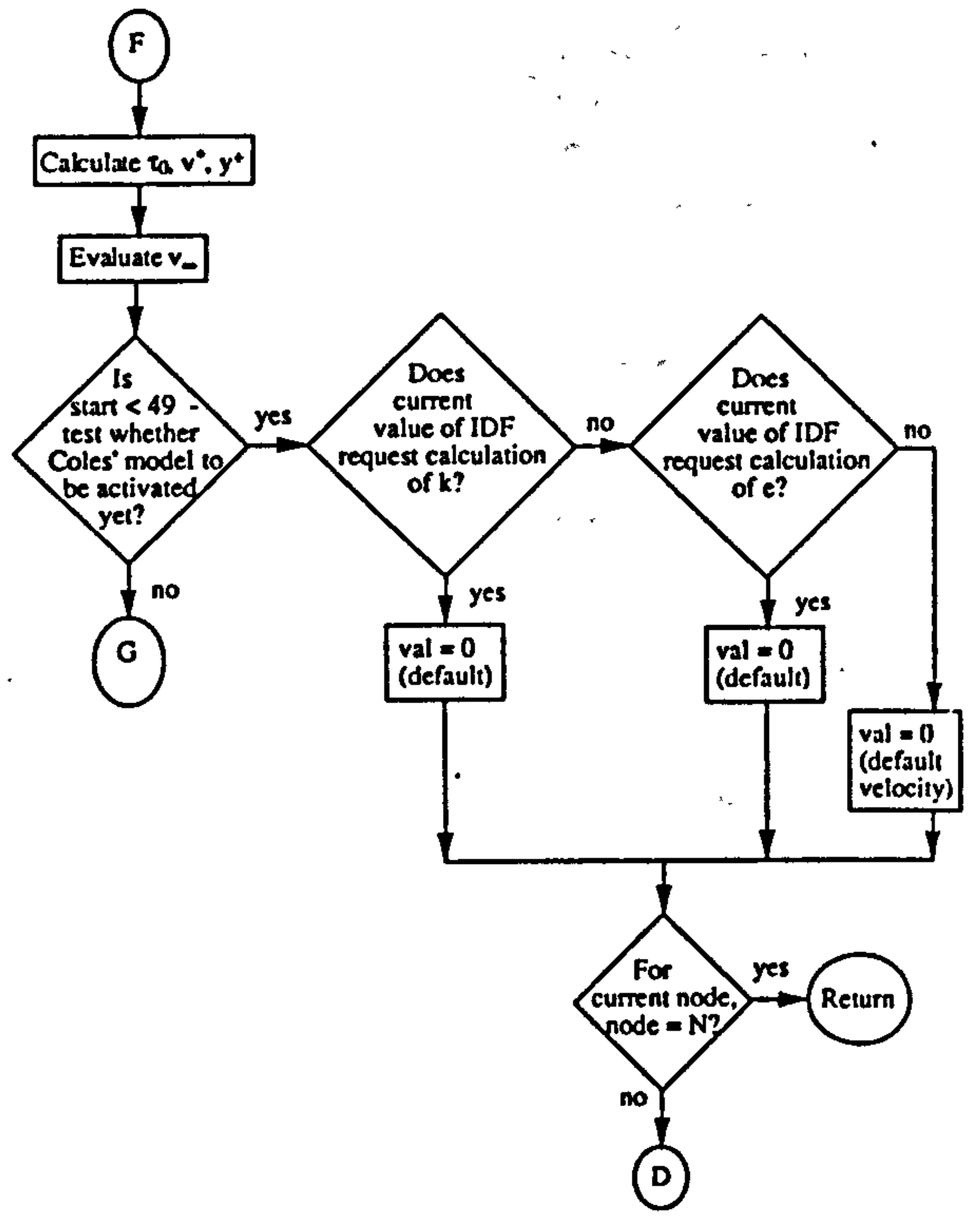
F
Calculate τ0, v*, y+
Evaluate v_
Is start < 49 - test whether Coles' model to be activated yet?
yes
no
G
Does current value of IDF request calculation of k?
yes
no
val = 0 (default)
Does current value of IDF request calculation of e?
yes
no
val = 0 (default)
val = 0 (default velocity)
For current node, node = N?
yes
Return
no
D

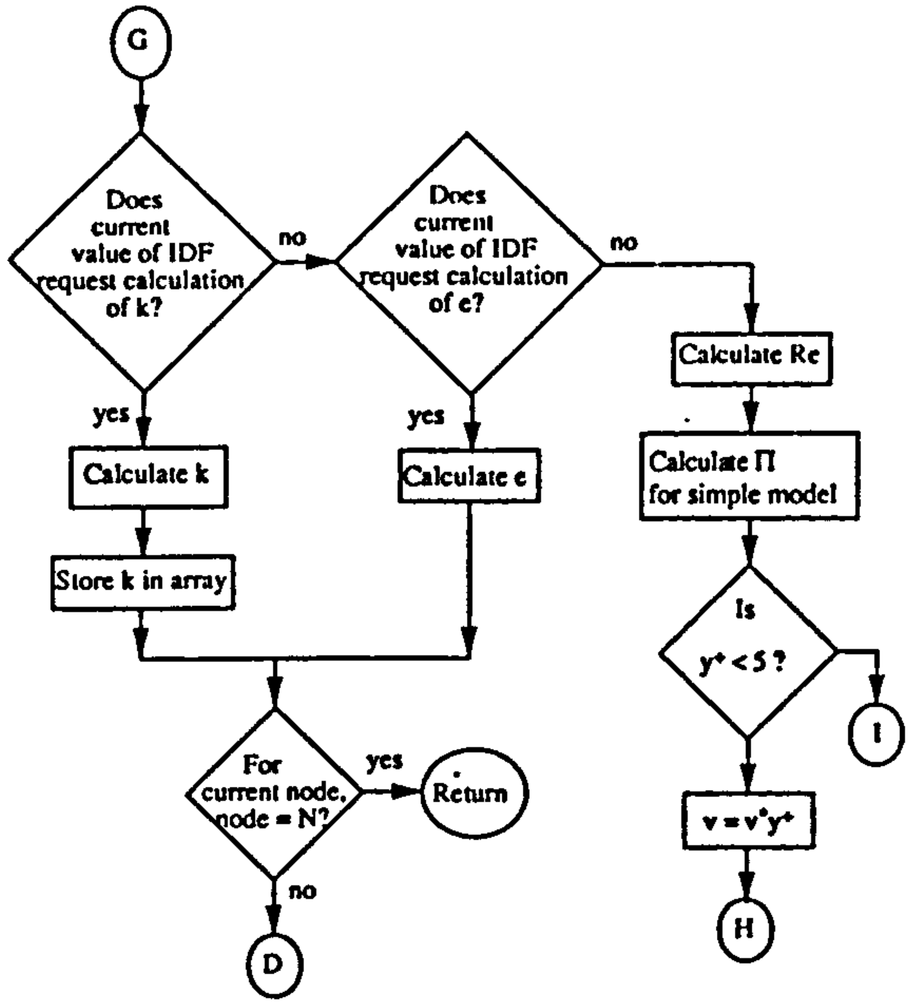
G
Does current value of IDF request calculation of k?
yes
Calculate k
Store k in array
no
Does current value of IDF request calculation of e?
yes
Calculate e
no
Calculate Re
Calculate Π for simple model
Is y+ < 5 ?
I
v = v*y+
H
For current node, node = N?
yes
Return
no
D

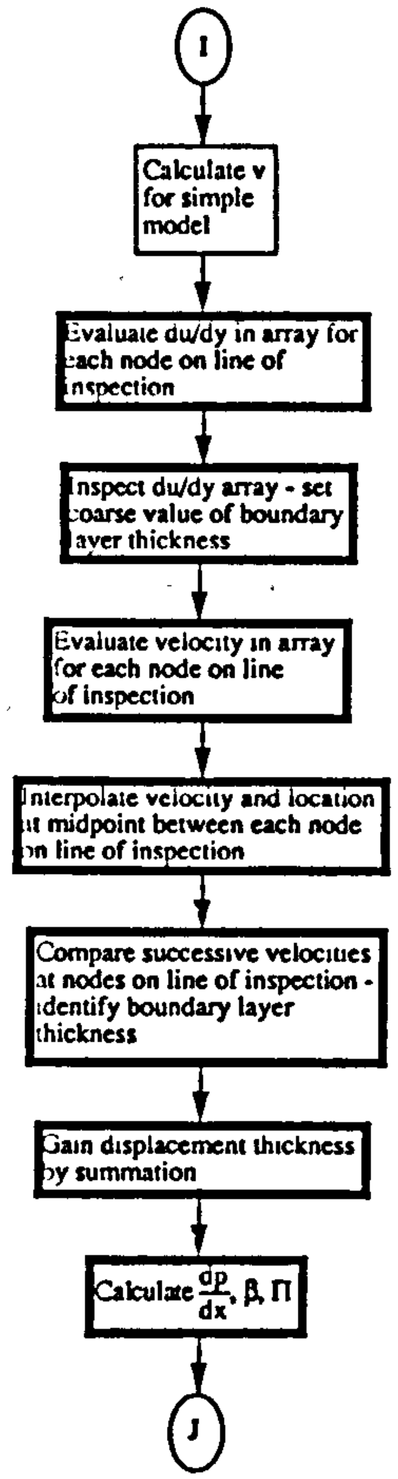
I
Calculate v for simple model
Evaluate du/dy in array for each node on line of inspection
Inspect du/dy array - set coarse value of boundary layer thickness
Evaluate velocity in array for each node on line of inspection
Interpolate velocity and location at midpoint between each node on line of inspection
Compare successive velocities at nodes on line of inspection - identify boundary layer thickness
Gain displacement thickness by summation
Calculate dp/dx, β, Π
J

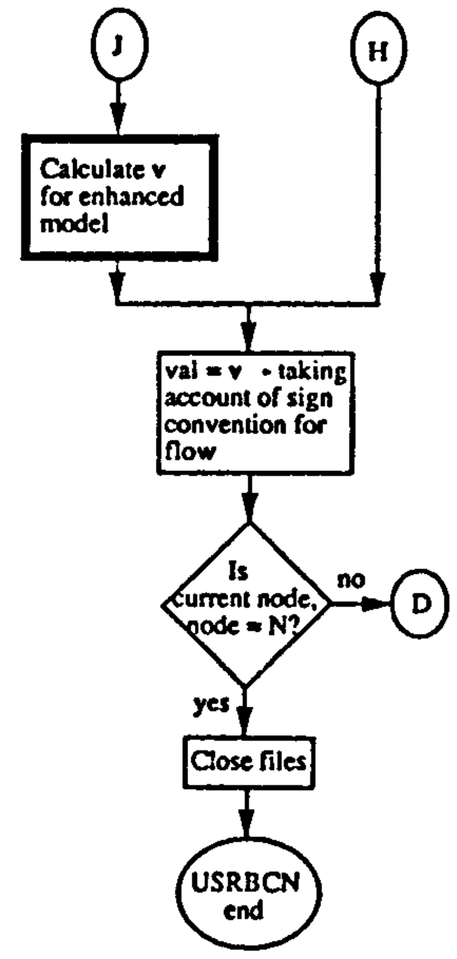
J
H
Calculate v for enhanced model
val = v - taking account of sign convention for flow
Is current node, node = N?
no
D
yes
Close files
USRBCN end

```
      subroutine usrini (inivar)
      include 'IMPLCT.COM'
      include 'PARUSR.COM'
      dimension inivar(*)
c
c     *** request derivatives of ux and uy ***
      inivar(kdu)=1
      inivar(kdv)=1
c
      return
      end
c
      SUBROUTINE USRSKE (NELT,NE,NG,SORCE,VARI,DVARI,NDFCD,LDOFU,SHP,
     1                   DSDX,XYZL,PROP,TIME,NPTS,ndp,MNDP,IERR,IOPT,
     2                   visct,viscl,den,mdvsc)
C
C     USER DEFINED SOURCES FOR KINETIC ENERGY OR DISSIPATION
C
C     NELT  = GLOBAL ELEMENT NUMBER
C     NE    = LOCAL ELEMENT NUMBER
C     NG    = GROUP NUMBER
C     SORCE = TURBULENT KINETIC ENERGY OR DISSIPATION (RETURNED VALUES)
C     VARI  = ARRAY OF SOLUTION VARIBLES AT INTEGRATION POINTS
C     DVARI = GRADIENTS OF SOLUTION VARIABLES AT INTEGRATION POINTS
C     LDOFU = pointer array for accessing vari and dvari information
C     XYZL  = X,Y,Z COORDINATES
C     SHP   = ELEMENT SHAPE FUNCTIONS
C     DSDX  = SHAPE FUNCTION DERIVATIVES IN THE X,Y,Z DIRECTION
C     PROP  = USER DEFINED PARAMETERS
C     MNDP  = FIRST DIMENSION OF SHAPE FUNCTION MATRICES
C     TIME  = TIME
C     NPTS  = NUMBER OF POINTS
C     IOPT = 0   ENERGY EQUATION
C     IOPT = N   TRANSPORT EQUATION FOR SPECIES N (0<N<16)
C     VISCT = TURBULENT VISCOSITY
C     VISCL = LAMINAR VISCOSITY
C     MDVSC = NUMBER OF COMPONENTS OF VISCOSITY ARRAY
C     IOPT = 0   KINETIC ENERGY SOURCES
C     IOPT = 1   DISSIPATION SOURCES
C
      INCLUDE 'IMPLCT.COM'
      INCLUDE 'PARUSR.COM'
c     ****** beware the second dimension of slope ***************
c     *** commonblocks for derivatives of ux and uy ***
c     *** at integration points and for x and y co-ords ***
      common/tlayer/ slopet2(1371:1415,4),slopet1(1416:1460,4),whyt
      common/blayerb/ slopeb2(606:617,4),slopeb1(561:572,4),whyb
      common/blayers/ slopes2(2:617,4),slopes1(1:616,4),whys
      common/blayerf/ slopef2(36:70,4),slopef1(1:35,4),whyf,start
      DIMENSION SORCE(NPTS),visct(npts),viscl(9,npts),den(npts)
      DIMENSION SHP(MNDP,NPTS),DSDX(MNDP,NPTS,NDFCD),XYZL(NPTS,NDFCD)
      DIMENSION PROP(*),VARI(NPTS,*),DVARI(NPTS,NDFCD,*),LDOFU(*)
      logical alive
c     *** arrays for storage of derivatives of ux and uy ***
c     *** at integration points ***
      dimension storet1(1416:1460,4),storet2(1371:1415,4)
      dimension storeb1(561:572,4),storeb2(607:617,4)
      dimension stores1(1:616,4),stores2(2:617,4)
      dimension storef2(36:70,4),storef1(1:35,4)
      integer start
      inquire(file='fred',exist=alive)
      if(.not.alive)then
        open(9,file='fred',status='new',form='formatted')
      else
        open(9,file='fred',status='old',form='formatted')
      endif
      iopt=0
      do 10 i=1,npts
        sorce(i)=0.
c       *** gain dux/dy (duy/dx for step face) ***
c       *** current values into storage ***
c       *** stored values to commonblock ***
c       ******* top ********
        if((nelt.ge.1416).and.(nelt.le.1460))then
          slopet1(nelt,i)=storet1(nelt,i)
          storet1(nelt,i)=dvari(i,2,ldofu(kdu))
        endif
        if((nelt.ge.1371).and.(nelt.le.1415))then
          slopet2(nelt,i)=storet2(nelt,i)
          storet2(nelt,i)=dvari(i,2,ldofu(kdu))
        endif
c       ******* back, upper reach ********
        if((nelt.ge.561).and.(nelt.le.572))then
          slopeb1(nelt,i)=storeb1(nelt,i)
          storeb1(nelt,i)=dvari(i,2,ldofu(kdu))
        endif
        if((nelt.ge.606).and.(nelt.le.617))then
          slopeb2(nelt,i)=storeb2(nelt,i)
          storeb2(nelt,i)=dvari(i,2,ldofu(kdu))
        endif
c       ******* step face ********
        if((nelt.ge.1).and.(nelt.le.616))then
          slopes1(nelt,i)=stores1(nelt,i)
          stores1(nelt,i)=dvari(i,1,ldofu(kdv))
        endif
        if((nelt.ge.2).and.(nelt.le.617))then
          slopes2(nelt,i)=stores2(nelt,i)
          stores2(nelt,i)=dvari(i,1,ldofu(kdv))
        endif
c       ******* front, lower reach ********
        if((nelt.ge.1).and.(nelt.le.35))then
          slopef1(nelt,i)=storef1(nelt,i)
          storef1(nelt,i)=dvari(i,2,ldofu(kdu))
        endif
        if((nelt.ge.36).and.(nelt.le.70))then
          slopef2(nelt,i)=storef2(nelt,i)
          storef2(nelt,i)=dvari(i,2,ldofu(kdu))
        endif
```

Figure A3.8. Subroutine listing, erasure.f: the simple Coles' law model of the backward facing step.

```
10     continue
c   *** gain thickness of Coles' element ***
c   ******* top ********
    if(nelt.eq.1415)then
      gauhgt2=xyzl(2,2)
    elseif(nelt.eq.1460)then
      gauhgt1=xyzl(1,2)
      gauhgt=(gauhgt1+gauhgt2)/2.
      whyt=abs(3.0-gauhgt)
    endif
c   ******* back, upper reach ********
    if(nelt.eq.561)then
      gauhgb1=xyzl(2,2)
    elseif(nelt.eq.607)then
      gauhgb2=xyzl(1,2)
      gauhgb=(gauhgb1+gauhgb2)/2.
      whyb=abs(1.0-gauhgb)
    endif
c   ******* step face ********
    if(nelt.eq.1)then
      gauhgs1=xyzl(3,1)
    elseif(nelt.eq.2)then
      gauhgs2=xyzl(1,1)
      gauhgs=(gauhgs1+gauhgs2)/2.
      whys=abs(4.0-gauhgs)
    endif
c   ******* front, lower reach ********
    if(nelt.eq.35)then
      gauhgf1=xyzl(2,2)
    elseif(nelt.eq.70)then
      gauhgf2=xyzl(1,2)
      gauhgf=(gauhgf1+gauhgf2)/2.
      whyf=abs(gauhgf)
    endif
    close(9)
C
    ZRO = 0.D0
    RETURN
    END
c
    SUBROUTINE USRBCN (VAL,NODE,IDF,TIME,SOL,ID,NDOF,NUMNP,LDOFU,
    1                  CONSTR)
    INCLUDE 'IMPLCT.COM'
    INCLUDE 'PARUSR.COM'
c   *** commonblocks for derivatives of ux and uy ***
c   *** at integration points and for x and y co-ords ***
c   ******** remember the postcode ********************
    common/tlayer/ slopet2(1371:1415,4),slopet1(1416:1460,4),whyt
    common/blayerb/ slopeb2(606:617,4),slopeb1(561:572,4),whyb
    common/blayers/ slopes2(2:617,4),slopes1(1:616,4),whys
    common/blayerf/ slopef2(36:70,4),slopef1(1:35,4),whyf,start
    DIMENSION SOL(*),ID(NUMNP,NDOF),CONSTR(*),LDOFU(*)
    dimension cay(1600)
    integer gelt1,start,gelt2,gelb1,gelb2,gelf1,gelf2,gels1,gels2
    integer flag,npole
    logical alive,kickin
c   ********** problem dependent things ******************
    data visk,destny,gnew,dia/2.2222e-5,1.,2.2222e-5,2.0/
    data bee,voncam,seemew/4.9,0.41,0.09/
    inquire(file='fred',exist=alive)
    if(.not.alive)then
      open(9,file='fred',status='new',form='formatted')
    else
      open(9,file='fred',status='old',form='formatted')
    endif
    inquire(file='alice',exist=kickin)
    if(.not.kickin)then
      open(10,file='alice',status='new',form='formatted')
    else
      open(10,file='alice',status='old',form='formatted')
    endif
c   ************** curious FIDAP(tm) constant ************
    ZRO = 0.D0
c   ************** calculate velocity gradients **************
c   *** slope 1 is near side of Coles' line w.r.t. wall ***
c   *** slope 2 is far side of same ***
c   *** also set y value for Coles' line ***
    imp=0
c   ****** back, upper reach *******
    if(node.eq.2)then
      dudy=(slopeb1(561,2)+slopeb2(607,1))/2.
c     *** iteration pass counter ***
      start=start+1
      why=whyb
    elseif(node.eq.236)then
      dudy=(slopeb1(570,4)+slopeb1(571,2)+
     c      slopeb2(615,3)+slopeb2(616,1))/4.
      why=whyb
    elseif(node.eq.267.and.npole.lt.3)then
      dudy=(slopeb1(571,4)+slopeb1(572,2)
     c     +slopeb2(616,3)+slopeb2(617,1))/4.
      why=whyb
c     *** npole governs derivative selection at node 267 ***
      npole=npole+1
    elseif((node.eq.23).or.(node.eq.44).or.(node.eq.65)
    c .or.(node.eq.86).or.(node.eq.107).or.(node.eq.128)
    c .or.(node.eq.149).or.(node.eq.170).or.(node.eq.191))
    c then
      imp=((node-2)/21)-1
      gelb1=562+imp
      gelb2=607+imp
      dudy=(slopeb1(gelb1-1,4)+slopeb1(gelb1,2)
     c      +slopeb2(gelb2-1,3)+slopeb2(gelb2,1))/4.
      why=whyb
c   ****** front, lower reach *******
    elseif(node.eq.1541)then
      dudy=(slopef1(35,4)+slopef2(70,3))/2.
      why=whyf
```

```
      start=start+1
     elseif((node.eq.283.and.flag.eq.3)
    c.or.(node.eq.320).or.(node.eq.357)
    c .or.(node.eq.394).or.(node.eq.431).or.(node.eq.468)
    c .or.(node.eq.505).or.(node.eq.542).or.(node.eq.579)
    c .or.(node.eq.616).or.(node.eq.653).or.(node.eq.690)
    c .or.(node.eq.727).or.(node.eq.764).or.(node.eq.801)
    c .or.(node.eq.838).or.(node.eq.875).or.(node eq.912)
    c .or.(node.eq.949).or.(node.eq 986).or.(node.eq.1023)
    c.or.(node.eq.1060).or.(node.eq.1097).or.(node.eq.1134)
    c.or (node.eq.1171).or.(node.eq.1208).or.(node.eq.1245)
    c.or.(node.eq.1282).or.(node.eq.1319).or.(node.eq.1356)
    c.or.(node.eq.1393).or.(node.eq.1430).or.(node.eq.1467)
    c.or.(node.eq.1504))then
       imp=((node-246)/37)-1
       gelf1=2+imp
       gelf2=37+imp
       dudy=(slopef1(gelf1-1,4)+slopef1(gelf1,2)
    c     +slopef2(gelf2-1,3)+slopef2(gelf2,1))/4.
       why=whyf
       if(idf.eq.5.and.node.eq.283.and.flag.eq.3)then
    c    *** flag governs derivative selection at node 283 ***
         flag=flag-3
       endif
    c  ****** step face *******
    c  ****** taking derivs in x direction *********
      elseif(node.eq.268)then
        dudy=(slopes1(526,4)+slopes1(571,3)+
    c       slopes2(527,2)+slopes2(572,1))/4.
        why=whys
        start=start+1
      elseif(node.eq.267.and.npole.eq.3)then
        dudy=(slopes1(571,4)+slopes1(616,3)+
    c       slopes2(572,2)+slopes2(617,1))/4.
        why=whys
        if(idf.eq.5)then
          npole=npole-3
        endif
      elseif((node.eq.269).or.(node.eq.270)
    c  .or.(node.eq.271)
    c.or.(node.eq.272).or.(node.eq.273).or.(node.eq.274)
    c.or.(node.eq.275).or.(node.eq.276).or.(node.eq.277)
    c.or.(node.eq.278).or.(node.eq.279).or.(node eq.280)
    c.or.(node.eq.281).or.(node.eq.282)
    c.or.(node.eq.283.and.flag.lt.3))then
        imp=(283-node)*35
        gels1=36+imp
        gels2=37+imp
        dudy=(slopes1(gels1-35,4)+slopes1(gels1,3)
    c       +slopes2(gels2-35,2)+slopes2(gels2,1))/4.
        why=whys
        if(node.eq.283)then
          flag=flag+1
        endif
    c  ****** top ********
      elseif(node.eq.20)then
        dudy=(slopct1(1416,1)+slopct2(1371,2))/2.
        why=whyt
        start=start+1
      elseif(node.eq.1506)then
        dudy=(slopct1(1460,3)+slopct2(1415,4))/2.
        why=whyt
      else
        if(node.lc.209)then
          imp=((node+1)/21)-1
          gelt1=1416+imp
          gelt2=1371+imp
        else
          imp=(node-212)/37
          gelt1=1426+imp
          gelt2=1381+imp
        endif
        dudy=(((slopet1(gelt1,1)+slopet1((gelt1-1),3))/2.)+
    c       ((slopct2(gelt2,2)+slopet2((gelt2-1),4))/2.))/2.
        why=whyt
      endif
    c  ************ calculate y+ and friends ****************
      shear0=visk*dudy
    c  * ** ***  remember physical senses  *** ** *
      shrmod=abs(shear0)
      walfrc=sqrt(shrmod/destny)
      whypls=(why*walfrc)/gnew
    c  ************ kidnap centreline velocity ***************
    c  *** define centreline node appropriate to ***
    c  *** current Coles' node ***
      if((node.eq.20).or.(node.eq.41).or.(node.eq.62).or.
    c  (node.eq.83).or.(node.eq.104).or.(node.eq.125).or.
    c  (node.eq.146).or.(node.eq.167).or.(node.eq.188).or.
    c  (node.eq.209).or.(node.eq.230))then
        knowd=node-9
      elseif(node.eq.1506)then
        knowd=1516
      elseif((node.eq.269).or.(node.eq.270).or.(node.eq.271)
    c  .or.(node.eq.272).or.(node.eq.273).or.(node.eq.274)
    c  .or.(node.eq.275).or.(node.eq.276).or.(node.eq.277)
    c  .or.(node.eq.278).or.(node.eq.279).or.(node.eq.280)
    c  .or.(node.eq.281).or.(node.eq.282).or.(node.eq.283)
    c  .or.(node.eq.268).or.(node.eq.267))then
        knowd=258
      elseif((node.eq.320).or.(node.eq.357)
    c  .or.(node.eq.394).or.(node.eq.431).or.(node.eq.468)
    c  .or.(node.eq.505).or.(node.eq.542).or.(node.eq.579)
    c  .or.(node.eq.616).or.(node.eq.653).or.(node.eq.690)
    c  .or.(node.eq.727).or.(node.eq.764).or.(node.eq.801)
    c  .or.(node.eq.838).or.(node.eq.875).or.(node.eq.912)
    c  .or.(node.eq.949).or.(node.eq.986).or.(node.eq.1023)
    c.or.(node.eq.1060).or.(node.eq.1097).or.(node.eq.1134)
    c.or.(node.eq.1171).or.(node.eq.1208).or.(node.eq.1245)
    c.or.(node.eq.1282).or.(node.eq.1319).or.(node.eq.1356)
    c.or.(node.eq.1393).or.(node.eq.1430).or.(node.eq.1467)
    c.or.(node.eq.1504).or.(node.eq.1541))then
       knowd=node-25
      else
       knowd=node+9
      endif
      if(knowd.eq.258.and.idf.eq.2)then
    c   *** require uy at cl. ***
       nadof=ldofu(kdv)
       ieq=id(knowd,nadof)
      else
    c   *** require ux at cl. ***
       nadof=ldofu(kdu)
       ieq=id(knowd,nadof)
      endif
      if(ieq.lt.0)then
       vinf=constr(-ieq)
      elseif(ieq.eq.0)then
       vinf=0.
      else
       vinf=abs(sol(ieq))
      endif
    c  ************ k-e database substream ****************
    c  *** idf=4 for k, idf=5 for e ***
      emel=voncam*why
      if(start.lt.50)then
    c   *** set k and e to default for first few passes ***
        if(idf.eq.4)then
          val = 0.003
          return
        elseif(idf.eq.5)then
          val=0.00364
          return
        endif
      else
        if(idf.eq.4)then
          cay(node)=sqrt(seemew)*emel*dudy*emel*dudy
          val=cay(node)
          if((node.eq.2).or.(node.eq.20))then
    c       *** protect inlet value ***
            val = 0.003
          endif
          return
        elseif(idf.eq.5)then
          epsil=seemew*cay(node)*cay(node)
    c         /(emel*emel*abs(dudy))
          val=epsil
          if((node.eq.2).or.(node.eq.20))then
    c       *** protect inlet value ***
            val=0.00364
          endif
          return
        endif
```

```
      endif
c     write(10,*) 'cay',cay(node),'node',node,'epsil',epsil
c     ********** Reynolds number and big pie **********
      reyno=(destny*dia*vinf)/visk
      if(reyno.le.5000.)then
        zedone=abs((reyno/425.)-1.)
        bigpi=0.55*(1.-exp((-0.243*sqrt(zedone))-(0.298*zedone)))
      else
        bigpi=0.55
      endif
c     ********** evaluate velocity at y=delta ************
c     ********** delta forced to wall *********************
c     ********** counter to decide which val to use ******
      if(start.lt.50)then
c     *** set to default for first few passes ***
        val=0.0
      else
        if(whypls.le.5.)then
c       *** relaminarization ***
          val=walfrc*whypls
        else
c       *** Coles' law ***
          val=walfrc*((log(whypls)/voncam)+bee
     c       +(2.*bigpi)/voncam)
        endif
c     ******* assign sign to velocity, remember top ********
c     ******* where coords are reversed, so du/dy -ve *******
        if((node.eq.20).or.(node.eq.41).or.(node.eq.62).or.
     c     (node.eq.83).or.(node.eq.104).or.(node.eq.125).or.
     c     (node.eq.146).or.(node.eq.167).or.(node.eq.188).or.
     c     (node.eq.209).or.(node.eq.212).or.(node.eq.249).or.
     c     (node.eq.286).or.(node.eq.323).or.(node.eq.360).or.
     c     (node.eq.397).or.(node.eq.434).or.(node.eq.471).or.
     c     (node.eq.508).or.(node.eq.545).or.(node.eq.582).or.
     c     (node.eq.619).or.(node.eq.656).or.(node.eq.693).or.
     c     (node.eq.730).or.(node.eq.767).or.(node.eq.804).or.
     c     (node.eq.841).or.(node.eq.878).or.(node.eq.915).or.
     c     (node.eq.952).or.(node.eq.989).or.(node.eq.1026).or.
     c     (node.eq.1063).or.(node.eq.1100).or.(node.eq.1137).or.
     c     (node.eq.1174).or.(node.eq.1211).or.(node.eq.1248).or.
     c     (node.eq.1285).or.(node.eq.1322).or.(node.eq.1359).or.
     c     (node.eq.1396).or.(node.eq.1433).or.(node.eq.1470).or.
     c     (node.eq.1506))then
          bing=-shear0
          val=sign(val,bing)
        else
          val=sign(val,shear0)
        endif
      endif
      if((node.eq.2).or.(node.eq.20))then
c     *** protect inlet condition ***
        val=1.0
      endif
      if((node.eq.2).and.(idf.eq.1))then
        write(9,*) 'start',start
      endif
      if(start.ge.7108)then
        write(10,*) 'node',node,'y+',whypls
      endif
c     ********** bedtime **********************************
      close(10)
      close(9)
      return
      end
```

```
      subroutine usrini (inivar)
      include 'IMPLCT.COM'
      include 'PARUSR.COM'
      dimension inivar(*)
c
c     *** request derivatives of ux and uy ***
      inivar(kdu)=1
      inivar(kdv)=1
      inivar(kdp)=1
c
      return
      end
c
      SUBROUTINE USRSKE (NELT,NE,NG,SORCE,VARI,DVARI,NDFCD,LDOFU,SHP,
     1                   DSDX,XYZL,PROP,TIME,NPTS,ndp,MNDP,IERR,IOPT,
     2                   visct,viscl,den,mdvsc)
C
C     USER DEFINED SOURCES FOR KINETIC ENERGY OR DISSIPATION
C
C     NELT  = GLOBAL ELEMENT NUMBER
C     NE    = LOCAL ELEMENT NUMBER
C     NG    = GROUP NUMBER
C     SORCE = TURBULENT KINETIC ENERGY OR DISSIPATION (RETURNED VALUES)
C     VARI  = ARRAY OF SOLUTION VARIBLES AT INTEGRATION POINTS
C     DVARI = GRADIENTS OF SOLUTION VARIABLES AT INTEGRATION POINTS
C     LDOFU = pointer array for accessing vari and dvari information
C     XYZL  = X,Y,Z COORDINATES
C     SHP   = ELEMENT SHAPE FUNCTIONS
C     DSDX  = SHAPE FUNCTION DERIVATIVES IN THE X,Y,Z DIRECTION
C     PROP  = USER DEFINED PARAMETERS
C     MNDP  = FIRST DIMENSION OF SHAPE FUNCTION MATRICES
C     TIME  = TIME
C     NPTS  = NUMBER OF POINTS
C     IOPT = 0   ENERGY EQUATION
C     IOPT = N   TRANSPORT EQUATION FOR SPECIES N (0<N<16)
C     VISCT = TURBULENT VISCOSITY
C     VISCL = LAMINAR VISCOSITY
C     MDVSC = NUMBER OF COMPONENTS OF VISCOSITY ARRAY
C     IOPT = 0   KINETIC ENERGY SOURCES
C     IOPT = 1   DISSIPATION SOURCES
C
      INCLUDE 'IMPLCT.COM'
      INCLUDE 'PARUSR.COM'
c     ****** beware the second dimension of slope ***************
c     *** commonblocks for derivatives of ux and uy ***
c     *** at integration points and for x and y co-ords ***
      common/vdriv/slope(1:1460,4),slide(1:1460,4)
      common/pdriv/px(1:1460,4),py(1:1460,4)
      common/whirr/ex(1:1460,4),ey(1:1460,4)
      common/thick1/whyb,whyf,whys,whyt
      common/thick2/yb(8),yf(8),ys(8),yt(8)
      common/velo/velx(1:1460,4),vely(1:1460,4)
      DIMENSION SORCE(NPTS),visct(npts),viscl(9,npts),den(npts)
      DIMENSION SHP(MNDP,NPTS),DSDX(MNDP,NPTS,NDFCD),XYZL(NPTS,NDFCD)
      DIMENSION PROP(*),VARI(NPTS,*),DVARI(NPTS,NDFCD,*),LDOFU(*)
      dimension store(1:1460,4),stash(1:1460,4),cave(1:1460,4)
      dimension hole(1:1460,4),sink(1:1460,4),bore(1:1460,4),h(16)
      logical alive
      integer punt
c     *** arrays for storage of derivatives of ux and uy ***
c     *** at integration points ***
      inquire(file='edna',exist=alive)
      if(.not.alive)then
        open(9,file='edna',status='new',form='formatted')
      else
        open(9,file='edna',status='old',form='formatied')
      endif
      iopt=0
c
      punt=punt+1
      do 10 i=1,npts
        sorce(i)=0
c       *** dvx/dy ***
        slope(nelt,i)=store(nelt,i)
        store(nelt,i)=dvari(i,2,ldofu(kdu))
c       *** dvy/dx ***
        slide(nelt,i)=stash(nelt,i)
        stash(nelt,i)=dvari(i,1,ldofu(kdv))
c       *** dp/dx ***
        px(nelt,i)=cave(nelt,i)
        cave(nelt,i)=vari(i,ldofu(kdp))
c       *** dp/dy ***
        py(nelt,i)=hole(nelt,i)
        hole(nelt,i)=vari(i,ldofu(kdp))
c       *** vx ***
        velx(nelt,i)=sink(nelt,i)
        sink(nelt,i)=vari(i,ldofu(kdu))
c       *** vy ***
        vely(nelt,i)=bore(nelt,i)
        bore(nelt,i)=vari(i,ldofu(kdv))
10      continue
      if((punt.ge.1).or.(punt.le.1460))then
        do 15 i=1,npts
          ex(nelt,i)=xyzl(i,1)
          ey(nelt,i)=xyzl(i,2)
15        continue
c       *** step face ***
        if(nelt.eq.1)then
          h(1)=xyzl(3,1)
        elseif(nelt.eq.2)then
          h(2)=xyzl(1,1)
          h(3)=xyzl(3,1)
        elseif(nelt.eq.3)then
          h(4)=xyzl(1,1)
          h(5)=xyzl(3,1)
        elseif(nelt.eq.4)then
          h(6)=xyzl(1,1)
          h(7)=xyzl(3,1)
```

Figure A3.9. Subroutine listing, circus.f: the enhanced Coles' law model of the backward facing step.

```
      elseif(nelt.eq.70)then
        h(2)=xyzl(1,2)
        h(3)=xyzl(2,2)
      elseif(nelt.eq.105)then
        h(4)=xyzl(1,2)
        h(5)=xyzl(2,2)
      elseif(nelt.eq.140)then
        h(6)=xyzl(1,2)
        h(7)=xyzl(2,2)
      elseif(nelt.eq.175)then
        h(8)=xyzl(1,2)
        h(9)=xyzl(2,2)
      elseif(nelt.eq.210)then
        h(10)=xyzl(1,2)
        h(11)=xyzl(2,2)
      elseif(nelt.eq.245)then
        h(12)=xyzl(1,2)
        h(13)=xyzl(2,2)
      elseif(nelt.eq.288)then
        h(14)=xyzl(1,2)
        h(15)=xyzl(2,2)
      elseif(nelt.eq.315)then
        h(16)=xyzl(1,2)
        do 30 i=1,8
          yf(i)=abs((h(i+i-1)+h(i+i))/2.)
30      continue
        why f=yf(1)
      endif
c     *** back, upper reach ***
      if(nelt.eq.561)then
        h(1)=xyzl(2,2)
      elseif(nelt.eq.606)then
        h(2)=xyzl(1,2)
      elseif(nelt.eq.651)then
        h(3)=xyzl(2,2)
      elseif(nelt.eq.696)then
        h(4)=xyzl(1,2)
      elseif(nelt.eq.741)then
        h(5)=xyzl(2,2)
      elseif(nelt.eq.786)then
        h(6)=xyzl(1,2)
      elseif(nelt.eq.831)then
        h(7)=xyzl(2,2)
      elseif(nelt.eq.876)then
        h(8)=xyzl(1,2)
      elseif(nelt.eq.921)then
        h(9)=xyzl(2,2)
      elseif(nelt.eq.966)then
        h(10)=xyzl(1,2)
      elseif(nelt.eq.1011)then
        h(11)=xyzl(2,2)
      elseif(nelt.eq.1056)then
        h(12)=xyzl(1,2)
      elseif(nelt.eq.1101)then
        h(13)=xyzl(2,2)
      elseif(nelt.eq.1146)then
        h(14)=xyzl(1,2)
      elseif(nelt.eq.1191)then
        h(15)=xyzl(2,2)
      elseif(nelt.eq.1236)then
        h(16)=xyzl(1,2)
        do 40 i=1,8
          yb(i)=abs(1.0-((h(i+i-1)+h(i+i))/2.))
40      continue
        why b=yb(1)
      endif
c     *** top ***
      if(nelt.eq.1056)then
        h(16)=xyzl(2,2)
      elseif(nelt.eq.1101)then
        h(15)=xyzl(1,2)
        h(14)=xyzl(2,2)
      elseif(nelt.eq.1146)then
        h(13)=xyzl(1,2)
        h(12)=xyzl(2,2)
      elseif(nelt.eq.1191)then
        h(11)=xyzl(1,2)
        h(10)=xyzl(2,2)
      elseif(nelt.eq.1236)then
        h(9)=xyzl(1,2)
        h(8)=xyzl(2,2)
      elseif(nelt.eq.1281)then
        h(7)=xyzl(1,2)
        h(6)=xyzl(2,2)
      elseif(nelt.eq.1326)then
        h(5)=xyzl(1,2)
        h(4)=xyzl(2,2)
      elseif(nelt.eq.1371)then
        h(3)=xyzl(1,2)
        h(2)=xyzl(2,2)
      elseif(nelt.eq.1416)then
        h(1)=xyzl(1,2)
        do 50 i=1,8
          yr(i)=abs(3.0-((h(i+i-1)+h(i+i))/2.))
50      continue
        why r=yr(1)
      endif
      if(pnt.eq.1460)then
        do 60 i=1,8
          write(9,*) yb,yb(i)
          write(9,*) yf,yf(i)
          write(9,*) ys,ys(i)
          write(9,*) yr,yr(i)
60      continue
      endif
c
      close(9)
      ZRO = 0.D0
      RETURN
      END
c
      SUBROUTINE USRBCN (VAL,NODE,IDF,TIME,SOL,ID,NDOF,NUMNP,LDOFU,
     1           CONSTR)
      INCLUDE 'IMPLCT.COM'
      INCLUDE 'PARUSR.COM'
c     *** commonblocks for derivatives of ux and uy ***
      common/vdriv/slope(1:1460,4),slide(1:1460,4)
      common/pdriv/px(1:1460,4),py(1:1460,4)
      common/whirl/cx(1:1460,4),cy(1:1460,4)
      common/thick1/why,why,wf,why,s,why,t
      common/thick2/yb(8,,yf(8),ys(8),yr(8)
      common/velo/velx(1:1460,4),vely(1:1460,4)
      DIMENSION SOL(*),IDOFU(NUMNP,NDOF),CONSTR(*),LDOFU(*)
      dimension cay(1600),cline(8),y(0:8),vo(0:8),ye(0:16),ve(0:16)
      integer gel1,start,gel2,gelb1,gelb2,gelf1,gelf2,gels1,gels2
      integer flag,npole,el1,el2
      logical alive,kickin,mango
c     ********** problem dependent things **********
      data visk,destry,gnew,dia/2.2222e-5,1.,2.2222e-5,2.0/
      data bee,voncam,seemew/4.9,0.41,0.09/
      data lol/1.e-10/
      inquire(file='fred',exist=alive)
      if(.not.alive)then
        open(9,file='fred',status='new',form='formatted')
      else
        open(9,file='fred',status='old',form='formatted')
      endif
      inquire(file='alice',exist=kickin)
      if(.not.kickin)then
        open(10,file='alice',status='new',form='formatted')
      else
        open(10,file='alice',status='old',form='formatted')
      endif
      inquire(file='gwen',exist=mango)
```

```
      if(.not.mango)then
        open(11,file='gwen',status='new',form='formatted')
      else
        open(11,file='gwen',status='old',form='formatted')
      endif
c     *************** curious FIDAP(tm) constant ************
      ZRO = 0.D0
c     *************** calculate velocity gradients **************
c     *** slope 1 is near side of Coles' line w.r.t. wall ***
c     *** slope 2 is far side of same ***
c     *** also set y value for Coles' line ***
      imp=0
c     ****** back, upper reach *******
      if(node.eq.2)then
        dudy=(slope(561,2)+slope(607,1))/2.
c       *** iteration pass counter ***
        start=start+1
        why=whyb
        line=1
        el1=0
        el2=561
        more=45
      elseif(node.eq.230)then
        dudy=(slope(570,4)+slope(571,2)+
     c       slope(615,3)+slope(616,1))/4.
        why=whyb
        line=1
        el1=570
        el2=571
        more=45
      elseif(node.eq.267.and.npole.lt.3)then
        dudy=(slope(571,4)+slope(572,2)
     c       +slope(616,3)+slope(617,1))/4.
        why=whyb
        line=1
        el1=571
        el2=572
        more=45
c       *** npole governs derivative selection at node 267 ***
        npole=npole+1
      elseif((node.eq.23).or.(node.eq.44).or.(node.eq.65)
     c .or.(node.eq.86).or.(node.eq.107).or.(node.eq.128)
     c .or.(node.eq.149).or.(node eq.170).or.(node.eq.191))
     c then
        imp=((node-2)/21)-1
        gelb1=562+imp
        gelb2=607+imp
        dudy=(slope(gelb1-1,4)+slope(gelb1,2)
     c       +slope(gelb2-1,3)+slope(gelb2,1))/4.
        why=whyb
        line=1
        el1=gelb1-1
        el2=gelb1
        more=45
c     ****** front, lower reach *******
      elseif(node.eq.1541)then
        dudy=(slope(35,4)+slope(70,3))/2.
        why=whyf
        start=start+1
        line=2
        el1=35
        el2=0
        more=35
      elseif((node.eq.283.and.flag.eq.3)
     c.or.(node.eq.320).or.(node.eq.357)
     c .or.(node.eq.394).or.(node.eq.431).or.(node.eq.468)
     c .or.(node.eq.505).or.(node.eq.542).or.(node.eq.579)
     c .or.(node.eq.616).or.(node.eq.653).or.(node.eq.690)
     c .or.(node.eq.727).or.(node.eq.764).or.(node.eq.801)
     c .or.(node.eq.838).or.(node.eq.875).or.(node.eq.912)
     c .or.(node.eq.949).or.(node.eq.986).or.(node.eq.1023)
     c.or.(node.eq.1060).or.(node.eq.1097).or.(node.eq.1134)
     c.or.(node.eq.1171).or.(node.eq.1208).or.(node.eq.1245)
     c.or.(node.eq.1282).or.(node.eq.1319).or.(node.eq.1356)
     c.or.(node.eq.1393).or.(node.eq.1430).or.(node.eq.1467)
     c.or.(node.eq.1504))then
        imp=((node-246)/37)-1
        gelf1=2+imp
        gelf2=37+imp
        dudy=(slope(gelf1-1,4)+slope(gelf1,2)
     c       +slope(gelf2-1,3)+slope(gelf2,1))/4.
        why=whyf
        line=2
        el1=gelf1-1
        el2=gelf1
        more=35
        if(idf.eq.5.and.node.eq.283.and.flag.eq.3)then
c         *** flag governs derivative selection at node 283 ***
          flag=flag-3
        endif
c     ****** step face *******
c     ****** taking derivs in x direction *********
      elseif(node.eq.268)then
        dudy=(slide(526,4)+slide(571,3)+
     c       slide(527,2)+slide(572,1))/4.
        why=whys
        start=start+1
        line=3
        el1=571
        el2=526
        more=1
      elseif(node.eq.267.and.npole.eq.3)then
        dudy=(slide(571,4)+slide(616,3)+
     c       slide(572,2)+slide(617,1))/4.
        why=whys
        line=3
        el1=616
        el2=571
        more=1
        if(idf.eq.5)then
          npole=npole-3
        endif
      elseif((node.eq.269).or.(node.eq.270)
     c .or.(node.eq.271)
     c.or.(node.eq.272).or.(node.eq.273).or.(node.eq.274)
     c.or.(node.eq.275).or.(node.eq.276).or.(node.eq 277)
     c.or.(node.eq.278).or.(node.eq.279).or.(node.eq.280)
     c.or.(node.eq.281).or.(node.eq.282)
     c.or.(node.eq.283.and flag.lt.3))then
        imp=(283-node)*35
        gels1=36+imp
        gels2=37+imp
        dudy=(slide(gels1-35,4)+slide(gels1,3)
     c       +slide(gels2-35,2)+slide(gels2,1))/4.
        why=whys
        line=3
        el1=gels1
        el2=gels1-35
        more=1
        if(node.eq.283)then
          flag=flag+1
        endif
c     ****** top ********
      elseif(node.eq.20)then
        dudy=(slope(1416,1)+slope(1371,2))/2.
        why=whyt
        start=start+1
        line=4
        el1=0
        el2=1416
        more=-45
      elseif(node.eq.1506)then
        dudy=(slope(1460,3)+slope(1415,4))/2.
        why=whyt
        line=4
        el1=1460
        el2=0
        more=-45
      else
        if(node.le.209)then
          imp=((node+1)/21)-1
          gelt1=1416+imp
          gelt2=1371+imp
        else
          imp=(node-212)/37
          gelt1=1426+imp
          gelt2=1381+imp
        endif
        dudy=(((slope(gelt1,1)+slope((gelt1-1),3))/2.)+
     c       ((slope(gelt2,2)+slope((gelt2-1),4))/2.))/2.
        why=whyt
        line=4
```

```
      el1=gelt1-1
      el2=gelt1
      more=-45
    endif
c   ********** calculate y+ and friends ***************
    shear0=visk*dudy
c   * ** ***  remember physical senses  *** ** *
    shrmod=abs(shear0)
    walfrc=sqrt(shrmod/destny)
    whypls=(why*walfrc)/gnew
c   ********** kidnap centreline velocity **************
c   *** define centreline node appropriate to ***
c   *** current Coles' node ***
    if((node.eq.20).or.(node.eq.41).or.(node.eq.62).or.
c   (node.eq.83).or.(node.eq.104).or.(node.eq.125).or.
c   (node.eq.146).or.(node.eq.167).or.(node.eq.188).or.
c   (node.eq.209).or.(node.eq.230))then
      knowd=node-9
    elseif(node.eq.1506)then
      knowd=1516
    elseif((node.eq.269).or.(node.eq.270).or (node.eq.271)
c   .or.(node.eq.272).or.(node.eq.273).or.(node.eq.274)
c   .or.(node.eq.275).or.(node.eq.276).or.(node.eq.277)
c   .or.(node.eq.278).or.(node.eq.279).or.(node.eq.280)
c   .or.(node.eq.281).or.(node.eq.282) or.(node.eq.283)
c   .or.(node.eq.268).or.(node.eq.267))then
      knowd=258
    elseif((node.eq.320).or.(node.eq.357)
c   .or.(node.eq.394).or.(node.eq.431).or.(node.eq.468)
c   .or.(node.eq.505).or.(node.eq.542).or.(node.eq.579)
c   .or.(node.eq.616).or.(node.eq.653).or.(node.eq.690)
c   .or.(node.eq.727).or.(node.eq.764).or.(node.eq 801)
c   .or.(node.eq.838).or.(node.eq.875).or.(node.eq.912)
c  .or.(node.eq.949).or.(node.eq.986).or.(node.eq.1023)
c.or.(node.eq.1060).or.(node.eq.1097).or.(node.eq.1134)
c.or.(node.eq.1171).or.(node.eq.1208).or.(node.eq.1245)
c.or.(node.eq.1282).or.(node.eq.1319).or.(node.eq.1356)
c.or.(node.eq.1393).or.(node.eq.1430).or.(node.eq.1467)
c.or.(node.eq.1504).or.(node.eq.1541))then
      knowd=node-25
    else
      knowd=node+9
    endif
    if(knowd.eq.258.and.idf.eq.2)then
c   *** require uy at cl. ***
      nadof=ldofu(kdv)
      ieq=id(knowd,nadof)
    else
c   *** require ux at cl. ***
      nadof=ldofu(kdu)
      ieq=id(knowd,nadof)
    endif
    if(ieq.lt.0)then
      vinf=constr(-ieq)
    elseif(ieq.eq.0)then
      vinf=0.
    else
      vinf=abs(sol(ieq))
    endif
c   *** find sol pressure at current node ***
    nadof=ldofu(kdp)
    ieq=id(knowd,nadof)
    pee=sol(ieq)
c   ********** k-e database substream ****************
c   *** idf=4 for k, idf=5 for e ***
    emel=voncam*why
    if(start.lt.49)then
c   *** set k and e to default for first few passes ***
c   *** main algorithm to be used from 12 onwards *****
      if(idf.eq.4)then
        val = 0.003
        return
      elseif(idf.eq.5)then
        val=0.00364
        return
      endif
    else
      if(idf.eq.4)then
        cay(node)=sqrt(seemew)*emel*dudy*emel*dudy
        val=cay(node)
        if((node.eq.2).or.(node.eq.20))then
c         *** protect inlet value ***
          val = 0.003
        endif
        return
      elseif(idf.eq.5)then
        epsil=seemew*cay(node)*cay(node)
c           /(emel*emel*abs(dudy))
        val=epsil
        if((node.eq.2).or.(node.eq.20))then
c         *** protect inlet value ***
          val=0.00364
        endif
        return
      endif
    endif
c   write(10,*) 'cay',cay(node),'node',node,'epsil',epsil
c   ********** Reynolds number and big pie ***********
    reyno=(destny*dia*vinf)/visk
    if(reyno.le.5000.)then
      zedone=abs((reyno/425.)-1.)
      bigpi=0.55*(1.-exp((-0.243*sqrt(zedone))-(0.298*zedone)))
    else
      bigpi=0.55
    endif
c   ********** evaluate velocity at y=delta ************
c   ********** delta forced to wall *********************
c   ********** counter to decide which val to use ******
    if(start.lt.49)then
c   *** set to default for first few passes ***
      val=0.0
    else
      if(whypls.le.5.)then
c       *** relaminarization ***
        val=walfrc*whypls
      else
        if(start.ge.385)then
c         *** boundary layer with pressure gradient ***
c         *** identify active Coles' line ***
          if(line.eq.1)then
            do 10 i=1,8
              y(i)=yb(i)
10            continue
          elseif(line.eq.2)then
            do 20 i=1,8
              y(i)=yf(i)
20            continue
          elseif(line.eq.3)then
            do 30 i=1,8
              y(i)=ys(i)
30            continue
          else
            do 40 i=1,8
              y(i)=yt(i)
40            continue
          endif
c         *** calculate velocity gradients along line
c         of inspection normal to Coles' line ***
          j=0
          do 50 i=1,8
            if(line.le.2)then
              if(el1.eq.0)then
                cline(i)=(slope(el2+(i-1)*more,2)
c                       +slope(el2+i*more,1))/2.
              elseif(el2.eq.0)then
                cline(i)=(slope(el1+(i-1)*more,4)
c                       +slope(el1+i*more,3))/2.
              else
                cline(i)=(slope(el1+(i-1)*more,4)
c                       +slope(el2+(i-1)*more
c                       ,2)+slope(el1+i*more,3)
c                       +slope(el2+i*more,1))/4.
              endif
            elseif(line.eq.3)then
              cline(i)=(slide(el1+(i-1)*more,3)
c                       +slide(el2+(i-1)*more
c                       ,4)+slide(el1+i*more,1)
c                       +slide(el2+i*more,2))/4.
            else
              if(el1.eq.0)then
                cline(i)=(slope(el2+(i-1)*more,1)
c                       +slope(el2+i*more,2))/2.
```

```
          elseif(el2.eq.0)then
            clinc(i)=(slopc(el1+(i-1)*more,3)
     c            +slope(el1+i*more,4))/2.
          else
            cline(i)=(slopc(el1+(i-1)*more,3)
     c            +slopc(el2+(i-1)*more
     c            ,1)+slopc(el1+i*more,4)
     c            +slopc(el2+i*more,2))/4.
          endif
        endif
c       *** if velocity gradient less than tolerance
c       then identify edge of boundary layer ***
        if(abs(cline(i)).le.tol)then
          j=i
          goto 60
        endif
50      continue
      if(j.eq.0)then
        j=8
      endif
60    delta=y(j)
c     *** calculate velocities along line of inspection
c     normal to Coles' line ***
      do 70 i=1,8
        if(line.le.2)then
          if(el1.eq.0)then
            vo(i)=(velx(el2+(i-1)*more,2)
     c            +velx(el2+i*more,1))/2.
          elseif(el2.eq.0)then
            vo(i)=(velx(el1+(i-1)*more,4)
     c            +velx(el1+i*more,3))/2.
          else
            vo(i)=(velx(el1+(i-1)*more,4)
     c            +velx(el2+(i-1)*more
     c            ,2)+velx(el1+i*more,3)
     c            +velx(el2+i*more,1))/4.
          endif
        elseif(line.eq.3)then
          vo(i)=(vely(el1+(i-1)*more,3)
     c          +vely(el2+(i-1)*more
     c          ,4)+vely(el1+i*more,1)
     c          +vely(el2+i*more,2))/4.
        else
          if(el1.eq.0)then
            vo(i)=(velx(el2+(i-1)*more,1)
     c            +velx(el2+i*more,2))/2.
          elseif(el2.eq.0)then
            vo(i)=(velx(el1+(i-1)*more,3)
     c            +velx(el1+i*more,4))/2.
          else
            vo(i)=(velx(el1+(i-1)*more,3)
     c            +velx(el2+(i-1)*more
     c            ,1)+velx(el1+i*more,4)
     c            +velx(el2+i*more,2))/4.
          endif
        endif
70      continue
      y(0)=0.
      vo(0)=0.
      ye(0)=0.
      ve(0)=0.
      k=2*j
c
      if(start.ge.385)then
        write(9,*) 'node',node,'line',line
c       write(9,*) 'line',line,'more',more
c       write(9,*) 'el1',el1,'el2',el2
c       write(9,*) 'j',j,'k-1',k
      endif
c
c     *** calculate velocities and locations at
c     mid-points between elements along line of
c     inspection normal to Coles' line ***
      do 80 i=2,k,2
        ve(i)=vo(i/2)
        ve(i-1)=(vo(i/2)+vo((i/2)-1))/2.
        ye(i)=y(i/2)
        ye(i-1)=((y(i/2)-y((i/2)-1))/2.)+y((i/2)-1)
80      continue
c       if((node.eq.269).and.(start.ge.385))then
c         do 84 i=0,k
c           write(9,*) 've(i)',ve(i)
c84         continue
c       endif
c       *** compare successive velocities along line of
c       inspection - identify edge of boundary layer ***
        do 90 i=2,k-1
          if(ve(i).ge.0.)then
            if(ve(i+1).lt.0.)then
              goto 100
            elseif(ve(i+1).lt.ve(i))then
              goto 100
            else
              toad=abs(ve(i+1)-ve(i))/abs(ve(i))
              if(toad.le.0.1)then
                goto 100
              endif
            endif
          else
            if(ve(i+1).gt.0.)then
              goto 100
            elseif(abs(ve(i+1)).lt.abs(ve(i)))then
              goto 100
            else
              toad=(abs(ve(i+1))-abs(ve(i)))/abs(ve(i))
              if(toad.le.0.1)then
                goto 100
              endif
            endif
          endif
90        continue
        goto 110
100       k=(i/2)*2
        if(start.ge.385)then
c         write(9,*) 'k-2',k
        endif
        delta=ye(k)
c       *** calculate displacement thickness ***
110     sum=0.
        do 120 i=1,k
          sum=sum+(1.-(abs(ve(i))/abs(ve(k))))
     c        *(ye(i)-ye(i-1))
120       continue
        delstr=sum
        k=k/2
        if(start.ge.385)then
c         write(9,*) 'k-3',k
          write(9,*) 'delta',delta,'delstr',delstr
          write(9,*)
        endif
        if(line.le.2)then
c         *** calculate pressure gradient at edge of
c         boundary ***
          if(el1.eq.0)then
            p2=(px(el2+k*more,3)
     c          +px(el2+(k-1)*more,4))/2.
            p1=(px(el2+k*more,1)
     c          +px(el2+(k-1)*more,2))/2.
            dp=p2-p1
            dx=ex(el2,3)-ex(el2,1)
            dpdx=dp/dx
          elseif(el2.eq.0)then
            p2=(px(el1+k*more,3)
     c          +px(el1+(k-1)*more,4))/2.
            p1=(px(el1+k*more,1)
     c          +px(el1+(k-1)*more,2))/2.
            dp=p2-p1
            dx=ex(el1,3)-ex(el1,1)
            dpdx=dp/dx
          else
            p2=(px(el2+k*more,1)
     c          +px(el2+(k-1)*more,2))/2.
            p1=(px(el1+k*more,3)
     c          +px(el1+(k-1)*more,4))/2.
            dp=p2-p1
            dx=(ex(el2,1)+ex(el2,3))/2.-
     c          (ex(el1,1)+ex(el1,3))/2.
            dpdx=dp/dx
          endif
        elseif(line.eq.3)then
          p2=(py(el1+k*more,1)
     c          +py(el1+(k-1)*more,3))/2.
```

```
      p1=(py(el2+k*more,2)
     c     +py(el2+(k-1)*more,4))/2.
      dp=p2-p1
      dy=(cy(el1,1)+cy(el1,2))/2.-
     c     (cy(el2,1)+cy(el2,2))/2.
      dpdy=dp/dy
    else
      if(el1.eq.0)then
        p2=(px(el2+(k-1)*more,3)
     c       +px(el2+k*more,4))/2.
        p1=(px(el2+(k-1)*more,1)
     c       +px(el2+k*more,2))/2.
        dp=p2-p1
        dx=ex(el2,3)-ex(el2,1)
        dpdx=dp/dx
      elseif(el2.eq 0)then
        p2=(px(el1+(k-1)*more,3)
     c       +px(el1+k*more,4))/2.
        p1=(px(el1+(k-1)*more,1)
     c       +px(el1+k*more,2))/2.
        dp=p2-p1
        dx=ex(el1,3)-ex(el1,1)
        dpdx=dp/dx
      else
        p2=(px(el2+(k-1)*more,1)
     c       +px(el2+k*more,2))/2.
        p1=(px(el1+(k-1)*more,3)
     c       +px(el1+k*more,4))/2.
        dp=p2-p1
        dx=(ex(el2,1)+ex(el2,3))/2.-
     c       (ex(el1,1)+ex(el1,3))/2.
        dpdx=dp/dx
      endif
    endif
c     *** calculate beta ***
    if(line.le.2)then
      beta=dpdx*delstr/shear0
    elseif(line.eq.3)then
      beta=dpdy*delstr/shear0
    else
      beta=dpdx*delstr/(-shear0)
    endif
    if((node.eq.542).and.(start.ge.385))then
      write(11,*) 'node',node,'beta',beta
      write(11,*) 'start',start,'A'
    endif
    if(beta.lt.-0.4)then
      beta=-0.4
    endif
    if((node.eq.542).and.(start.ge.385))then
      write(11,*) 'node',node,'beta',beta
      write(11,*) 'start',start,'B'
    endif
c     *** calculate wake parameter ***
      c=-0.4-beta
      pi=(-0.76+sqrt(0.5776-(1.68*c)))/0.84
c
      if((line.eq.3) and.(pi.gt.5.))then
        pi=5.
      endif
c
      eta=why/delta
      if(start.ge.385)then
        write(9,*) 'eta',eta
      endif
c     *** full Colcs' law ***
      wakfcn=2.*eta*eta*eta-3.*eta*eta
c
      val=walfrc*((log(whypls)/voncam)+bee
     c     +(((2.*pi)/voncam)*(wakfcn)))
    else
      val=walfrc*((log(whypls)/voncam)+bee
     c     +(2.*bigpi)/voncam)
    endif
  endif
c   ******* assign sign to velocity, remember top ********
c   ******* where coords are reversed, so du/dy -ve *******
  if((node.eq.20).or.(node.eq.41).or.(node.eq.62).or.
 c   (node.eq.83).or.(node.eq.104).or.(node.eq.125).or.
 c   (node.eq.146).or.(node.eq.167).or.(node.eq.188).or.
 c   (node.eq.209).or.(node.eq.212).or.(node.eq.249).or.
 c   (node.eq.286).or.(node.eq.323).or.(node.eq.360).or.
 c   (node.eq.397).or.(node.eq.434).or.(node.eq.471).or.
 c   (node.eq.508).or.(node.eq.545).or.(node.eq.582).or.
 c   (node.eq.619).or.(node.eq.656).or.(node.eq.693).or.
 c   (node.eq.730).or.(node.eq.767).or.(node.eq.804).or.
 c   (node.eq.841).or.(node.eq.878).or.(node.eq.915).or.
 c   (node.eq.952).or.(node.eq.989).or.(node.eq.1026).or.
 c   (node.eq.1063).or.(node.eq.1100).or.(node.eq.1137).or.
 c   (node.eq.1174).or.(node.eq.1211).or.(node.eq.1248).or.
 c   (node.eq.1285).or.(node.eq.1322).or.(node.eq.1359).or.
 c   (node.eq.1396).or.(node.eq 1433).or.(node.eq.1470).or.
 c   (node.eq.1506))then
      bing=-shear0
      val=sign(val,bing)
    else
      val=sign(val,shear0)
    endif
  endif
  if((node.eq.2).or.(node.eq.20))then
c   *** protect inlet condition ***
    val=1.0
  endif
  if(start.ge.445)then
    write(10,*) 'start',start,'whypls',whypls
    write(10,*) 'node',node,'line',line
    write(10,*) 'p1',p1,'p2',p2
    if(line.ne.3)then
      write(10,*) 'pee',pee,'dx',dx
      write(10,*) 'dpdx',dpdx,'delstr',delstr
    else
      write(10,*) 'pee',pee,'dy',dy
      write(10,*) 'dpdy',dpdy,'delstr',delstr
    endif
    if(line.le.3)then
      write(10,*) 'shear0',shear0,'beta',beta
    else
      write(10,*) 'shear0',-shear0,'beta',beta
    endif
    write(10,*) 'pi',pi,'val',val
  endif
  if((node.eq.542).and.(start.ge.385))then
    write(11,*) 'node',node,'beta',beta
    write(11,*) 'start',start,'C'
  endif
c   ********** bedtime **********************************
  close(11)
  close(10)
  close(9)
  return
  end
```

Appendix A4. Calculated Solution Variables from the Enhanced Coles' Law Model of the Backward Facing Step.

The following table lists the values of selected solution variables for the final iteration of the enhanced Coles' law model of the backward facing step. These values were calculated within the subroutine circus.f, whose workings are described in Sections 5.3.4 and 5.3.5.

Distance along Coles' line (m)	Boundary layer thickness (m)	Pressure gradient (N/m)	Clauser's parameter	Stress at wall (kg/ms2)	Wake parameter
0.24	0.245	0.78e-1	101298.9	0.11e-6	5.0
0.50	0.245	-0.78e-1	101298.9	-0.25e-5	5.0
0.77	0.245	-0.78e-1	101298.9	-0.88e-5	5.0
1.05	0.120	-0.74e-3	1.5	-0.18e-4	1.4
1.35	0.120	0.41e-2	-0.4	-0.26e-4	0.13e-7
1.67	0.120	0.16e-1	-0.4	-0.32e-4	0.13e-7
2.01	0.120	0.28e-1	-0.4	-0.36e-4	0.13e-7
2.36	0.074	0.42e-1	-0.4	-0.38e-4	0.13e-7
2.73	0.074	0.53e-1	-0.4	-0.37e-4	0.13e-7
3.12	0.074	0.59e-1	-0.4	-0.34e-4	0.13e-7
3.54	0.074	0.61e-1	-0.4	-0.28e-4	0.13e-7
3.97	0.074	0.55e-1	-0.4	-0.18e-4	0.13e-7
4.43	0.074	0.55e-1	-0.4	-0.67e-5	0.13e-7
4.91	0.074	0.55e-1	-0.4	0.47e-5	0.13e-7
5.42	0.550	0.25e-1	414.6	0.15e-4	30.5
5.96	0.550	0.15e-1	141.9	0.24e-4	17.5
6.53	0.174	0.78e-2	16.5	0.29e-4	5.5
7.13	0.174	0.44e-2	7.6	0.35e-4	3.5
7.76	0.120	0.22e-2	2.2	0.41e-4	1.7
8.42	0.120	-0.47e-3	-0.4	0.48e-4	0.13e-7
9.12	0.120	-0.28e-2	-0.4	0.54e-4	0.13e-7
9.86	0.120	-0.65e-2	-0.4	0.57e-4	0.13e-7
10.63	0.120	-0.63e-2	-0.4	0.59e-4	0.13e-7
11.45	0.120	-0.81e-2	-0.4	0.60e-4	0.13e-7
12.32	0.120	-0.64e-2	-0.4	0.60e-4	0.13e-7
13.23	0.120	-0.74e-2	-0.4	0.60e-4	0.13e-7
14.19	0.120	-0.56e-2	-0.4	0.61e-4	0.13e-7
15.20	0.120	-0.67e-2	-0.4	0.61e-4	0.13e-7
16.27	0.120	-0.57e-2	-0.4	0.63e-4	0.13e-7
17.39	0.120	-0.70e-2	-0.4	0.64e-4	0.13e-7
18.58	0.120	-0.67e-2	-0.4	0.66e-4	0.13e-7
19.83	0.120	-0.76e-2	-0.4	0.66e-4	0.13e-7
21.14	0.120	-0.78e-2	-0.4	0.68e-4	0.13e-7
22.53	0.174	-0.85e-2	-0.4	0.67e-4	0.13e-7
24.00	0.120	0.0	0.0	0.69e-4	0.4